Donald M. McGuire
14 June, 1982

A Climatology and Oceanographic Analysis of the California Pacific Outer Continental Shelf Region

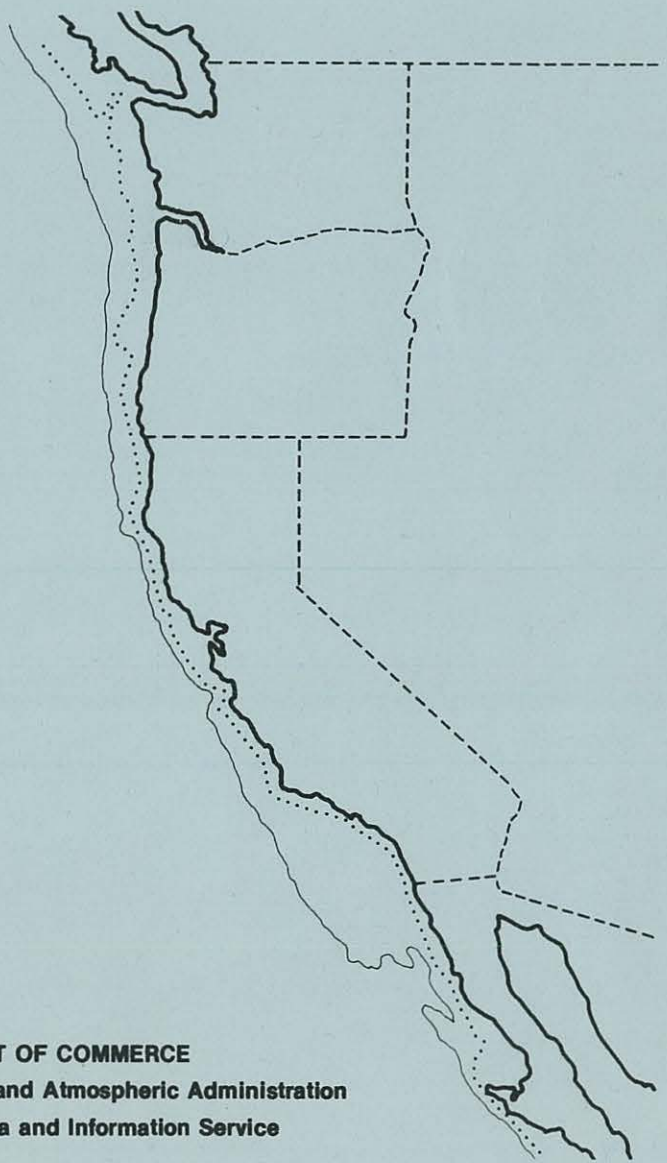

U.S. DEPARTMENT OF COMMERCE
National Oceanic and Atmospheric Administration
Environmental Data and Information Service

A Climatology and Oceanographic Analysis of the California Pacific Outer Continental Shelf Region

Editors
Fredric A. Godshall
Robert G. Williams

Edited Version of
Final Report to the Bureau of Land Management, U.S. Department of the Interior; produced under Interagency Agreement (AA551-IA9-2)

Authors
R. G. Williams, R. W. Reeves, F. A. Godshall, S. W. Fehler, NOAA
G. R. Halliwell, K. C. Vierra, C. N. K. Mooers, University of Delaware
M. D. Earle, K. Bush, Marine Environments Corporation

September 1981

U.S. DEPARTMENT OF COMMERCE
Malcolm Baldrige, Secretary

National Oceanic and Atmospheric Administration
John V. Byrne, Administrator

Environmental Data and Information Service
Thomas D. Potter, Director

CONTENTS

CONTENTS (continued)

ACRONYM LIST

ART	– Airborne Radiation Thermometer
BLM	– Bureau of Land Management
CALCOFI	– California Cooperative Oceanic Fisheries Investigation
CODAR	– Coastal Ocean Dynamics Application Radar
CODE	– Coastal Ocean Dynamics Experiment
CPOCS	– California Pacific Offshore Continental Shelf
CUE	– Coastal Upwelling Experiment
EDIS	– Environmental Data and Information Service
FNWC	– Fleet Numerical Weather Central
GEK	– Geomagnetic Electrokinetograph
MAST	– Marine Atlas Summary Tables
MBT	– Mechanical Bathythermographs
NAVOCEANO	– U.S. Naval Oceanographic Office
NCC	– National Climatic Center
NDBO	– NOAA Data Buoy Office
NMFS	– National Marine Fisheries Service
NOAA	– National Oceanic and Atmospheric Administration
NODC	– National Oceanographic Data Center
NOS	– National Ocean Survey
NWS	– National Weather Service
OCS	– Offshore Continental Shelf
PMEL	– Pacific Marine Environmental Laboratory
POCS	– Pacific Offshore Continental Shelf

SCCWRP	– Southern California Coastal Water Research Project
SCUDS	– Surface Current Data System
SSMO	– Summary of Synoptic Meteorological Observations
SST	– Sea-Surface Temperature
STD	– Salinity-Temperature-Depth
XBT	– Expendable Bathythermographs

1. INTRODUCTION

The Marine Environmental Assessment Division of the Center for Environmental Assessment Services, National Oceanic and Atmospheric Administration (NOAA) has utilized meteorological archives from the National Climatic Center (NCC, Asheville, NC 28801) and the National Oceanographic Data Center (NODC, Washington, DC 20235) to produce climatological and oceanographic analyses of the outer continental shelf region of California (Figure 2.1). A final report of this work, "A Climatology and Oceanographic Analysis of the California Pacific Outer Continental Shelf Region," was prepared (September 1980) under Interagency agreement (AA551-IA9-2) between NOAA and the Bureau of Land Management (BLM), U.S. Department of Interior. The report contains summaries of historical physical and chemical oceanographic and meteorological observations, interpretation of the summaries, evaluation of the data with respect to BLM information requirements for bottom land lease management, and recommendations for improvement of the data base. Because of the size of this report (1182 pages) only a limited number of copies were produced. In order to make copies of the important marine data summaries and interpretations available for general distribution, this edited version of the full report has been published. Copies of the full report may be obtained from the National Technical Information Service (5235 Port Royal Rd., Springfield, VA 22161).

A number of authors contributed to the original report (Reference 4). They are as follows: R. G. Williams (Project Director), R. W. Reeves, F. A. Godshall, and S. W. Fehler, (NOAA); G. Halliwell, K. Vierra, and C. N. K. Mooers (University of Delaware); and M. D. Earle and K. Bush (Marine Environments Corporation).

2. SOURCES OF DATA

R. G. Williams

2.1 METEOROLOGICAL DATA

The meteorological data used in this study included hourly surface observations from the coastal military and civilian stations (Figure 2.1) and standard ship marine surface observations from ships in transit.

The observational records for the 11 coastal and island stations used in this study are listed in Table 2.1. Observations were taken on an hourly basis until 1965 for the civilian stations and 1972 for the naval stations, at which times the frequency was reduced to 3-hourly per day. The Air Force and Army stations generally made hourly observations and the Coast Guard made 3-hourly per day.

Standard Ship Marine Surface Observations consist of data acquired by ships in transit for the period roughly from the middle 1800 s to 1974, with primary observational period from the 1930 s to 1974. From this data set, monthly summaries were prepared for 146 1° x 1° square areas (identified by Marsden square numbers mapped in Figure 2.1) off the California and Baja California coasts (Reference 3). The number of observations for each 1° square area varies considerably over the region with the greatest number occurring on normal shipping channels.

Limited editing was performed on the data at NCC before the compilation of tabular summaries. This procedure, known as the Marine Data Array edit, consists of producing cumulative frequency distributions for each parameter. Anomalies are identified from the statistical summaries and suspect data are edited subjectively by a meteorologist. Thus, extreme data points of a distribution are likely to be eliminated. A disadvantage of this procedure is that it renders, as questionable, any subsequent rare event analysis.

A separate set of meteorological data was obtained from NCC by the subcontractor at the University of Delaware for use in the current meter and sea surface temperature analyses. These stations are shown in Figure 2.2 with information summarized in Table 2.2. The following parameters were processed for each station: pressure, east-west and north-south wind components, and air temperatures. Data were obtained for the period 1970 through 1978 for six stations (Arcata, San Francisco, Point Mugu, San Nicolas Island, San Clemente Island, and Imperial Beach). For S.E. Farallon Island, digital data were only available for 1970 and 1971, but were obtained because most current meters were deployed near these islands during 1970 and 1971. All data had a sampling interval of three hours.

The source data tapes were read and the time series stored on disk by variable, station, and year. These time series were edited in two steps:

- First, all values outside of physically reasonable bounds (Table 2.3) were rejected.
- Next, a first-difference edit was performed for each time series where, if the difference between a given value and either the value following or the value preceding it in the time series was greater than three times the average value of all first differences in the time series, that value was rejected and replaced by a missing value spacer. Linear interpolation was then used to fill the resulting gaps in the time series. None of these gaps were greater than 24 hours in length.

Table 2.1
Coastal and Islands Stations and Their Locations, Periods of Record, and Number of Observations

Station	Latitude	Longitude	Period	Number of Observations
Arcata (FAA)	40.9	124.1	12/49-1/79	84,856
Pt. Arena (CG)	39.0	123.7	1/67-12/76	29,170
S.E. Farallon (CG)	37.7	123.0	1/62-12/71	29,183
Monterey (FAA)	36.6	121.9	3/45-2/72	55,992
Ft. Ord (AAF)	36.7	121.8	4/60-12/70	28,931
Pt. Arguello (CG)	34.6	120.7	1/69-12/78	28,743
Vandenburg (AFB)	34.6	120.5	7/51-12/75	49,393
Pt. Mugu (NF)	34.1	119.1	3/46-1/79	94,519
San Nicolas I. (NF)	33.2	119.4	4/45-1/79	54,901
San Clemente I. (NF)	33.0	118.6	4/60-12/78	49,196
Imperial Beach (NAS)	32.6	117.1	1/52-12/78	63,672

The station type is indicated by the following abbreviations:

FAA	Federal Aviation Agency
CG	Coast Guard
AAF	Army Air Field
AFB	Air Force Base
NF	Naval Facility
NAS	Naval Air Station

Table 2.2
Coastal Meteorological Station Information

Station	Latitude (deg., min.)		Longitude (deg., min.)		Elevation (m)	Anemometer Height (m)	Start Date	End Date
Arcata, CA	40	59	124	06	69	6.1	1/1/70	12/31/78
S.E. Farallon Island, CA	37	42	123	00	9.1	6.7	1/1/70	12/31/71
San Francisco, CA	37	37	122	23	7.7	6.1	1/1/70	12/31/78
Point Mugu, CA	34	07	119	07	3.4	4.0	1/1/70	12/31/78
San Nicolas Island, CA	33	15	119	27	173	3.0	1/1/70	12/31/78
San Clemente Island, CA	33	01	118	35	5.2	7.9	1/1/70	12/31/78
Imperial Beach, CA	32	34	117	07	6.4	6.1	1/1/70	12/31/78

Table 2.3
Physically Reasonable Bounds for Atmospheric Forcing Variables

Variable	Units	Lower Bound	Upper Bound
sea level pressure	mb	950	1060
east-west wind	m/s	-50	50
north-south wind	m/s	-50	50
air temperature	°C	-40	45

The edited data were then 40-hour, low pass filtered and subsampled to six hours. Time series of semi-monthly averages of all variables for 1970 through 1978 were computed for the seven stations with available data for this entire interval, and used to study long period fluctuations in the atmospheric forcing variables.

2.2 OCEANOGRAPHIC DATA

The oceanic data and information used in this study have been drawn from many sources according to the type of data. In general, data on ocean currents are scarce, especially in regard to direct measurements of current by moored current meters and drogues. In many areas, very few observations of nutrients have been made. The distribution of archived physical and chemical observations throughout the study area is generally irregular in space and time, resulting in adequate coverage of source areas, and inadequate or no coverage in other areas. Such distributions are exemplified by Figures 2.3 and 2.4 which show the locations of archived hydrographic casts during the months of May and November. This nonuniformity of the spatial distribution of observations increases the uncertainty in the mean data fields, as represented by the climatological charts.

The distributions of the observations are presented by type in this chapter. Maps are given showing the total number of observations by 1° square. In the subsequent sections of data summaries, specific distributions of the observations by month and by season are presented as required to explain conclusions drawn from the analysis.

2.2.1 Station Data Archives (Nansen Cast/STD)

The principal data source for the physical and chemical oceanographic studies is the station data file at NODC, which consists of both water sample data (acquired by Nansen or Niskin bottles), and electronic STD sensors. This file is subdivided into a physical subfile consisting of the directly measured quantities of temperature and salinity at depth, and the computed density (sigma-t), and dynamic depth anomaly (delta). The chemical file consists of observations of dissolved oxygen, phosphate, nitrate, and silicate. The total number of these observations in the study area, along with the expected accuracies, are given in Table 2.4. The total number of oceanographic observations in the study area by 1° square, including mechanical and expendable bathythermographs (MBT and XBT), are given in Figures 2.5 through 2.13.

Quality control was performed on all analyzed physical oceanographic station data acquired within the study area. The variables include temperature, salinity, sigma-t, and dynamic depth anomaly. Because natural scatter in dissolved oxygen and nutrient chemicals is naturally quite high, and the number of observations small, no quality control was done on these data prior to analysis.

Table 2.4
Oceanographic Data for the Pacific Region Available at NODC

MEASURED QUALITY	NO. OF OBSERVATIONS	EXPECTED ACCURACY	REMARKS
Temperature (MBT)	72,275	on the order of ± 0.5°C and ± 3 m	cover period 1944 to present; accuracy highly dependent on calibration methods and handling; being replaced by XBT
Temperature (XBT)	18,621	± 0.1°C ± 2 m	cover period 1962 to present; repeatability of digitized XBT record is ± 0.2°C and ± 2 m
Temperature (Nansen cast or STD)	33,784	± 0.02°C ± 0.02°/oo	NODC does not distinguish between temperatures and salinities from Nansen casts or from Nansen casts or from STD sensors
Oxygen	25,287	± 0.04 m1/1	
Nitrate	2,835	± 5%	
Nitrite	914		
Phosphate	8,044	± 10%	
Silicate	3,180	± 8%	
Surface Currents	74,645		Covers period 1850 through 1974; relies on large numbers of observations to reduce error

The quality control consisted primarily of determining that the data fall within physically realistic limits specified as follows:

Variable	Accepted Limits
Temperature	0° - 28°C (degrees celsius)
Salinity	30 ppt - 37 ppt (parts per thousand)
Sigma-t	22-28
Dynamic Depth Anomaly	0-3 dynamic meters

Data falling outside these ranges were discarded. The surviving data were then examined for values excessively far from the center of the distributions (assuming that the populations are normal). The criterion employed was that the variables must lie within the 99 percent limits of the student's t-distribution (student's t-distribution was employed because of the small number of data points in some areas).

Finally, a gradient test was applied to each Nansen or STD cast to ascertain that all vertical profiles retained for analysis are physically realizable. The gradient limits employed were:

Variable	Gradient
Temperature	0.5°C/m (degrees celsius per meter)
Salinity	0.3 ppt/m (parts per thousand per meter)
Sigma-t	0.4/m (per meter)
Dynamic Depth Anomaly	0.3 dynm/m (dynamic meters per meter)

When one bad data point in a cast was identified, the entire cast was rejected. The net result of the quality control procedures was that approximately 1.5 percent of the casts were rejected (500 out of 34,000 casts).

No additional quality control beyond that routinely performed by NODC was carried out for the MBT and XBT observations.

2.2.2 Ship-Drift Archive

The source of data for this study is the Surface Current Data System (SCUDS) file of ship-drift observations at NODC (Reference 1). These data were screened by NODC for duplication and obvious navigational errors. Observations were not included which were made under conditions of high winds and waves (winds-33 kt; waves-12 ft.), or when the interval between observations exceeded 12 hours. Set is recorded to the nearest degree true; drift, to the nearest tenth of a knot. The distribution of these observations is shown in Figure 2.14.

2.2.3 Current Meter Archives

Geodyne 101 film-recording current meter records from the U.S. Naval Oceanographic Office (NAVOCEANO) for the years 1970, 1971, and 1974 were considered for this study. The arrays of meters, each consisting of one or more moorings, were deployed as listed in Table 2.5. In addition, data from three meters deployed off Southern California were obtained from the Scripps Institution of Oceanography, as listed in Table 2.6. Of the 52 NAVOCEANO meters, data were obtained for 44 of them. Data for the remaining eight were never digitized from the film records, due to the poor quality of the films. Of these meters, 10 had to be rejected due to meter malfunctions, which were determined by visual inspections of the time series plots, as shown in Table 2.7. All Scripps meters had good records.

Table 2.5
NAVOCEANO Current Meter Array Information

ARRAY NO.	MOORING NO.	LATITUDE	LONGITUDE	WATER DEPTH (m)	DEPLOYMENT DATE	RECOVERY DATE	NO. OF METERS	METER DEPTHS (m)
1	1	37°54'24"	123°23'00"	125[a]	1/6/70	unknown	3	25,101,116
2	1	37°54'39"	123°25'33"	143	2/22/70	3/27/70	4	27,82,136,138
2	2	37°54'30"	123°21'30"	110	2/23/70	3/22/70	2	69,103
3	1	37°55'00"	123°19'30"	104	5/12/70	6/15/70	4	21,31,98,100
3	2	37°52'29"	123°24'01"	140[a]	5/12/70	6/14/70	4	26,54,132,135
4	1	37°55'00"[b]	123°19'30"[b]	130	8/28/70	9/26/70	4	5,57,123,126
4	2	37°52'30"	123°21'30"	121	8/28/70	9/26/70	4	5,52,114,116
5	1	41°36'00"	124°23'00"	97	11/6/70	11/19/70	4	27,48,91,93
5	2	41°27'00"	124°27'00"	134	11/5/70	12/3/70	3	24,75,128
5	3	37°55'03"	123°19'32"	104[a]	11/12/70	12/6/70	4	20,53,94,96
5	4	37°52'32"	123°21'30"	110	11/12/70	12/6/70	4	25,59,103,105
6	1	37°42'58"	123°27'01"	2190[a]	1/25/71	2/10/71	2	2024,2176
6	2	37°38'03"	123°21'34"	2416[a]	1/26/71	2/11/71	3	2264,2410,2412
7	1	38°10'05"	123°26'43"	284	11/24/71	12/5/71	4	30,102,277,279
8	1	38°07'45"	123°39'48"	1829	11/12/74	11/21/74	3	18,1676,1824

[a] Depth approximate - determined from a National Ocean Survey bathymetric chart.

[b] The position of this mooring may be in error. The depth at this position of 104 m, and it is located 7 km from the 130 m isobath.

Table 2.6
Scripps Current Meter Information

Meter No.	Latitude	Longitude	Meter Depth (m)	Water Depth (m)	Deployment Date	Start Time	Length of Record (hr)
S1	34°13.6′	120°00.5′	276	576	5/6/70	0700	93
S2	34°13.6′	120°00.5′	426	576	5/6/70	0900	93
S3	32°52.0′	117°15.0′	13	33	3/21/70	0000	480

37 NAVOCEANO and 3 Scripps meters had acceptable records for processing. Four of the NAVOCEANO meters had short records less than one week long, and two of the four Scripps meters also had records less than one week long. This left a total of 31 meters with records longer than one week. (Charts of meter locations, depths, times of deployment, etc., for the current meters are presented in Appendix C of the unabridged report, Reference 5). Most meters were deployed near the shelfbreak off Central California (near 38°N). Only four NAVOCEANO meters with records longer than one week were deployed off Northern California (array five, moorings one and two). The four Scripps meters, only two of which had records longer than one week, were the only meters deployed in the Southern California Bight.

During current meter data processing, linear interpolation was used to fill the data gaps. For all meters, only a few missing data values had to be filled. Time series of north-south and east-west current components were computed from the speed and direction for all meters. Time series of current components were rotated to alongshelf and across-shelf components according to the local bathymetry. Two sets of filtered time series were created for the current components: three-hour low passed series subsampled to one hour, and 40-hour low passed series subsampled to six hours.

2.2.4 Coastal Sea Level Data

Coastal sea level stations (Figure 2.15) hourly data were obtained from the National Ocean Survey (NOS) for 1970 through 1978. The data were then subjected to the same editing procedure as the meteorological data for the current meter analysis. Because of the very large tidal signal, a modified interpolation scheme had to be used. For all data gaps longer than three hours, 25-hour averages were computed on each side of the gaps. These averaged values, which represented values 12.5 hours prior to the beginning of the gap and 12.5 hours following the end of the gap, were used to compute the interpolated values used to replace the missing data.

Two data sets were created for analysis. First, 40-hour low passed time series were computed and subsampled to six hours. Time series of semi-monthly averaged sea level were also computed.

2.2.5 Data for the Sea Surface Temperature Analysis

Sea surface temperatures were digitized from the semi-monthly *Fishing Information Supplements* produced by the National Marine Fisheries Service (NMFS) (Reference 2) for the period 1972 through 1978. The domain within which temperatures were digitized is shown by the grid in Figure 2.16. Temperature values were digitized at a spacing of one degree of both latitude and longitude, at points centered on integer values of both latitude and longitude. In order to extend the temperature coverage to the coast, temperature values were digitized at some points just landward of the coast, by extrapolation of the temperature contours. A total of 119 times series were thus obtained.

Table 2.7
Current Meter Data Summary

METER NO.	METER DEPTH (m)	START DATE	START TIME	END DATE	RECORD LENGTH (hr.)	SAMPLING INTERVAL	COMMENTS
111	25					10′	Data not available
112	101					10′	Data not available
113	116					10′	Data not available
211	27					10′	Rejected-meter malfunction
212	82					10′	Rejected-meter malfunction
213	136					10′	Rejected-meter malfunction
214	138	2/23/70	0252	3/23/70	682	10′	
221	69					10′	Rejected-data values all zero
222	103	2/23/70	1010	3/22/70	673	10′	
311	21	5/12/70	0825	6/14/70	796	10′	
312	31					10′	Data not available
313	98	5/12/70	0825	6/13/70	736	10′	
314	100	5/12/70	0825	5/18/70	149	10′	
321	26					10′	Data not available
322	54	5/12/70	2140	6/15/70	813	10′	
323	132					10′	Data not available
324	135					10′	Rejected-record only 6 hours long
411	5	8/28/70	0309	9/27/70	718	10′	Not rejected-questionable shallow depth
412	57	8/31/70	0629	9/23/70	565	10′	
413	123	8/28/70	0309	9/02/70	131	10′	
414	126	8/28/70	0309	9/20/70	566	10′	
421	5					10′	Rejected-meter malfunction
422	52	8/28/70	0613	9/01/70	92	10′	
423	114	8/31/70	0813	9/26/70	568	10′	
424	116	8/28/70	0613	9/20/70	562	10′	
511	27	11/06/70	0355	11/09/70	90	10′	
512	48	11/06/70	0355	11/19/70	344	10′	
513	91	11/06/70	0355	11/19/70	335	10′	
514	93					10′	Data not available

Table 2.7 (continued)

METER NO.	METER DEPTH (m)	START DATE	START TIME	END DATE	RECORD LENGTH (hr.)	SAMPLING INTERVAL	COMMENTS
521	24					10′	Rejected-meter malfunction
522	75	11/05/70	0358	11/18/70	331	10′	
523	128	11/05/70	0358	11/18/70	337	10′	
531	20	11/12/70	0430	12/06/70	576	10′	
532	53	11/12/70	0430	12/04/70	538	10′	
533	94					10′	Data not available
534	96	11/12/70	0430	11/29/70	443	10′	
541	25	11/12/70	0633	11/21/70	233	10′	
542	59	11/12/70	0633	12/06/70	584	10′	
543	103	11/12/70	0633	12/06/70	584	10′	
544	105	11/12/70	0633	12/04/70	530	10′	
611	2024					10′	Rejected-meter malfunction
612	2176					10′	Rejected-meter malfunction
621	2264					10′	Rejected-meter malfunction
622	2410	1/26/71	0430	2/09/71	342	10′	
623	2412	1/26/71	0430	2/10/71	357	10′	
711	30	11/24/71	1712	12/07/71	296	5′	
712	102	11/24/71	1712	12/06/71	290	5′	
713	277	11/24/71	1712	12/07/71	313	5′	
714	279	11/24/71	1712	12/06/71	293	5′	
811	18	11/13/74	0008	11/22/74	228	15′	
812	1676	11/13/74	0008	11/21/74	212	15′	
813	1824	11/13/74	0008	11/22/74	228	15′	
S1	276	5/06/70	0700	5/10/70	93	60′	
S2	426	5/06/70	0900	5/10/70	93	60′	
S3	13	3/21/70	0000	4/10/70	486	60′	

2.2.6 Special Data Sets

Certain data sets, not yet in the NODC archives, but made available through the courtesy of the principal investigators, were received too late in the study to incorporate into the archive data for statistical analysis. Limited use of these observations was made for special purposes, such as examining hydrographic structure in the region of current meter observations. Three such data sets are:

- CALCOFI hydrographic observations acquired since 1969
- The Pacific Marine Environmental Laboratory (PMEL) STD cruise off northern California
- Hydrographic observations by certain Soviet vessels, on file at World Data Center A for Oceanography in the form of printed log sheets

2.2.7 Water Level Elevation Data

The storm surge analysis incorporated derived statistics from the literature, e.g., obtained from California tide stations operated by the NOS, and from wave observations obtained and described by the U.S. Army Corps of Engineers.

The surface wind wave analysis employed both visual wave observation data, obtained from NCC, and derived statistics obtained by the California Coastal Engineering Data Network, and the U.S. Army Coastal Engineering Center. These sources of data are discussed in Chapter 3.

Chapter 7 describes the water elevation data which were used in this study in connection with analysis of storm surge, surface wind wave conditions, and tsunami occurrence along the California coast. The tsunami characteristics were obtained from derived statistics and model results from the published literature, particularly from studies performed by the U.S. Army Corps of Engineers.

REFERENCES

1. Waters, W., 1976. New Surface Current Data Available, EDS, Environmental Data Service, National Oceanic and Atmospheric Administration, U.S. Department of Commerce, Washington, D.C., pp 21–22.

2. Fishing Information and Fishing Information Supplement charts, National Oceanic and Atmospheric Administration/National Marine Fisheries Service (NOAA/NMFS), Southwest Fisheries Center, La Jolla, California.

3. User's Guide to NODC Services, Key to Oceanographic Records Documentation No. 1 (Revised February 1974), U.S. Department of Commerce, NOAA, Washington, D.C., 72 pp.

4. Williams, R.G., R.W. Reeves, F.A. Godshall, S.W. Fehler, 1980. A Climatology and Oceanographic Analysis of the California Pacific Outer Continental Shelf Region, Final Report to the Bureau of Land Management, U.S. Department of Commerce, NOAA, Washington, D.C., 1182 pp.

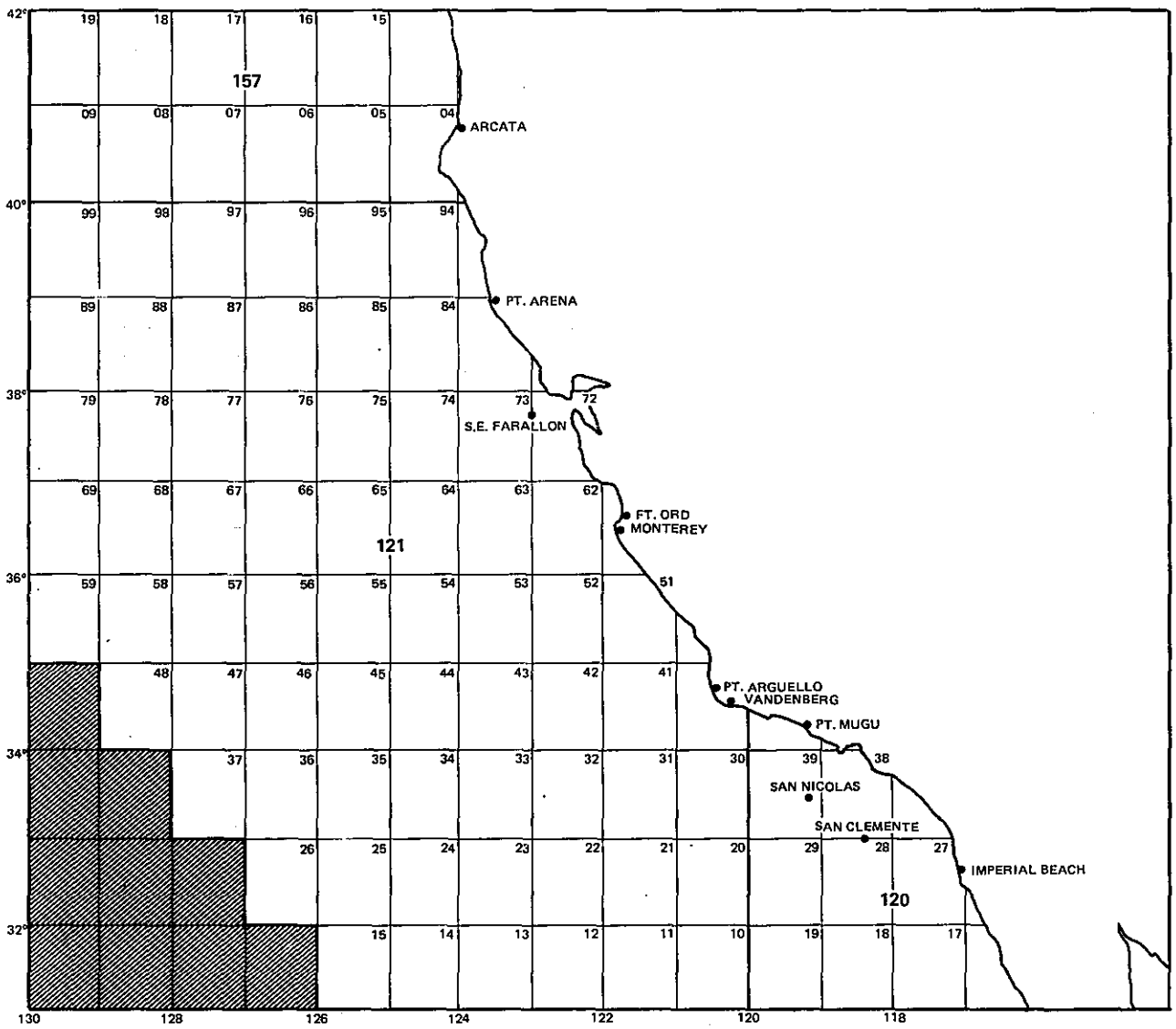

Figure 2.1. Meteorological Stations

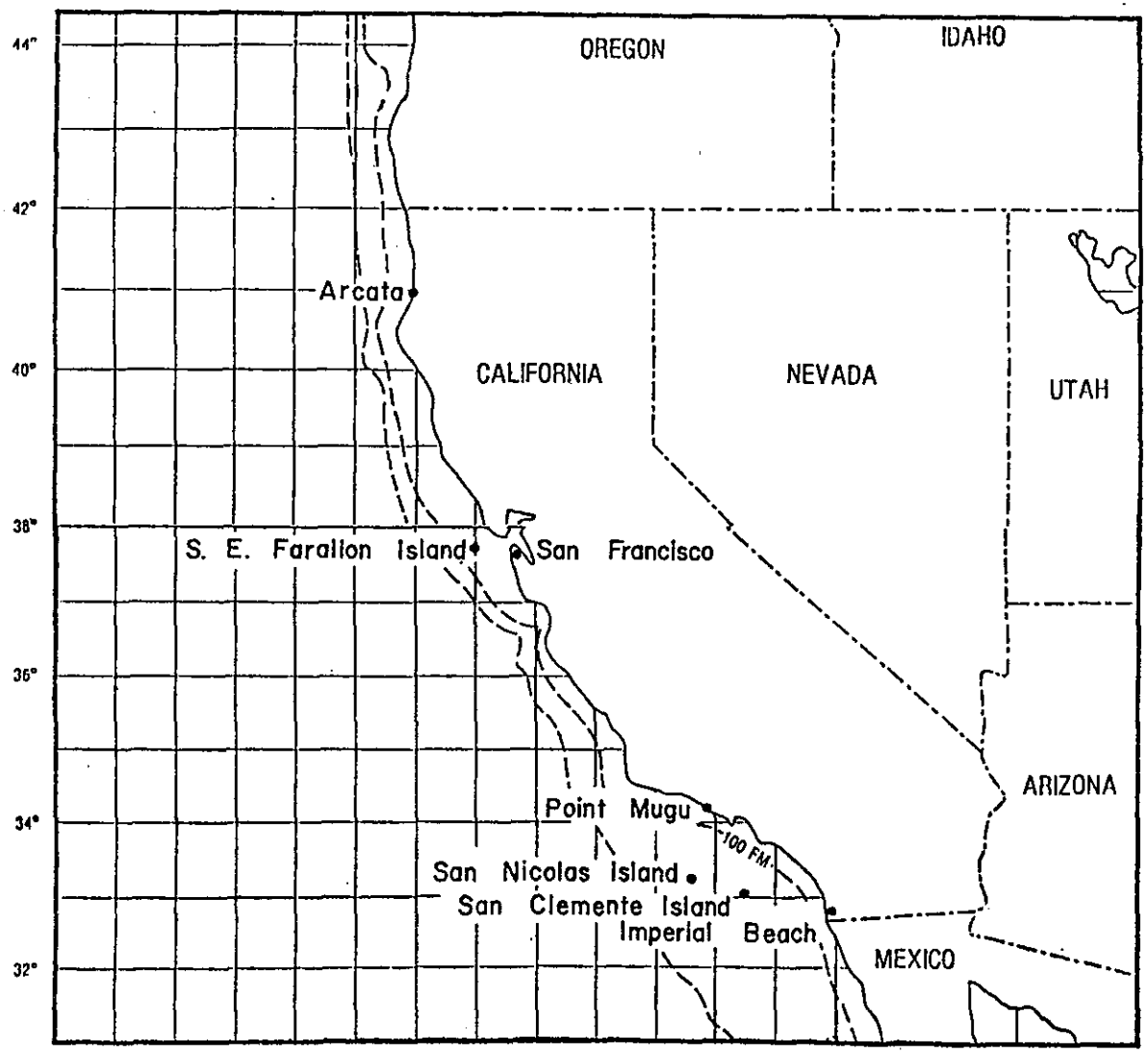

Figure 2.2. Meteorological Stations Used for the Current Meter Data Analysis

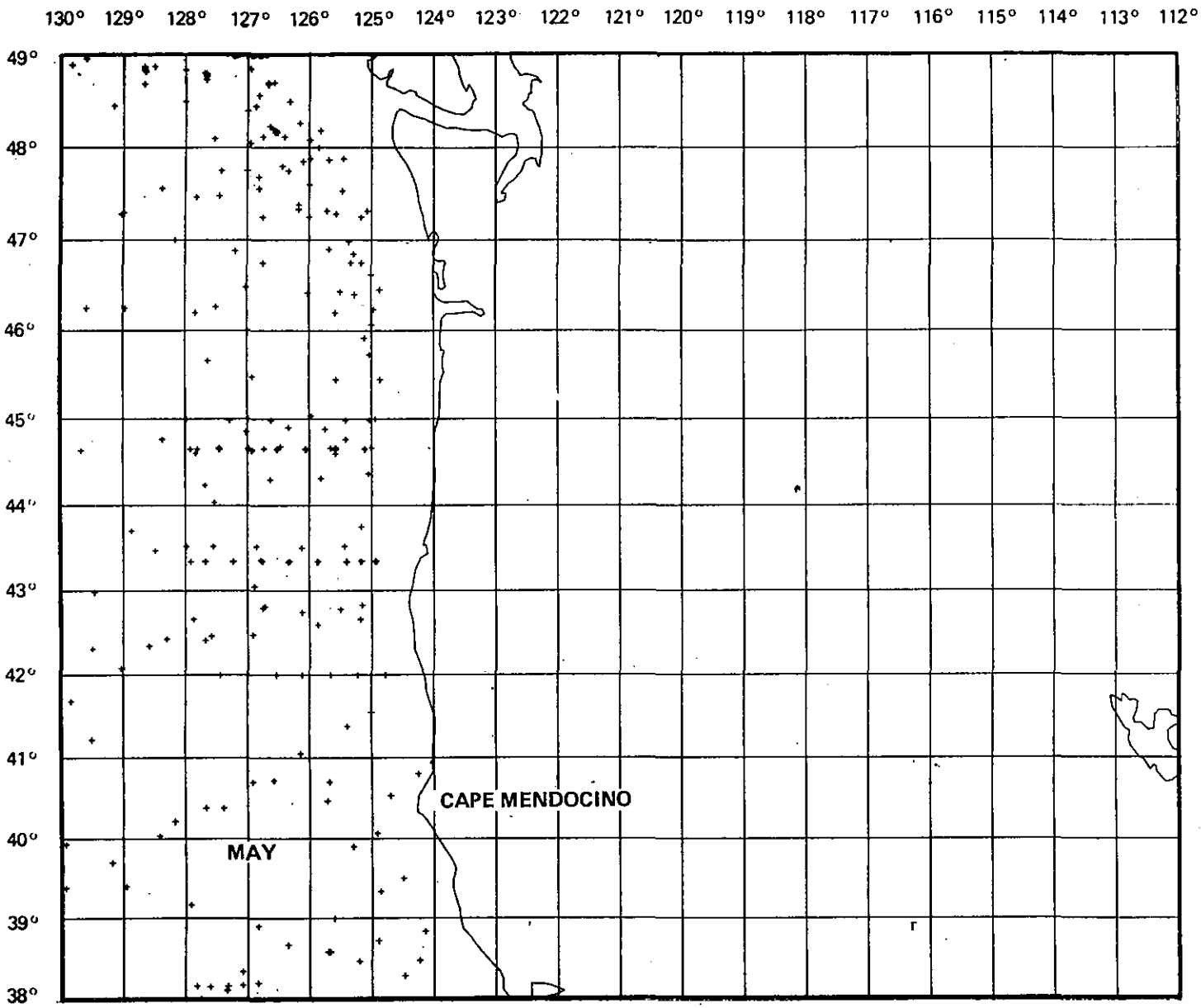

Figure 2.3. Location of Archived Hydrographic Casts During the Month of May

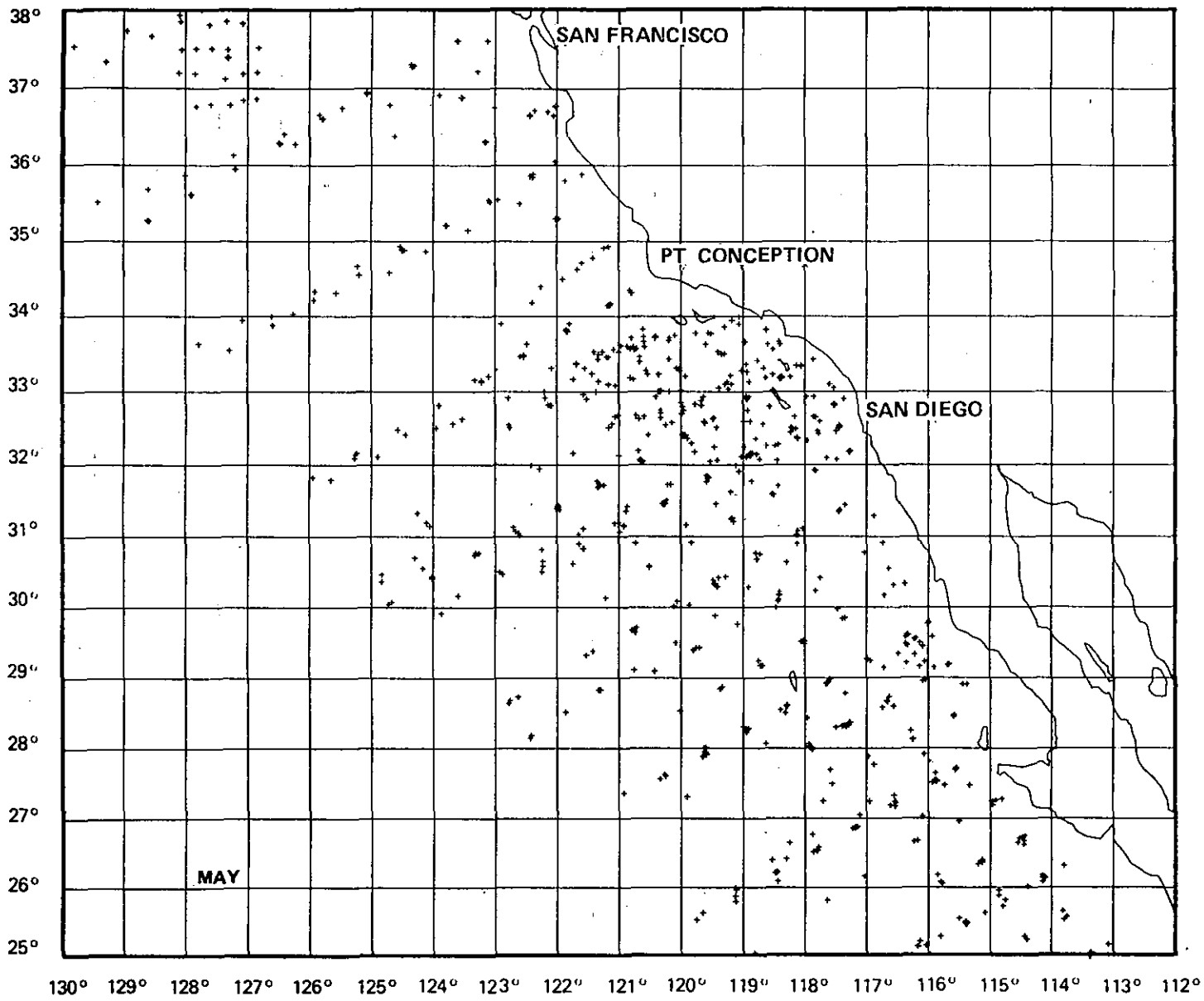

Figure 2.3. Location of Archived Hydrographic Casts During the Month of May (continued)

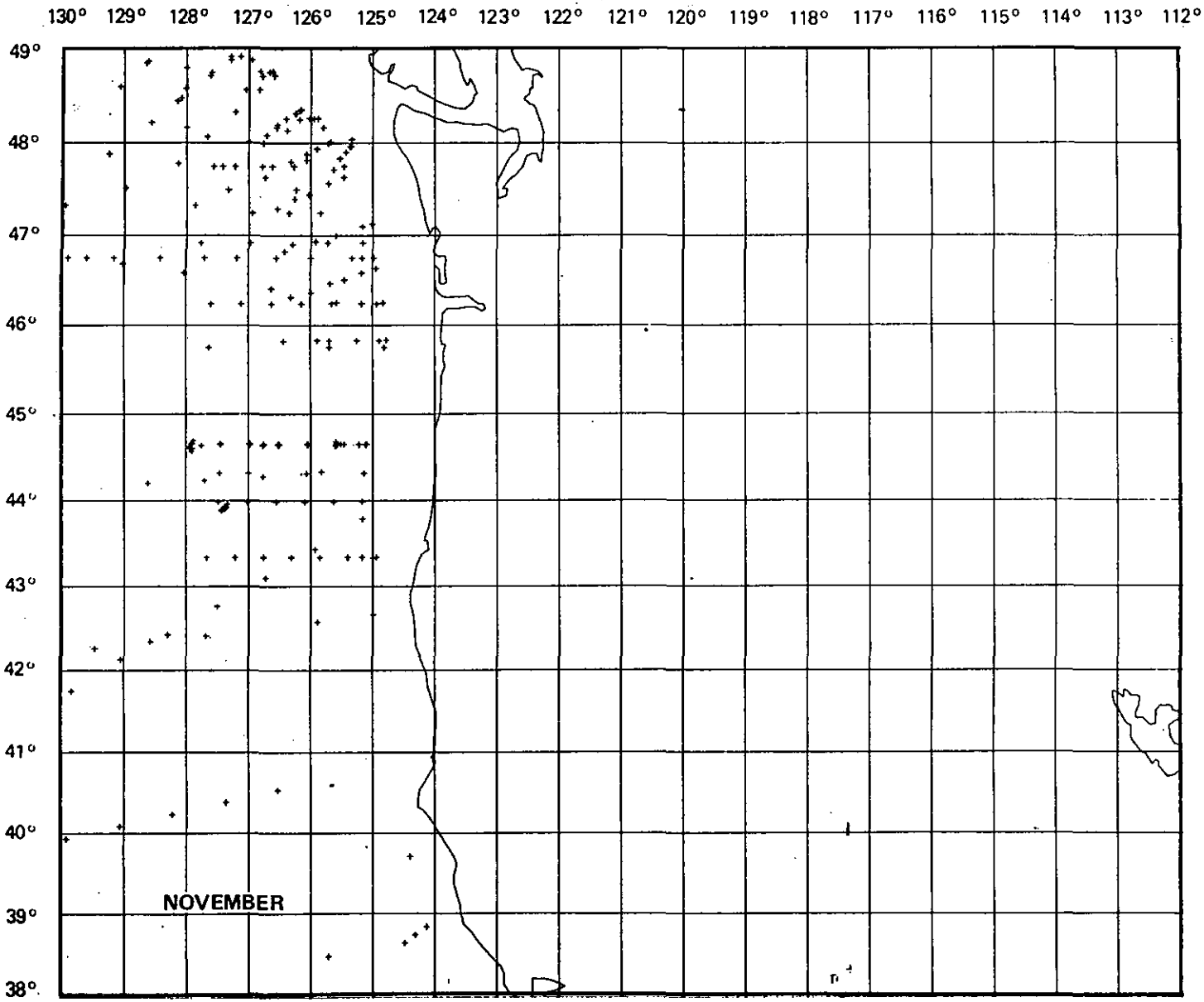

Figure 2.4. Location of Archived Hydrographic Casts During the Month of November

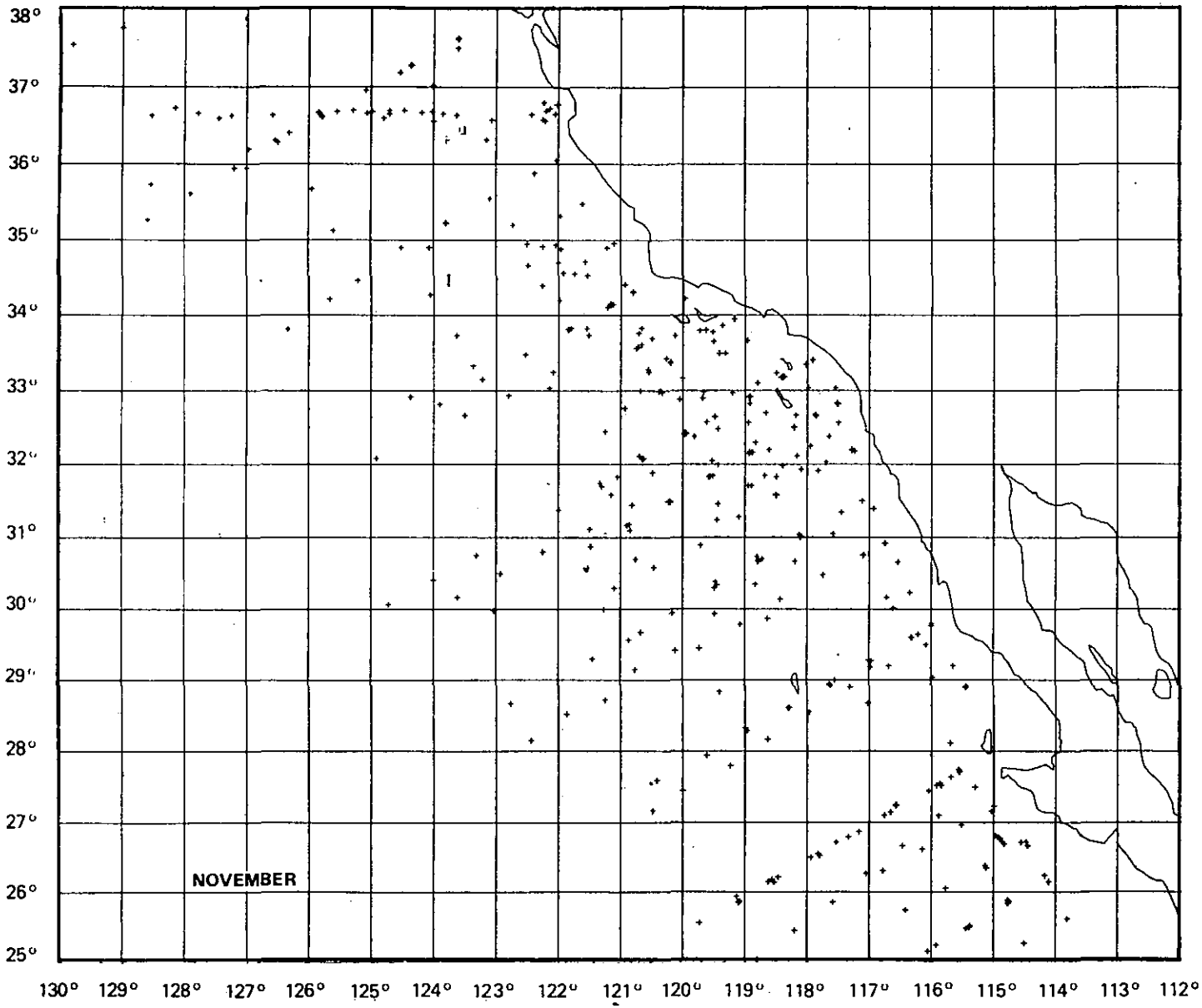

Figure 2.4. Location of Archived Hydrographic Casts During the Month of November (continued)

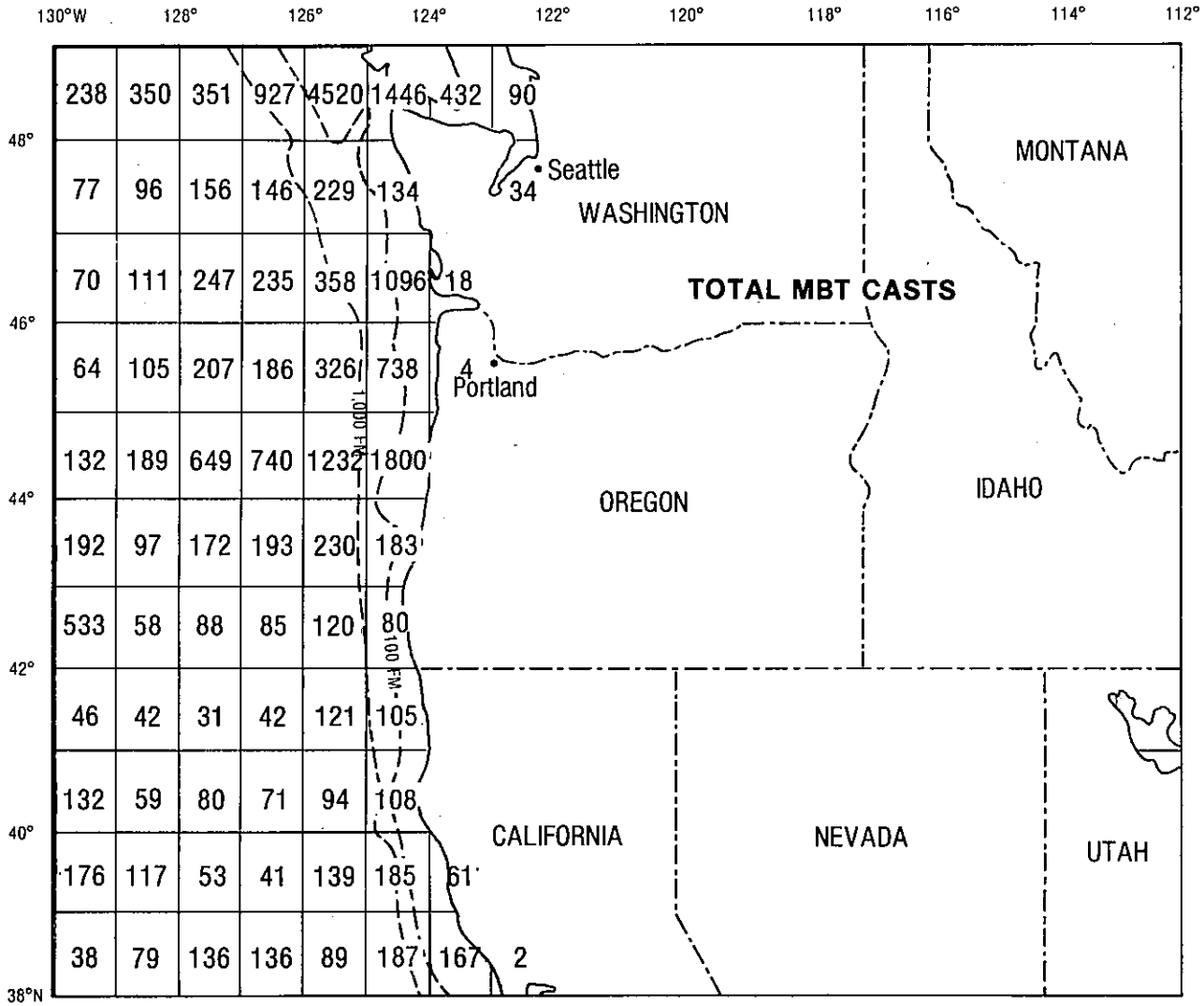

Figure 2.5. The Number of Archived Mechanical Bathythermograph (MBT) Observations by 1 degree Square

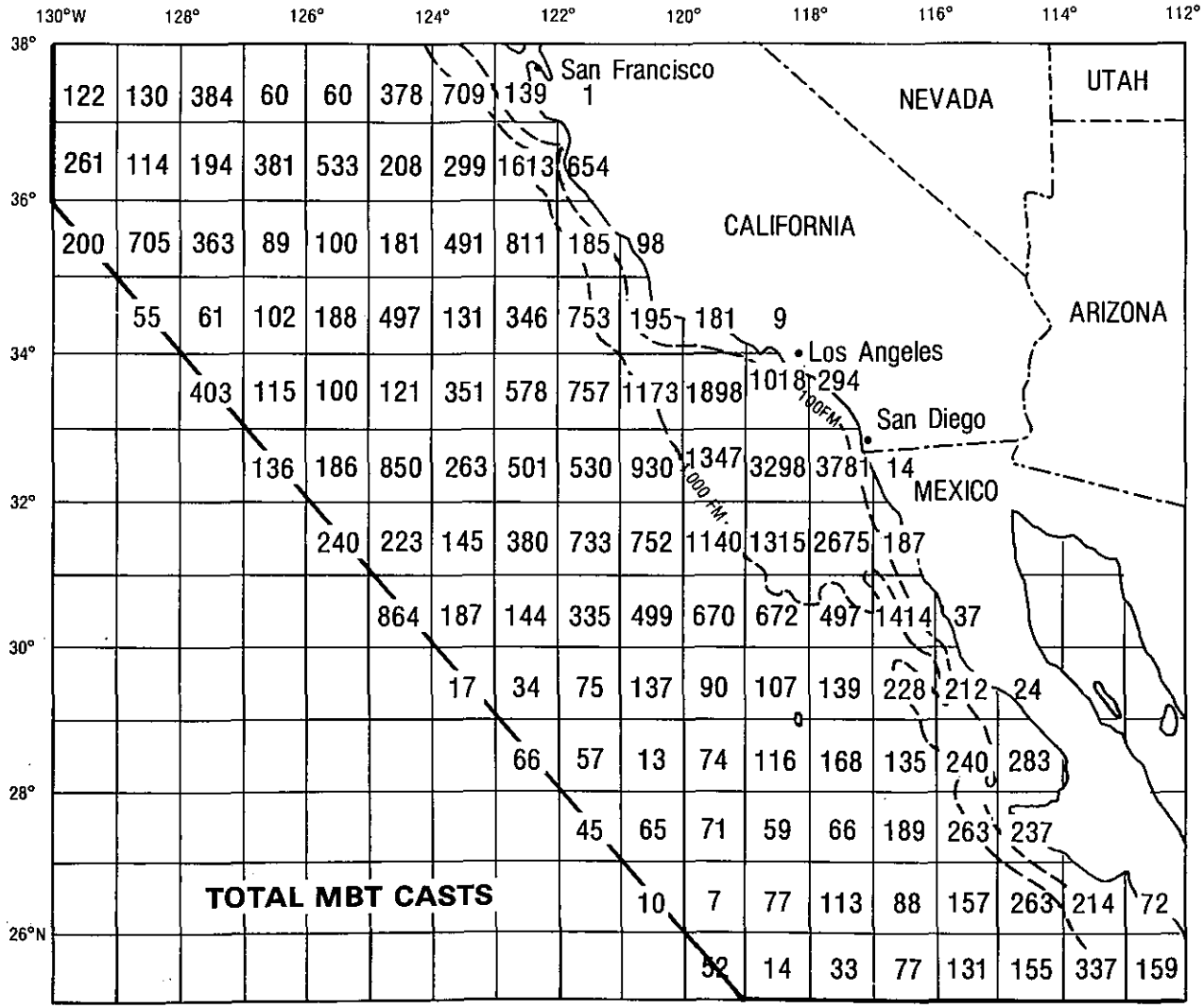

Figure 2.5. The Number of Archived Mechanical Bathythermograph (MBT) Observations by 1 degree Square (continued)

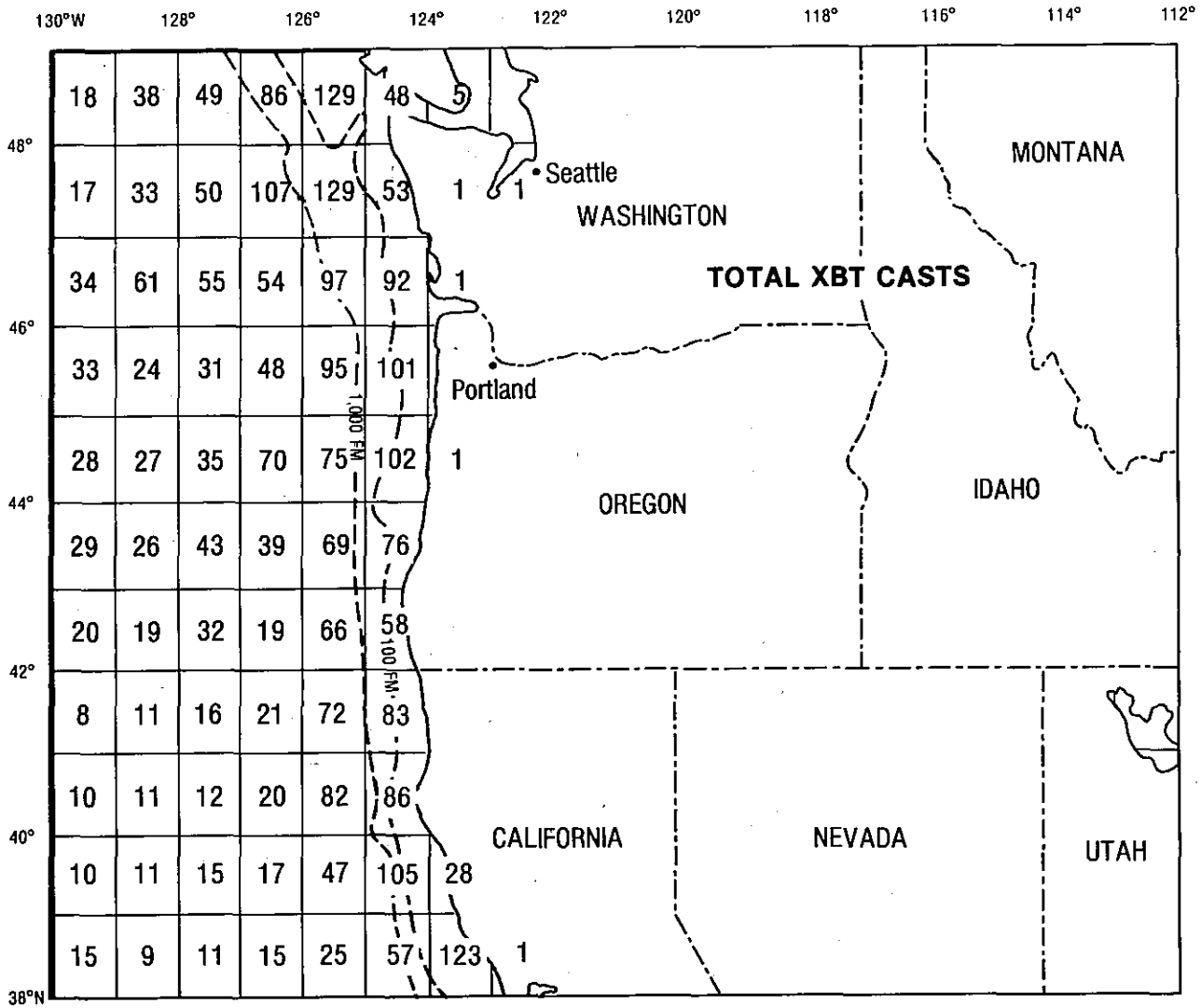

Figure 2.6. The Number of Archived Expendable Bathythermograph (XBT) Observations by 1 degree Square

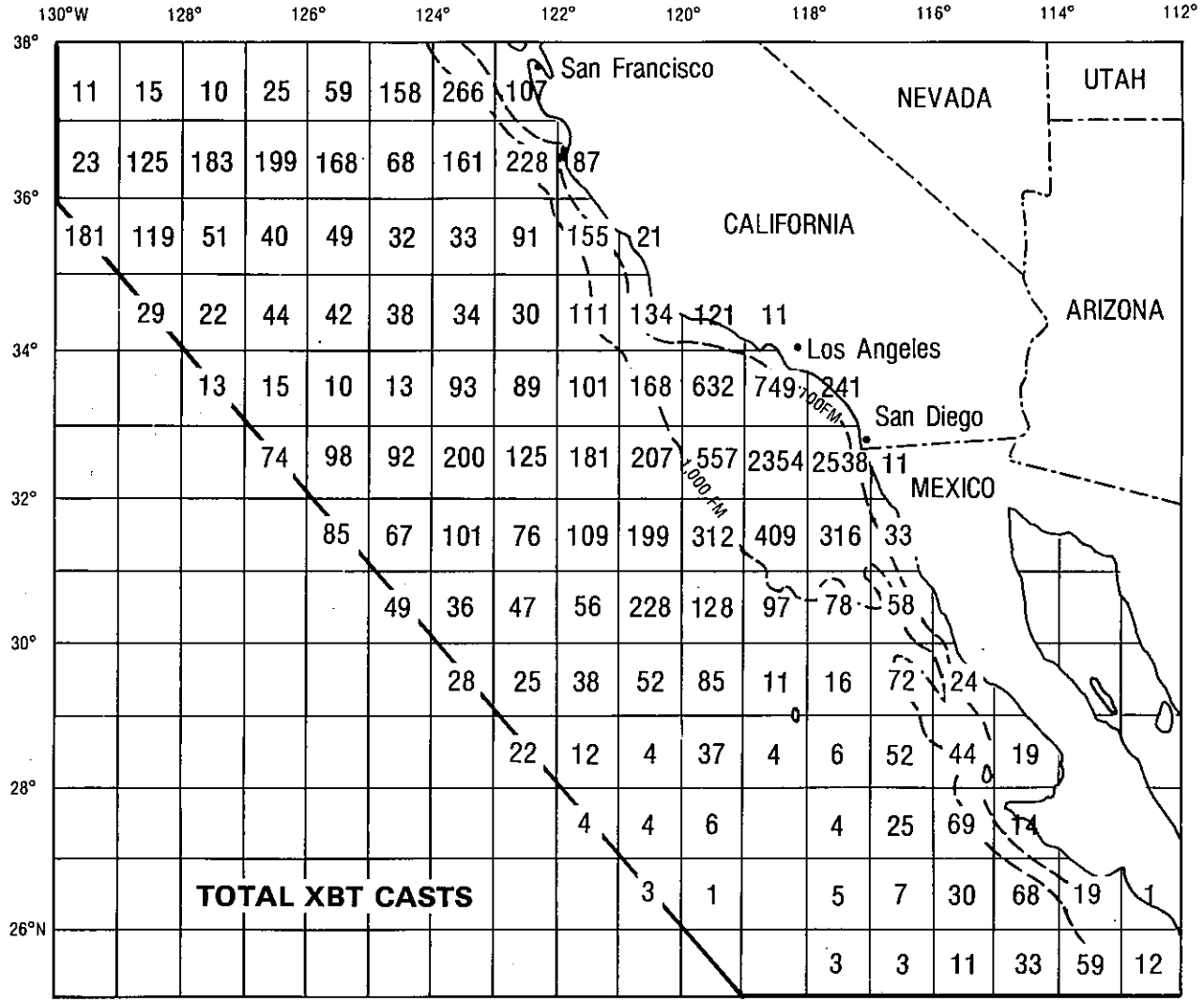

Figure 2.6. The Number of Archived Expendable Bathythermograph (XBT) Observations by 1 degree Square (continued)

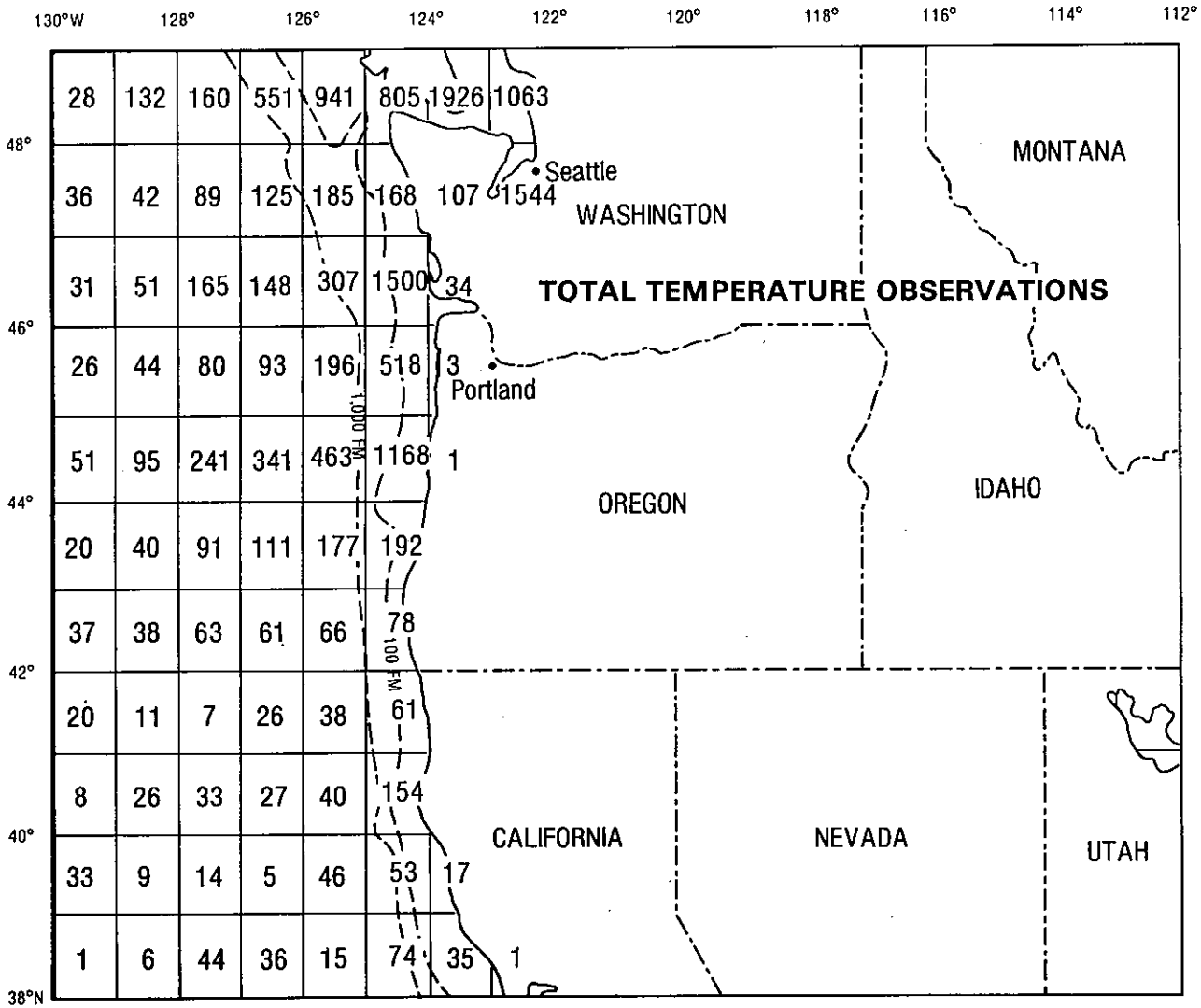

Figure 2.7. The Number of Archived Temperature Soundings from Nansen Casts and STD Casts by 1 degree Square

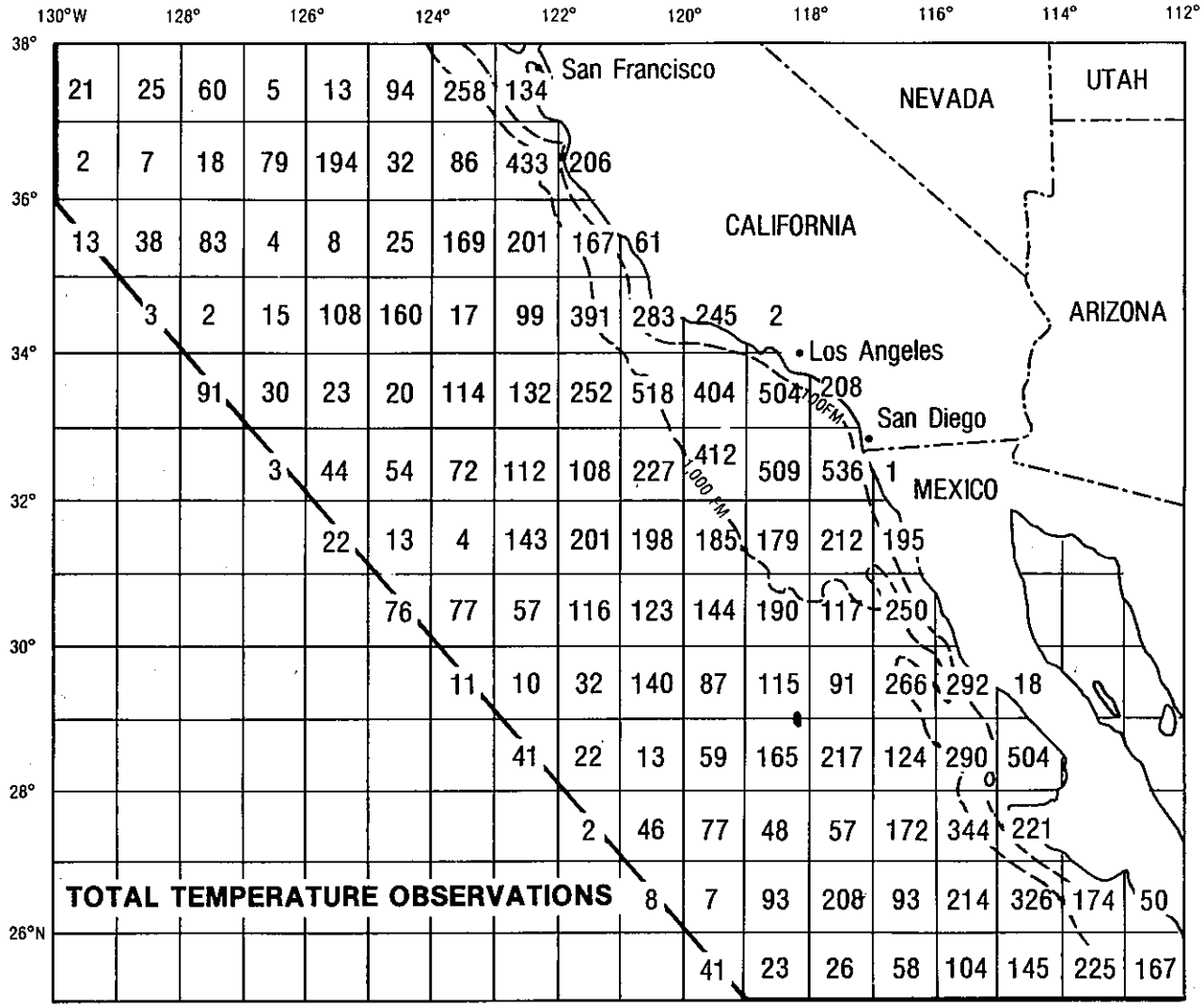

Figure 2.7. The Number of Archived Temperature Soundings from Nansen Casts and STD Casts by 1 degree Square (continued)

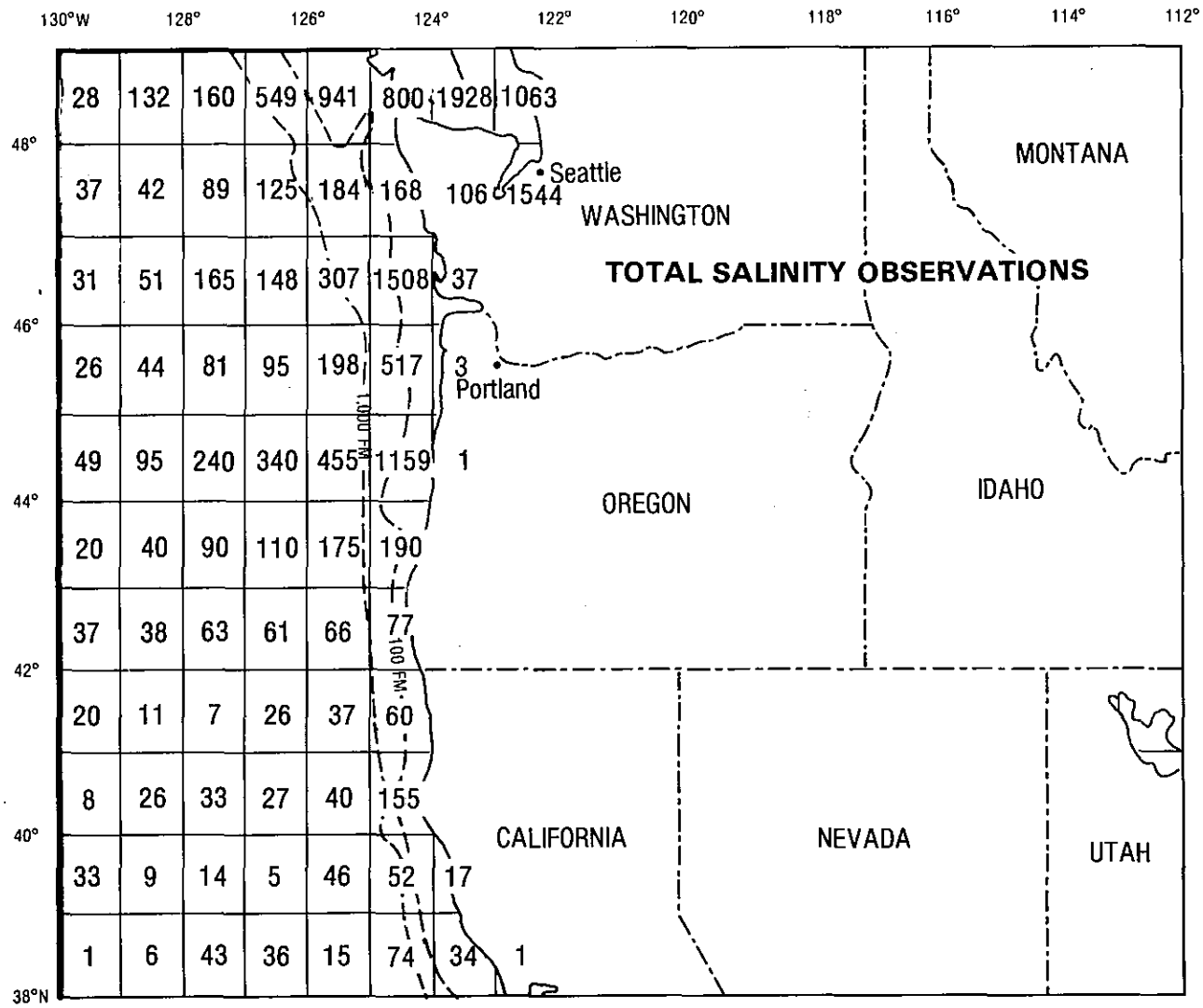

Figure 2.8. The Number of Archived Salinity Soundings from Nansen Casts and STD Casts by 1 degree Square

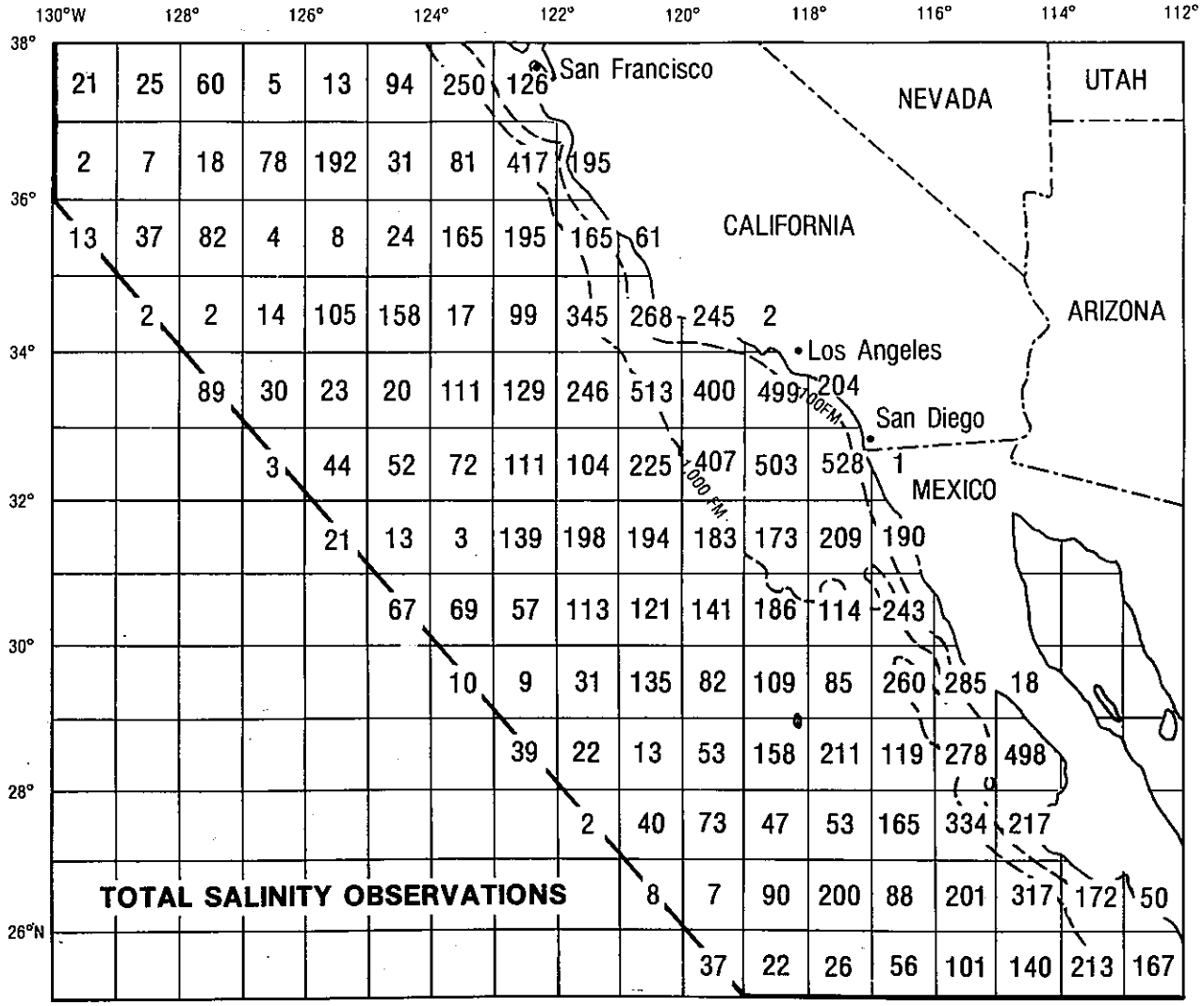

Figure 2.8. The Number of Archived Salinity Soundings from Nansen Casts and STD Casts by 1 degree Square (continued)

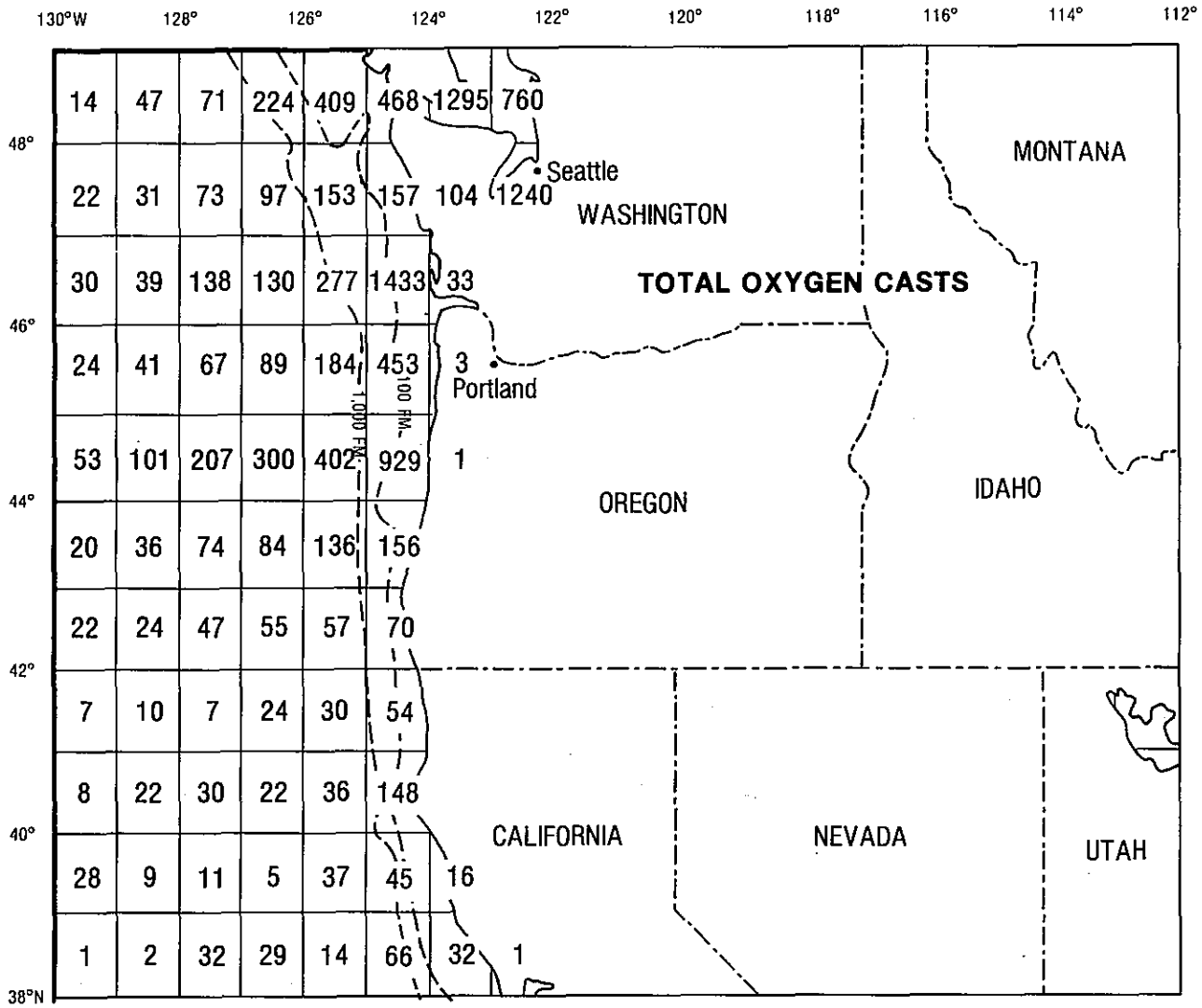

Figure 2.9. The Number of Archived Oxygen Soundings by 1 degree Square

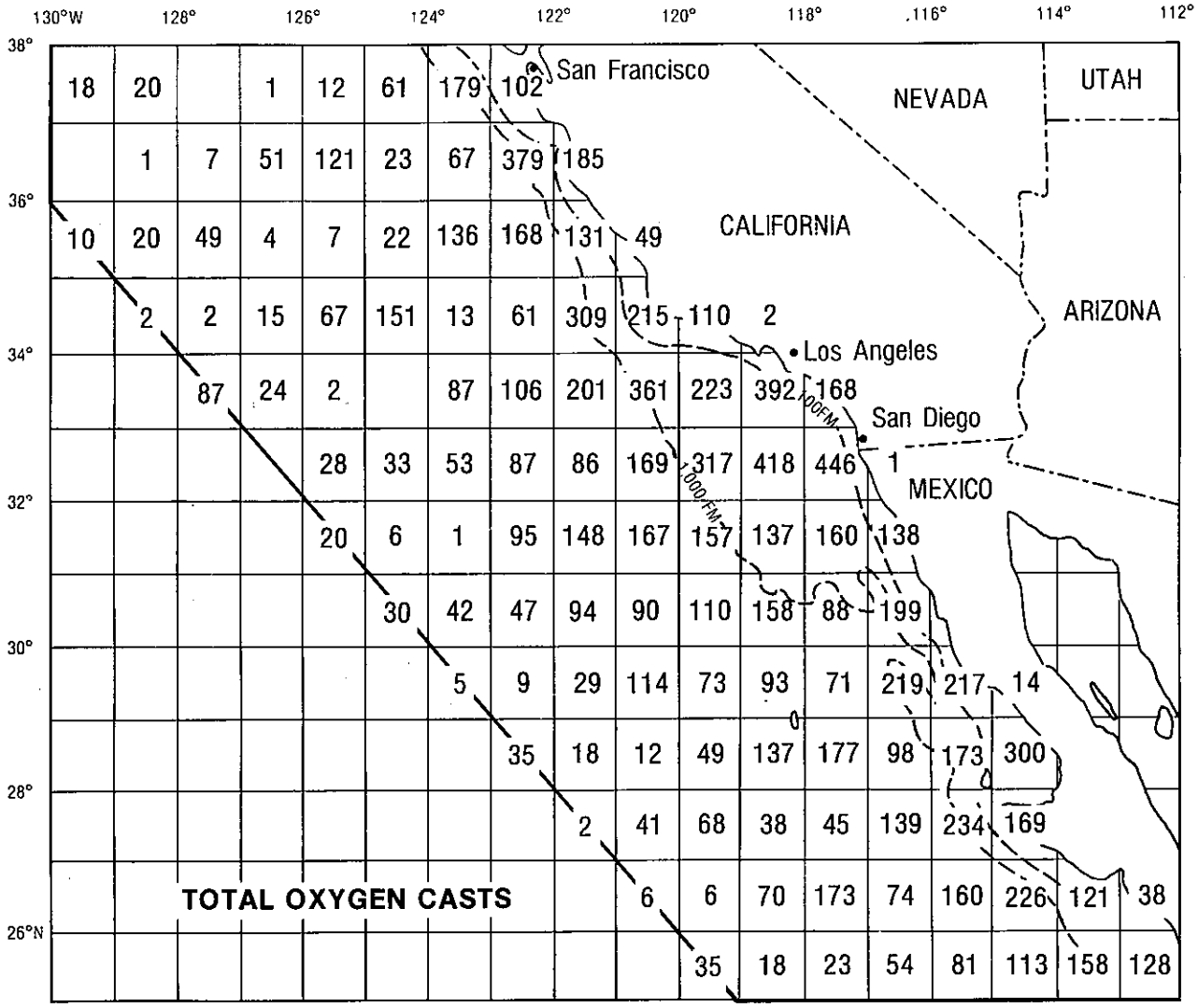

Figure 2.9. The Number of Archived Oxygen Soundings by 1 degree Square (continued)

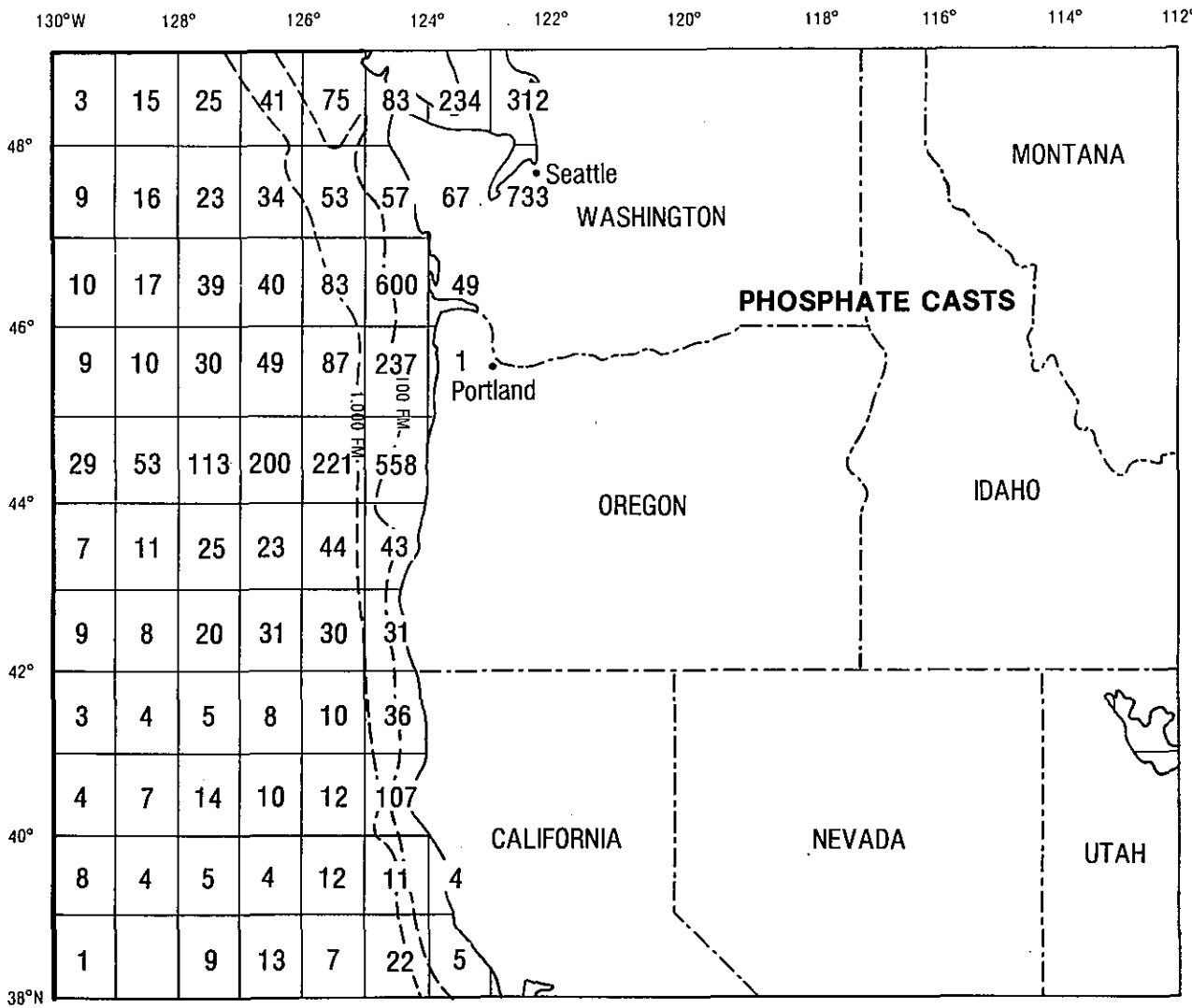

Figure 2.10. The Number of Archived Phosphate Soundings by 1 degree Square

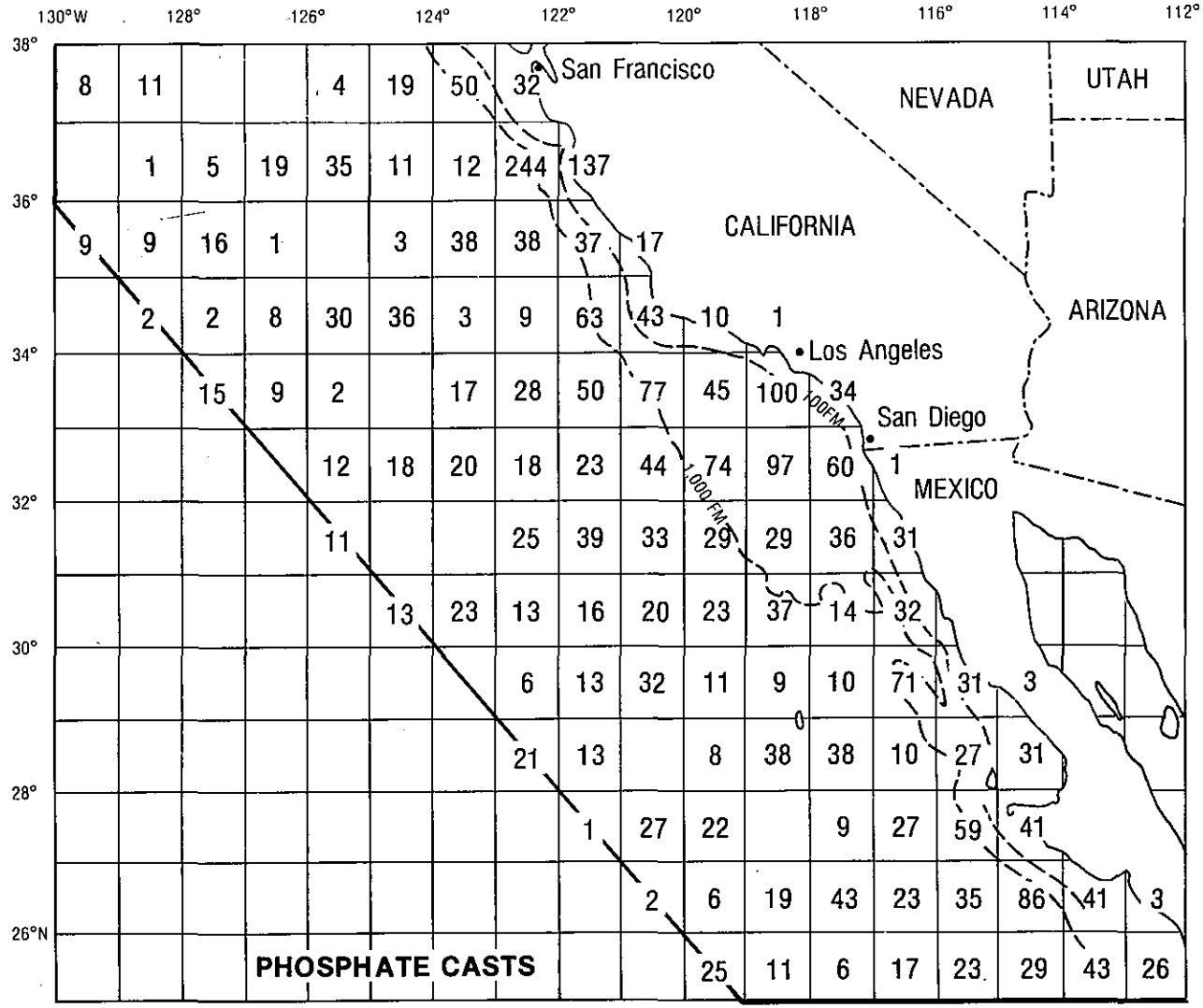

Figure 2.10. The Number of Archived Phosphate Soundings by 1 degree Square (continued)

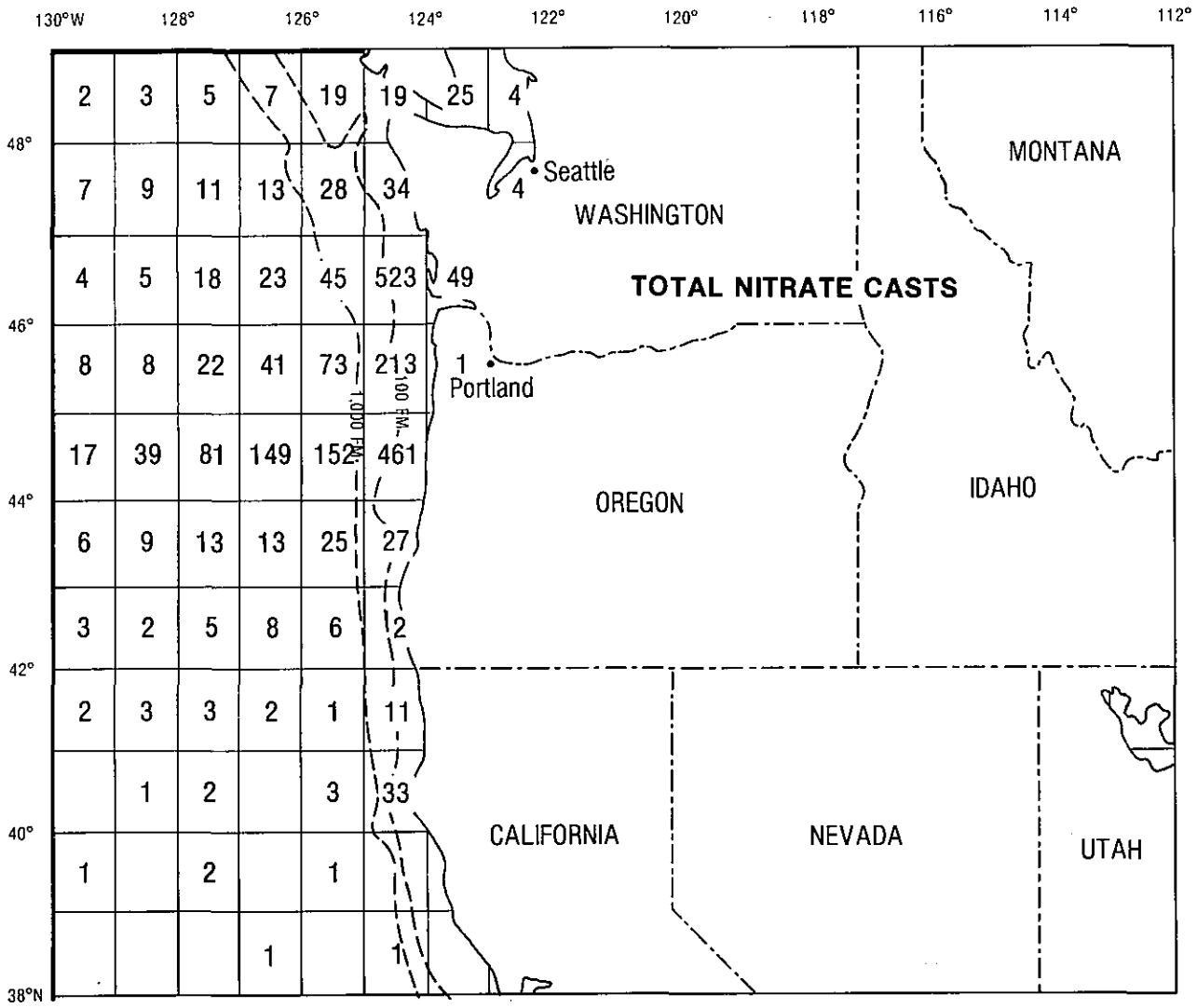

Figure 2.11. The Number of Archived Nitrate Soundings by 1 degree Square

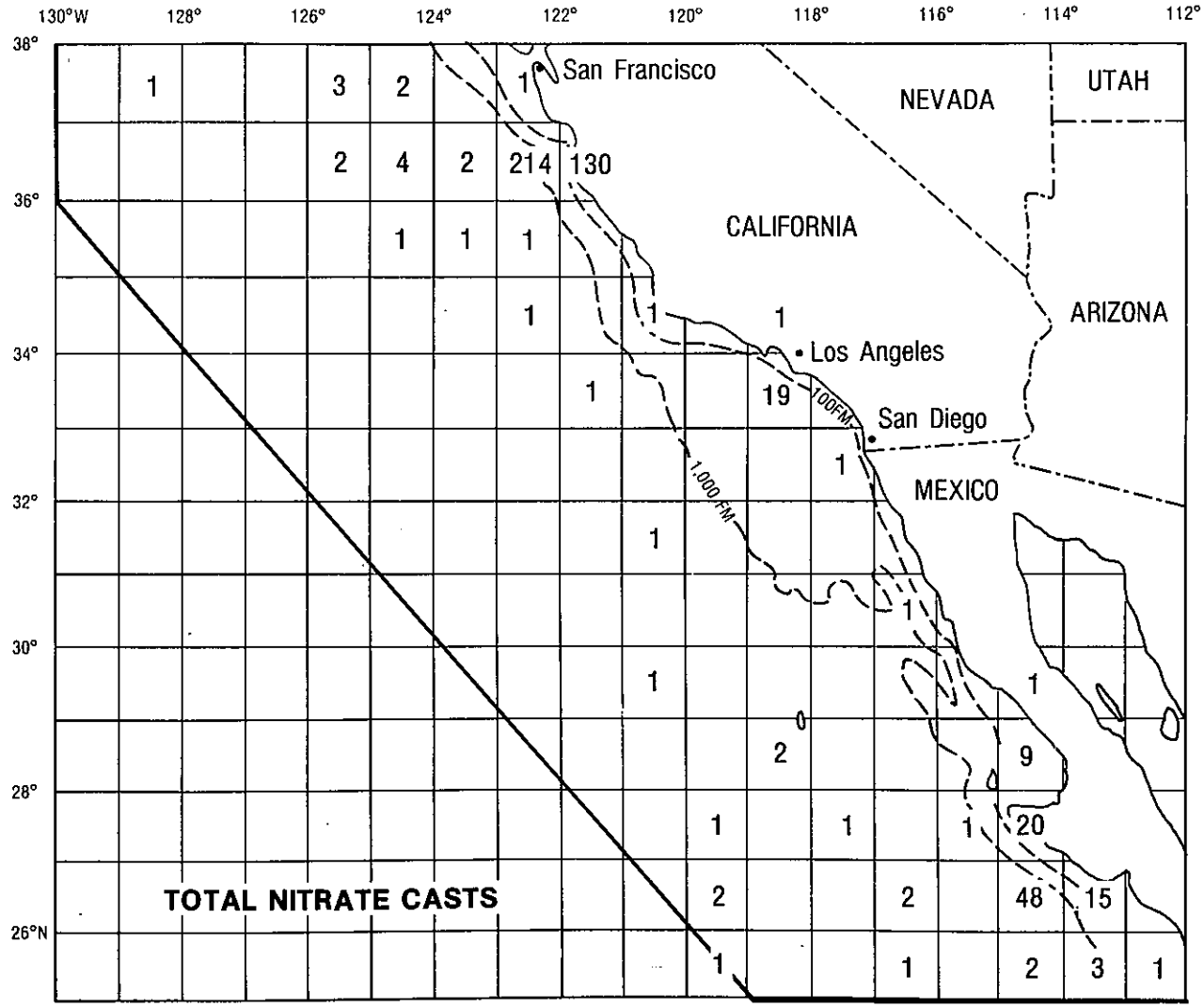

Figure 2.11. The Number of Archived Nitrate Soundings by 1 degree Square (continued)

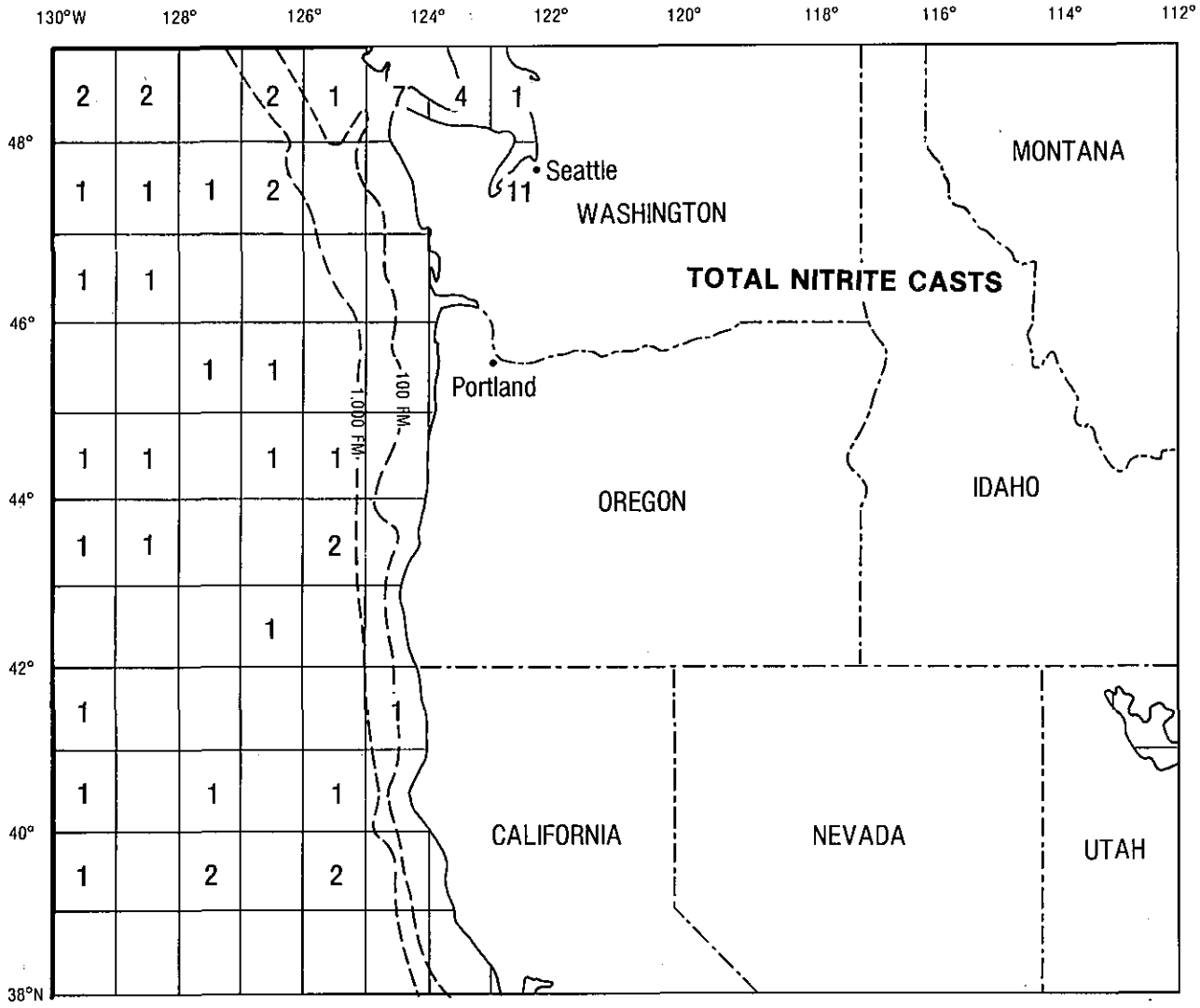

Figure 2.12. The Number of Archived Nitrite Soundings by 1 degree Square

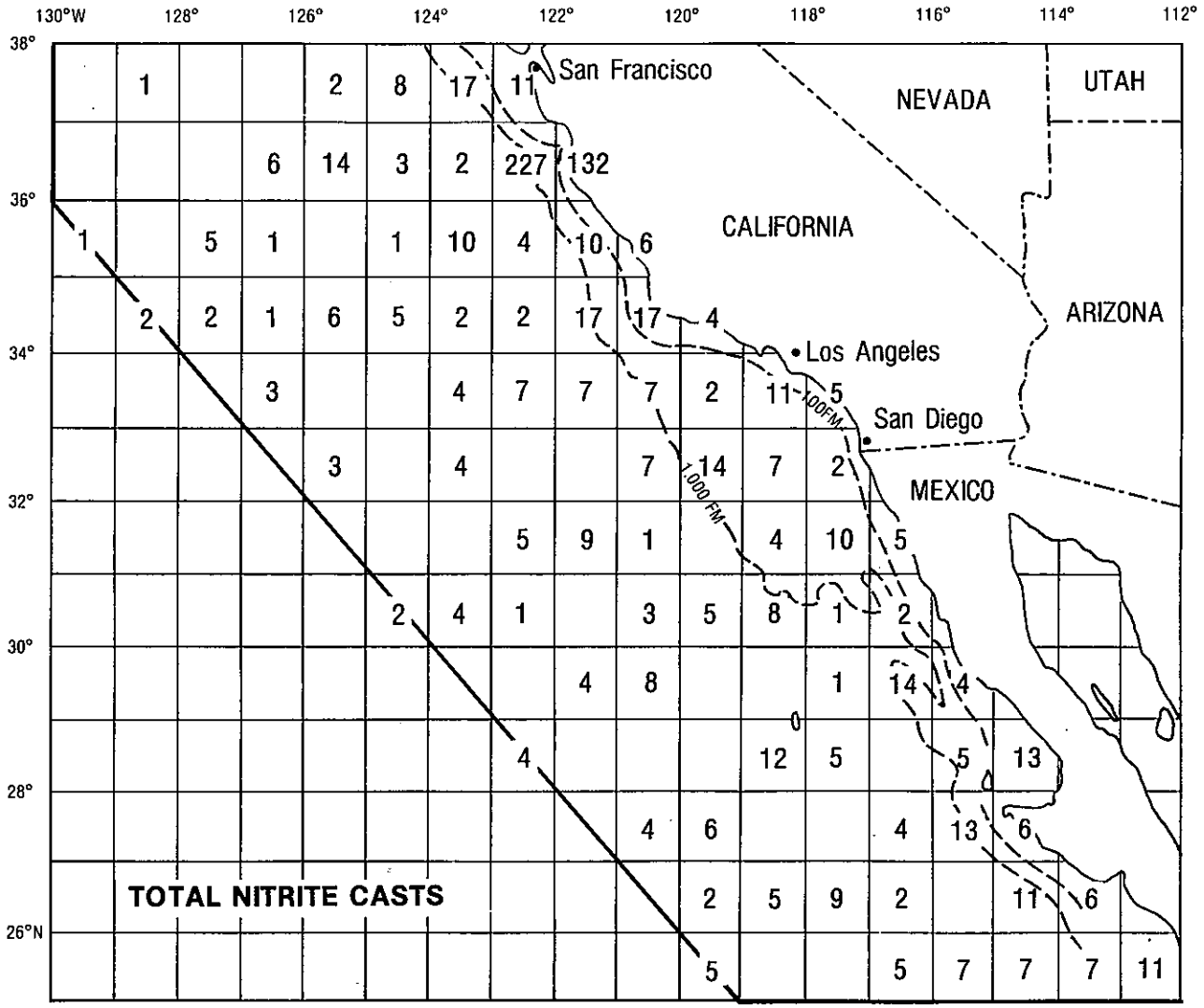

Figure 2.12. The Number of Archived Nitrite Soundings by 1 degree Square (continued)

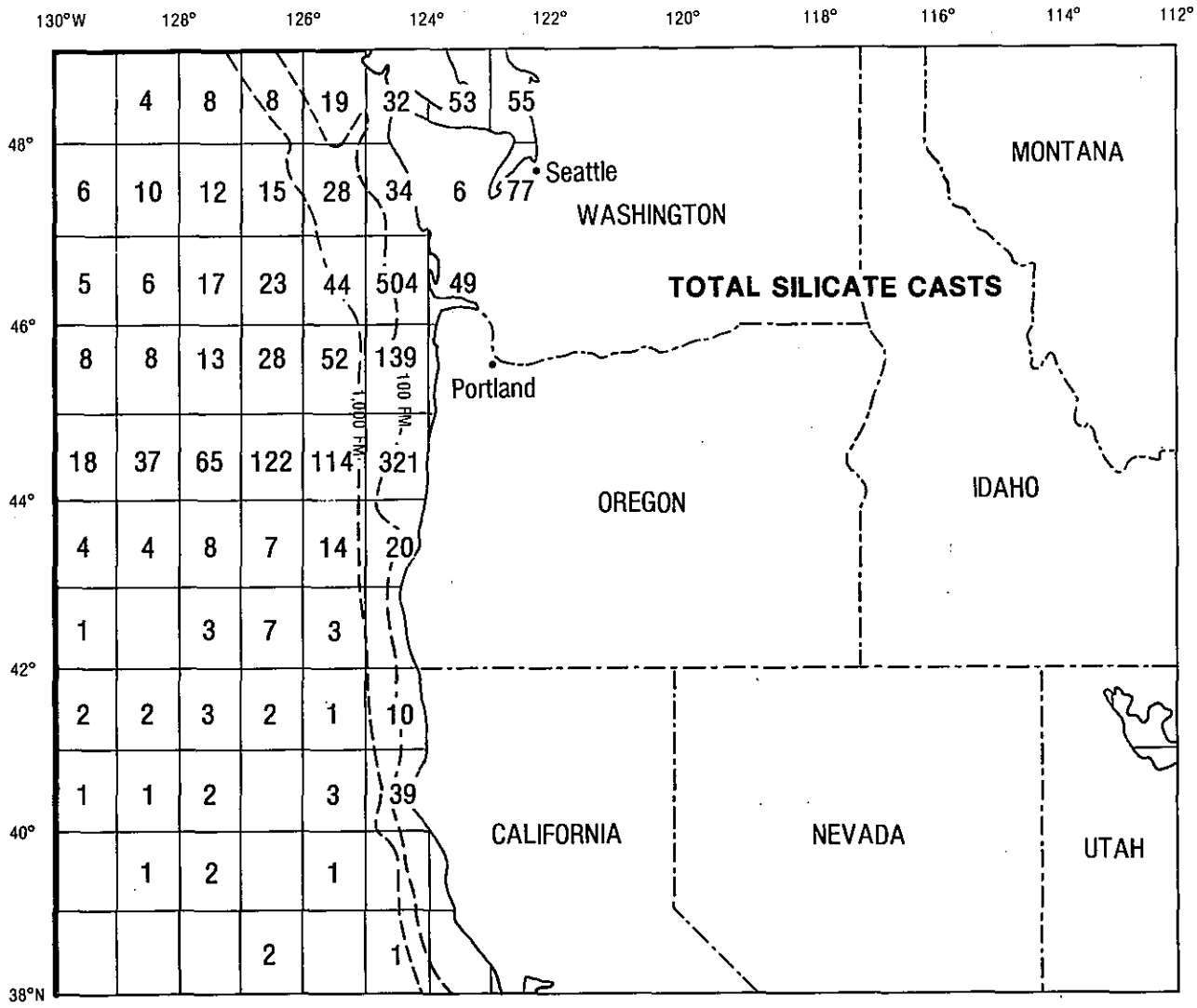

Figure 2.13. The Number of Archived Silicate Soundings by 1 degree Square

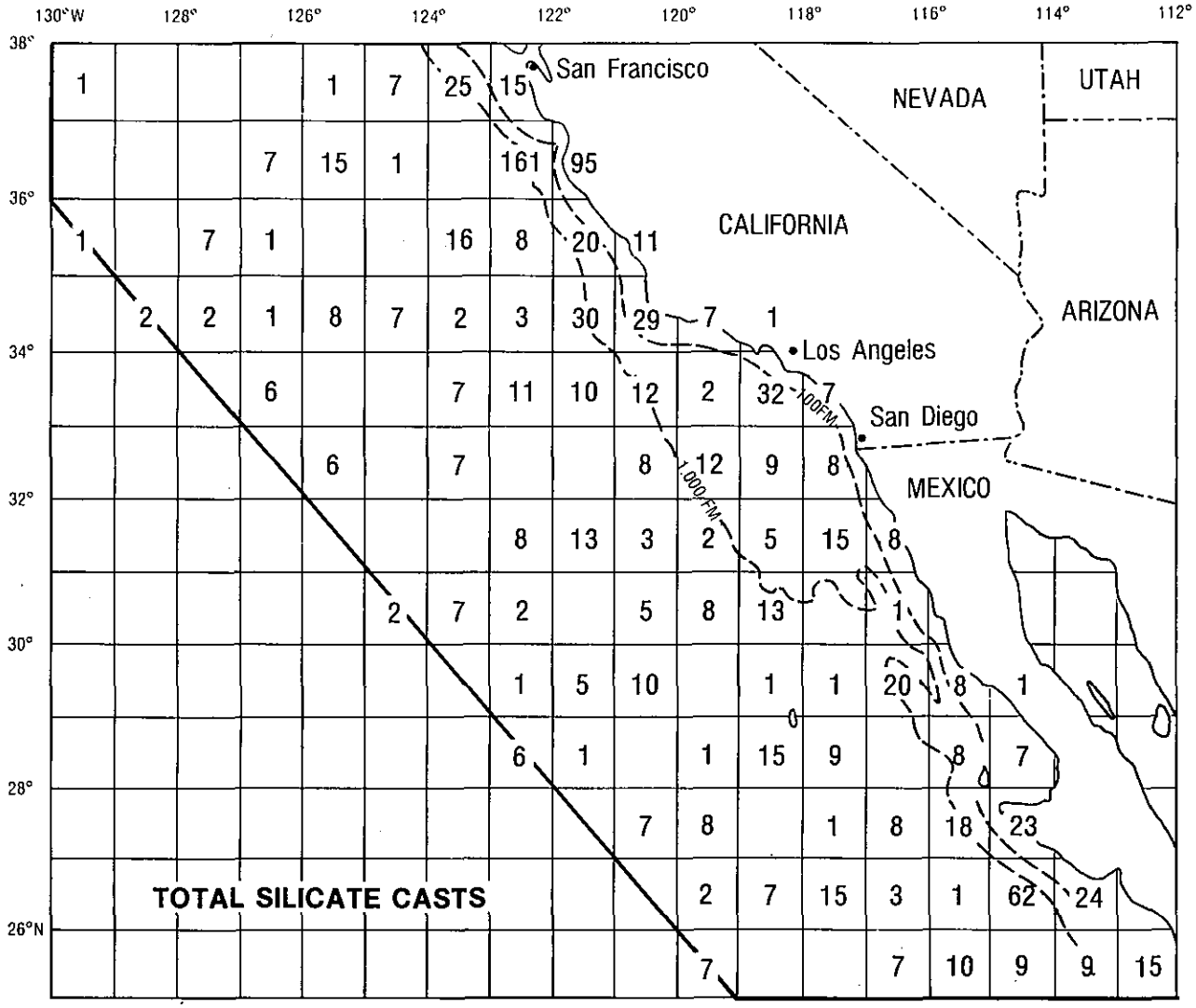

Figure 2.13. The Number of Archived Silicate Soundings by 1 degree Square (continued)

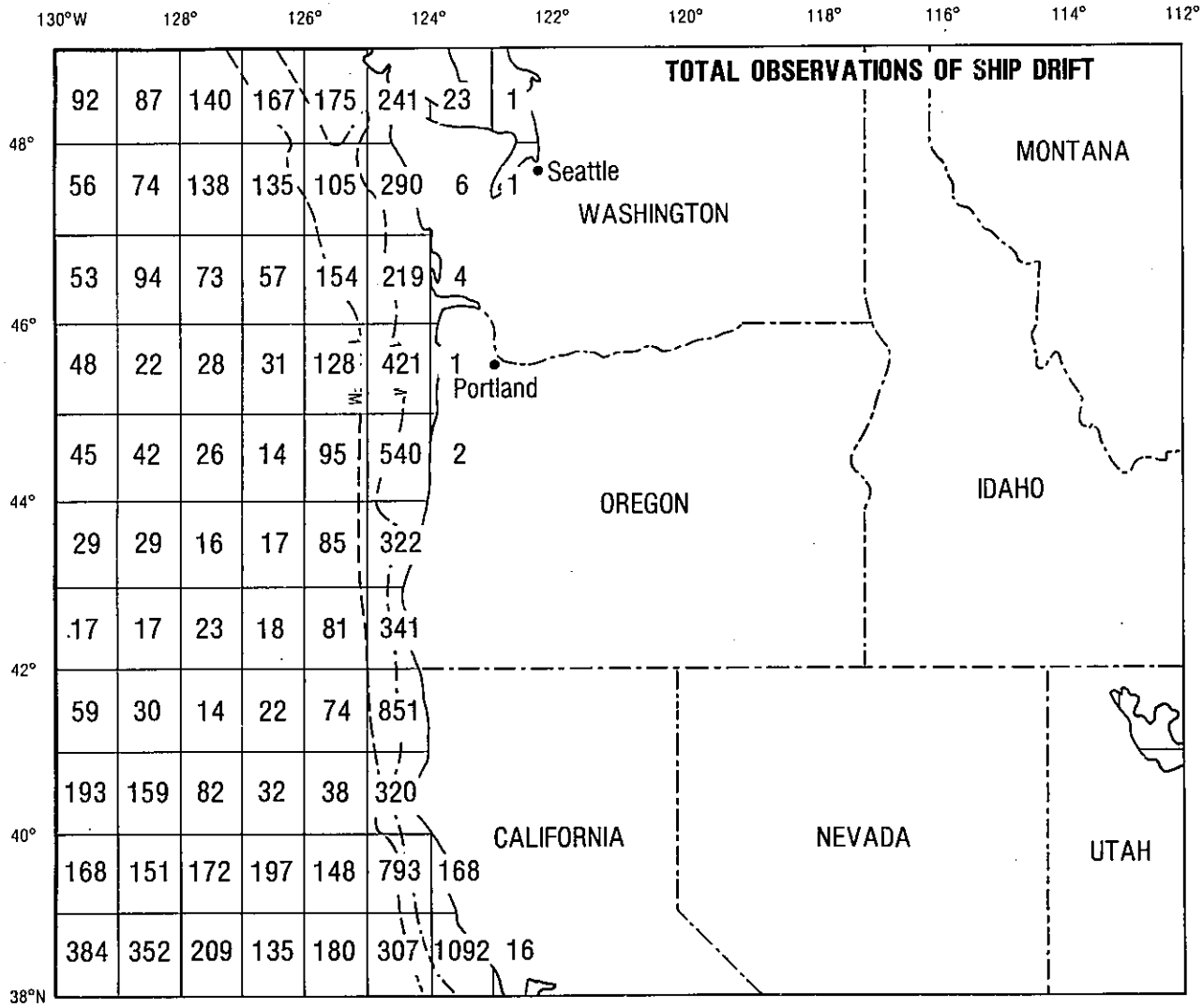

Figure 2.14. The Number of Archived Observations of Surface Current Inferred from Ship-Drift by 1 degree Square

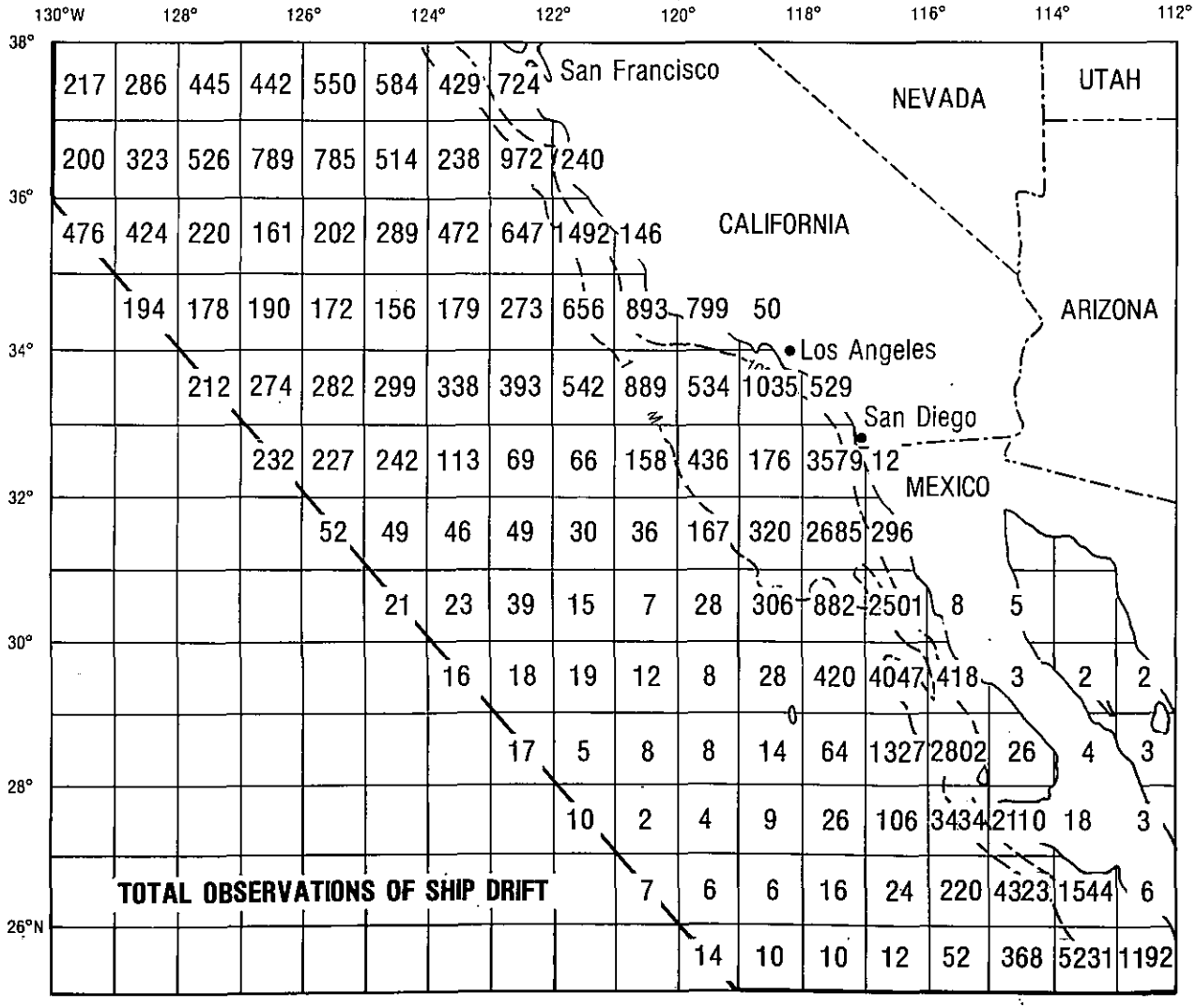

Figure 2.14. The Number of Archived Observations of Surface Current Inferred from Ship-Drift by 1 degree Square (continued)

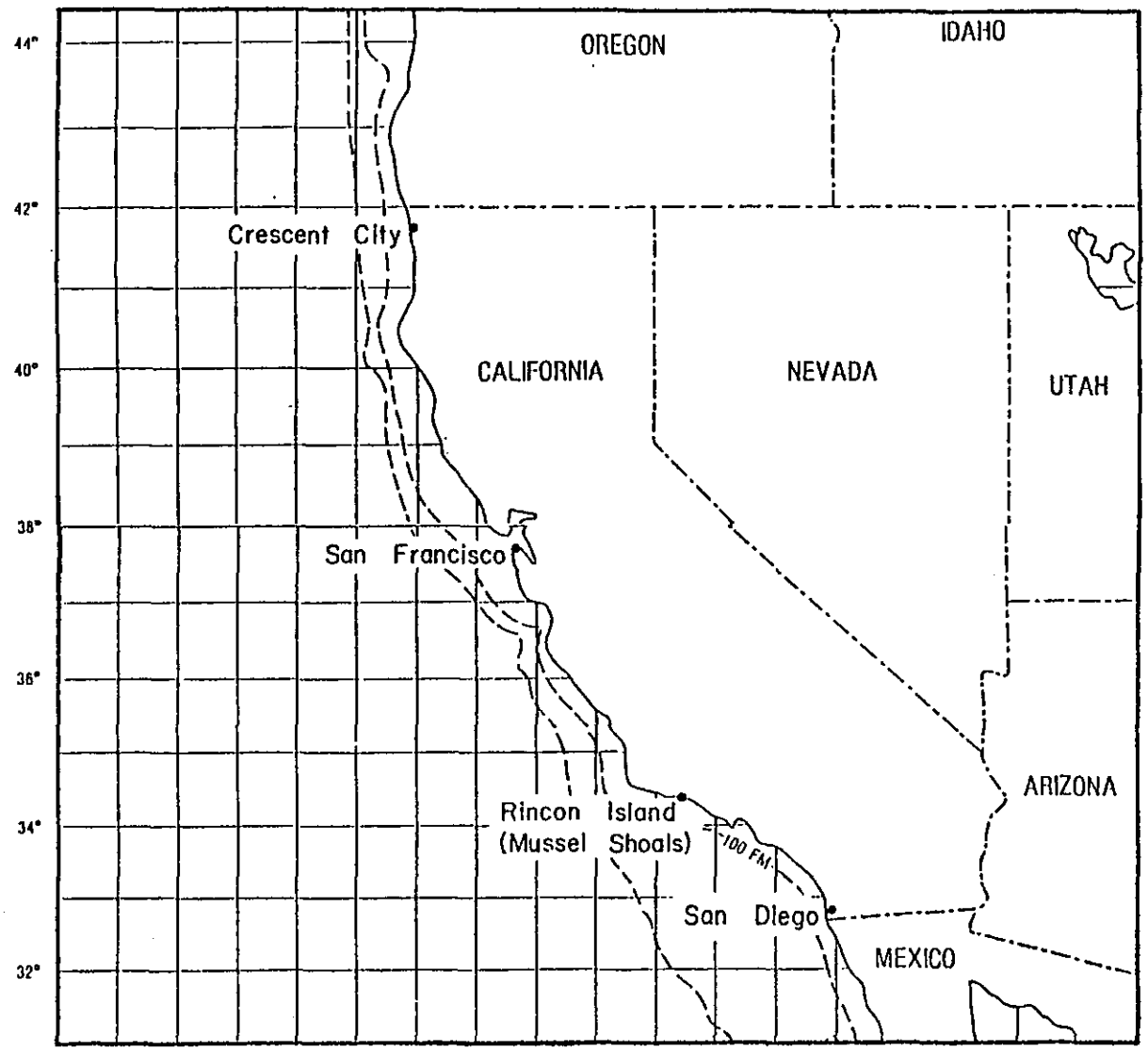

Figure 2.15. Coastal Sea Level Stations

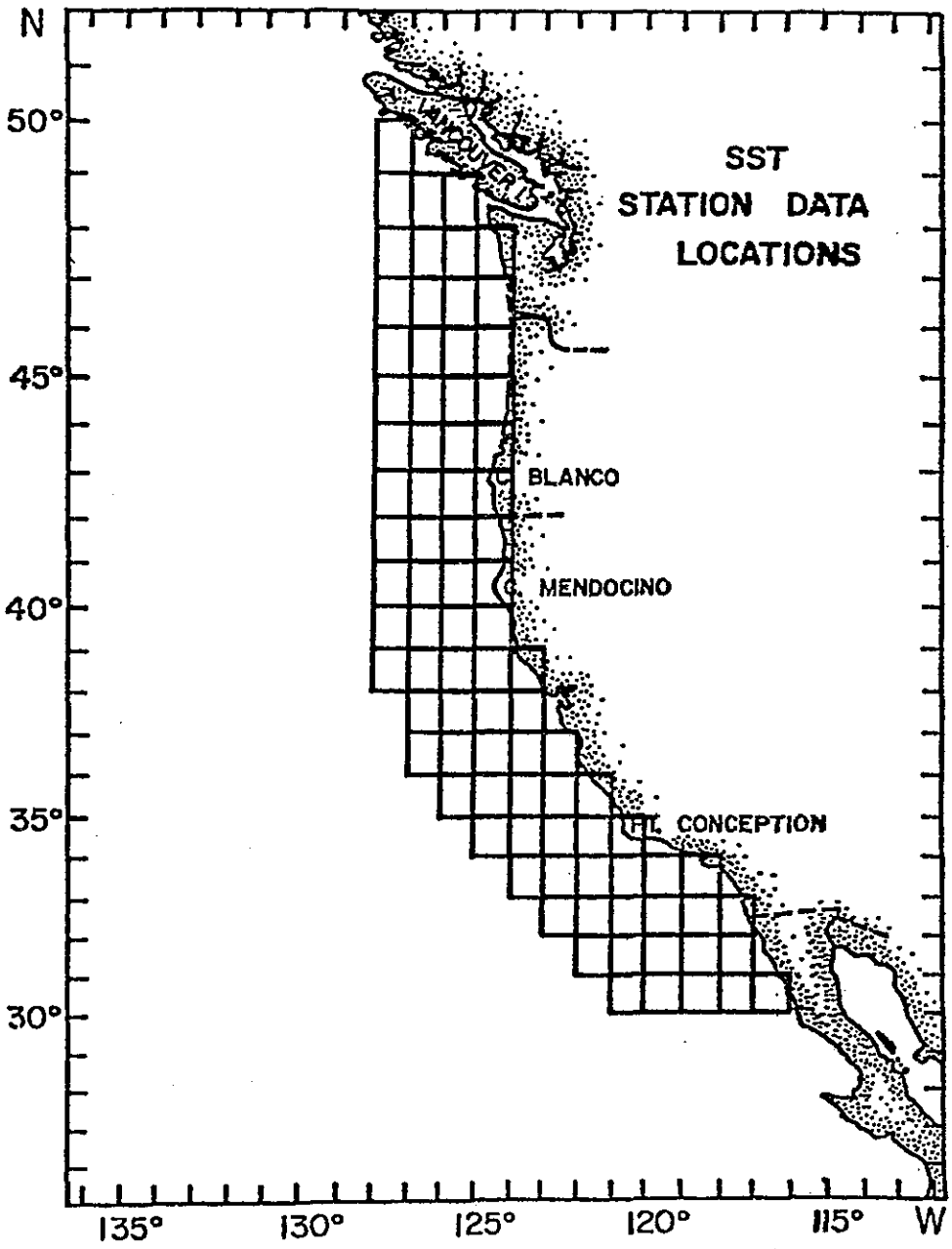

Figure 2.16. The Sea Surface Temperature Grid

3. METEOROLOGY

R. W. Reeves, F. A. Godshall and P. Pytlowany

The transport and dispersion of pollutants in the marine environment depends largely on the atmospheric flow characteristics. Oceanborne pollution is transported by the currents, which are driven by the large-scale surface winds. The large-scale circulation features are determined by the mean pressure pattern, whose orderly migratory behavior allows for easier interpretation of changes in the circulation. The details of the seasonal changes will be discussed in Section 3.1.

The purpose of the meteorological data summaries is to provide background statistics on mean flow characteristics, reductions in visibility, and the probability of occurrence of extreme events.

3.1 SEASONAL VARIATION OF MEAN SURFACE FLOW

The most important feature of the sea-level pressure distribution in the California coastal region is the subtropical anticyclone over the eastern Pacific. The anticyclone is strongest during the summer months and occupies its most northerly position at that time. The center of the anticyclone lies between 30°N and 40°N, and 140°W-150°W. The combination of a strong anticyclone over the Pacific and a semipermanent low over the desert Southwest produces a strong pressure gradient in the vicinity of coastal California with a geostrophic wind from the northwest.

Toward autumn, both the anticyclone and the desert low weaken, thus reducing the geostrophic flow along the coast. The pressure pattern becomes more cellular in structure in the winter with mean centers of high pressure over the continental northwestern United States and the eastern Pacific around 30°N. The mean pressure gradients are considerably weakened during January in the California coastal region. In the spring, the low off the Aleutians weakens and the subtropical Pacific anticyclone gradually becomes a single cell east to west covering the entire Pacific. The pressure gradient then begins to strengthen with the reestablishment of the desert low, and the annual cycle begins anew.

The general surface flow off coastal California can be deduced from the mean surface pressure patterns just described. During the winter, the flow over the open ocean is generally westerly off northern California and northwesterly off southern California. During the spring the speed increases and the mean flow becomes uniform over the entire area; after April the flow is from the northwest in all areas over the open ocean. The mean northwesterly flow continues through summer, with mean speeds as high as 18 knots off the northern California coast. The weakening of the subtropical anticyclone in the autumn leads to a weakening of the flow, with backing to a more westerly flow, especially off the northern coast. See Figures 3.1 through 3.12.

3.1.1 Wind Variability

A measure of wind steadiness (constancy) is the ratio of the magnitude of the vector mean wind speed to the mean scalar speed expressed as a percentage. In the northern part of the study region, steadiness of 10–20% during

winter (Figures 3.1, 3.2) is attributed to passing storms. The large magnitude of steadiness in summer in the northern areas and throughout the year in southern areas is attributed to the influence of the subtropical anticyclones of the central Pacific region.

Steadiness values by themselves reveal only limited information about wind variability. Much more information is obtained from frequency tables of wind direction vs. wind speed plotted in the form of wind roses (Figure 3.35). Wind roses (Attachment) for the midseason months (January, April, July, and October) were constructed for selected coastal and island stations (Attachment, Figures 3.36 through 3.41) and a selection of offshore 1° square areas (Figures 3.42 through 3.48). The wind roses illustrate some of the results obtained from the steadiness information. For example, over the southern areas there is a clear wind direction mode at northwest during the entire year. Over the northern areas, a distinct wind direction mode occurs only during the summer, the prevailing direction being north. During the winter, the influence of passing storms, with their attendant wind shifts, produces a broader distribution about the mode. The prevailing wind is westerly during January. The wind roses for the coastal stations are more complicated and show effects of topography and local circulation. For example, the normal wind direction at Arcata in northern California is southeast to east during January and east wind is most frequent at Imperial Beach. Only during the summer months do most stations possess modal direction from the west to north.

The island station roses are the ones most similar to the open ocean. The normal direction at S.E. Farallon is north to northwest throughout the year, and from the northwest for San Nicolas Island. San Clemente Island possesses a broader mode with maximum frequency evenly distributed among the directions southwest, west, and northwest.

The lack of agreement between coastal stations and those over the open ocean is due to two factors: the influence of local topography and the land-sea breeze.

3.1.2 Wind Stress

A direct consequence of the surface atmospheric wind is the stress produced by the wind on the ocean's surface in the same direction as the wind. The mean stress is along the California coast for much of the year, producing important effects in the coastal region. The southward directed wind stress along the coast produces an offshore transport of water in the upper ocean layer. Subsurface water of lower temperature is brought to the surface to replace that which has been transported away from the coast. This has important consequences in the summer when the diurnal land-sea breeze transports warm moist Pacific air shoreward over the cool water. The result is often a bank of fog in coastal regions. A detailed stress analysis over the California current was performed by Nelson (Reference 2). February and August maps (Figures 3.13 and 3.14) of offshore wind stress vectors illustrate seasonal change in ocean circulation wind forcing. The maximum eastward-directed stress occurs during the summer months when the flow around the subtropical anticyclone is strongest. The maximum values occur at 200-300 km offshore.

3.2 SIGNIFICANT CLIMATOLOGICAL FEATURES

Many of the significant climatological features of the California coastal area can be deduced from the mean pressure or wind patterns. The subtropical anticyclone over the Pacific with its accompanying west to northwest flow in the eastern Pacific suggests that the air arriving at the coast has had a long fetch over water. This gives California a typical maritime climate whose most significant feature is a lack of weather extremes.

The enhanced pressure gradient during summer produces a strong north to northwest flow which drives the California current and draws cool water up to the surface from below. Thus, a band of cool water is maintained off the coast through much of the year.

During summer, the relatively warm moist Pacific air transported over the cold water forms an advection fog which is carried inland when there exists a strong shoreward component of the flow. Heating from below dissipates the fog bank as it is carried inland during the late afternoon. The fog then recedes to the coast during the night.

The rarity of cyclone passages, except for the northern coastal region in winter, reduces the incidence of high winds. Occasionally, tropical storms make their way up the Baja California coast, but their primary effect is a drenching rain rather than damaging winds.

The statistics for S.E. Farallon Isl. help to demonstrate some of the significant features just discussed. During January, a minimum temperature of freezing or below occurs less than 0.1 percent of the time, while the maximum temperature exceeds 65° F only 0.1 percent of the time. During July, the temperature range is narrower, with temperatures below 49° F occurring less than 0.1 percent of the time and observations exceeding 65° F occurring 0.4 percent of the time.

Wind speeds exceeding 33 knots occur about 1 percent of the time in January but less than 0.1 percent during July. Fog occurs 31 percent of the time during July, but only 9 percent during January. Thunderstorms are extremely rare, occurring less than 0.1 percent of the time in July and never in January. The relative humidity is high most of the time, which is typical for a maritime climate. The relative humidity is greater than 90 percent for approximately 2/3 of the observations in January, but for only 83 percent of the observations in July.

3.3 INFLUENCE OF SEA BREEZE

The topographic features of the California coastal region play an important role in the flow characteristics and thus in the transport of atmospheric pollutants. This distribution of land, sea, mountains, valleys, and coastal plains has important local effects on the large-scale flow. During the daytime the land is heated more strongly than the sea, resulting in the creation of flow from sea to land. A diurnal pattern ensues, with a sea breeze occurring during the day and a land breeze occurring at night. A similar effect takes place along the slopes of mountains. The differential heating creates an upslope flow during the day and downslope flow during the night. During the day the differential heating causes a flow of air from sea to coastal plain or basin and up the slopes of the coastal range. At night the flow is reversed, down the slopes and toward the sea. This local, diurnal circulation has a modulating effect on the larger-scale circulation. Thus, a prevailing large-scale onshore flow would be strengthened in the daytime and weakened at night. These effects are indicated by differences in coastal station and offshore 1° summary area wind roses (Figures 3.36-3.48).

The mean wind speeds during summer were somewhat greater than during winter, with the flow generally parallel to the coast during both seasons. Over land, the daytime heating is stronger during summer than winter, producing a stronger sea breeze circulation in summer. This was shown for southern California in Reference 3. The mean streamline pattern for the afternoon (Figure 3.15) shows landward flow across the coastal range. For example, air moving inland over the Los Angeles area is transported over the San Gabriel Mountains to the northeast. The onshore flow can often persist beyond midnight. The offshore flow and downslope winds become organized after midnight when the land has cooled considerably. The island stations still show flow parallel to the coast (Figure 3.16) but with a slight component toward land. Thus, the exact position of the average oceanic extent of the land breeze is not known, but lies somewhere between the coast and about 15 miles offshore. Inland penetration of the sea breeze is stronger than seaward penetration of the land breeze. The reason lies partly in the fact that the mean flow which is parallel to the coast brings cold water to the surface, heightening the temperature contrast between land and sea during the daytime. At night, the coastal land areas may be only slightly cooler than the coastal waters, inhibiting development of the land breeze. Inland, the nocturnal cooling produces a reverse of the daytime mountain-valley

circulation as the cool air drains into the valleys. Thus, there is downslope flow from the San Gabriel Mountains into the San Fernando Valley and Los Angeles Basin. Very often, air which is transported north and east of the industrial areas during the day by a strong sea breeze and upslope circulation remains trapped in the lowlands to the southwest of the San Gabriel Mountains at night. Photochemical pollutants carried inland in southern California from the populated areas have affected the forested areas as far as 75 miles inland (Reference 4).

During the winter when the subtropical anticyclone is weakest, the speed of the prevailing flow is reduced. This leads to a reduction in the upwelling along the coast and thus a reduced cooling at the sea surface. The seasonal land area cooling with reduction in sea surface cooling considerably weakens the land-sea temperature contrast. While there is still a marked diurnal variation in the land temperature, the daytime heating does not produce a strong land-sea temperature difference in winter, and the sea breeze is not fully developed. At night, the strong cooling of the land leads to a marked land breeze which can extend seaward some distance. The mean flow off the southern California coast for nighttime shows that the land breeze can extend 12 miles away from the coast. The data are not plentiful between the islands and the coast, and data from San Clemente and San Nicolas Island yield conflicting evidence as to seaward extent of the land breeze. Santa Catalina Island, about 25 miles from the coast, reports mean flow toward land, but San Clemente Island, which is more than twice as far from the coast, possesses mean easterly (seaward) flow. The wind, however, may be affected by local terrain features. Over land, the valley and canyons which have outlets to the ocean exhibit air drainage to the sea during the night.

3.4 ADVECTION AND DIFFUSION OF OFFSHORE AIR POLLUTANTS

The southern part of the study region is under the influence of the belt of Pacific subtropical anticyclones which are more intense during summer. Subsidence associated with the anticyclones produces a temperature inversion in offshore areas generally based at 300-500 ft. (Reference 5). During summer, cold surface water along the coast increases the atmospheric stability; thus air masses in offshore areas are expected to be more stable than over land areas. Additional stabilizing of the coastal boundary layer can occur after onset of the sea breeze during the daytime when a cool marine layer undercuts the warmer air over land (Reference 6 and 7). The general lack of climatological information about over-water atmospheric stability hinders assessment of diffusion potential for the study region.

A classification of atmospheric stability and measure of the potential for atmospheric diffusion is the Pasquill Stability Index (Reference 8). Index A (a condition with high potential for mixing) through Index F (a low potential for mixing) may be related quantitatively to pollutant dispersion.

The relationships between the stability indices and spreading of a plume of gaseous pollutant are given in Reference 9. Estimates of the indices may be made from routinely available meteorological measurements (Reference 10 and Reference 11). The climatological frequency of the stability indices at several of the coastal meteorological stations in the study region are given in Table 3-1.

Index D is associated with a neutrally stable atmosphere, which implies a lapse rate of 1°C per 100 meters. Table 3.1 shows a higher frequency of these indices at the southern coastal stations than at northern stations.

Stable atmospheric conditions are expected to occur more frequently in offshore areas; therefore in the assessment of diffusion potential in the Pacific Outer Continental Shelf study area, prevailing stable conditions are assumed.

An evaluation of the magnitude of atmospheric diffusion for a *worst case* hypothetical scenario was adopted to illustrate the potential of a coastal impact from offshore release of air pollutants. Dr. Isaac van der Hoven (affiliated with the Air Resources Laboratory of NOAA, Technical Advisor for air pollution analysis) assumed for the worst case, high volume release of pollutants from a *process stack* and a *flare stack* (Reference 6) at a hypothetical release site 3 miles from shore with a direct onshore breeze. Relative mixing under stable conditions over water is assumed with a fumigation process on the shore line.

Table 3.1
Relative Annual Frequency of Pasquill Stability Indexes

	Stability Index					
	A	B	C	D	E	F
Arcata	0.6	4.4	8.1	60.9	7.5	18.4
San Francisco	0.1	5.3	11.7	55.7	12.7	14.4
Vandenberg AFB	0.7	7.2	11.9	22.8	26.7	30.7
Pt. Arguello	0.8	4.1	11.0	27.4	29.9	26.3
Pt. Mugu	0.3	6.9	13.6	21.9	20.6	36.7
Imperial Beach	0.4	9.3	14.8	17.9	22.2	35.3

Tabular results are percentage of meteorological observations associated with indicated Index (calm winds excluded). Index F includes all stabilities greater than E.

$$X/Q = (\sqrt{2\pi}\, u\, (\sigma_y + h/8)\, (h + 2\sigma_z))^{-1}$$

X is the pollutant concentration at the receptor, Q is the released volume, u is the wind speed, h is the virtual stack height (Reference 12), and the vertical and horizontal spreading factors σ_z and σ_y respectively, are estimated for stability conditions E and F. Under varying wind speeds, the relative mixing X/Q, is computed on the surface at the shoreline and these computation results are given in Table 3.2. In consideration of the physical characteristics of pollutant release from a typical *process stack* and a *flare stack* (Reference 6) and ambient winds ranging from 1 to 10 kt, the virtual release heights for the pollutants was calculated to be 118-140 ft. and 106-160 ft. respectively, under stable conditions. These heights are less than the mean height of the subsidence inversion in summer in the southern part of the study region (Reference 5). Therefore, the shoreline mixing ratios would be as presented in Table 3.2. However, lowering of the subsidence inversion may occur and at some time, restrict the virtual height of the pollutant release, which would produce lower mixing ratios at the shore. Unfortunately, no statistics concerning the range of height of the subsidence inversion are available. In northern areas, the restriction of virtual heights may not occur as often because these inversions are not expected to be as frequent or as intense as those in the southern areas.

A general approach to air pollution control for multiple sources may be established on the basis of a pollutant concentrations standard. A common basis is the concentration which is expected to be exceeded less than 1 percent of the time (Reference 13). Therefore, for the purpose of addressing the 1 percent occurrence, hypothetical trajectories of air pollutants were generated from wind climatology using statistical procedures (Reference 14). The geographical position of offshore pollutant sources, from which 12-hour trajectories are expected to carry pollutants onto the coast 1 percent or less of the time, are shown in Figure 3.17. Assuming a stability index F, mixing ratios of about $1{:}5 \times 10^{-8} - 1{:}5 \times 10^{-7}$ were estimated using the measured distance from shore to hypothetical offshore release sites and empirically defined plume spreading constants (Reference 9).

Since the two analyses of the air pollution mixing potential presented here address two different scales of meteorological circulation features, the small potentials are additive. Advection of pollutants over the three mile distance is probably associated with a sea breeze circulation; the offshore sites associated with 1 percent of advection

Table 3.2
Volumetric Mixing Ratios for Offshore
Air Pollutants from Selected Sources

Process Stack		Stability Index
Slightly Stable Atmospheric Conditions		(E)
*Wind Speed	Mixing Ratios	
1	1: 7 X 10^{-6}	
2	1: 3.7 X 10^{-6}	
5	1: 1.5 X 10^{-6}	
10	1: 7.9 X 10^{-7}	
Stable Atmospheric Conditions		(F)
*Wind Speed	Mixing Ratios	
1	1: 1.2 X 10^{-5}	
2	1: 6.4 X 10^{-6}	
5	1: 2.7 X 10^{-6}	
10	1: 1.4 X 10^{-6}	
Flare Stack		
Slightly Stable Atmospheric Conditions		(E)
*Wind Speed	Mixing Ratios	
1	1: 6.5 X 10^{-6}	
2	1: 3.5 X 10^{-6}	
5	1: 1.6 X 10^{-6}	
10	1: 8.4 X 10^{-7}	
Stable Atmospheric Conditions		(F)
*Wind Speed	Mixing Ratios	
1	1: 1.1 X 10^{-5}	
2	1: 6.1 X 10^{-6}	
5	1: 2.8 X 10^{-6}	
10	1: 1.5 X 10^{-6}	

*Wind Speed (kts)

scenarios are probably associated with regional scales of meteorological features. Therefore, for planning purposes, a sea breeze can be assumed to be a daily circulation feature in summer, and mixing potentials (even those associated with subsidence inversion height of half of the normal height) are on the order of $1:1 \times 10^{-5}$. In winter and in northern coastal areas, local sea breeze circulation may not be a daily coastal circulation feature, therefore the *worst pollution case* may be a less frequent event than during summer and in southern areas. Without specific information about local air pollution regulations and location of air pollution release sites, no assessment of the likely violation of coastal air pollution regulations can be made.

3.5 APPLICATION OF CORRECTIONS TO OFFSHORE WINDS

Forecasting the movement of airborne or oceanborne pollutants requires, at the very least, an estimate of the wind over and downwind of the pollution source region. Unfortunately, there are few observations over the open ocean, so one is forced to rely on nearby coastal or island stations for estimates of the wind. Coastal stations are affected by local topographic features as well as by the diurnal land-sea breeze circulation; thus reliable estimates of the flow offshore using coastal winds are not easily obtained. The greater variability of the winds at the coastal stations compared to the offshore areas is a reflection of local topography and the land-sea breeze effects. This is especially noticeable in the summertime patterns.

Although the island station wind statistics are expected to be more representative of the surrounding oceanic area than the coastal stations wind statistics, the wind speeds at the island stations are often less than the speeds over the water areas. This is a common bias between land stations and shipboard stations. When such systematic differences are known to exist between island and ocean wind measurements, then adjustments can be made to the island winds to reflect actual speeds over the ocean. Systematic differences in wind direction are also possible. The subtropical anticyclone is strong during summer and the lack of migrating storms in the summer is reflected in the high steadiness values. The nearly constant flow over the open oceans exhibits a curved pattern typical on the east side of the anticyclone, the flow northwesterly off the northern California coast and northerly off the southern California coast. Thus there are, in the mean, predictable differences in the directions of the flow from region to region over the water. There are three reporting island stations off the California coast: S.E. Farallon, San Clemente, and San Nicolas Islands. S.E. Farrallon and San Nicolas were selected to represent the flow off the northern and southern California coasts, respectively. Mean adjustments to the wind direction and speed were computed for each 1° square area which would give agreement between the 1° squares and the island stations. Maps of these correction factors for the 1° areas off northern California based on S.E. Farrallon and for the 1° areas off southern California based on San Nicolas Island are shown in Figures 3.18 through 3.21 for summer and winter.

3.6 SURFACE AIR TRAJECTORIES

The trajectory is computed as follows: a hypothetical source is selected within a 1° square area. The data from a nearby island station is used and assumed to be applicable to the 1° square area, with approximate adjustment to its speed and direction as determined by mean differences between the island station and the 1° square area. The displacement for a 3-hour period is computed, and a new starting location is determined for the next 3-hour computation. In this manner trajectories were computed for 12-hour periods.

Five locations were selected as possible point sources of air pollution. The wind statistics for S.E. Farallon were found to be most nearly representative of the statistics for the ocean areas off northern California, while San Nicolas Island data were used to represent the flow characteristics off southern California. Based on the corrections discussed in Section 3.5, the time series at San Nicolas Island were used to construct climatological trajectories off southern California, and the time series for S.E. Farallon were used for locations off northern California. The trajectories off the southern California coast for summer and winter display similar characteristics with the main transport to the southeast. Isopleths representing the percentage of trajectories (1, 3, and 10 percent) which pass through a $1^\circ \times 1^\circ$ square area 12 hours after initialization are shown for selected locations (Figures 3.22 and 3.23). The trajectories for the northern areas reflect the greater variability of the wind with its weaker tendency for northwesterly flow.

3.7 VISIBILITY ANALYSIS

The production of advection fog off the California coast was described in Section 3.1. During the summer, the strong flow from the northwest produces the optimum condition for advection fog, with upwelling of cold water beneath the warm, moist air from the anticyclone. This condition is reflected in the visibility statistics: at S.E. Farallon, the visibility is less than 2 n. mi. 24 percent of the time in July as compared to 11 percent in January. Most coastal and island stations reflect the same general behavior, except for southern California when reduction in visibility below 2 n. mi. shows no preference between summer and winter.

The frequency of visibilities below given threshold values for 1° square areas are shown for representative winter and summer months (Figures 3.24 and 3.25). During the summer, the frequency of reduced visibility generally decreases sharply away from the coast, although this trend is not as dramatic off the northern California coast. Reduction in visibility in southern areas, to less than 2 n. mi. occurs 1 – 2 percent in some areas. The frequency of reduced visibility is generally higher for coastal and island stations.

During the winter, there does not appear to be a systematic trend away from the coast or with latitude. The frequency of visibilities below 2 n. mi. is generally 10 – 15 percent off both southern and northern coasts.

For extremely dense fog (visibilities less than 1/2 mile), San Nicolas Island reports greatest frequency for the periods around sunrise during the summer months.

3.8 EXTREME WIND SPEED ANALYSIS

The more-or-less continuous record of observations from S.E. Farallon yielded a reliable data set from which to estimate the return period of gale force winds ($>$ 34 knots). The data suggest a higher probability of gale conditions in the winter, a condition expected by the more frequent passage of midlatitude storms. During winter there is about a 90 percent probability that an occurrence of gale winds will be followed by a similar occurrence within 48 days. For summer this probability drops to about 25 percent. Statistics for Pt. Arguello reveal the same trend from winter to summer, but with too few occurrences of gales in June and July to compute a reliable return period. During winter, the probability averages around 75 percent for return periods of less than 48 days.

REFERENCES

1. Crutcher, H.L. and J.M. Meserve, 1970. Selected Level Heights, Temperatures, and Dew Points for the Northern Hemisphere. NAVAIR 50-1C-52, Commander, Naval Weather Service Command.

2. Nelson, C.S., 1977. Wind Stress and Wind Stress Curl over the California Current, NOAA Tech. Rept. NMFS SSRF-714, U.S. Department of Commerce, NOAA, NMFS, 87 pp.

3. DeMarrais, G.A., G.C. Holzworth and C.D. Hosler, 1965. Meteorological summaries pertinent to atmospheric transport and dispersion over Southern California, U.S. Weather Bureau Technical Paper No. 54, Washington, D.C.

4. Edinger, J.G., M.H. McCutchan, P.R. Miller, B.C. Ryan, M.J. Schroeder and J.V. Behar, 1972. Penetration and Duration of Oxidant Air Pollution in the South Coast Air Basin of California. Journal of the Air Pollution Control Association 22, pp. 882–886.

5. Neiburger, M., D.J. Johnson and Chen Wu Chien, 1961. Studies of the Structure of the Atmosphere over the Eastern Pacific Ocean in Summer, 1, The Inversion of the Eastern North Pacific Ocean, UCLA Publication in Meteorology (Chap. 4).

6. AeroVironment Inc., 1977. Air Quality Analysis of the Southern California Bight in Relation to Potential Impact of Offshore Oil and Gas Development. Final Report to the Bureau of Land Management (Contract No. AA550-CT7-18), Pasadena, CA., Unpublished.

7. Angell, J.K., C.R. Dickson, and W.H. Hoecker, Jr., 1974. Relative Dispersion Within the Los Angeles Basin as Estimated from Tetroon Trials, Technical Memorandum NOAA TM ERL ARL-46, Silver Spring, MD, 34 pp.

8. Pasquill, F., 1961. The Estimation of the Dispersion of Windborne Material, Meteor. Mag. 90; **1063**, pp. 33–49.

9. Turner, B.D., 1969. Workbook of Atmospheric Dispersion Estimates, U.S. Department of Health, Education, and Welfare, National Air Pollution Control Administration, Cincinnati, Ohio, 84 pp.

10. Gifford, F.A., 1961. Use of Routine Meteorological Observation for Estimating Atmospheric Dispersion, Nuclear Safety, **2 (4)**, pp. 47–51.

11. Doty, S.R., B.L. Wallace and G.C. Holzworth, 1976. A Climatological Analysis of Pasquill Stability Categories Based on "STAR" summaries, National Climatic Center, NOAA, Asheville, NC, 51 pp.

12. Briggs, G.A., 1965. A Plume Rise Model Compared with Observation, Journal of the Air Pollution Control Association (15), pp. 433–438.

13. Schueneman, J.J., 1968. Air Pollution Control Administration, Air Pollution, A.C. Stern ed., Vol. 3, Chap. 52, Academic Press, New York, pp. 719–793.

14. Williams, R.G. and F.A. Godshall, 1977. Summarization and interpretation of historical physical oceanographic and meteorological information for the Mid-Atlantic region, Final Report to the Bureau of Land Management, U.S. Department of Commerce, National Oceanic and Atmospheric Administration, Washington, D.C., 295 pp.

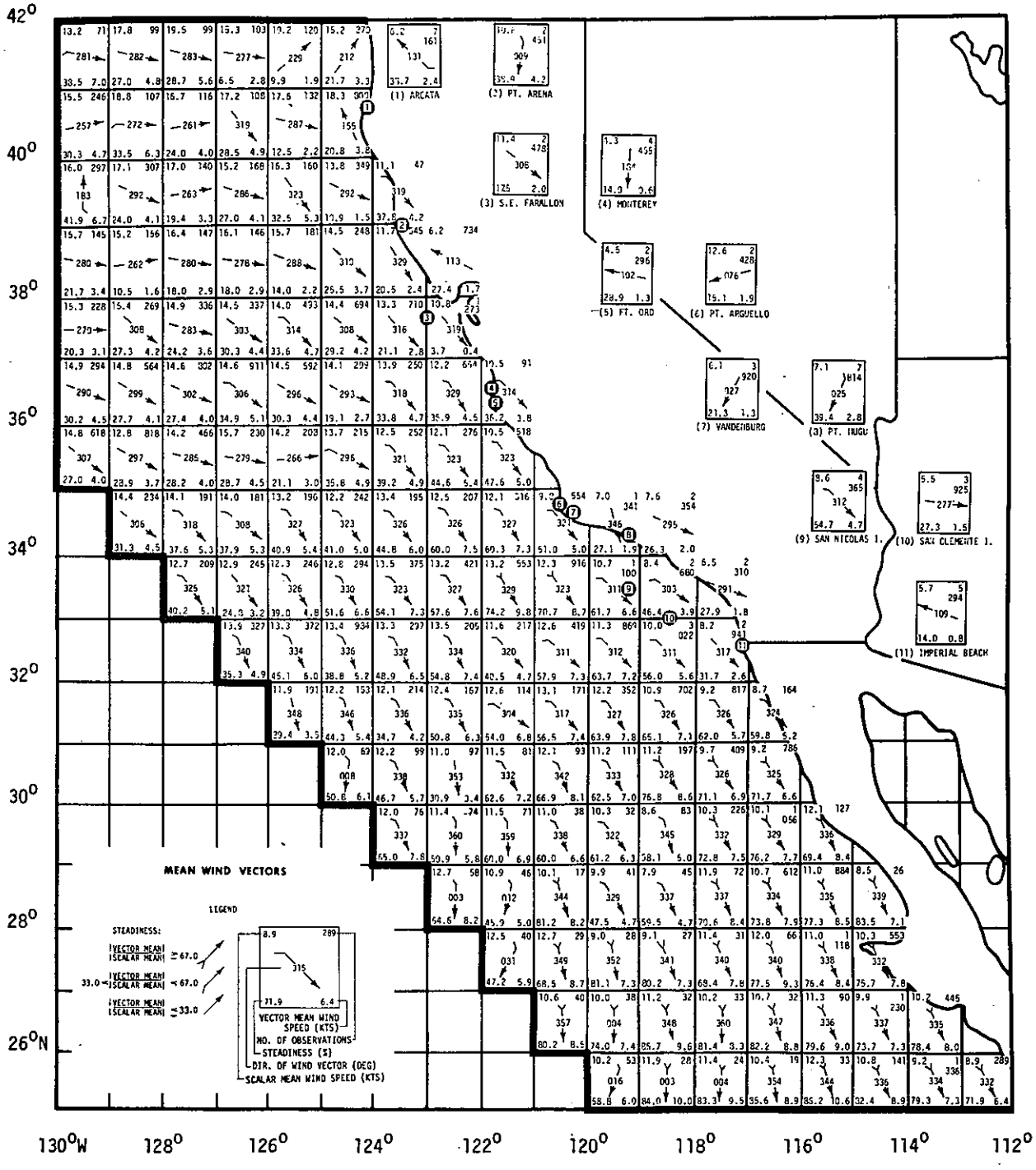

Figure 3.1. Monthly Mean Wind Vectors for January

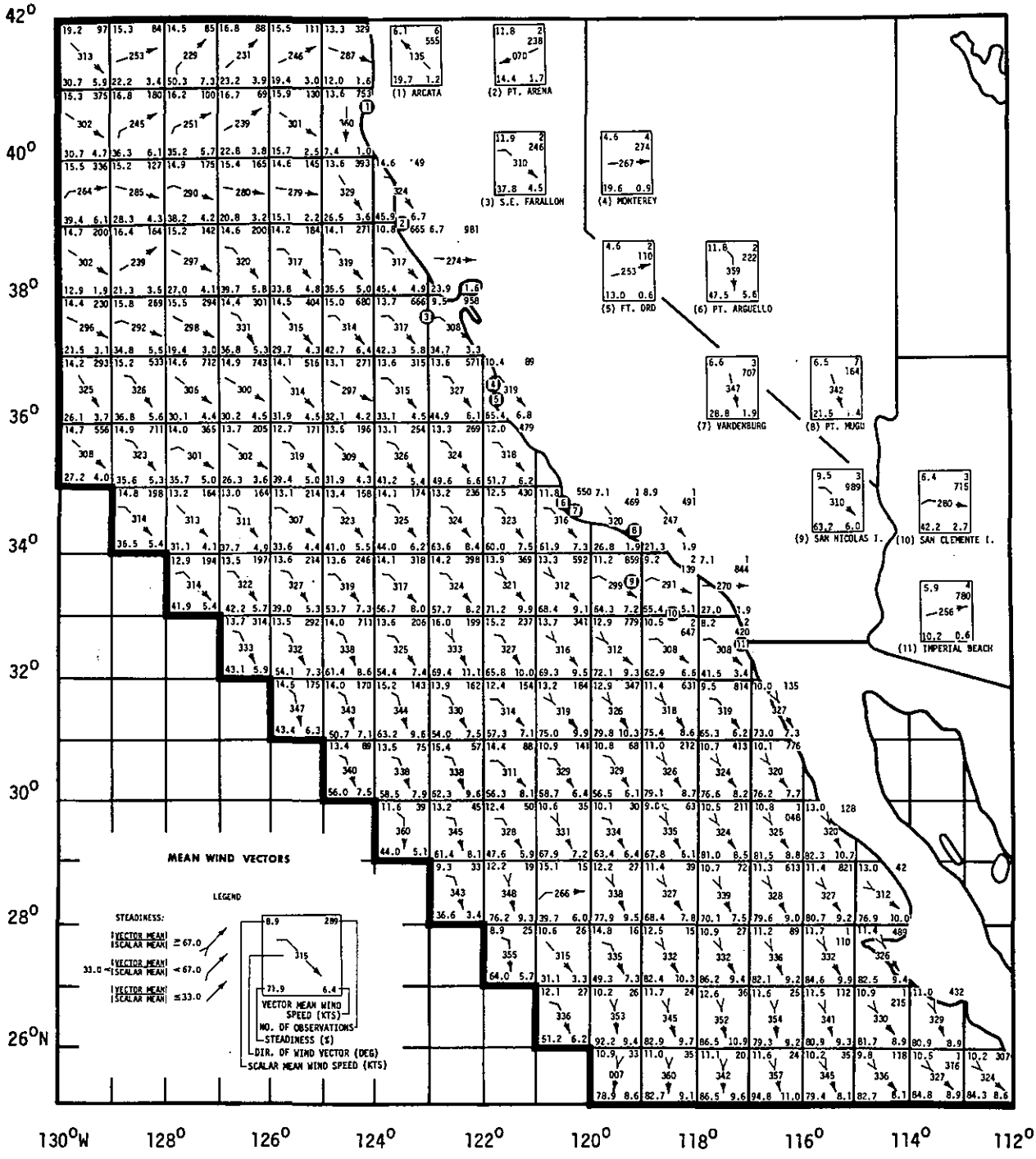

Figure 3.2. Monthly Mean Wind Vectors for February

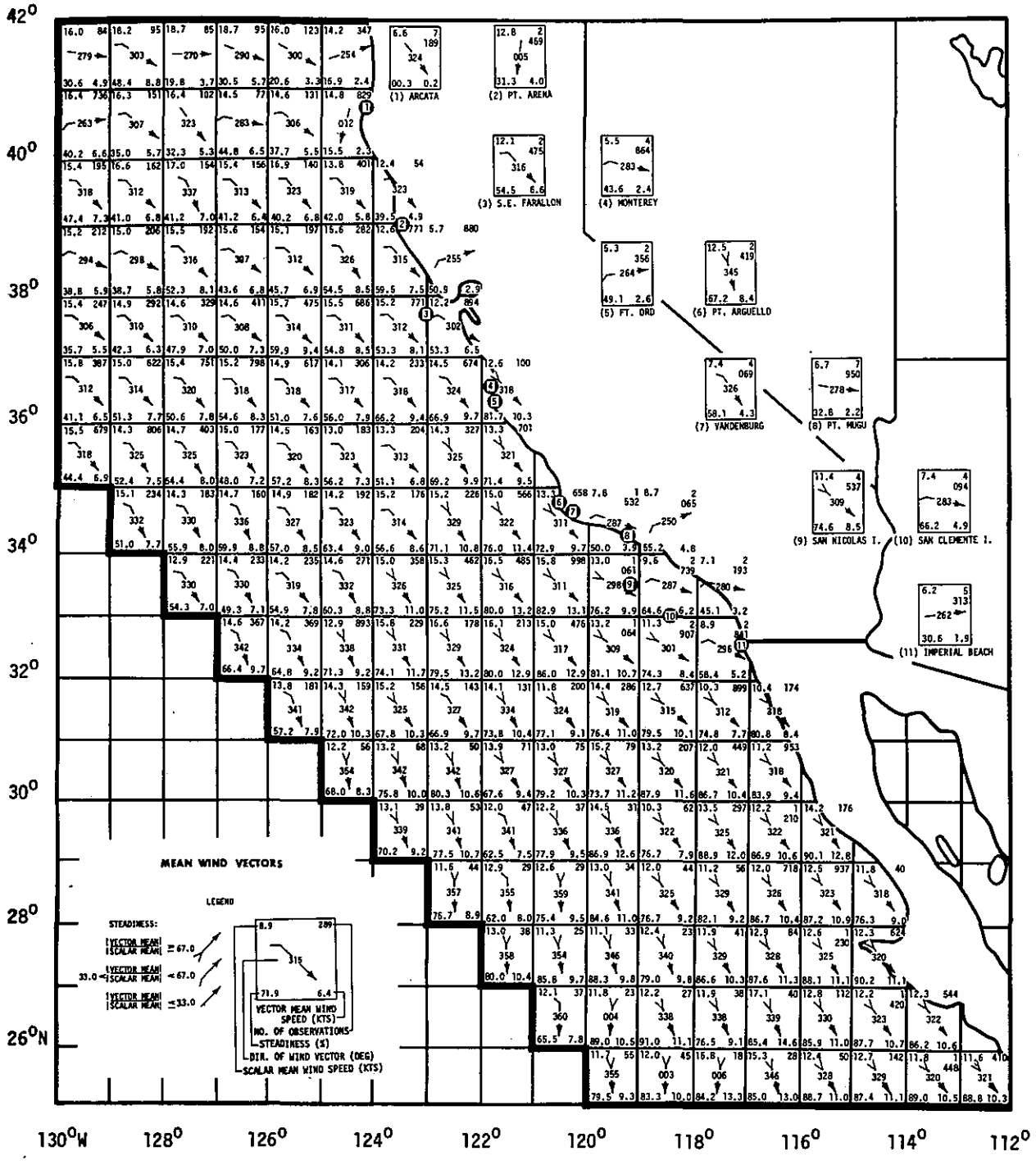

Figure 3.3. Monthly Mean Wind Vectors for March

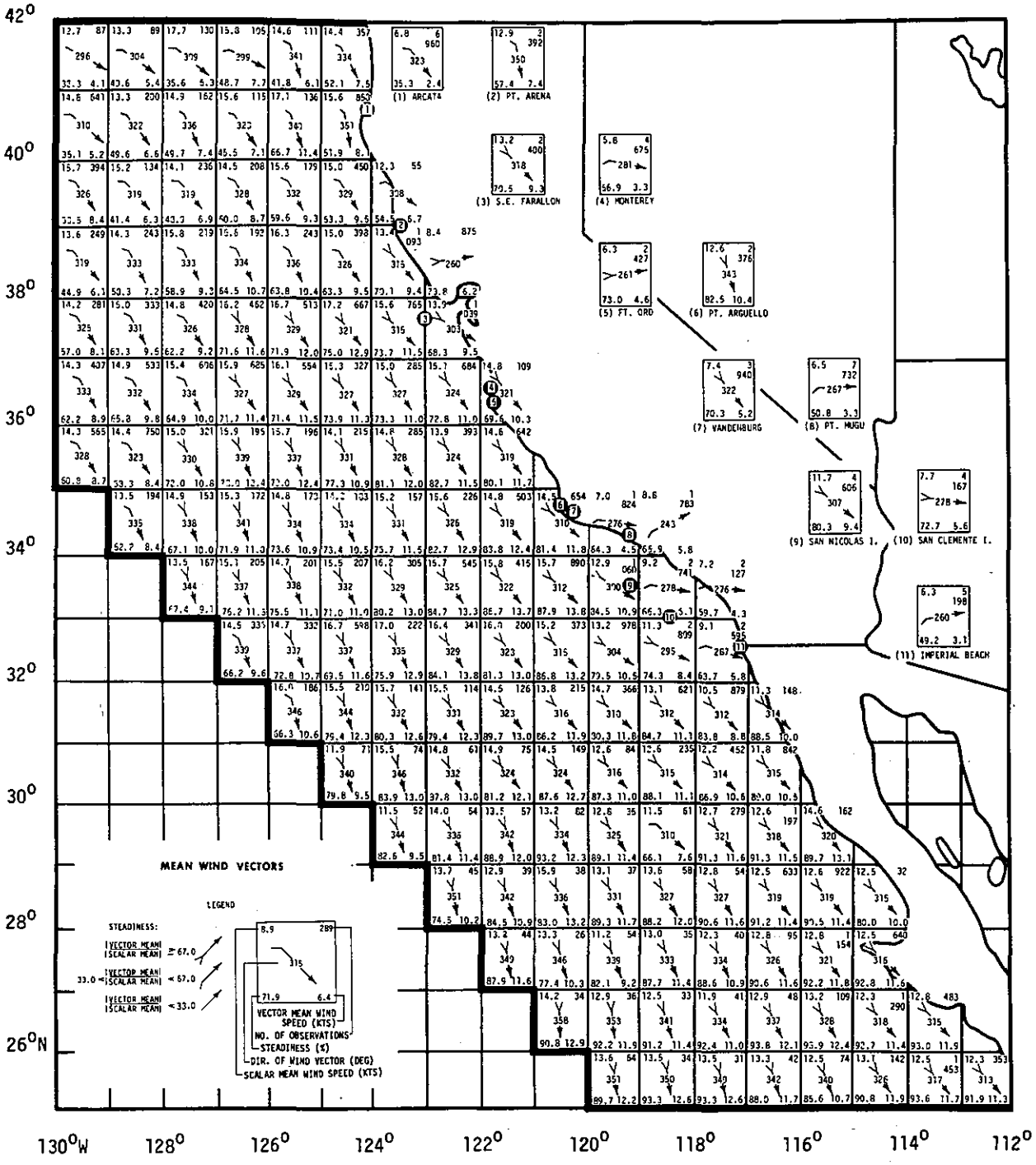

Figure 3.4. Monthly Mean Wind Vectors for April

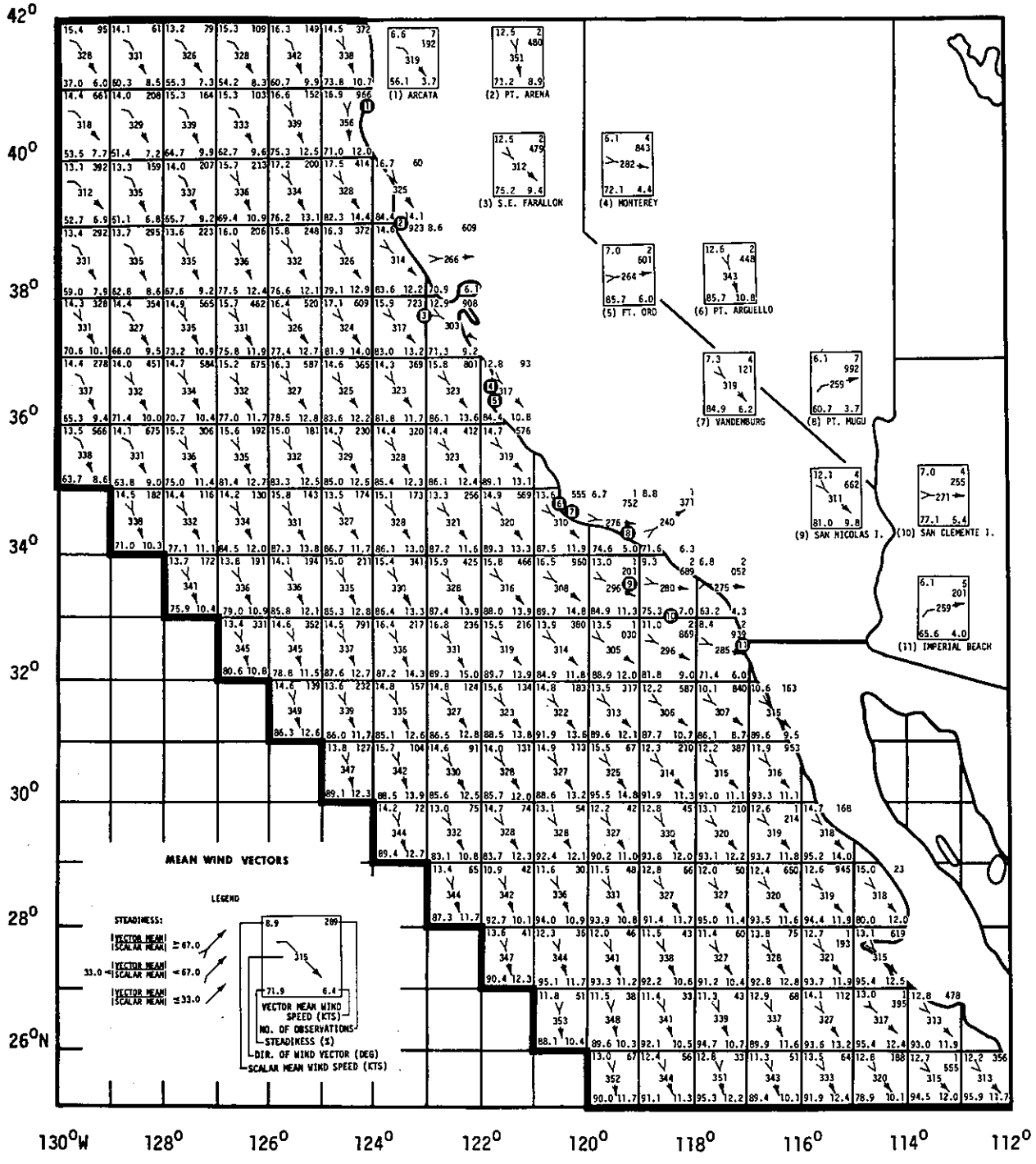

Figure 3.5. Monthly Mean Wind Vectors for May

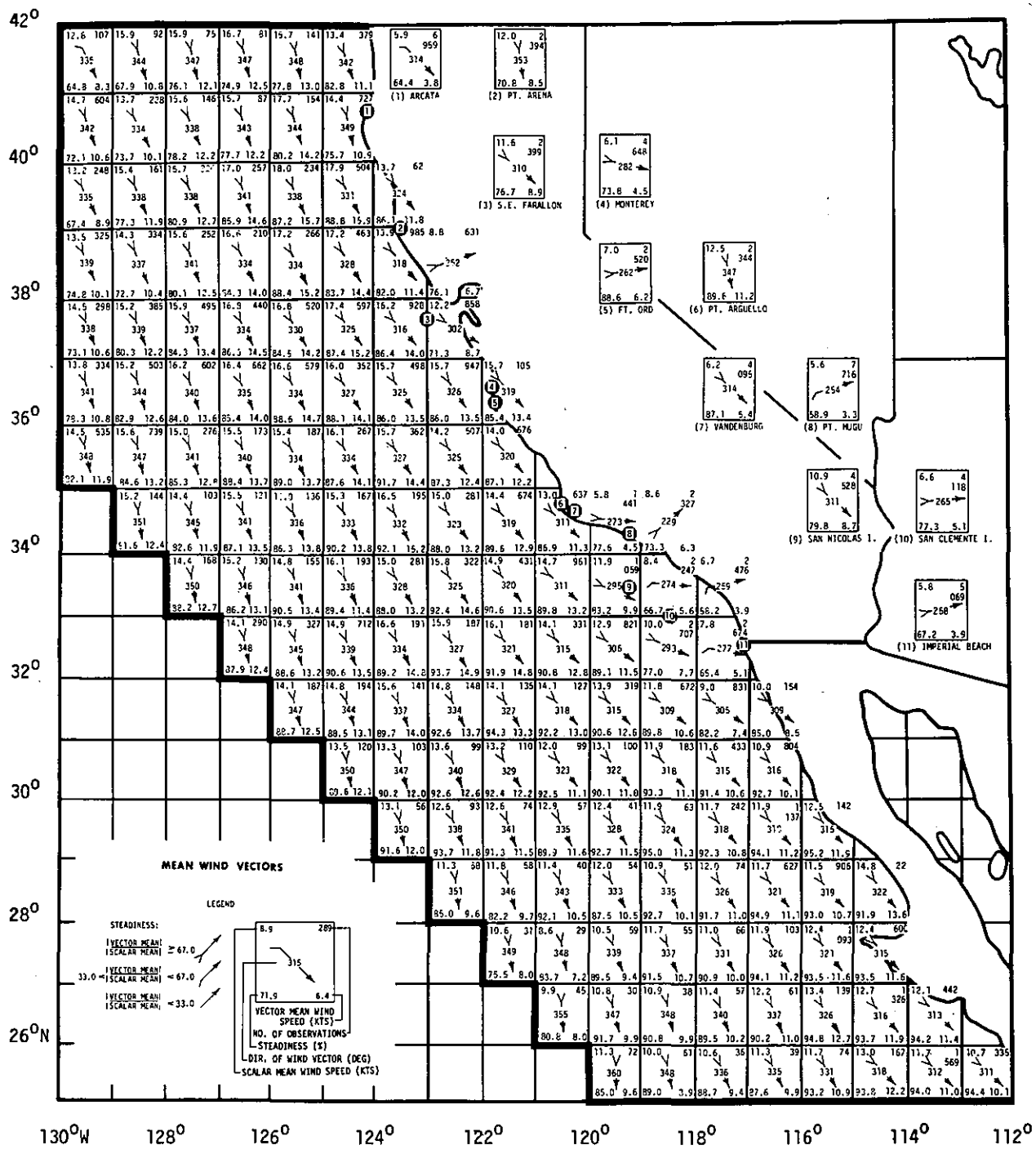

Figure 3.6. Monthly Mean Wind Vectors for June

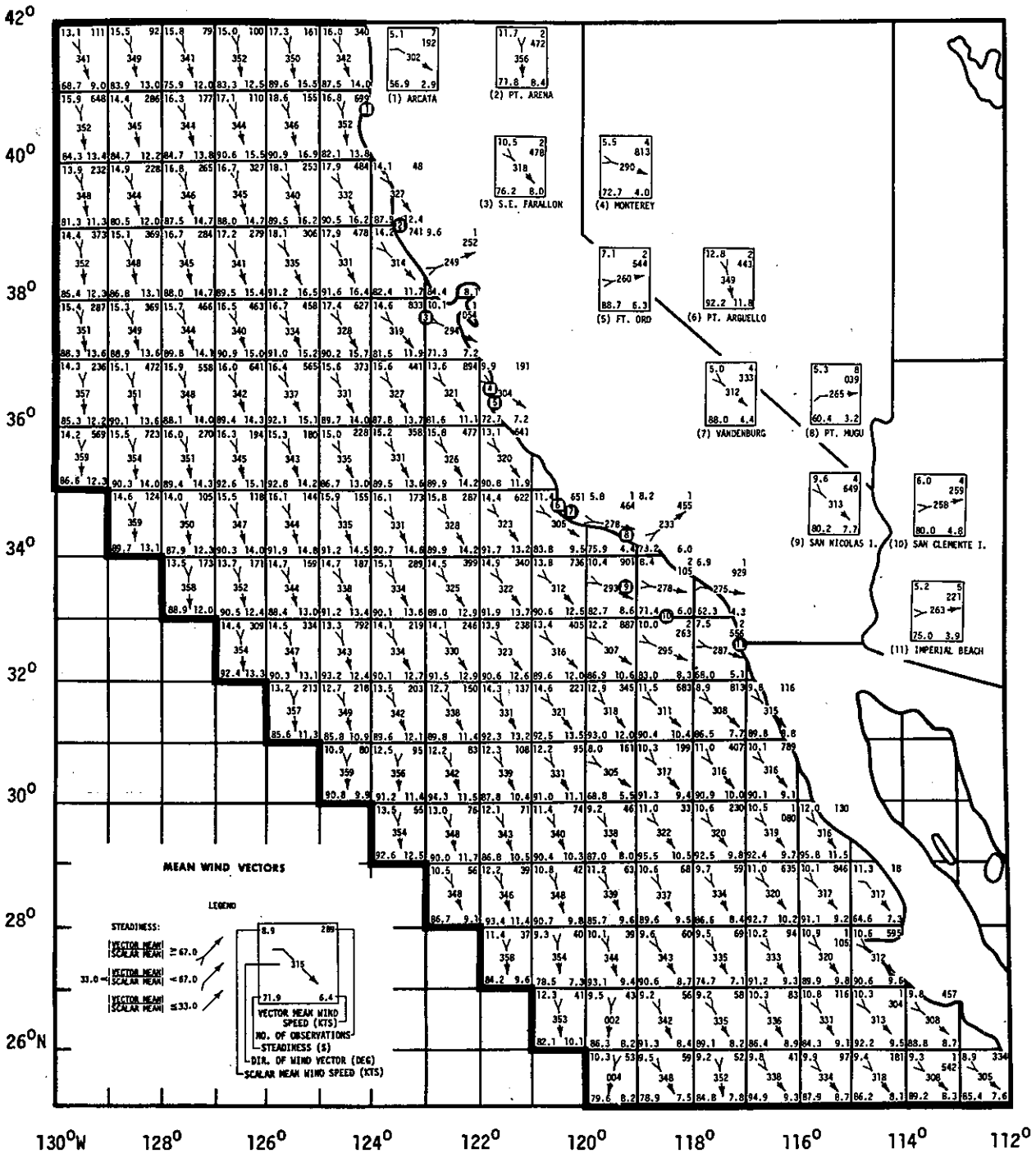

Figure 3.7. Monthly Mean Wind Vectors for July

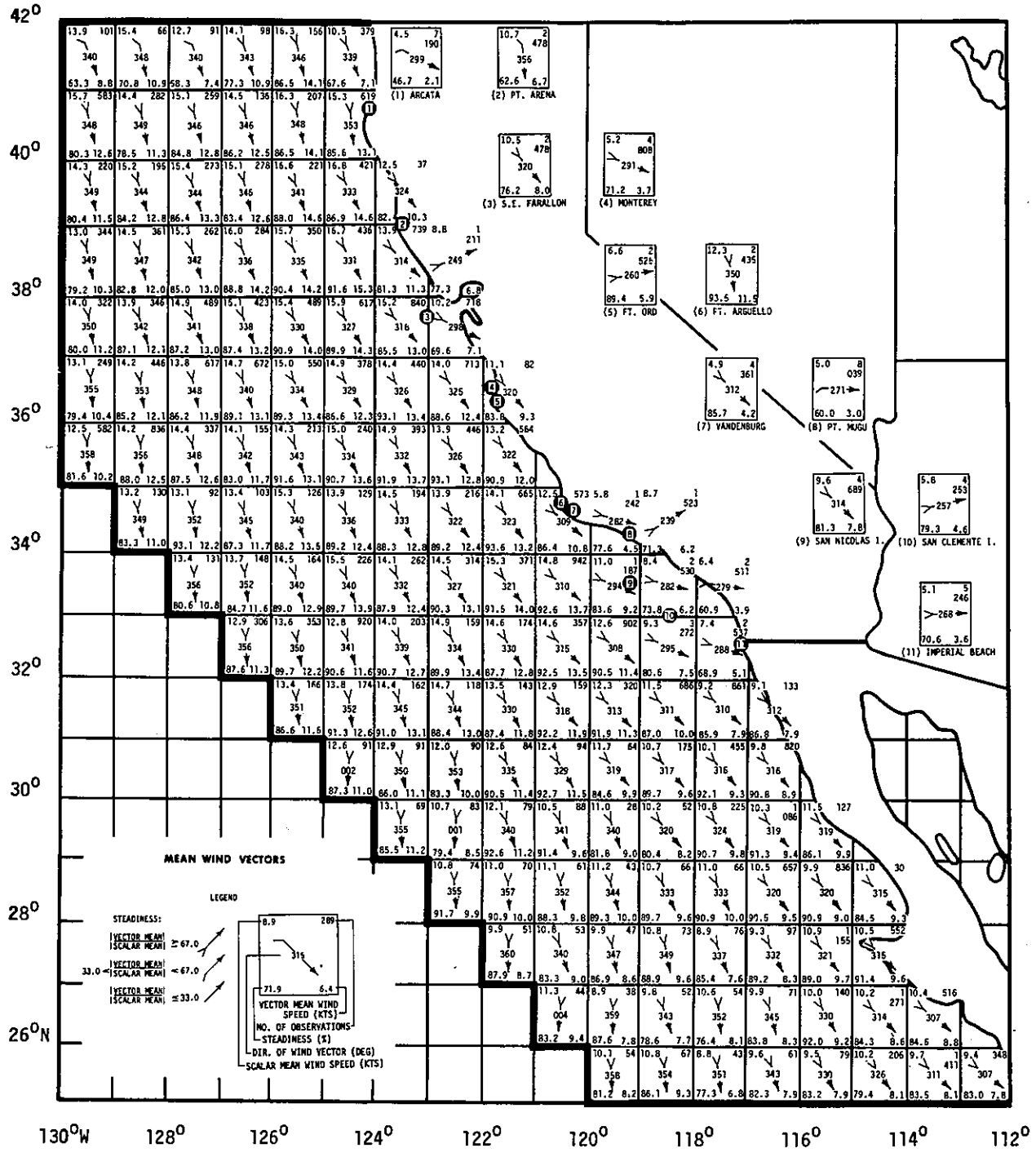

Figure 3.8. Monthly Mean Wind Vectors for August

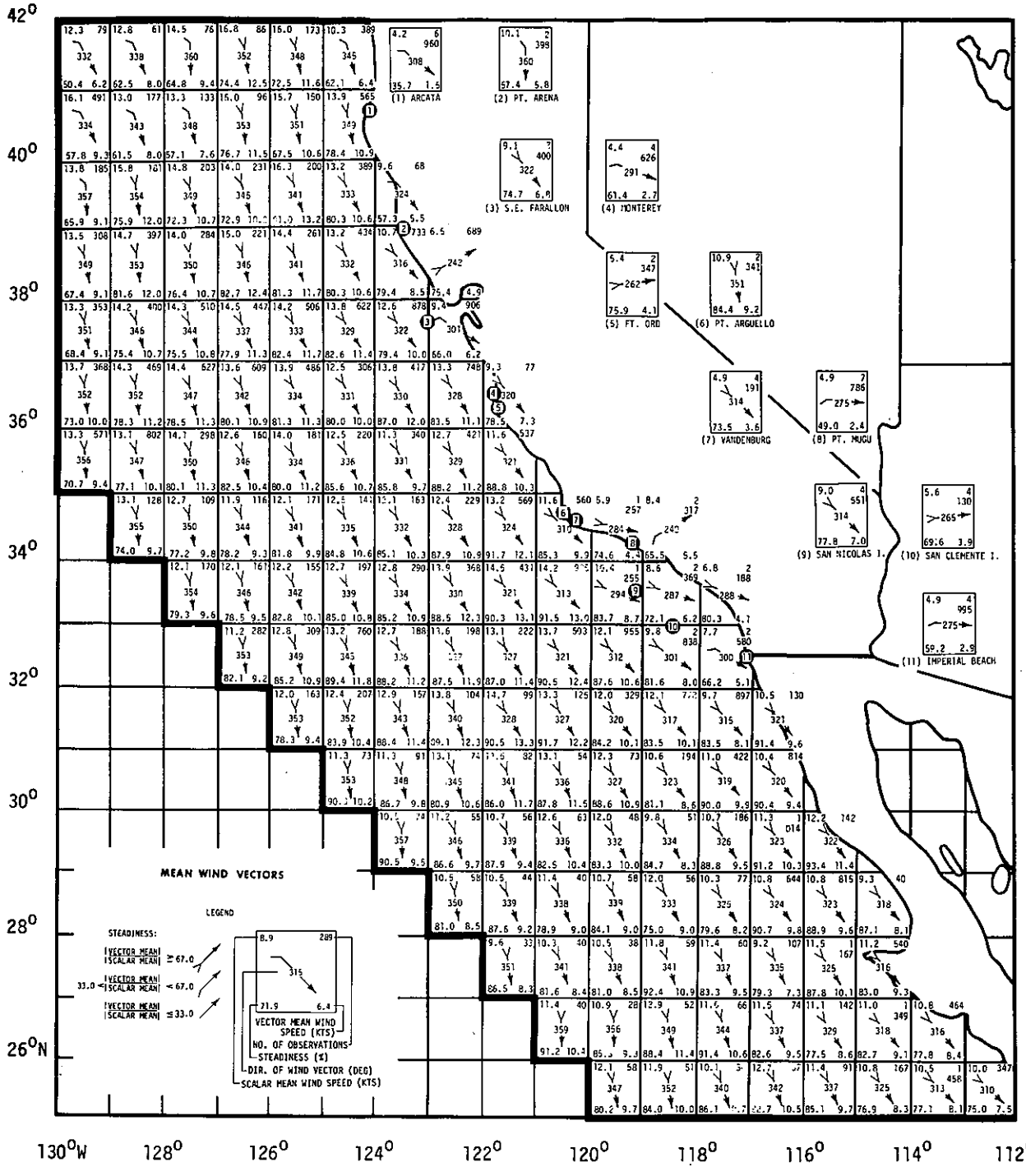

Figure 3.9. Monthly Mean Wind Vectors for September

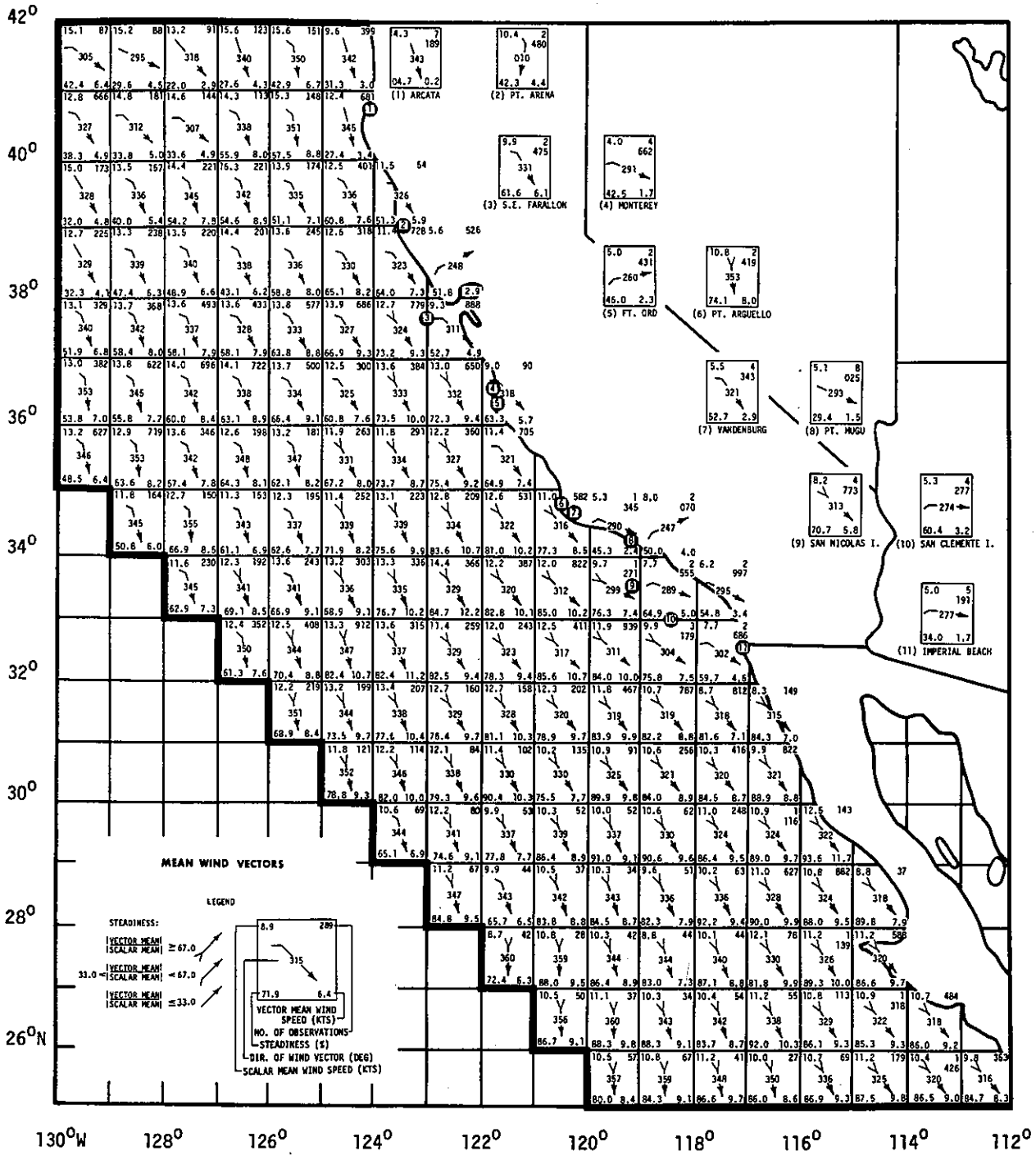

Figure 3.10. Monthly Mean Wind Vectors for October

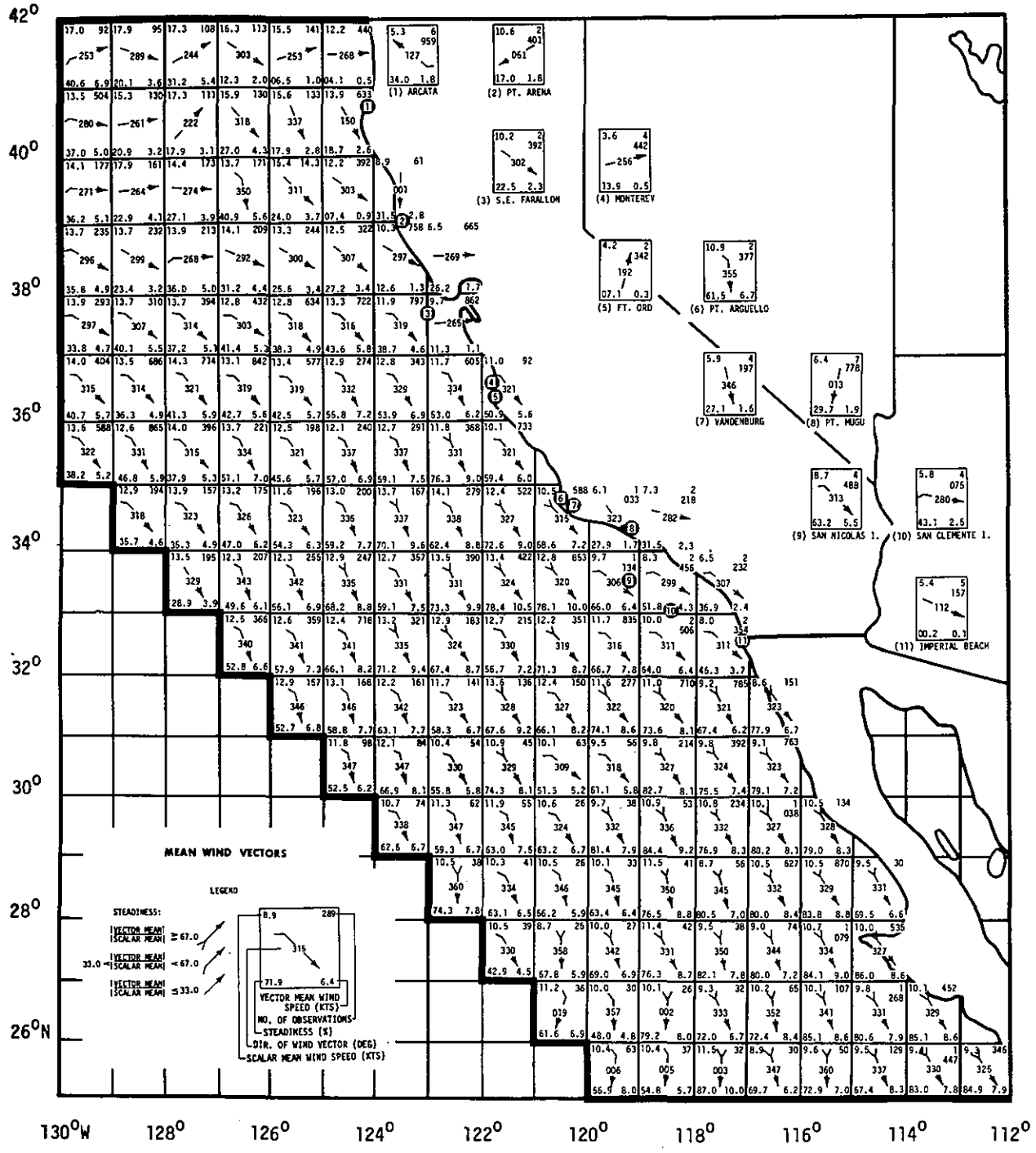

Figure 3.11. Monthly Mean Wind Vectors for November

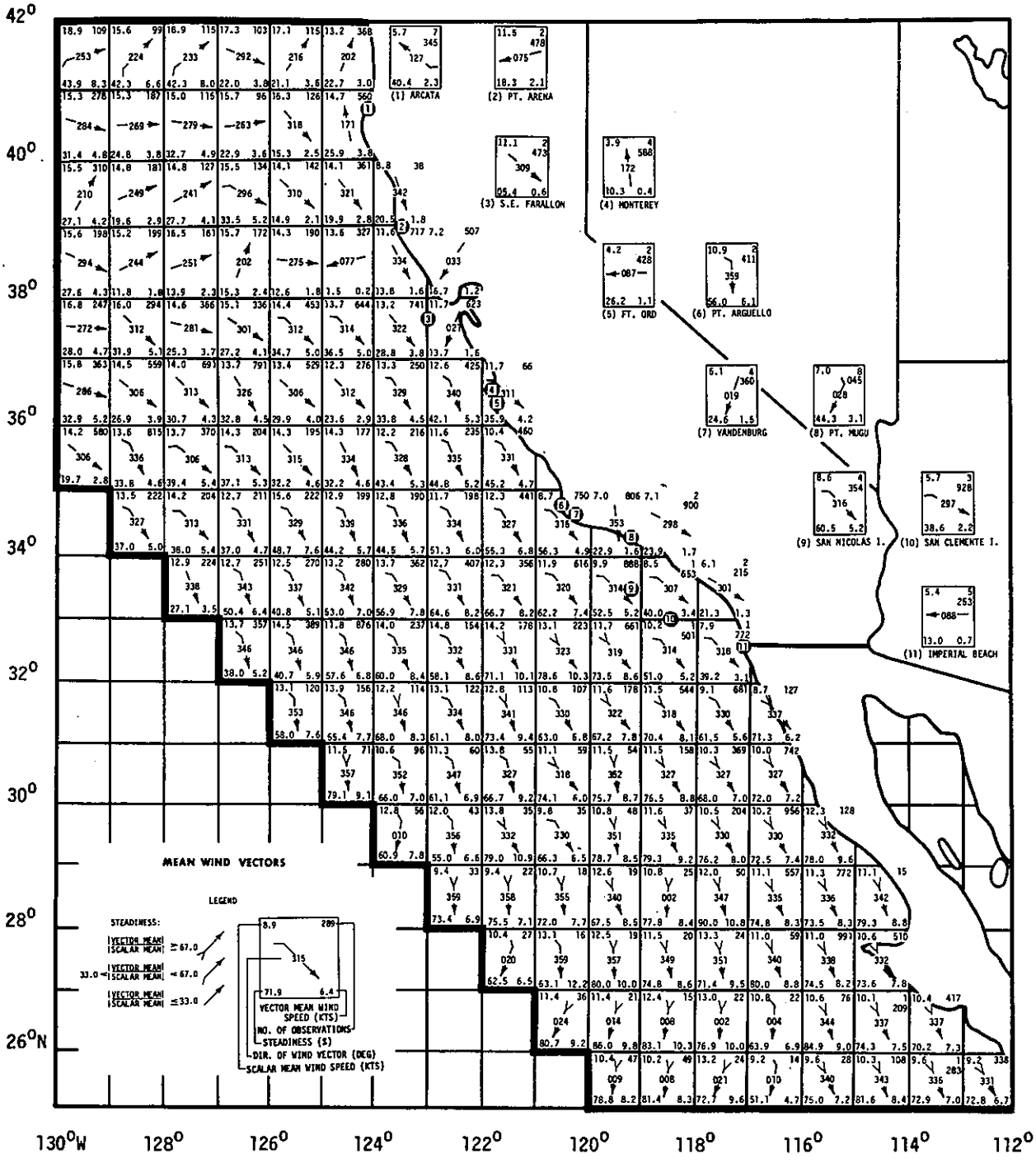

Figure 3.12. Monthly Mean Wind Vectors for December

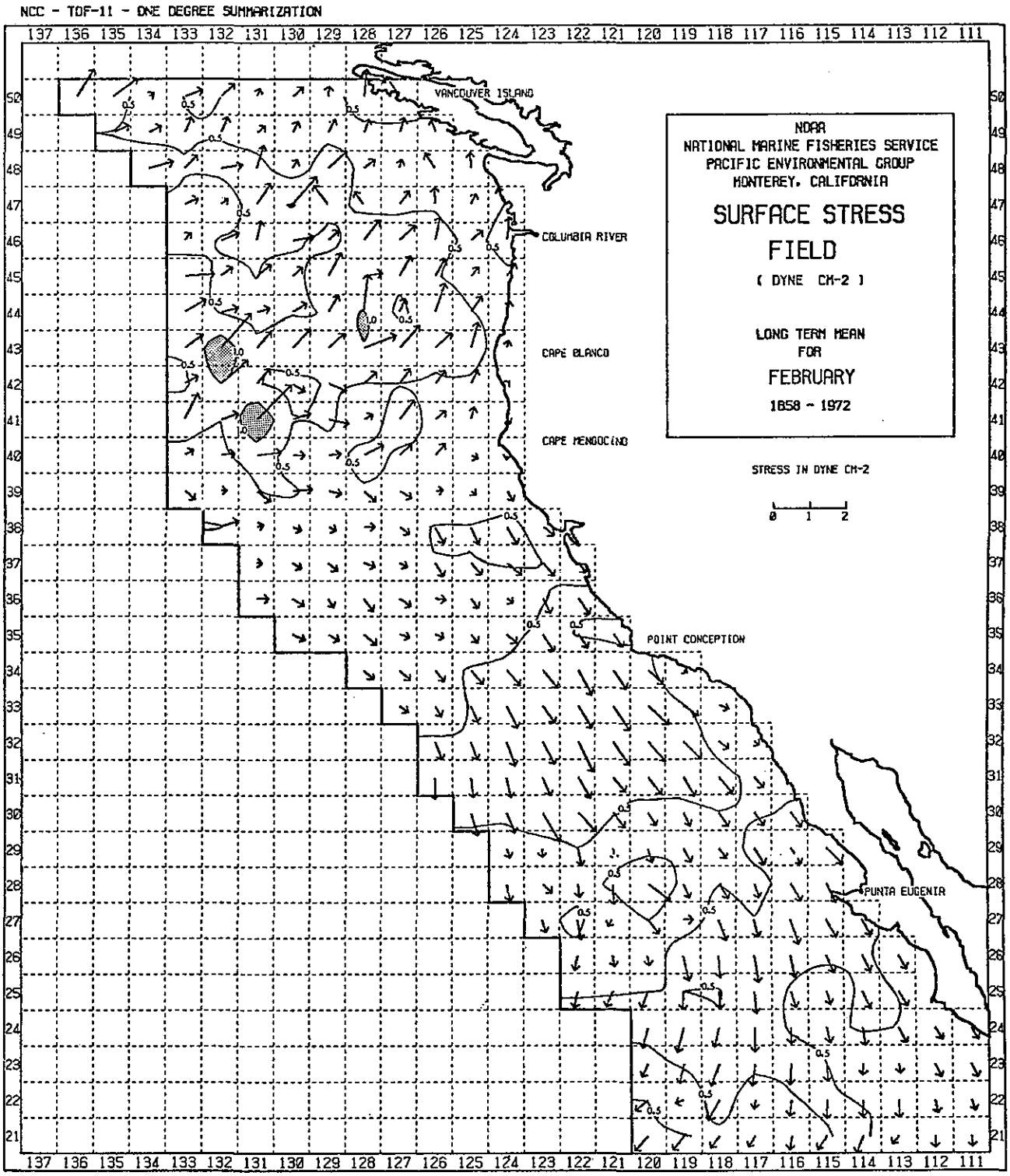

Figure 3.13. Resultant Surface Wind Stress Vectors for February

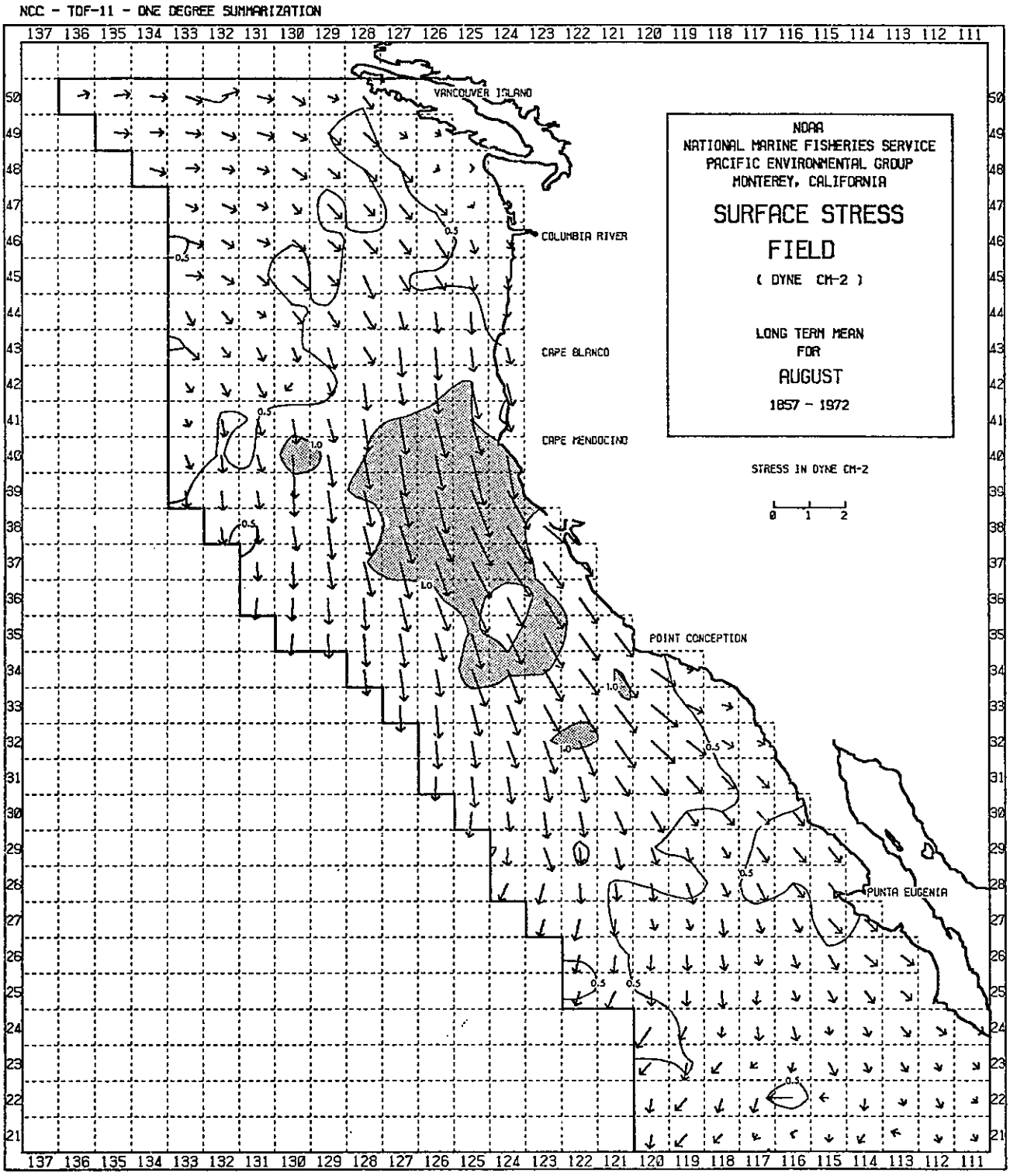

Figure 3.14. Resultant Surface Wind Stress Vectors for August

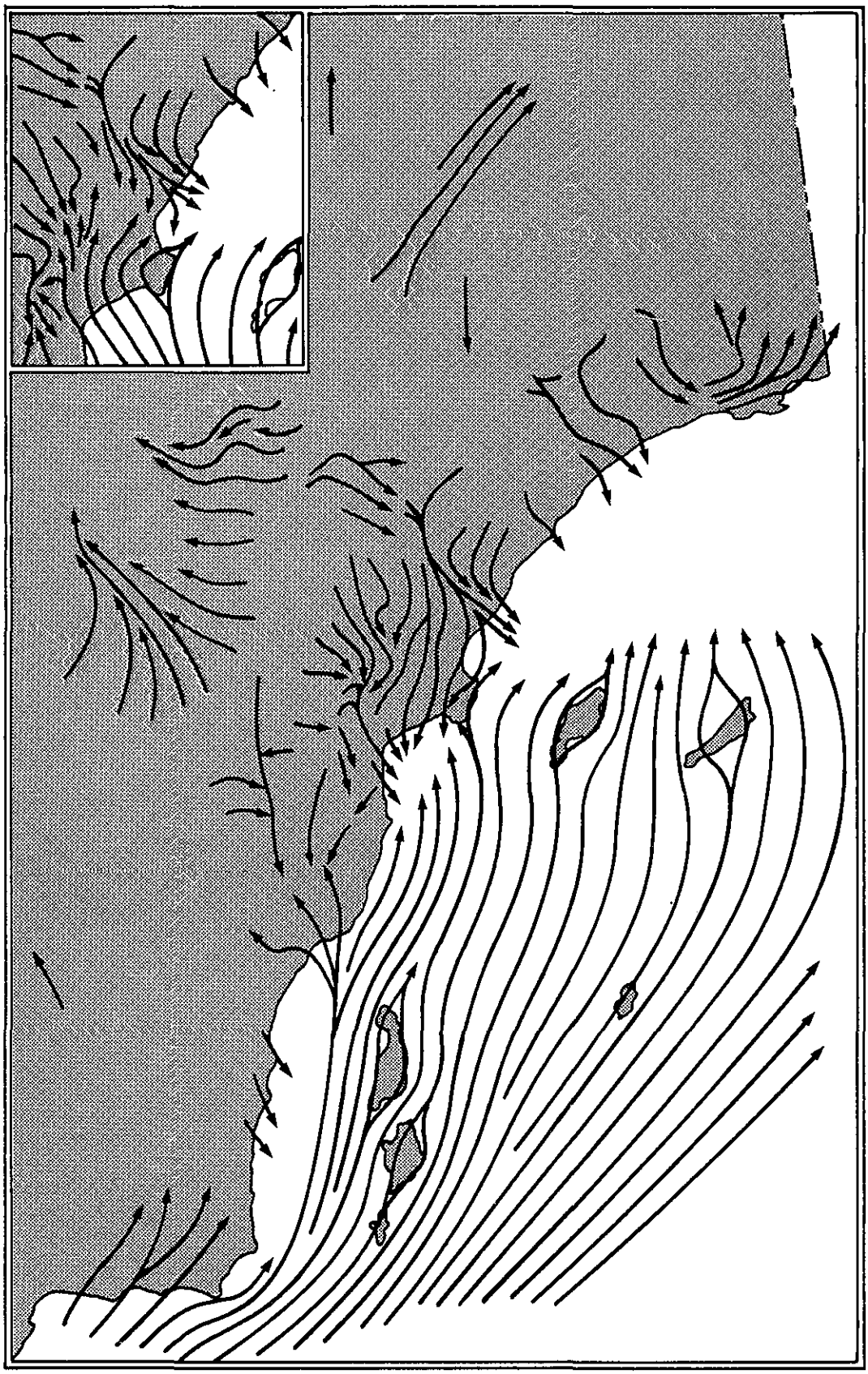

Figure 3.15. Streamline Chart for Southern California for July, 1200-1800 PST (after DeMarrais, Holzworth, and Hosler, 1965)

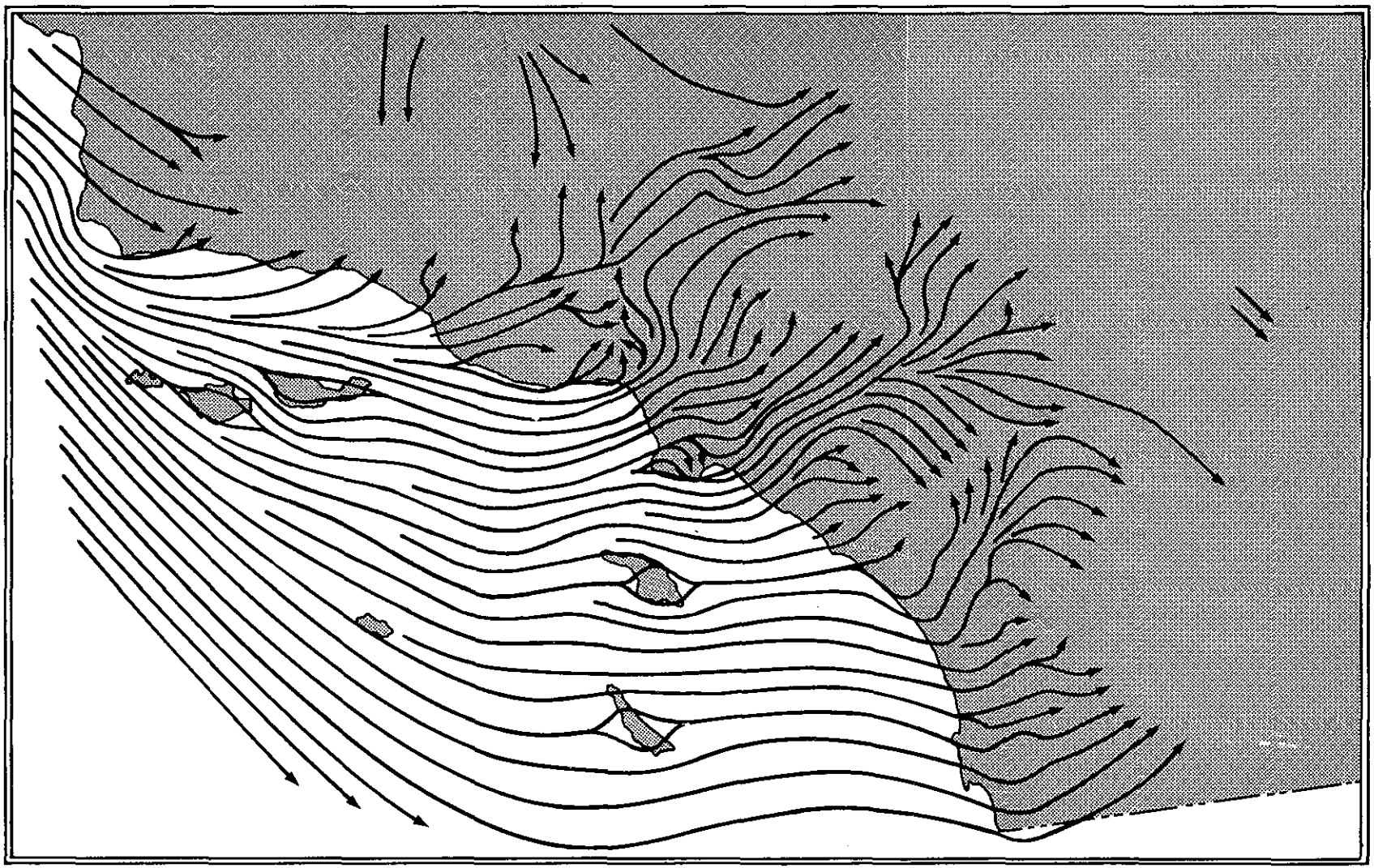

Figure 3.16. Streamline Chart for Southern California for July, 0000-0500 PST (after DeMarrais, Holzworth, and Hosler, 1965)

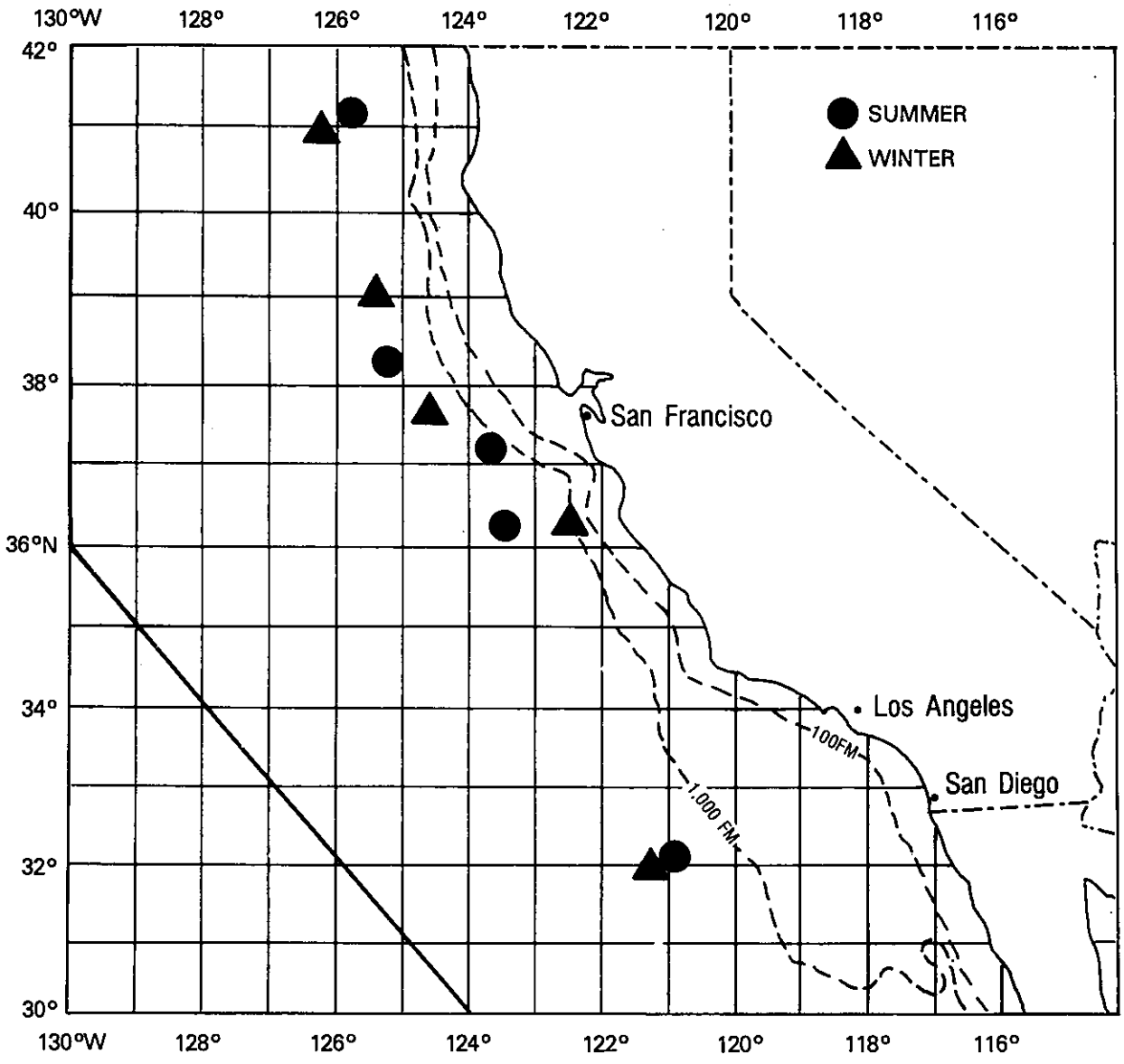

Figure 3.17. Hypothetical Air Pollutant Sources from Which Air Pollutants Are Expected to Reach Coastal Areas Within 12 Hours of Advection at 1 Percent of the Time.

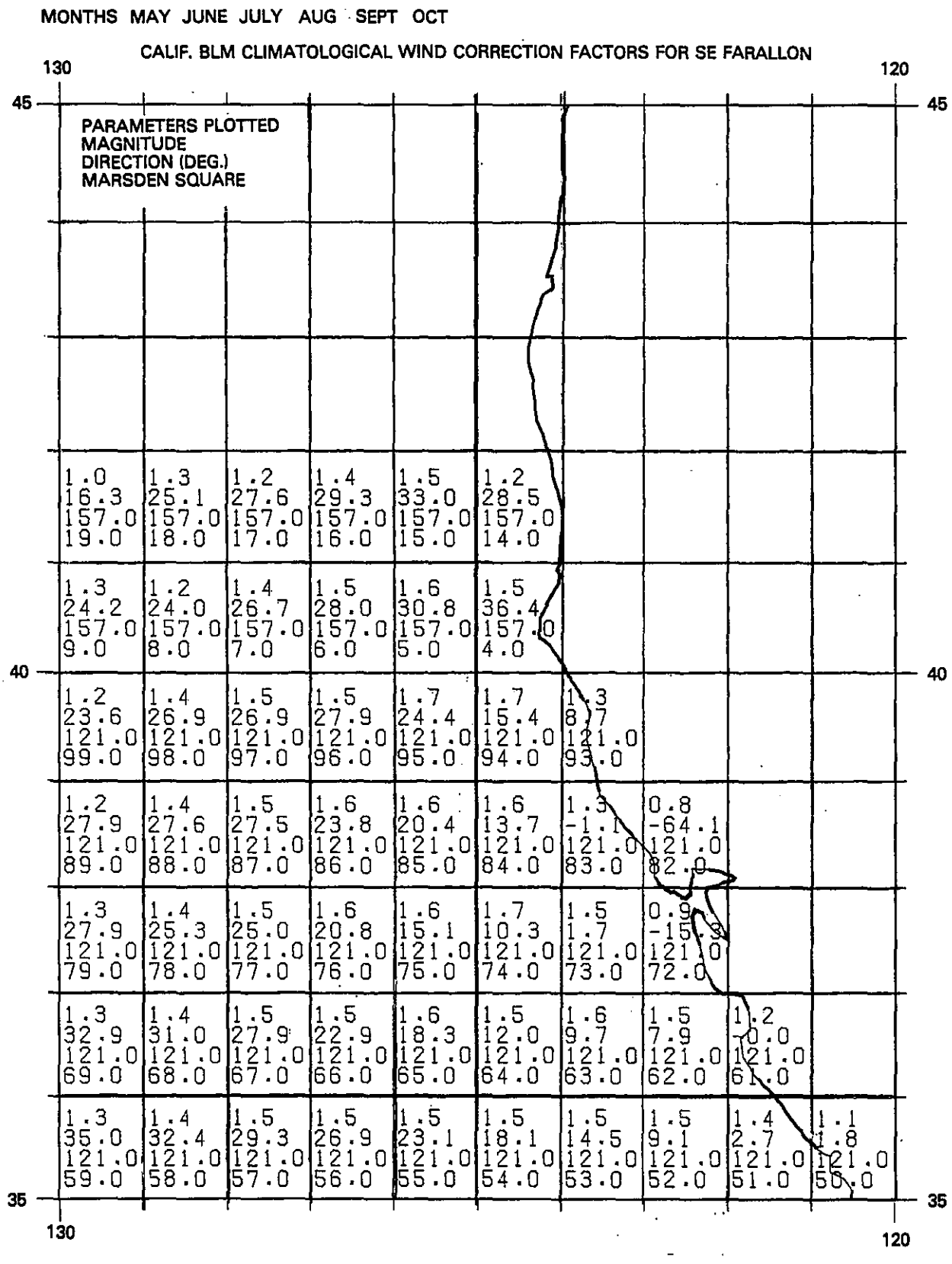

Figure 3.18. Wind Speed and Direction Adjustment Factors for S.E. Farallon Island for Summer

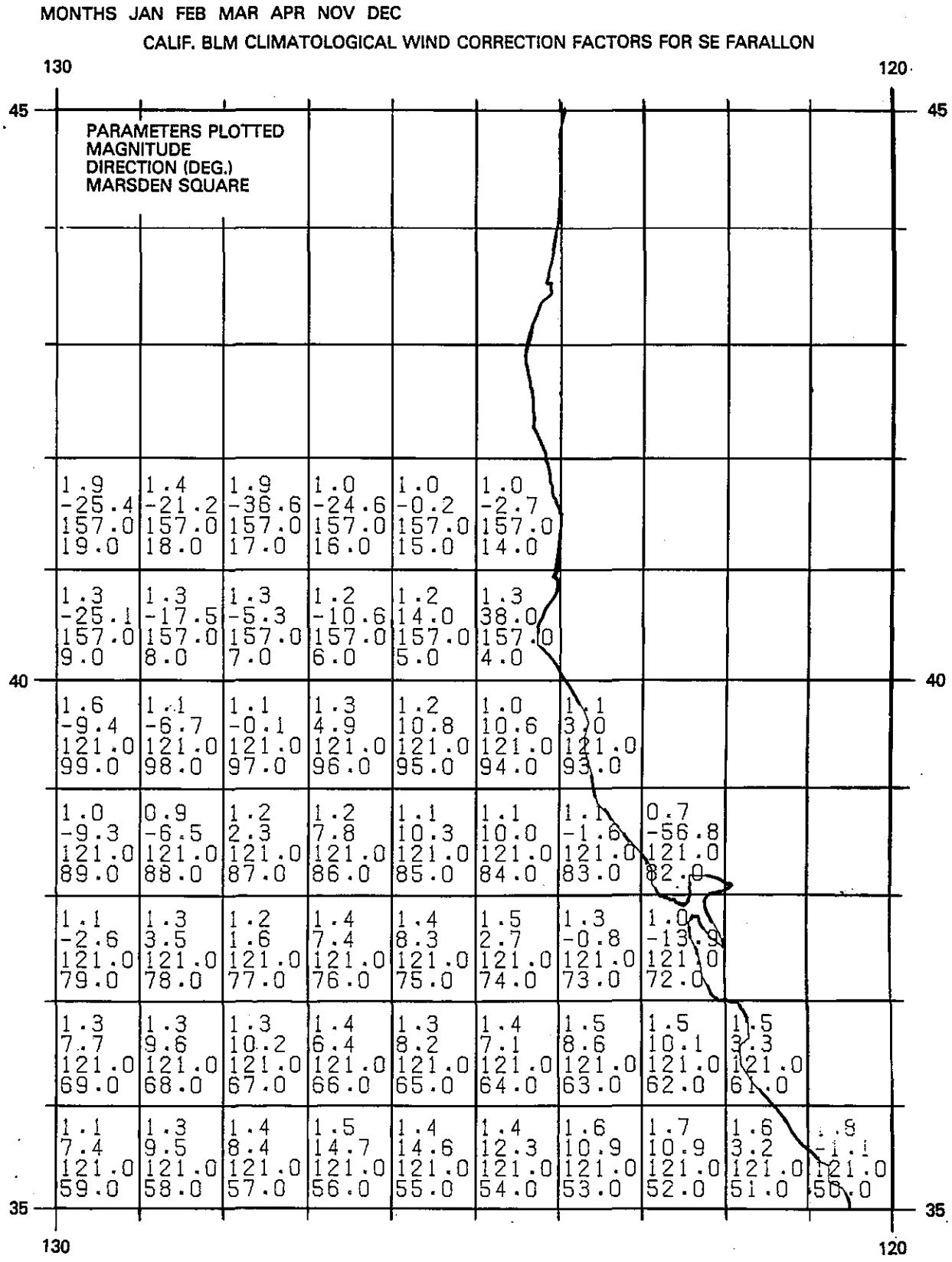

Figure 3.19. Wind Speed and Direction Adjustment Factors for S.E. Farallon Island for Winter

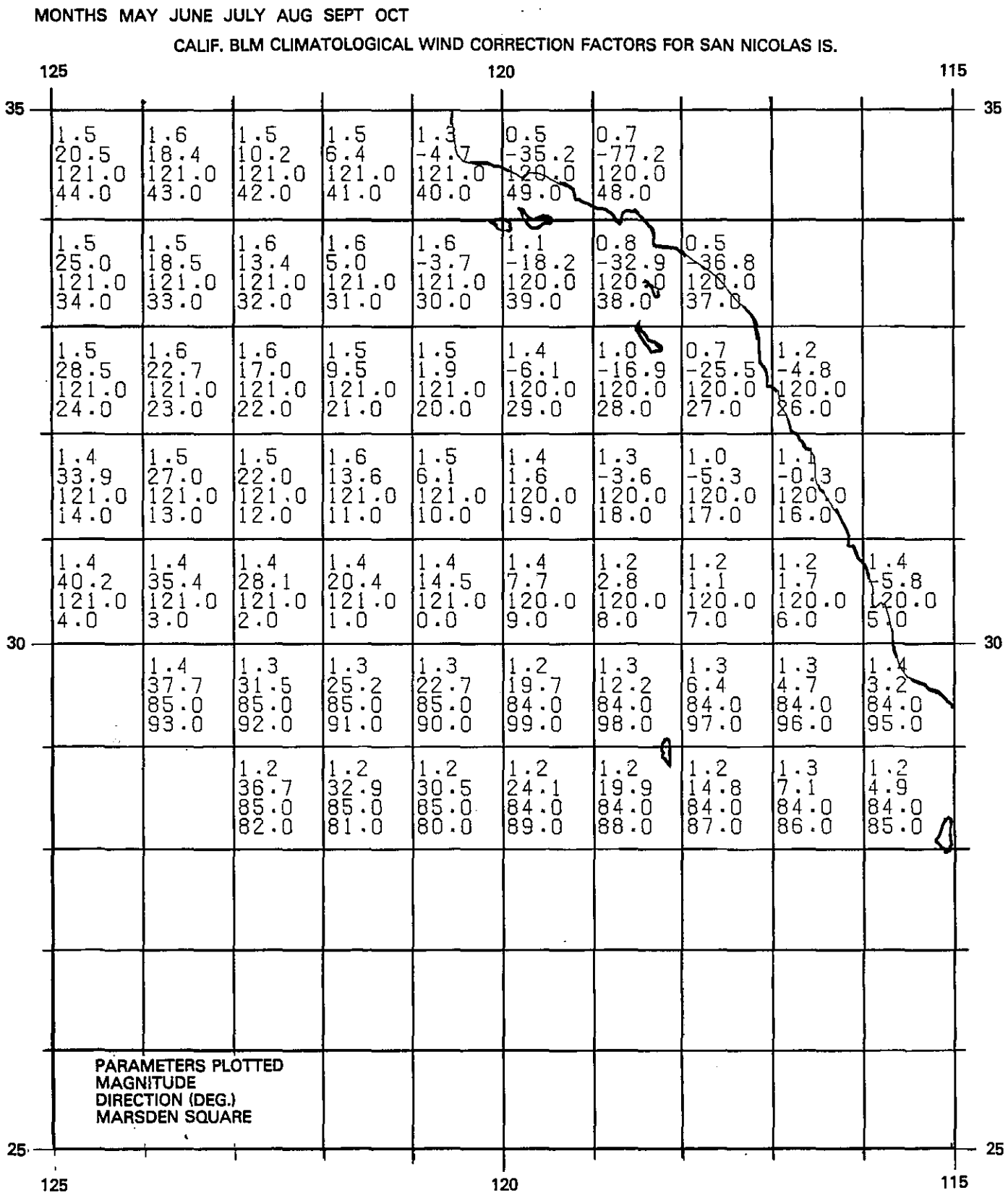

Figure 3.20. Wind Speed and Direction Adjustment Factors for San Nicolas for Summer

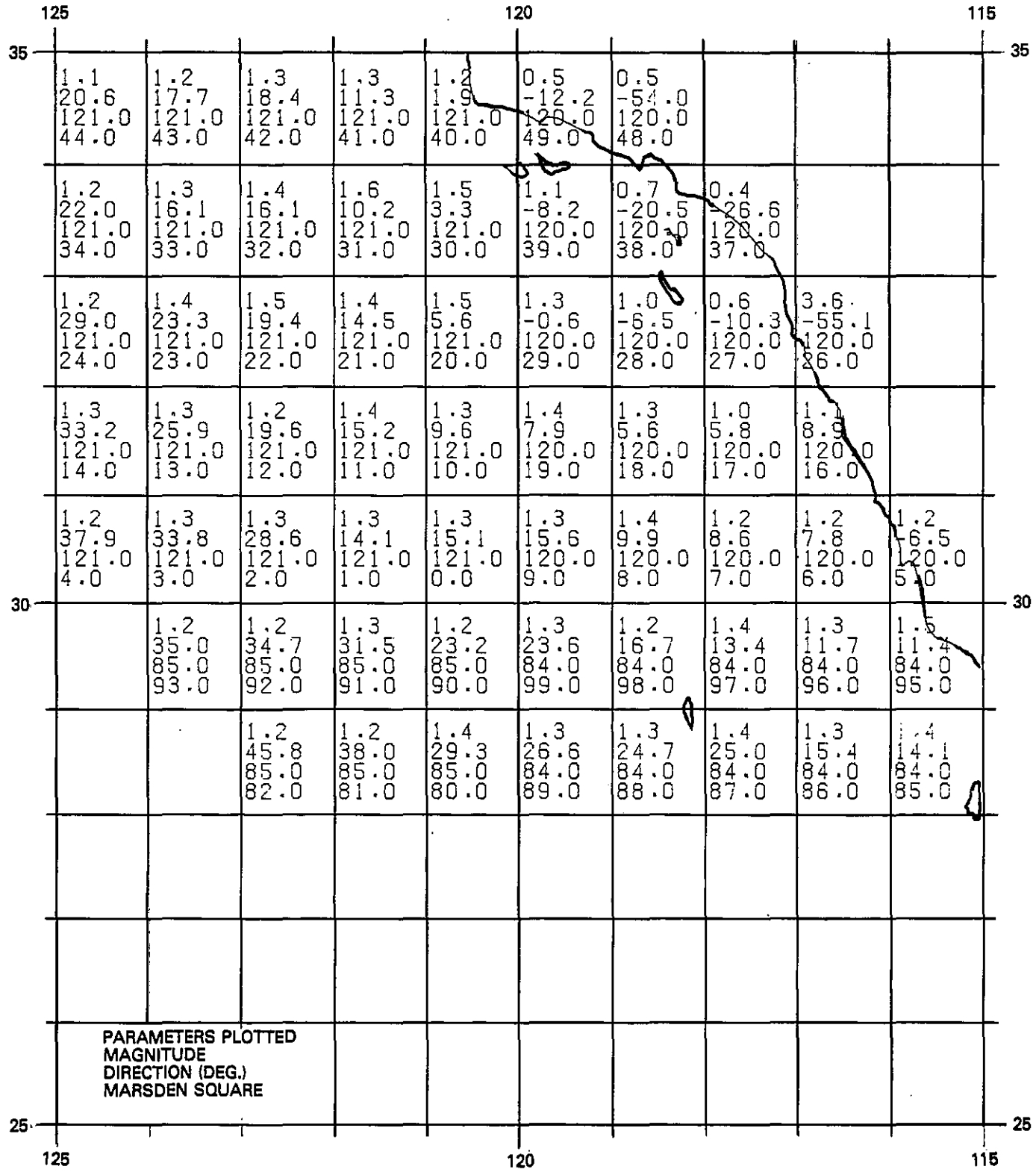

Figure 3.21. Wind Speed and Direction Adjustment Factors for San Nicolas for Winter

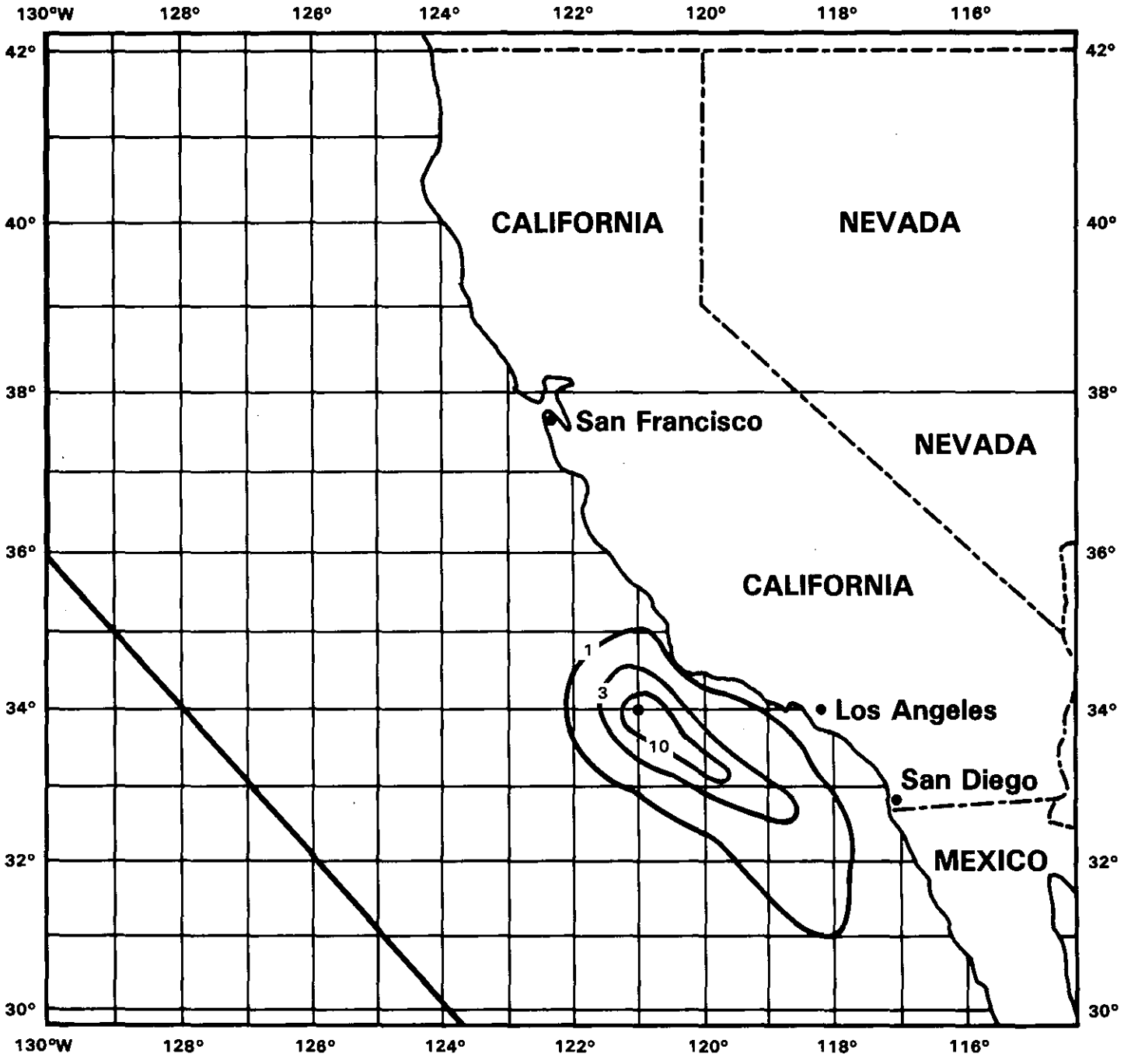

Figure 3.22. Coverage of Winter Air Trajectories for 12 Hours Using Adjusted San Nicolas Data. The Number 1% Indicates that 1% of the Trajectories Pass Through a 1° Square Area, Centered at a Point on the Isopleth, within 12 Hours.

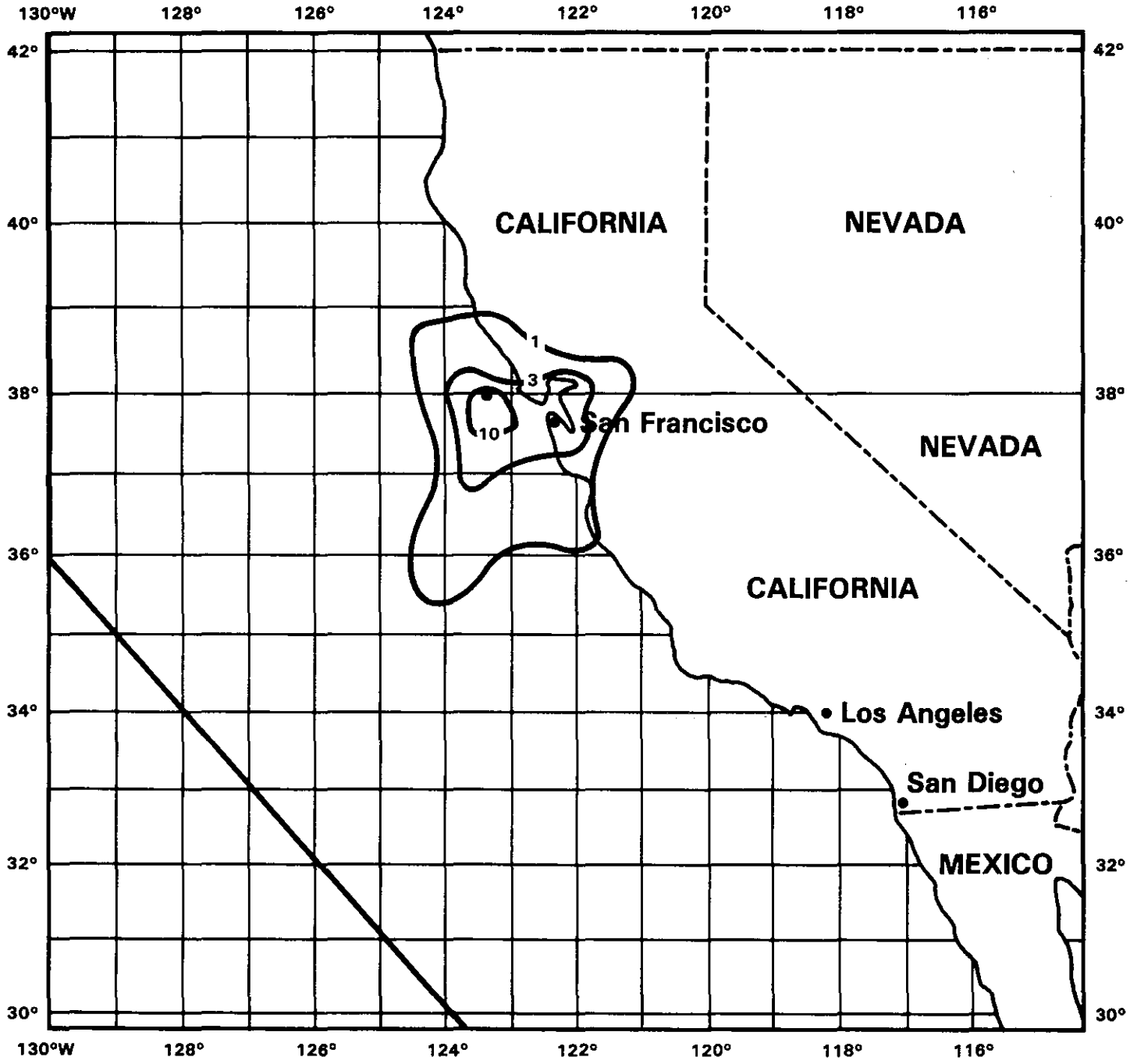

Figure 3.23. Coverage of Summer Air Trajectories for 12 Hours Using Adjusted S.E. Farallon Data. The Number 1% Indicates that 1% of the Trajectories Pass Through a 1° Square Area, Centered at a Point on the Isopleth, within 12 Hours.

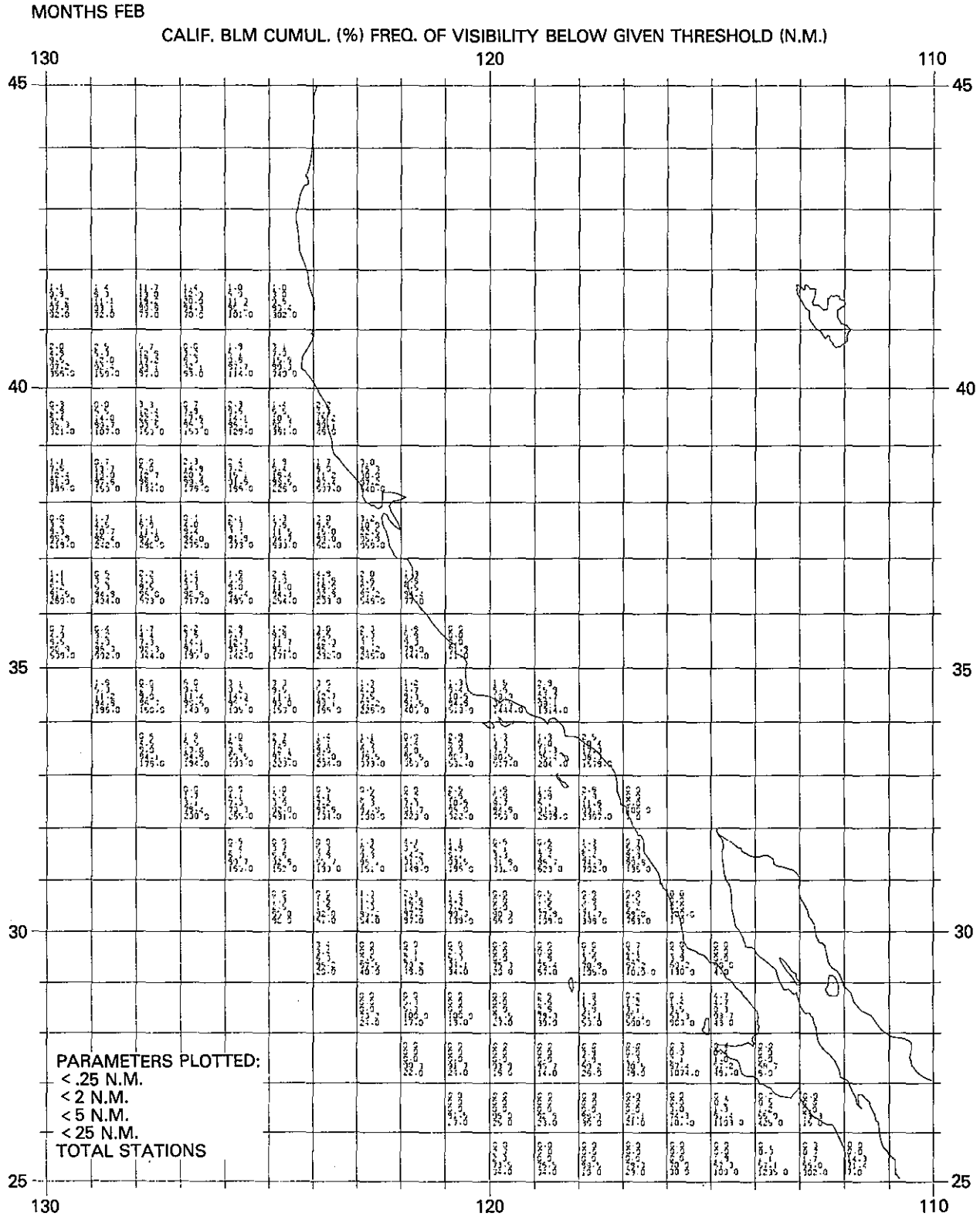

Figure 3.24. Frequency of Visibilities Below Given Threshold Values for 1°-square Ocean Areas for February

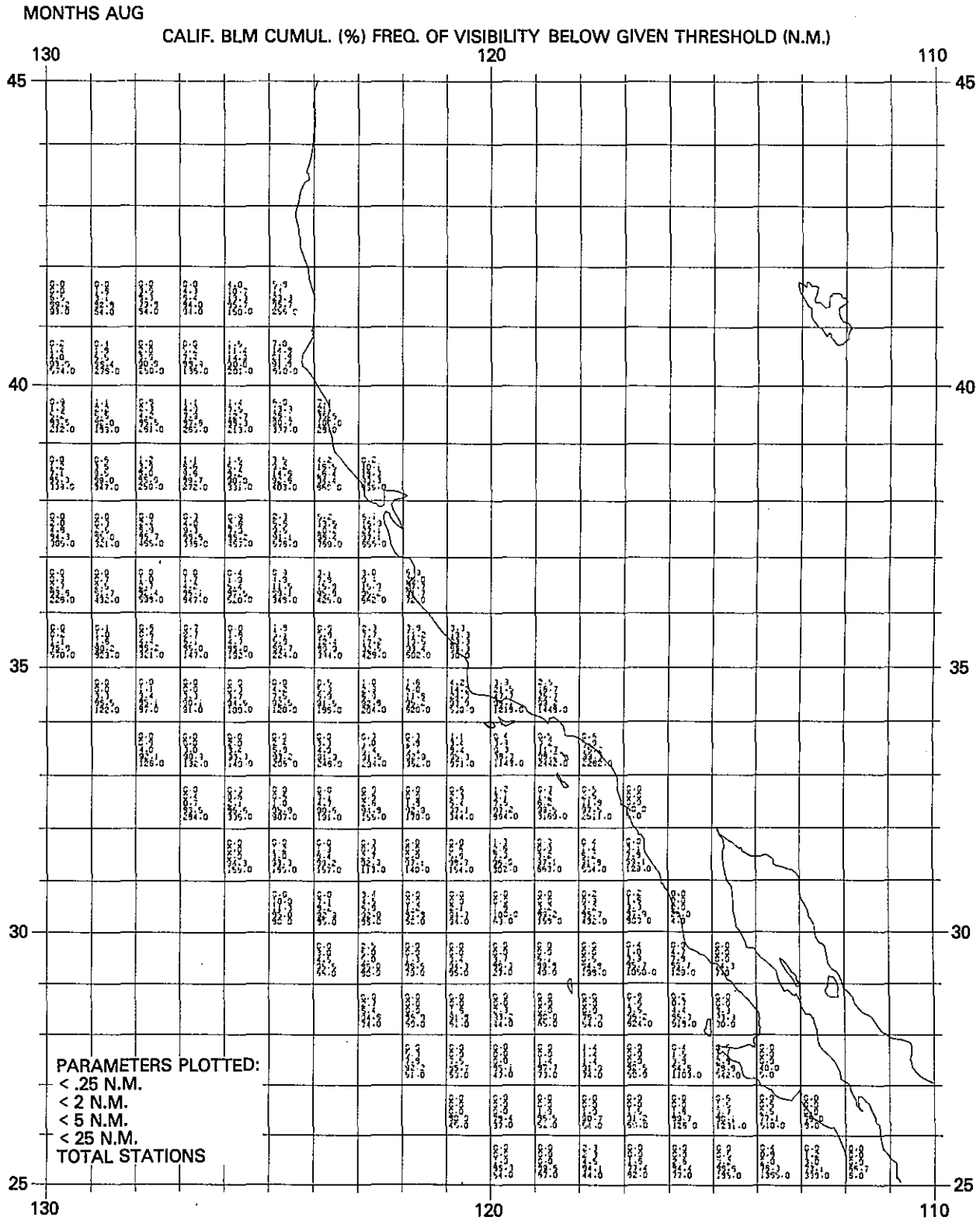

Figure 3.25. Frequency of Visibilities Below Given Threshold Values for 1°-square Ocean Areas for August

WIND ROSES

Detailed information can be obtained from frequency tables of wind direction or wind speed plotted in the form of wind roses. Wind roses for the midseason months (January, April, July, and October) were constructed for selected coastal and island stations (Figures 3.27–3.32). A selection of representative offshore 1° square area wind roses appear in Figures 3.33–3.39.

The numbers along the horizontal bar of the wind rose are the percentages of all winds in the following speed (kts) categories: 4-6, 7-10, 11-16, 17-21, 22-27, 28-33, 34-40, 41-47, and > 47 knots. The length of the bar represents 100% minus the percentage in the 0-3 kt category. The numbers at the end of the direction bars are the percentages of winds from that direction.

9 categories of speed

0-3 kts
4-6 kts
7-10 kts
11-16 kts
17-21 kts
22-27 kts
28-33 kts
34-40 kts
41-47 kts
> 47 kts

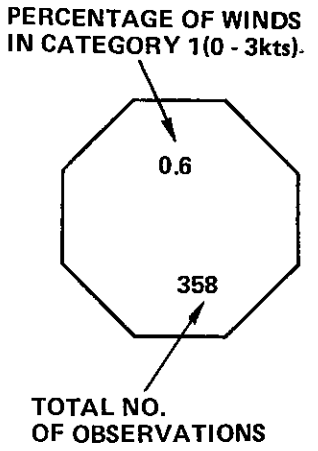

Figure 3.26. Wind Roses

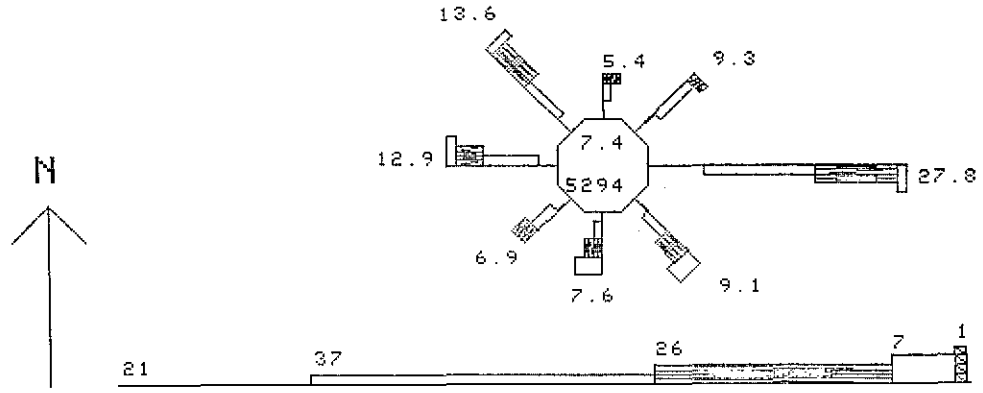

(a) January

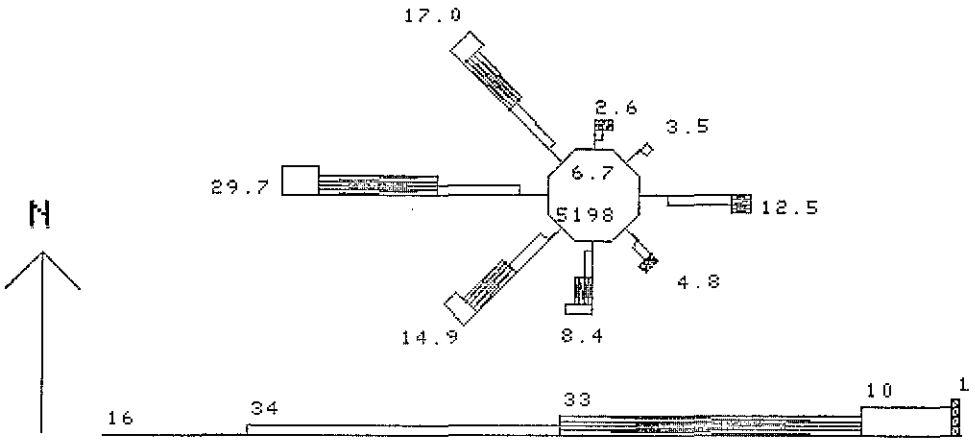

(b) April

Figure 3.27. Coastal Station Wind Roses – Imperial Beach

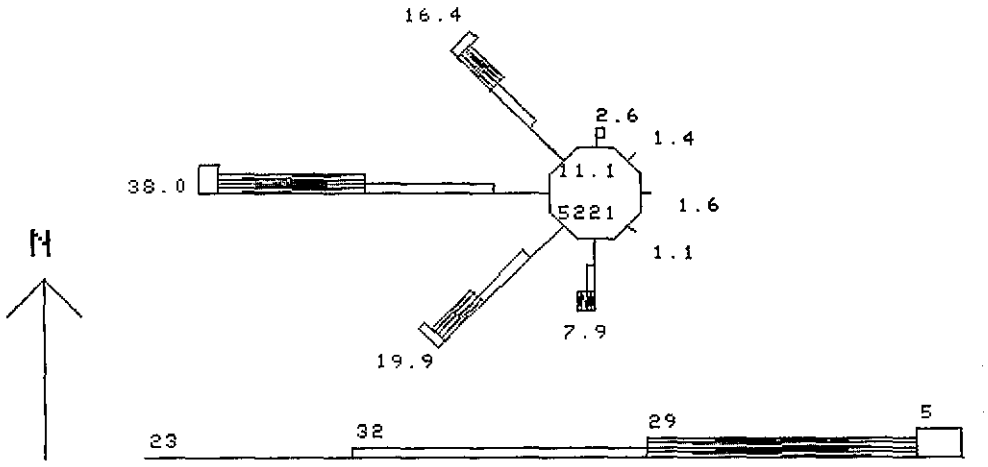

(c) July

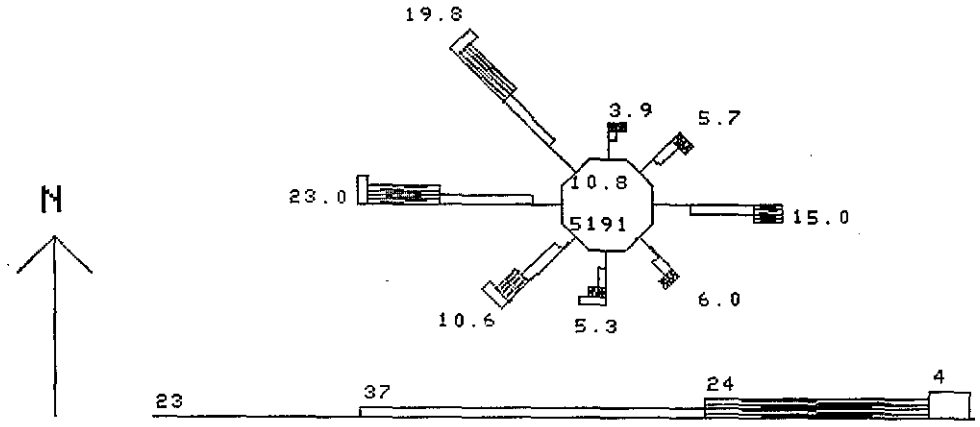

(d) October

Figure 3.27. Coastal Station Wind Roses -- Imperial Beach (cont'd)

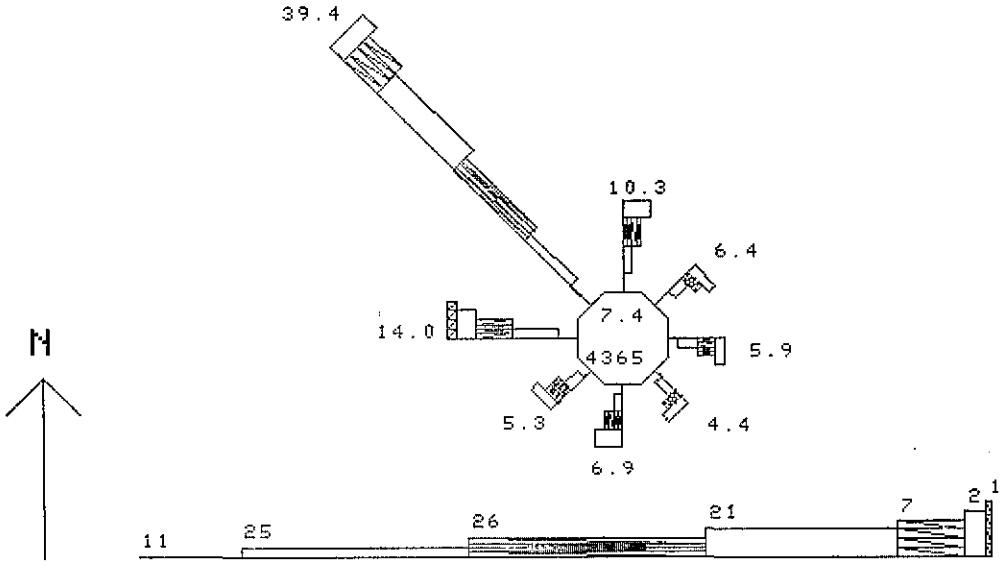

(a) January

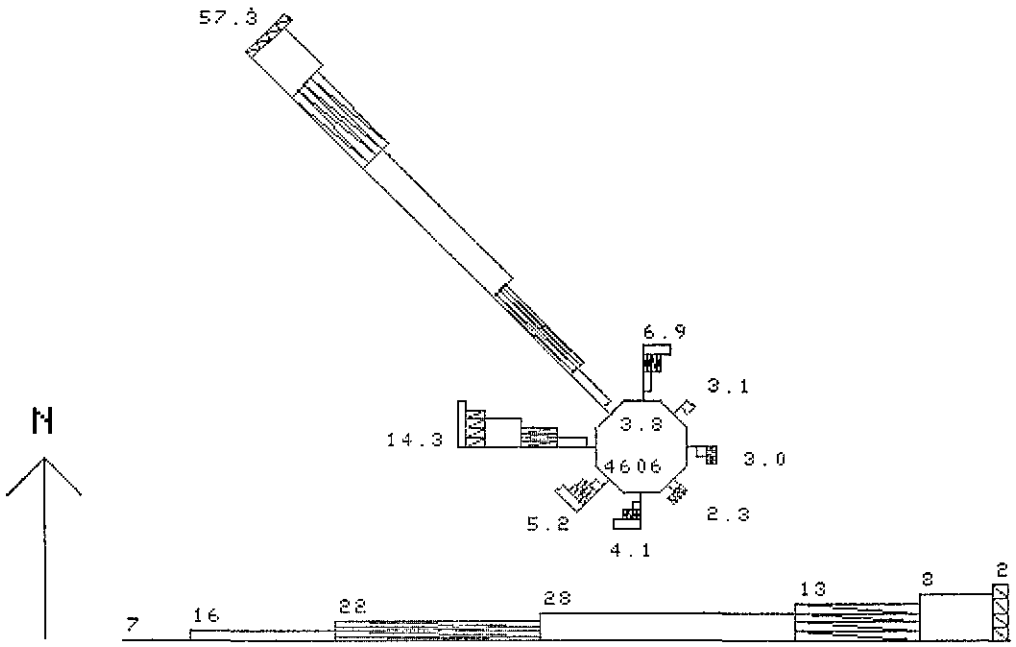

(b) April

Figure 3.28. Coastal Station Wind Roses -- San Nicolas Island

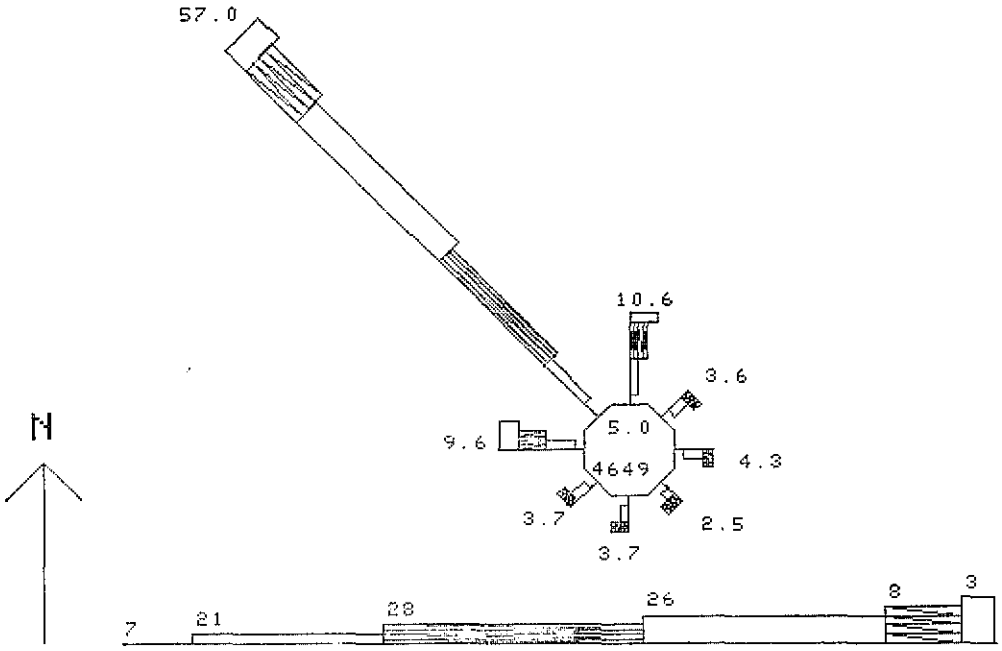

(c) July

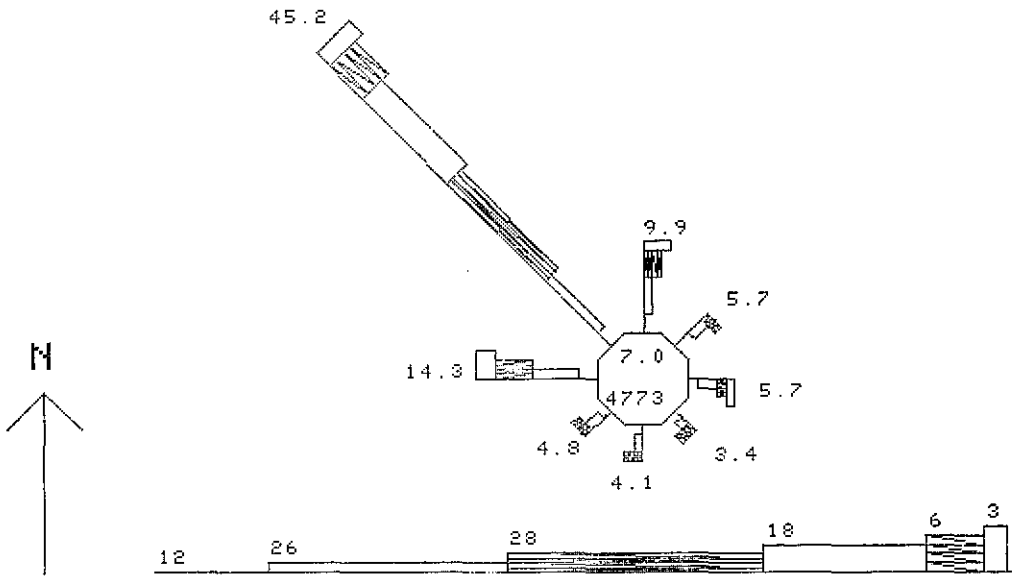

(d) October

Figure 3.28. Coastal Station Wind Roses – San Nicolas Island (cont'd)

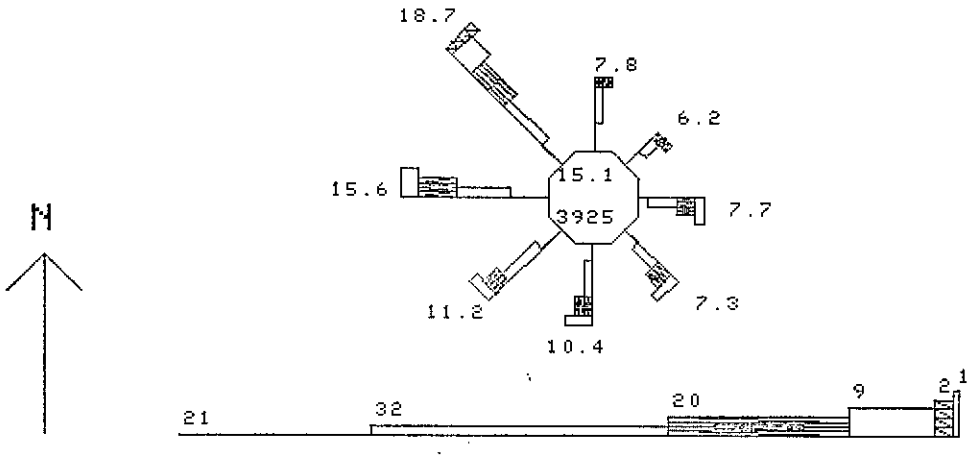

(a) January

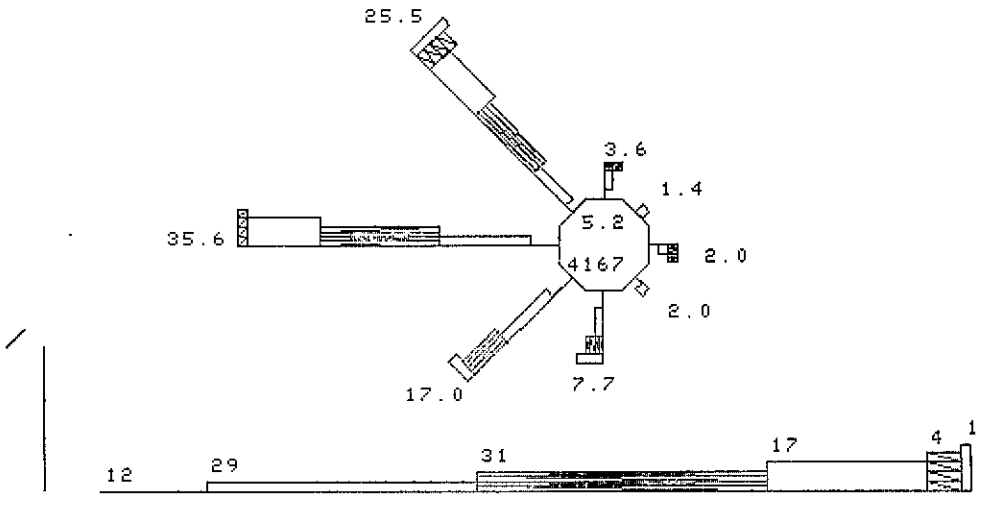

(b) April

Figure 3.29. Coastal Station Wind Roses – San Clemente

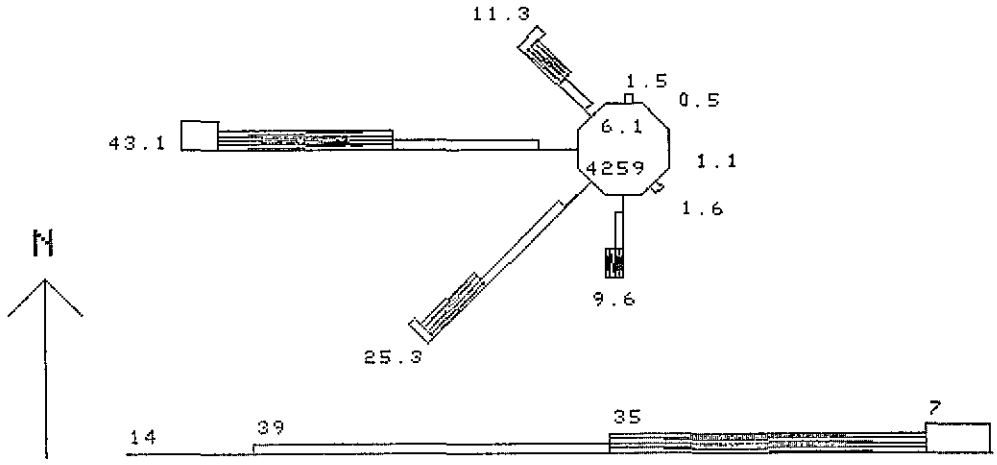

(c) July

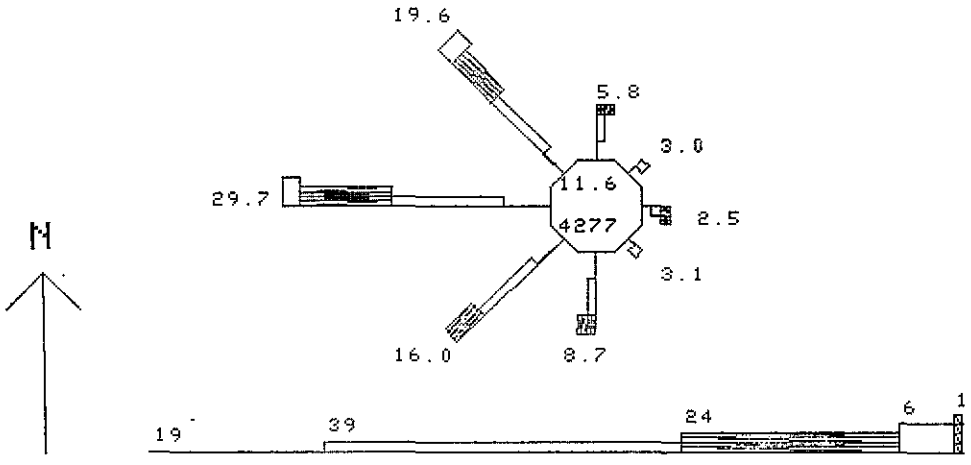

(d) October

Figure 3.29. Coastal Station Wind Roses – San Clemente (cont'd)

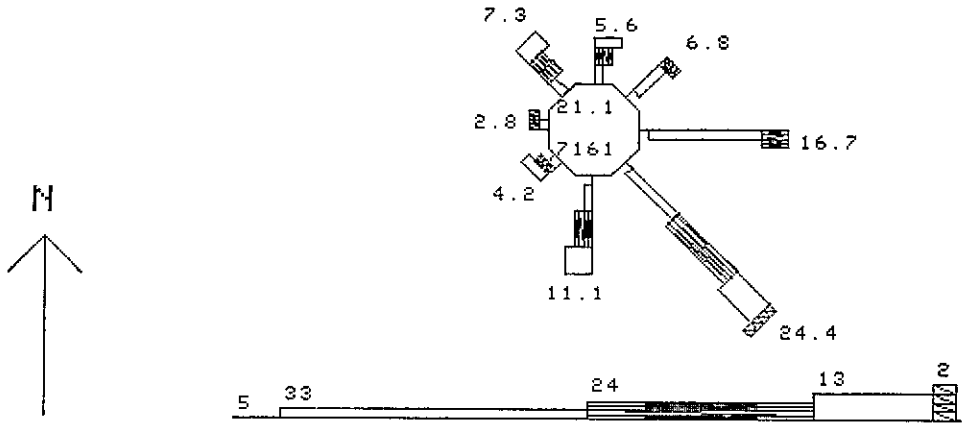

(a) January

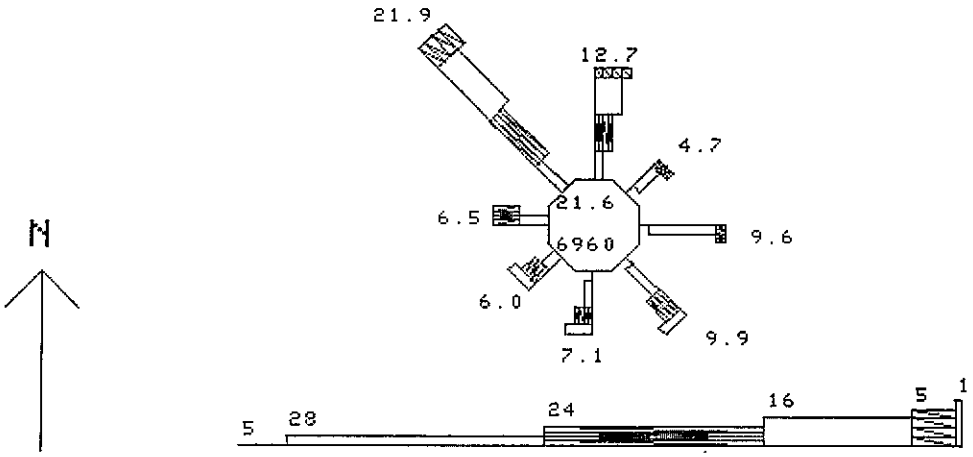

(b) April

Figure 3.30. Coastal Station Wind Roses – Arcata

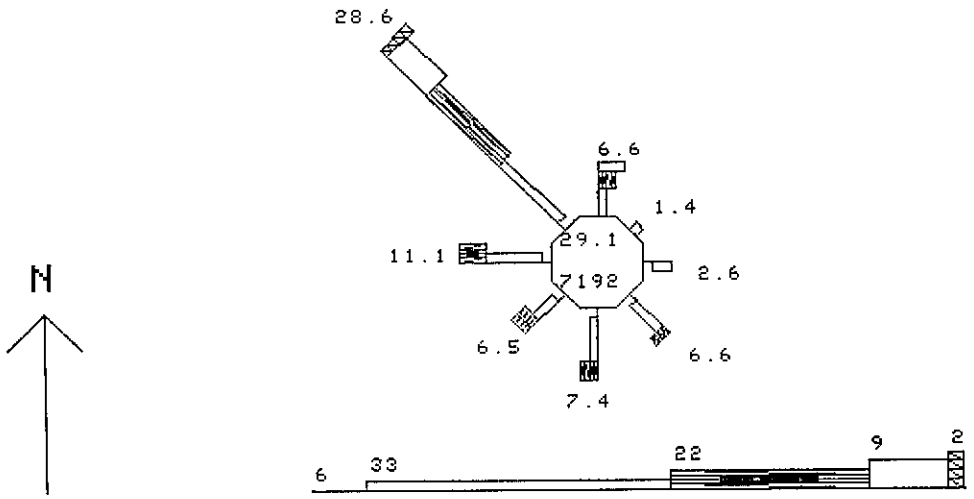

(c) July

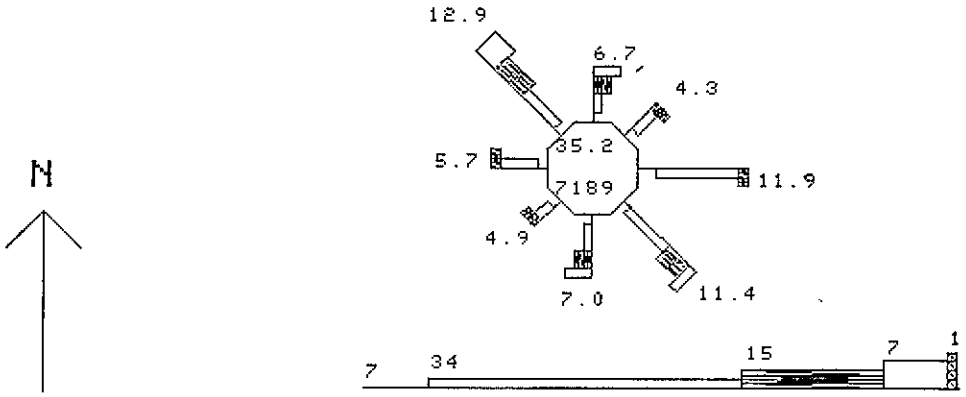

(d) October

Figure 3.30. Coastal Station Wind Roses – Arcata (cont'd)

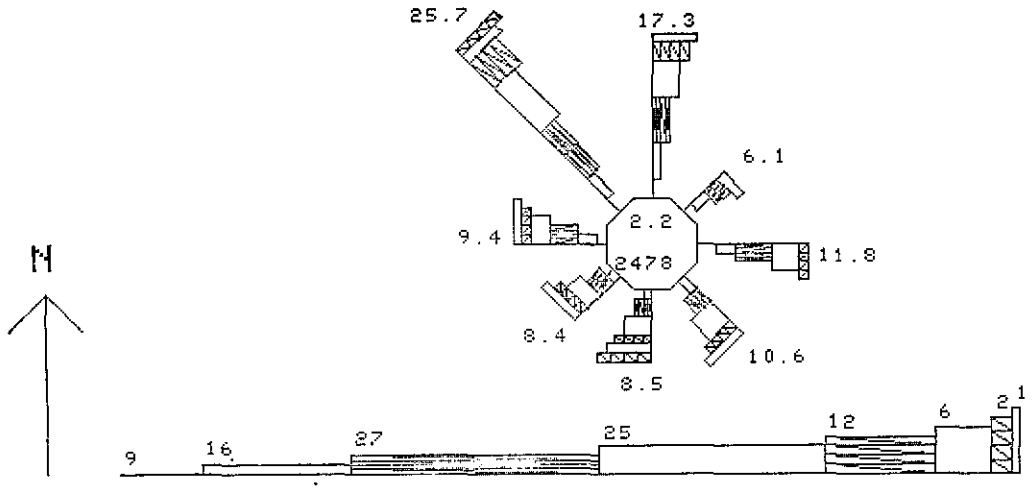

(a) January

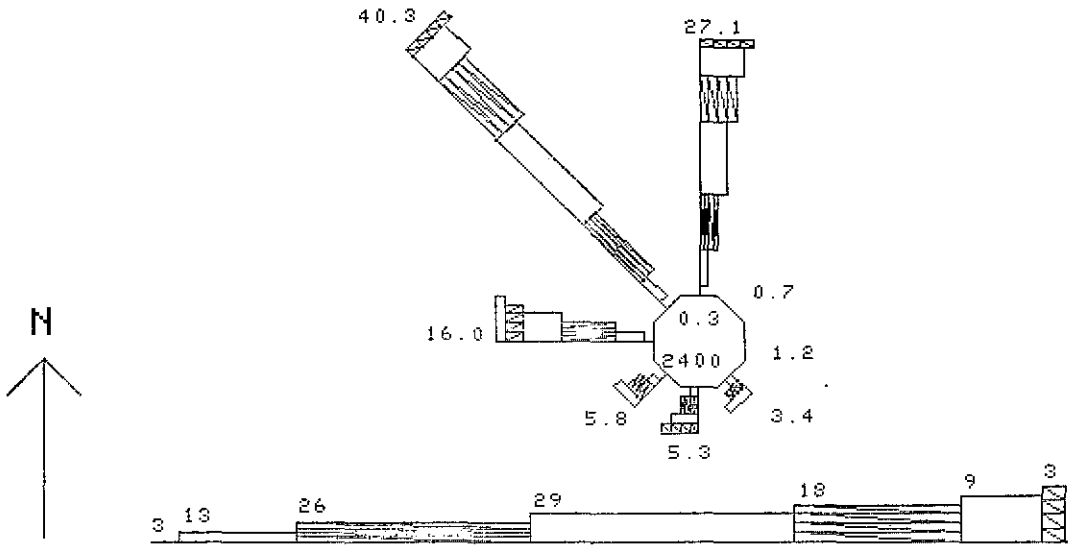

(b) April

Figure 3.31. Coastal Station Wind Roses – S.E. Farallon Island

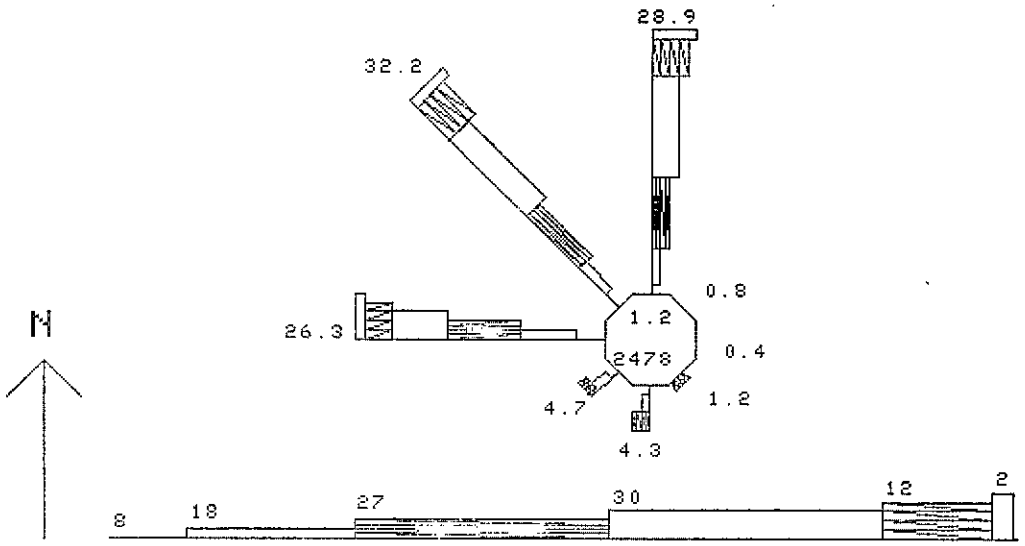

(c) July

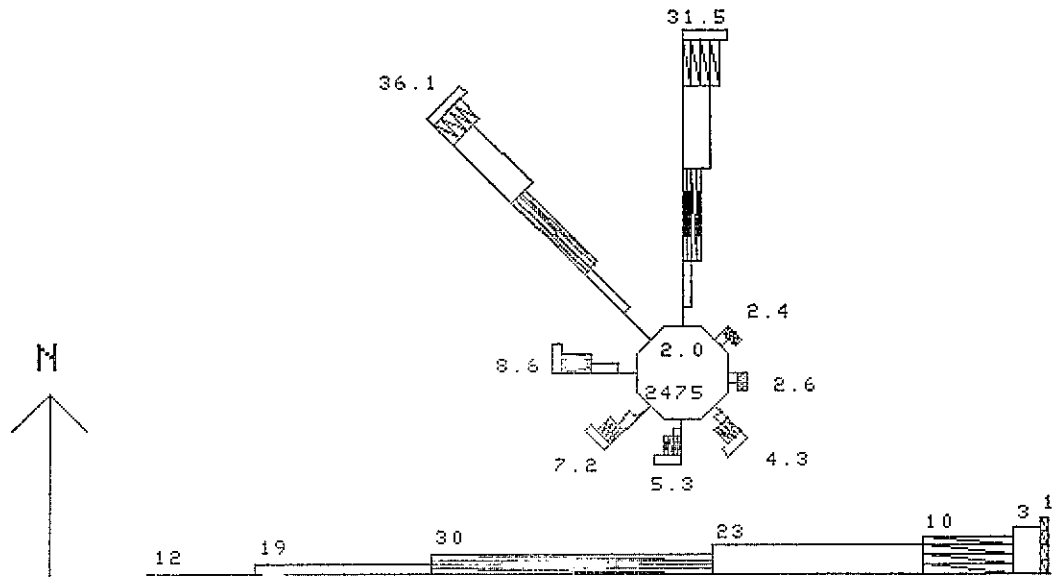

(d) October

Figure 3.31. Coastal Station Wind Roses – S.E. Farallon Island (cont'd)

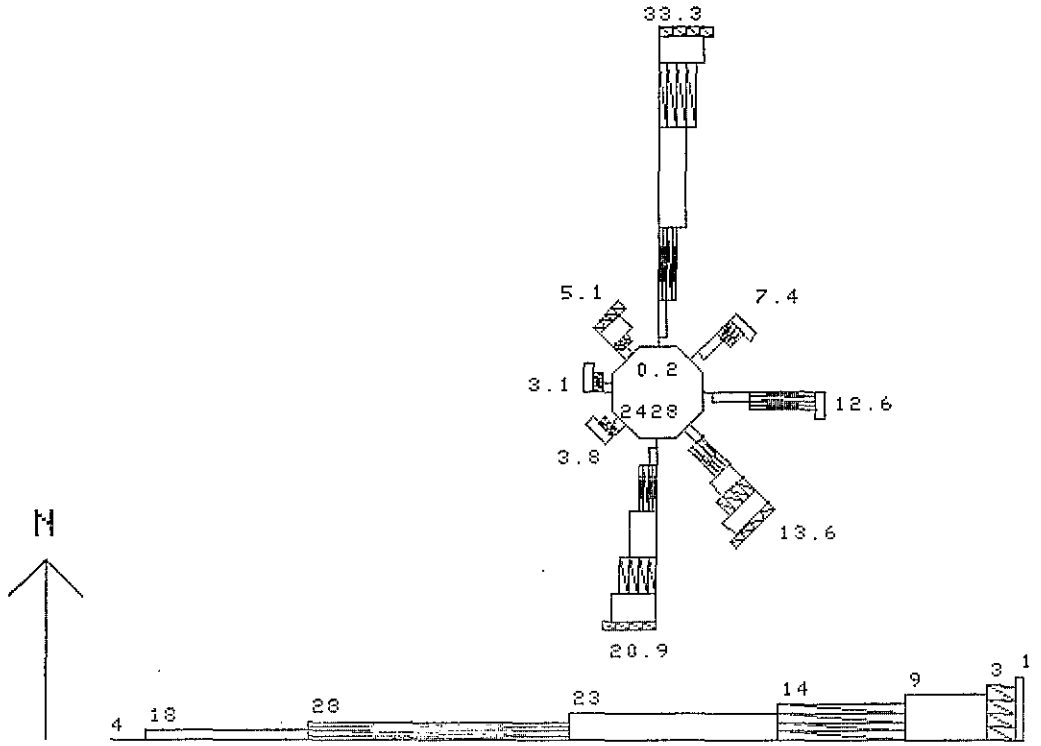

(a) January

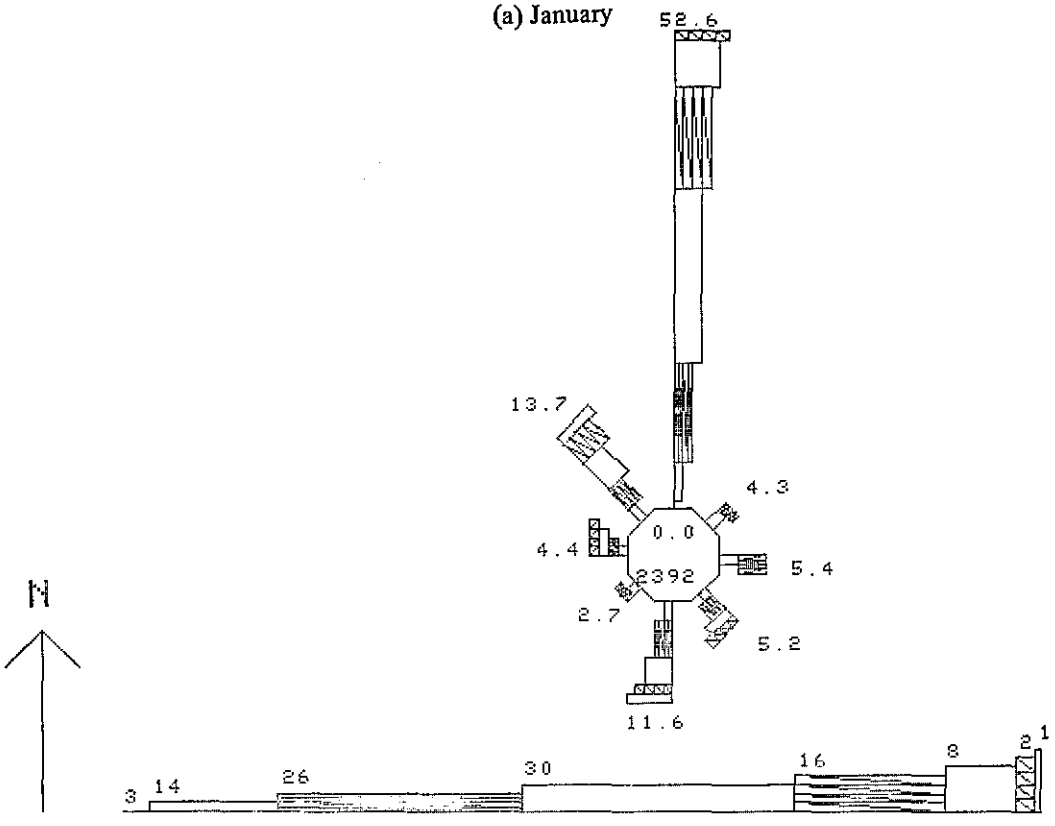

(b) April

Figure 3.32. Coastal Station Wind Roses – Point Arena

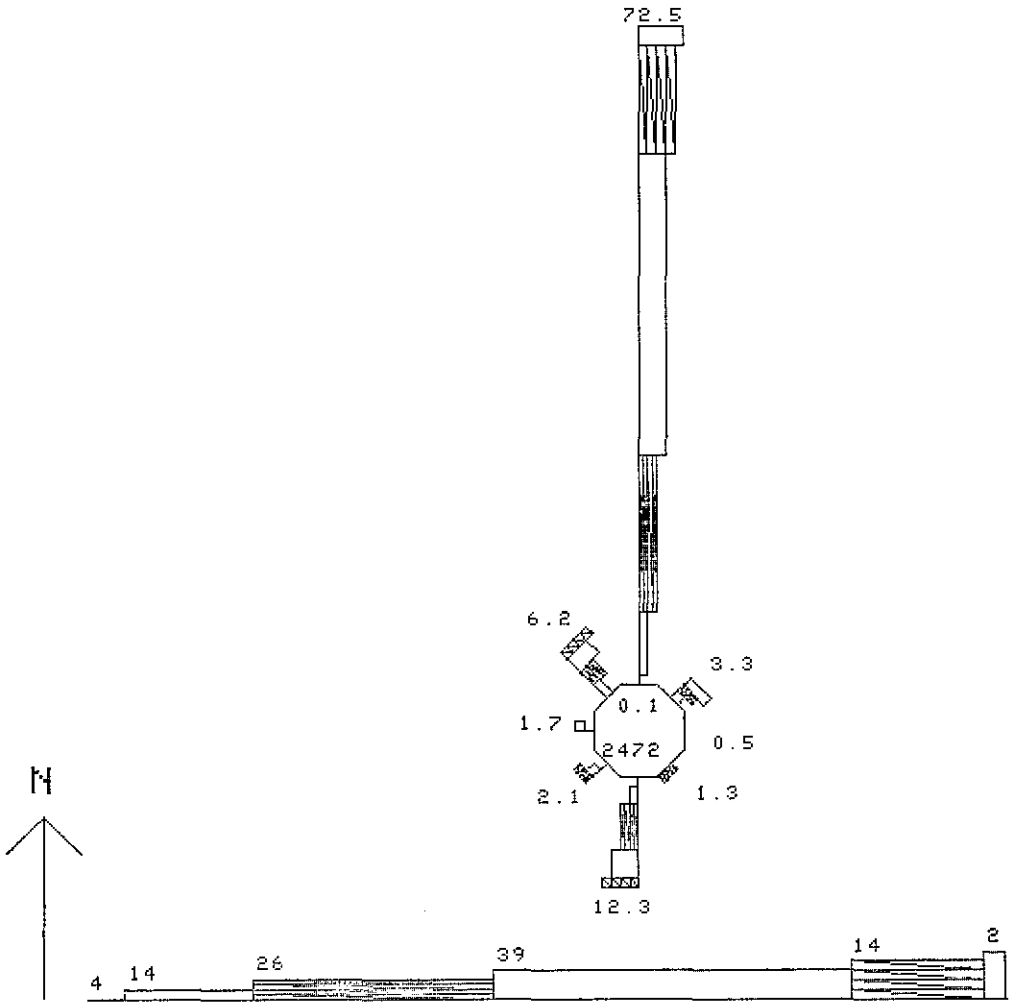

(c) July

Figure 3.32. Coastal Station Wind Roses -- Point Arena (cont'd)

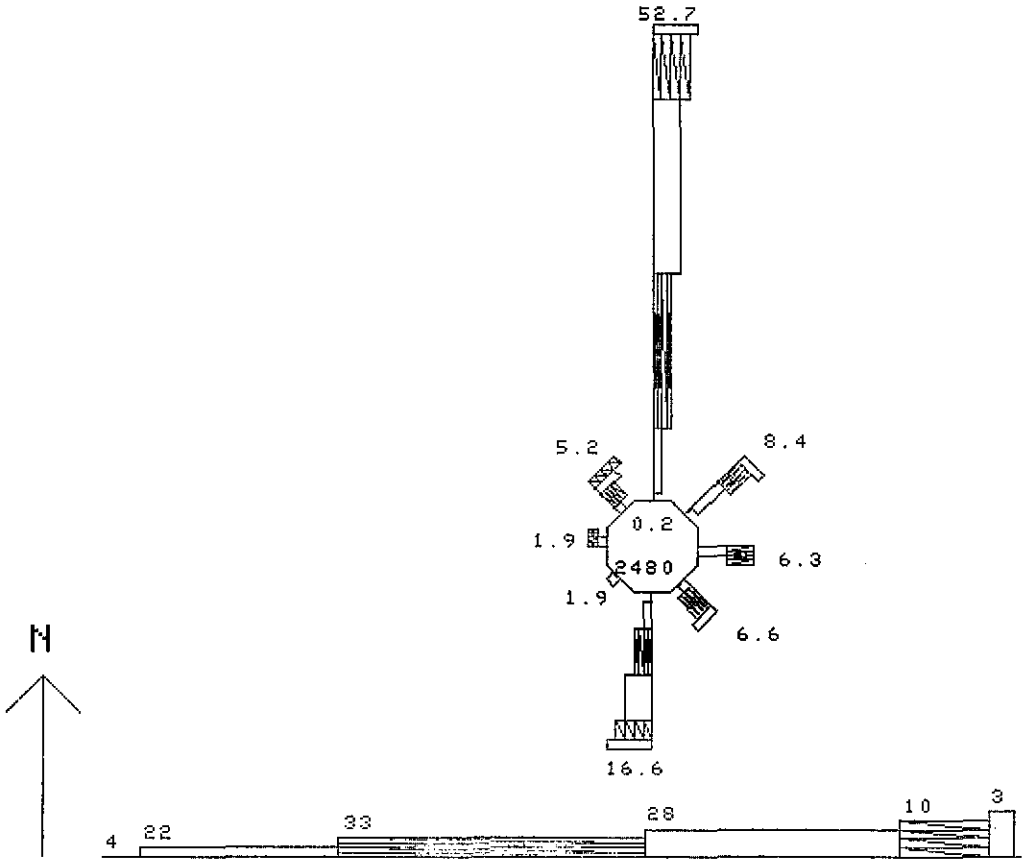

(d) October

Figure 3.32. Coastal Station Wind Roses – Point Arena (cont'd)

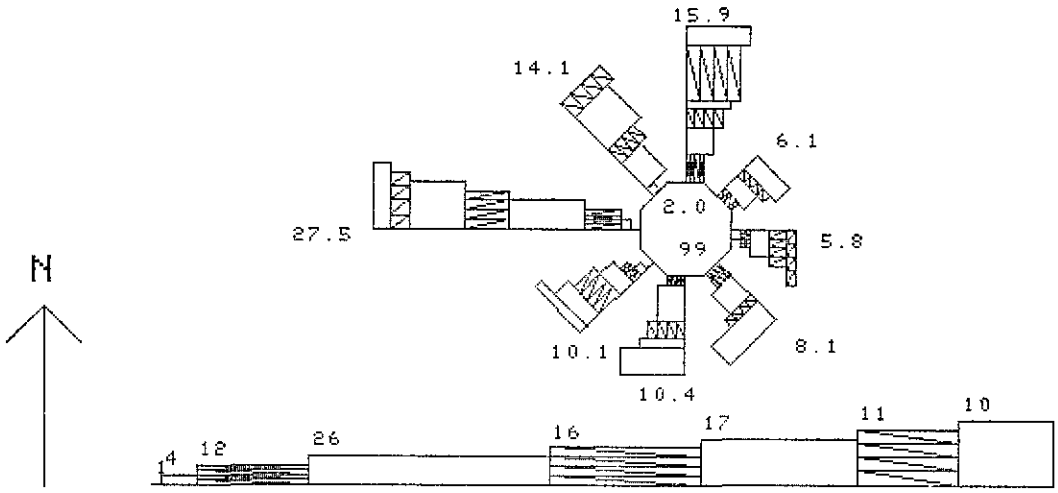

(a) January

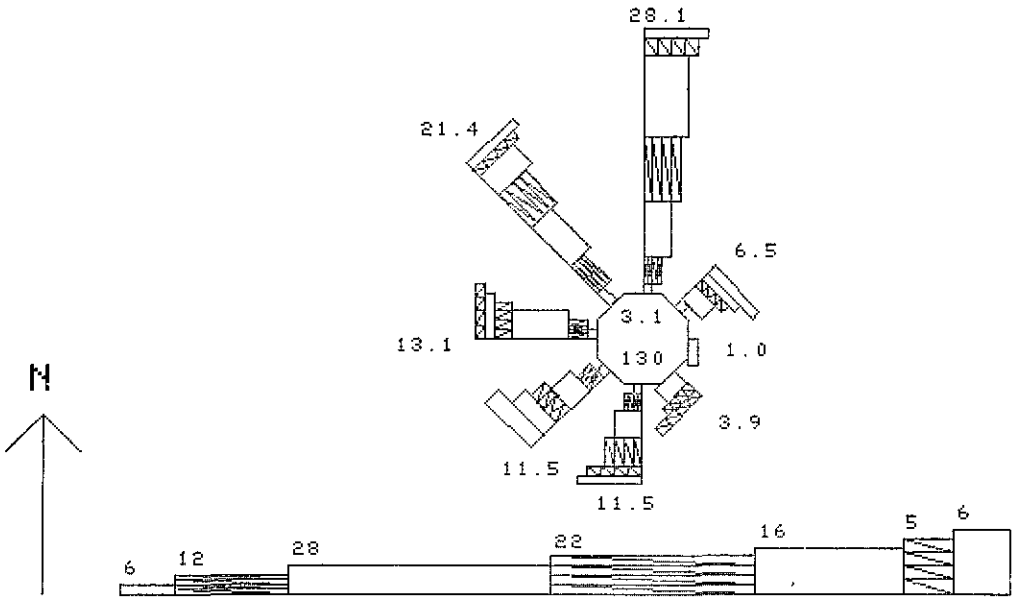

(b) April

Figure 3.33. Marine Area Wind Roses – MSQ 5717

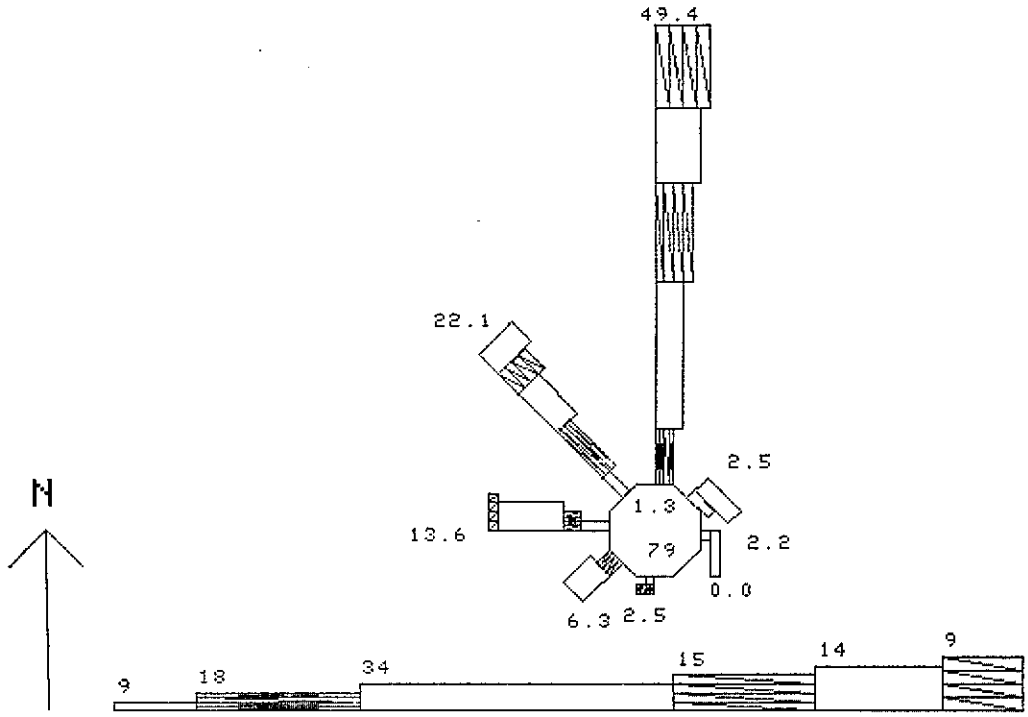

(c) July

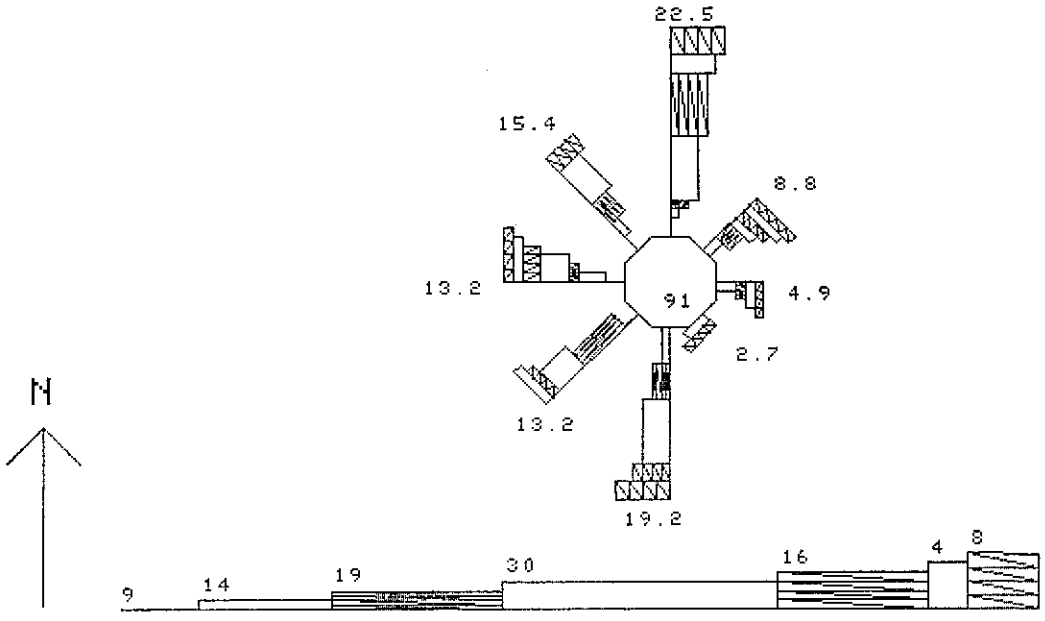

(d) October

Figure 3.33. Marine Area Wind Roses – MSQ 5717 (cont'd)

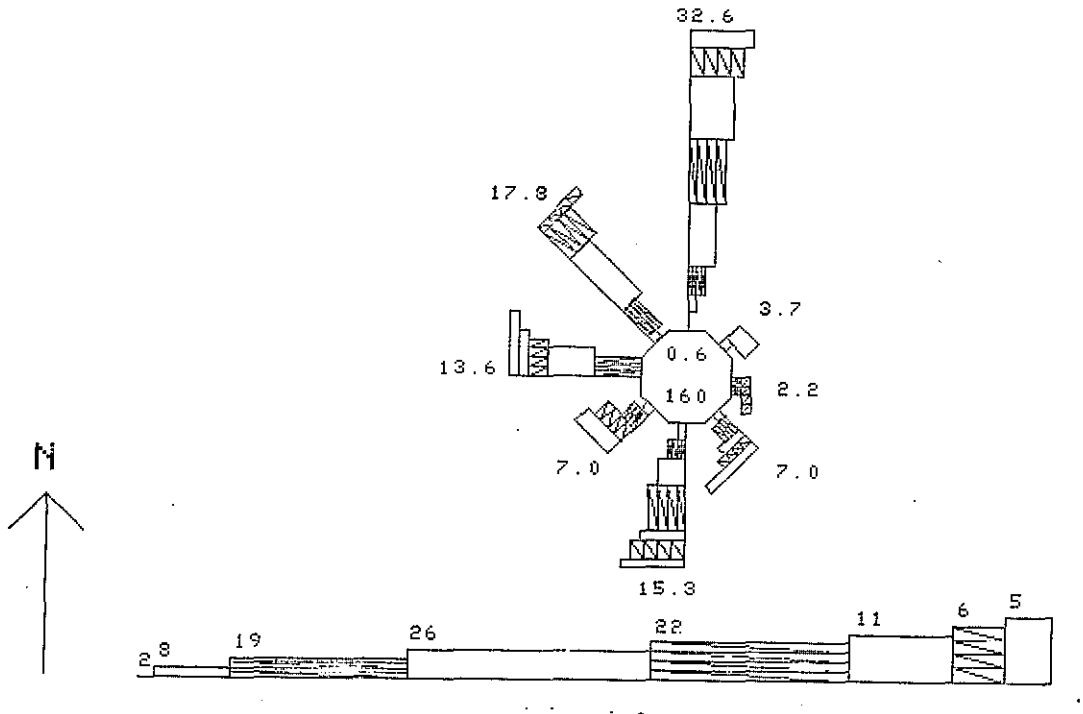

(a) January

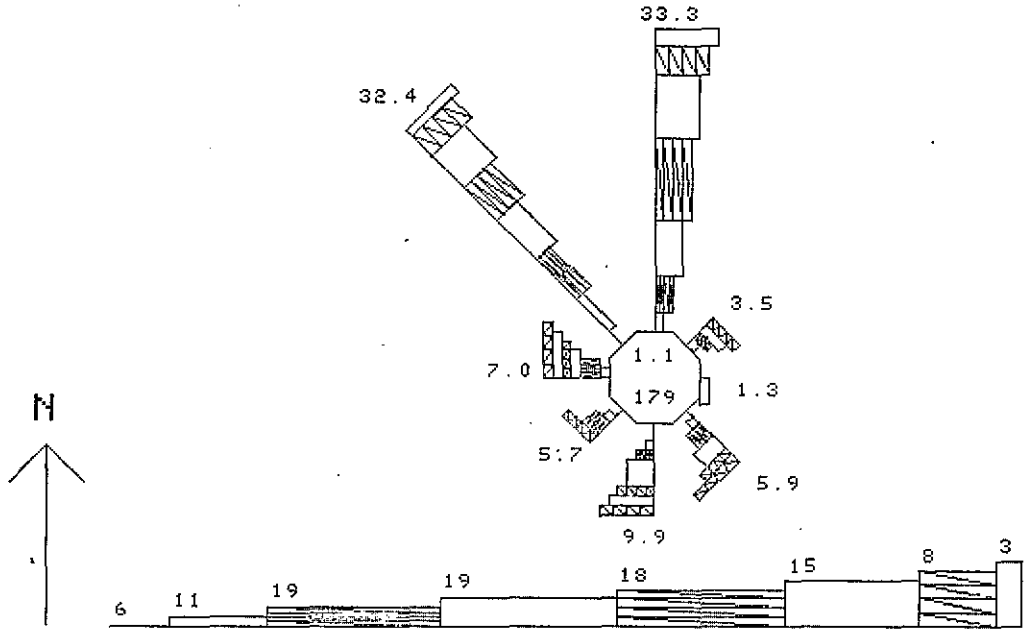

(b) April

Figure 3.34. Marine Area Wind Roses – MSQ 2195

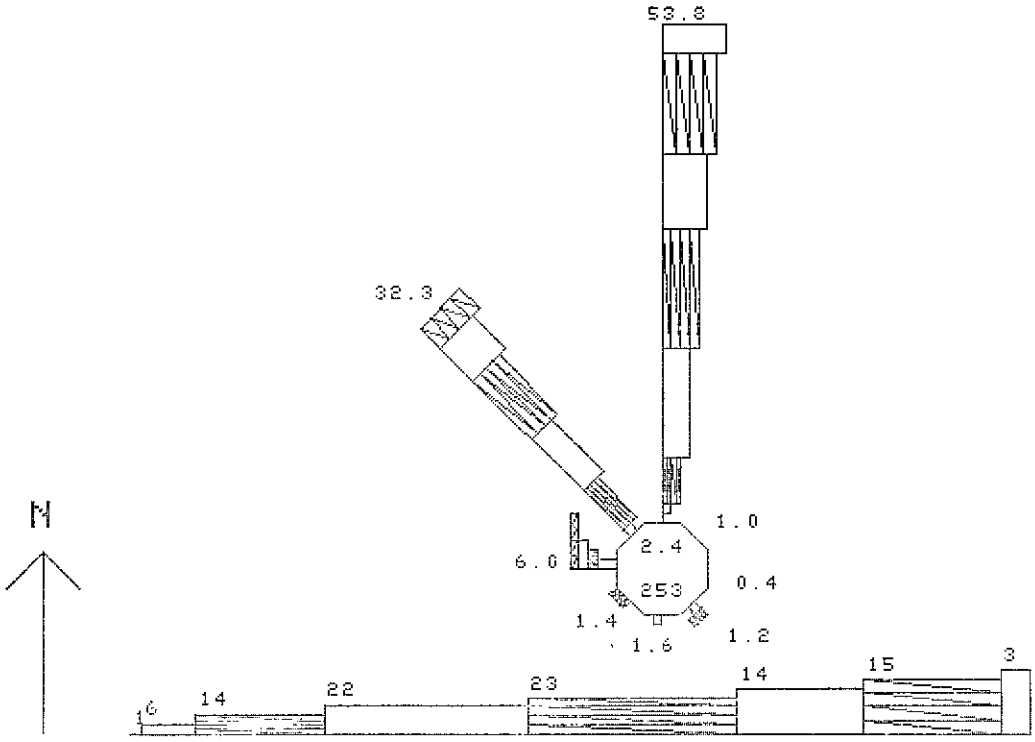

(c) July

Figure 3.34. Marine Area Wind Roses – MSQ 2195 (cont'd)

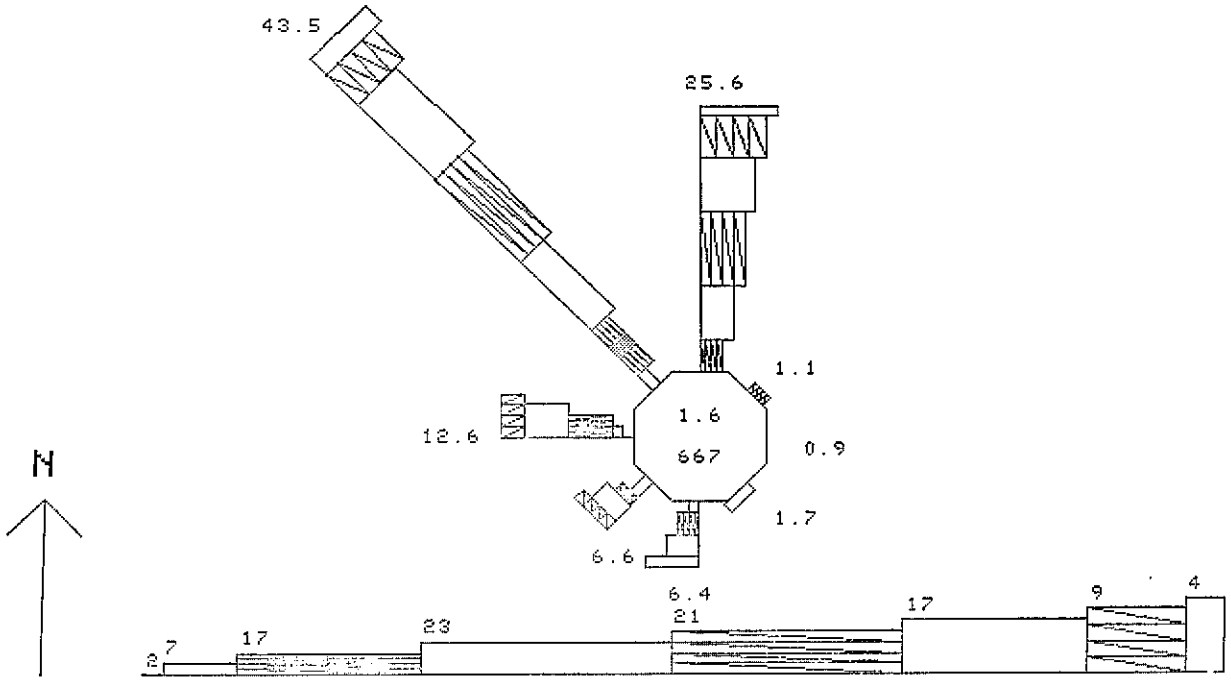

(a) January

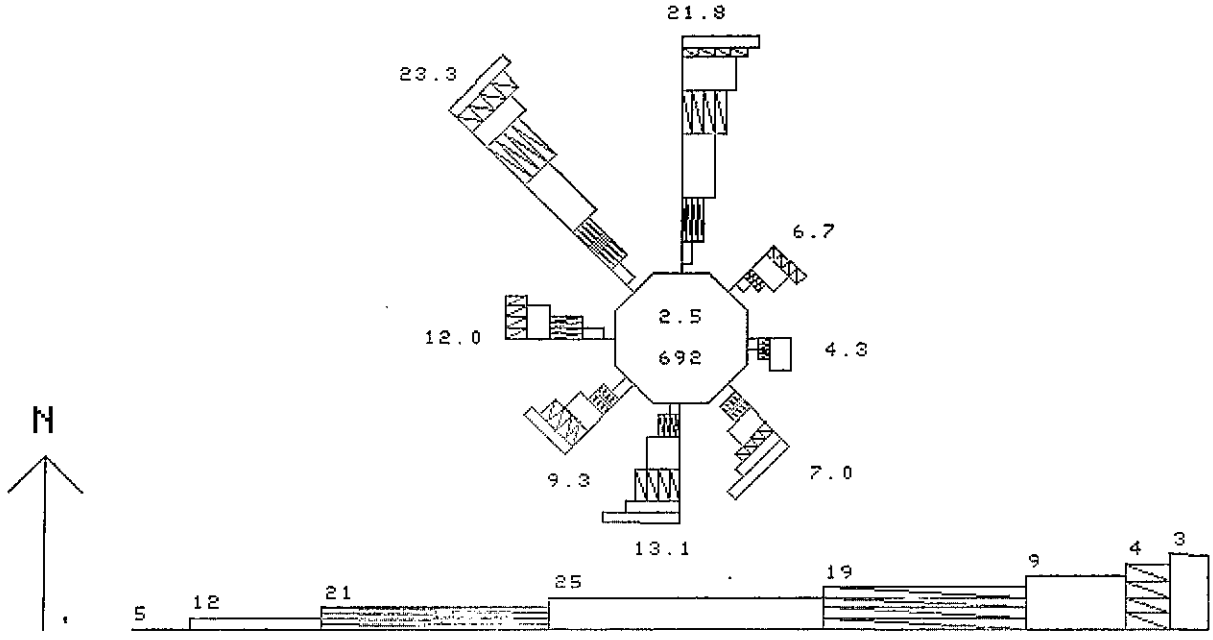

(b) April

Figure 3.35. Marine Area Wind Roses – MSQ 2174

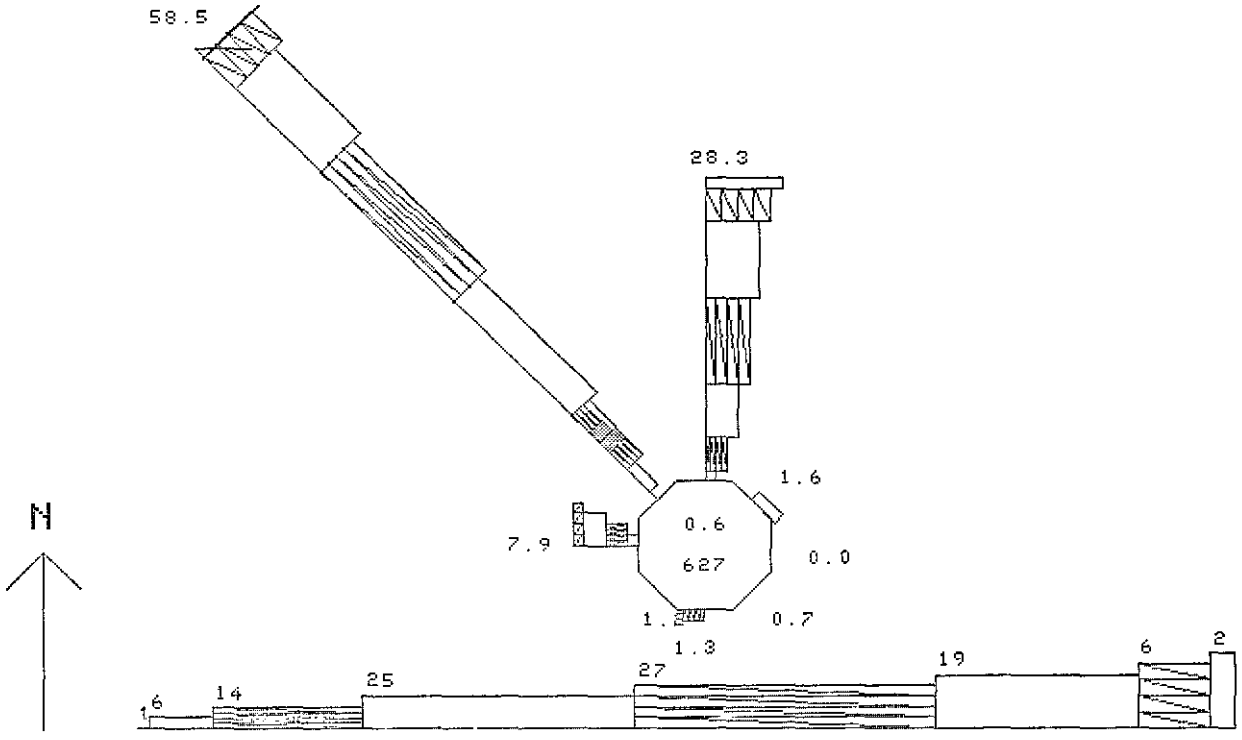

(c) July

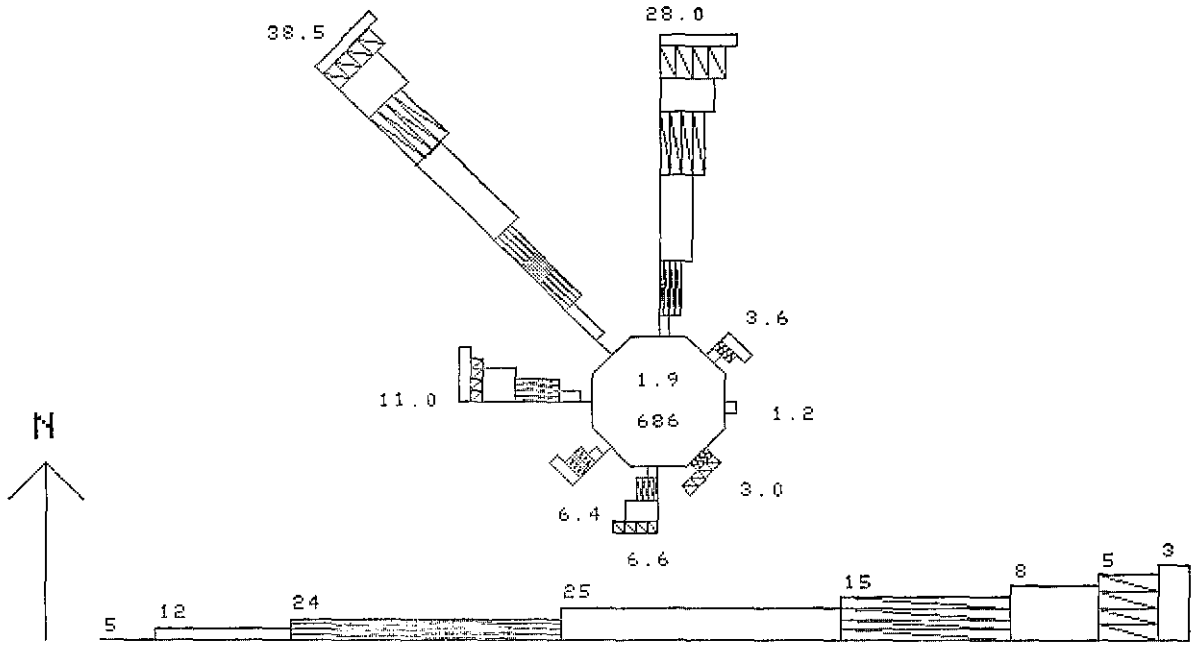

(d) October

Figure 3.35. Marine Area Wind Roses – MSQ 2174 (cont'd)

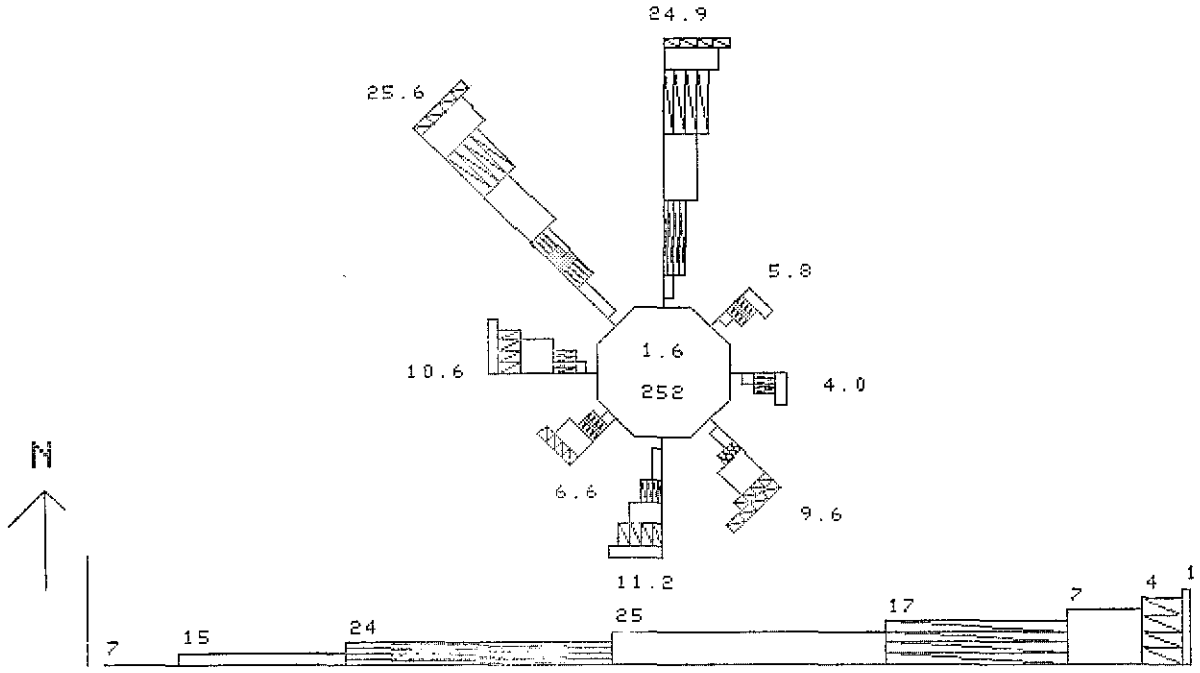

(a) January

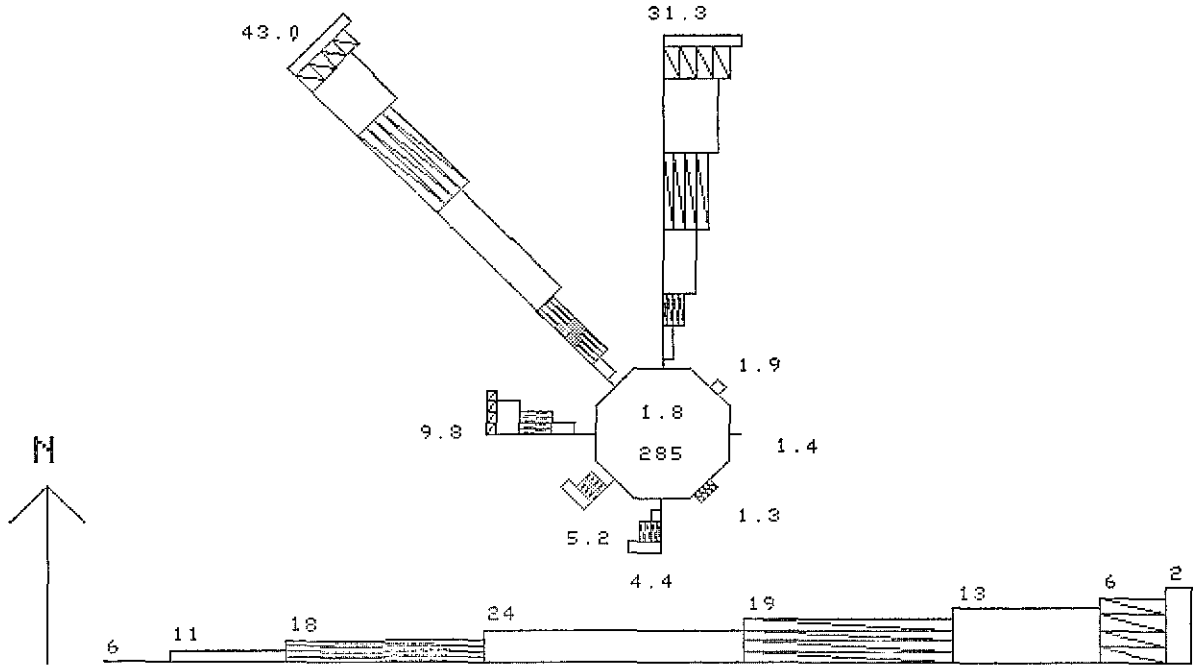

(b) April

Figure 3.36. Marine Area Wind Roses – MSQ 2153

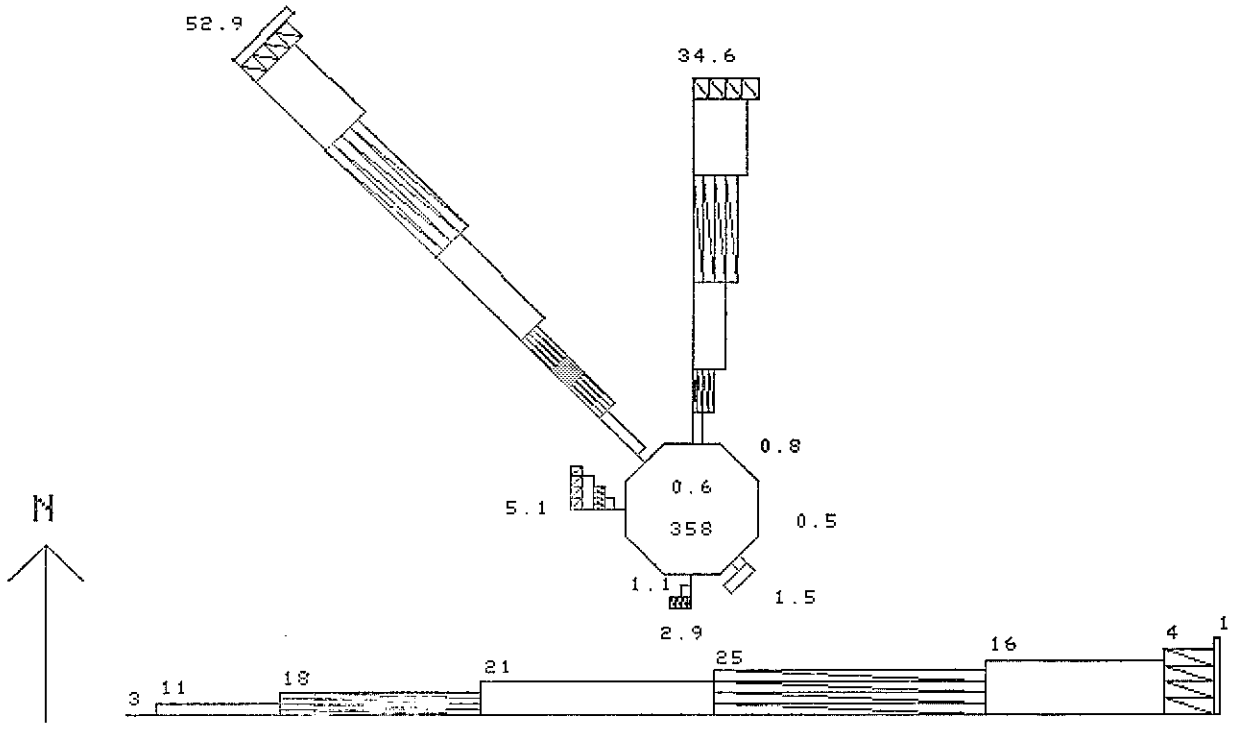

(c) July

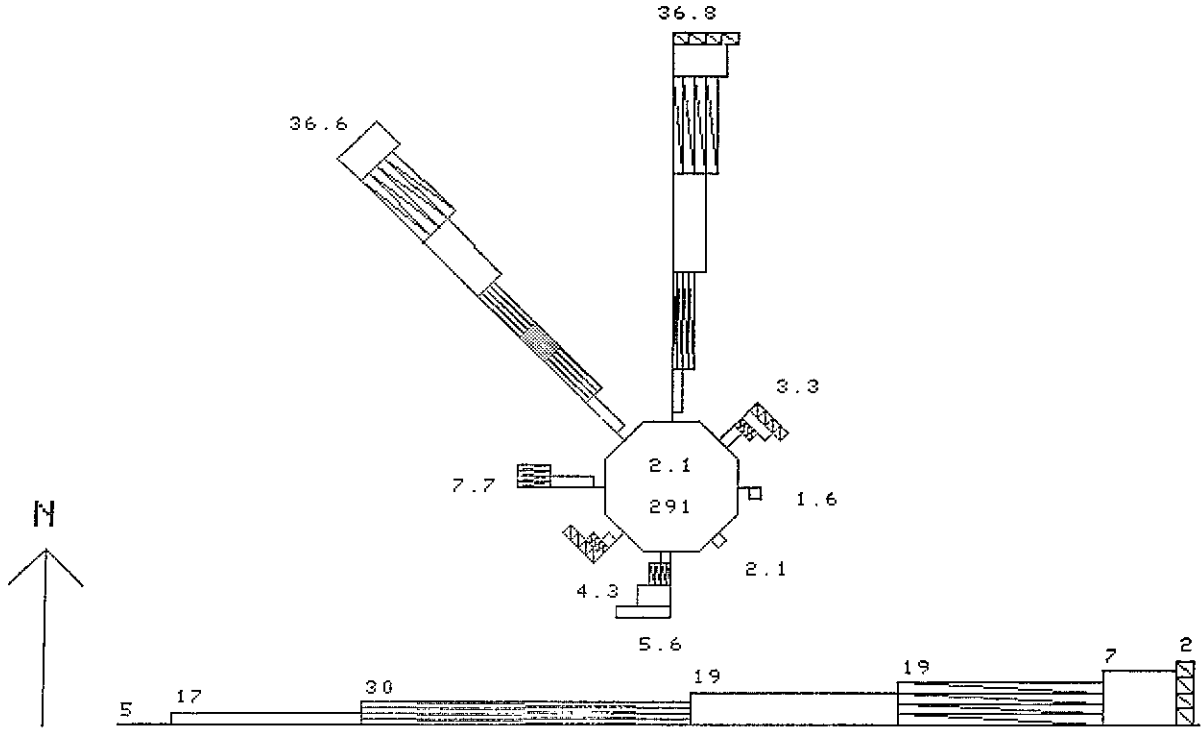

(d) October

Figure 3.36. Marine Area Wind Roses – MSQ 2153 (cont'd)

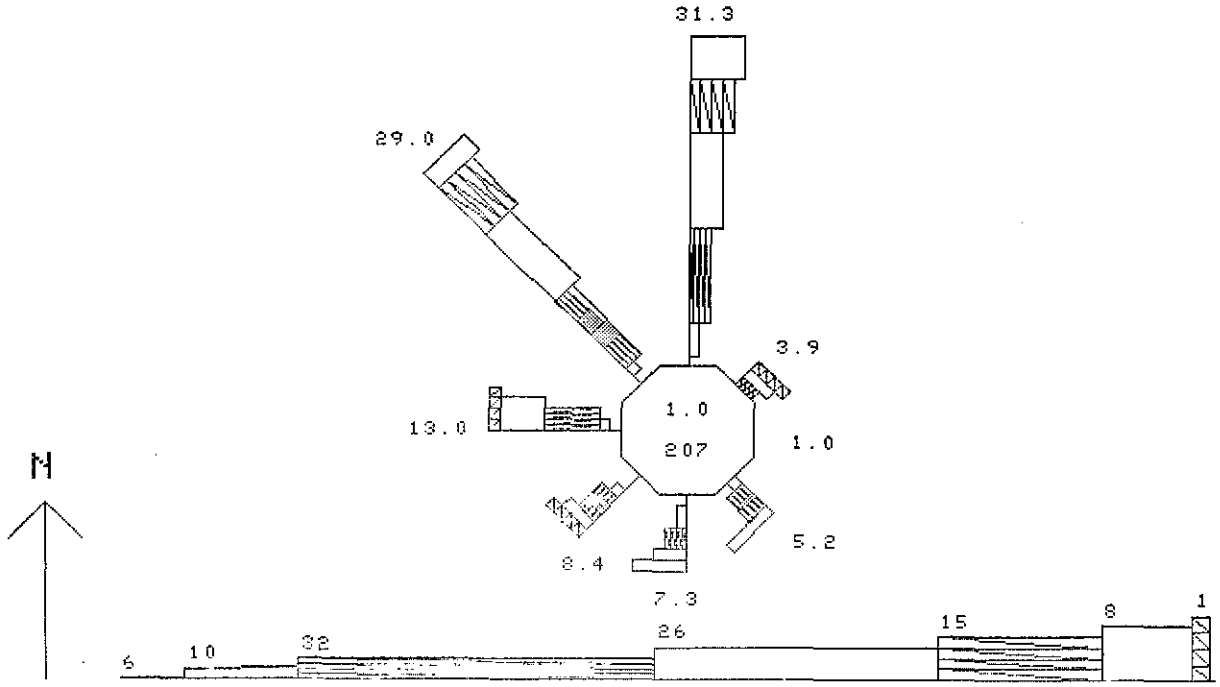

(a) January

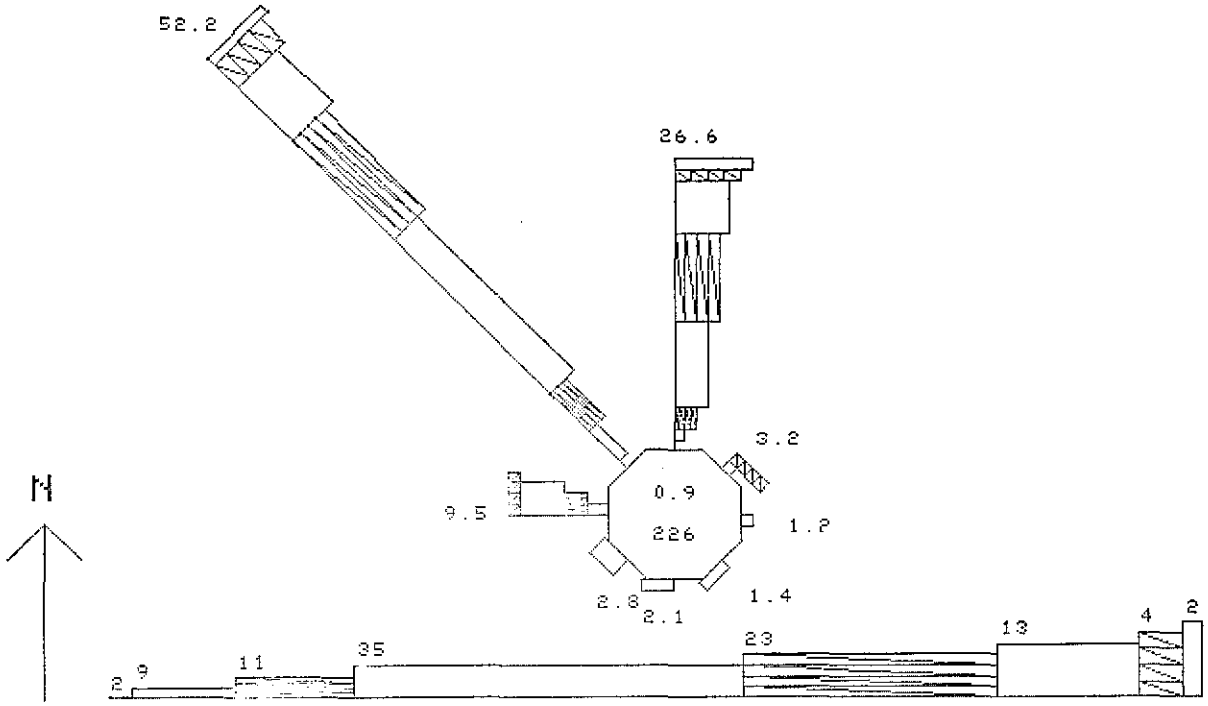

(b) April

Figure 3.37. Marine Area Wind Roses -- MSQ 2142

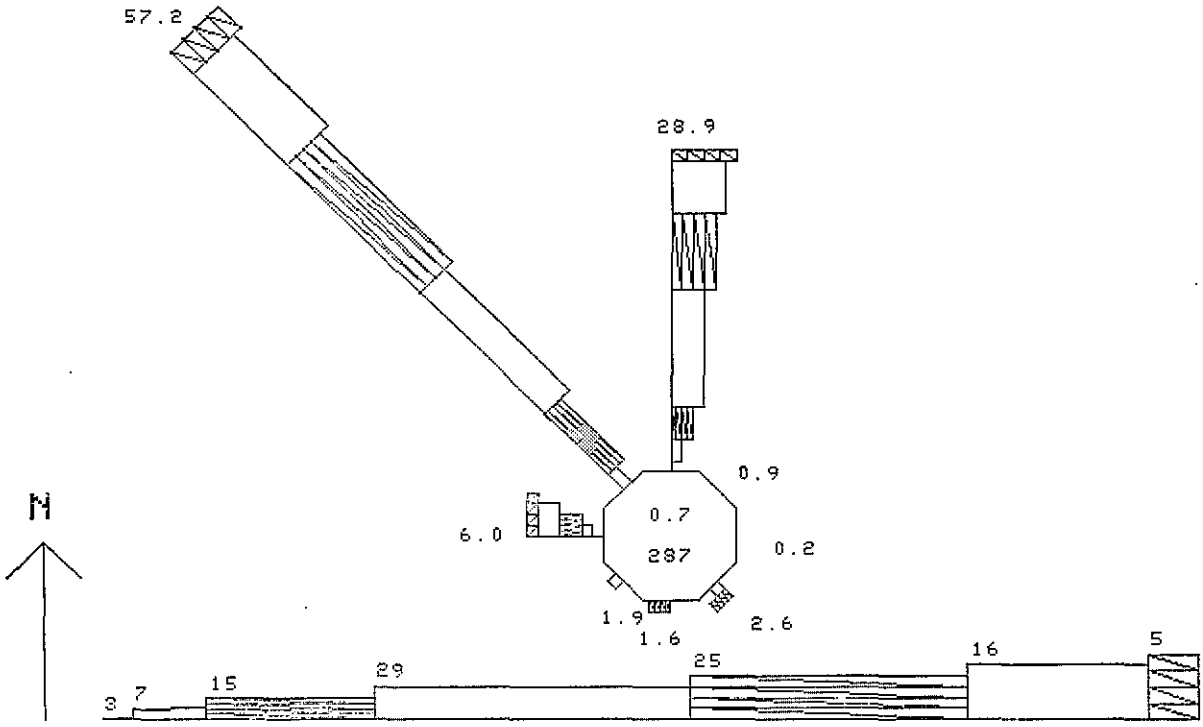

(c) July

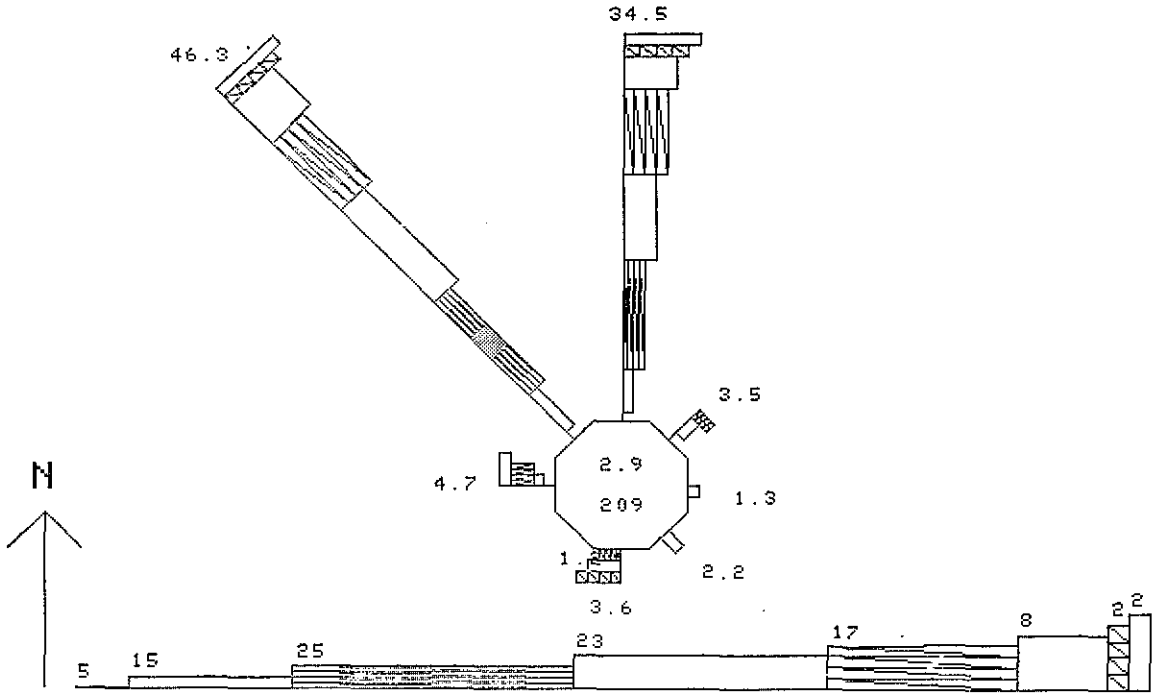

(d) October

Figure 3.37. Marine Area Wind Roses – MSQ 2142 (cont'd)

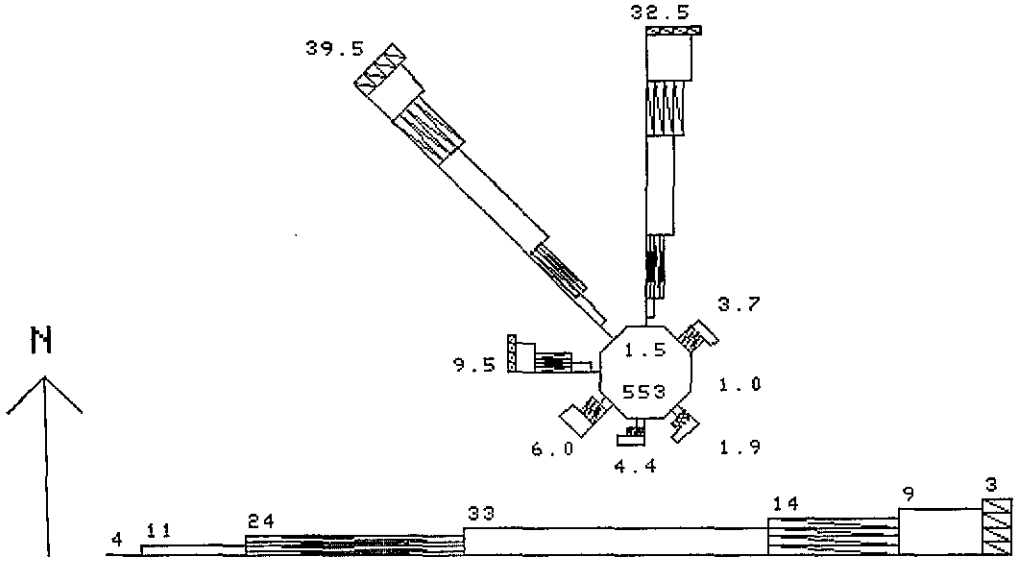

(a) January

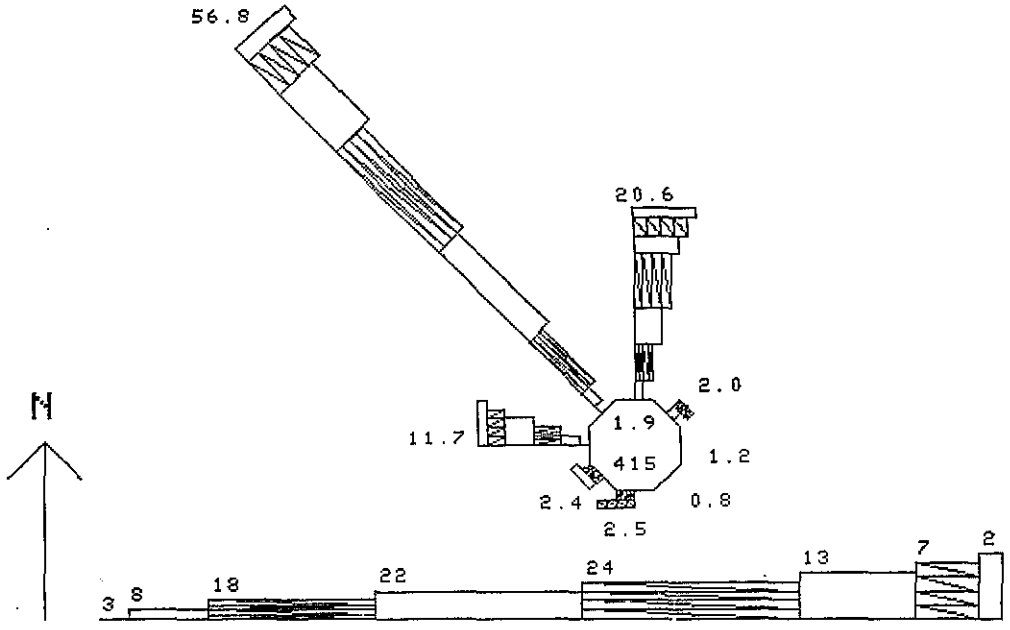

(b) April

Figure 3.38. Marine Area Wind Roses – MSQ 2131

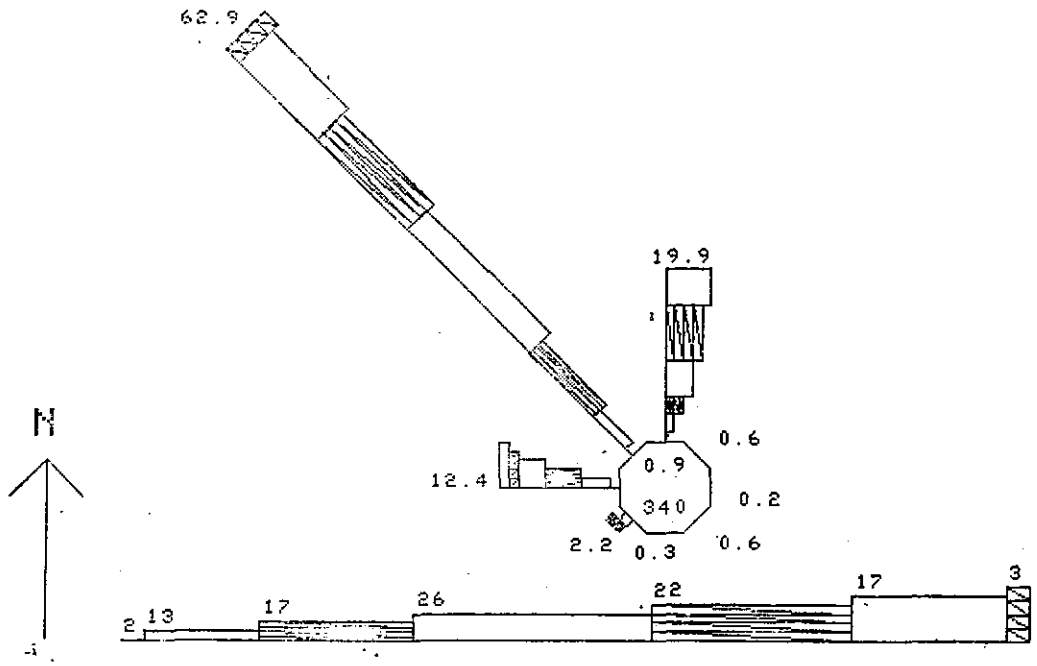

(c) July

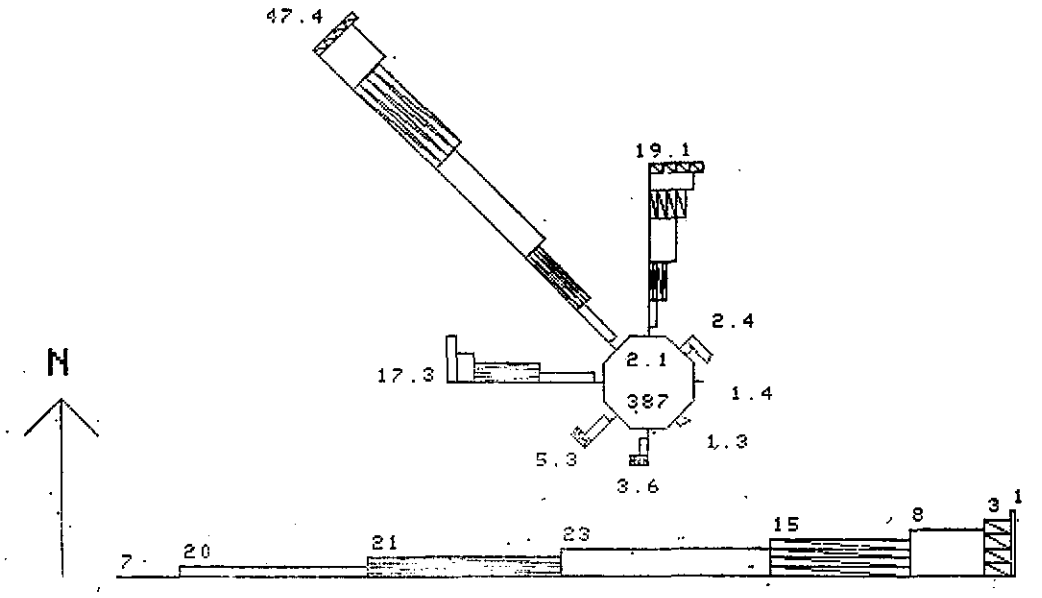

(d) October

Figure 3.38. Marine Area Wind Roses – MSQ 2131 (cont'd)

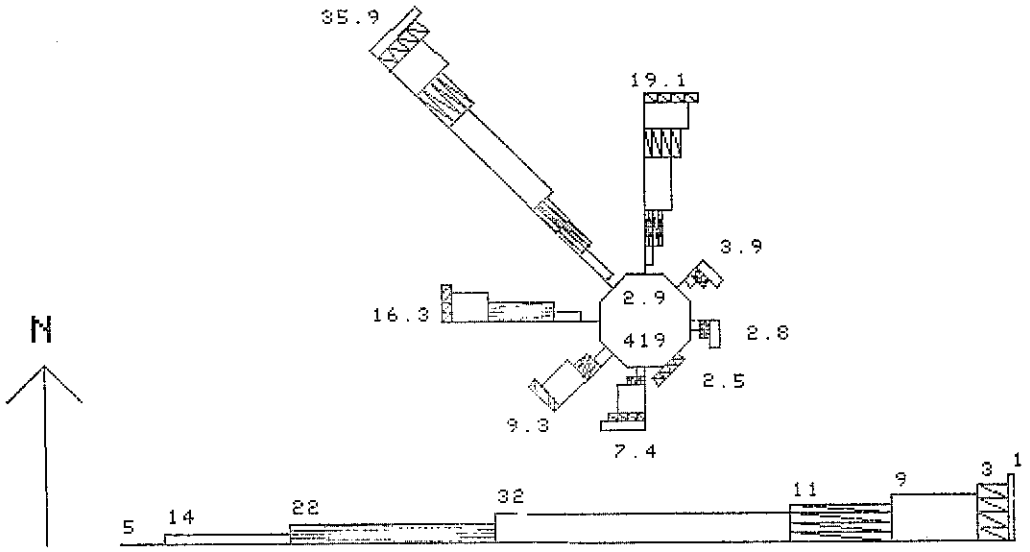

(a) January

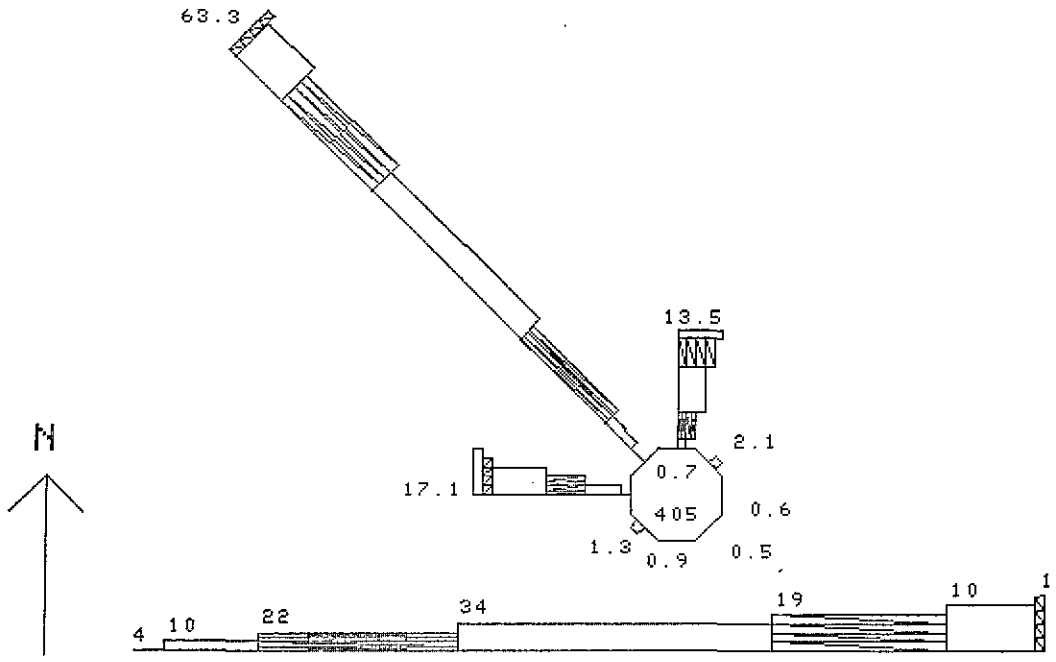

(b) April

Figure 3.39. Marine Area Wind Roses -- MSQ 2120

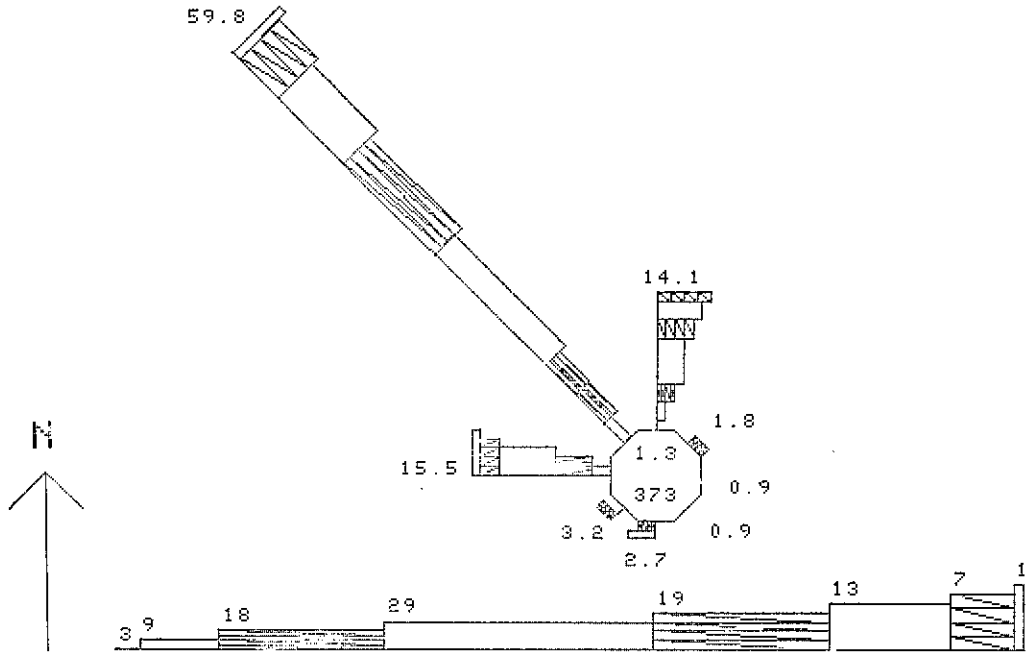

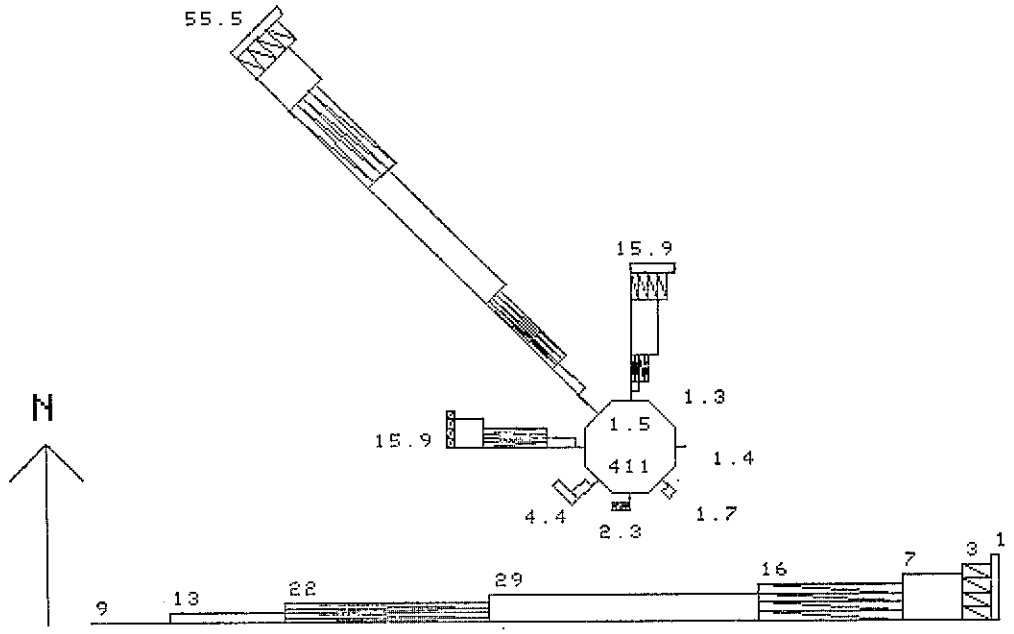

(d) October

Figure 3.39. Marine Area Wind Roses – MSQ 2120 (cont'd)

4. OCEAN CURRENTS

G. Halliwell, R.G. Williams, K. Vierra
and C.N.K. Mooers

4.1 GENERAL DESCRIPTION OF THE REGIONAL CIRCULATION

The California Current system is driven primarily by the wind stress patterns over the North Pacific Ocean. The California Current system variability is controlled primarily by interactions between the subtropical high pressure cell over the North Pacific Ocean and the atmospheric thermal low located over California/Nevada. The wind field produces southward oceanic flow in spring and summer in response to southward-directed wind stress. Associated Ekman transport results in a circulation away from the coast in the near-surface layers, with concomitant upwelling of cold, salty water from below.

In late fall and early winter, northerly winds weaken and winds are at times from the southwest. This wind regime produces a northward flow along the coast, called a Davidson Current (Reference 1). Offshore, the mean flow continues southward. The onset of this period is often rapid, accompanied by a rise in surface temperature and a deepened mixed layer (References 2 and 3). The end of the Davidson Current period and the onset of upwelling can also occur suddenly (Reference 4).

Along the coast, an undercurrent flows northward at depths below 200 m. When upwelling weakens or ceases, the core of the undercurrent propagates upward toward the surface, occasionally allowing northward flow to reach the surface (Reference 5). When southward winds relax along the coast during fall, the undercurrent surfaces to form the Davidson Current.

In the Southern California Bight, a cyclonic eddy is often found, which includes a countercurrent along the coast and a split in flow at Point Conception, where one branch flows southwest joining with the California Current to form the western part of the eddy, and one branch flows northward along the coast as a narrow countercurrent.

There is much variation in nomenclature in the literature for these flows. In her comprehensive monograph on the California Current system, Hickey (Reference 6) defines the constituents of the system as follows:

- The California Current—The equatorward flow of water off the coast
- The California Undercurrent—A subsurface northward flow that occurs below the main pycnocline and seaward of the continental shelf
- The Davidson Current—A northward flowing nearshore current associated with winter wind patterns north of Point Conception
- The Southern California Countercurrent (also called the Southern California Eddy)—A northward flow in the Southern California Bight south of Point Conception and inshore of the Channel Islands

4.1.1 The California Current

The California Current is a wide, sluggish body of water characterized by relatively low temperature and salinity. It is about 600-1000 km in width, and 100-500 m deep (Reference 7). Estimates of the transport are on the order of 10-12 x 10^6 m^3/sec, (References 5, 8, and 9). The mean speed is about 12.5-25 cm/sec, although speeds as high as 50 cm/sec have been observed, primarily within eddies or meanders (Reference 10). Peak velocities in the current occur in summer, following several months of persistent northwesterly winds (Reference 10). In spring, the current moves closer to the coast, resulting in the disappearance of the Davidson Current, and sometimes even the countercurrent (Reference 11).

In winter, the California Current moves farther offshore, as the Davidson Current develops along the coast. The flow in the California Current is not uniform, but rather is characterized by streaks of relatively high velocity interspersing very slowly moving water. For example, off Cape Mendocino, two southward flows are formed: one about 125 km off the coast during February through October; the second, a broader flow located about 475 km offshore from February through September, when it is strongest (Reference 6). This offshore flow tends to merge with the inshore flow in winter. Off Point Conception, a southward nearshore maximum is found during April and May. Hickey (Reference 6) has presented numerous cross sections of flow perpendicular to the coast which document these streaks from Cape San Lazaro to Washington.

4.1.2 The California Undercurrent

The California Undercurrent flows inshore the California Current northward along the continental slope. This current is not often continuous along the entire California Coast, but is particularly well developed in summer, with a width of 40-50 km (Reference 3). Mean speeds are low, on the order of 5-10 cm/sec (Reference 10). The Undercurrent region is characterized by high temperature and salinity, since it is a northward movement of equatorial water (Reference 12).

Wooster and Jones (Reference 13) observed the Undercurrent off Baja California and noted that it could be distinguished from surrounding water by a high salinity maximum (34.3 ppt). Farther north, the high salinity core thinned to a narrow band just seaward of the 200 m isobath. Wickham (Reference 14) determined that off Monterey, streaks of equatorial water (the undercurrent) occur between 200 and 500 m, interspersed with California Current water (Figure 4.1) which may have speeds as high as 20-40 cm/sec.

4.1.3 The Davidson Current

The Davidson Current is probably the surface expression of the Undercurrent north of Point Conception. The Davidson Current is found off California from mid-November to mid-February, when southerly winds occur along the coast (Reference 15). During the period of persistent northwesterly winds in spring and summer, northward flow is usually confined to deep water over the continental shelf, continental slope, and farther offshore. Most of the evidence for this current comes from drift bottle data, as geostrophic currents are difficult to calculate nearshore. Schwartzlose and Reid (Reference 10) found that the Davidson Current attained speeds as high as 15-30 cm/sec. These drift bottle studies revealed that the Davidson Current is usually a continuous feature along the West Coast of the United States in winter, not merely a succession of eddies. Off Point Conception, the Davidson Current has a width of about 80 km and widens to the north (Reference 16). Burt (Reference 29) showed evidence for the existence of the Davidson Current off Oregon during October through March.

4.1.4 Southern California Countercurrent/Southern California Eddy

The Southern California Countercurrent is the inshore part of a large semipermanent eddy which rotates cyclonically in the Southern California Bight south of Point Conception. The eddy is formed as the Countercurrent diverges at Point Conception, with flows moving toward the north and to the southwest. Geostrophic current estimates indicate that the Countercurrent occurs in all seasons, although it appears best developed in winter (Reference 17). Geostrophic speeds in the Countercurrent were determined to be on the order of 12-18 cm/sec (Reference 18). One investigator (Reference 19) found the eddy to occur during all months except March through May. Velocity maxima in the Countercurrent during winter as high as 35 to 40 cm/sec have been observed (Reference 17). Another investigator (Reference 8) estimated the half-rotation time of the eddy to be 10 to 20 days. Tsuchiya (Reference 20) has noted that the circulation in this region is more complex than anywhere else off California. He notes that inshore of a line connecting Point Conception and Cortes Bank, the flow is northerly; to the west it is southerly. This line, then, roughly delineates the center of the eddy. Shoreward of the Countercurrent, southeastward flow is often present (Reference 20). However, Tsuchiya notes the following complications in the flow pattern:

- The large eddy contains smaller eddies of varying scale (Reference 19).
- The California Current moves inshore in April and May, often eliminating the Countercurrent. In other months, the Countercurrent may increase in intensity and displace the California Current offshore.

4.1.5 Current Variability

Most of the energy in oceanic motions is not contained in the mean flow, but rather in the transient features, such as eddies, meanders, tidal currents, inertia currents, etc. (References 21 and 22). This situation is also true in the California current region. As early as 1942, Sverdrup (Reference 5) noted that "...in the California Current...no high velocities are encountered except within local eddies." Within the high temperature tongues, flow is northward; within the low temperature tongues, flow is southward. Zones of upwelling along the coast are evident from very low sea surface temperature separated by higher temperature regions (References 5 and 28). This cold, upwelled water was believed to rise from a depth of not more than 200 m, at a rate of about 20 m a month (Reference 23).

Griggs (Reference 24) noted that eddies are capable of dominating the coastal circulation pattern, regardless of wind stress. Several investigators found through analysis of CALCOFI data that eddies are common features off the California coast. Wilkinson (Reference 26) studied a number of eddies, six of which were located off California. Of these six eddies, two were anticyclonic, and four were cyclonic. Dynamic height differences across the eddies were less than five dyn/cm. Wilkinson believed these eddies originated from instabilities in the mean current because they persisted for several months. The westward propagation of eddies off California has been verified in Reference 27 by analysis of fluctuations in the depths of isotherms, and Reid *et al.* (Reference 25) attributed much of the lateral mixing off California to eddies.

In the subsequent paragraphs of this section, the mean circulation will be analyzed by means of maps of dynamic topography, ship drift, analysis of drift bottle returns, and a few direct measurements of current. Current variability will be studied by analysis of current meter records, wind and sea level records, and by surface temperature patterns observed from satellites, aircraft, and regular ship measurements. For purposes of this study, we use the following terminology for current variability, adapted from Reference 21.

Descriptive Term	Time Scale	Example
Sub-Synoptic	Months	Seasonal Variations
Synoptic	2–30 days	Eddies, meanders
Mesoscale	Hours–a few days	Tides, interia currents

4.2 MEAN SURFACE CIRCULATION AND SPATIAL VARIABILITY

4.2.1 Mean Geostrophic Surface Circulation

Maps of monthly mean dynamic topography, from which the geostrophic flow is inferred, are presented and analyzed in this section. The maps were contoured by hand from 1/2° square averages to the dynamic depth anomaly relative to the 500 dbar surface. Although monthly charts of dynamic topography have been produced in the CALCOFI Atlas No. 4 (References 11 and 6), the importance of the circulation to the present study indicated the need for a new set based on all available archive observations. The maps are presented as Figures 4.2 through 4.13. Although the maps cover the area from 25°N to 49°N, the discussion will focus on the area off the California coast and northern Baja California.

The January map (Figure 4.2) indicates geostrophic flow to the southeast, generally parallel to the coast off California with speeds on the order of 5-10 cm/sec, 200 km from the coast. Off Oregon and Washington, the flow has a component toward the coast. There are indications of northward flow along the coast north of San Diego and southwest of Cape Mendocino and divergence in the flow off Cape Mendocino; one branch moving southward, at about 126-128°W, and one branch moving northward north of 41°N. Very low current speeds, less than 5 cm/sec toward the southeast, are indicated to the south of San Diego. The February (Figure 4.3) dynamic topography is similar.

In March (Figure 4.4), generally southeast flow prevails off California, with very weak currents north of 42°N, parallel to the coast. Southward flow along the coast is indicated at all locations south of Cape Mendocino. A velocity streak of about 20 cm/sec occurs in the southeastward flow at the shelfbreak southwest of Cape Mendocino. At 39°N at the shelfbreak, the flow meanders seaward. Again, streaks in speed of about 20 cm/sec occur about 150 km southwest of Los Angeles and off Baja California at 31°N. There are indications of an eddy in this region, as well as a rotation of the flow to the northwest north of Punta Eugenia. The California Current seems to be closer inshore than in the previous two months (Reference 6).

In April (Figure 4.5), very slow eastward flow is indicated north of 43°N. There is a large meander south of Cape Mendocino which begins at the shelfbreak and extends seaward to 128°W, with speeds as high as 15 cm/sec. Generally, southeast flow is found south of this meander. Speeds as high as 15 cm/sec occur 150 km southwest of Los Angeles. There is an indication of northward flow between San Diego and Los Angeles. Meandering occurs off Baja California at 30°N with a wavelike pattern of flow on the order of 5-10 cm/sec toward the southeast off Punta Eugenia. Similar flow patterns are indicated during May, June and July (Figures 4.6–4.8).

In August (Figure 4.9), the distribution of the observations north of San Francisco is poor, making inference of details of the flow difficult. The pattern of meanders observed in the previous two months is generally smoother. The flow turns sharply toward the east at 31°N, 120°W. A meander appears northwest of Punta Eugenia. There is no evidence in August of the presence of the Southern California Eddy.

In September (Figure 4.10), meanders occur off Cape Blanco, Cape Mendocino, and San Francisco. There is a strong turning of the current eastward at about 32°N, 120°W, indicating the presence of the Southern California Eddy. An anticyclonic eddy is found southwest of northern Baja, at about 29.5°N, 118°W with velocities on the order of 5-15 cm/sec. There is a streak in velocity at 15 cm/sec seaward of the shelfbreak southwest of Cape Mendocino.

In October (Figure 4.11), low velocities are found inshore of the shelfbreak. Streaks in velocity, on the order of 20 cm/sec occur about 400 km seaward of Monterey. There is a strong rotation at 31°N, 120°W to form the lower branch of the Southern California Eddy. There is an indication of an eddy off Punta Eugenia at 27°N, 116°W.

In November (Figure 4.12), weak flow is found inshore of about 250 km off the coast. The distribution of observations is poor north of San Francisco, resulting in great uncertainty in the current field (Figure 2.3). A velocity streak of about 15-20 cm/sec occurs about 300 km off the coast between San Francisco and Los Angeles. There is a turning to the east at 32°N, 120°W, to form the Southern California Eddy. A meander is found off Baja at about 20°N.

In December (Figure 4.13), the distribution of observations is again poor. Indications of northward flow are found all along the coast from northern Baja California to Washington. The flow is northward around Point Conception, with return southward flow offshore a line from Point Conception to the Channel Islands. The general mean flow further offshore is to the southeast at about 5 cm/sec. There is a turn in flow from southeast to east to northeast at about 32°N, 122°W.

4.2.2 Surface Currents from Ship Drift

The monthly distribution of ship drift observations is very uneven with large areas containing no observations. Current deduced from ship drift for areas with small numbers of observations (less than 30) are suspect, because this method depends on the cancellation of periodic variations from tide by averages of observations. Monthly current maps are presented in Figures 4.14 through 4.21, although greater statistical stability would be attainable with seasonal summaries. The variability in the currents observed from the ship drift data is discussed in Section 4.9.2.

In January (Figure 4.14), northward flow prevails along the coast north of Cape Blanco. Generally southward flow is found south of 39°N. Low speeds are found on the order of 0.1-2 kts (5-10 cm/sec) in agreement with the magnitude of the geostrophic currents calculated from the dynamic topography. The highest observed speed is 0.63 kts (32.5 cm/sec). The flow is generally to the south-southeast, or perhaps 20° to the right of the mean winds and also the geostrophic current, which both tend to parallel the coastline. Other similarities with the geostrophic flow (Figure 4.2) are the eastward flow above 32°N, and the northwestward flow from Los Angeles to Point Conception, forming the Southern California Eddy. The southward flow off San Diego to Punta Eugenia and south appears more nearly parallel to the coast than the geostrophic current (Figure 4.2). A similar flow is found in February.

In March (Figure 4.15), southward flow occurs along the coast south of 46°N. The flow off Cape Mendocino is highly variable. There is generally southerly flow south of 38°N, with velocities on the order of a 0.1 kt (5 cm/sec) with a few speeds as high as 15 cm/sec. Again the general flow pattern consists of southerly currents, which may be an indication of deflection of the basic geostrophic flow to the right by the mean winds. Southeasterly flow is found in the Southern California Bight in agreement with the dynamic topography chart (Figure 4.4); the highest observed speed in the Bight is 0.26 kts (13 cm/sec). Southeasterly flow is found off Baja California. The southern California Eddy is not evident, in agreement with Hickey (Reference 6).

In April (Figure 4.16), southerly flow occurs along the coast south of 48°N. There is high variability in the flow off Cape Mendocino indicating the divergence in current west of 128°W. Generally southerly flow is found south of 39°N. There is no correlation with the meander observed on the dynamic topographic chart (Figure 4.5) southwest of Cape Mendocino. Currents are fairly uniform to the southeast in the Southern California Bight, and off Baja California. The highest observed speed in this region is 0.41 kts (21 cm/sec) off Punta Eugenia. Again, there is no indication of the Southern California Eddy, indicating that the California Current has moved inshore. Similar flows are found during May, June and July.

In August (Figure 4.17), the flow near the coast is approximately parallel to the shoreline from 28°N to Point Conception. Seaward of 122°W, the flow is generally to the south-southwest. Speeds as high as 0.71 kt (36 cm/sec) are found, but the more typical speeds are on the order of 0.2 kt of 10 cm/sec. Northward flow occurs off Los Angeles; seaward flow occurs off Point Conception and also off Punta Eugenia, probably indicative of upwelling.

In September (Figure 4.18), the current is again southward very near the coast north of Point Conception. Between 38°N and 41°N, the offshore flow has a westerly component; south of 36°N, the flow is more southerly. Indications of the Southern California Eddy are present. The flow is again offshore at Point Conception and Punta Eugenia, indicating possible upwelling. Off Baja California, the current is weaker than in previous months, and in some cases, is flowing northward, the reverse of the flow observed in January through August.

In October (Figure 4.19), the southward flow along the coast is weakened; in fact, northward flow occurs north of Cape Blanco indicating the possible onset of the Davidson Current. Off Cape Mendocino, the flow is again highly variable. South of 38°N, the current is more easterly than in the summer (upwelling) months indicating a geostrophic trend (relaxing of the winds). The Southern California Eddy appears well developed. Currents are very weak south of Punta Eugenia.

In November (Figure 4.20), northward flow is evident along the coast at most locations from San Diego to Washington. This direction of flow indicates the development of the Countercurrent and Davidson Currents. The circulation beyond the continental slope is still primarily toward the south-southeast. The Southern California Eddy appears well developed but with very low speeds on the order of 0.5 kt or 5 cm/sec. Southward flow prevails from 31°N to Punta Eugenia. A cyclonic eddy is found south of Punta Eugenia.

In December (Figure 4.21), northward flow along the coast is prevalent at most locations north of Point Conception (the Davidson Current). The flow off Cape Mendocino is highly variable. The general offshore circulation pattern west of 123°W shows a much more easterly set than in previous months, probably indicating that, with weakening mean wind stress, the flow is approaching geostrophic. Speeds range between 0.02 and 0.32 kts (1-15 cm/sec). The Southern California Eddy is evident; southward flow prevails from 32°N to Punta Eugenia. Evidence of a cyclonic eddy persists south of Punta Eugenia.

4.3 MEAN CIRCULATION PATTERNS DEDUCED FROM SURFACE DRIFTERS

Drifter releases from several studies were used to determine mean alongshelf circulation patterns. The drifter trajectories (lines connecting the release point with the recovery point) were taken from figures within the publications of several studies (Table 4.1) and combined on monthly charts. Surface drifter trajectories were drawn by solid lines, and bottom drifter trajectories by dotted lines. Most drifters released were surface drifters. The charts showed the expected seasonal cycle in mean current patterns. In winter, most drifters released within 2° longitude of the coast traveled poleward off Washington and Oregon. Most of the few releases off Baja California traveled equatorward. The spring transition, or the transition from poleward to equatorward near-surface alongshelf flow over the shelf and slope, typically occurs around January or February in the Southern California Bight, Section 4.6. By March

Table 4.1
Summary of Drifter Studies Conducted off the West Coast

Study	Type	Location	Time Period	Number of Stations	Number of Releases/ Station	Number Released	Number Recovered	Percentage Recovered	Comments
Wyatt, B., et al., (1972)	Drift Bottles	Oregon	1961 to 1971	----	----	21,285	2,937	13.8%	Drift bottles releases were made during 80 out of the 120 months of the period.
Squire, J. L. (1969)	Seabed Drifters	Monterey Bay	5/25/62 2/15/63	(25) (24) 49 Total	(5) (-) ----	(115) (120) 245	(9) (6) 15	(7.8%) (15.0%) 11.4%	There were 125 seabed drifters in the first deployment in May, but seven were damaged when dropped from the aircraft.
Burt, W.V., and B. Wyatt, (1964)	Drift Bottles	Oregon	6/58 to 5/61	----	----	6,207	803	12.9%	The study area was 0 to 45 miles offshore Northern and Central Oregon, but beginning 6/60 to 5/61 the area consisted of the entire Oregon Coast. 70.5 of the returns came from within 40 miles of shore.
Schwartzlose, R. S. (1963)	Surface Drift Bottles	Entire West Coast	10/54 to 6/60	----	12	52,650	2,439	4.6%	Only examples of results are shown by this study (Table III).
Squire, J. L. (1969)	Surface Drift Cards	Southern & Central California	3/64 to 2/66	----	10	8,320	377	4.5% 5.7% Southern Area 3.5% Central Area	Drops were made every 3 months from March 1964 to February 1965 and monthly drops from March 1965 to February 1966.

Table 4.1 (Continued)

Study	Type	Location	Time Period	Number of Stations	Number of Releases/ Station	Number Released	Number Recovered	Percentage Recovered	Comments
Ingraham, W.J., Jr. and J.R. Hastings (1976)	Surface Drift Bottles	Vancouver Island & Washington	4/64 7/64 11/64 11/65	21 (Varied from period to period)	12	1,104	226	20.5%	On the average 276 drifters were dropped per period.
Griggs, G. B. (1974)	Seabed & Surface Drifters	Pt. Año Nuevo to Pt. Cypress	11/71 to 4/73 (monthly drops)	36	10 (5 Surface & 5 Seabed)	4,500	1,305	29% 34.3% Surface 23.0% Seabed	The values for the number of stations and number of releases/station were cited in the text but differ from that cited for the stations.
Blankovich, D. D. (1973)	Olson-Type Drift Cards	Monterey Bay	9/71 to 4/73 (monthly drops)	20-33 (Varied from month to month)	5-20	5,478	1,253	22.9%	42% of the recoveries were from releases that were deployed greater than 2 miles offshore, and 58% were within 2 miles.
Schwartzlose, R.A. and J.L. Reid, Jr. (1972)	Surface Drift Bottles	California Coast & Baja, California	12/69 1/69 4/69	----	----	----	----	----	This study did not include statistics about the drift bottle releases.

(Figure 4.22), virtually all trajectories were equatorward. Drifters released in April (Figure 4.23) traveled both equatorward and poleward off Washington and Oregon, indicating that reversals in the average equatorward flow were important. Summer period trajectories are illustrated by the July drift (Figure 4.24). During November (Figure 4.25), poleward flow prevailed. The long trajectories (many hundreds of kilometers) of some drifters indicated that the Davidson Current may at times be continuous alongshelf for at least hundreds of kilometers.

Nearshore and short-trajectory releases off Southern California traveled poleward in January (Figure 4.26), with those released farther offshore traveling equatorward in the California Current. This pattern supports the presence of the Southern California Eddy, with the poleward-flowing Southern California Countercurrent located inshore of the equatorward-flowing California Current. In February (Figure 4.27) through May, almost all drifters traveled equatorward; a period when the Southern California Eddy was weakest. The transition from poleward to equatorward flow occurs earlier in the Southern California Bight than off Central and Northern California, occurring in late January and February in the Bight, and in late March off Central and Northern California, Section 4.6. In June (Figure 4.28), some drifters released to the south of the Channel Islands moved straight inshore or inshore and poleward. Most nearshore releases traveled equatorward. In November (Figure 4.29), most releases traveled poleward, while in December (Figure 4.30), some traveled poleward and some equatorward, indicating that reversals of the poleward flow inshore of the California Current can be important.

4.4 SUBSURFACE GEOSTROPHIC FLOW

Flow at subsurface levels has been principally determined from hydrographic observations using the geostrophic approximation. A few direct measurements have been made in the region of the California Undercurrent.

In this study, subsurface flow was examined by analysis of $1/2^{\circ}$ square averages of all available archive data on dynamic height at the 200 m level referred to the 500 dbar level. Because of the small number of available observations, especially in northern California, seasonal averages have been used for the seasons similar to those defined in Reference 3:

Winter, or "Davidson Current Period" – December and January
Spring or "Upwelling Period" – May, June and July
Fall or "Oceanic Period" – September and October

In the winter period (Figure 4.31), geostrophic velocities are very low at the 200 m level, generally less than 5 cm/sec and, more typically, 1-2 cm/sec. Northward flow appears all along the coast from Baja California to Washington. A trough line in the dynamic topography is indicated which separates the northward flow of equatorial water from the southward flow of subarctic water of the California Current (Figure 4.32).

In the late spring-early summer period, during peak upwelling, geostrophic speeds are generally higher south of Point Conception, of the order 5-7 cm/sec, in agreement with Reference 6. North of Point Conception, the flow tends to be broken up into eddies; overall, the northward transport appears less in summer than in winter, also indicated in Reference 6. The trough line is further inshore, indicating the California Current has moved inshore, thus constraining the Countercurrent system closer to the coast. Eddy-like features in the flow appear north of Cape Mendocino.

In the fall (Figure 4.33), speeds appear slightly less than in the peak upwelling season. The trough line lies further offshore, indicating a seaward movement of the axis of the California Current. Flow to the north of San Francisco appears broken up into a number of incoherent eddies. A large cyclonic eddy of very low velocities appears to be located off Cape Blanco at about 42°N, 127°W.

It should be emphasized that we have presented the seasonal average geostrophic flow. The currents at any given time may be quite different, as can be seen in Figure 4.34 (Reference 11), which shows geostrophic flow calculated from CALCOFI cruise 4905 (April-May, 1949). In this situation, the flow in the Southern California Bight exhibits a small anticyclonic eddy off San Diego, and general southeastward flow. Details in the subsurface flow in the Southern California Bight have recently been examined in Reference 20.

4.5 MEAN CURRENTS DETERMINED FROM DIRECT CURRENT MEASUREMENTS

NAVOCEANO current meter arrays were deployed near the shelfbreak northwest of the Farallon Islands at depths less than 200 m during 1970 and 1971; the depth-time distribution of the mean vectors from these meters, along with semimonthly averaged wind stress from the Farallon Islands, is presented in Figure 4.35.

The mean current vectors showed, in general, the expected annual cycle of mean alongshelf current speed, Figure 4.35. (Information on the data records of each meter are discussed in Section 2.2.3)

4.6 MEAN CIRCULATION INFERRED FROM ALONGSHELF WIND STRESS, SEA LEVEL PRESSURE, AND COASTAL SEA LEVEL

Time series of alongshelf wind stress, sea level pressure, and coastal sea level for 1970 through 1978 were 15-day low pass filtered, then subsampled to an interval of seven days. These time series (Figures 4.36 through 4.39) for four meteorological-sea level station pairs: Crescent City/Arcata in Northern California, San Francisco/San Francisco in Central California, Rincon Island (Mussel Shoals)/Point Mugu just equatorward of Point Conception, and San Diego/Imperial Beach in extreme Southern California were barometrically adjusted to remove the static fluctuations due to pressure variability at sea level.

At all four meteorological stations, alongshelf wind stress was more equatorward in summer than in winter. The largest amplitude of this annual cycle, which was very strong equatorward (hence, upwelling-favorable) occurred at San Francisco in summer. Nelson (Reference 38) showed that the maximum southward wind along the west coast in summer occurs between Cape Mendocino and San Francisco.

Sea level pressure had a minimum in summer and a maximum in winter along the entire California coast. This cycle resulted from the formation of the thermal low pressure region over the southwestern United States in summer. The formation of this low, coupled with the northward migration of the subtropical high pressure region over the eastern North Pacific Ocean, produced the strong equatorward wind stress in summer, since the pressure gradient between the high and low was strongest during this season.

Adjusted sea level was lowest in winter and highest in summer. A substantial part of this seasonal cycle is due to the seasonal cycle of alongshelf wind stress and the resulting set-up and set-down of sea level due to cross-shelf Ekman transport (Reference 39).

Huyer, *et al.* (Reference 4) noted that the 1973 and 1975 transitions from the winter to the summer flow regimes occurred within a period of days, due to strong equator wind stress events. Thus, off the California coast, the transition from winter to spring circulation patterns could also be abrupt. Huyer, *et al.* (Reference 4) also noted that during these two years, adjusted coastal sea level was a good indicator of the time of this transition, as a rapid drop in sea level accompanied the onset of upwelling circulation. Although they did not discuss it, their data showed a sharp increase in adjusted coastal sea level in late October, 1973, which apparently signaled the transition to winter

circulation (the onset of the Davidson Current), and which was forced by a strong poleward wind stress event. They unfortunately did not have accompanying current meter data during this transition to determine if a large increase in poleward flow accompanied this sea level change, but it is probably a safe assumption that it did.

The time series of adjusted coastal sea level in Figures 4.36 through 4.39 were used to perform a census of the times of occurrence of both the spring and fall transitions for the four locations along the California coast. The mean transition time and the standard deviation of the transition time (in weeks) were computed (Table 4.2). Transition times occur earlier in the year going southward along the California coast; the spring transition actually occurs in winter off the Southern California coast. Thus, nearshore southward flow begins earlier in the year in the Southern California Bight (Section 4.3); the fall transition actually occurs in summer. Most surface drifters released nearshore in the Bight from July through September traveled poleward.

4.7 ESTIMATES OF SEASONAL MEAN CURRENTS

One objective of this study was the production of maps of mean current vectors on a regular grid for application in pollutant spill trajectory models. Inputs to the preparation of these maps include the currents computed from ship drift, geostrophic currents, wind drift currents derived from the mean wind stress, currents from surface drifters, and current meter data.

Examination of these data sets has shown that existing observations of any one type are insufficient to prepare reliable circulation charts on a monthly basis. Hence, we have combined the data according to the distinct circulation seasons, after Skogsberg (Reference 40) as follows: The Davidson Current Period, December-January; The Upwelling Period, May-June-July; The Oceanic Period, September-October. Transition months which may fall into one of two seasons are not included in the average as they increase the "noise" in the data fields.

Surface drifters were deemed of little help for our analysis as they indicate only the general direction and (in some cases) rough orders of magnitude of current speed. There are insufficient current meter observations to provide more than a few point measurements of currents. Also, these observations were generally at depth, hence these were not included in the surface current charts.

The procedure followed was to plot mean dynamic depth anomaly of 1° square by season, and to compute mean geostrophic velocities relative to 500 bar on a 1° grid by first differences (Figures 4.40, 4.42 and 4.44). Surface currents from ship drift were also computed by 1° square by season, for comparison (Figures 4.41, 4.43 and 4.45). The geostrophic charts indicated mean currents of relatively low speed (order 0.1 kts), and generally parallel to the coast in direction. The ship drift current charts indicated higher speeds and directions to the right of the geostrophic current vectors, typically 5° to 20°. Comparison with the literature (Reference 6) also indicated that our geostrophic speeds were generally low, and that the observed current flows at a small angle to the coast and to the isobaths.

These considerations led us to add a mean wind drift current component (Reference 41) to the geostrophic current to produce better agreement with previous knowledge and observations. Our justification for this procedure is that, according to Ekman (Reference 41) the ocean surface current is the vector sum of the wind stress-induced current and the geostrophic current.

The seasonal wind stress was obtained by averaging the monthly 1° square wind stress components given by Nelson (Reference 39), and computing the surface drift current by Ekman's formula (Reference 41), with an eddy viscosity coefficient of 100 (which corresponds to taking 3 percent of the wind speed), but using a deflection of 10° rather than 45°. The latter deflection produced currents at too large a cross-isobath angle as compared to the generally

Table 4.2
Approximate Times of Occurrence of the Spring and Fall Transitions at Four Locations along the California Coast, 1970 through 1978

Year	Station Pair	Spring Transition	Fall Transition
1970	Arcata/Crescent City	Early Apr.	Late Oct.
	San Francisco/San Francisco	Early Apr.	Early Nov.
	Pt. Mugu/Rincon Is.	Mid-Apr.	Mid-Aug.
	Imperial Beach/San Diego	(Late 1969)	Early Oct.
1971	Arcata/Crescent City	Late Jan.	Early Dec.
	San Francisco/San Francisco	Mid-Feb.	Early Sep.
	Pt. Mugu/Rincon Is.	Early Feb.	Mid-July
	Imperial Beach/San Diego	Early Dec. (1970)	Late July
1972	Arcata/Crescent City	Late Apr.	Early June
	San Francisco/San Francisco	Early Apr.	Mid-July
	Pt. Mugu/Rincon Is.	Early Mar.	Late July
	Imperial Beach/San Diego	Late Nov. (1971)	Mid-July
1973	Arcata/Crescent City	Late Mar.	Mid-Nov.
	San Francisco/San Francisco	Mid-Mar.	Mid-Dec.
	Pt. Mugu/Rincon Is.	Late Mar.	(none)
	Imperial Beach/San Diego	Late Mar.	(none)
1974	Arcata/Crescent City	Mid-Apr.	Late Nov.
	San Francisco/San Francisco	Early May	Mid-Sep.
	Pt. Mugu/Rincon Is.	(none)	Late July
	Imperial Beach/San Diego	(none)	Early Aug.
1975	Arcata/Crescent City	Late Mar.	Mid-Jan. (1976)
	San Francisco/San Francisco	Late Mar.	Mid-Jan. (1976)
	Pt. Mugu/Rincon Is.	Mid-Jan.	(none)
	Imperial Beach/San Diego	Mid-Jan.	Early Aug.
1976	Arcata/Crescent City	Mid-Mar.	Late Sep.
	San Francisco/San Francisco	Early Mar.	Late July
	Pt. Mugu/Rincon Is.	(none)	Early July
	Imperial Beach/San Diego	Mid-Feb.	Late June
1977	Arcata/Crescent City	Mid-Mar.	Early Oct.
	San Francisco/San Francisco	Mid-Mar.	Mid-Sep.
	Pt. Mugu/Rincon Is.	Early Mar.	Mid-Aug.
	Imperial Beach/San Diego	Early Mar.	Late July

Table 4.2 (Continued)

Year	Station Pair	Spring Transition	Fall Transition
1978	Arcata/Crescent City	Early May	Early Oct.
	San Francisco/San Francisco	Early May	Late Sep.
	Pt. Mugu/Rincon Is.	Late Mar.	Mid-Aug.
	Imperial Beach/San Diego	Late Mar.	Mid-Aug.
1970-1978 Mean	Arcata/Crescent City	Late Mar.	Late Oct.
	San Francisco/San Francisco	Late Mar.	Late Sep.
	Pt. Mugu/Rincon Is.	Early Mar.	Late July
	Imperial Beach/San Diego	Late Jan.	Late July
1970-1978 Standard Deviation (weeks)	Arcata/Crescent City	9	4
	San Francisco/San Francisco	8	4
	Pt. Mugu/Rincon Is.	3	4
	Imperial Beach/San Diego	5	7

accepted current pattern, resulting in excessive transport away from the coast. There is great uncertainty in the deflection angle, but it is generally agreed on the basis of field and laboratory experiments that 45° is much too large. The factor of 10° has been suggested by Stolzenbach *et al.* (Reference 42) in his review of empirical oil spill and surface drift studies. We have used 10° as our deflection angle.

The chart for December-January (Figure 4.40) indicates mean currents everywhere less than 0.3 kt and in most locations less than 0.2 kt. The amount of dynamic topography data for the region north of Cape Mendocino is considered insufficient to delineate the pattern of flow. Between Cape Mendocino and Point Conception, the flow is highly variable. This variability agrees with the low persistence seen in the ship drift charts for this region. South of Point Conception, a fairly coherent mean flow to the southeast prevails. This procedure for 1° square summary areas does not resolve the Davidson or Countercurrent Systems; yet there is some indication on the chart of mean northward flow off San Francisco.

Unfortunately, the ship drift chart for December-January, (Figure 4.41) lacks data in the area north of Cape Mendocino. The coastal currents are better resolved in the ship drift chart: the Southern California Eddy, and the generally northward flow along the coast between Point Conception and Cape Blanco. The persistence values indicate that the flow off Cape Mendocino, and just north of San Francisco is highly variable.

In May, June, and July, the geostrophic/wind stress current chart (Figure 4.42) indicates strong southward flow with a confused eddy or meander off Cape Mendocino. Average speed is on the order of 0.3 kts. There is a suggestion of the *turn-in* of current off San Diego, forming the lower half of the Southern California Eddy. The ship drift current chart for this period (Figure 4.43) shows general agreement in speed and direction. The eddy off Cape Mendocino also can be seen. The flow is toward the southeast in the Southern California Bight which probably indicates a very near surface drift current superimposed on the deep flow, which agrees with the fact that the Southern California Eddy is weakest or nonexistent in spring (Reference 6).

The geostrophic/wind stress current chart for September-October (Figure 4.44) indicates flow generally toward the southeast, less strong than May, June, and July, but stronger than December-January. Northward flow is indicated along the coast in the Southern California Bight. The ship drift current chart for September-October (Figure 4.45) also indicates currents of intermediate strength between summer and winter. The area northwest of Cape Mendocino contains few observations. The flow off Cape Mendocino is seen to be highly variable with mean northward flow about 100 km from the coast. The Southern California Eddy is seen with northward flow inshore the channel islands.

4.8 MEAN CIRCULATION ANALYSIS CONCLUSIONS

Currents over the shelf and slope off the California coast have two seasonal extremes. From Point Conception northward, flow over most of the shelf is typically poleward throughout the water column from late autumn through the winter, and equatorward throughout the rest of the year. The poleward flow has been named the Davidson Current. The transition from the winter to spring (upwelling) flow regimes usually occurs over a period of days. Equatorward flow, which is strongest near the surface, and coastal upwelling are both strongest during the spring due to strong equatorward wind stress. Mean poleward flow during spring is typically found only in deep water over the continental slope and farther offshore at this time of the year, and is named the California Undercurrent. The equatorward wind stress weakens somewhat during the summer and early fall. Nearsurface equatorward flow decreases in speed and upwelling decreases in intensity. The California Undercurrent is found closer to the surface and closer inshore during this period, and poleward flow is often observed nearbottom over the outer shelf. Some researchers have named this the "Oceanic" period. Usually around midautumn relatively abrupt transition to winter flow occurs over a period of several days to a couple of weeks when the mean equatorward wind stress decreases substantially in intensity or becomes poleward. Most researchers now believe that the onset of poleward flow is accomplished by the surfacing of the California Undercurrent (Reference 6).

Long-term mean flow in the Southern California Bight is dominated by the Southern California Eddy. This is a cyclonic eddy, the offshore side of which is formed by the California Current which flows equatorward from Point Conception. Poleward flow exists inshore of the California Current to form the nearshore side of this eddy. This poleward flow is weakest in the spring, when equatorward flow is often observed. At some times, equatorward flow forms shoreward of the poleward flow, resulting in poleward flow sandwiched between two equatorward flows. A transition from mean poleward flow to weak poleward or equatorward flow occurs on average in January, and a transition back to mean poleward flow occurs on average in July. These transitions correspond to the transitions observed off central and northern California, but occur about three months earlier. The period of weakest poleward flow occurs during the period of strongest equatorward alongshelf wind stress, which occurs earlier over the Southern California Bight than over the central and northern California coasts. Maximum equatorward stress is observed in April in the Southern California Bight and in July off Oregon (Reference 38).

The spring and fall transition times are approximate for the entire California coast. These can occur plus or minus several weeks from the mean time. Thus, mean current vectors must be used with caution during these transition periods, as discussed in Section 4.6.

Data of all kinds were found to be sparse, especially off northern California. The CALCOFI hydrographic data set is probably the best available off the California coast, but poor resolution nearshore limits its usefulness in analyzing circulation over the shelf and slope. Hydrographic and ship drift data from NODC files, when sorted by 1° squares, is very poorly distributed, with large numbers of observations in a relatively few 1° squares located offshore of major population centers and off parts of Oregon and Washington, but relatively few observations in the remainder of the domain. Thus, ship drift and dynamic topography charts off the west coast of the U.S. tend to be unstable over a large part of this domain. Only 31 moored current meter records longer than one week were available off the California coast, and most of these were moored during 1970 and 1971 near the shelfbreak to the northwest of the Farallon Islands. Four of these meters were deployed near the shelfbreak off northern California, and only one of these meters was deployed in the Southern California Bight.

The available hydrographic, ship drift, moored current meter, and drifter data tend to support existing knowledge of currents over the shelf and slope off California, but cannot provide good estimates of monthly long-term mean currents over the large majority of this domain. These data sets show the expected seasonal changes in mean near-surface flow, as discussed at the beginning of this section. (Adjusted coastal sea level at four stations along the California coast for 1970 through 1978 were used to estimate the transition times between poleward and equatorward nearsurface flow.) Ship drift charts show seaward component to mean surface current vectors at all times of the year; mean speeds are on the order of 10 cm/s for both the poleward and equatorward flow periods. Some drifter and current meter data contain evidence for the existence of an anticyclonic eddy between San Francisco and Monterey Bays during summer and early fall, which result in poleward flow nearshore between the bays and offshore flow at the shelfbreak near 38°N (References 11 and 6). In addition to the spatial structure in the current field, temporal variability on both interannual time scales and on time scales less than one month (synoptic) is very important. The interannual variability has been discussed in Section 4.6. Many of the features seen on the dynamic topographic charts may be the result of interannual variability. The spatial structure of, and the synoptic-scale variability in, the current field off the west coast, and the implications of these to the prediction of oil spill movement, will be discussed in Section 4.9.

The seasons were defined to be centered on the three discernible circulation regimes (Reference 40), i.e., the winter or Davidson Current Period in December-January; the spring or the upwelling period in May, June and July; and fall or the Oceanic period in September-October. Transition months were not included, since, as explained in the section on coastal sea level, (4.6), charts of average circulation based on data from assorted years would have little meaning.

Geostrophic current charts (produced from 1° summaries) were found to be too low in speed, and lacked the seaward deflection with respect to the isobaths noted in the literature and apparent from the ship drift charts. Consequently, a mean wind-stress induced current vector was added to the geostrophic current vectors, at a 10° deflection angle, based on recent literature. General agreement in speed and direction was obtained between the ship-drift and geostrophic current estimates, although the geostrophic/wind stress current fails to clearly delineate the coastal currents. Many areas still contain data gaps, especially in winter.

4.9 STRUCTURE AND VARIABILITY

The geostrophic interior velocity off the California coast has greater variability in summer than in winter, as shown by dynamic topography charts. Ship drift charts, which are sensitive to near-surface drift current, show greater current variability in winter than in summer. Near-surface drift currents have the largest variability in winter due to large wind stress fluctuations with periods of one to several days due to storms and fronts. In summer, wind stress fluctuations are less energetic and occur at longer periods, since storms and fronts are relatively weak and interstorm time scales are longer. Hence, the summer fluctuations are more capable of forcing adjustments in the mass field, and thus driving fluctuations in geostrophic interior velocity. In summer, stratification is greater due to upwelling and the formation of the seasonal thermocline offshore, allowing the summer wind stress fluctuations to be more effective in forcing this variability.

From the current meter data, semidiurnal tides, diurnal tides, inertial oscillations and low-frequency (< 0.5 cpd) oscillations contribute roughly equal fractions of the total current variance on average. Typical amplitudes of each of these components average several centimeters per second. Correlations among current velocity, wind stress, and adjusted coastal sea level were in general poor, in contrast to results obtained off Oregon (Reference 4) by Huyer, probably because sea level stations, wind stress stations, and current meter locations were usually separated by at

least 50 to 100 km. No obvious seasonal or depth dependence over the shelf is observed in the amplitudes of these fluctuations. Low frequency variability is especially important to consider in predicting the transport of spilled oil. Large deviations from expected means, and even current reversals alongshelf, can occur for periods up to several days.

The flow field can have significant structure alongshelf. In monthly-mean average current charts, seaward deflections of mean alongshelf currents are observed. In satellite images, very complex structures are usually observed (Reference 43). Offshore-flowing plumes of water tens of kilometers wide and occasionally extending several hundred kilometers offshore are often observed, especially near major capes, such as Cape Mendocino. Transient cyclonic and anticyclonic eddies are often observed along the entire California Coast. Thus, over a time scale of days, the path of spilled oil may deviate substantially from the expected smooth alongshelf mean flow.

REFERENCES

1. Reid, J.L., Jr., 1960. Oceanography of the Northern Pacific Ocean during the last ten years, CALCOFI Rept. 7, pp. 77–90.

2. Bolin, R.L. and D.P. Abott, 1962. Studies on the Marine Climate and Phytoplankton of the Central Coastal Area of California, 1954-1960, California Cooperative Oceanic Fisheries Investigations Progress Report, IX, 1 July 1960 to 30 June 1962, Marine Research Committee, California Department of Fish and Game, Sacramento, CA, pp. 23–45.

3. Winzler and Kelly, Inc., 1977. A Summary of Knowledge of the Central and Northern California Coastal Zone and Offshore Areas, Volume I, Physical Conditions, Book 1 PB-274 210, Winzler and Kelly Consulting Engineers, Eureka, CA, 189 pp.

4. Huyer, A., E.J.C. Sobey, and R.L. Smith, 1979. The Spring Transition in Currents over the Oregon Continental Shelf, J. Geophysical Research, 84 (C11), pp. 6995–7011.

5. Sverdrup, H.U., M.W. Johnson, and R.H. Fleming, 1942. The Oceans: Their Physics, Chemistry, and General Biology, Prentice-Hall, Inc., New York, 1087 pp.

6. Hickey, B.M., 1979. The California Current System–Hypotheses and Facts, Progress in Oceanography, 8(4), pp. 191–279.

7. Wooster, W.S. and J.L. Reid, Jr., 1963. Eastern Boundary Currents. The Sea, Volume 2, John Wiley & Sons, New York, pp. 253–276.

8. Emery, K.O., 1960. The Sea Off Southern California, John Wiley & Sons, New York, 366 pp.

9. Pavlova, Y.V., 1966. Seasonal Variations of the California Current, Oceanology, 6(6), pp. 806–814.

10. Schwartzlose, R.A. and J.L. Reid, Jr., 1972. Nearshore Circulation in the California Current, CALCOFI Rept. 16, pp. 57–65.

11. Wyllie, J.G., 1966. Geostrophic Flow of the California Current at the Surface and at 200 meters, CALICOFI, Atlas No. 4, 288 pp.

12. Tibby, R.B., 1941. The Water Masses of the West Coast of North America, Journal of Marine Research, **4(2)**, pp. 112–121.

13. Wooster, W.S. and J.H. Jones, 1970. California Undercurrent off Northern Baja California, Journal of Marine Research, **28(2)**, pp. 235–250.

14. Wickham, J.B., 1975. Observations of the California Countercurrent, Journal Marine Research, **33(3)**, pp. 325–340.

15. Kolitz, B.L., 1971. Descriptive Physical Oceanography in the Monterey Bay Region during the 1971 Upwelling Season, Report, University of Miami, Miami, FL, 39 pp.

16. Tsuchiya, M., 1975. California Undercurrent in the Southern California Bight, CALCOFI Rept. 18, pp. 155–158.

17. Maloney, N. and K.M. Chan, 1974. A Summary of Knowledge of the Southern California Coastal Zone and Offshore Areas, Vol. I, Sept. 1974, The Southern California Ocean Studies Consortium of the California State Universities and Colleges, Report to Bureau of Land Management, Department of Interior, Washington, D.C.

18. Sverdrup, H.U. and R.H. Fleming, 1941. The Waters off the Coast of Southern California, March to July, 1937. Bulletin, Scripps Institute of Oceanography, University of California, La Jolla, CA, **4**, pp. 261–378.

19. Schwartzlose, R.A., 1963. Nearshore Currents of the Western United States and Baja California as Measured by Drift Bottles. CALCOFI Rept. 9, pp. 15–22.

20. Tsuchiya, M., 1980. Onshore Circulation in the Southern California Bight, 1974-1977, Deep-Sea Research, (in press).

21. Monin, A.S., V.M. Kamenkovich, and V.G. Kort, 1977. Variability of the Oceans, John Wiley & Sons, New York, 241 pp.

22. Munk, W.H., 1978. Variable Ocean Structure in Advances in Oceanography, H. Charnock, G. Deacon, Ed., Plenum Press, New York.

23. McEwen, G.F., 1934. Rate of Upwelling in the Region of San Diego Computed from Serial Temperatures, Fifth Pacific Science Congress, Canadian Proceedings 1933, 3, pp. 1793.

24. Griggs, G.B., 1974. Nearshore current patterns along Central California Coast, Estuarine Coastal Mar. Sci., 2, pp. 395–405.

25. Reid, J.L., Jr., R.A. Schwartzlose and D.M. Brown, 1963. Direct Measurements of a Small Surface Eddy off Northern Baja California, Journal of Marine Research, **21**, pp. 205–218.

26. Wilkinson, D.L., 1972. An Apparent Similarity Among Ocean Eddies, Deep-Sea Research, **19**, pp. 895–898.

27. Bernstein, R.L., 1974. Mesoscale Ocean Eddies in the North Pacific, Westward Propagation Science, **183 (4120)**, pp. 71–72.

28. Huyer, A., R.L. Smith and R.D. Pillsbury, 1974. Observations in a Coastal Upwelling Region During a Period of Variable Winds (Oregon Coast, July 1972), Tethys **6**, pp. 391–404.

29. Burt, W.V. and B. Wyatt, 1964. Drift Bottle Observations of the Davidson Current Off Oregon, Studies on Oceanography, K. Yoshida, ed., University of Washington Press, Seattle, WA, pp. 156–165.

30. Ingraham, W.J., Jr. and J.R. Hastings, 1976. Seasonal Surface Currents off the Coasts of Vancouver Island and Washington as Shown by Drift Bottle Experiments, 1964-1965, NOAA Tech. Rept., NMFS SSRF-699, 9 pp.

31. Blankovich, D.D., 1973. A Drift Card Study in Monterey Bay, California, September 1971-April 1973, Tech. Publ. 73-4, Moss Landing Marine Laboratories, Moss Landing, CA, 79 pp.

32. Wyatt, B., W.V. Burt and J.G. Pattullo, 1972. Surface Currents Off Oregon as Determined from Drift Bottle Returns, J. Phys. Oceanogr., **2(3)**, pp. 286–293.

33. Squire, J.L., 1969. Observations on Cumulative Bottom Drift in Monterey Bay Using Seabed Drifters, Limnol. Oceanography, **14(1)**, pp. 163–167.

34. Reid, J.L., Jr., and R.A. Schwartzlose, 1962. Direct Measurements of the Davidson Current Off Central California, J. Geophy. Res., **67(6)**, pp. 2491–2497.

35. Huyer, A., and R.L. Smith, 1974. A Subsurface Ribbon of Cool Water Over the Continental Shelf Off Oregon, J. Phys. Oceanogr., **4(3)**, pp. 381–391.

36. Reed, R.K. and D. Halpern, 1976. Observations of the California Undercurrent Off Washington and Vancouver Island, Limnol. Oceanogr., **21(3)**, pp. 389–398.

37. Kundu, P.K. and J.S. Allen, 1976. Some Three-Dimensional Characteristics of Low-Frequency Current Fluctuations Near the Oregon Coast, J. Phys. Oceanogr., **6(2)**, pp. 181–199.

38. Nelson, C.S., 1977. Wind Stress and Wind Stress Curl Over the California Current, NOAA Tech. Rep. NMFS SSRF-714, U.S. Department of Commerce, NOAA, NMFS, 87 pp.

39. Bretschneider, D.E., 1980. Non-Tidal/Sea Level Variations at Monterey, California. Masters Thesis, U.S. Naval Post Graduate School, Monterey, CA.

40. Skogsberg, T., 1936. Hydrography of Monterey Bay, California Thermal Conditions, 1929-1933, Am. Phil. Soc. Trans., 29, 152 pp.

41. Ekman, V.W., 1905. On the Influence of the Earth's Rotation on Ocean Current,. Ark. Mat. Altr. Fye., **2(11)**, pp. 1–52.

42. Stolzenbach, K.D., O.S. Madsen, E.E. Adams, A.M. Pallack, and C.K. Cooper, 1976. A review and evaluation of basic techniques for predicting the behavior of surface oil slicks, MIT Dept. of Civil Engineering, Ralph M. Parsons Laboratory, May.

43. Bernstein, R.L., L. Breaker and R. Whritner, 1977. California Current Eddy Formation. Ship, Air, and Satellite Results, Science, **195**, pp. 353–359.

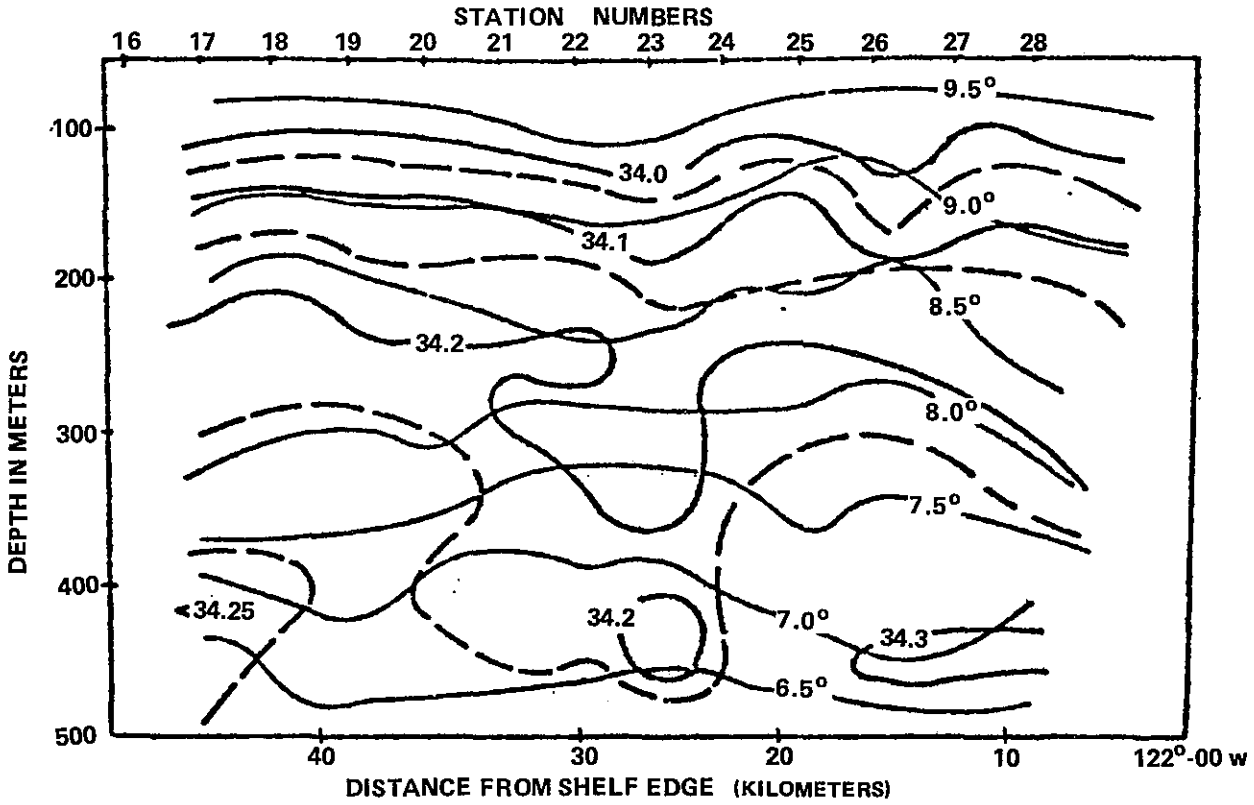

Figure 4.1. Temperature (°C) and Salinity (o/oo) on a Vertical Section at Latitude 36°20′ N, 3-7 August, 1972 (from Wickham, 1975, Reference 14)

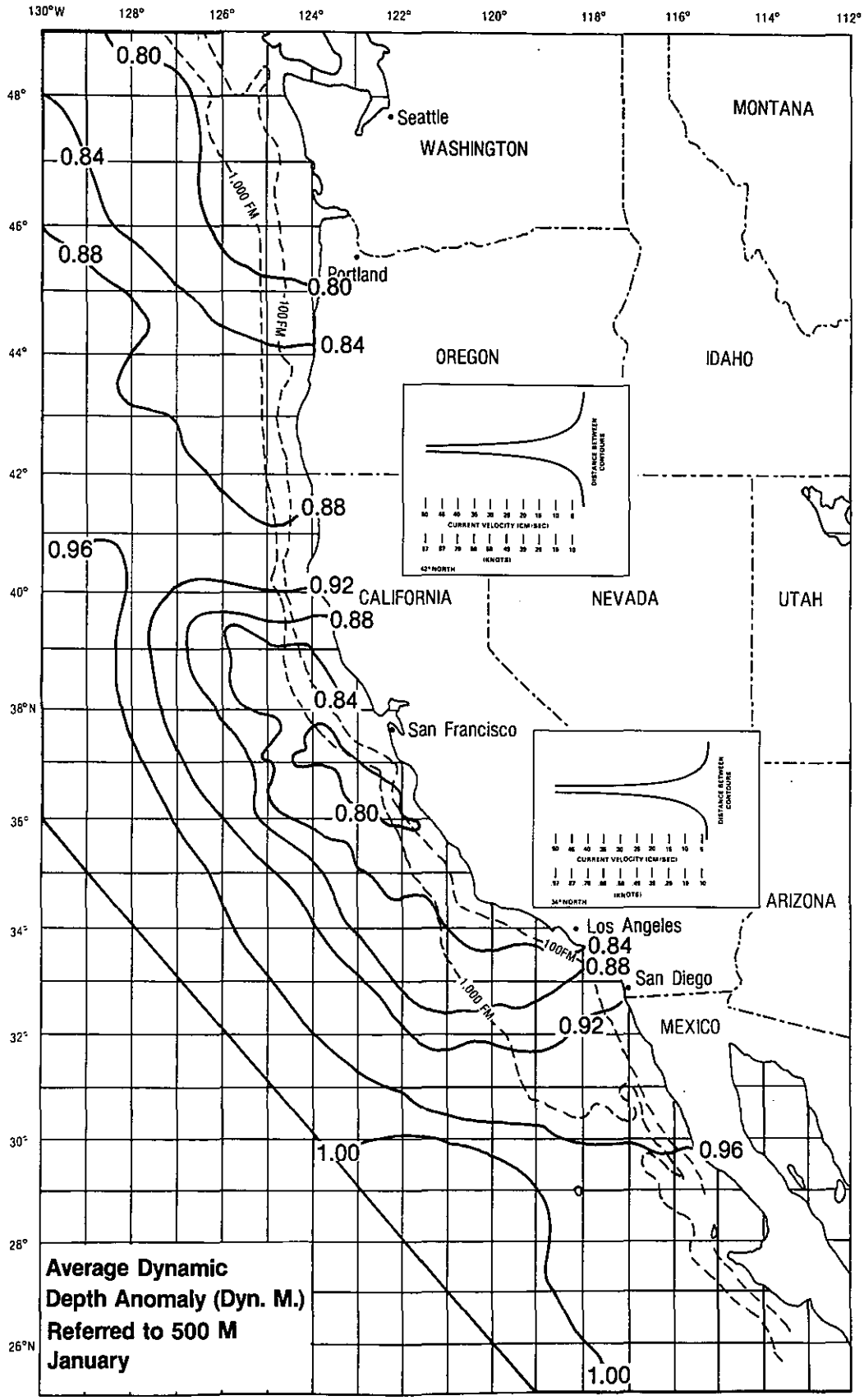

Figure 4.2. Dynamic Topography (dyn-m) of the Sea Surface Referred to 500 dbar—January

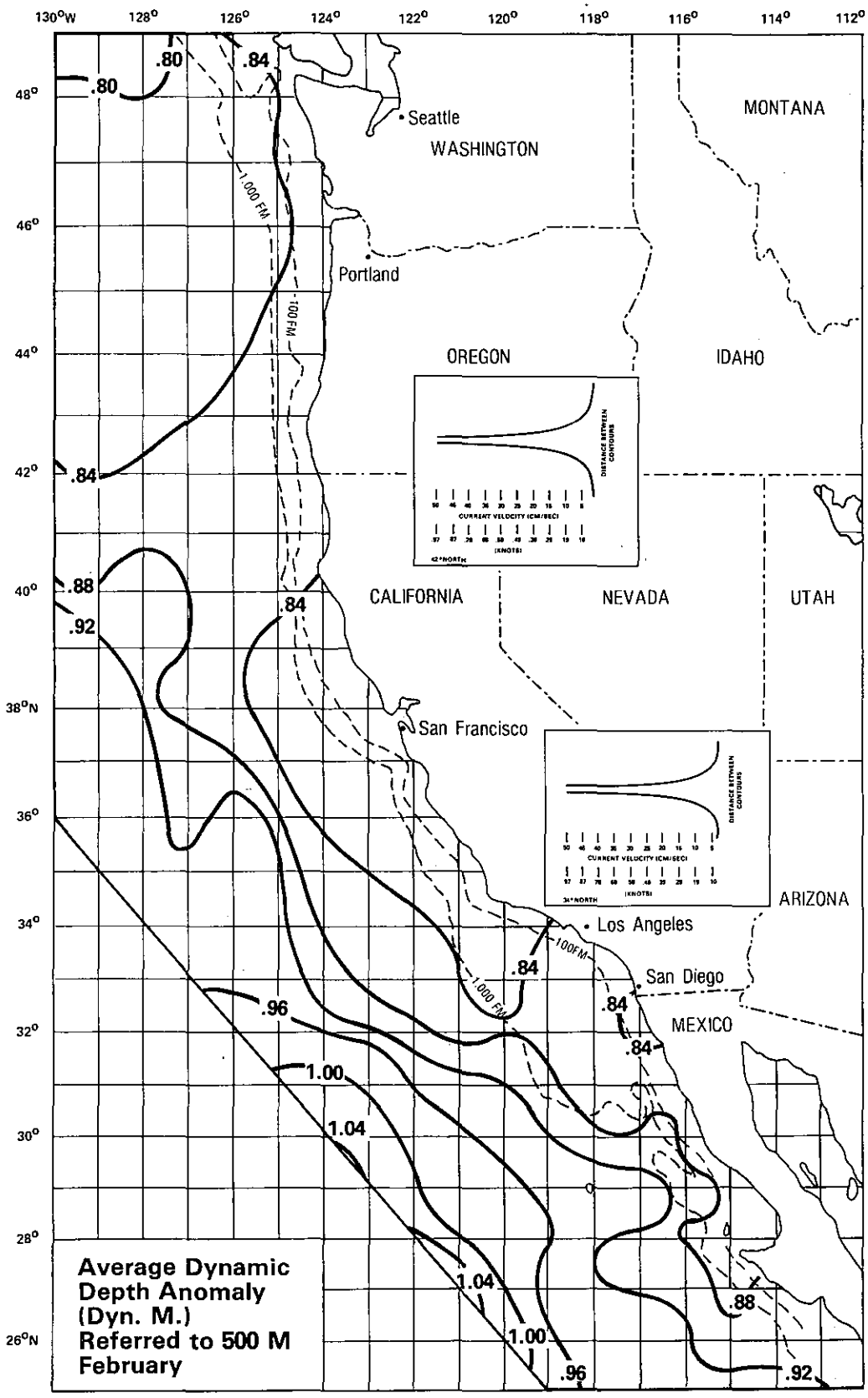

Figure 4.3. Dynamic Topography (dyn-m) of the Sea Surface Referred to 500 dbar—February

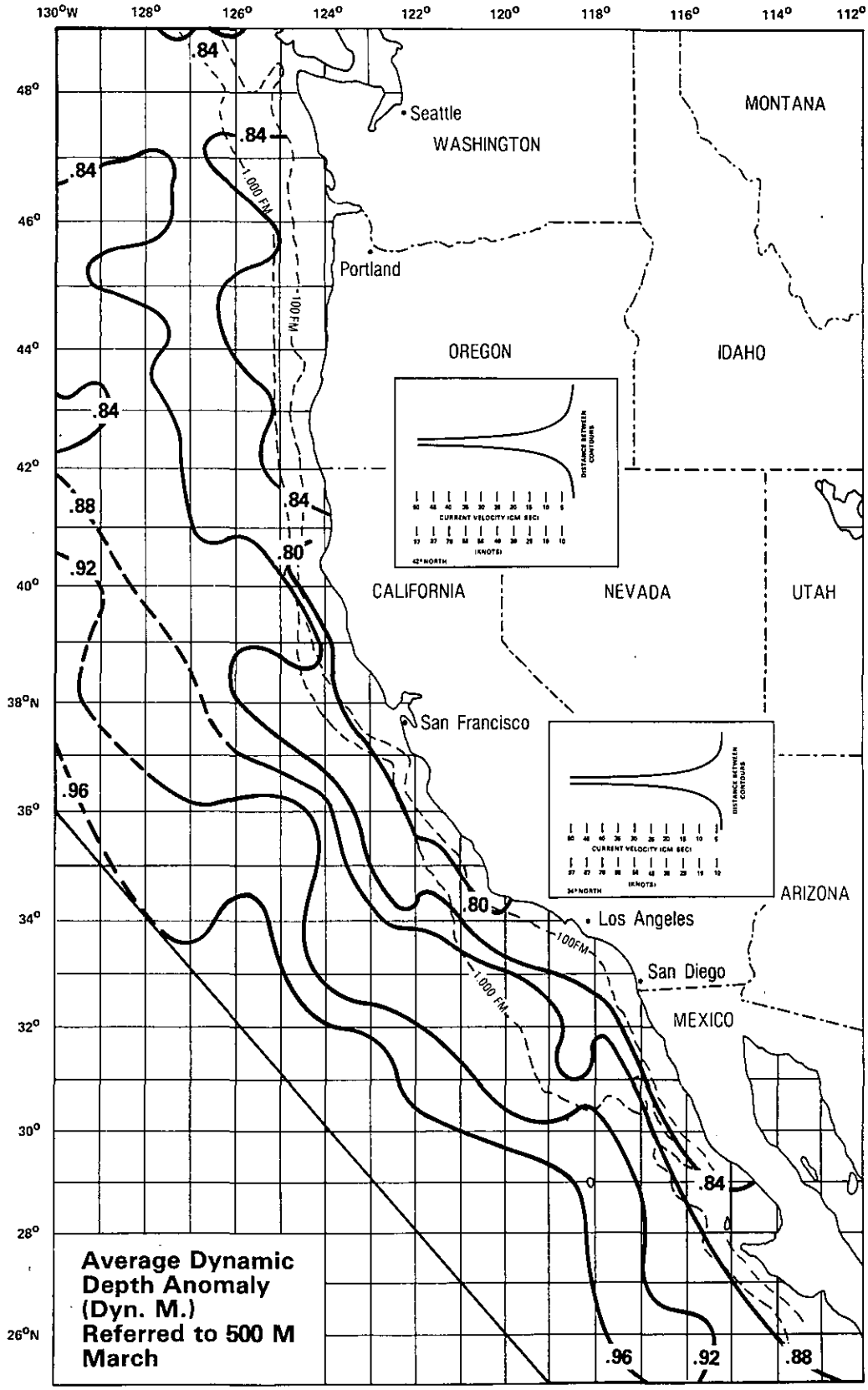

Figure 4.4. Dynamic Topography (dyn-m) of the Sea Surface Referred to 500 dbar–March

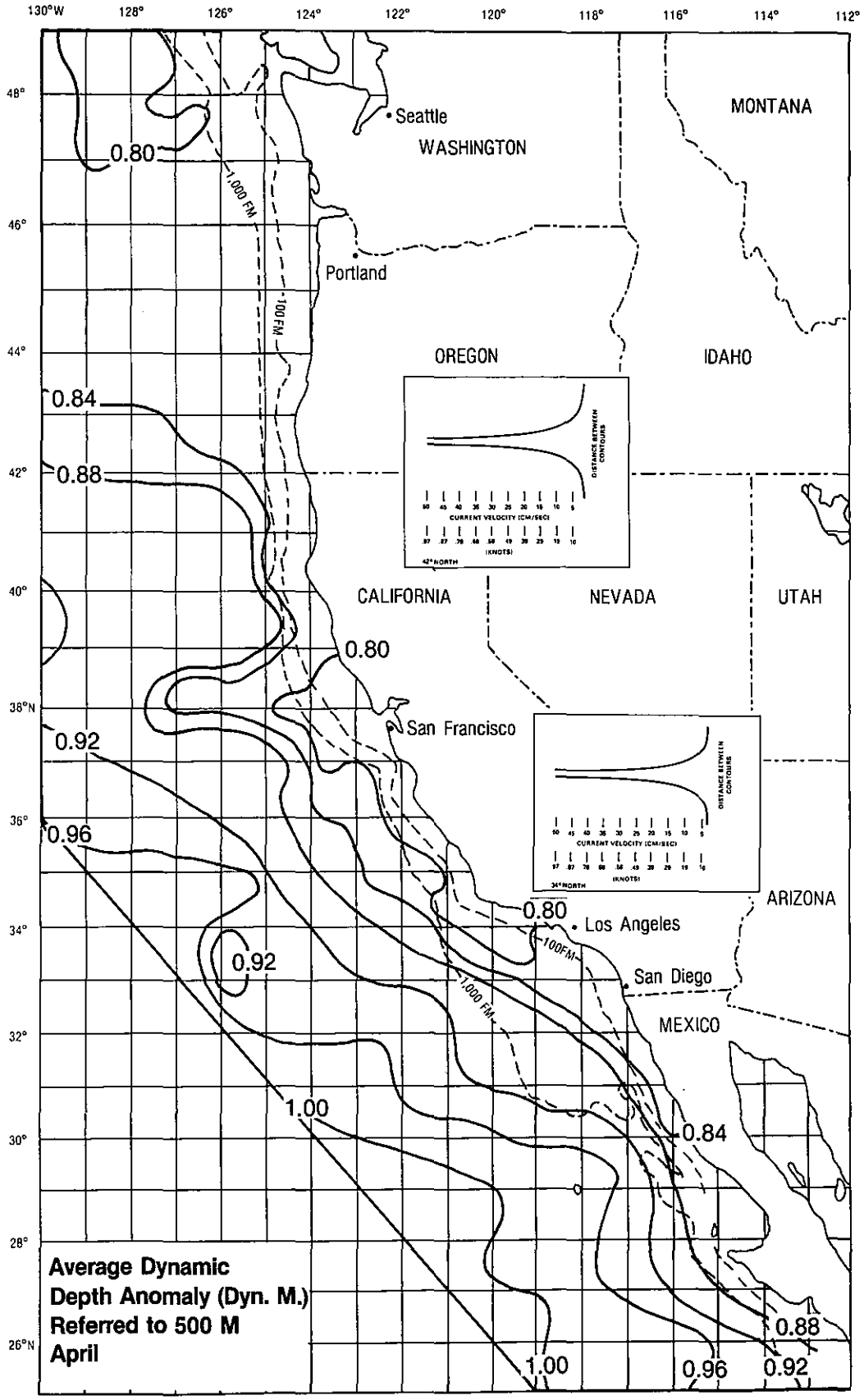

Figure 4.5. Dynamic Topography (dyn-m) of the Sea Surface Referred to 500 dbar—April

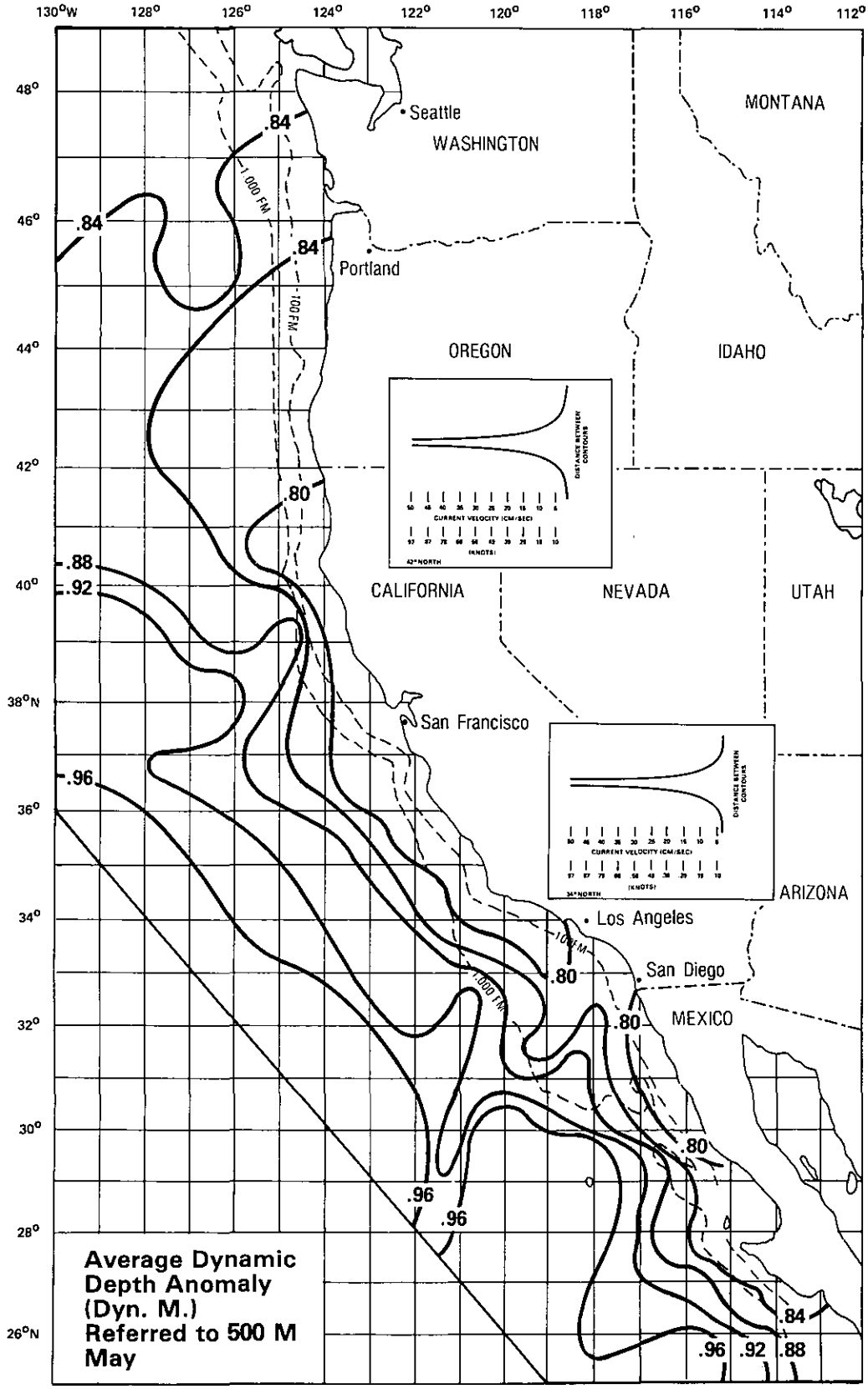

Figure 4.6. Dynamic Topography (dyn-m) of the Sea Surface Referred to 500 dbar–May

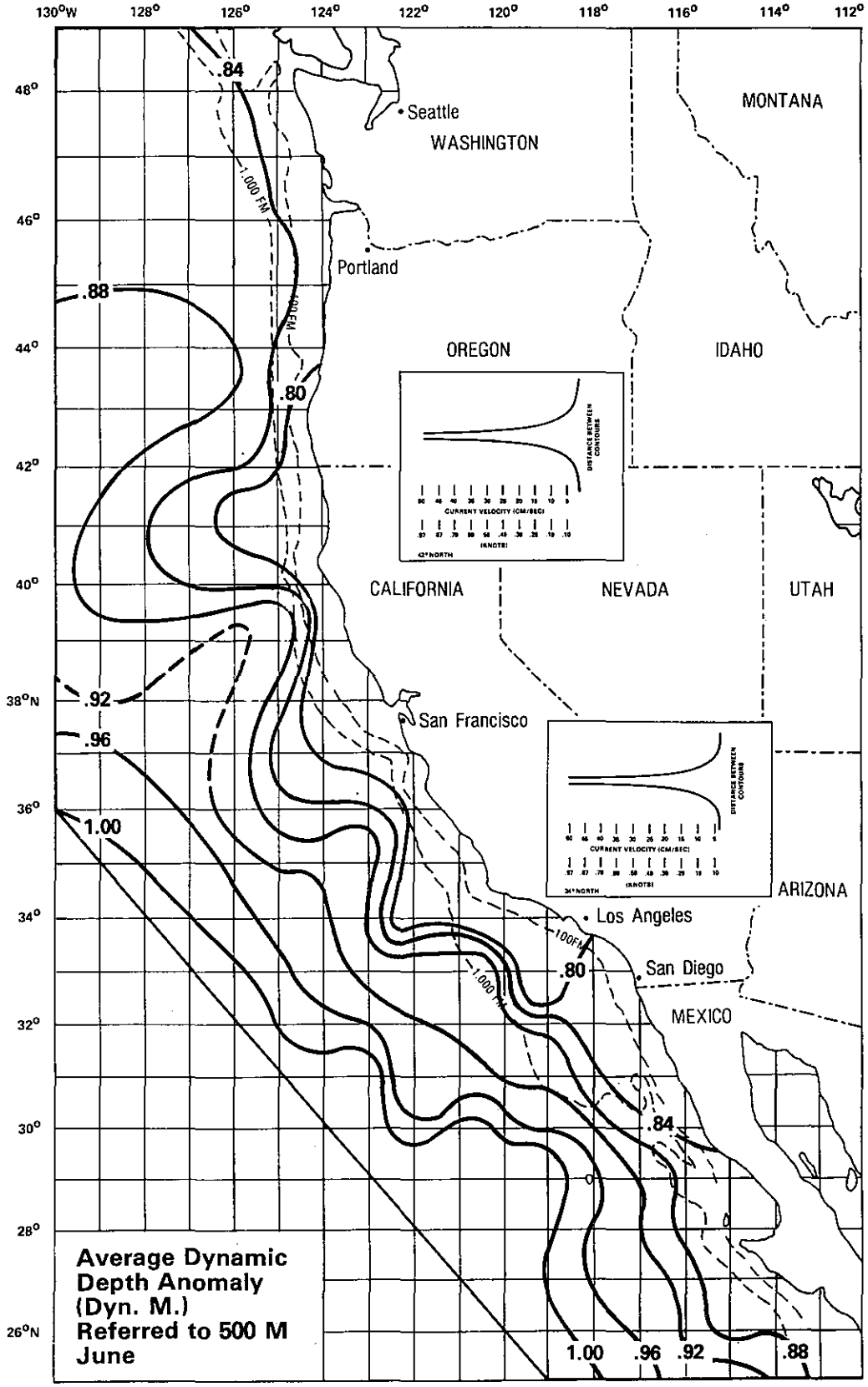

Figure 4.7. Dynamic Topography (dyn-m) of the Sea Surface Referred to 500 dbar—June

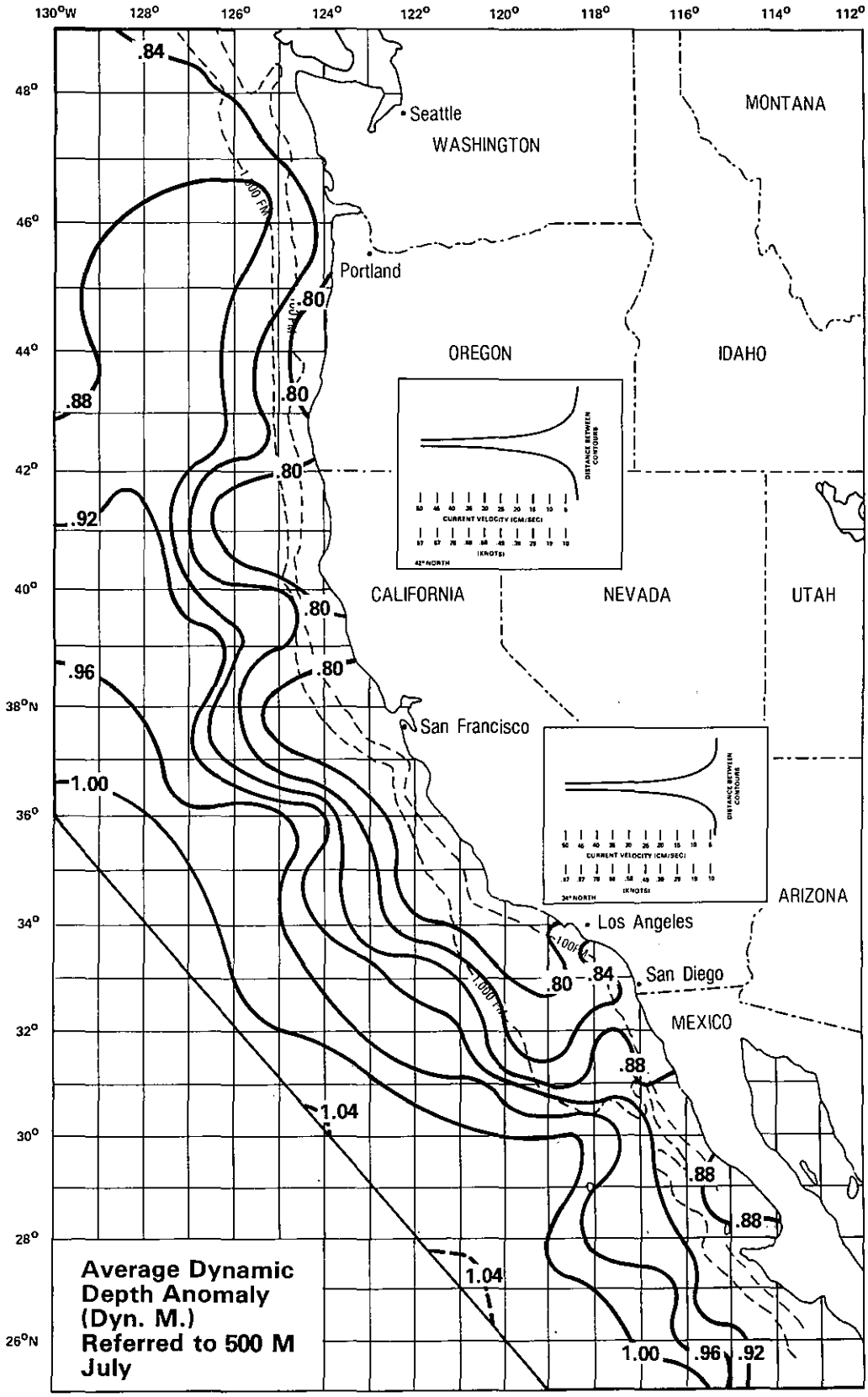

Figure 4.8. Dynamic Topography (dyn-m) of the Sea Surface Referred to 500 dbar—July

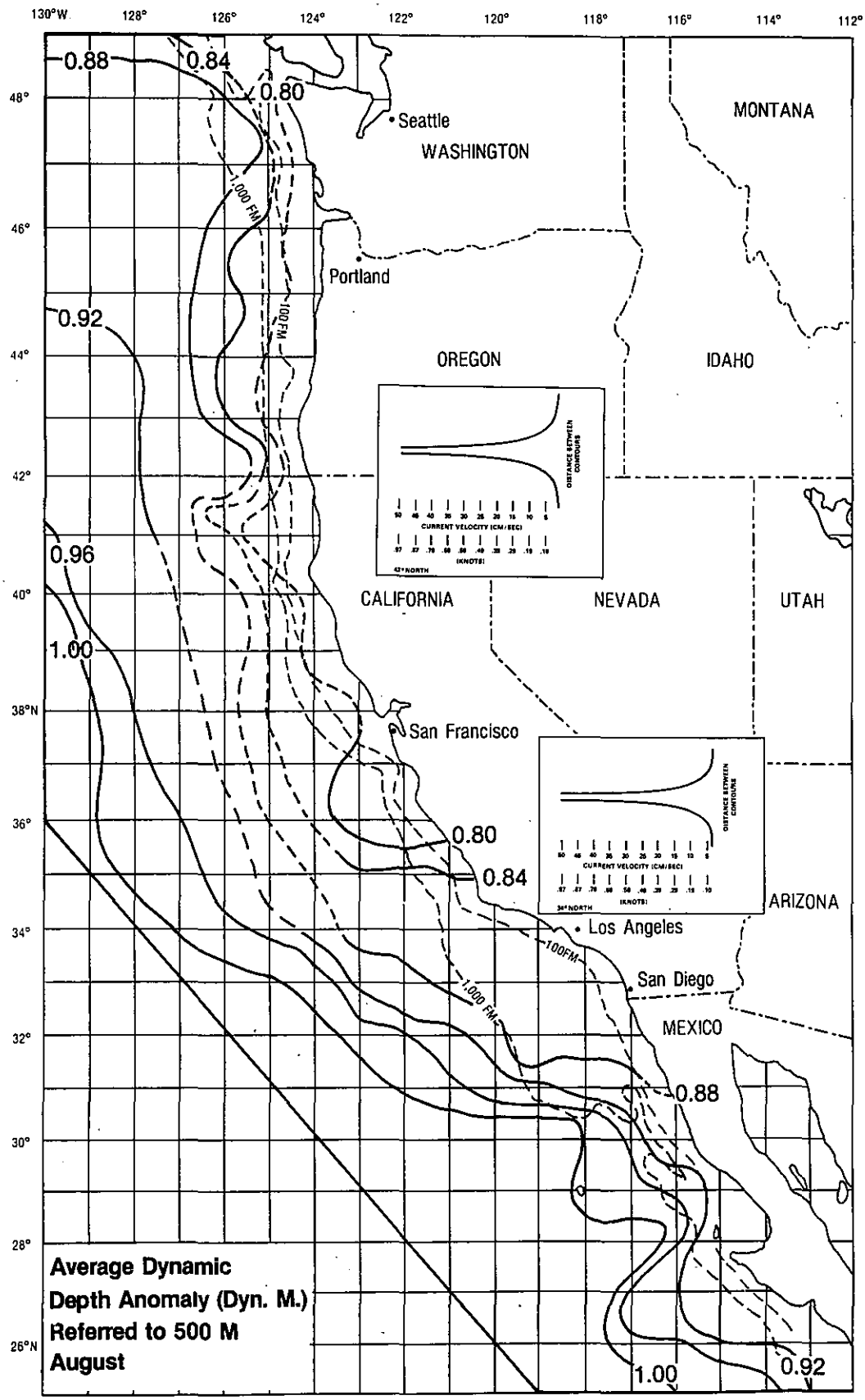

Figure 4.9. Dynamic Topography (dyn-m) of the Sea Surface Referred to 500 dbar—August

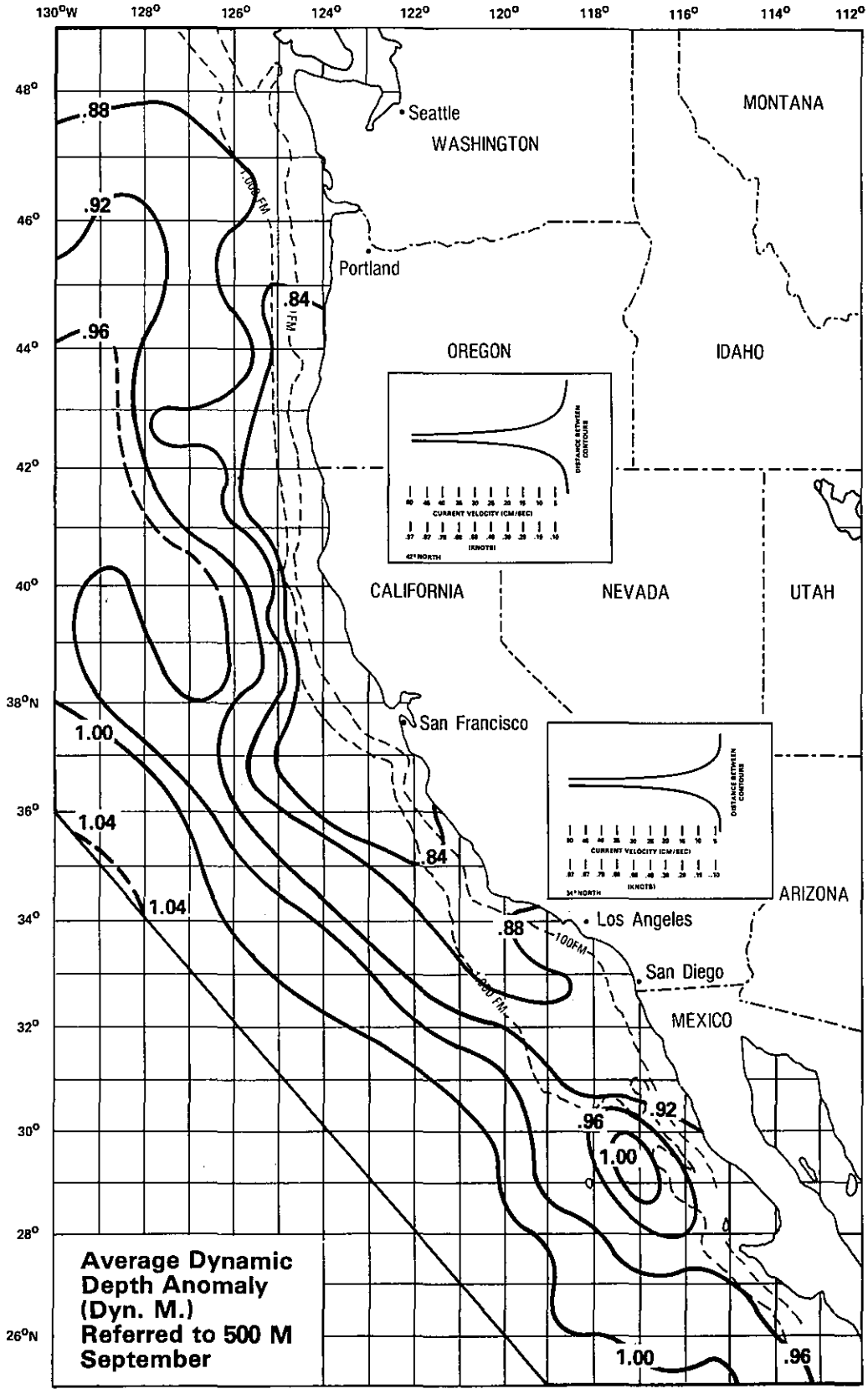

Figure 4.10. Dynamic Topography (dyn-m) of the Sea Surface Referred to 500 dbar—September

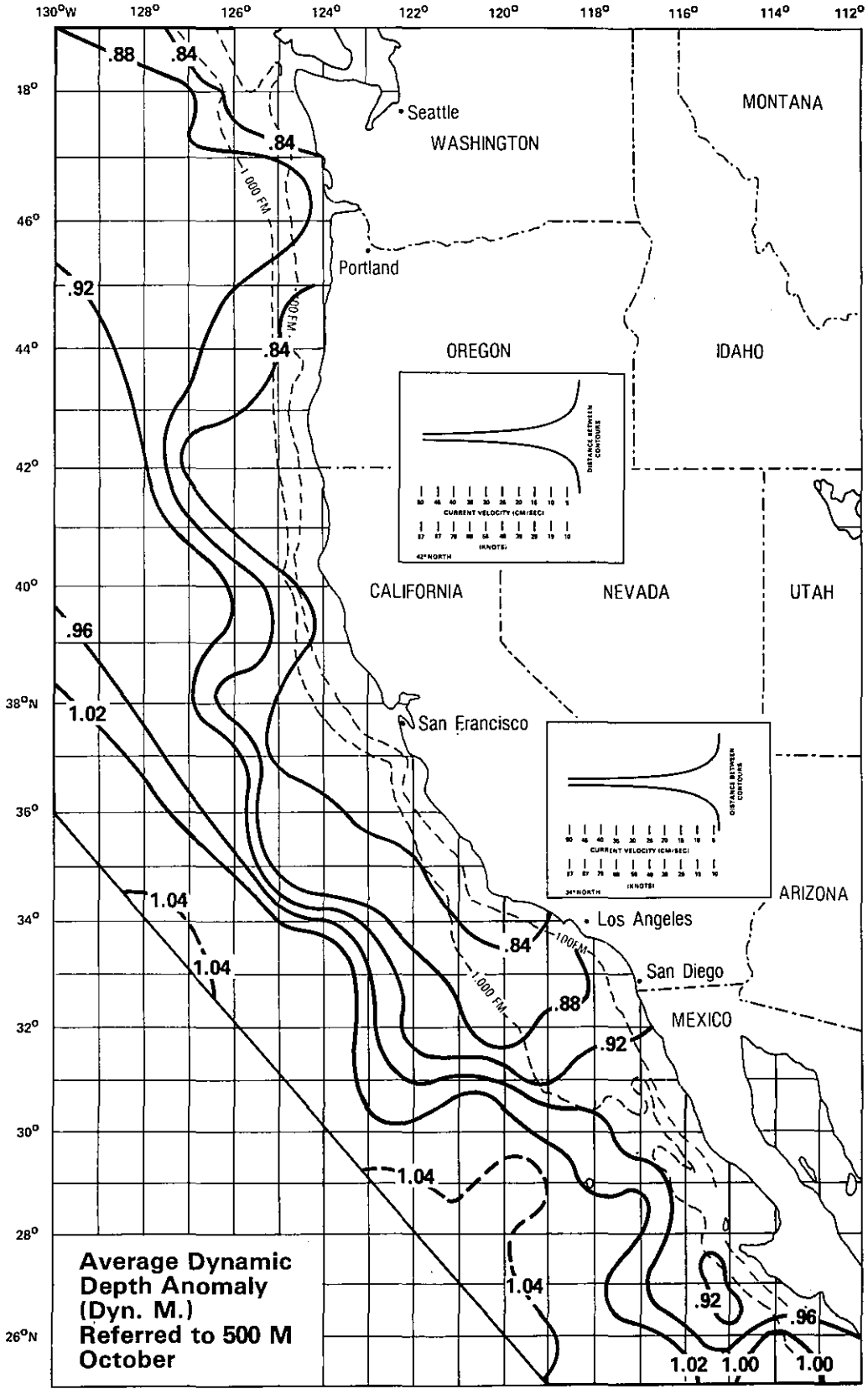

Figure 4.11. Dynamic Topography (dyn-m) of the Sea Surface Referred to 500 dbar—October

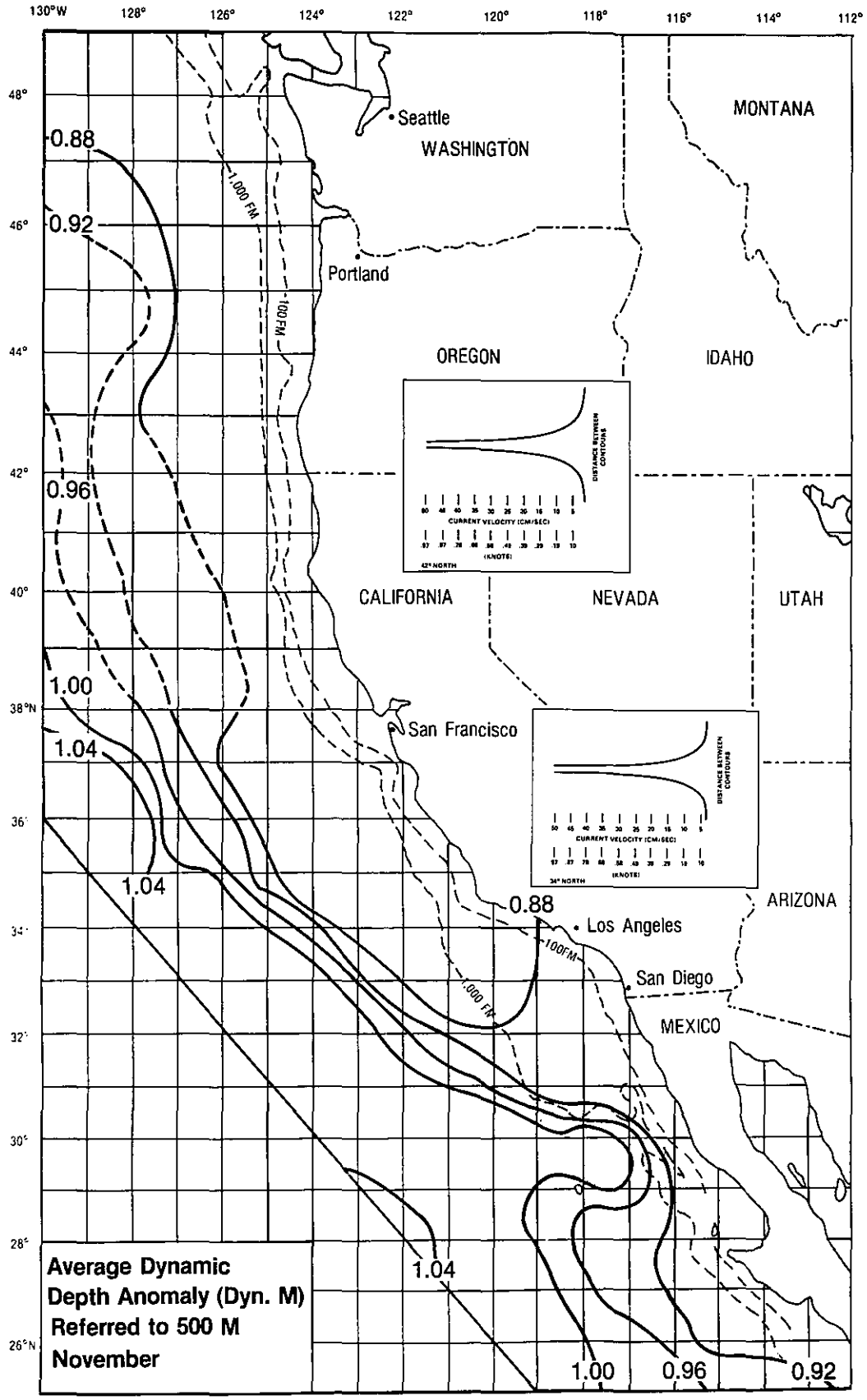

Figure 4.12. Dynamic Topography (dyn-m) of the Sea Surface Referred to 500 dbar–November

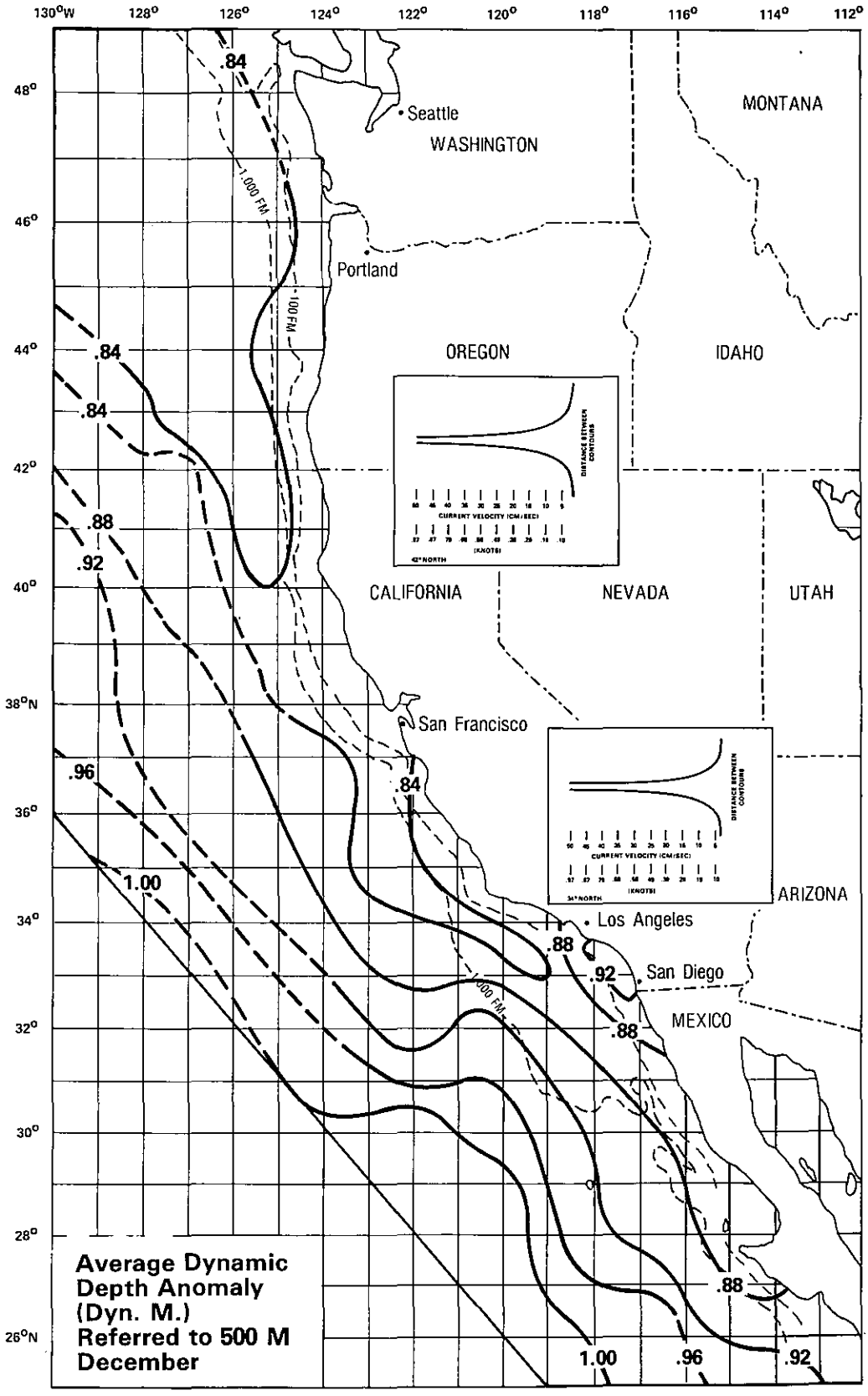

Figure 4.13. Dynamic Topography (dyn-m) of the Sea Surface Referred to 500 dbar–December

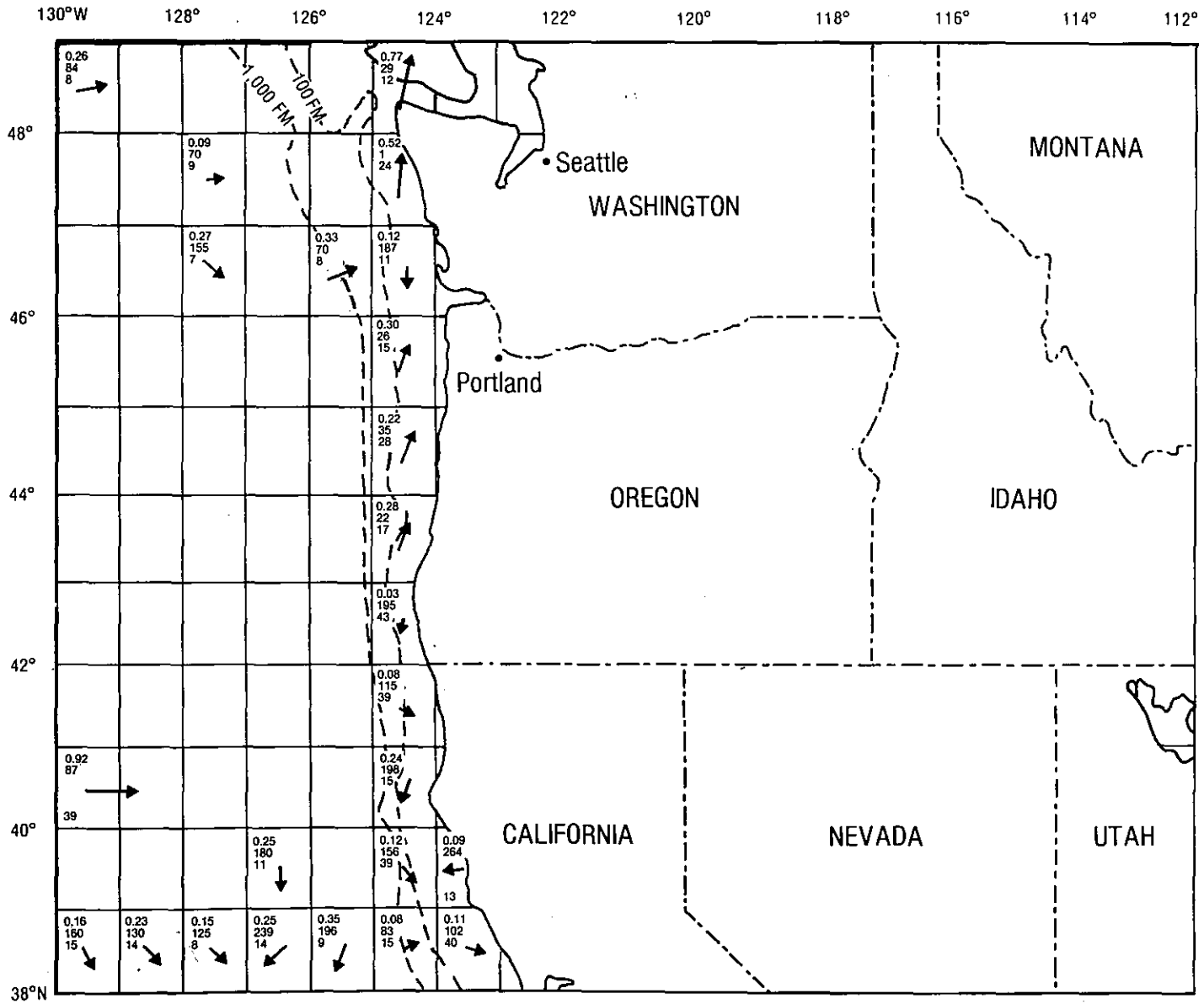

Figure 4.14. Surface Currents in January Computed From the NODC Ship Drift File

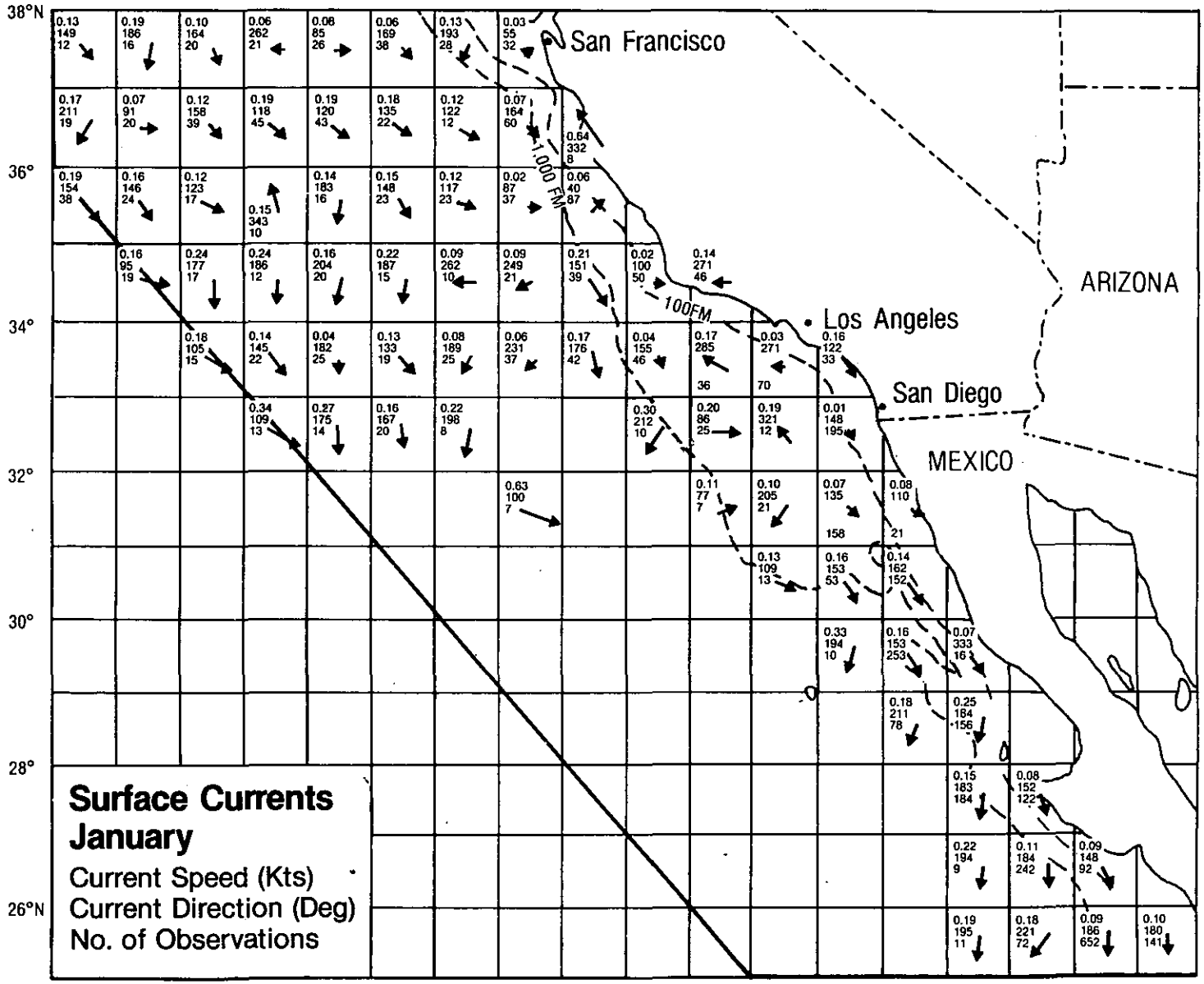

Figure 4.14. Surface Currents in January Computed From the NODC Ship Drift File (cont'd)

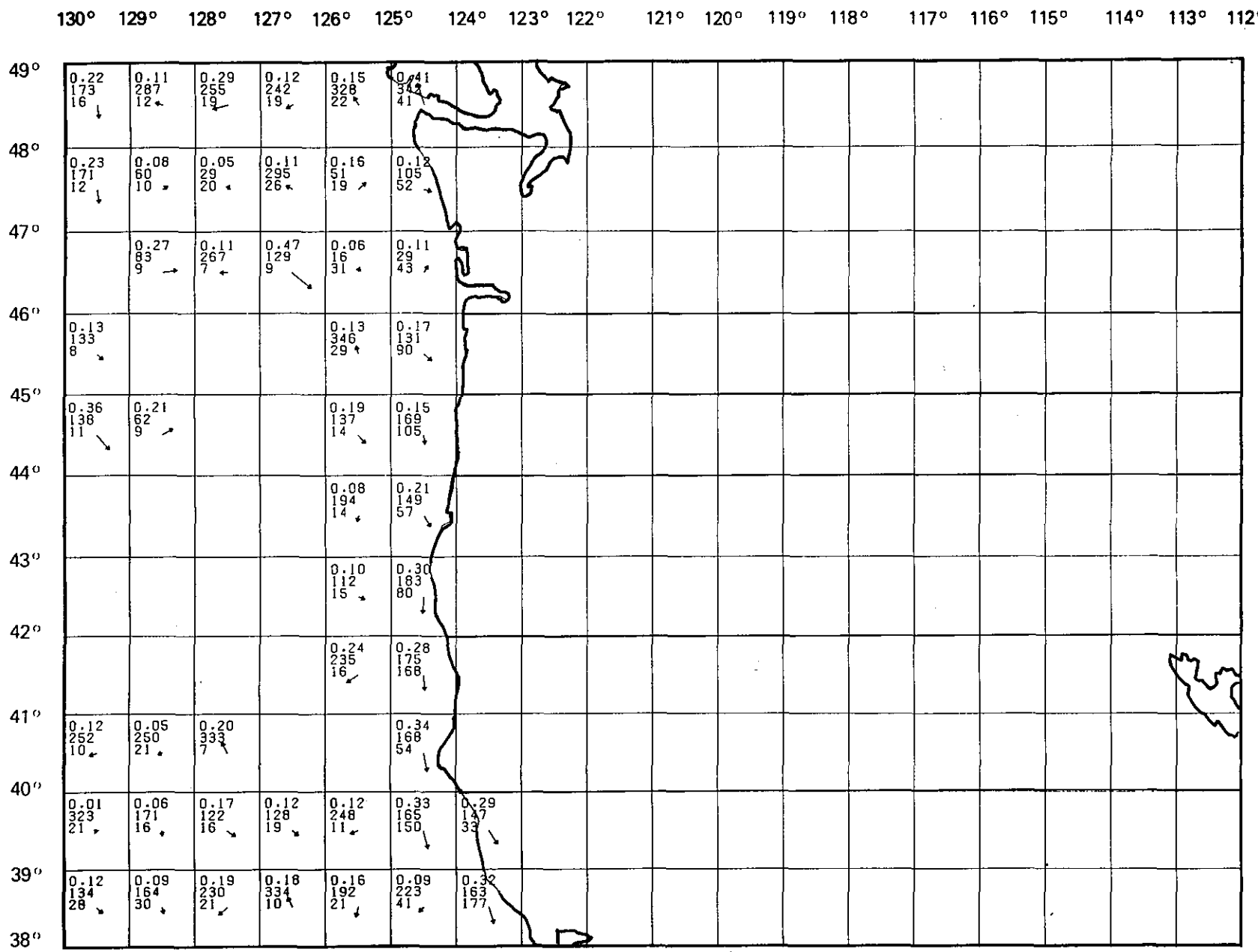

Figure 4.15. Surface Currents in March Computed From the NODC Ship Drift File

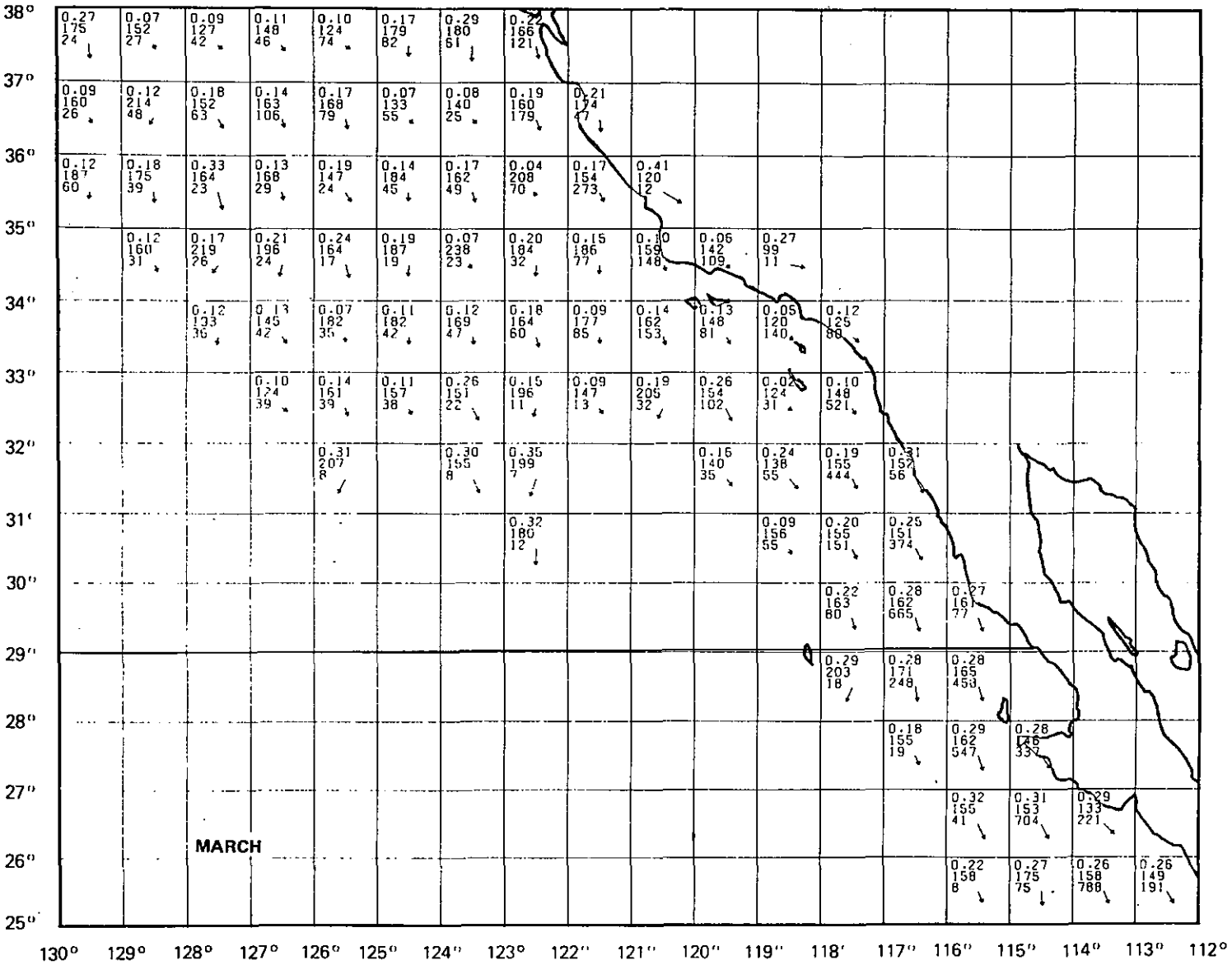

Figure 4.15. Surface Currents in March Computed From the NODC Ship Drift File (cont'd)

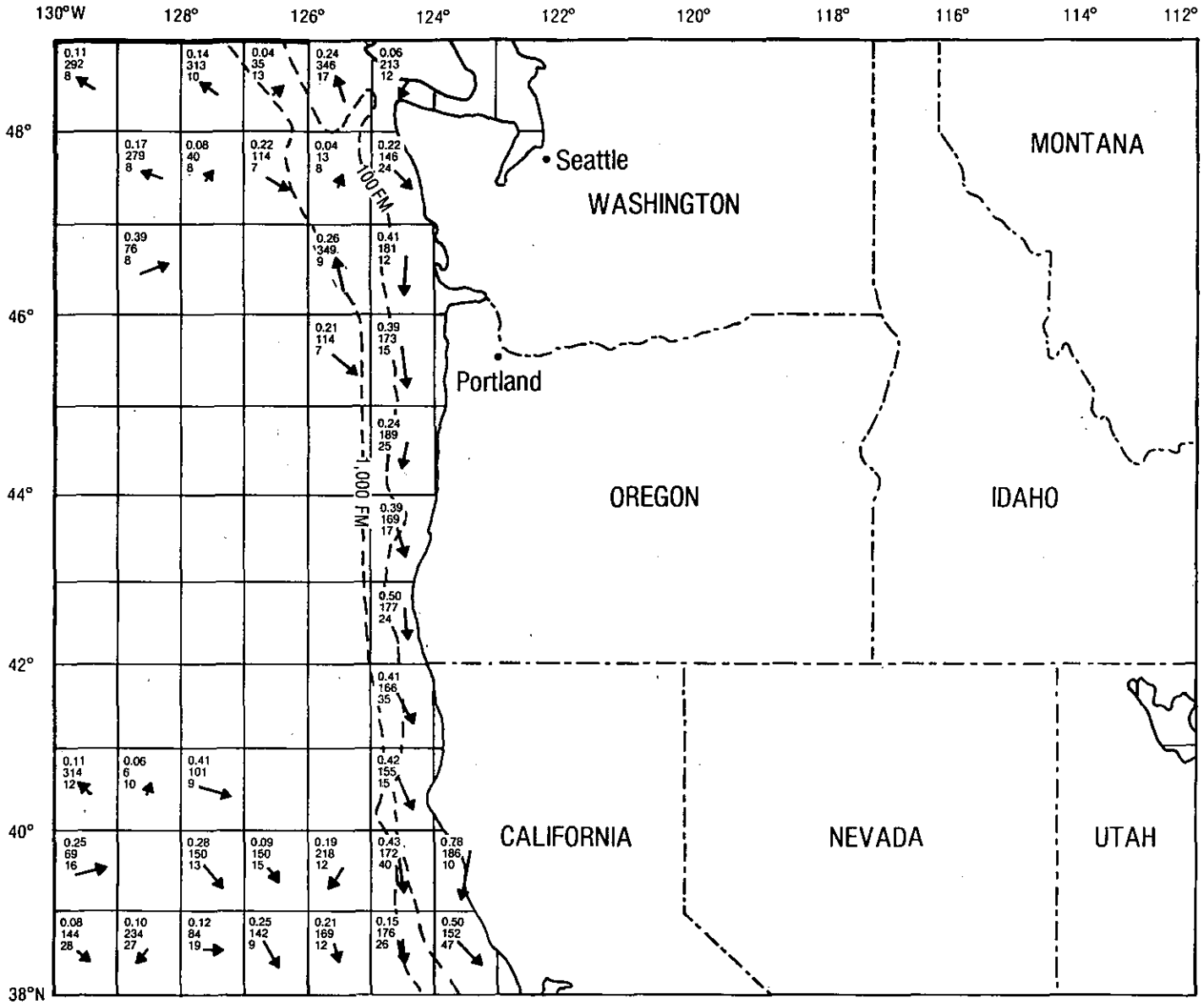

Figure 4.16. Surface Currents in April Computed From the NODC Ship Drift File

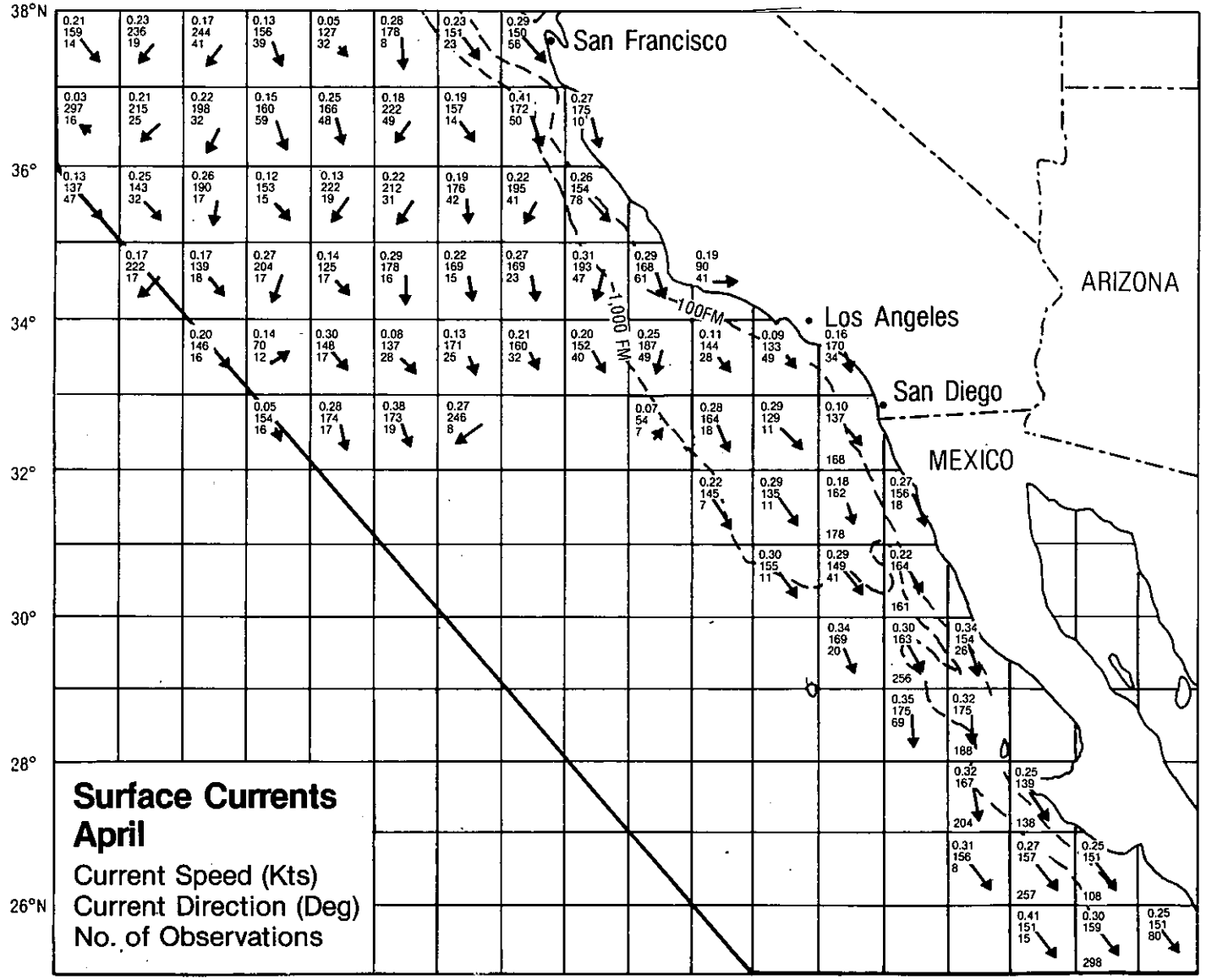

Figure 4.16. Surface Currents in April Computed From the NODC Ship Drift File (cont'd)

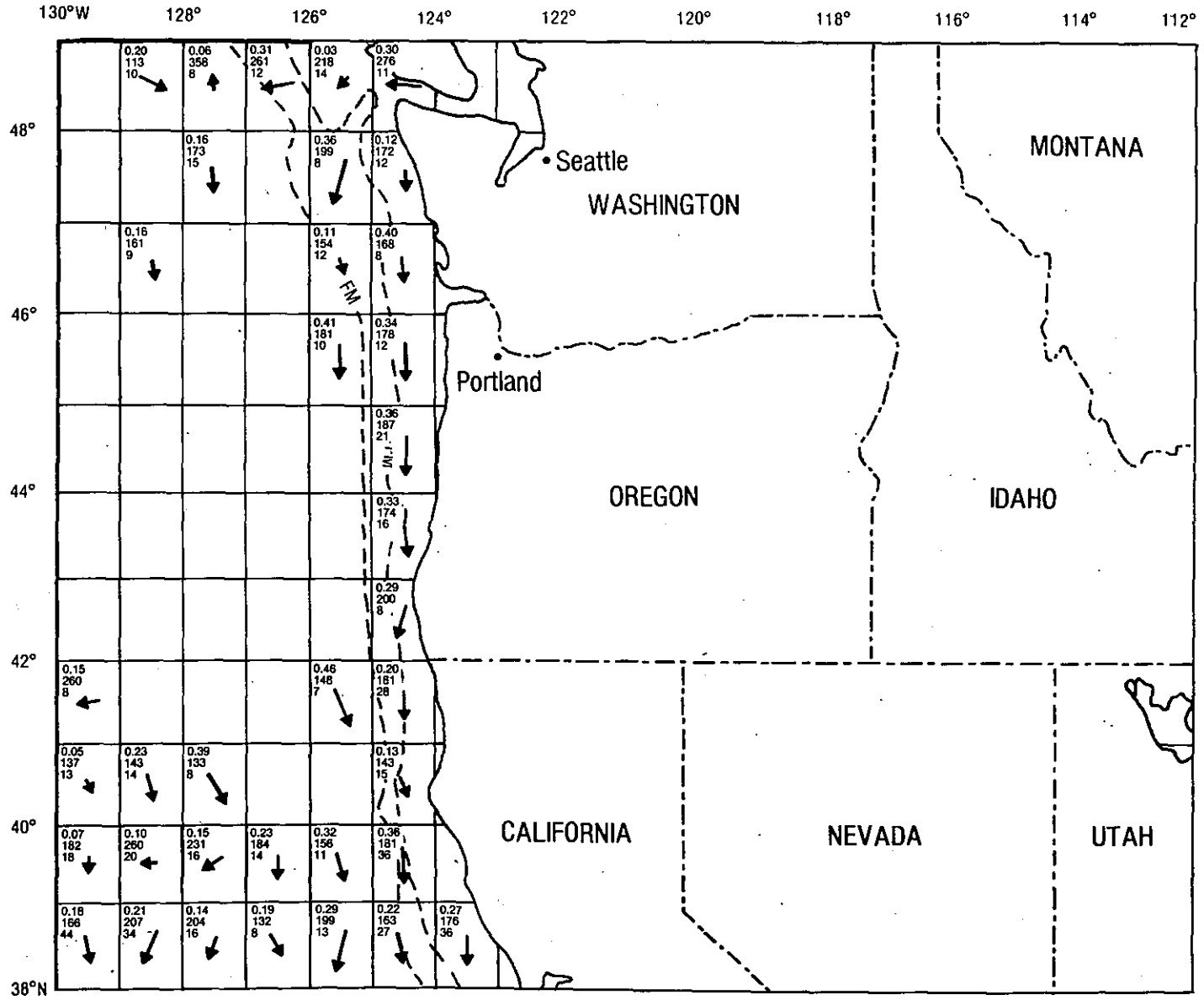

Figure 4.17. Surface Currents in August Computed From the NODC Ship Drift File

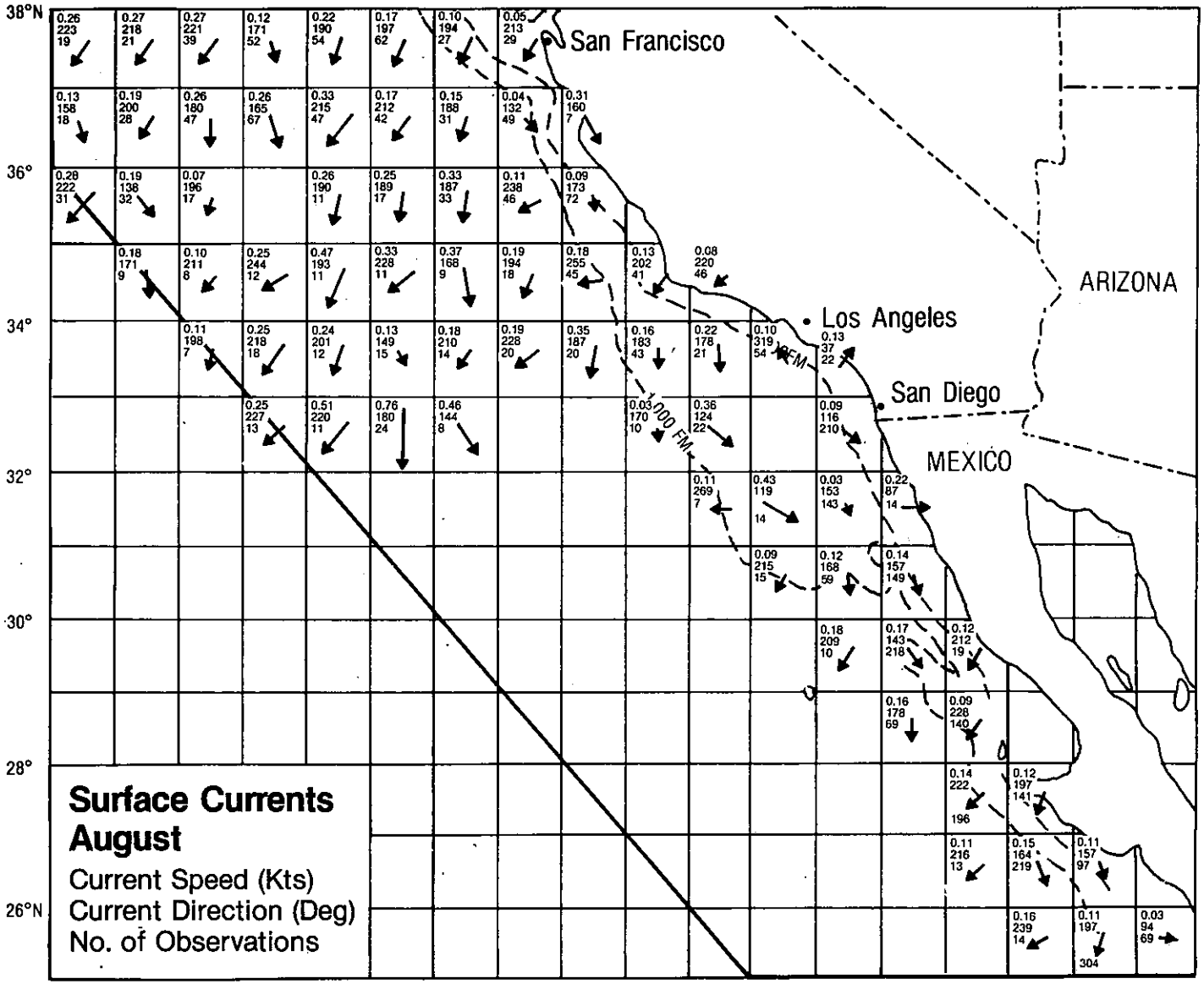

Figure 4.17. Surface Currents in August Computed From the NODC Ship Drift File (cont'd)

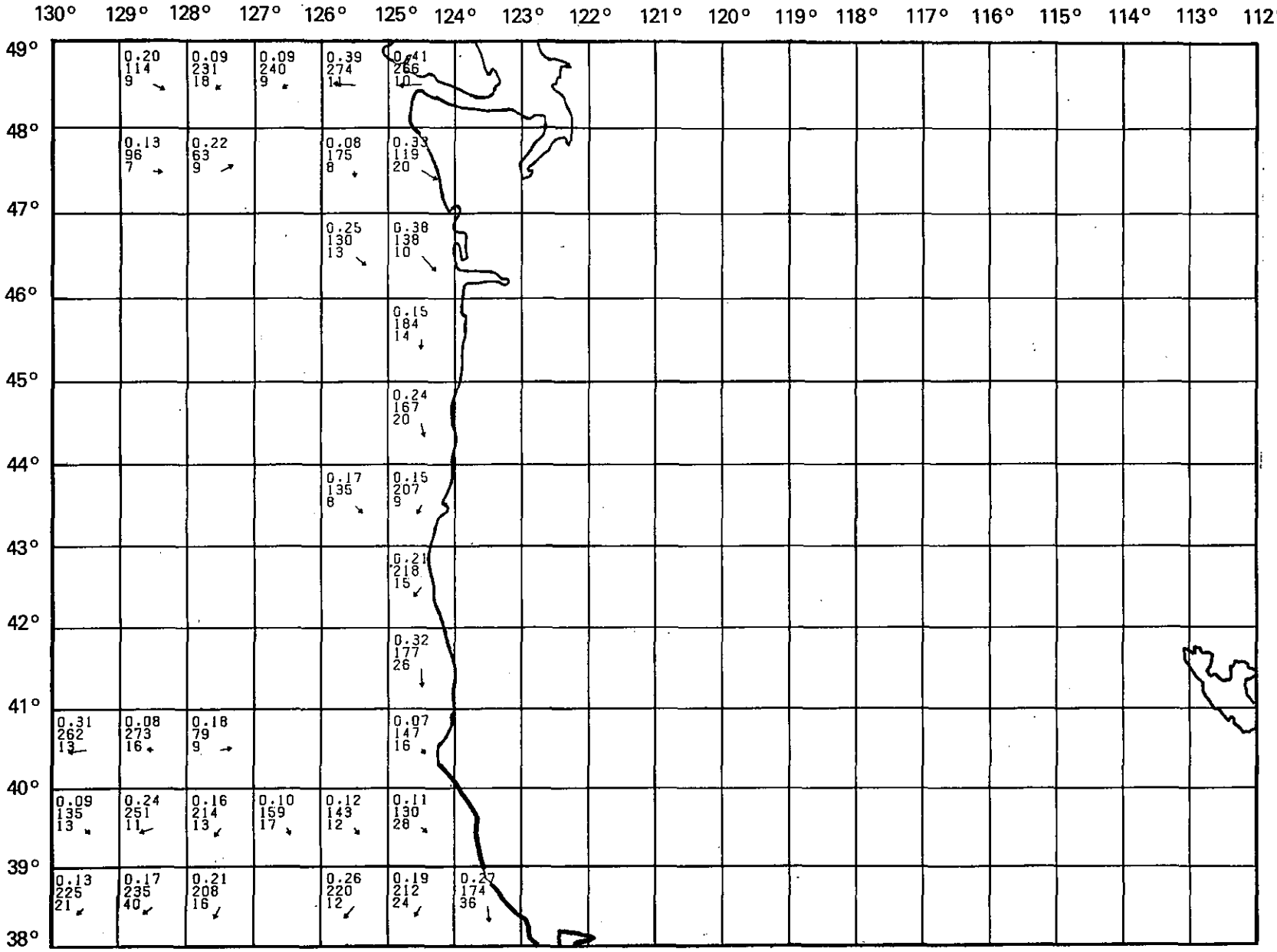

Figure 4.18. Surface Currents in September Computed From the NODC Ship Drift File

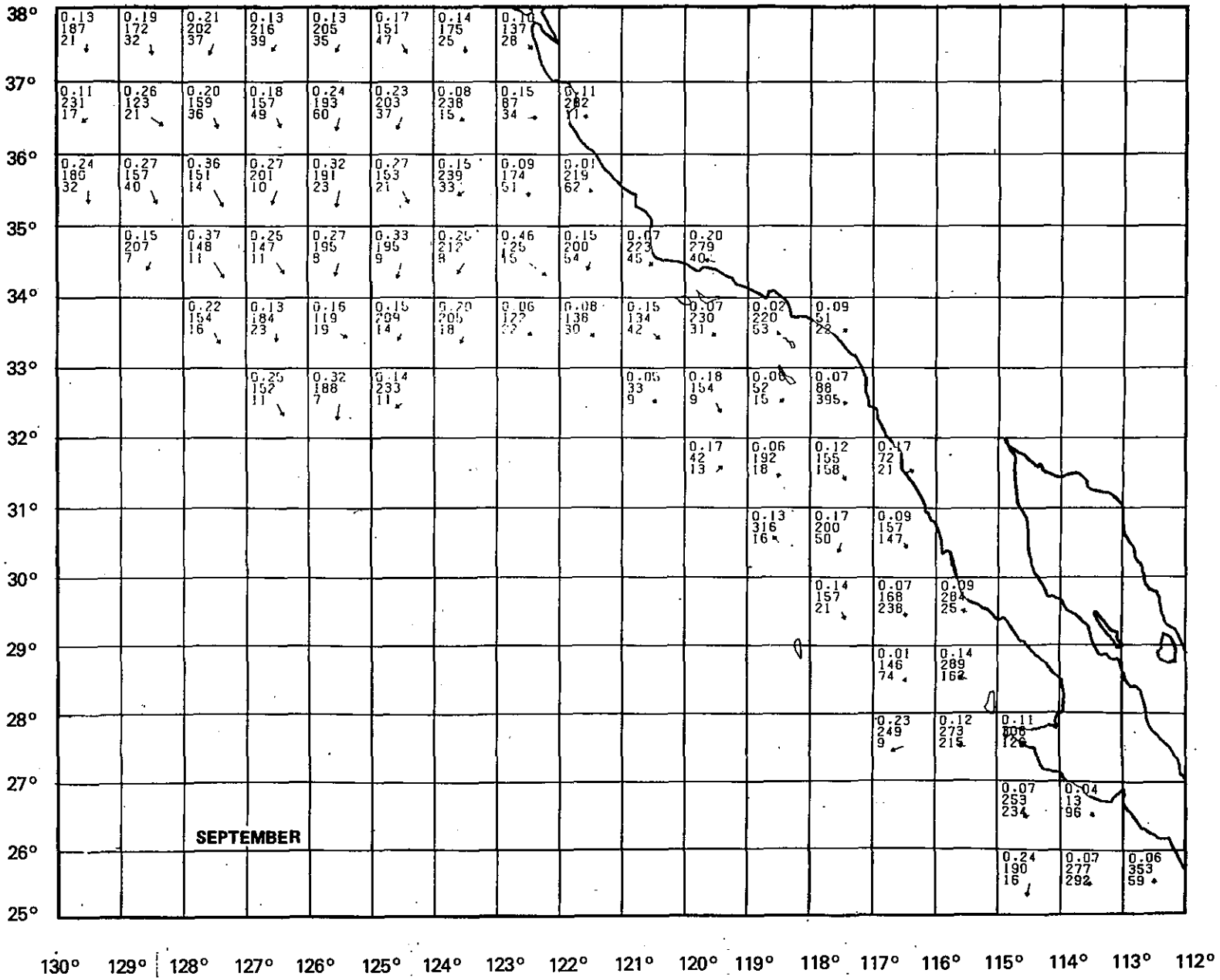

Figure 4.18. Surface Currents in September Computed From the NODC Ship Drift File (cont'd)

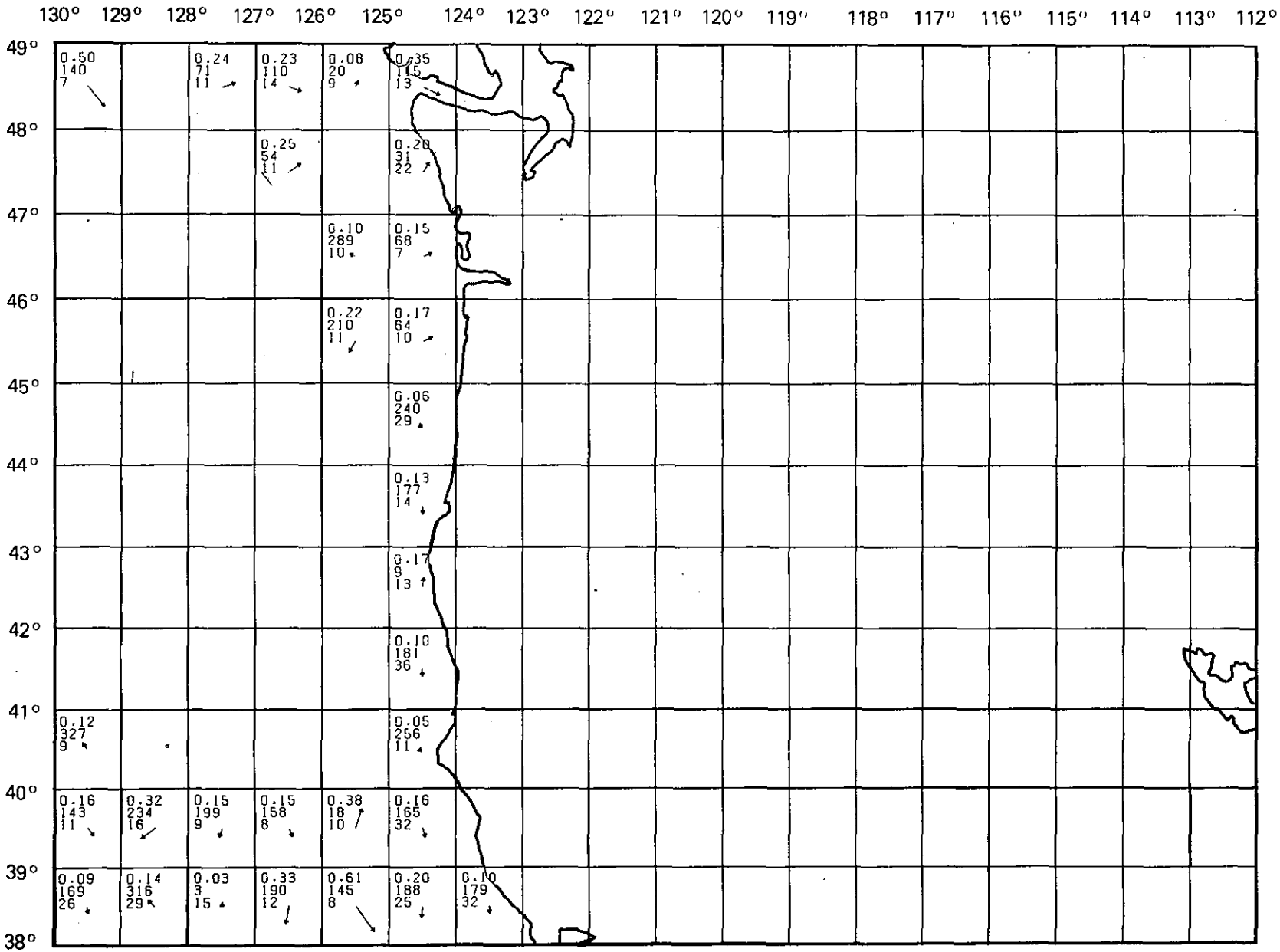

Figure 4.19. Surface Currents in October Computed From the NODC Ship Drift File

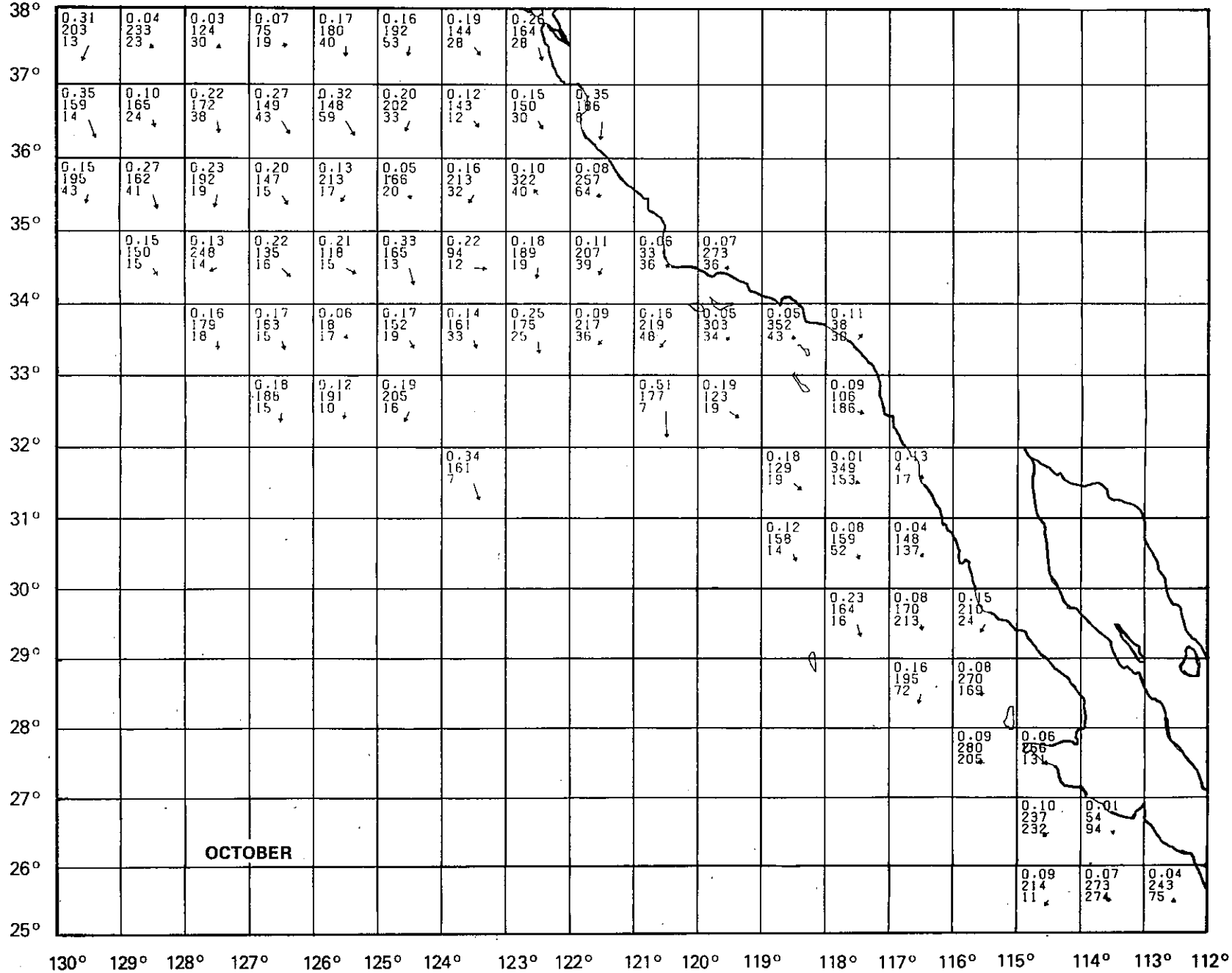

Figure 4.19. Surface Currents in October Computed From the NODC Ship Drift File (cont'd)

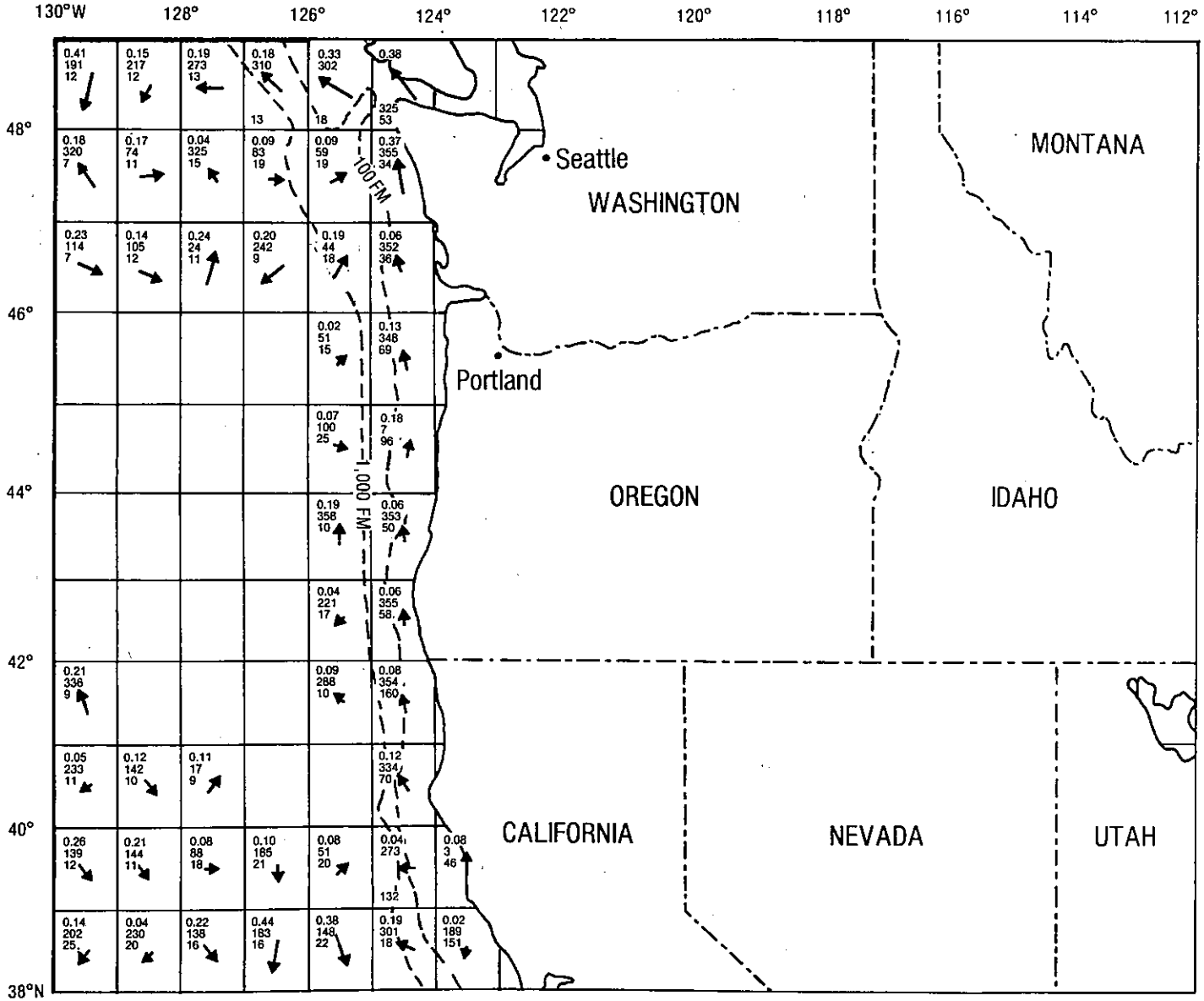

Figure 4.20. Surface Currents in November Computed From the NODC Ship Drift File

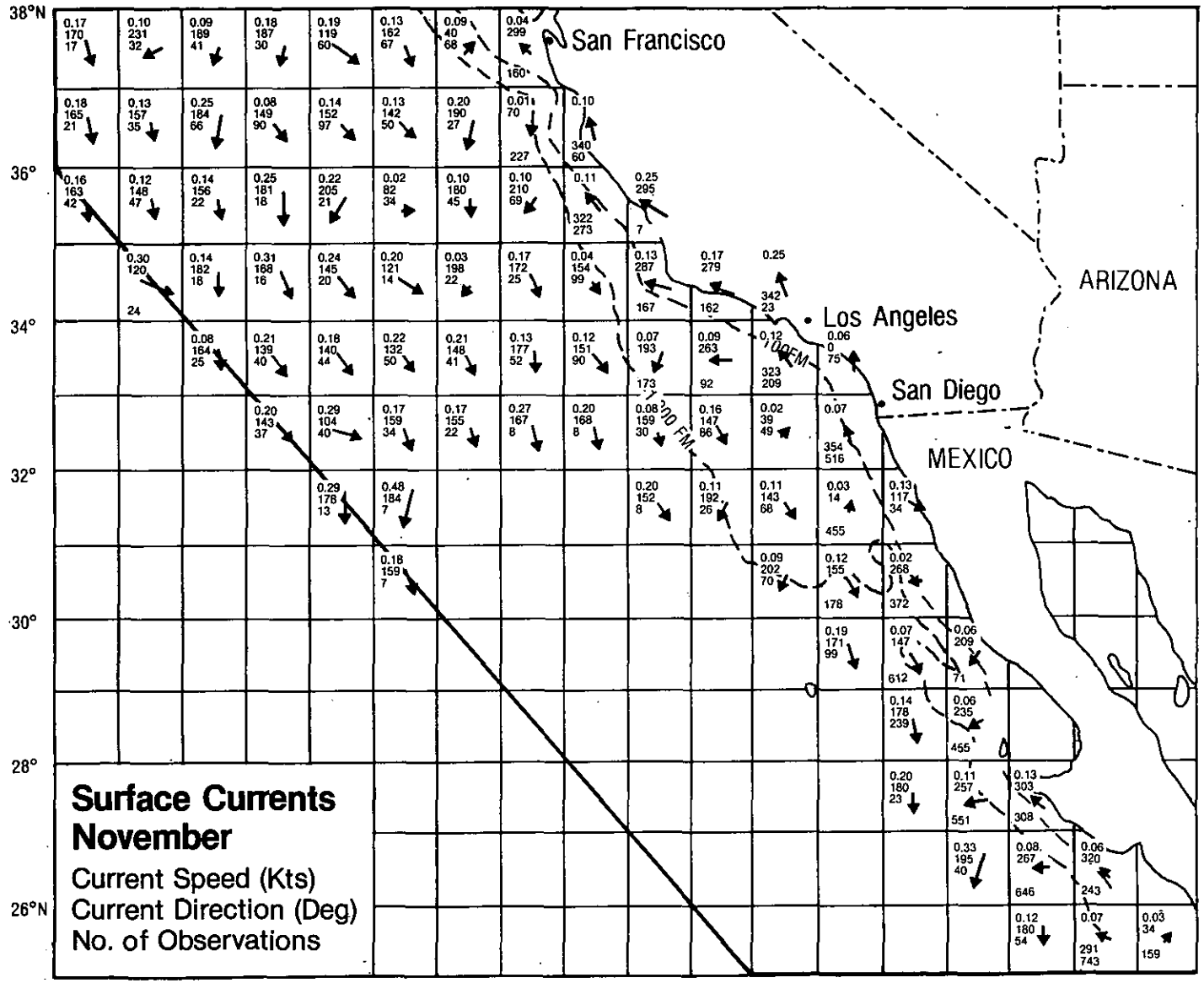

Figure 4.20. Surface Currents in November Computed From the NODC Ship Drift File (cont'd)

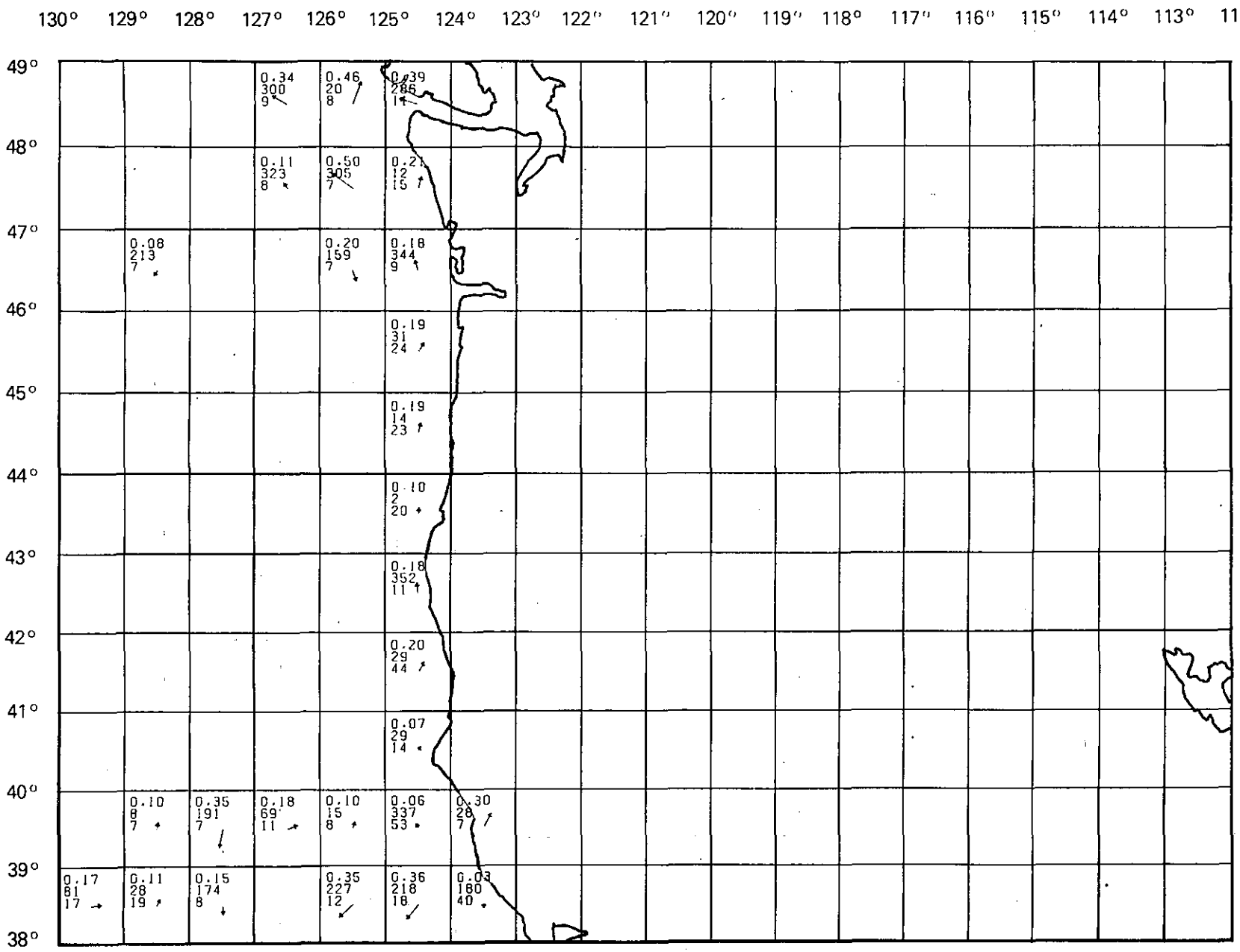

Figure 4.21. Surface Currents in December Computed From the NODC Ship Drift File

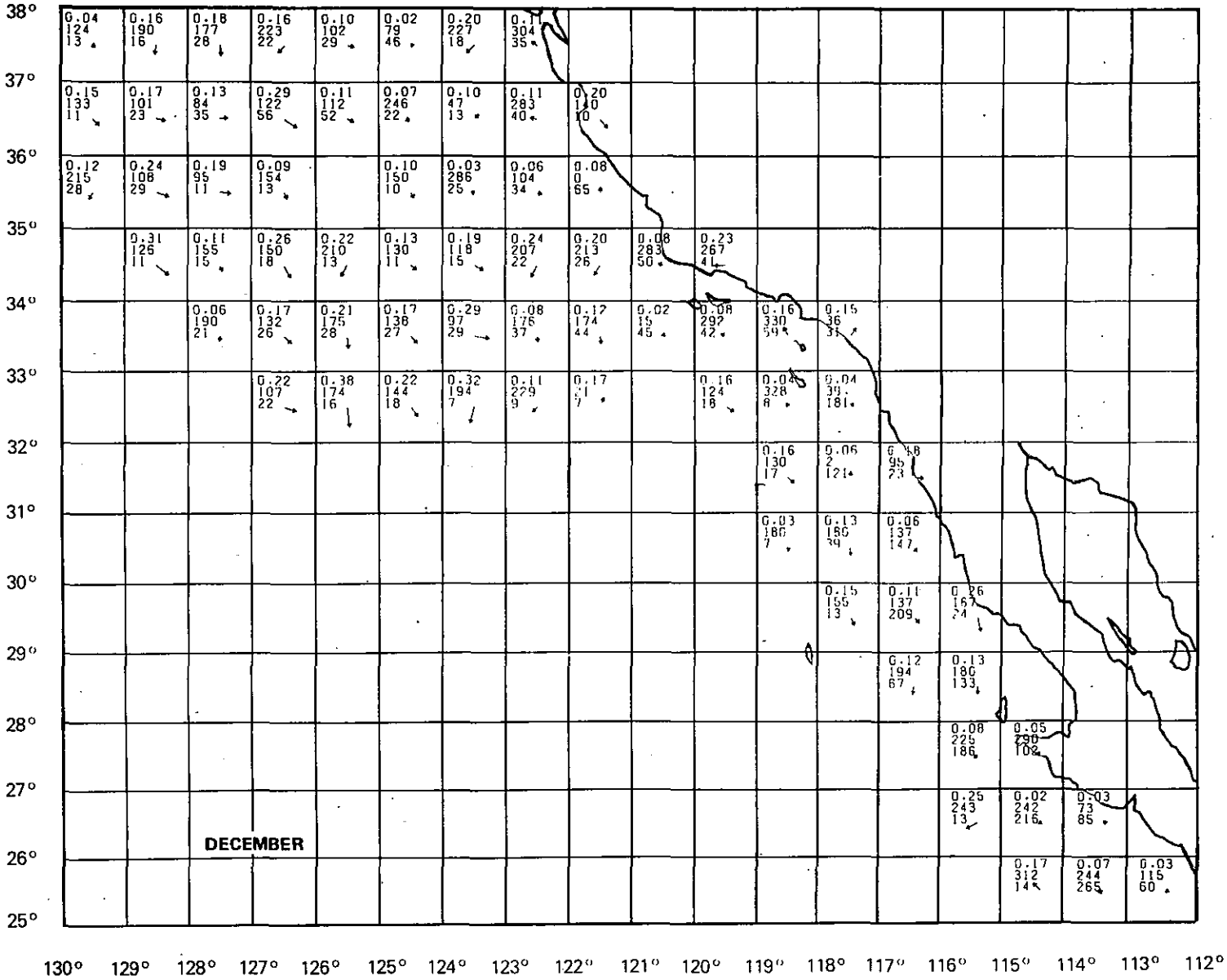

Figure 4.21. Surface Currents in December Computed From the NODC Ship Drift File (cont'd)

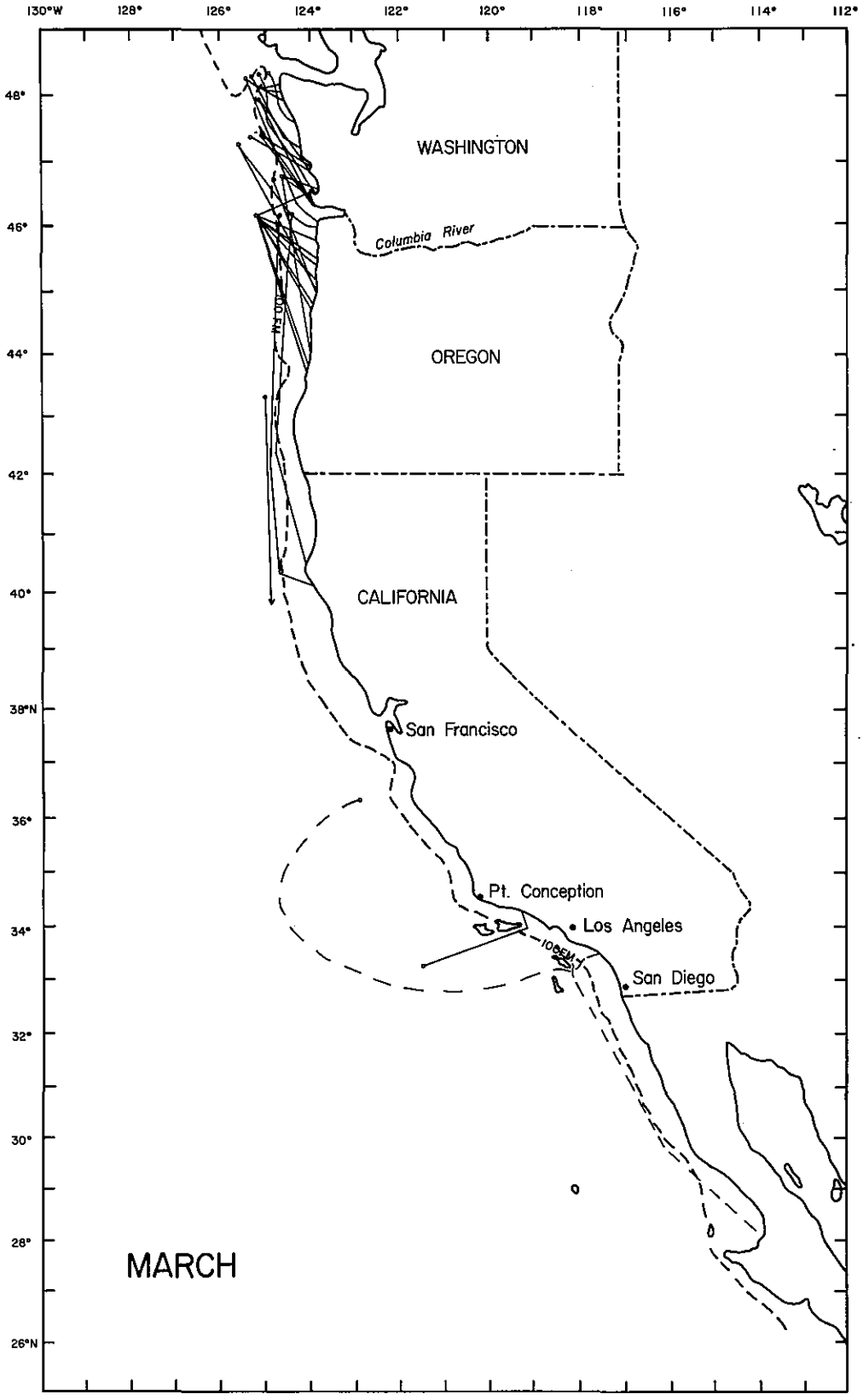

Figure 4.22. Long Trajectory Drifters for March

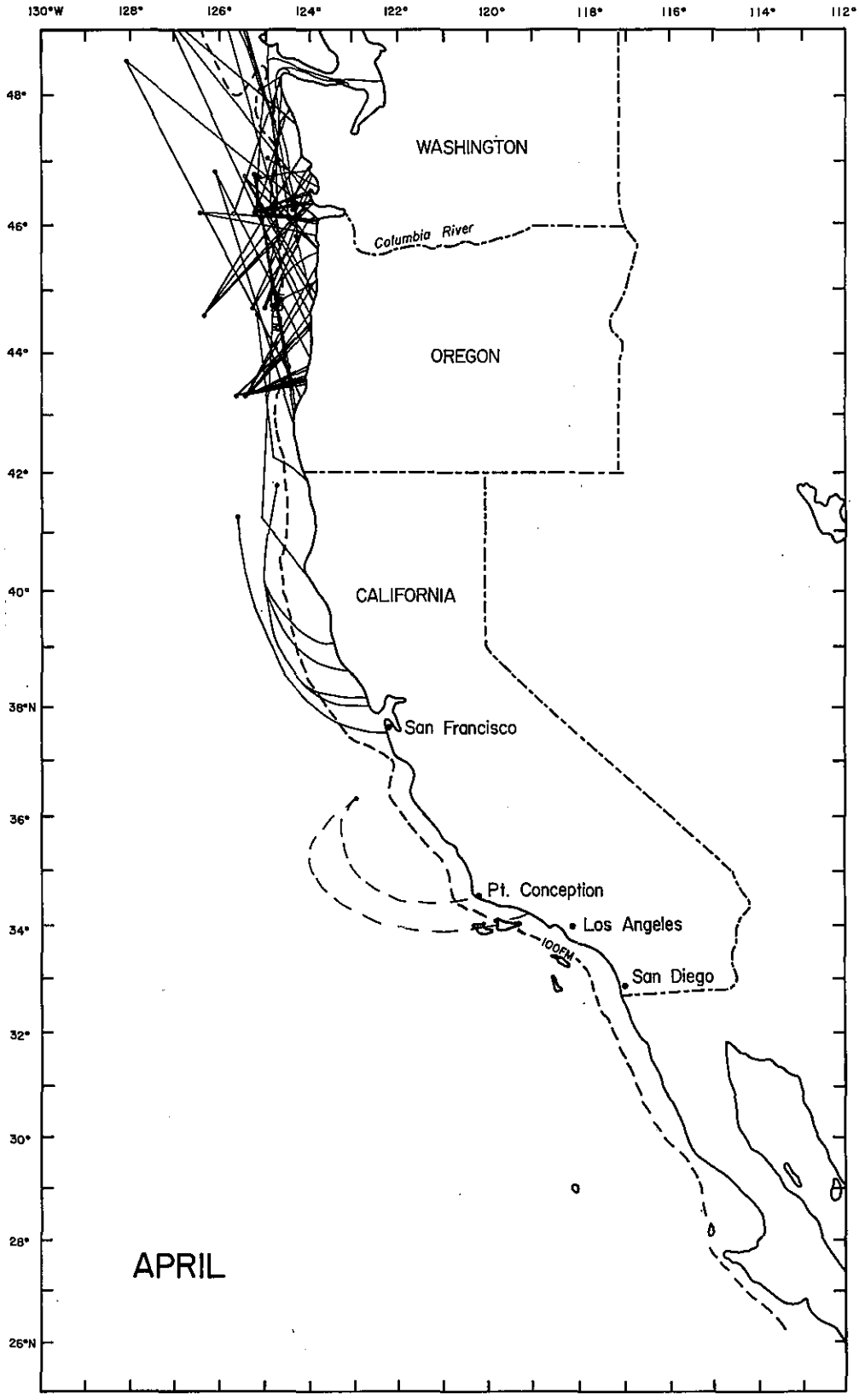

Figure 4.23. Long Trajectory Drifters for April

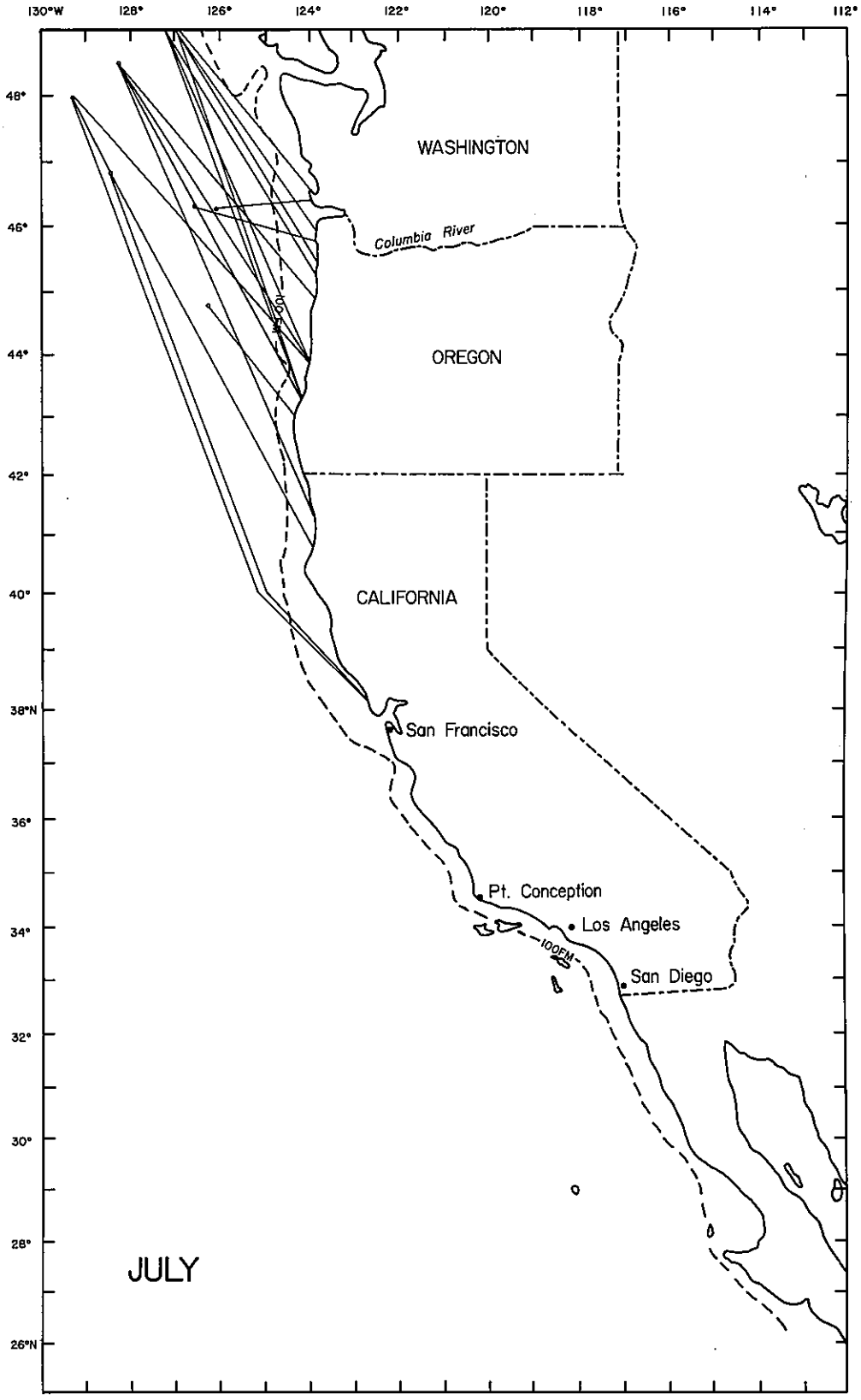

Figure 4.24. Long Trajectory Drifters for July

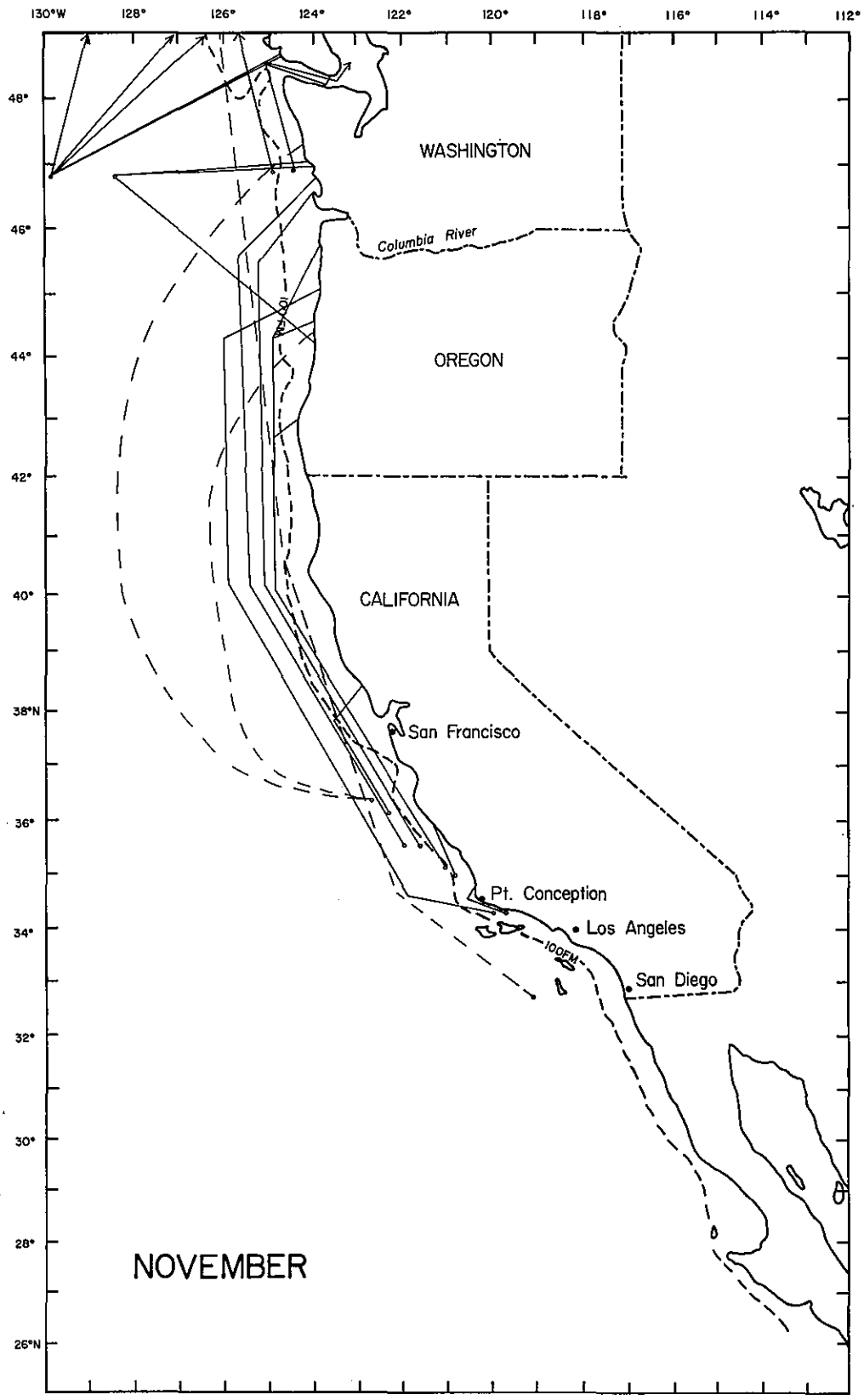

Figure 4.25. Long Trajectory Drifters for November

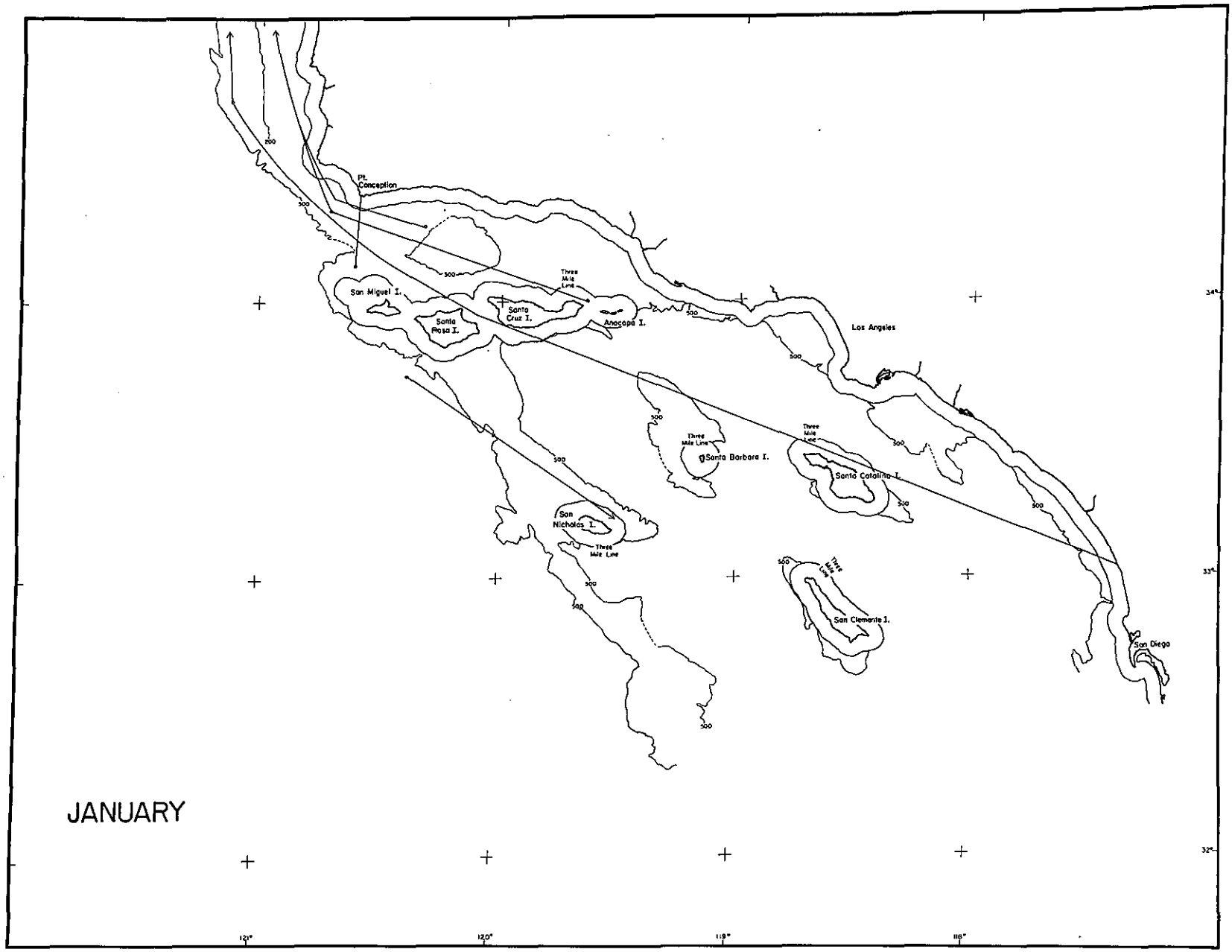

Figure 4.26. Nearshore Drifter Releases for January off Southern California

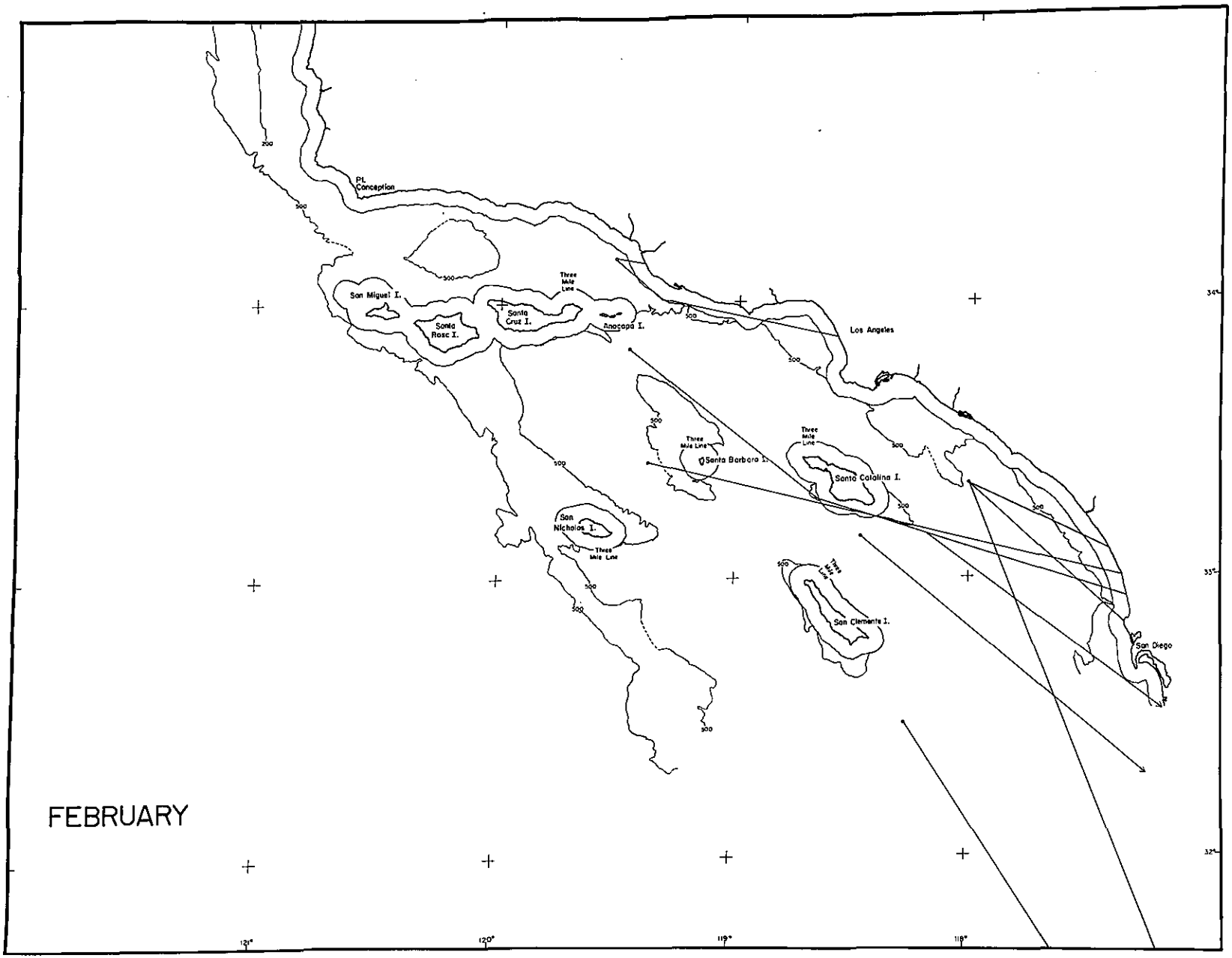

Figure 4.27. Nearshore Drifter Releases for February off Southern California

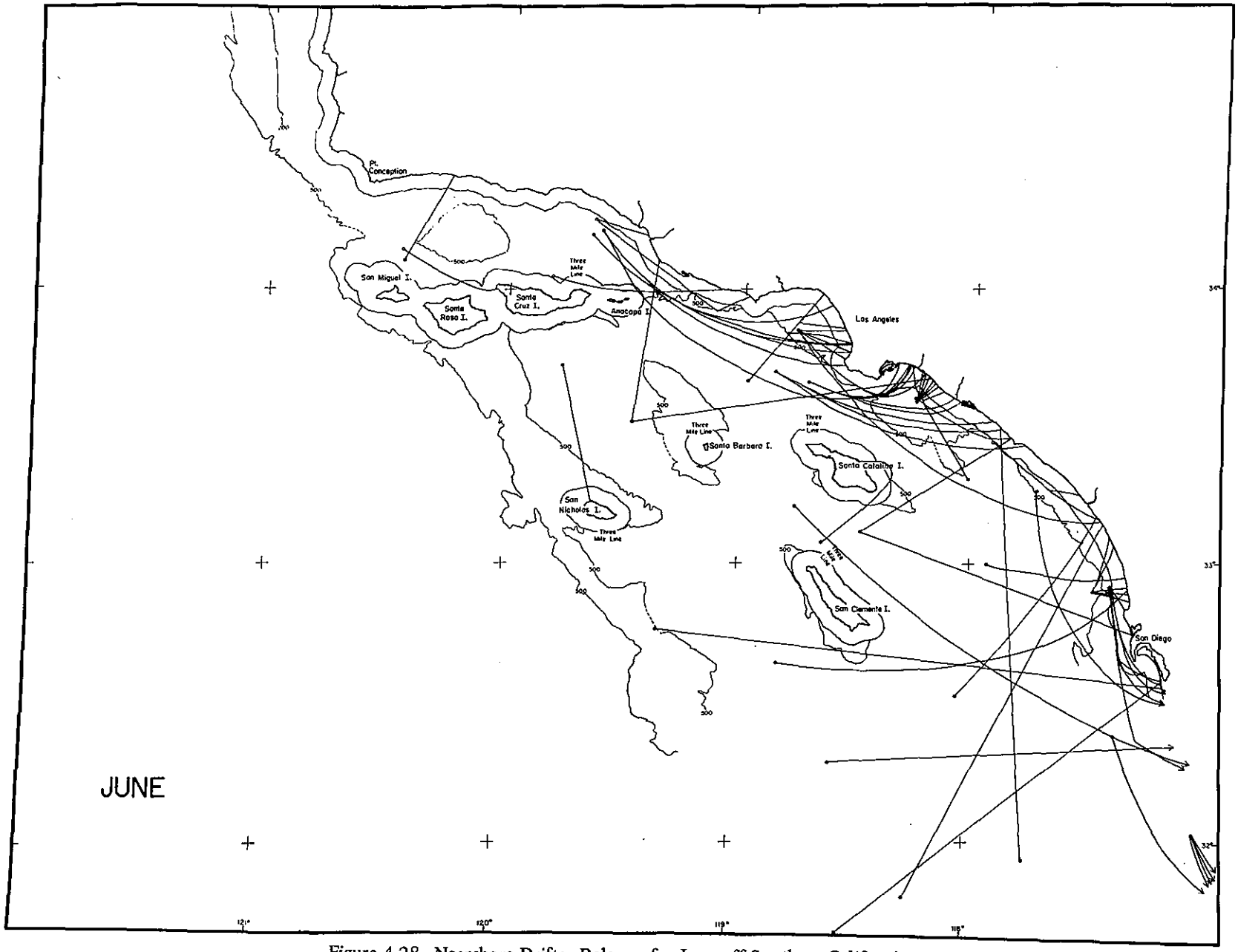

Figure 4.28. Nearshore Drifter Releases for June off Southern California

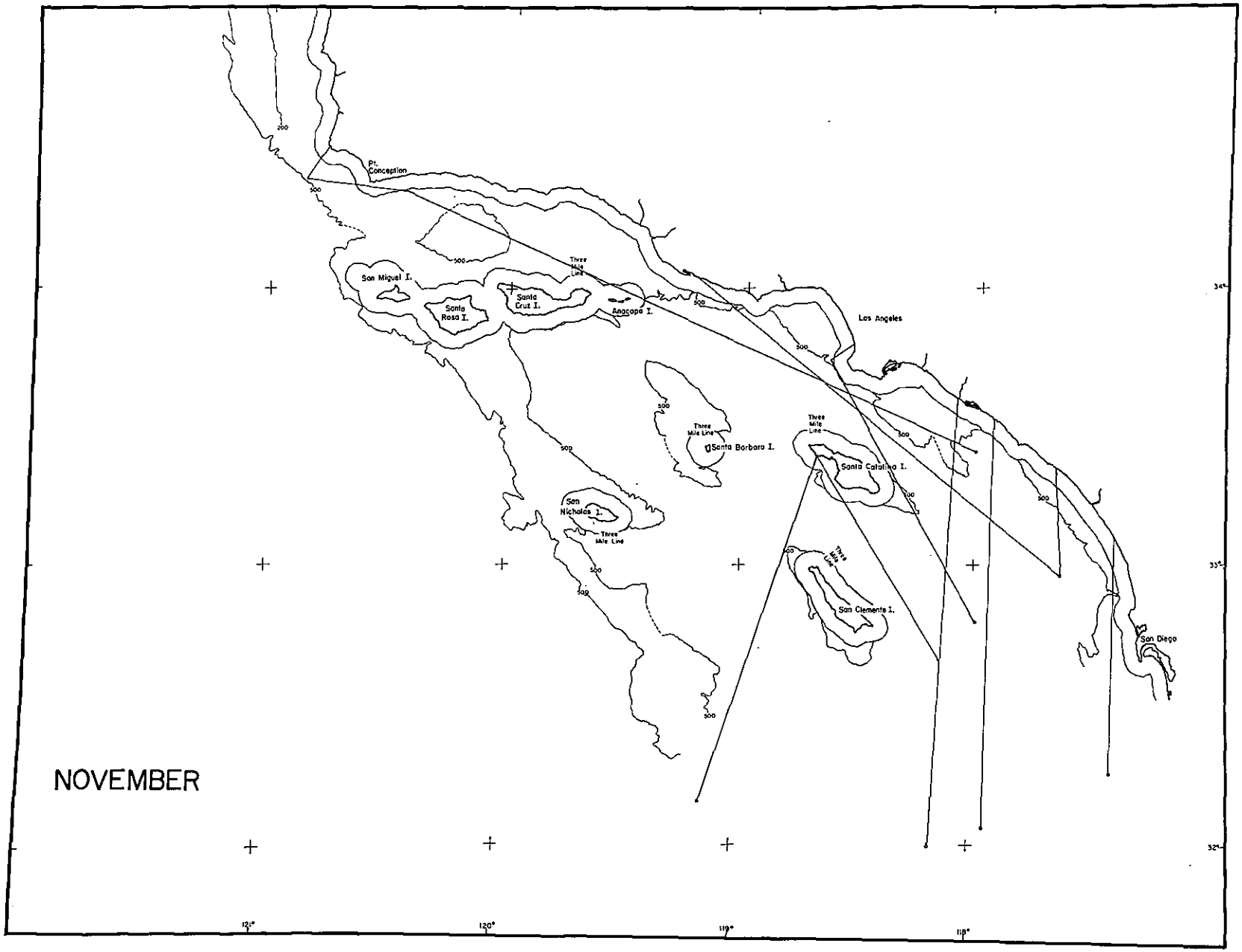

Figure 4.29. Nearshore Drifter Releases for November off Southern California

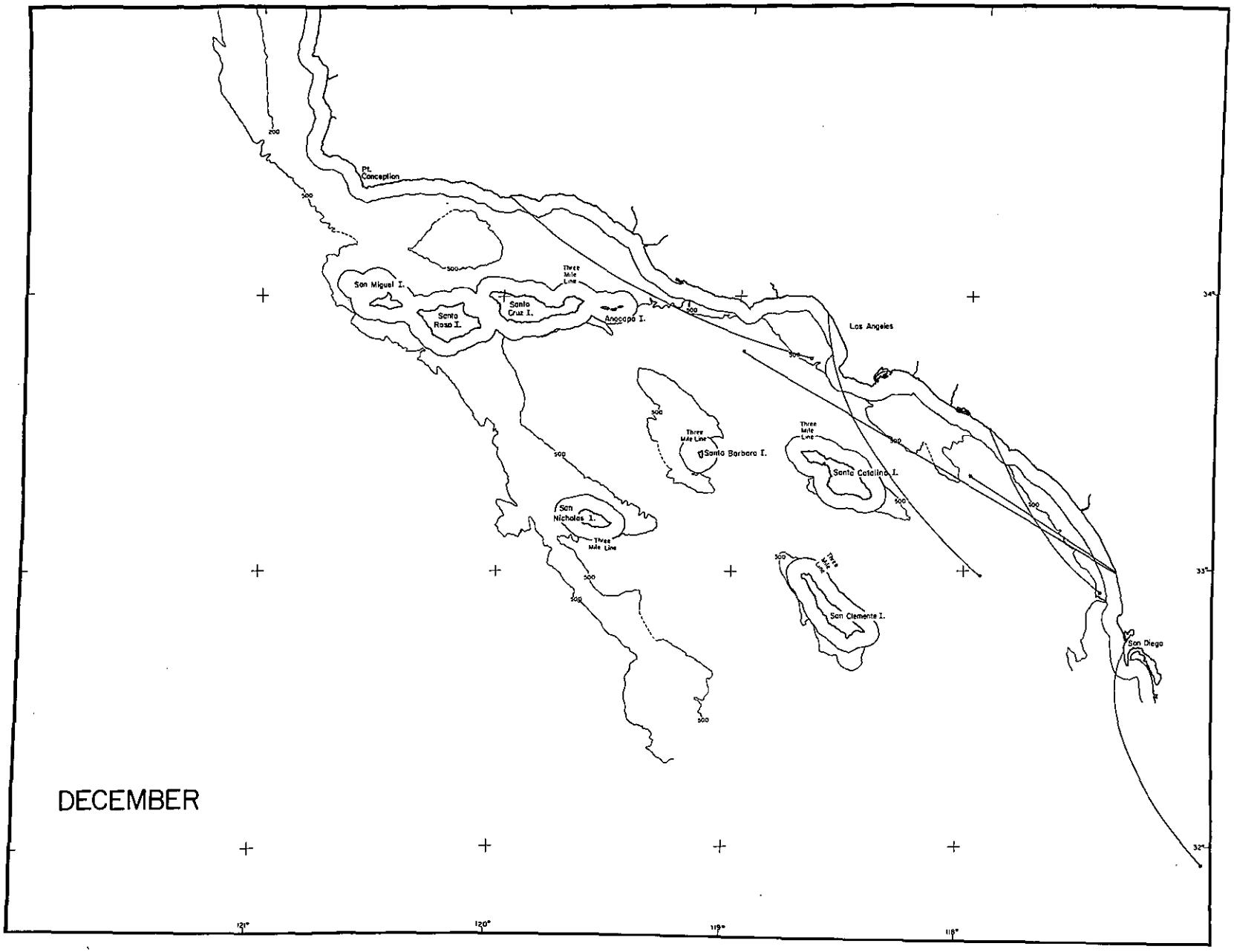

Figure 4.30. Nearshore Drifter Releases for December off Southern California

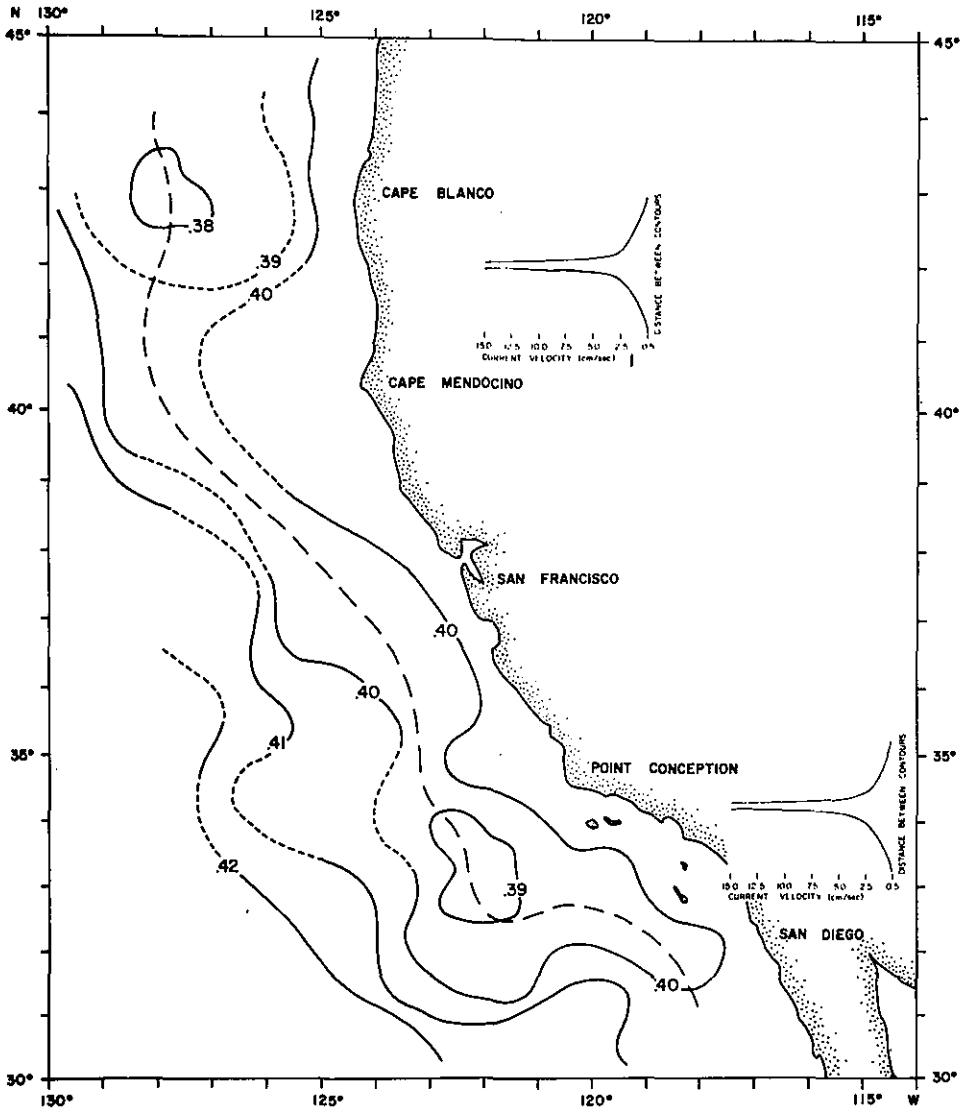

Figure 4.31. Dynamic Topography (dyn-m) of the 200 m Level Relative to 500 dbar, December-January. The Large Dashed Line Separates Equatorward from Poleward Flow. The Dashed Contours Indicate High Uncertainty.

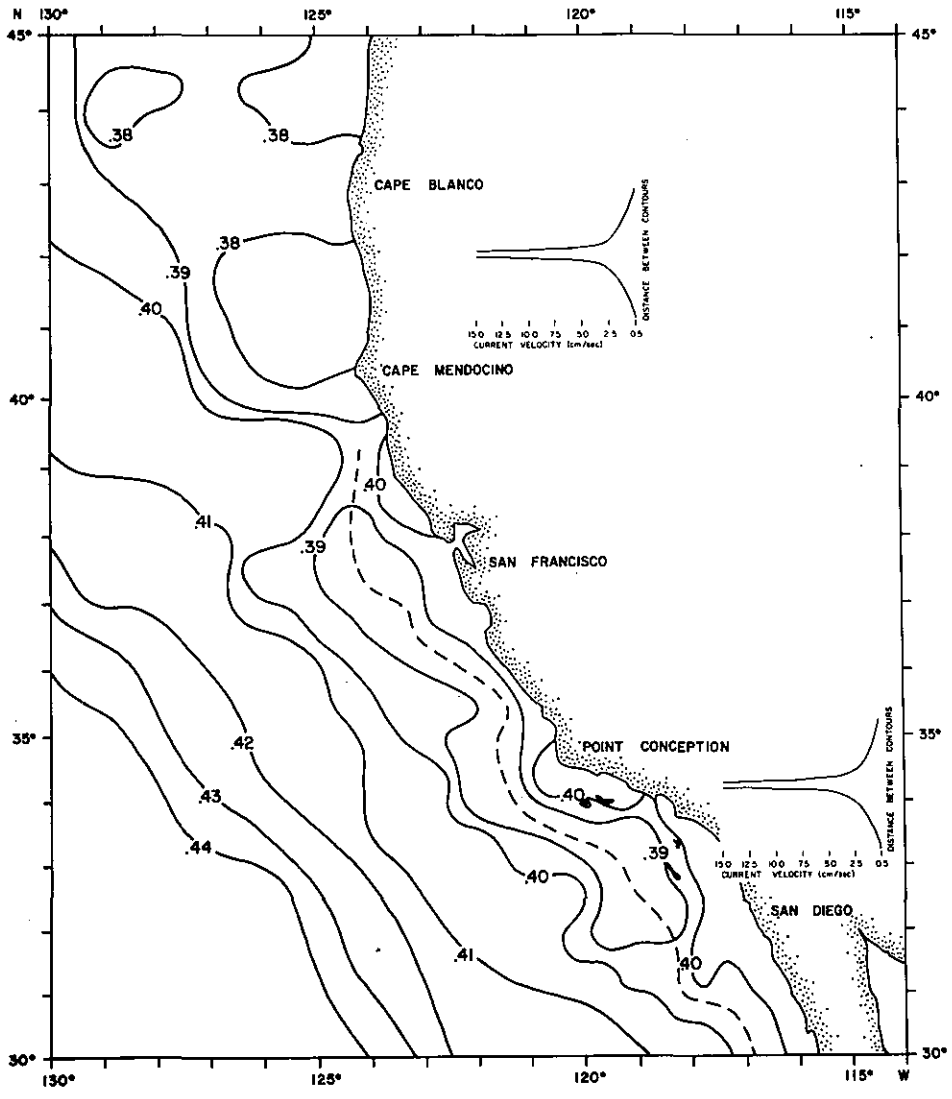

Figure 4.32. Dynamic Topography (dyn-m) of the 200 m Level Relative to 500 dbar, May, June, July. The Large Dashed Line Separates Equatorward from Poleward Flow. The Dashed Contours Indicate High Uncertainty.

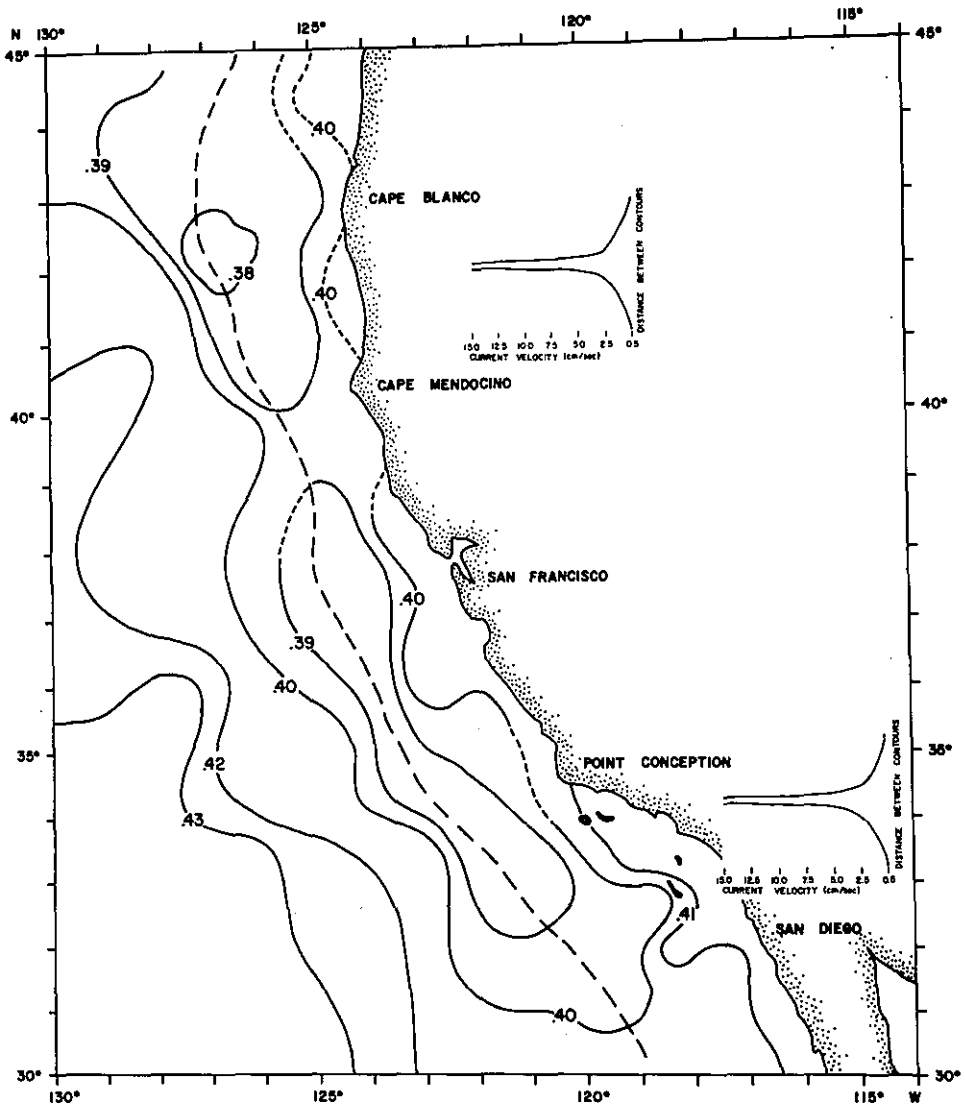

Figure 4.33. Dynamic Topography (dyn-m) of the 200 m Level Relative to 500 dbar, September-October. The Large Dashed Line Separates Equatorward from Poleward Flow. The Dashed Contours Indicate High Uncertainty.

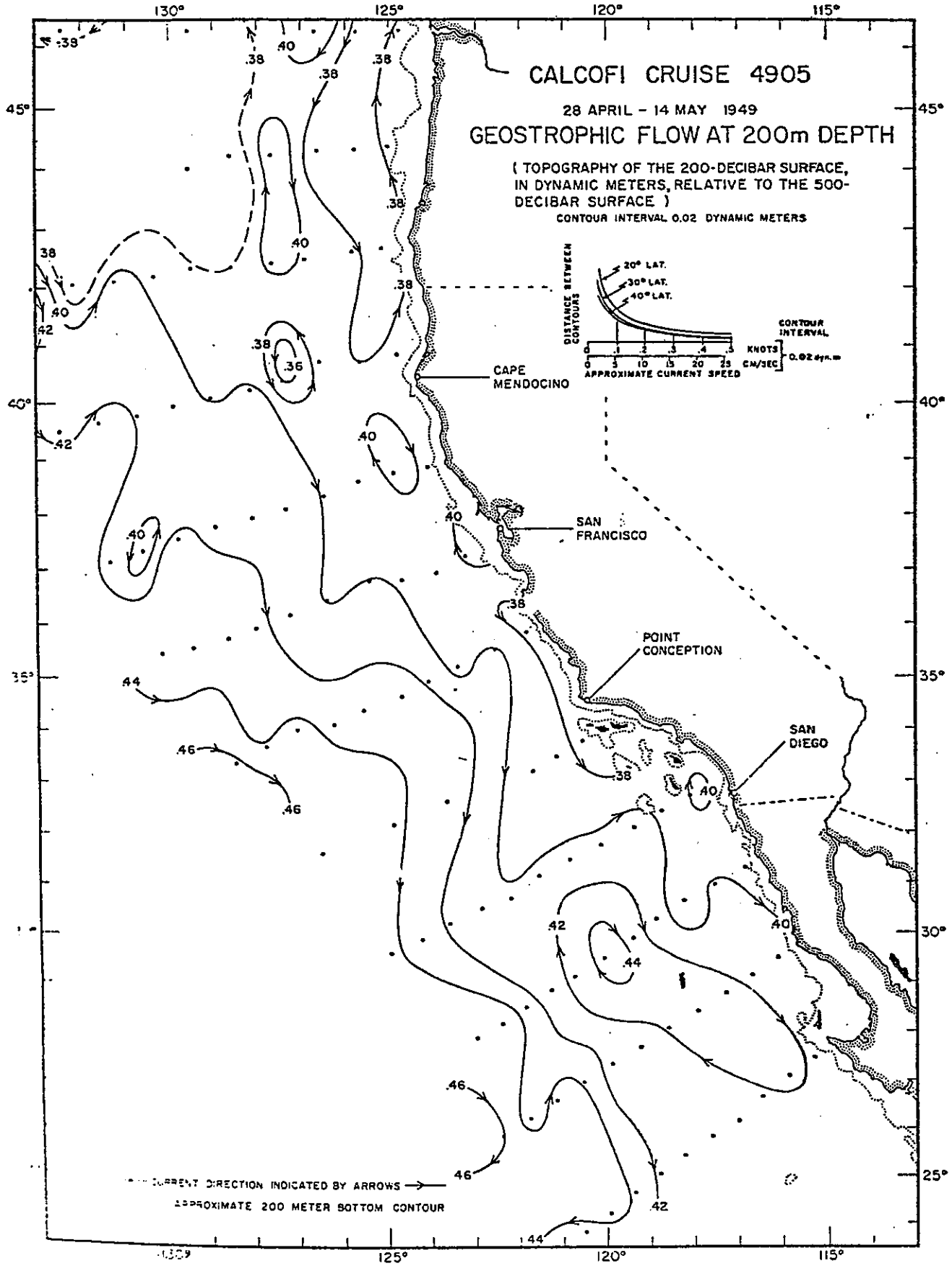

Figure 4.34. Dynamic Topography of the 200 m dbar Referred to 500 m dbar

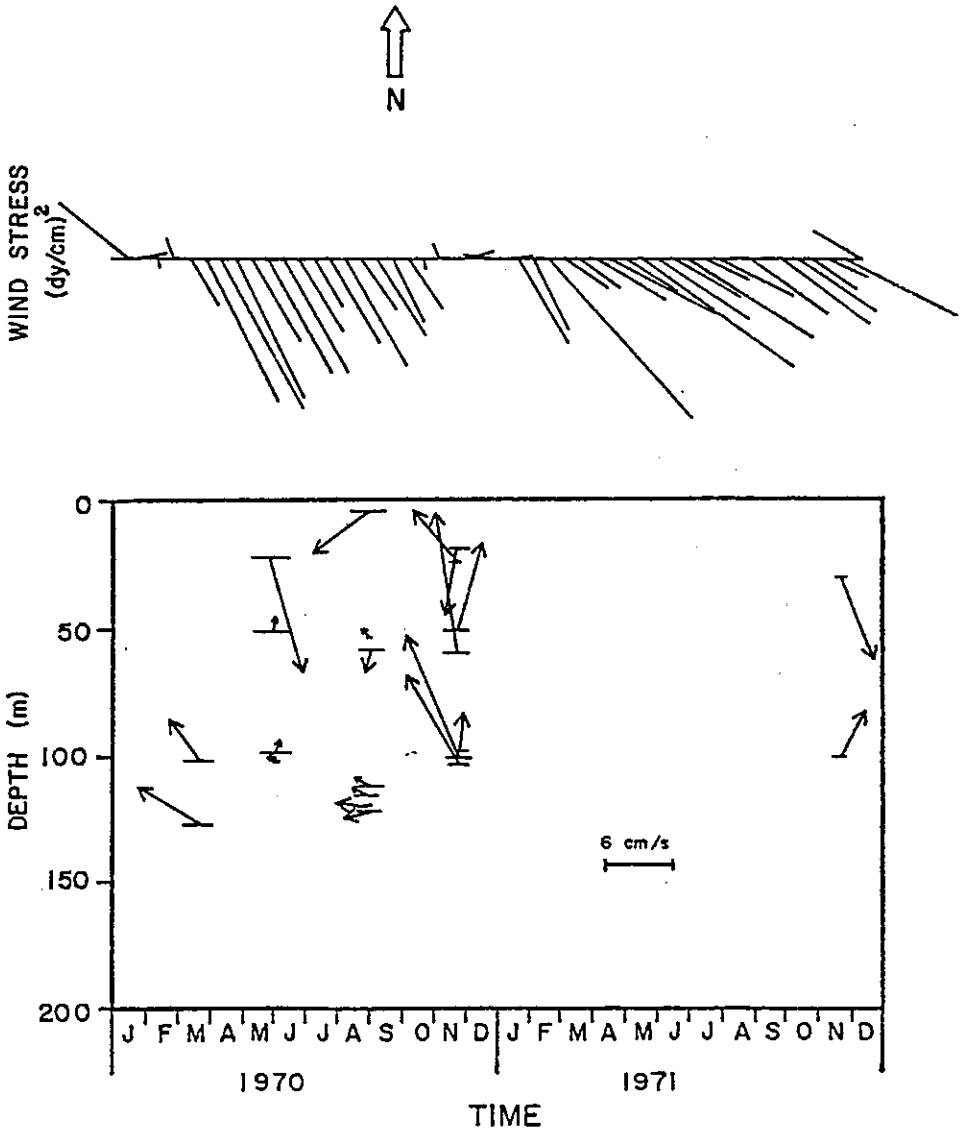

Figure 4.35. Farallon Island Semimonthly Averaged Wind Stress and Mean Current Vectors as a Function of Depth and Time for 1970 and 1971. (Horizontal lines at base of current vectors show the period of record.)

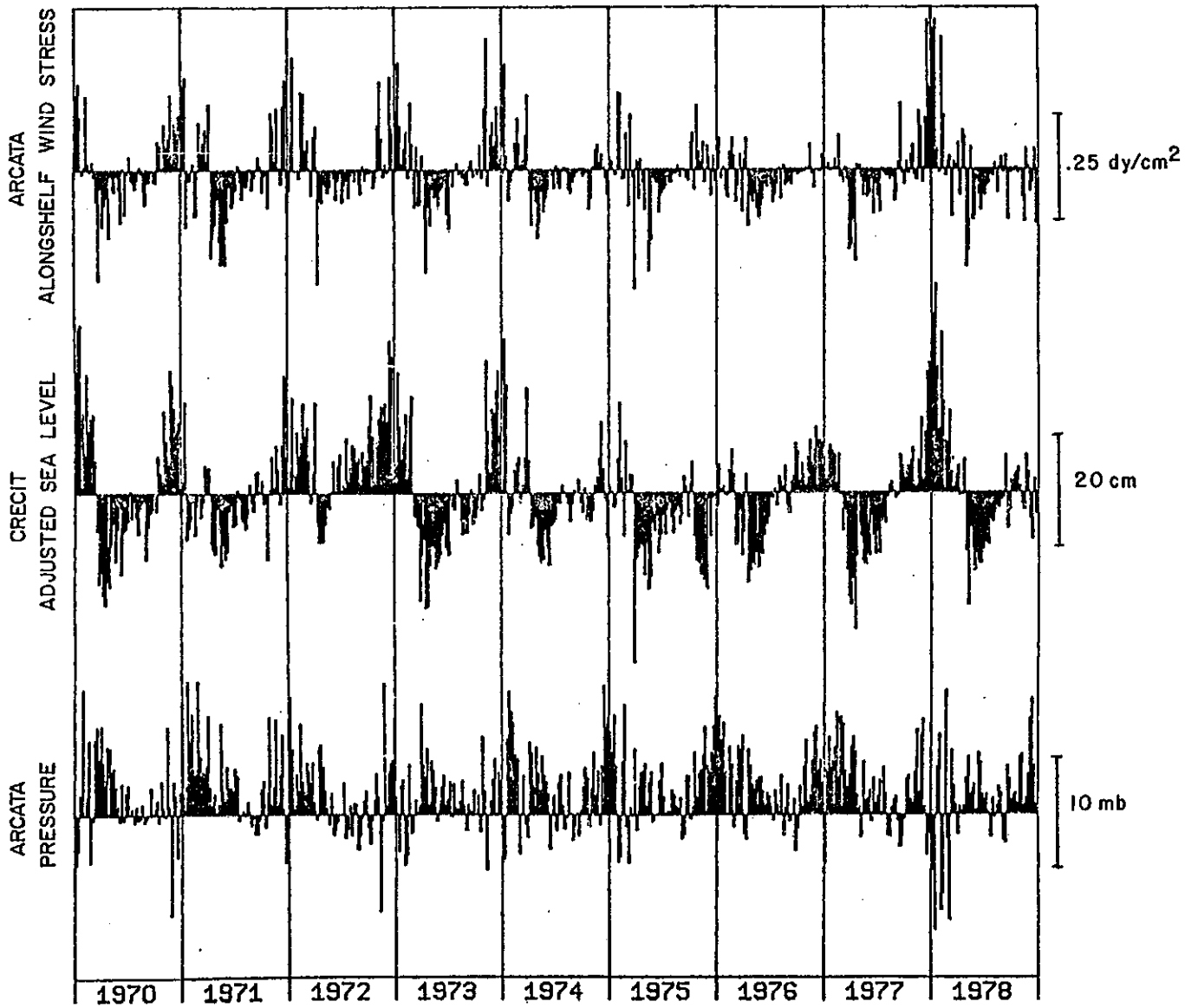

Figure 4.36. Alongshelf Wind Stress and Sea Level Pressure for Arcata, and Adjusted Coastal Sea Level for Crescent City, 1970 Through 1978

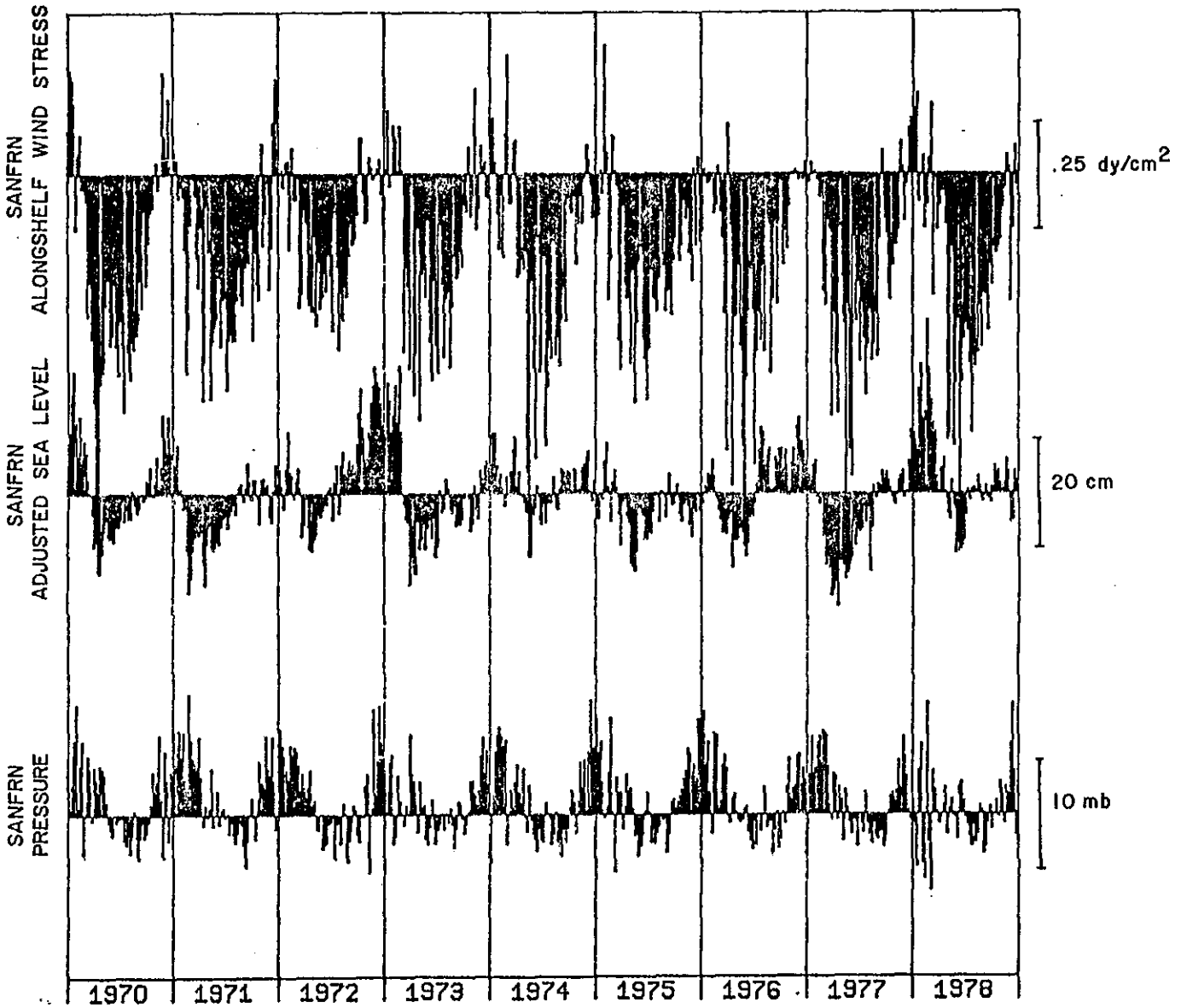

Figure 4.37. Alongshelf Wind Stress and Sea Level Pressure for San Francisco, and Adjusted Coastal Sea Level for San Francisco, 1970 Through 1978

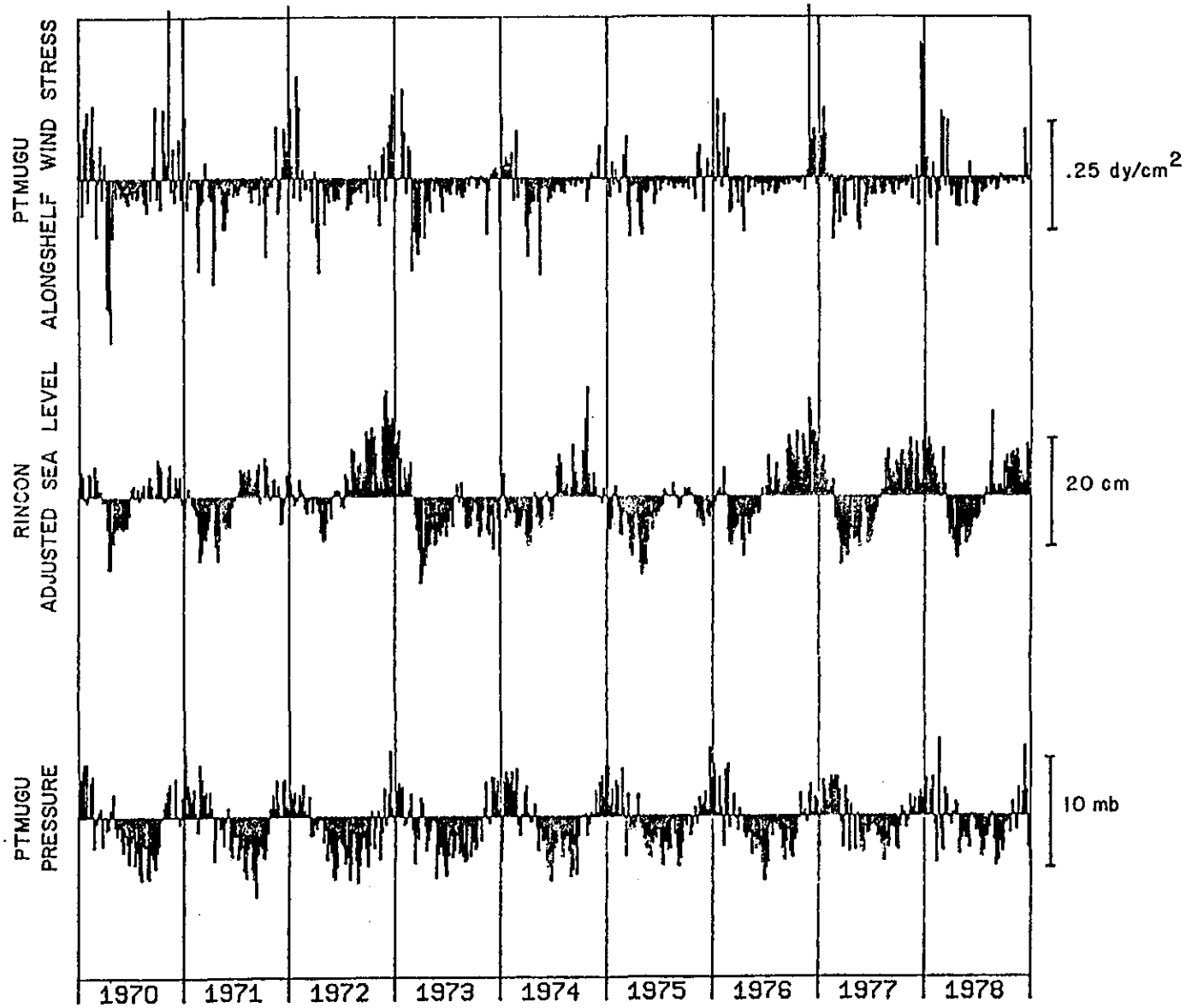

Figure 4.38. Alongshelf Wind Stress and Sea Level Pressure for Point Mugu, and Adjusted Coastal Sea Level for Rincon Island (Mussel Shoals), 1970 Through 1978

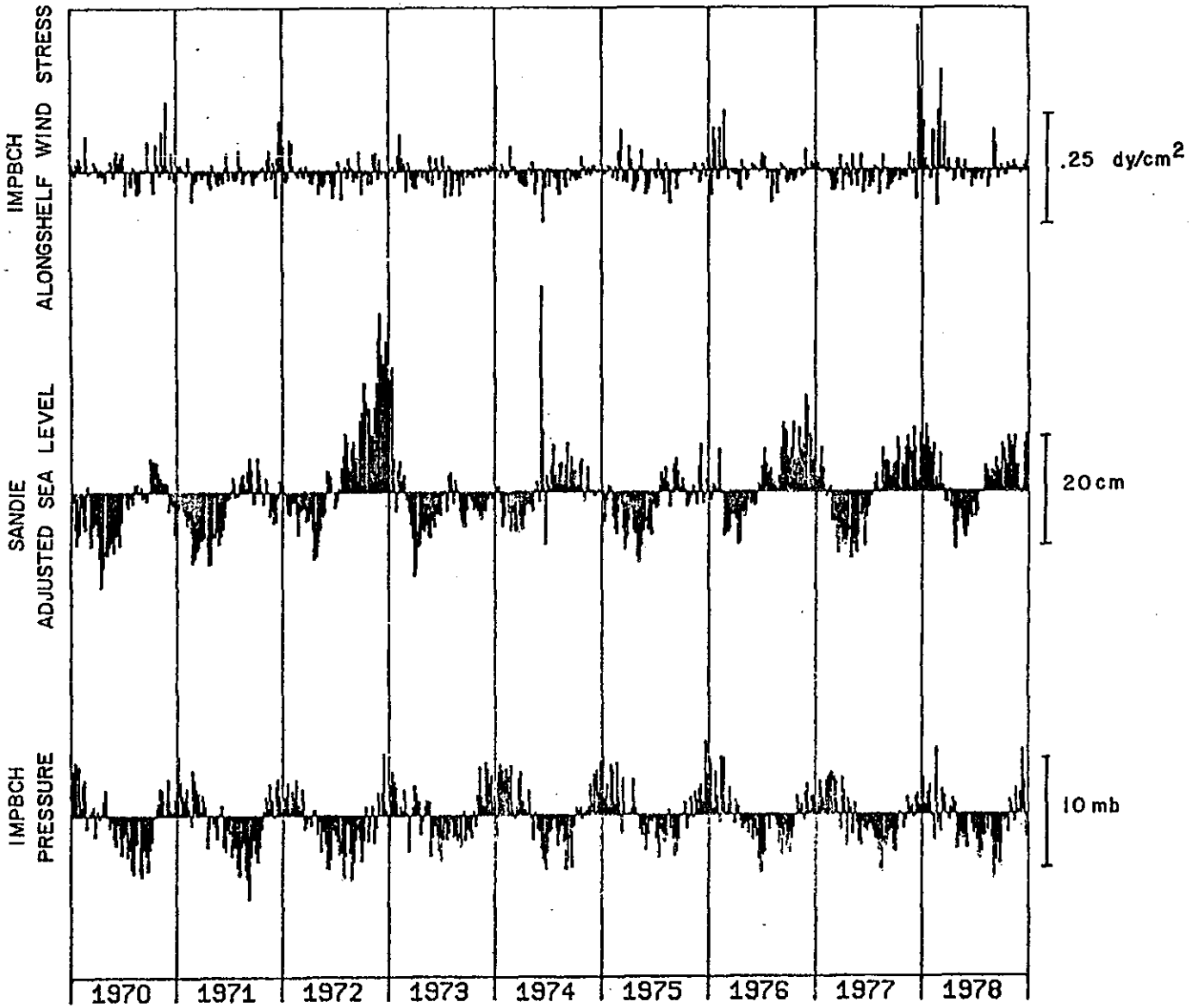

Figure 4.39. Alongshelf Wind Stress and Sea Level Pressure for Imperial Beach, and Adjusted Coastal Sea Level for San Diego, 1970 Through 1978

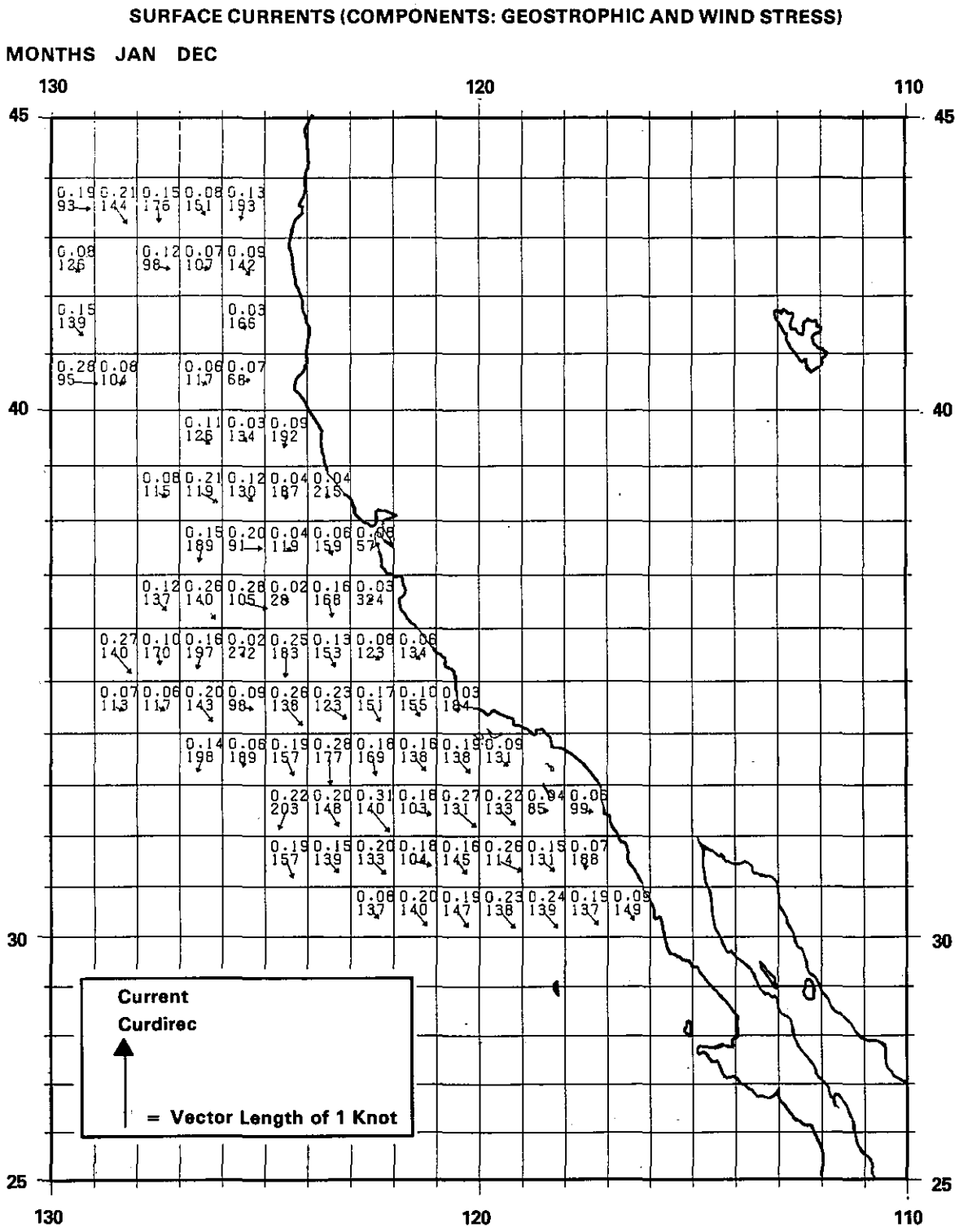

Figure 4.40. Surface Currents (Components: Geostrophic and Wind Stress)

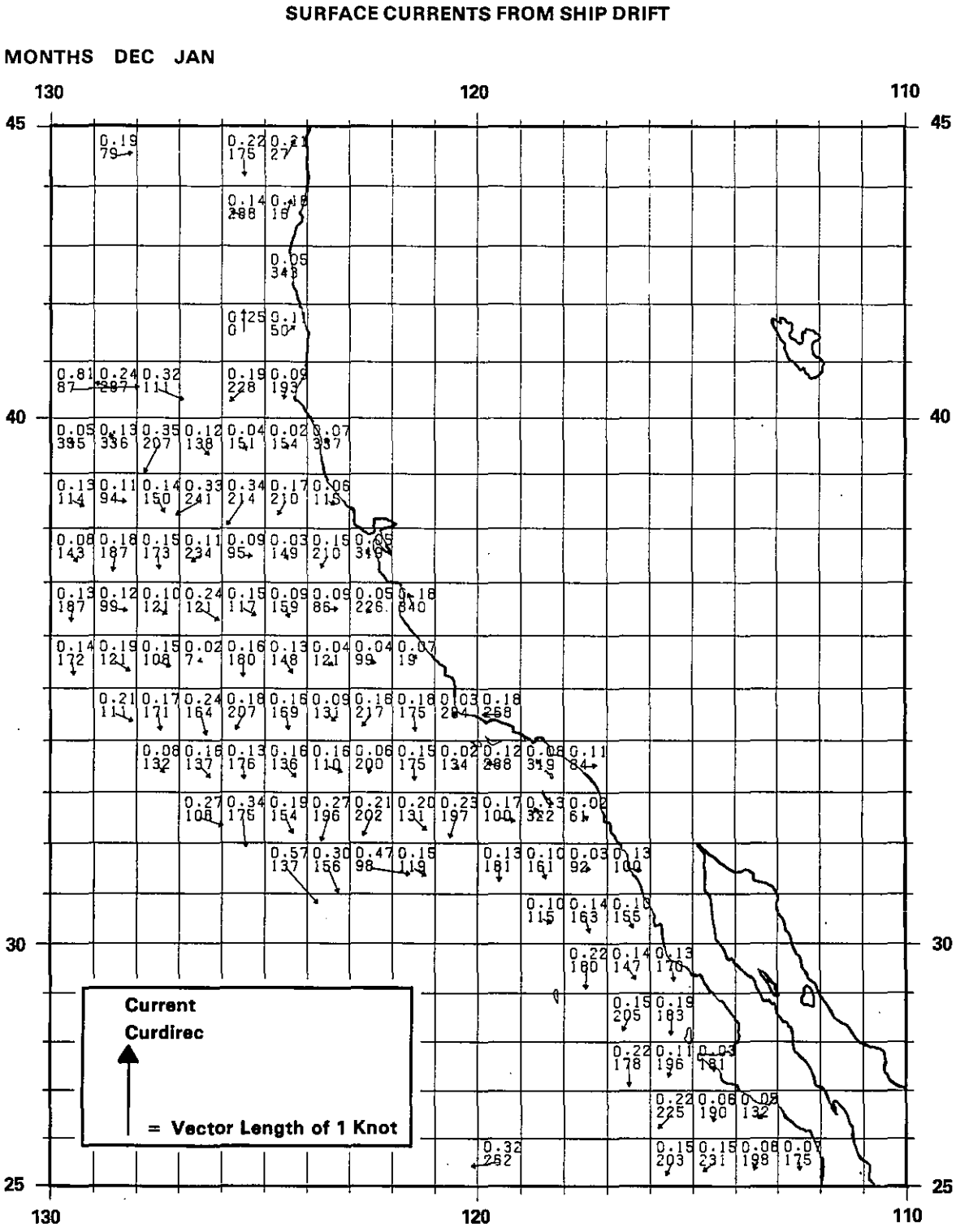

Figure 4.41. Surface Currents from Ship Drift

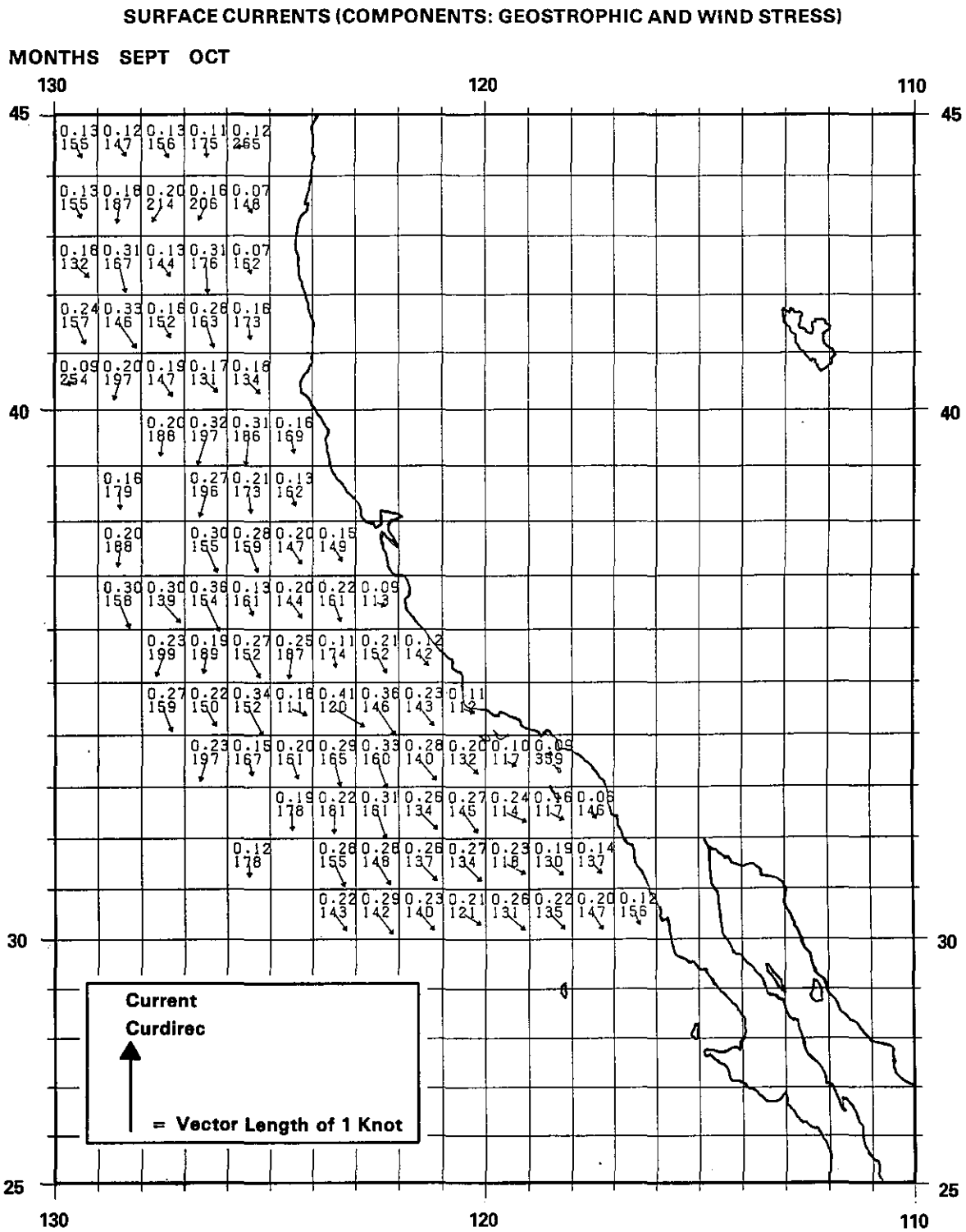

Figure 4.42. Surface Currents (Components: Geostrophic and Wind Stress)

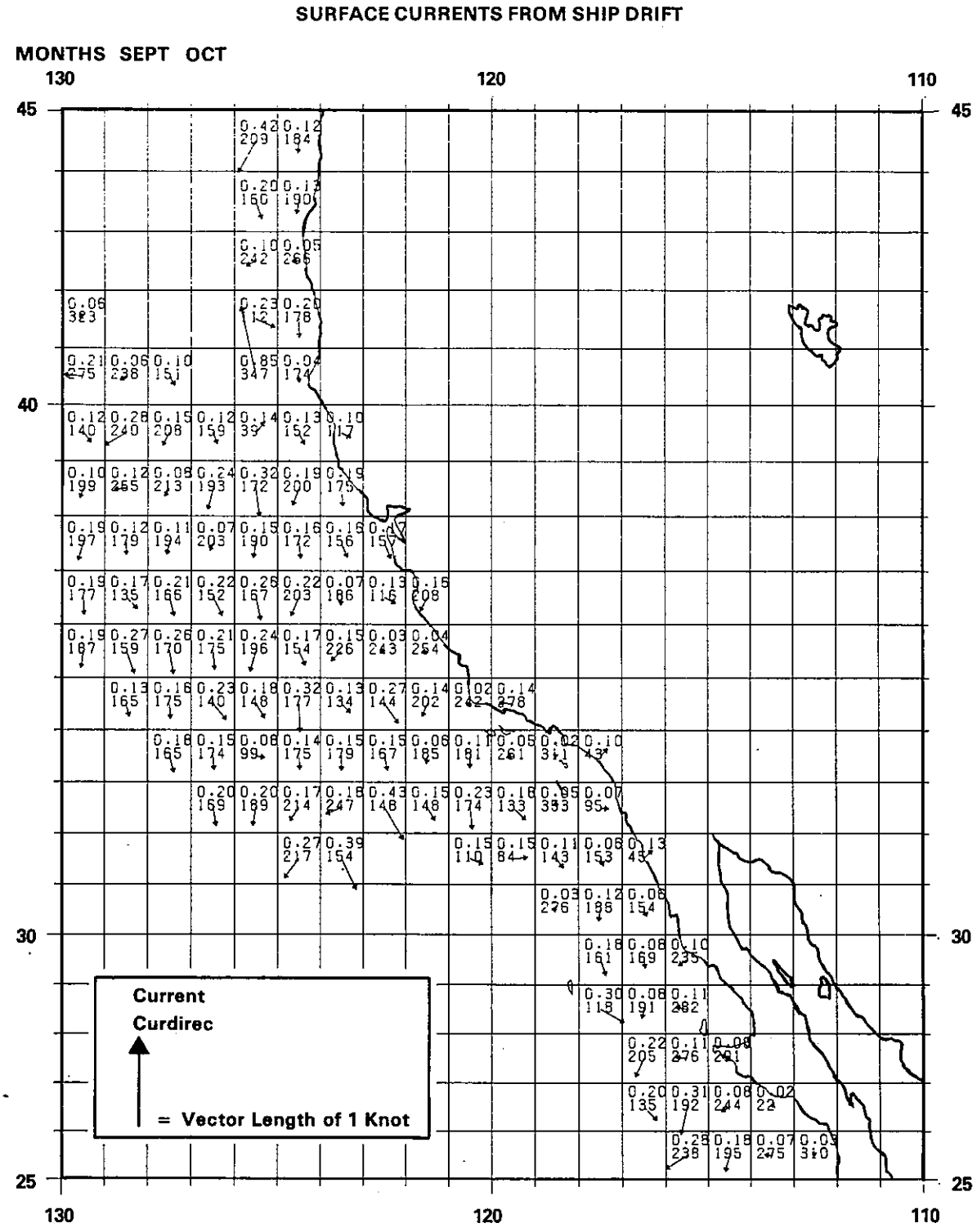

Figure 4.43. Surface Currents from Ship Drift

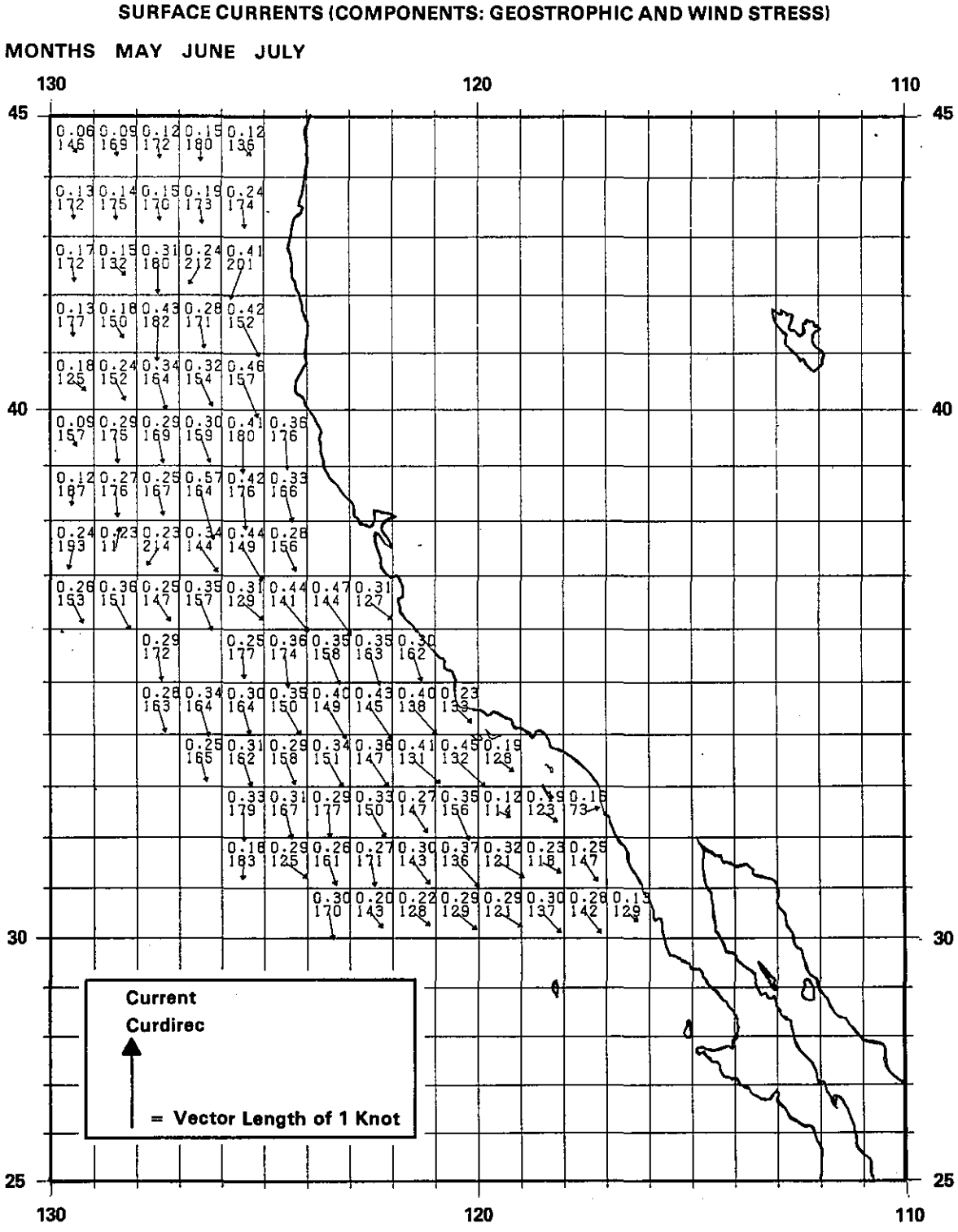

Figure 4.44. Surface Currents (Components: Geostrophic and Wind Stress)

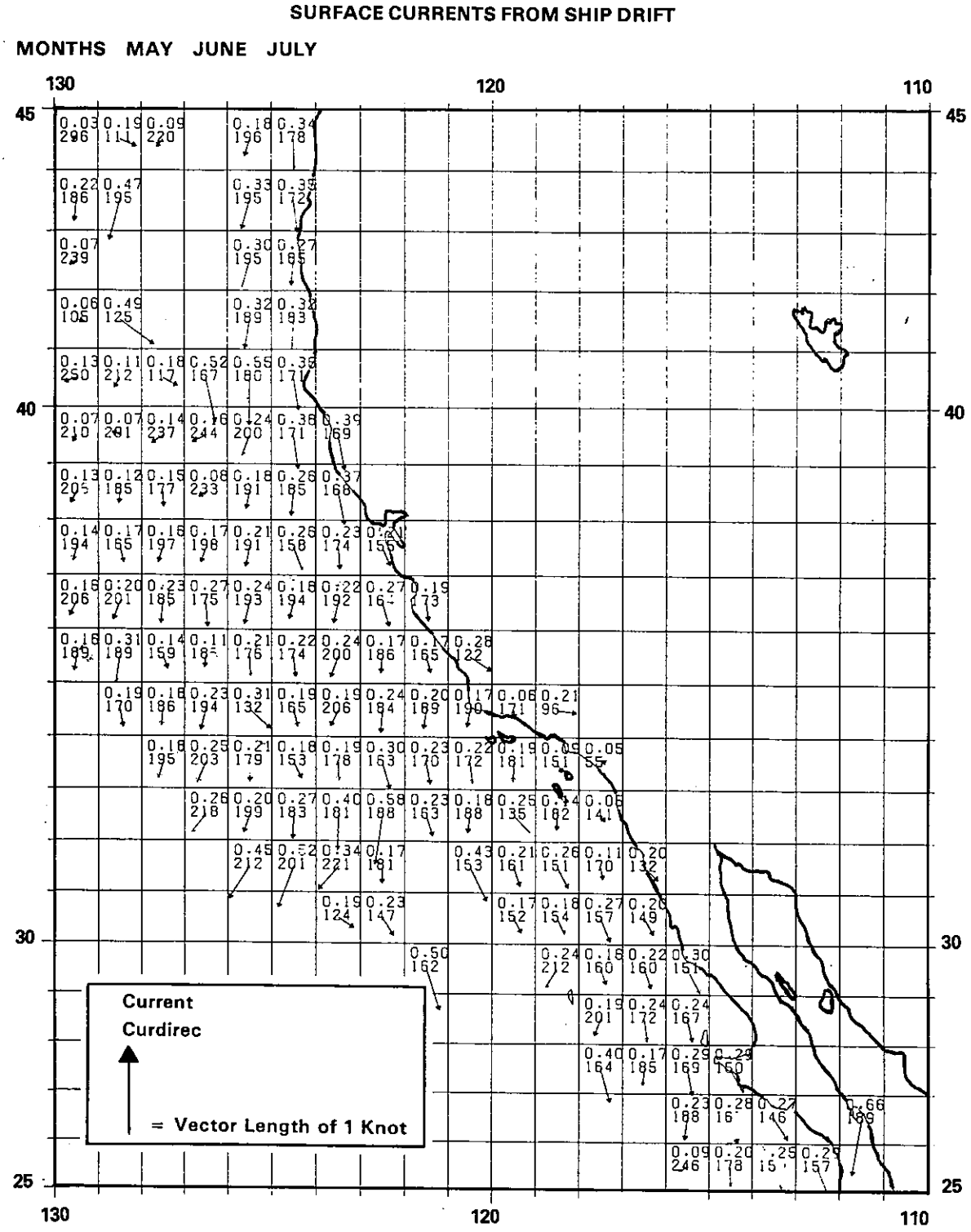

Figure 4.45. Surface Currents from Ship Drift

5. WATER MASSES AND PHYSICAL PROPERTIES IN THE STUDY REGION

R. G. Williams and F. A. Godshall

5.1 INTRODUCTION

In general, water mass definition has been based on temperature salinity (T-S) correlations. Reference 1 defines water masses as "more or less homogeneous volumes of water characterized by defined relationships of physiochemical properties such as temperature and salinity T-S." Because of the proximity of sources of fresh water, the delineation of homogeneous water masses is less rigorous in coastal areas than in the open ocean, with a corresponding diversity in terminology. The distribution of water masses in the California study region can be understood in terms of the confluence of major currents of the North Pacific gyre and associated eastern boundary currents, which are characterized by distinctive water masses.

Subarctic water flowing eastward in the North Pacific Current is low in temperature and salinity, but high in dissolved oxygen and phosphates. The average temperature is between 2° and 4°C, and the salinity at the surface may be as low as 32 ppt, although it increases to 34 ppt at a depth of a few hundred meters (Reference 2). This current splits into two branches before hitting the American coasts: one branch flows northward into the Gulf of Alaska while the other flows southward. Considerable mixing takes place along the western boundary with Central North Pacific water which is low in nutrients and relatively high in temperature (15°C) and salinity (34.40 ppt) (Reference 3).

In the southeastern part of the study region, Equatorial Pacific water (below 200 m), high in temperature, salinity, and phosphate, and low in dissolved oxygen, flows northward along the coast (Reference 3). The Equatorial Pacific water mass has a nearly linear T-S correlation between T = 15°C, S = 35.15 ppt, and T = 8°C, S = 34.6 ppt. At 800 m, the temperature is approximately 5.5°C, and there is a salinity minimum between 34.50 ppt and 34.58 ppt. Below 1000 m, the temperature decreases toward the bottom to 1.3°C, and the salinity increases to 34.70 ppt (Reference 2). Subtropical water, which is low in phosphate, flows northward at the surface in this region.

The northward subsurface flow along the coast, the California Undercurrent, appears to be transporting equatorial water, northward inshore and sometimes below, the general southward surface flow. This current extends from lower Baja, California as far north as Vancouver Island where mixing has decreased the temperature to 7°C and the salinity to 33.9 ppt (Reference 4).

The meeting and mixing of these water masses has led many investigators to describe the waters of the California region as a *transition zone*. For example, Reference 5 describes the waters at depths of 150 to 1000 m along the coast of California as being a mixture of two extreme water masses. These water masses are identified from characteristic T-S curves as Subarctic North Pacific water and Equatorial Pacific water. Subarctic water extends over the Pacific Ocean north of 43°N and Equatorial water extends from the equator to 20°N. A region of transition exists between these water masses adjacent to the west coast of North America and extends to distances of more than 600 miles from the coast. The distribution of temperature and salinity in this transition region can be expressed in terms of percentages of Equatorial Water (Figure 5.1, 5.2). The transition between the subarctic waters and the equatorial waters which form a wedge along the coast is shown in Figure 5.3 (Reference 5).

Seasonal variations of water masses in the California study region are principally the result of variations in surface heat flux, precipitation and coastal runoff, local winds, and ocean circulation (Reference 7). Temperature shows the greatest seasonal variation. Offshore, the seasonal variation is a result of vertical heat flux at the air-sea interface. In January and February a well mixed surface layer exists with a sharp thermocline below. In spring, a thin, warm surface layer forms a new thermocline which deepens as summer passes. By August, the thermocline has reached the depth of the winter thermocline (Reference 3). In the north, this results in a temperature variation of 5°-7°C and in the south a variation of 2°-3°C (Reference 6). Near the coast, upwelling and seasonal cooling bring colder water to the surface. North of 34°N, strong upwelling reduces the seasonal range and the cool period is lengthened (Reference 8); the temperature range is only 2°-3°C (Reference 6) and at 40°N, a March temperature average of 10°C and an August average of 11°C (Reference 3) is reported. Upwelling occurs earlier (seasonally) in the region between 28°N and 34° (during the period of the offshore seasonal minimum); consequently, the seasonal range is increased to 5°-7°C. References 8 and 6 reported a March average temperature of 12°C and an August average of 19°C at 30°N. South of 28°N, the winter countercurrent brings warm water northward, delays the minimum temperature until spring and increases the seasonal range which is on the order of 5° to 7°C (References 8 and 6).

In oceanic areas of the region the seasonal variation in salinity depends only on evaporation and precipitation and only amounts to 0.4 to 0.5 ppt (Reference 6). However, in coastal areas, e.g., near the Columbia River, variations depend on river discharge, which is least in winter and greatest in late spring and summer. Locally, in the upper 10 to 20 meters, the variation may be as great as 2-3 ppt (Reference 3).

North of 34°N, nearshore upwelling of deep water in the spring and summer causes a wide range of salinity values with the maximum salinity occurring in summer (Reference 8). The variation here may be as great as 0.8 ppt (Reference 6). South of 28°N the countercurrent brings highly saline water northward in winter and the salinity range here is also high with the maximum occurring in winter (Reference 8). The region between 28° and 34°N is affected by both upwelling and the countercurrent and the two effects tend to compensate and keep the salinity variation low on the order of 0.2 to 0.3 ppt (Reference 6). These seasonal variations of temperature and salinity off the west coast of North America are succinctly depicted in Figure 5.4 (Reference 3). Subsurface oxygen maxima occur in the summer and fall which in the north is as high as 7 ml/liter and in the south 5.5 ml/liter (Reference 3). Upwelling also causes replenishment of phosphate at the surface which may be as high as 1 μg at/liter, but this variation is not as regular as temperature and salinity (Reference 9).

In this study, water mass properties analysis involves the classification and mapping of water structure by vertical T-S profiles (Reference 10) from the surface to 250 m depth for representative months, along with examination of T-S scatter plots for each month of the year for selected areas. From this analysis, the literature, and from the seasonal march of wind stress which influences water mass distribution, it was decided to summarize the data in three seasons. Transition months have been discarded in the averaging because transitional characteristics tend to "smear out" seasonal distinctions. The representative groups of months for summary in this report are as follows:

- Winter or Davidson Current Season (December - January)
- Spring or Upwelling Season (May - June - July)
- Autumnal or Oceanic Season (September - October)

The months selected for the upwelling season were a compromise, since upwelling begins early in the year off Baja California and progresses up the coast to Oregon in late summer (Chapter 4).

5.2 MEAN DISTRIBUTION OF WATER MASSES

5.2.1 Water Mass Classification

The first step in examining the distribution of water masses in the California study region was to classify the vertical T-S relationships from the surface to 250 m depth (Reference 10). The ASD procedure was developed by Reference 10 and was applied in the Mid-Atlantic study of Williams and Godshall (Reference 13) and the Georges Bank study (Reference 14). This analysis provides an overview of water structure by emphasizing the main features in the data and serves as a guide for further detailed analysis.

Four representative months (February, June, September and December) were chosen for the ASD analysis to identify seasonal extremes. Up to seven water structures can be distinguished by this method. However, it was found from application that no more than three water structures could be meaningfully differentiated. Because the computer program for the classification is limited to 700 soundings in any given month, it was necessary to subsample the data in some cases (i.e., using only every other or every third sounding). This procedure should not significantly affect the results.

The water mass structure for February depicted by the ASD classification is seen in Figure 5.5. The main feature in the geographical distribution of water structures is a transition or frontal zone running southwest from just north of San Francisco to about 33°N, 128°W, which separates warm, relatively saline water, most likely of equatorial origin (structure 1), from cooler, less saline water of subarctic origin (structure 2). There is a third water structure, found primarily in the Southern California Bight area which is quite similar to structure 1, but exhibits a greater range in temperature and salinity. This general distribution corresponds most nearly to the characterization of the study region (Reference 5) as a transition zone between subarctic waters to the north, flowing southward in the California current, and water of equatorial origin, flowing northward along the coast as the California countercurrent system, primarily as a subsurface flow. (See Section 4.)

Water structure 1 has a range of about 1 ppt in salinity, centered on a mean of about 33.5 ppt. Temperature ranges from about 17.5°C at the surface to 9°C at 200 m depth. Water structure 3 is similar, but somewhat less homogeneous than 1. Mean salinity is again about 33.5 ppt, but the distribution is skewed left, with a few salinities as low as 32 ppt. Temperature varies from about 20°C at the surface to 9°C at 200 m. This water is found primarily in the Southern California Bight, possibly a consequence of the large cyclonic eddy generally located there which would tend to confine the waters of this region to continued circulation within the eddy. There are two "blobs" of structure 3 water north of the boundary zone between structures 1 and 2. These are probably indicative of either mixing processes at the boundary, or advection of nearshore water seaward.

Structure 3 water is the most highly stratified, with a surface sigma-t of 23.5 and a sigma-t of 26.0 at 200 m. Structure 1 water has a surface sigma-t at about 24.3, and a sigma-t of 26.0 at 200 m. Structure 2 is the least stratified, with a surface sigma-t of 24.5, and a sigma-t of 26.0 at 200 m. Structure 2 water, henceforth referred to as Californian water, following Kin'dyushev (Reference 6), to distinguish it from the water of equatorial origin, or southern water to the south, has a mean salinity of about 32.7 ppt and a range of about 2 ppt. Temperature varies from 13°C at the surface to 8°C at 200 m depth. This water is more nearly homogeneous than the water farther south and is a mixture of subarctic water and the subtropical waters found to the west of the California Current.

In June (Figure 5.6), the transition zone has penetrated further south, to about 33.5°N at 124°W. Along the coast, however, southern water was expanded in an area off San Francisco. Structure 3 water has contracted in an area within the Southern California Bight. Seasonal modification since January is evident primarily in terms of surface heating. Structure 1 warmed to about 20°C at the surface, with a corresponding decrease to 23.0 in sigma-t.

Higher salinities than in February are evident, possibly resulting from upwelling. Structure 2 has warmed to about 16°C at the surface; fewer low salinities occur than in February. Structure 3 is slightly warmer at the surface with again, fewer low salinities. In general then, seasonal change has produced higher surface temperatures, some higher salinities, and more stable stratification.

In September, the transition zone (Figure 5.7) has retreated northward to about 36°N at 124°W, and has moved northward along the coast past Cape Mendocino. Structure 3 water is again located primarily in the Southern California Bight area, and also in a "blob" a little south of San Francisco. Structure 1 exhibits little change in temperature from June; salinity is somewhat lower, as it is in structures 2 and 3. Near-surface temperatures in structure 2 are lower, with few temperatures above 12.5. Structure 3 has reached a peak of 22.5°C in near-surface temperature. Stratification has been enhanced in structure 3, with near-surface sigma-t of 23.0, whereas stratification in the California structure 2 water has lessened, with near-surface sigma-t at about 24.5. Structure 1 is essentially unchanged in stratification. Values near 200 m are relatively unchanged, indicating little seasonal influence at that depth (Figure 5.7).

In December, the transition zone (Figure 5.8) has moved southward along an arc from Monterey Bay to 35.5°N and thence northwest to 39°N, 130°W. Structure 3 water is found off San Diego and Los Angeles, and also in an area south of Monterey just below the transition zone. The absence of subtropical water further north along the coast is surprising; in view of the development of the Davidson Current (Section 4.1.3), it may simply reflect the lack of data in the northern California region.*

It is interesting to compare the results of the ASD classification with an analysis of percentage content of water masses by Reference 6, Figure 5.9. The transition zone is shown in Kin'dyushev's analysis by the isoline of 50 percent content of Californian water. His analysis in February shows the transition area further south than in our Figure 5.5. Again in November, he shows the transition zone as being further south than our analysis (Figure 5.10), except right along the coast. The methods are not, of course, directly comparable, both in data used and in layer of the Californian water mass (Kin'dyushev is looking at the depth of water mass cores rather than fixed slices) but the general features of the water mass distribution are in agreement.

5.2.2 Hydrographic Features

Further insight into the distribution of water masses can be gained by examining specific sections of temperature and salinity. For example, Figure 5.11 shows the vertical T-S profiles for a section made perpendicular to the coast south of Cape Mendocino by the Soviet research vessel R/V OGON July 24-25, 1972. The offshore profiles show a mixed layer about 25 m deep above a thermocline which becomes increasingly shallow toward the coast, until very near the coast, where nearly homogeneous conditions prevail. Below the thermocline, temperature decreases gradually to about 4.5°C at 500 m. Salinity is low near the sea surface, about 32.8 ppt; increases rapidly in a halocline region about 100 m thick starting at 50 m, then increases slowly with depth to about 34.0 ppt at 500 m. Generally speaking, both the thermocline and the halocline deepen moving seaward, the thermocline always being above the halocline.

Further south (32°N), a winter hydrographic section through the Southern California Bight by R/V DAVID STARR JORDAN (Figure 5.12) shows a deep mixed layer, increasing in depth from about 30 m near the coast to about 75 m at 121°W. A small thermocline region of about 50 m in thickness is found below the mixed layer. A halocline occurs below the thermocline at about 100 m depth. Surface temperatures are about 15°C, bottom temperatures 5-8°C, while salinity is about 33.25 ppt at the surface and about 34 ppt at 500 m. Sections made in this same area in summer show the development of a shallow seasonal thermocline.

*Structures 1 and 3 show the effect of autumnal cooling of near-surface waters, reducing the magnitude of the stratification and thus facilitating stronger vertical mixing. The T-S distribution of structure 2 appears to be similar to that of September.

5.3 DISTRIBUTION OF PHYSICAL PROPERTIES

In this section (Figures 5.13 through 5.21), the distribution of physical properties and dissolved oxygen is presented for three depths: 0, 100 m, 200 m and for three seasons: Davidson Current (December, January), Upwelling (May, June, July), and Oceanic (September, October).

5.4 STABILITY

An important quantity which parameterizes vertical mixing is the flux Richardson number, which is proportional to the ratio of the product of the vertical density gradient and the acceleration due to gravity to the product of the mean water density and the vertical shear of horizontal velocity. Unfortunately, the flux Richardson number cannot be calculated from National Archive data, since measurements of velocity shear are not available. However, implications regarding the extent of vertical mixing are often drawn from the analysis of water stability (Reference 17). More recent studies use a parameter, closely related to the stability, called the Brunt-Vaisala frequency N (Reference 18) defined as follows:

$$N^2(z) = \frac{g}{\rho}\frac{dp}{dz} - \frac{g^2}{c^2}$$

where

ρ = local water density
g = acceleration of gravity
c = speed of sound

The last term, involving the speed of sound, is usually neglected in upper oceanic layers. If N^2 (z) is positive, the water is stable (i.e., the buoyancy forces will oppose vertical displacement of fluid parcels from their rest positions). If N^2 (z) is negative, the buoyancy force will reinforce a vertical displacement of fluid parcels, so that they accelerate away from their original positions. N^2 (z) = 0 is, of course, neutral buoyancy.

In practice, high values of N^2 (z), values of a few minutes (expressed in terms of period, the reciprocal of frequency), occur in strongly stratified oceanic regions, where vertical mixing is inhibited. Low values of N^2 (z) (on the order of hours) occur in quasi-homogeneous areas where mixing is not inhibited and hence deep stirring of the waters from the surface often occurs. Such regions are characterized by a deep mixed layer, or by the complete absence of a thermocline, as occurs in subarctic waters.

Upper ocean stability has been analyzed in Reference 19 in terms of the distribution of seasonal mean Brunt-Vaisala frequency, for 5° square summary areas. Their seasons are defined as follows:

- Winter–January, February, March
- Spring–April, May, June
- Summer–July, August, September
- Autumn–October, November, December

While these definitions of seasons and spatial resolution are not ideal for the California study area, their results are sufficient to delineate the main features of the distribution of stability in the study area.

5.4.1 Distribution of Brunt-Vaisala Frequency

Figure 5.22 shows the summary areas used in Reference 19 for their computation of Brunt-Vaisala frequency. In all areas the highest values of Brunt-Vaisala frequency occur, as would be expected, at the depth of the maximum gradient within the pycnocline, typically between 20 and 125 m (Figure 5.23). The between-area differences of the magnitude of maximum Brunt-Vaisala frequency (order 0.014 rad/sec, or 7.4 min) indicate that the differences in mean mixing potential attributable to the static stability are small among these areas. Stability is minimum in either winter or spring, when strong wind stirring and surface cooling have deepened the mixed layer. Stability is highest in fall, when winds are generally weakest, and insolation has had its effect in creating the seasonal thermoclines (pycnocline). Note that the area of high stability extends from the seasonal pycnocline through the main pycnocline.

In area 1213, the Southern California Bight, the part of the water column of maximum stability is very close to the surface, about 20 m depth in spring, summer and autumn. Values of N^2 (z) are minimal in winter. Within the water column maximum N^2 values occur at about 70 m in depth (0.011 rad/sec) and are highest in fall (nearly 0.015 rad/sec, or 7 minutes period) at about 20 m depth, which indicates autumnal vertical mixing is suppressed in the upper water volume.

5.4.2 Distribution of Mixed Layer Depth

The mixed layer depth chart provides a practical means of estimating the extent of mixing in the upper layers of the ocean. Again, as in the case of the Brunt-Vaisala frequency distribution, the estimate is qualitative rather than quantitative. In this section, we examine charts of the depth of the ocean mixed layer from Reference 20.

In January, the mixed layer reaches its maximum depth off Southern California, about 50 m (Figure 5.24a). Within the mixed layer strong vertical mixing can occur as the buoyancy force is very weak. The northward flowing Countercurrent and Davidson Currents, and the associated absence of upwelling are probably the cause of this maximum in coastal mixed layer depth; farther seaward at 130° west the layer depth is on the order of 100 m, and continues to deepen with distance from the coast. This is probably the result of cooled, relatively unstable surface waters being overturned by winter storms.

In April (Figure 5.24b), the onset of the upwelling season, layer depths are considerably more shallow; 20 m off San Diego and 30 m off San Francisco. Layer depth is deeper at 130° W, reaching about 120 m, which may result from intensification of the California Current and steady northwesterly winds.

In June (Figure 5.24c), near the peak of the upwelling season, layer depth is very shallow (10 m) in the Southern California Bight. In regions of strong upwelling, the thermocline "breaks the surface" and hence reduces the mixed layer to almost zero thickness. Offshore the mixed layer is much more shallow than in April. This results from surface solar heating, which creates a shallow seasonal thermocline above the main thermocline. Figure 5.23 shows that Brunt-Vaisala frequency is high throughout the area between the thermoclines, thus suppressing vertical mixing.

In September (Figure 5.24d), the mixed layer is very shallow throughout the study region; in fact, this is the month of minimum depth. The combination of continued upwelling and surface heating has driven the isotherms very close to the surface. Near-surface vertical mixing would be strongly suppressed under these conditions.

5.5 LONG PERIOD FLUCTUATION OF PHYSICAL OCEANOGRAPHIC CHARACTERISTICS OF COASTAL WATER

Long period fluctuations of the wind field are highly correlated with long period fluctuations of the coastal station-observed water temperature and broad-scale characteristics of the general atmospheric circulation over the Pacific Ocean (References 21, 22, and 23). Part of the long period fluctuations of the general atmospheric circulation have been associated with low latitude periodic fluctuations (e.g., a 24-month period oscillation–the biennial oscillation).

Considering the magnitude and period of coastal water temperature fluctuations (Reference 23) and meridional transport by the California Current system (Reference 24), the aperiodic fluctuations are of greater magnitude than periodic changes. The changes in the current system produce changes in the geographic location of the regionally characteristic water masses (Section 5.1) and therefore, local changes in salinity, dissolved oxygen concentration, and temperature.

5.5.1 Fluctuation of the California Current System

The California Current flows southward along the coast. North of Cape Mendocino it brings cool, relatively low saline surface water south which is gradually mixed with relatively more saline water south of the Cape (Reference 25). In winter the northward directed California Countercurrent and Davidson Current bring relatively warm saline water northward along the coast. One observer (Reid, private communication) suggested that decreased southward transport is associated with increased northward transport of warm water masses and therefore contributing to any trend toward warmer coastal water associated with decreased upwelling.

Huang (Reference 26) showed that cold relatively saline bottom waters upwelled along the coast must produce change in the local geopotential of the sea surface. These changes, considering geostropic flow, tend to produce flow augmenting local southward surface drift. A significant (3.6 cm mean) decadal difference (1948-1957 compared with 1958-1969) in sea level at San Diego (Reference 22) was associated with a decadal difference in southward, meridional transport by the California Current. The cool coastal water period (1948-1957) was associated with lower coastal sea level and relatively large southward water transport (Huang, private communication).

5.5.2 Fluctuation of Water Temperature and Salinity

During the period 1948-1957, anomalously low surface water temperature was observed along the entire California coast (References 23 and 25). Temperature anomalies in more recent periods have also indicated that there is considerable coherence in temporal water temperature variations along the coast (References 21 and 27). Summaries of monthly averaged coastal water temperature observations from stations at Pacific Grove, S.E. Farallon Islands, Port Hueneme, and Blunt's Reef Light Ships (Reference 23) indicated that anomalously low temperature water was found along the coast during the period 1961-1962, and 1969 was in a period of high temperature anomaly. A twelve-month running mean of these coastal station data, expressed as temperature anomalies, are graphed in Figure 5.25a. These data may be compared with offshore temperature data collected during the CALCOFI program (Figure 5.25b). From the comparison, it is evident that the coastal station water temperatures are highly correlated with the offshore temperature.

Figures 5.26 and 5.27, maps of 10 m water temperature produced during the California Cooperative Oceanic Fisheries Investigations (CALCOFI) for summer 1961 and 1969, respectively, show representative special distributions of water temperatures over the study region during periods of anomalously cool and warm coastal water temperatures and Figures 5.28 and 5.29 show representative distributions of salinity during the low and high temperature anomaly periods.

The apparent effect on the regional salinity distribution produced by the California Countercurrent, seen in Figure 5.29, seems to be obscured by the effects of intense coastal upwelling deduced for the period 1961-1962 (Figure 5.28).

5.5.3 Long Period Fluctuations, Conclusions

From the charts of the summer season's surface temperature in 1961 (Figure 5.26) and in 1969 (Figure 5.27), it is evident that year to year variation of coastal water temperature may be about 2°C. Near Point Conception, this is about 50 percent of the mean annual temperature variation. Along the coast of Lower California, these year to year variations are equal in magnitude to about 30 percent of the annual variation (Figures 5.25a and 5.25b). Therefore, it is concluded that the long period fluctuations of temperature are significant factors of the coastal water temperature climatology. The long period variation in surface salinity is also large compared to the annual variation (30-50 percent of the annual) (Figures 5.28, 5.29, 5.30(a) and 5.30(b)).

5.6 WATER MASS ANALYSIS CONCLUSIONS

Kin'dyushev (Reference 6) has defined a complex pattern of water masses in the study region, including four surface water masses, and three-subsurface water masses in the upper 500 m of the water column. This viewpoint contrasts with the earlier studies of References 5 and 15, who viewed the California coastal waters as an interaction or transition zone between subarctic water and equatorial water.

The result of our ASD analysis tends to agree with the latter point of view, at least in the upper 200 m. We have differentiated three water structures, two of which are quite similar. The first structure we call southern water. It is primarily an equatorial water mass that has been reduced in temperature and salinity by mixing with temperate waters. In the upper 200 m, it has a mean salinity of about 33.4 ppt, and varies between 33 and 34 ppt. Temperature ranges from about 8°C to 20°C. This water structure is found over most of the southern part of the study area (i.e., found south of Point Conception and also pressed against the coast north to San Francisco). The ASD procedure discriminated a second, slightly different water structure of somewhat higher mean temperature and salinity (33.6 ppt), primarily resident in the Southern California Bight area. The third water structure has a lower mean salinity, about 33 ppt, with a larger range in salinity, about 32° ppt to 33.8 ppt and a temperature range of about 7°C to 17°C. This water structure appears to arise from a modified subarctic water mass, which we call Californian. Hence our description is given in terms of two basic water structures, modified equatorial (southern), and modified subarctic (Californian), and is in general agreement with References 5 and 15. A mixing or transition zone between these structures runs generally along a curve oriented northeast to southwest intersecting the coast within a degree or two of San Francisco.

The distribution of these water masses is determined largely by the currents. The California Current transports Californian water southward in the upper 200 m. The Countercurrent/Undercurrent system transports southern water northward along the coast. In winter, north of Point Conception when the subsurface Countercurrent and Davidson Current are most intense, significant northward transport of southern water should occur. When northerly winds strengthen in spring, the Davidson Current breaks up into a series of eddies, and upwelling of cold, salty water commences. The relationship between the northward flowing coastal currents and the slow, northward drift of southern water offshore is unknown (Reference 12).

Seasonal modification of the water masses is effected largely by the annual solar heating cycle and by the onset of upwelling resulting from variations in the wind stress. Precipitation and coastal runoff play a smaller role. In the northern California coastal region, temperature is about the same in winter as in summer, but in winter, near-surface salinity is lower because of the termination of upwelling, and because of dilution due to winter rains. The

band of highly saline upwelled water which prevents the intrusion of Californian water in late spring and summer is absent in winter, and thus the Californian water can reach the coastline (Reference 28). This conclusion is corroborated by our ASD analysis, which showed large scatter in salinity in both December (Figure 5.8) and June (Figure 5.6).

In Southern California Bight area, our ASD analysis shows near-surface salinities for the southern water on the order of 33.5 ppt, whereas in June, salinities are on the order of 33.7 ppt, in agreement with Reference 29 who asserted that salinities are lowest in this region in winter.

In conclusion, there are two fundamental water structures in the California POCS region. The first is a southern water structure, equatorial in origin exemplified by Figure 5.16. The second is a basically subarctic water structure, transported into the study area by the California Current, exemplified by Figure 5.15. Seasonal modification of these water masses is brought about both by the annual solar heating cycle, and by the annual wind regime which produces changes in upwelling intensity.

We have found the three season concept describes adequately the water mass characteristics of the region, as have other observers (References 30 and 11). There are essentially two basic hydrographic regimes: "Summer," in which there is southward flow along the coast north of Point Conception, and hence a transport of Californian water; and "Winter," in which there is northward flow along the coast, and transport of southern water to the north. The first corresponds to the "Upwelling Season," which, overall, peaks in May, June and July. The second corresponds to the "Davidson Current Period," and peaks in December and January. The third season, the "Oceanic Season," is simply a less intense version of the Upwelling Season. Transition months have not been included in the summaries, because the transition from one season to another is often very rapid but varies from year to year. Hence, long-term averages would have little meaning.

Spring, or the intense upwelling season, is initiated by strong northerly winds. The region of maximum southward wind stress begins early in the year (March) off Baja, California, and progresses up the coast, reaching a maximum in June in the region of Point Conception-Cape Mendocino, and, in July, to the north of Cape Mendocino (Reference 31). These wind stress variations produce a seasonal March in the coast upwelling, which is shown in Figure 5.31, based on results by Bakun (Reference 31).

The isotherms and isopycnals run generally parallel to the coast during the upwelling season; dissolved oxygen is generally above saturation value near the surface, but is lower nearshore. During winter, when the Davidson Current prevails and upwelling is suppressed, the isotherms cut the coastline at an angle which increases from north to south (Figure 5.13).

Northerly winds produce the strongest upwelling off Baja, California in early spring, and off northern California in summer; the most intense upwelling areas follow the migration of maximum meridional wind stress (Reference 32). North of Point Conception, in late fall and winter, the countercurrent intensifies and in winter extends all the way to the surface as the Davidson Current develops a reduction in upwelling and change in water properties (Reference 12). The cessation of upwelling, combined with winter rains, lowers near-surface salinity along the coast (Reference 28). A major residual effect of winter rain is a tongue of low-salinity waters (the Columbia River plume) which extends toward the southwest in May-June-July (Figure 5.16) reducing surface salinities in the surface layers of the California current, while at the same time surface heating is increasing temperatures, thus intensifying the stratification.

Seasonal variation in near-surface temperature and salinity is summarized in Figure 5.4 (Reference 3) and is also summarized by us from NODC data for four 2° square summary areas, along with sigma-t, in Figure 5.30. The maximum seasonal influence is seen to be on temperature. Far offshore along 129°-120°W, temperatures of the upper layers of the ocean follow the annual atmospheric heating cycle, with about a 1-month phase lag. For example, off Cape Blanco, temperature is lowest in March (about 8°C) and highest in September (about 17°C) giving a range of 9°C. The range decreases toward the south, so that off Punta Eugenia there is a minimum of about 17°C in March and a maximum of about 30°C in September, or a 3°C range. Further inshore, upwelling complicates this simple pattern. Between Cape Mendocino and Point Conception, the temperature range is small because upwelling occurs during the heating season, and northward currents of warmer water prevail during the cooling season (Figure 5.4, Reference 3).

The temperature range increases south of Point Conception to about 5°C off San Diego (15°C in March; 20°C in September). Off northern Baja California, in the upwelling zone, temperature is about 14°C in March and 20°C in September and October. From here south, the upwelling increases the seasonal range because upwelling occurs during the cooling period and the Countercurrent prevails during the warming period (Reference 3). Because the variations in the solar heating cycle are stronger, seasonal variations also increase north of Cape Mendocino.

In salinity, the evaporation minus precipitation effects produce rather incoherent salinity fluctuations in the offshore regions (Reference 3). In the nearshore areas, the upwelling and Countercurrent result in significant salinity fluctuations. The two effects tend to cancel each other between 28°N to 34°N (Reference 3). Off Cape Mendocino, salinity variations on the order of 1° ppt occur, within a minimum salinity in January and a maximum salinity in July. Off Point Conception, the range is only about 0.4 ppt, from 33.2 ppt in February to 33.4 ppt in July. Off Punta Eugenia the range is larger or with a salinity maximum of 34.2 ppt in January and a minimum of 33.6 in September, when upwelling is at a low ebb.

The changes in salinity can be seen to correspond to the upwelling intensity (Figure 5.31). Intraseasonal variability tends to be higher in the northern part of the study area than in the southern. Two observers (Reference 28) find that off Crescent City, summer temperatures can fluctuate 5° to 7°, while salinity fluctuates 1 to 3.5 ppt. In winter, large variations in salinity (several ppt) occurred nearshore due to runoff. However, variations of several kilometers offshore are much lower.

Seasonal variability in density is on the order of 0.5 in sigma-t nearshore, in the Southern California Bight, with minimum values occurring in winter on the order of 24.9, due to rainfall and runoff, and summer values of 25.0 due to evaporation, Maloney, et al. and Muromstev (References 29 and 33) observed that in the California Current, minimum densities occurred in late spring and maximum densities in winter within the top 25 m of the water column. To the north (e.g., off Cape Mendocino), however, our analysis has shown (Figure 5.18) that near-surface density reaches a maximum during the upwelling season, and a minimum during the Davidson Current period, with a range of nearly 2 sigma-t units. Farther offshore, beyond the upwelling regime, surface density is a maximum in early spring (March-April), and minimum in later summer (September).

Our analysis has shown that in the Southern California Bight area, subsurface density in the layer between 25-75 m depth is a maximum in the upwelling season (May, June, July), and is a minimum in December-January. North of Port Conception subsurface density is still highest in the upwelling season. The seasonal variability is about 0.5 sigma-t units at this level. Below 150 m season variability is small (Figure 5.18). Seasonal variability in dissolved oxygen follows the temperature distribution quite closely (Reference 3).

Vertical stability, as an indicator of vertical mixing potential, has been examined qualitatively by means of the shape of the Brunt-Vaisala frequency N (z) profile with depth using results from Reference 19 and by the depth of the mixed layer using results found in Reference 20. The N (z) profiles are generally similar throughout the CPOCS study region, with relatively high values near the pycnocline depth, on the order of 0.012-0.015 rad/sec (7-8 minutes). This implies strong stratification and a suppression of vertical mixing through the pycnocline.

The mixed layer near the coast reaches its maximum depth during the winter months of January and February, because of convective cooling at the surface and mechanical wind stirring. Layer depths of 50 m are typical at this time of year. Seaward, the mixed layer deepens to about 100 m at 130°W, as expected, from the general circulation.

In spring, with the onset of upwelling, layer depths shoal to about 25 m near the coast but deepen offshore to about 120 m at 130°W, which may be an indication of intensification of the California Current.

As the season progresses upwelling continues and the mixed layer depth decreases to almost zero near the coast, while the Brunt-Vaisala frequency is quite high near the surface. These conditions would tend to confine spilled pollutants to very near the surface. In September, mixed layer depth is minimal throughout the study region, being less than 10 m near the coast in southern California, 20 m off San Francisco, and 50 m in the offshore areas where seasonal surface heating has resulted in a seasonal thermocline. By December, winter conditions have again been established. Hence, in general, the strongest vertical mixing will occur in winter and early spring in the offshore area; the least vertical mixing will occur in late summer in the Southern California Bight area.

Long period fluctuations have been associated with low latitude periodic fluctuations in the wind field, such as the bienniel oscillation (Reference 22). However, aperiodic changes appear to be larger than periodic changes. Aperiodic sea level anomalies have been associated with anomalous transport by the California Current. Huang (Reference 26) found that cool coastal water during the period 1948-1957 was associated with lower coastal sea level and an increase in southward water transport.

In general, the archive temperature, salinity, and oxygen data are adequate to describe monthly variations at 1° or 2° resolution in most parts of the Southern California Bight area and south to Punta Eugenia. North of San Francisco there is a dearth of observations and only a seasonal description can be made with reasonable statistical reliability.

The archive data is also insufficiently dense to resolve the hydrographic features associated with the California Countercurrent system (Reference 34). It is important to resolve these features because the nearshore hydrography has a significant influence on the dispersion and fate of spilled pollutants. Observations of the vertical current shear combined with temperature and salinity are badly needed at several locations in order to characterize the vertical mixing by means of the gradient Richardson number.

REFERENCES

1. Defant, A., 1961. Physical Oceanography, Permagon Press Ltd., New York, 729 pp.

2. Sverdrup, H. U., M. W. Johnson and R. H. Fleming, 1942. The Oceans: Their Physics, Chemistry and General Biology, Prentice-Hall, Inc., New York, 1087 pp.

3. Reid, J. L., Jr., 1960. Oceanography of the Northern Pacific Ocean During the Last Ten Years, CALCOFI Rep., 7, pp. 77-90.

4. Hickey, B. M., 1979. The California Current System–Hypotheses and Facts, Progress in Oceanogr., **8(4)**, pp. 191-279.

5. Tibby, R. B., 1941. The Water Masses of the West Coast of North America, J. Mar. Res., **4(2)**, pp. 112-121.

6. Kin'dyushev, V. I., 1970. Seasonal Variations of Water Masses in the California Region of the Pacific Ocean, Oceanol., **10(4)**, pp. 456-464.

7. Huyer, A., 1977. Seasonal Variation in Temperature, Salinity and Density Over the Continental Shelf off Oregon, Limnol. Oceanogr., 22, pp. 442-453.

8. Lynn, R. J., Seasonal Variation of Temperature and Salinity at 10 Meters in the California Current, California Cooperative Oceanic Fisheries Investigations Progress Report, July 2, 1963 to June 30, 1966. Marine Resources Committee, California Department of Fish and Game, Sacramento, California, pp. 157-186.

9. Reid, J. L., Jr., G. I. Roden and J. G. Wyllie, 1958. Studies of the California Current System, CALCOFI Rep., 1 July 1956 - 1 January 1958, pp. 28-56.

10. Jalickee, J. B. and D. R. Hamilton, 1977. Objective Analysis and Classification of Oceanographic Data Tellus, 29, pp. 545-560.

11. Skogsberg, T., 1936. Hydrography of Monterey Bay, California Thermal Conditions, 1929-1933, Am. Phil. Soc. Trans., 29, 152 pp.

12. Hickey, B. M., 1979. Variability of the California Undercurrent During Summer, 1972 (Abstr.) EOS (Trans., Am. Geophys. Union), 60(46), p. 856.

13. Williams, R. G. and F. A. Godshall, 1977. Summarization and Interpretation of Historical Physical Oceanographic and Meteorological Information for the Mid-Atlantic Region. Final Report to the Bureau of Land Management, U.S. Department of Commerce, National Oceanic and Atmospheric Administration, Washington, D.C., 295 pp.

14. Godshall, F. A., R. B. Williams, J. M. Bishop, F. Everdale, and S. W. Fehler, 1980. A Climatological and Oceanographic Analysis of the Georges Bank Study Region of the Outer Continental Shelf. Final Report to the Bureau of Land Management, U.S. Department of the Interior, U.S. Department of Commerce, National Oceanic and Atmospheric Administration, Environmental Data and Information Service, Washington, D.C.

15. Sverdrup, H. U. and R. H. Fleming, 1941. The Waters off the Coast of Southern California, March to July 1937, Bull., Scripps Inst. Oceanogr., University of California, La Jolla, California, 4, pp. 261-378.

16. Neumann, G., and W. J. Pierson, Jr., 1966. Principles of Physical Oceanography, Prentice-Hall, Inc., Englewood Cliffs, New Jersey, 545 pp.

17. Hesselberg, T., and H. U. Sverdrup (1914, 1915): Die Stabilitatsverhaltnisse des Seewassers bei vertikalen Verschiebungen, Bergens Museums Aarbok, No. 14 (1914) and Bergens Museums Aarbok, No. 15 (1915).

18. Phillips, O. M., 1966. The Dynamics of the Upper Ocean, Cambridge University Press, Cambridge, Massachusetts, 261 pp.

19. Bell, T. H., Jr., A. B. Mays and W. P. DeWitt, 1974. Upper Ocean Stability, A Compilation of Density and Brunt-Vaisala Frequency Distributions for the Upper 500 m of the World Ocean, NRL Report 7799, Naval Research Laboratory, Washington, D.C.

20. Wyllie, J. G. and R. J. Lynn, 1971. Distribution of Temperature and Salinity of 10 meters, 1960-1969 and Mean Temperatures, Salinity and Oxygen at 150 meters, 1950-1968, in the California Current, Marine Res. Comm., California Cooperative Oceanic Fisheries Investigations, Atlas No. 15.

21. Godshall, F. A., L. J. Allison, E. R. Kreins and G. Warnechke, 1969. The association of monthly average cloud cover, derived from meteorological satellite data, and sea surface temperature with the large scale circulation over the tropical Pacific Ocean, Joint conference on the general circulation of the atmosphere, London, England: unpublished.

22. Namias, J., 1971. Space Scales of Sea-surface Temperature Patterns and Their Causes, Fish. Bull. **70(3)**, pp. 611-617.

23. Allison, L. J., J. Steranka, R. J. Holub, J. Hansen, F. A. Godshall and C. Prabhakara, 1972. Air-sea Interaction in the Tropical Pacific Ocean, NASA Tech. Note (NASA TN D-6684), National Aeronautics and Space Administration, Washington, D.C., 84 pp.

24. Fofonoff, N. P., 1960. Transportation Computations for the North Pacific Ocean, Fish. Res. Bd. Canada, MS Rept. Series Oceanogr. Limnol.

25. Reid, J. L., Jr., 1959. Oceanography of the Northeastern Pacific Ocean During the Last Ten Years. California Cooperative Oceanic Fisheries Investigations, Reports Vol. VII, 1 January 1958 to 30 June 1950; pp. 77-90.

26. Huang, J. C. K., 1972. Recent Decadal Variation in the California Current System, J. Phy. Oceanog., Vol 2, **10**, pp. 382-390.

27. Vierra, K. C., 1980. Sea-Surface Temperature Variability of the California Current System. CMS-5-80, College of Marine Studies, University of Delaware.

28. Bourke, R. H. and J. G. Pattullo, 1974. Seasonal variation of the water mass along the Oregon-Northern California Coast, Limnol. Oceanogr., **19**, pp. 190-198.

29. Maloney, N. and K. M. Chan, 1974. A Summary of Knowledge of the Southern California Coastal Zone and Offshore Areas, Vol I, Sept. 1974, The Southern California Ocean Studies Consortium of the California State Universities and Colleges, Report to the Bureau of Land Management, Department of Interior, Washington, D.C.

30. Winzler and Kelly, Inc., 1977. A Summary of Knowledge of the Central and Northern California Coastal Zone and Offshore Areas, Volume I, Physical Conditions, Book 1 PB-274 210, Winzler and Kelly Consulting Engineers, Eureka, California, 189 pp.

31. Bakun, A., 1978. Coastal Upwelling off Western North America, 1975, Ocean Variability: Effects on U.S. Marine Fishery Resources-1975, NOAA Tech. Rep. NMFS Circular 416, J. R. Goulet, Jr. and E. D. Haynes, eds., pp. 89-103.

32. Wooster, W. S. and J. L. Reid, Jr., 1963. Eastern Boundary Currents, The Sea, Vol. 2, John Wiley & Sons, New York, pp. 253-276.

33. Muromstev, A. M., 1963. The principal hydrological features of the Pacific Ocean, Trans. from the Russian. Nat. Sci. Fdn., Washington, D.C., 417 pp.

34. Wickham, J. B., 1975. Observations of the California Countercurrent, Journal Marine Research, **33(3)**, pp. 325-340.

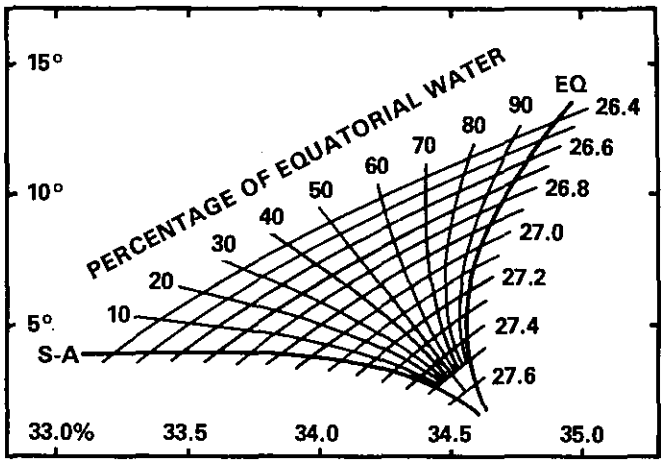

Figure 5.1 Temperature-Salinity "fan of mixing" Used by Tibbey (1941) in his Description of the California Coastal Region as a Transition Zone Between Equatorial and Subarctic Water

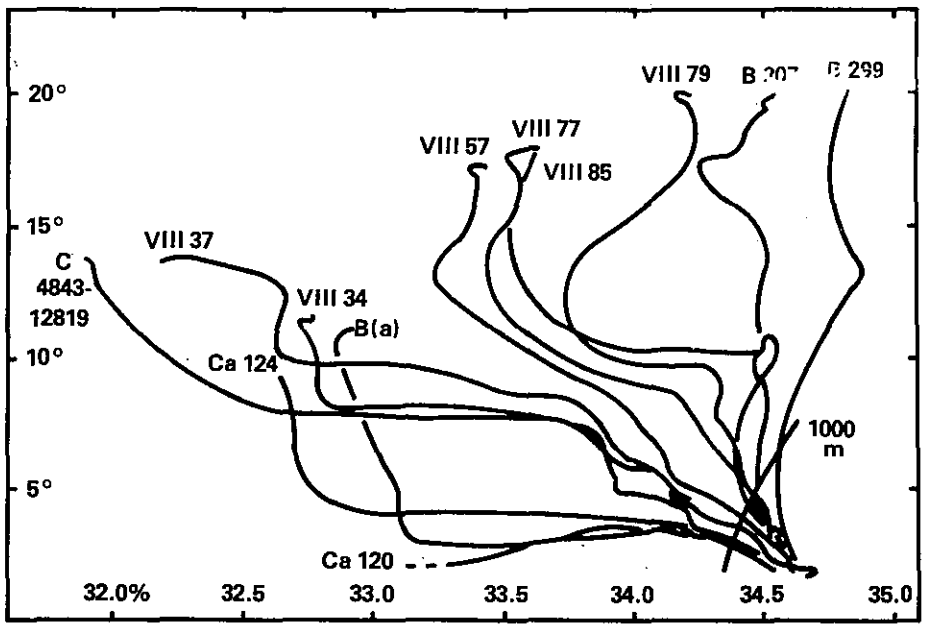

Figure 5.2 Temperature-Salinity Curves of Stations in the Eastern North Pacific from Off the Aleutian Islands to Central America (Tibbey, 1941)

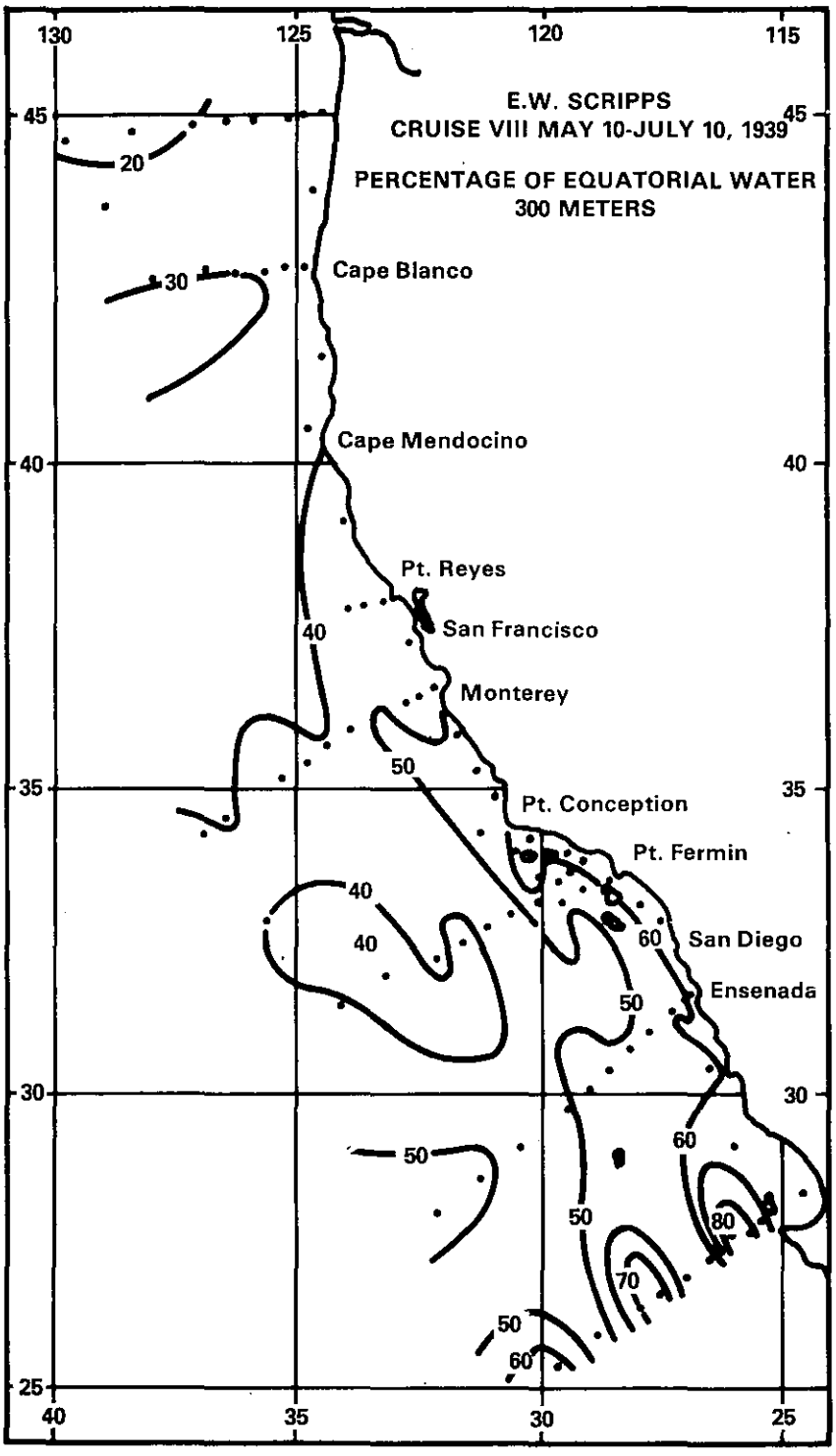

Figure 5.3 The Percentage Content of Equatorial Water at 300 Meters

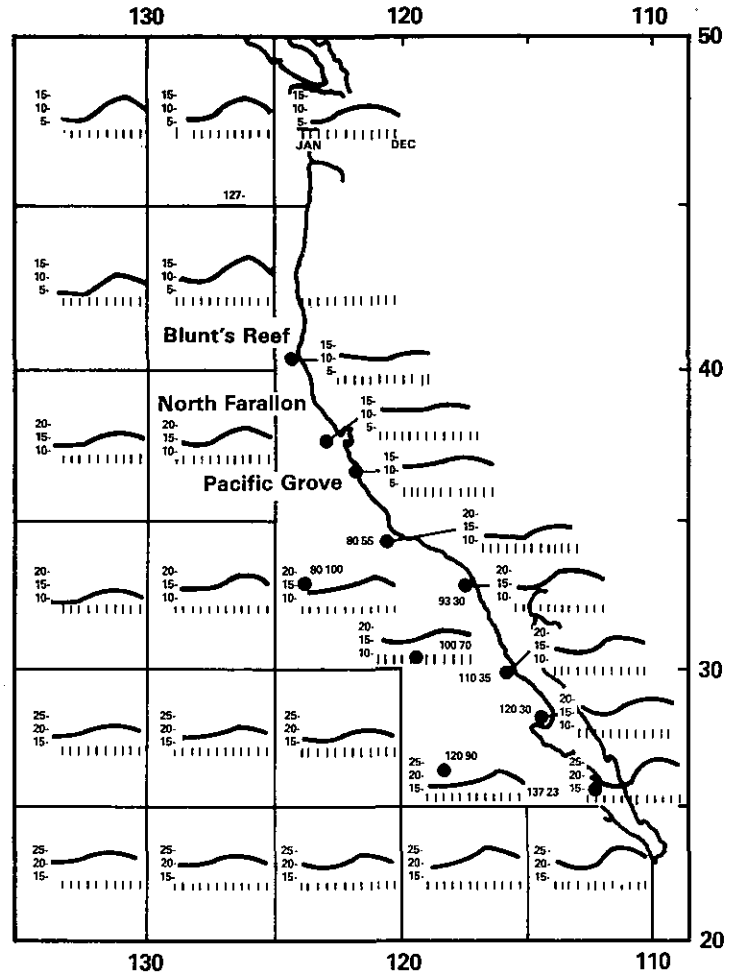

(a) Temperature in degrees Centigrade. Values over five-degree squares are from Robinson (1957); values at Blunt's Reef, North Farallon Island and Pacific Grove are from U.S. Coast and Geodetic Survey (1956); values at numbered stations are from CALCOFI data (1949-55).

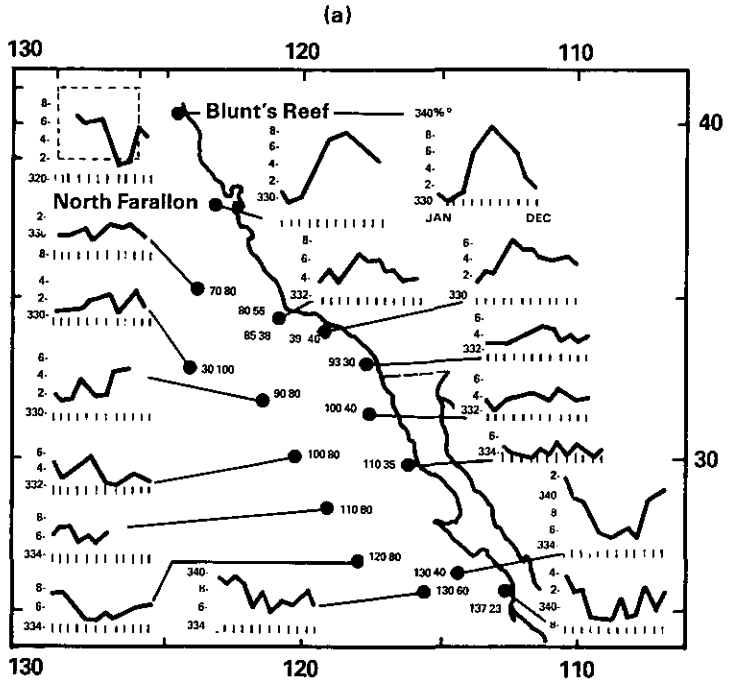

(b) Salinity in parts per million. Values at Blunt's Reef and North Farallon Island are from U.S. Coast and Geodetic Survey (1954).

Figure 5.4. Seasonal Variation of Temperature and Salinity at the Surface Off the Western Coast of North America (Reid, 1960)

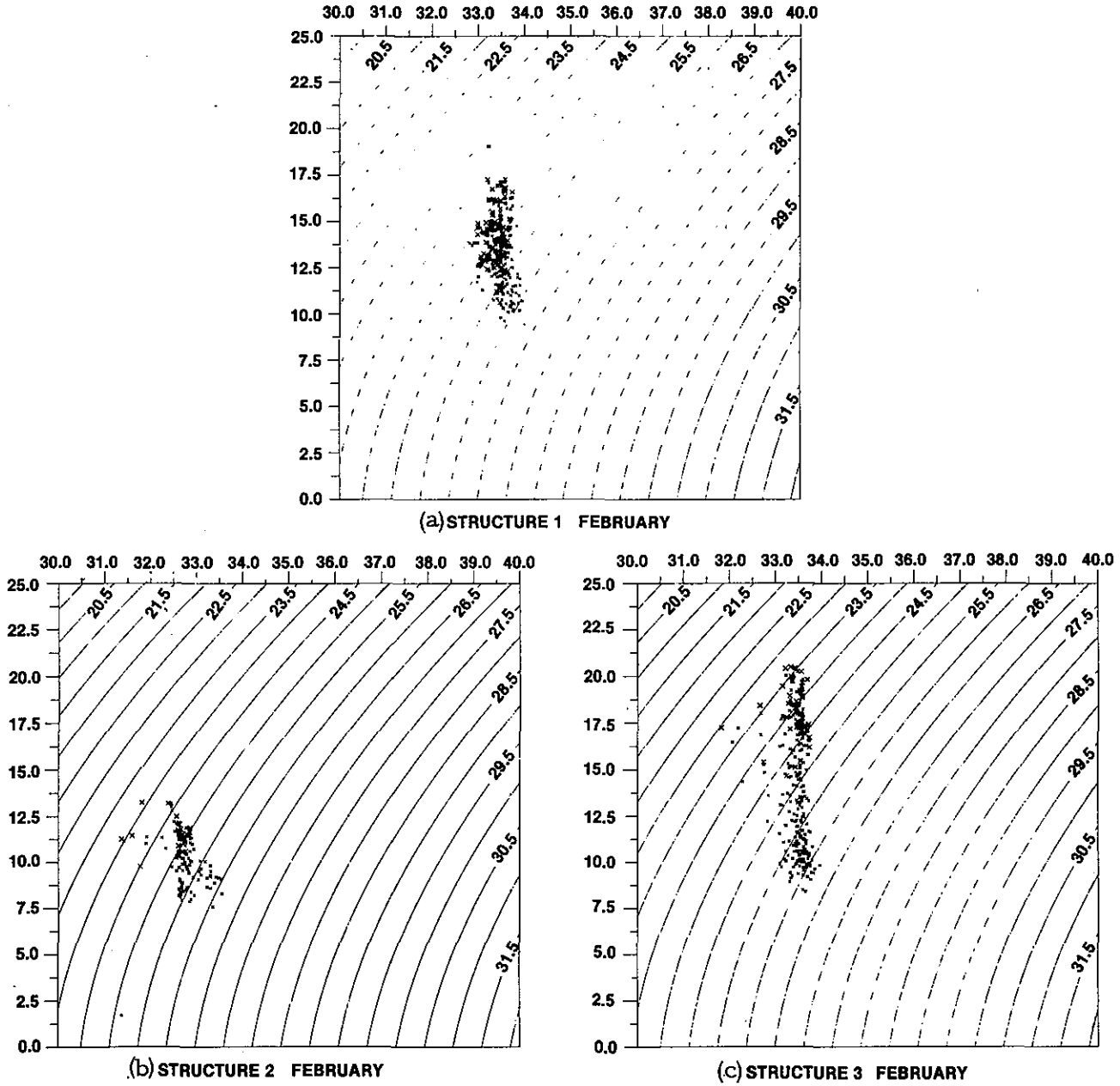

Figure 5.5 Classification of water structures in February by the ASD method

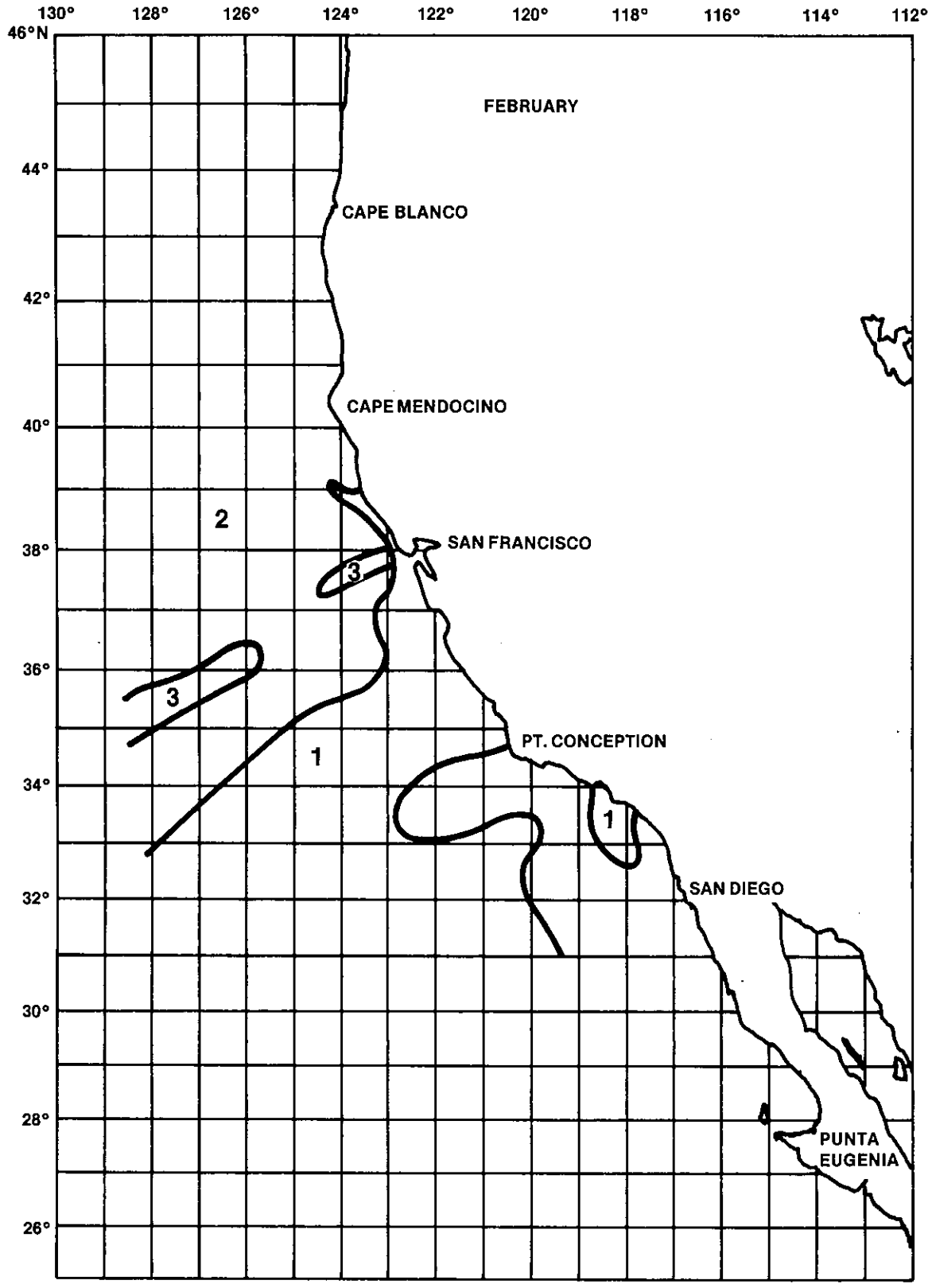

"Geographical distribution of water structures"

Figure 5.5 Classification of water structures in February by the ASD method (continued)

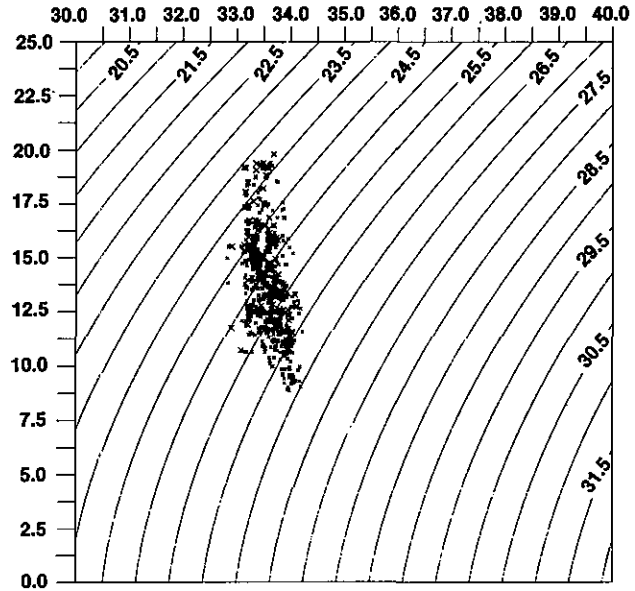

(a) STRUCTURE 1 JUNE

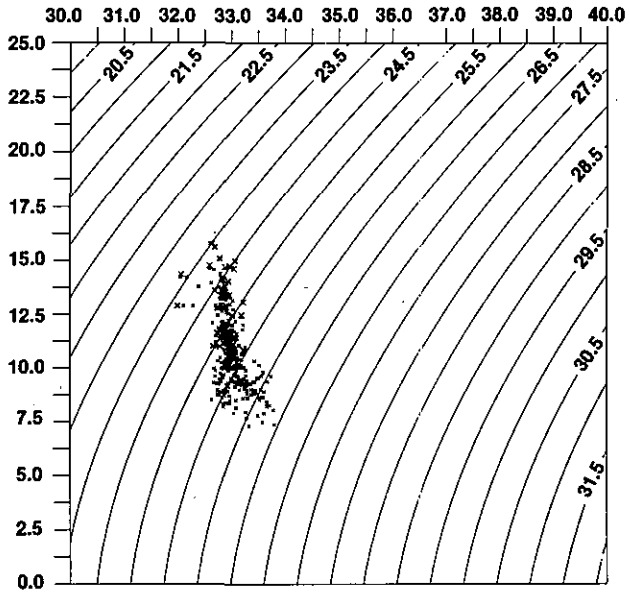

(b) STRUCTURE 2 JUNE

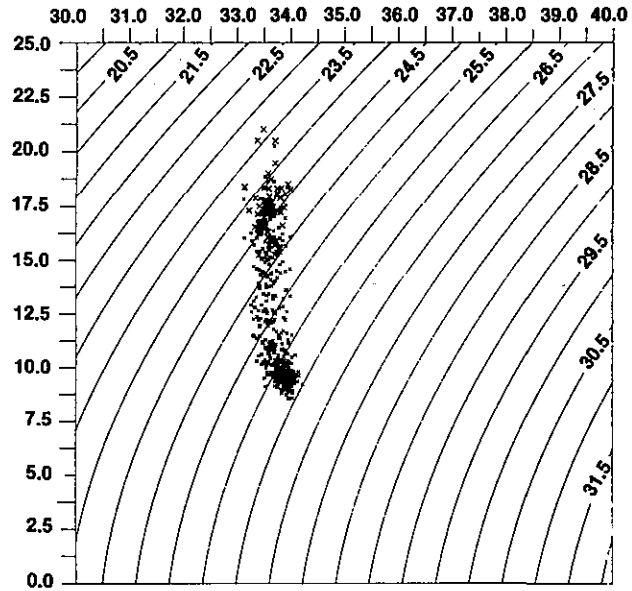

(c) STRUCTURE 3 JUNE

Figure 5.6 Classification of water structures in June by the ASD method

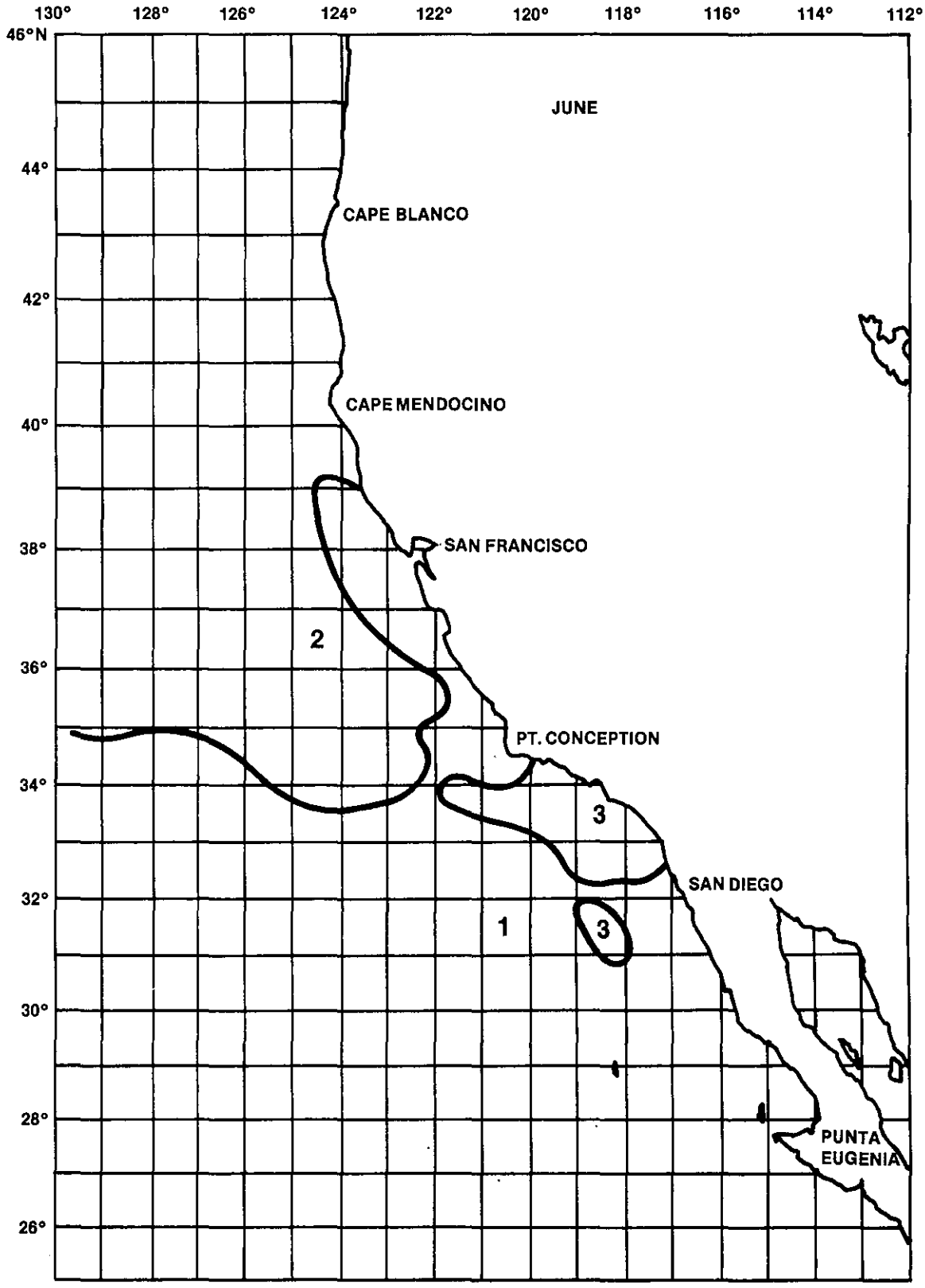

"Geographical distribution of water structures"

Figure 5.6 Classification of water structures in June by the ASD method (continued)

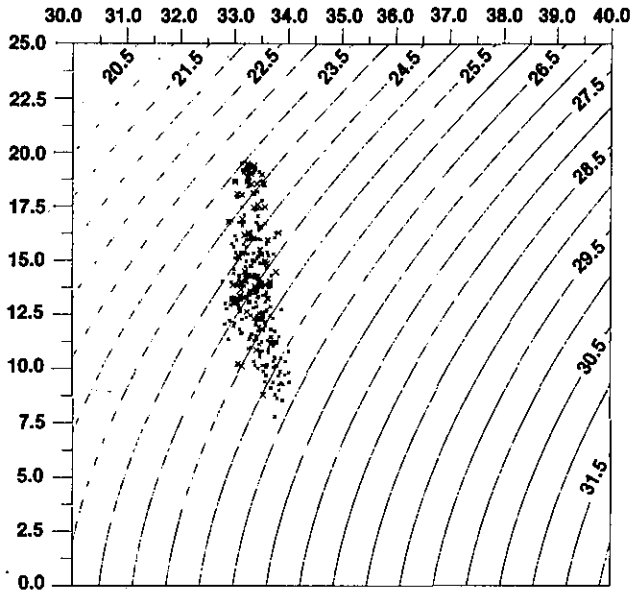

(a) STRUCTURE 1 SEPTEMBER

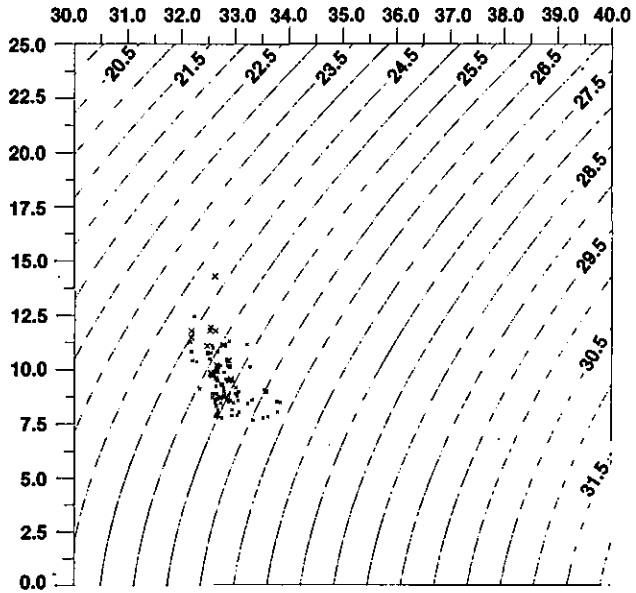

(b) STRUCTURE 2 SEPTEMBER

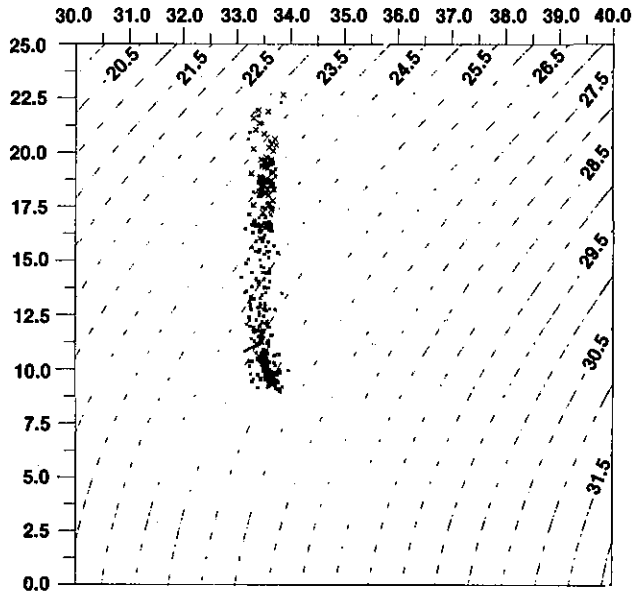

(c) STRUCTURE 3 SEPTEMBER

Figure 5.7 Classification of water structures in September by the ASD method

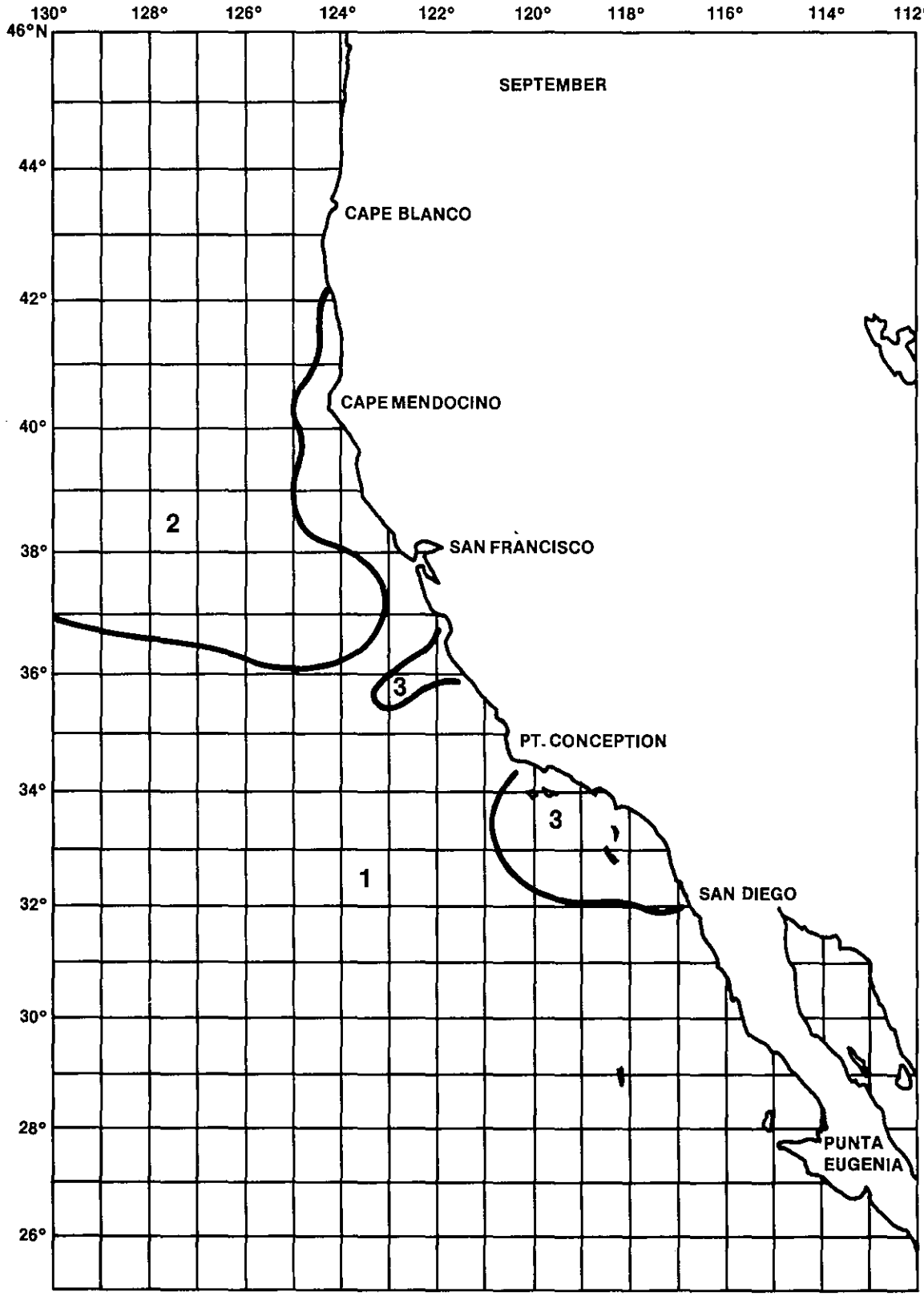

"Geographical distribution of water structures"

Figure 5.7 Classification of water structures in September by the ASD method (continued)

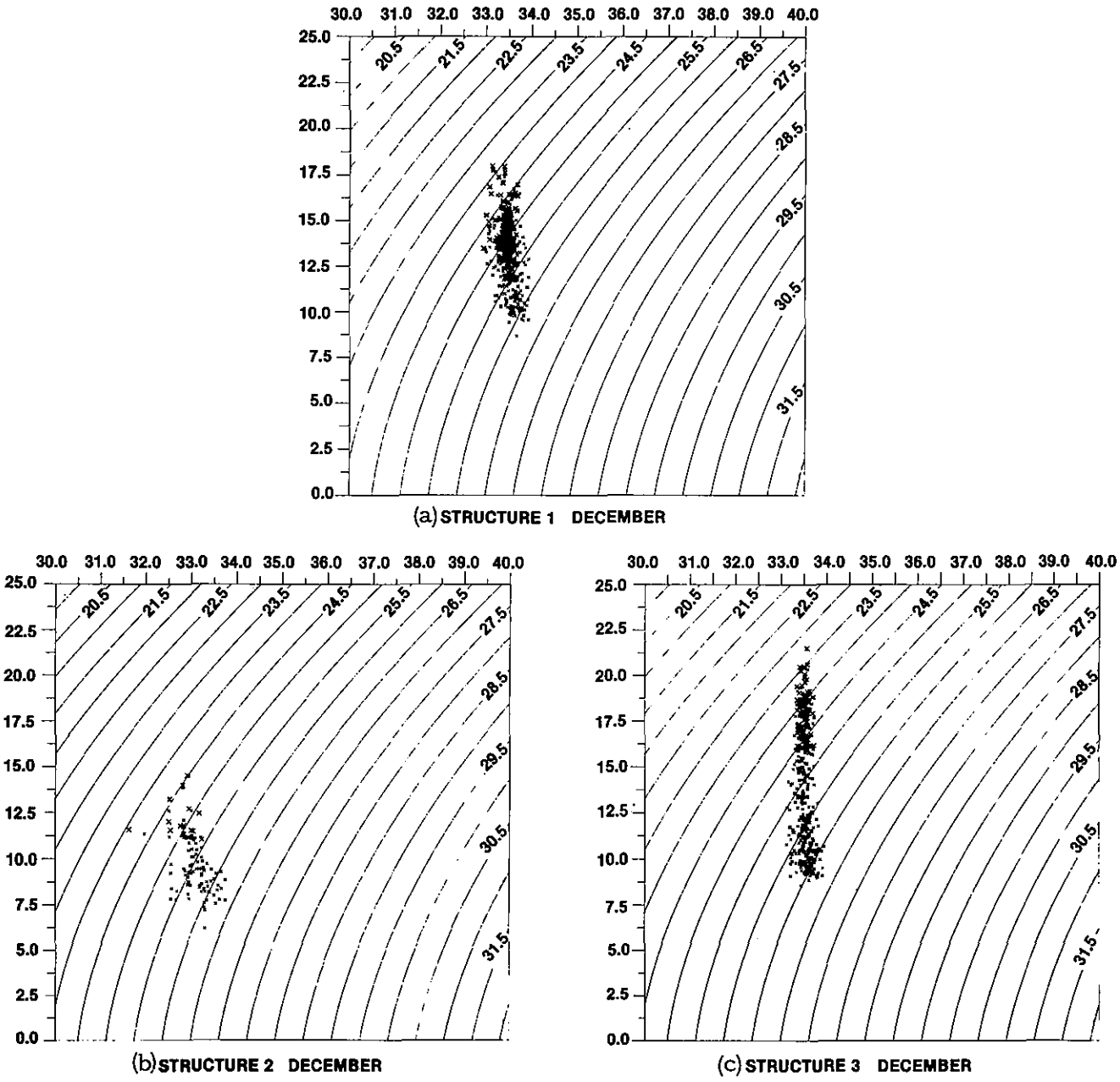

Figure 5.8 Classification of water structures in December by the ASD method

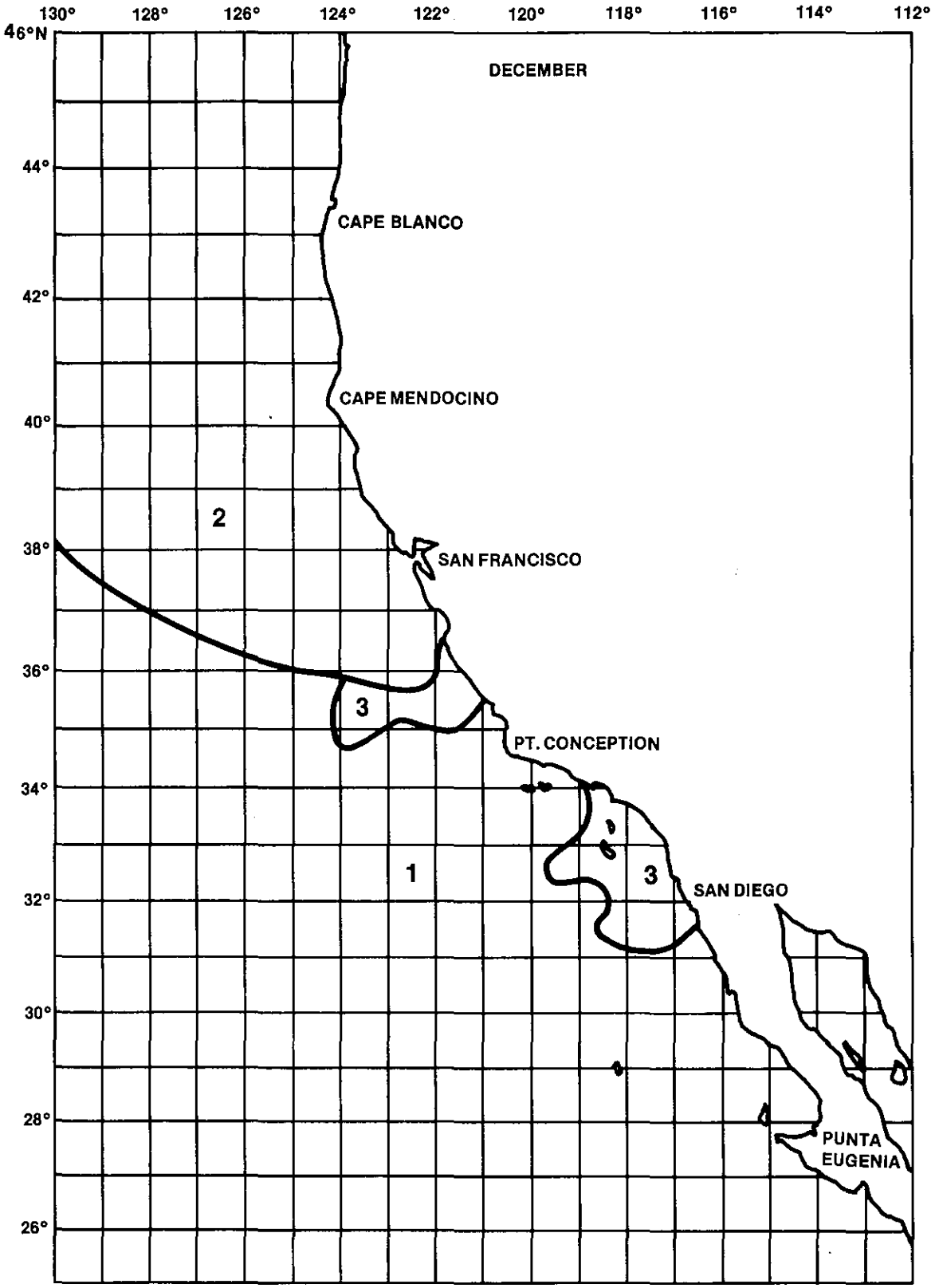

"Geographical distribution of water structures"

Figure 5.8 Classification of water structures in December by the ASD method (continued)

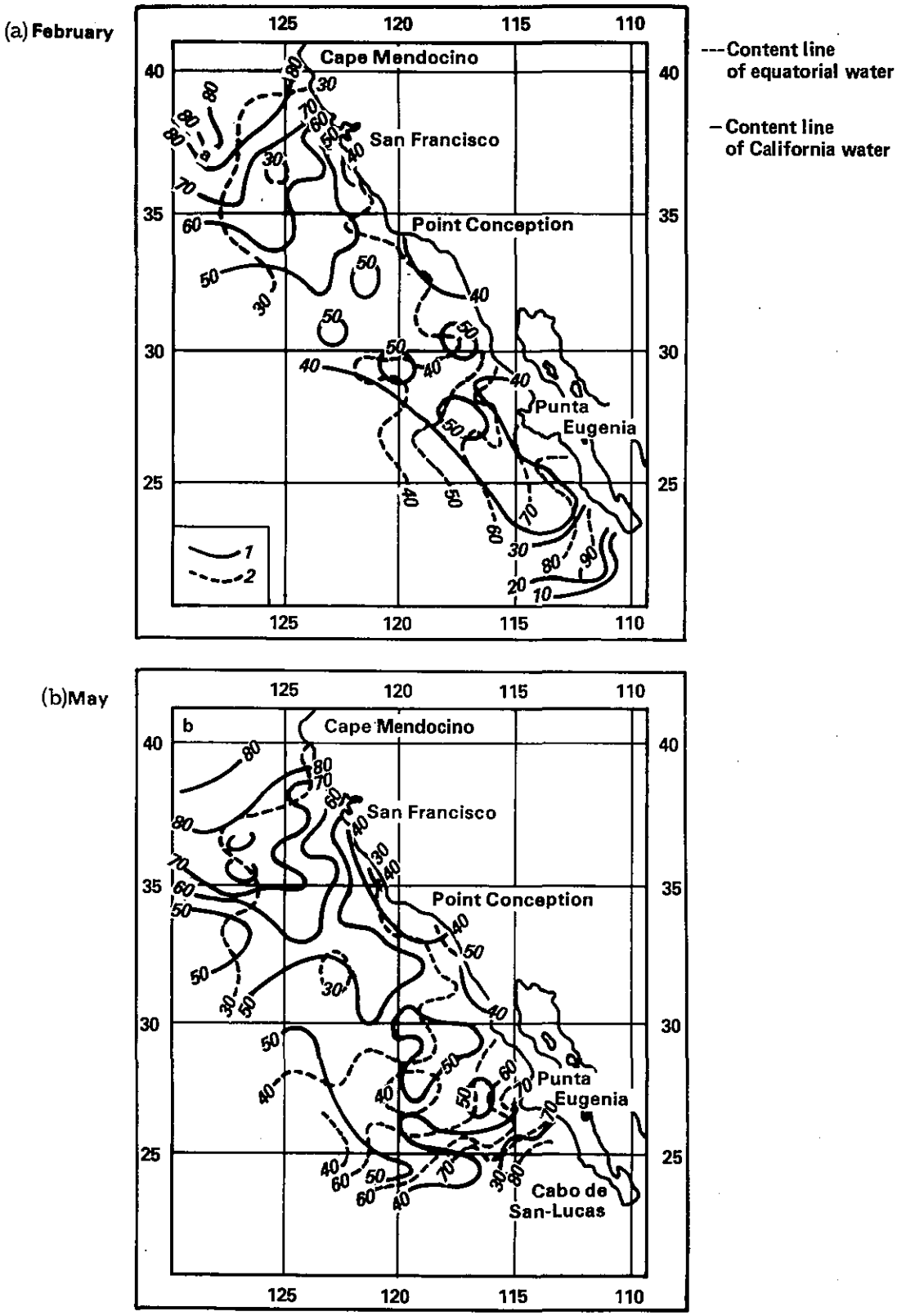

Figure 5.9. Distribution of the California and Equatorial Water Masses (in %) in Different Seasons of the Year (Kin'dyushev, 1970)

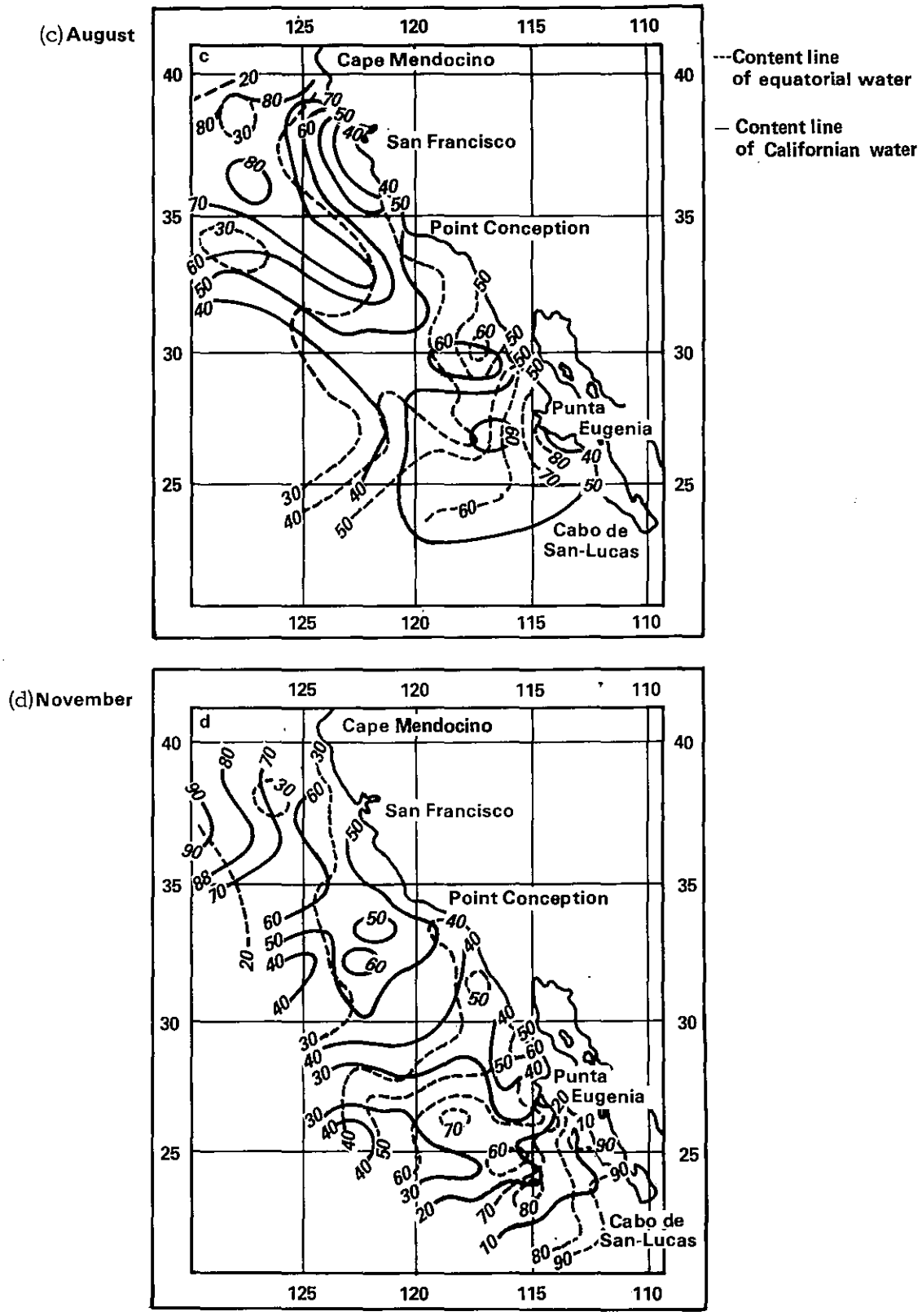

Figure 5.9. Distribution of the California and Equatorial Water Masses (in %) in Different Seasons of the Year (Kin'dyushev, 1970) (continued)

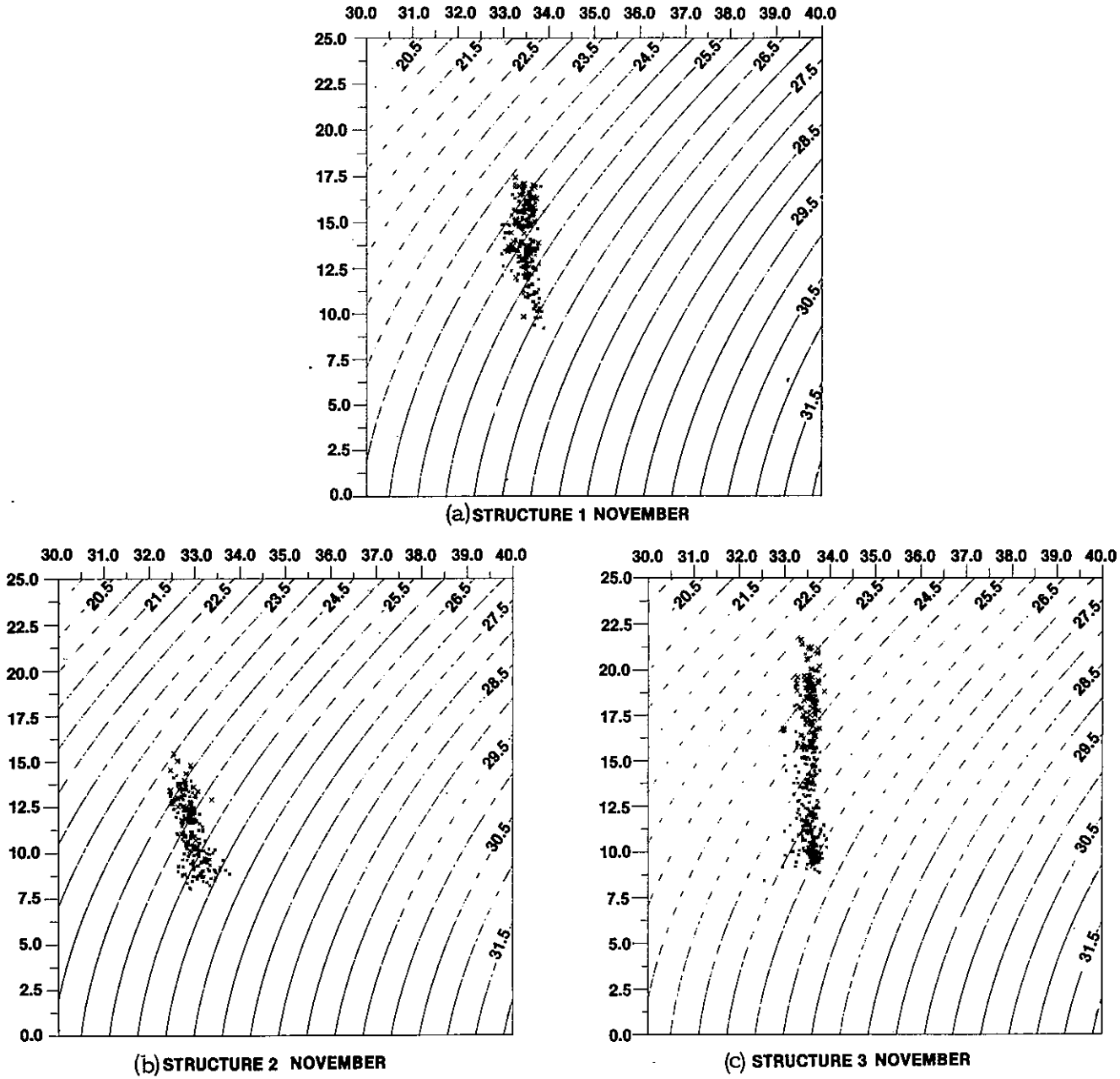

Figure 5.10 Classification of water structures in November by the ASD method

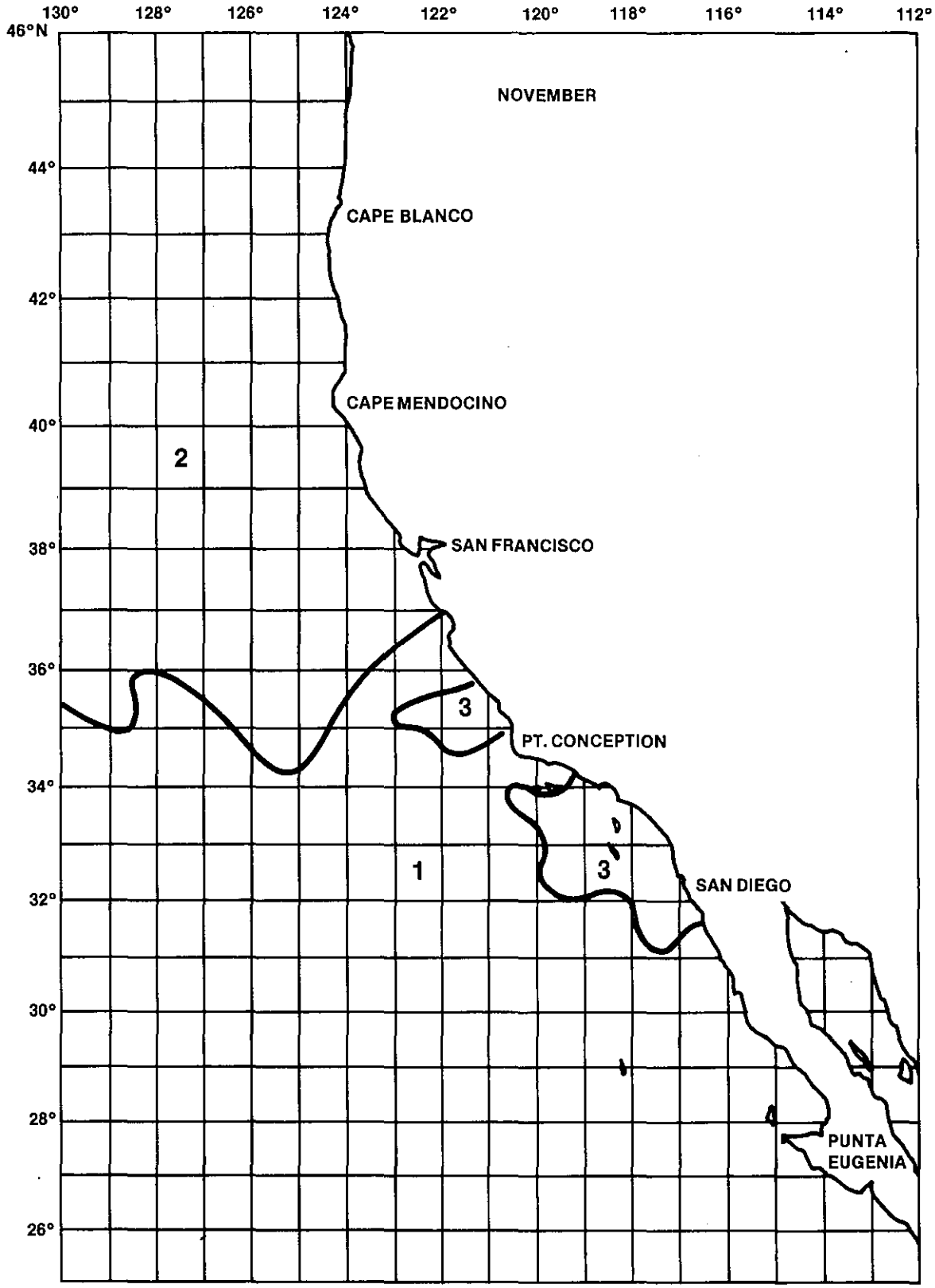

"Geographical distribution of water structures"

Figure 5.10 Classification of water structures in November by the ASD method (continued)

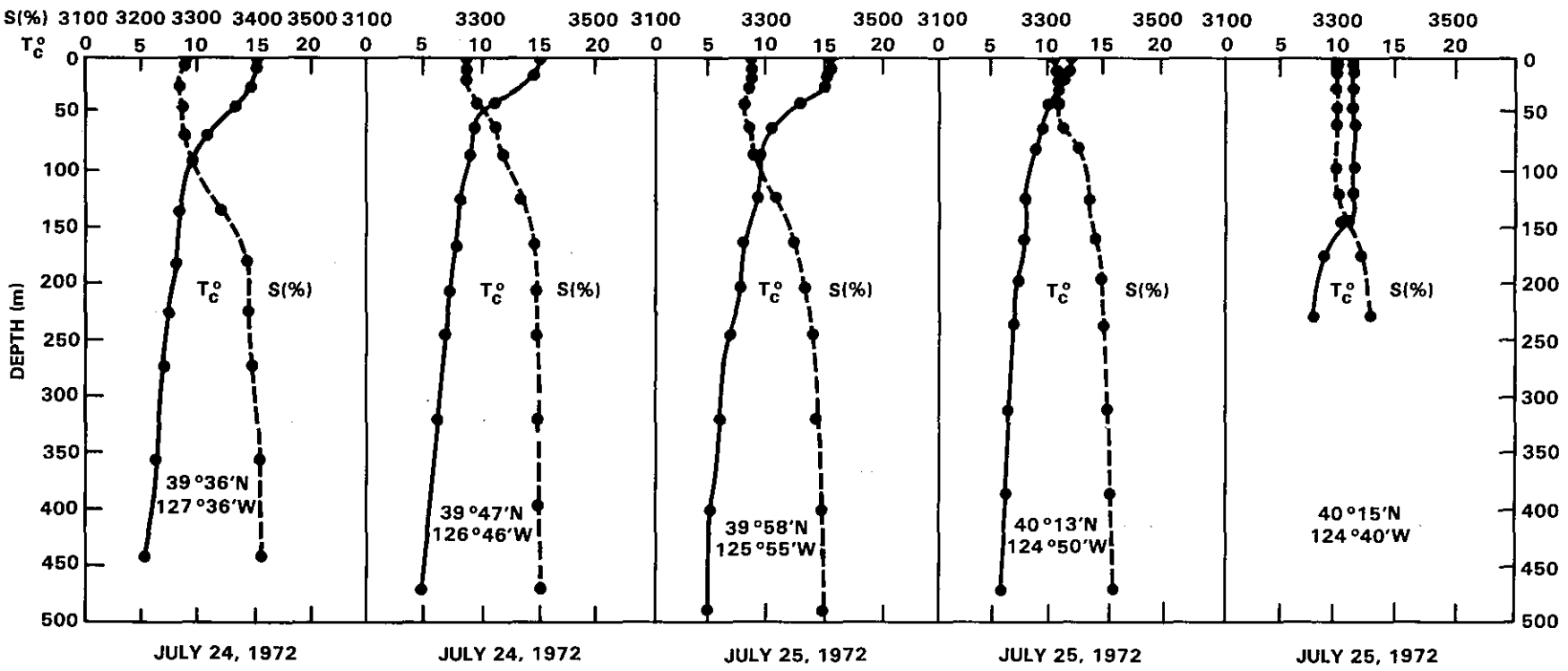

Figure 5.11 Temperature and salinity vs. depth profiles, R/V OGON (USSR), July 1972

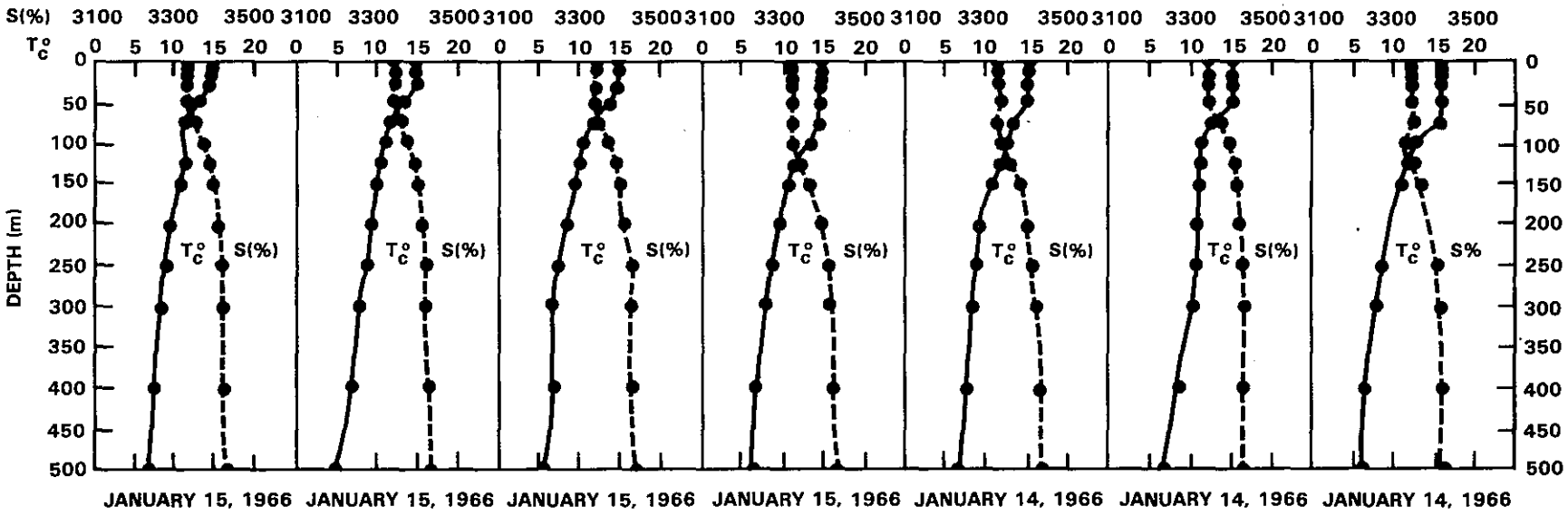

Figure 5.12 Temperature and salinity correlations, R/V David Starr Jordan, January 1960

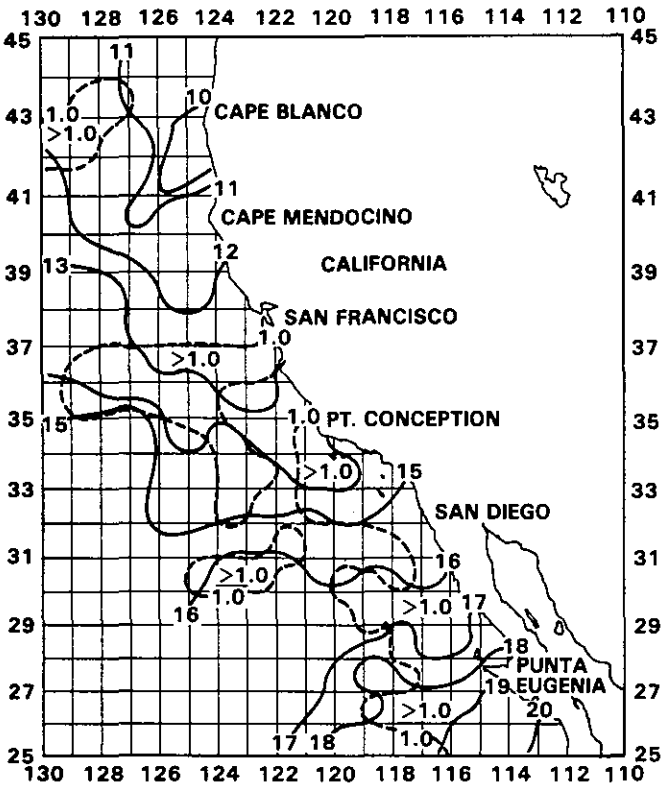

(a) Temperature (°C) – December - January

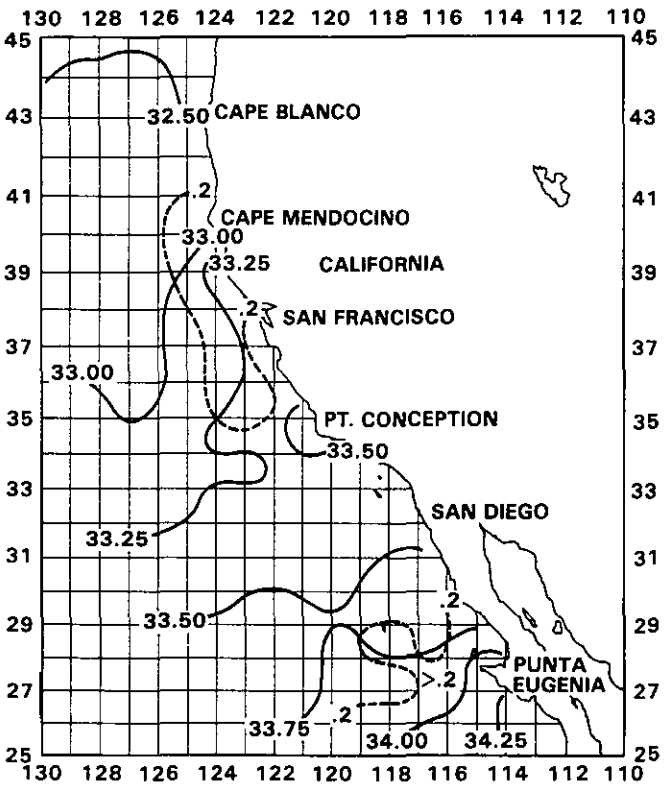

(b) Salinity (ppt) – December-January

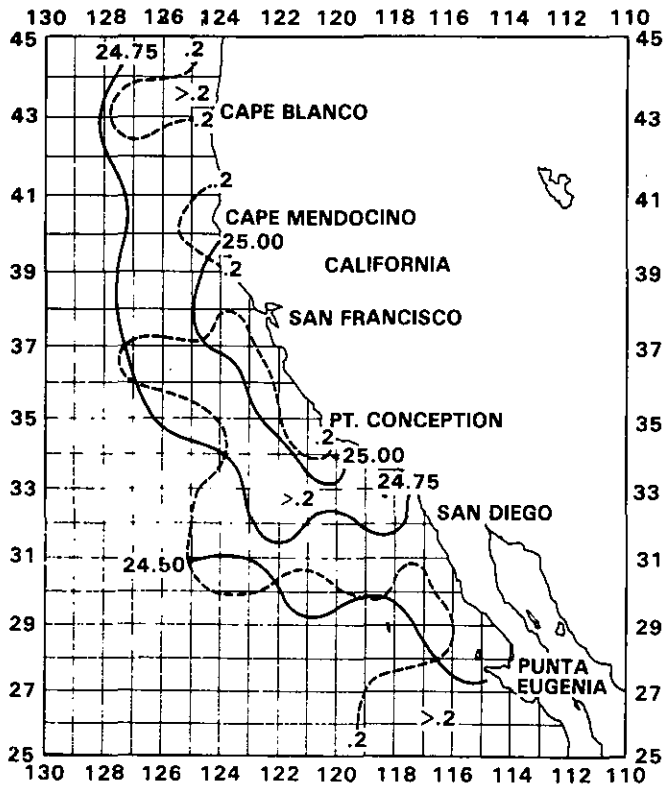

(c) Sigma-t – December-January

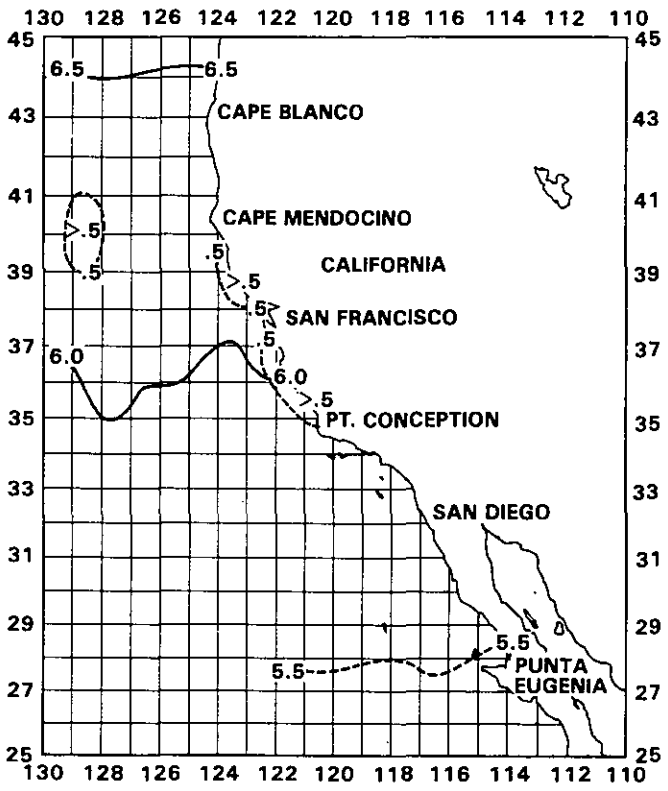

(d) Dissolved Oxygen (ml/l)
December-January

——Mean – – –Standard Deviation

Figure 5.13. Physical Properties at the
Sea Surface December-January

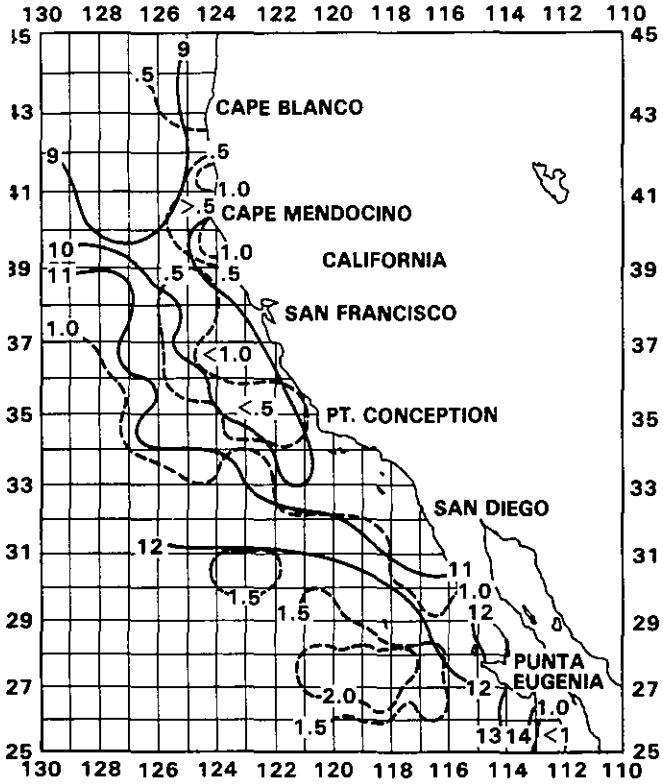

(a) Temperature (°C) – December-January

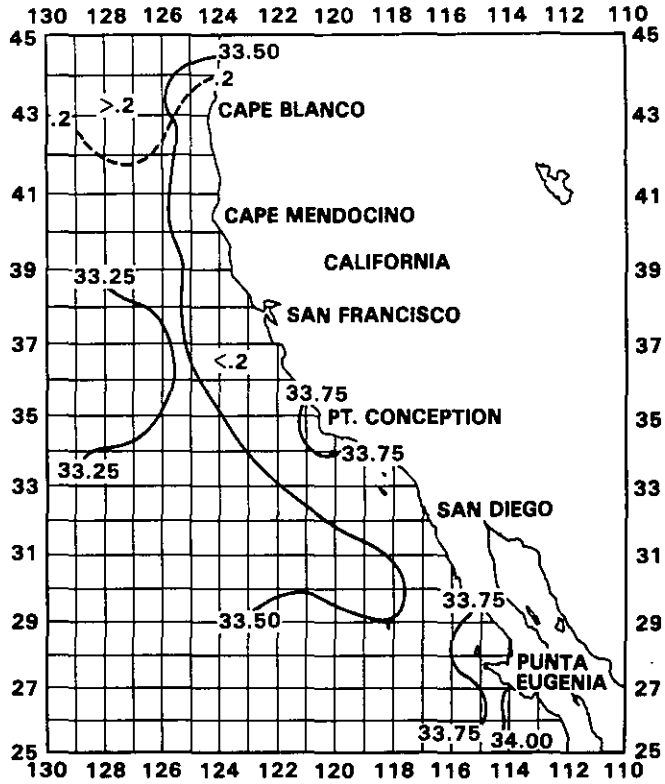

(b) Salinity (ppt) – December-January

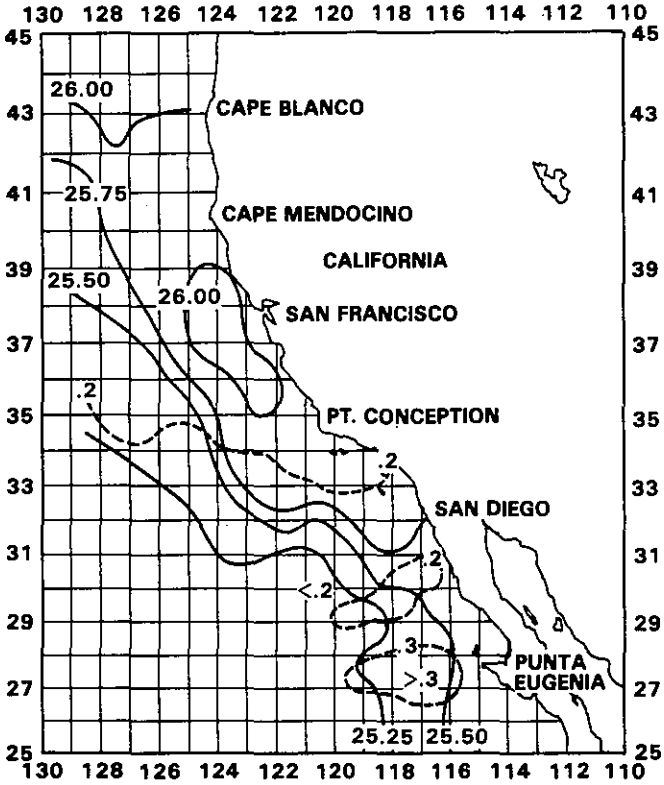

(c) Sigma-t – December-January

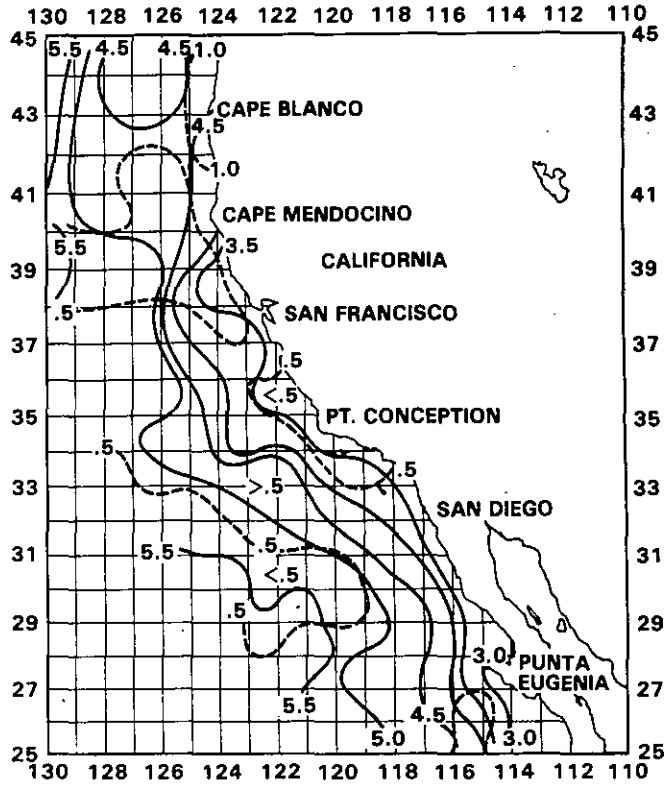

(d) Dissolved Oxygen (ml/l) December-January

—— Mean – – – Standard Deviation

Figure 5.14. Physical Properties at 100 m
December-January

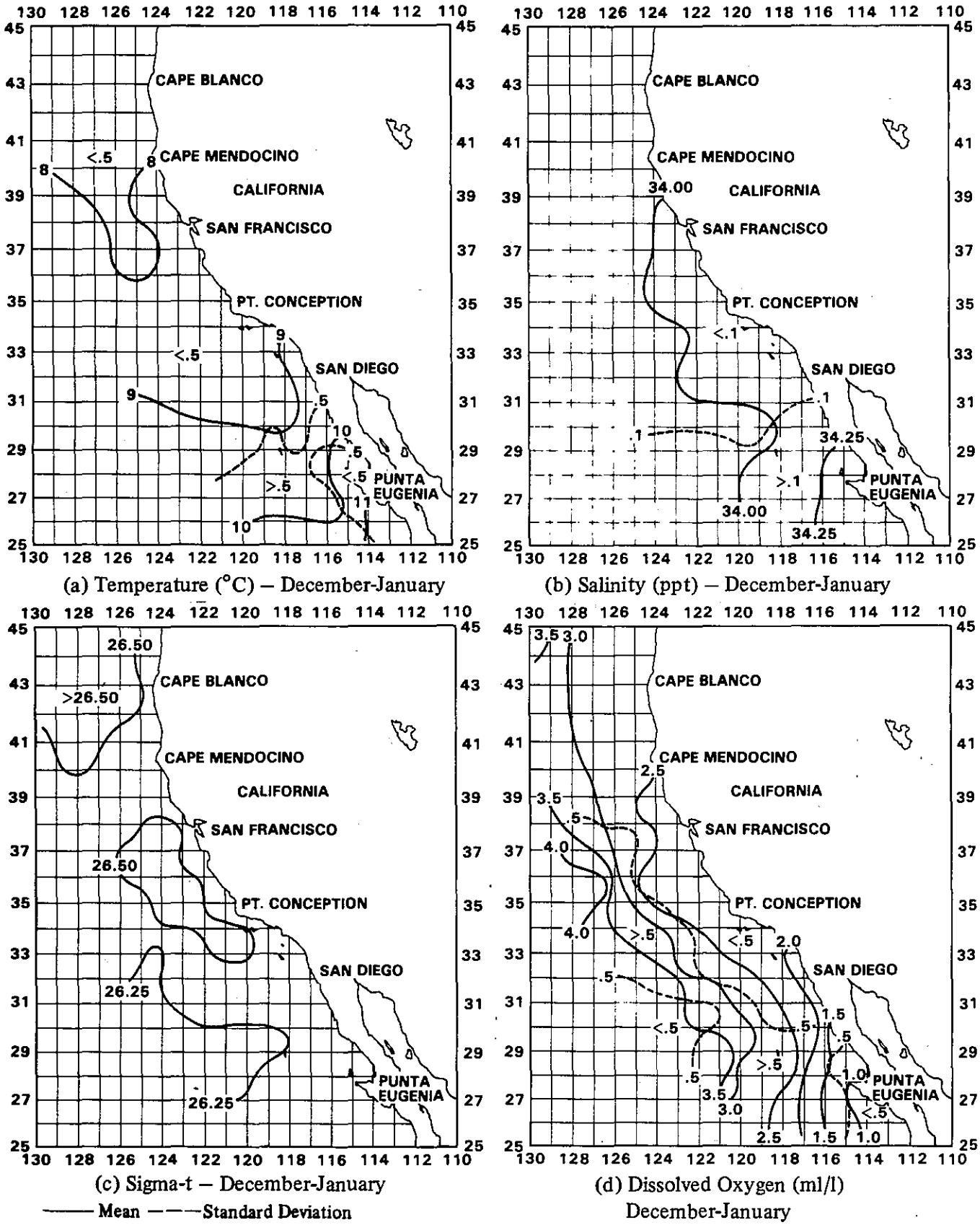

(a) Temperature (°C) – December-January

(b) Salinity (ppt) – December-January

(c) Sigma-t – December-January

(d) Dissolved Oxygen (ml/l) December-January

——— Mean – – – Standard Deviation

Figure 5.15. Physical Properties at 200 m
December-January

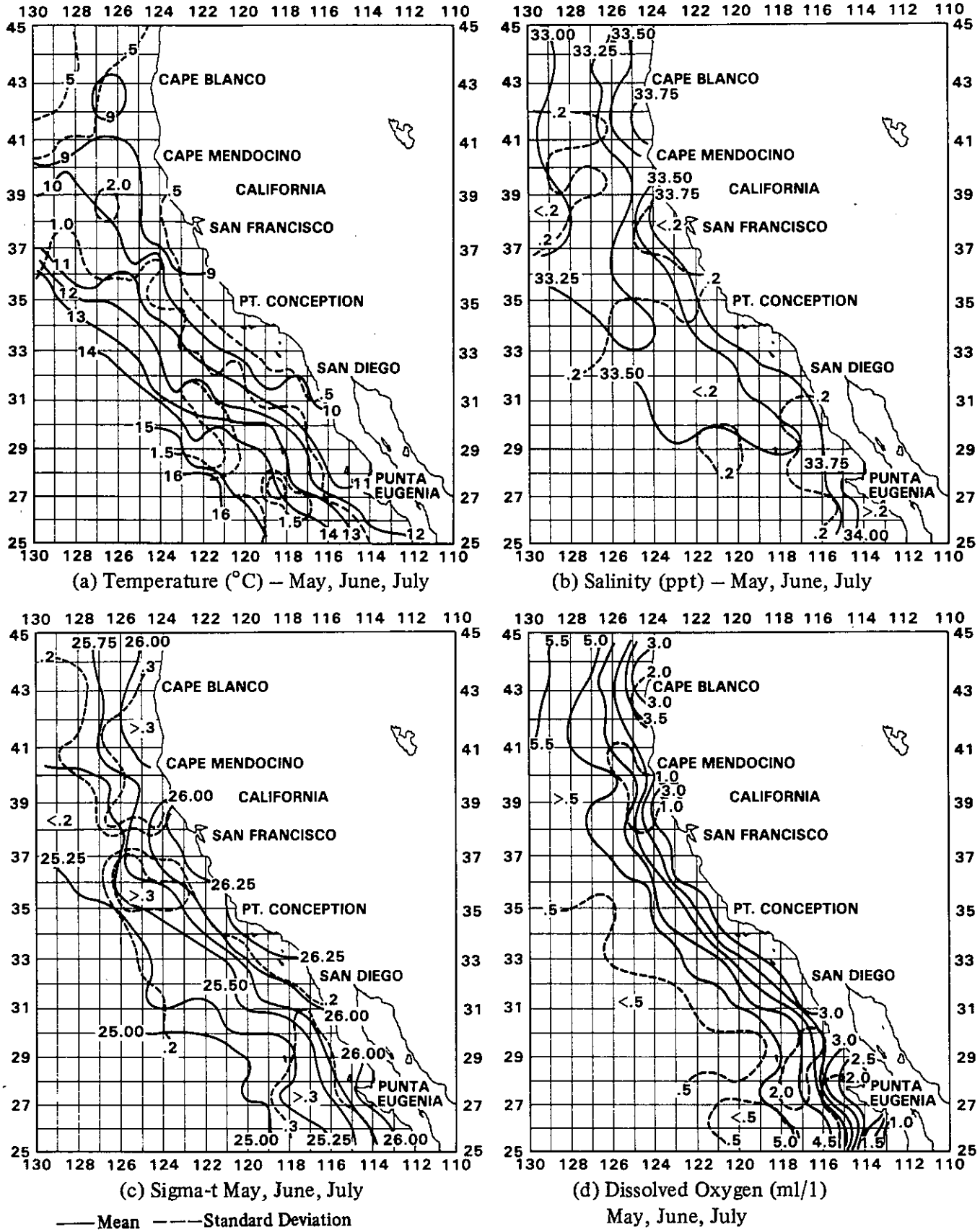

Figure 5.16. Physical Properties at the Sea Surface May-June-July

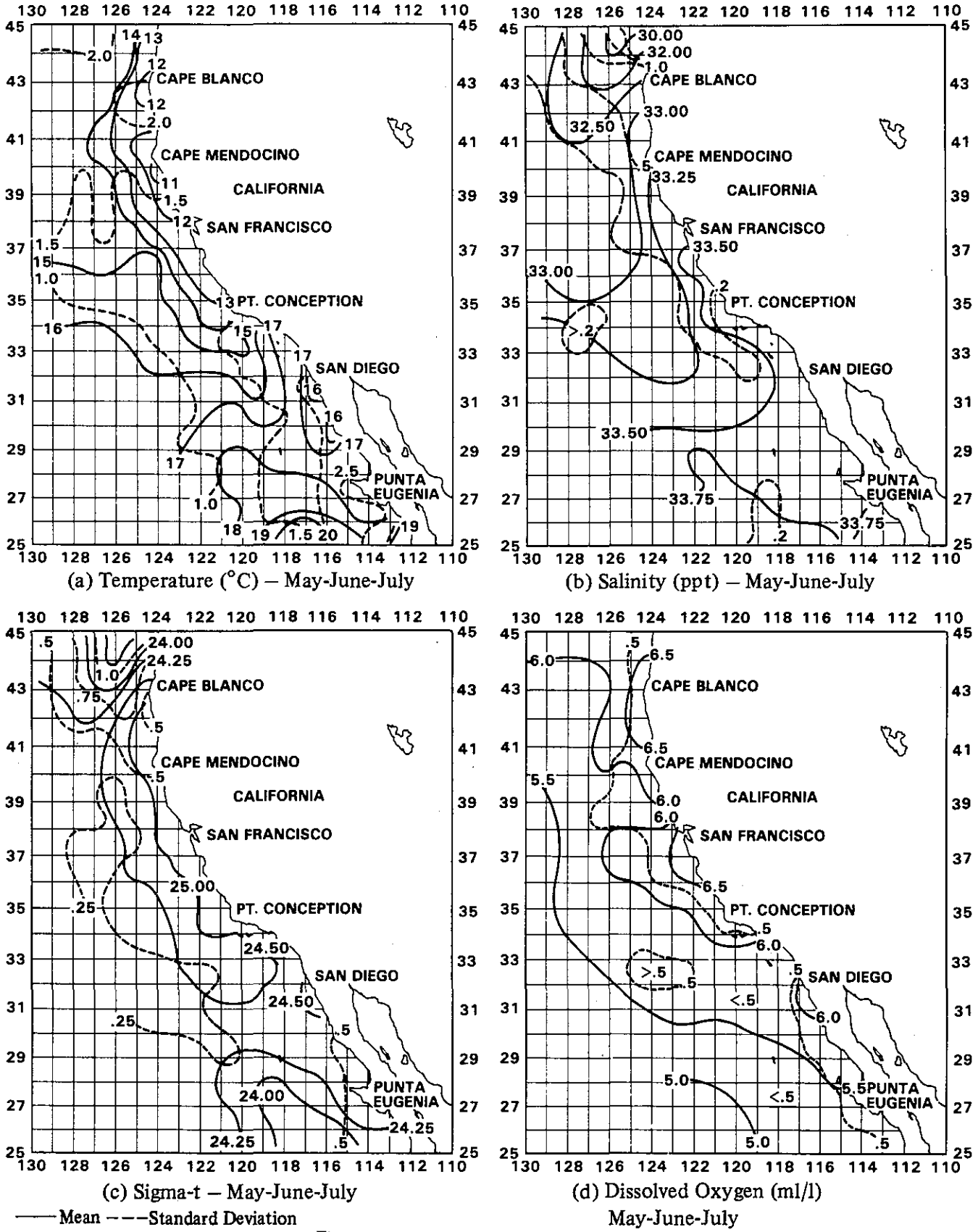

Figure 5.17. Physical Properties at 100 m
May-June-July

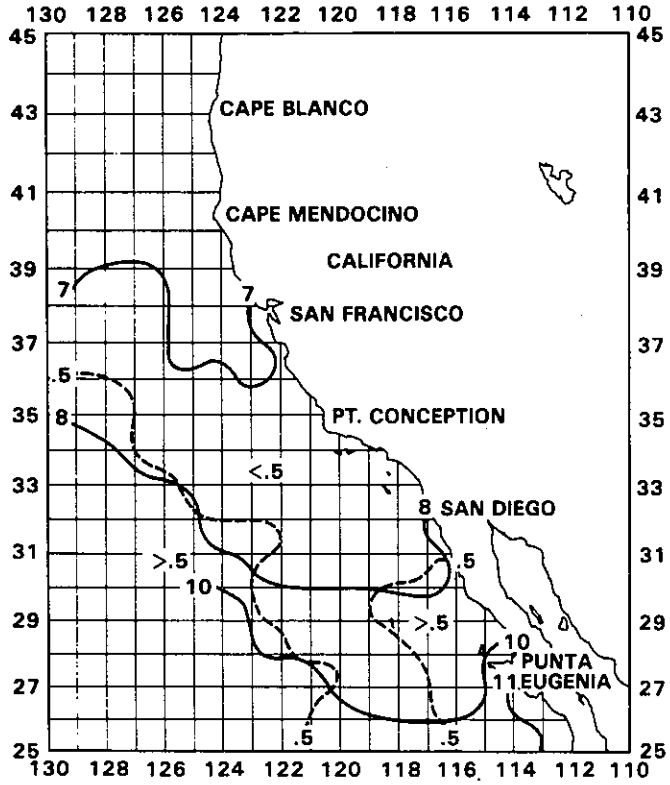

(a) Temperature (°C) – May, June, July

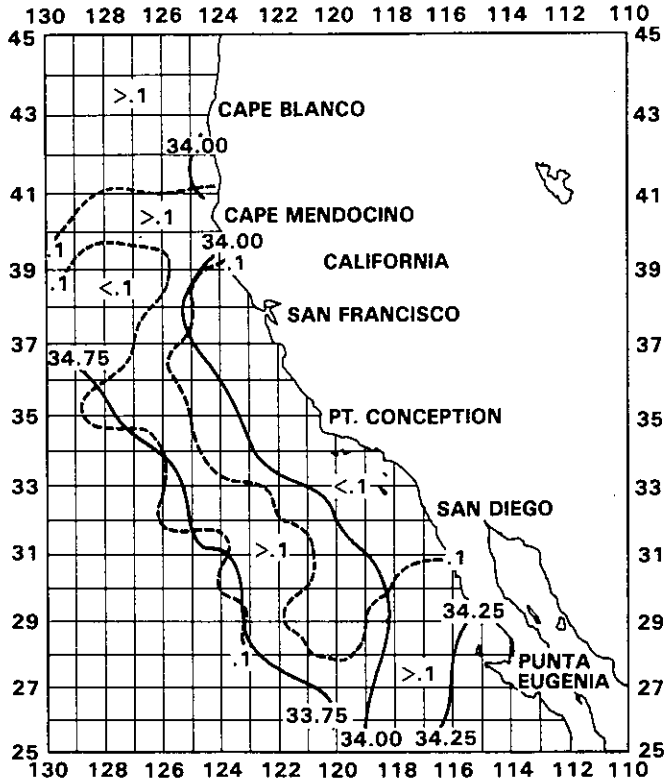

(b) Salinity (ppt) – May, June, July

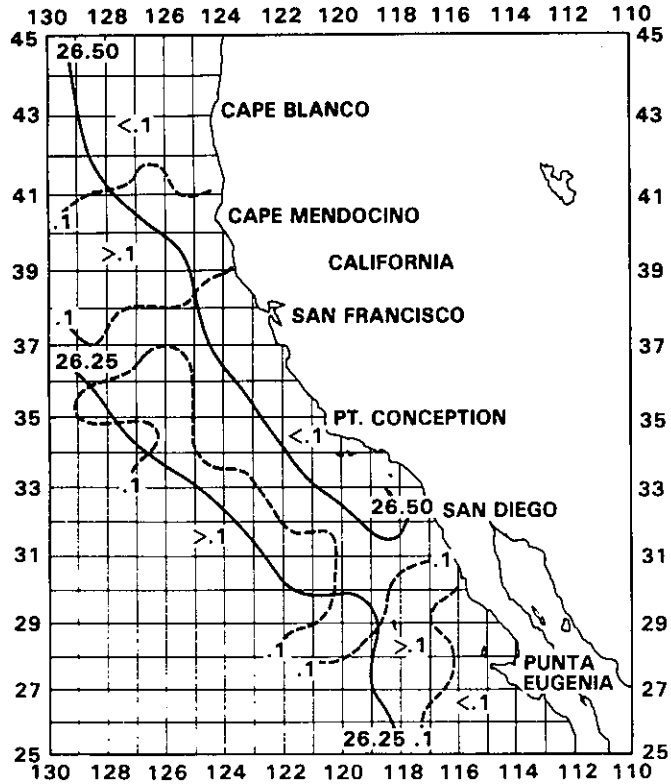

(c) Sigma-t – May, June, July

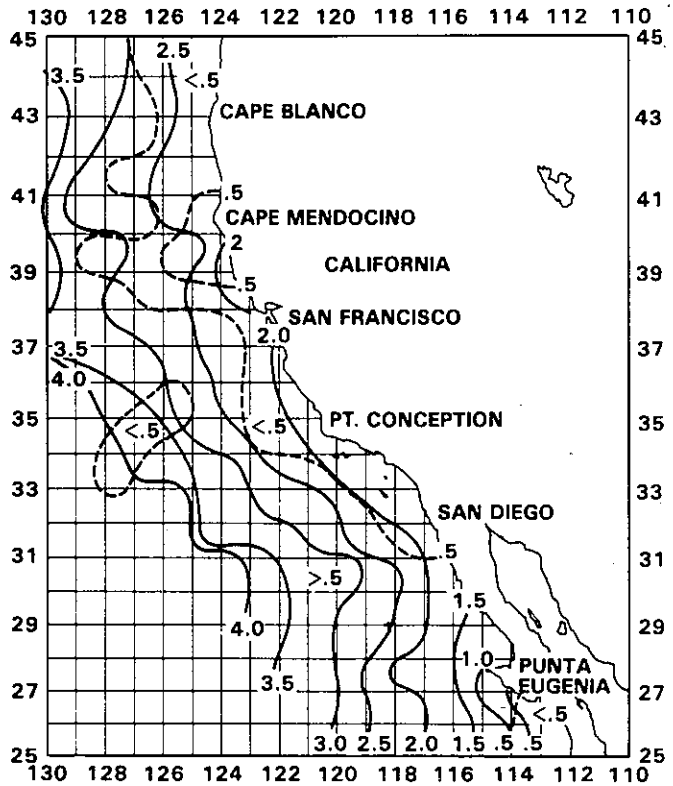

(d) Dissolved Oxygen (ml/l) May, July

——Mean ———Standard Deviation

Figure 5.18. Physical Properties at 200 m
May-June-July

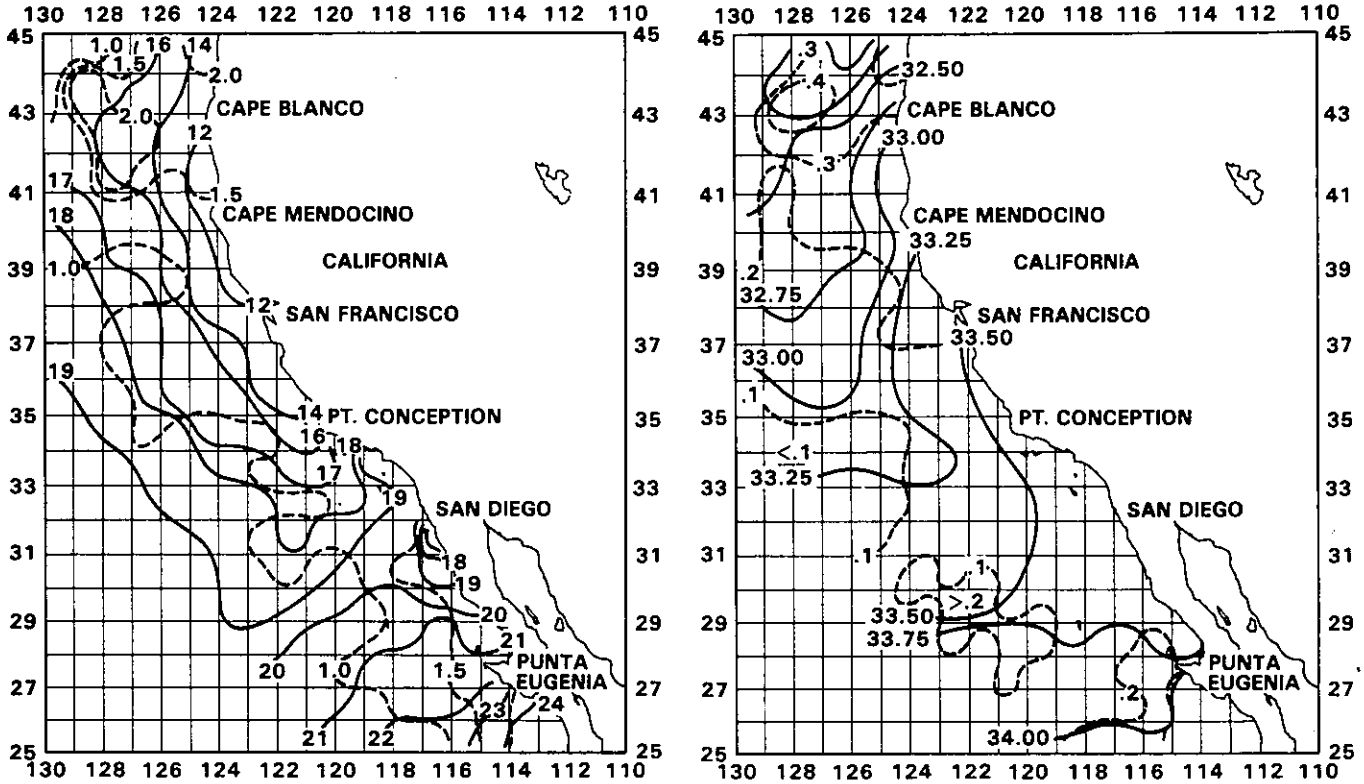

(a) Temperature (°C) – September , October

(b) Salinity (ppt) – September, October

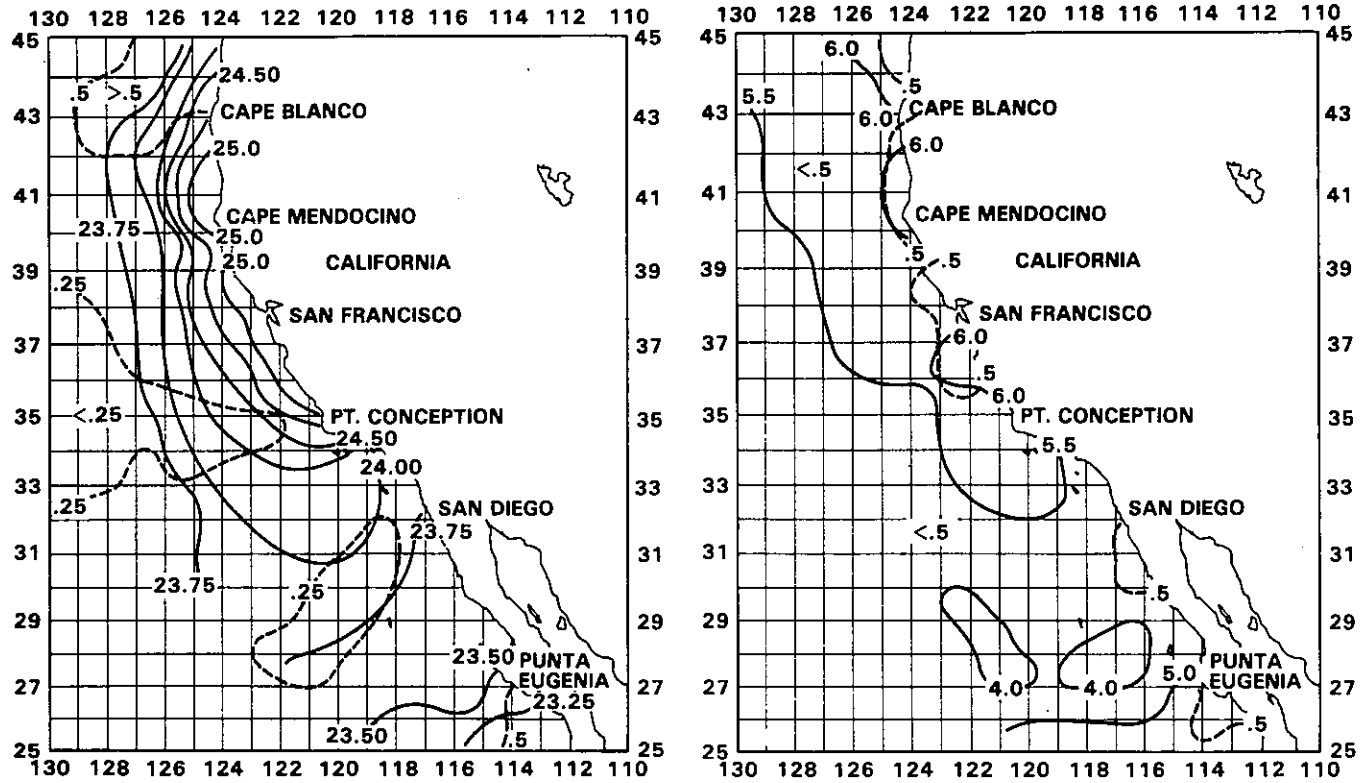

(c) Sigma-t – September, October

——Mean – – –Standard Deviation

(d) Dissolved Oxygen (ml/l)
September, October

Figure 5.19. Physical Properties at the
Sea Surface September-October

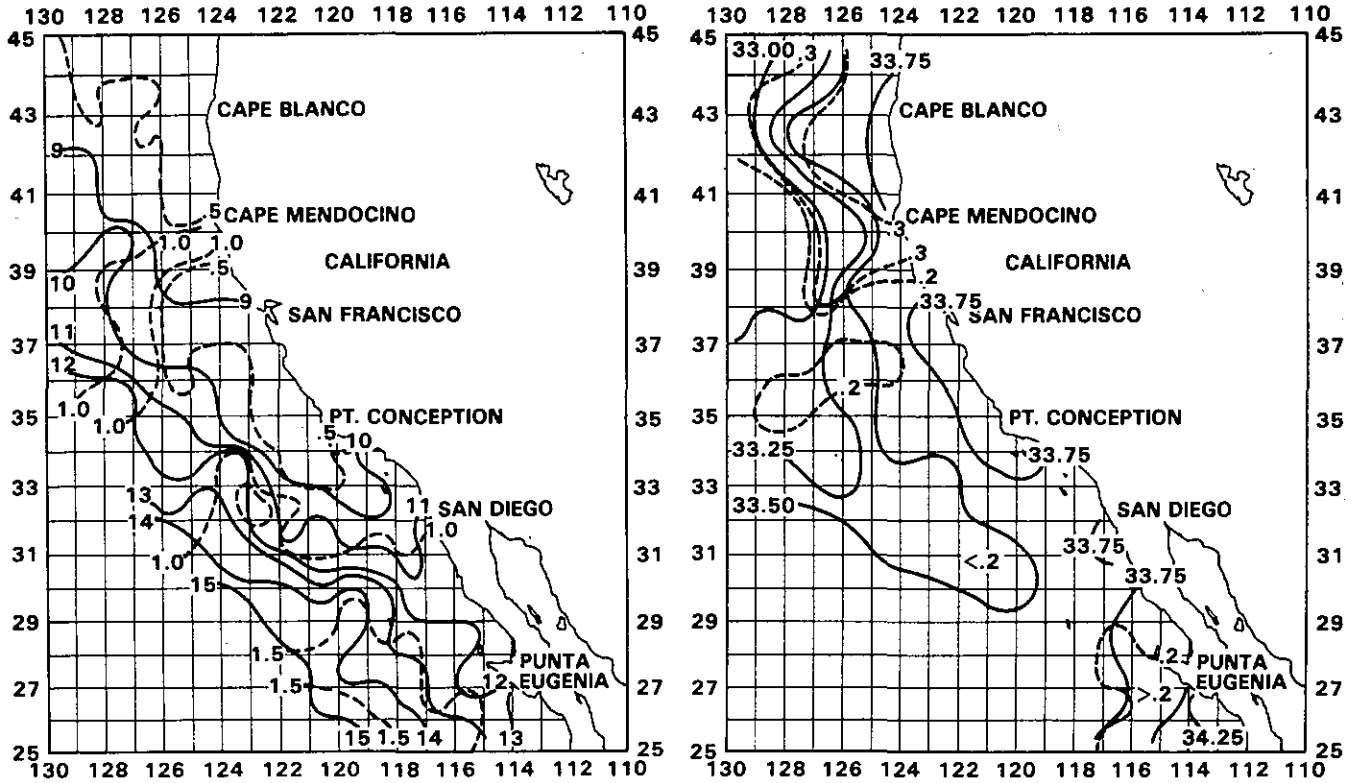

(a) Temperature (°C) – September, October

(b) Salinity (ppt) – September, October

(c) Sigma-t – September, October

(d) Dissolved Oxygen (ml/1) September, October

——Mean ——— Standard Deviation

Figure 5.20. Physical Properties at 100 m
September-October

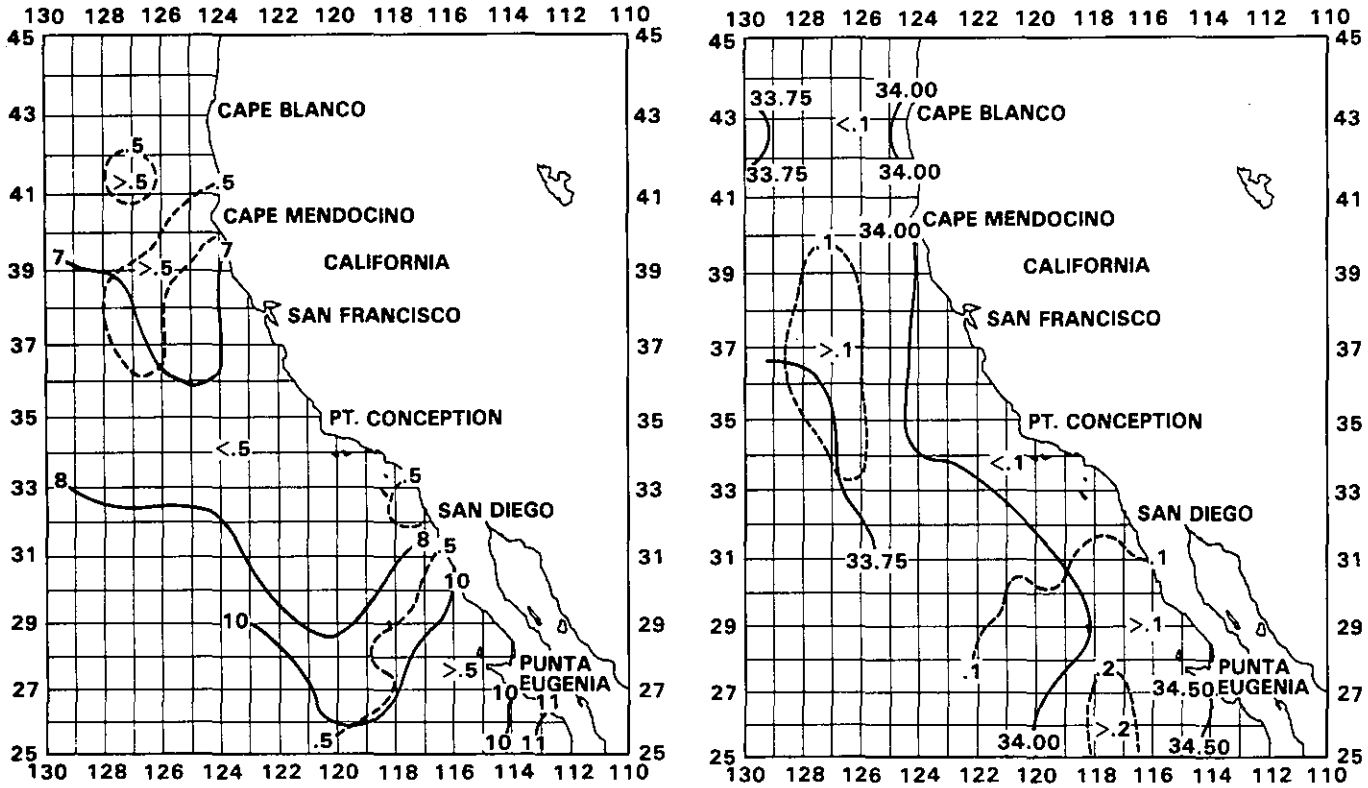

(a) Temperature (°C) – September, October

(b) Salinity (ppt) – September, October

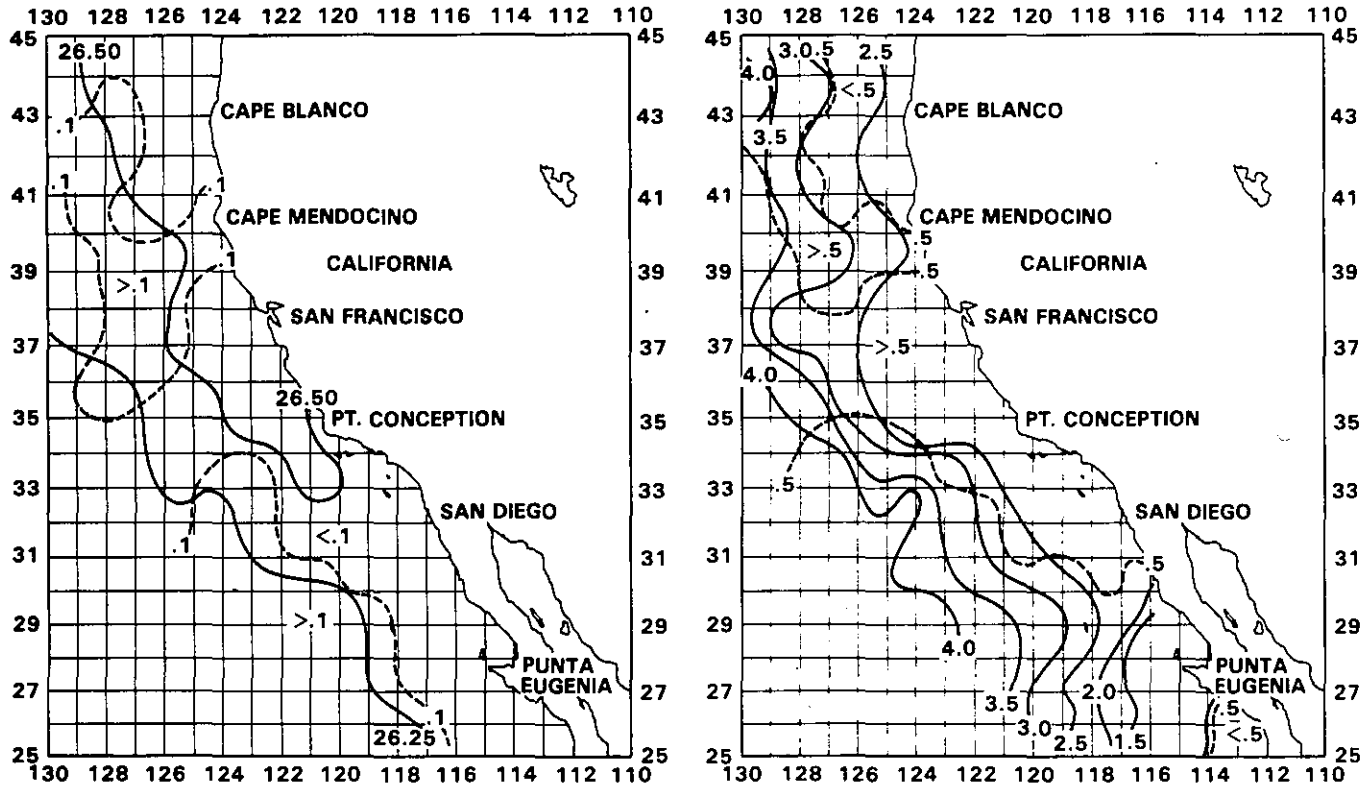

(c) Sigma-t – September, October

(d) Dissolved Oxygen (ml/l)
September, October

——Mean – – – Standard Deviation

Figure 5.21. Physical Properties at 200 m
September-October

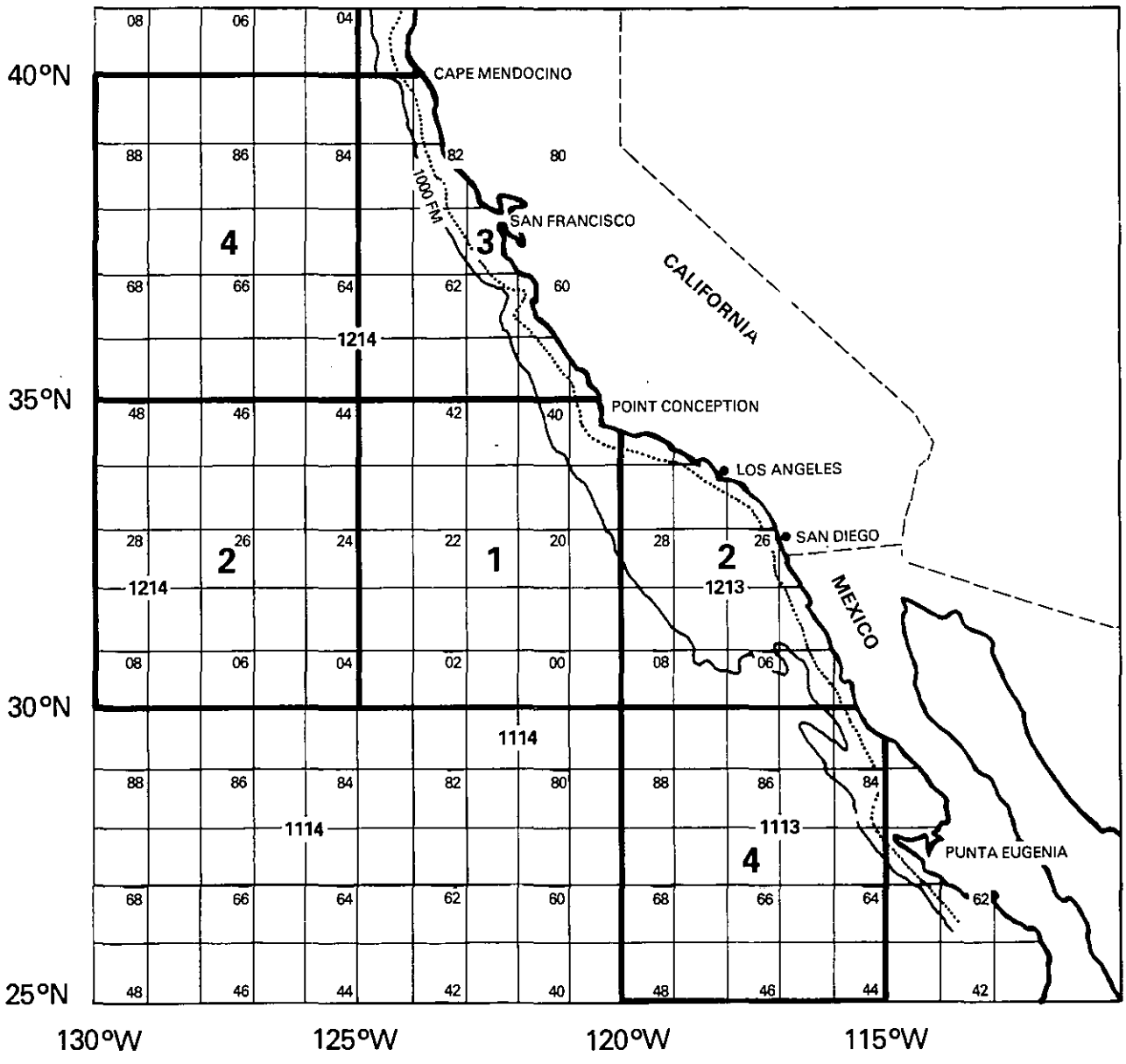

Figure 5.22 Data Summary Areas Used in Stability Analysis. (The large numerals denote the 5° square area within the 4-digit 10° square areas.)

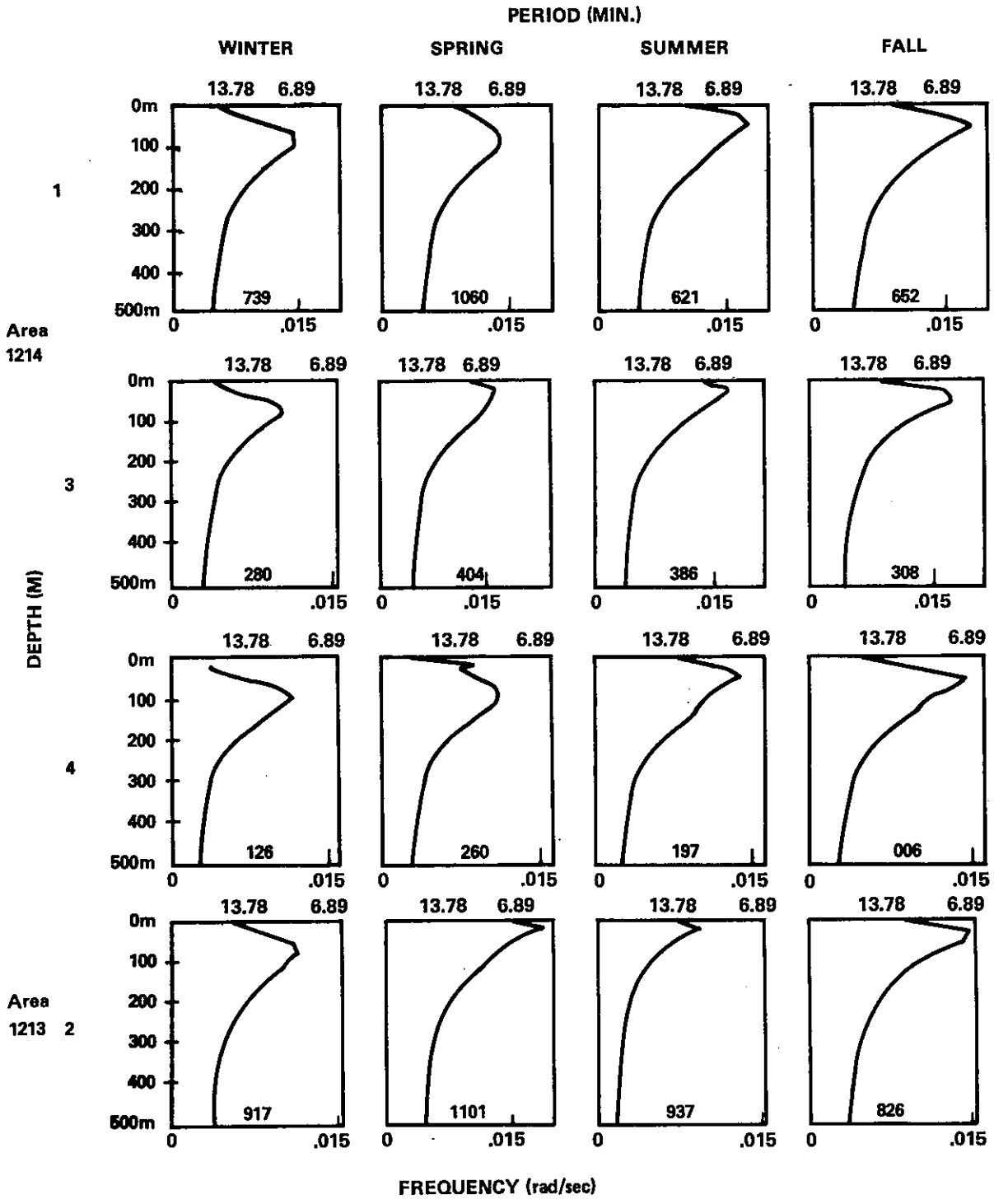

Figure 5.23 Water column stability for 5° summary areas as expressed by the Brunt-Vaisala frequency. (–) Brunt-Vaisala frequency is expressed in radians per second on the lower scale, and in terms of the period in minutes on the upper scale. The number of stations included in the average is indicated at the bottom of the frame. The 5° summary area within each 10° square is indicated by the large numbers on left (Bell, Mays, DeWitt, 1974).

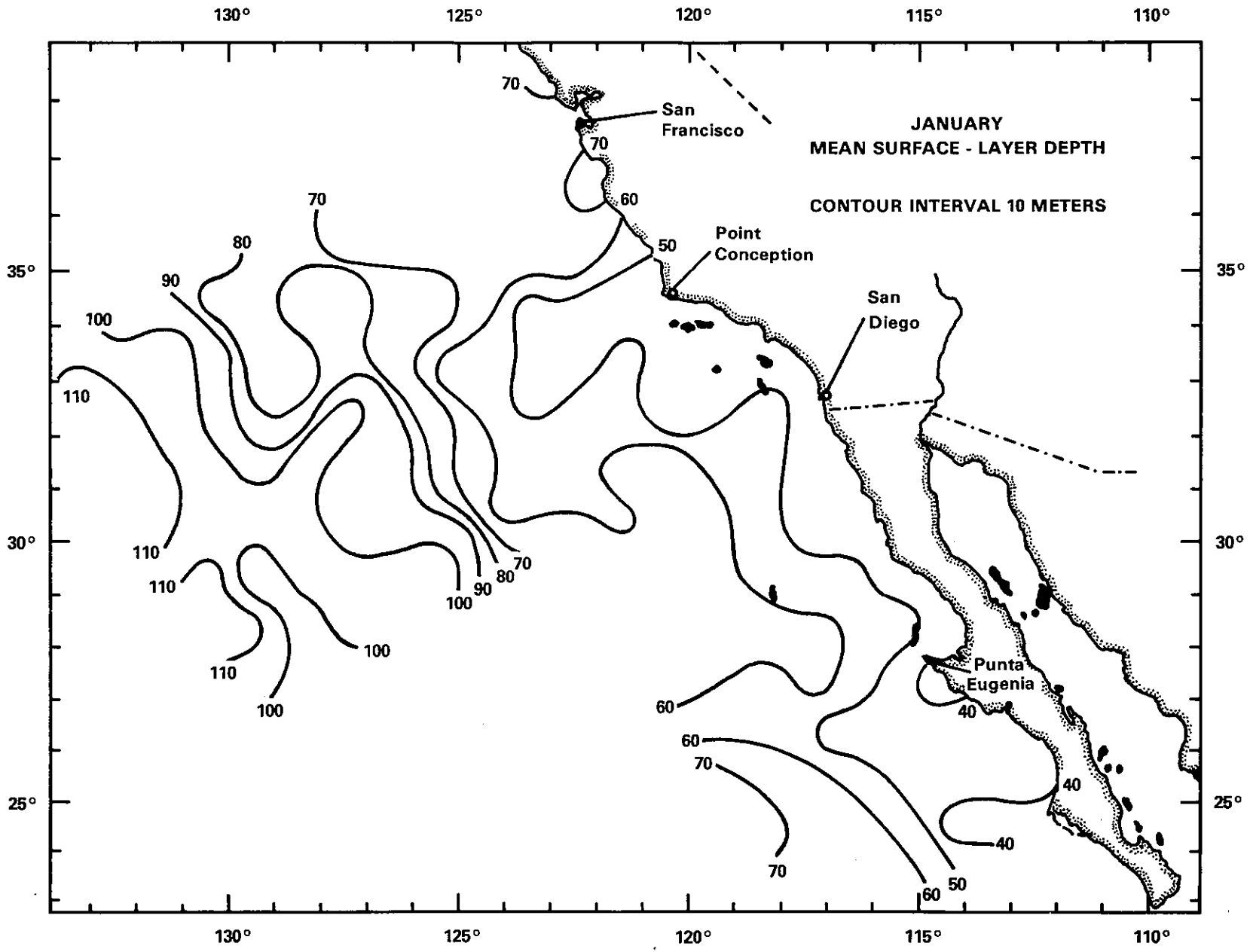

Figure 5.24(a). Mean Surface-Layer Depth, January (Wyllie and Lynn, 1971)

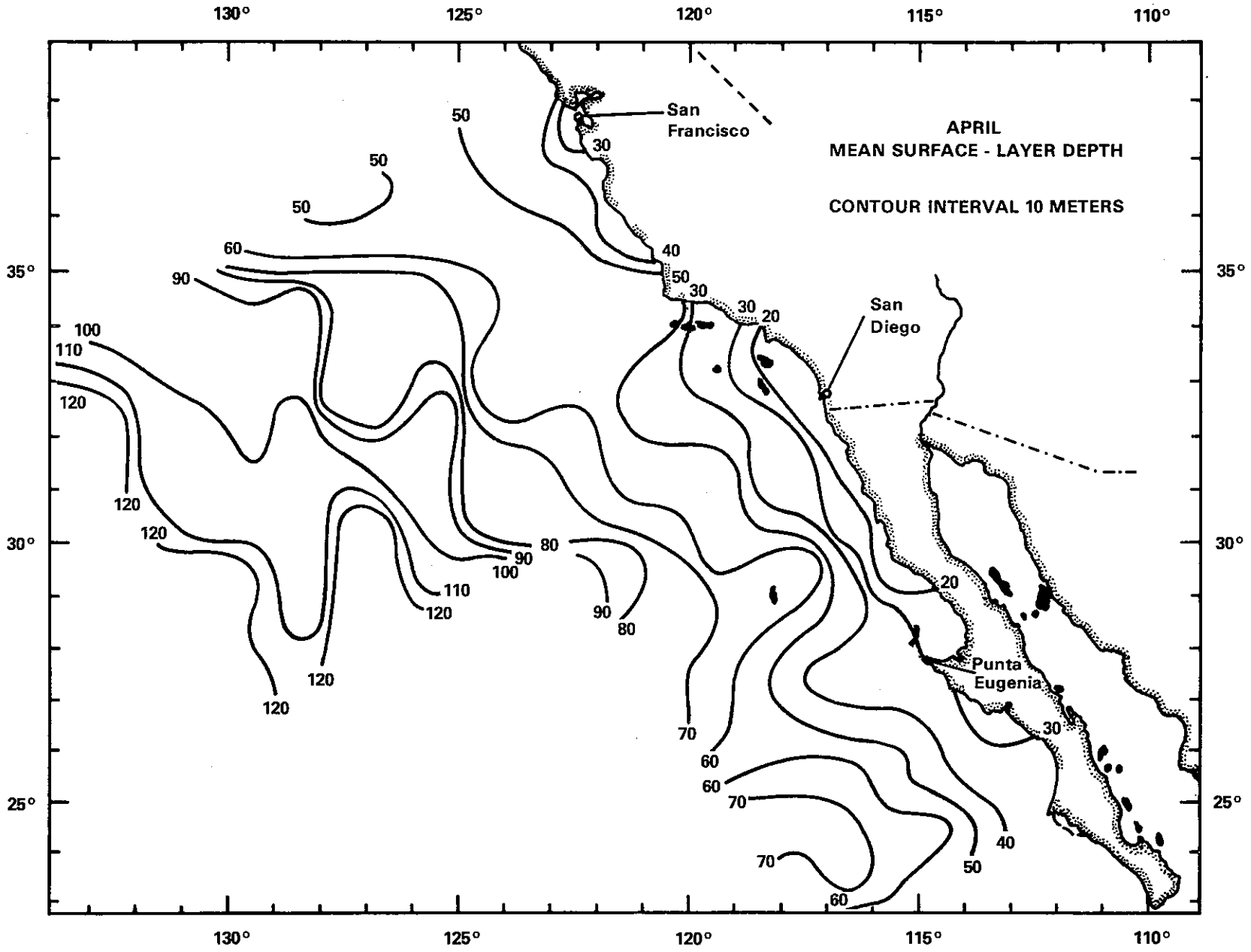

Figure 5.24(b). Mean Surface-Layer Depth, April (Wyllie and Lynn, 1971)

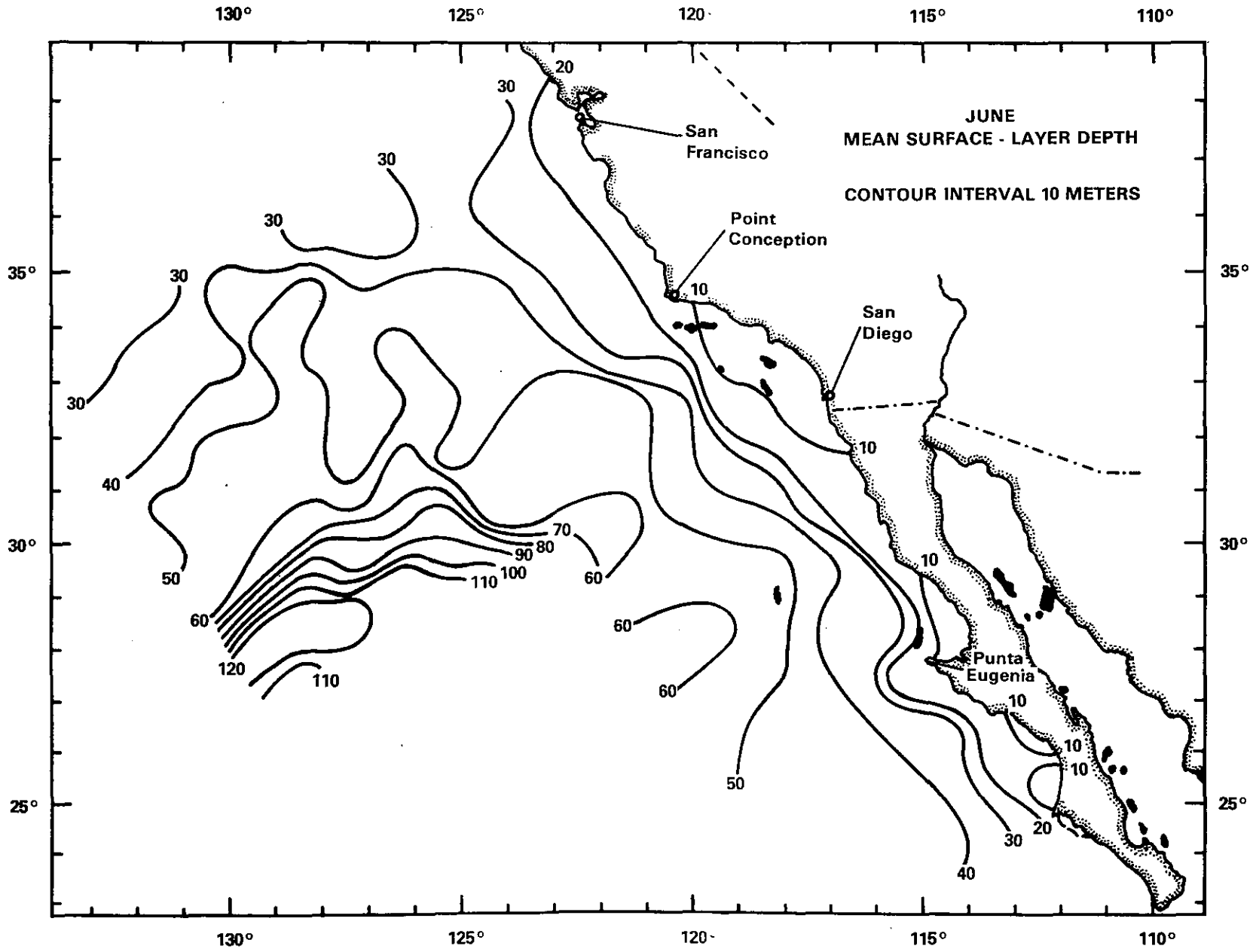

Figure 5.24(c). Mean Surface-Layer Depth, June (Wyllie and Lynn, 1971)

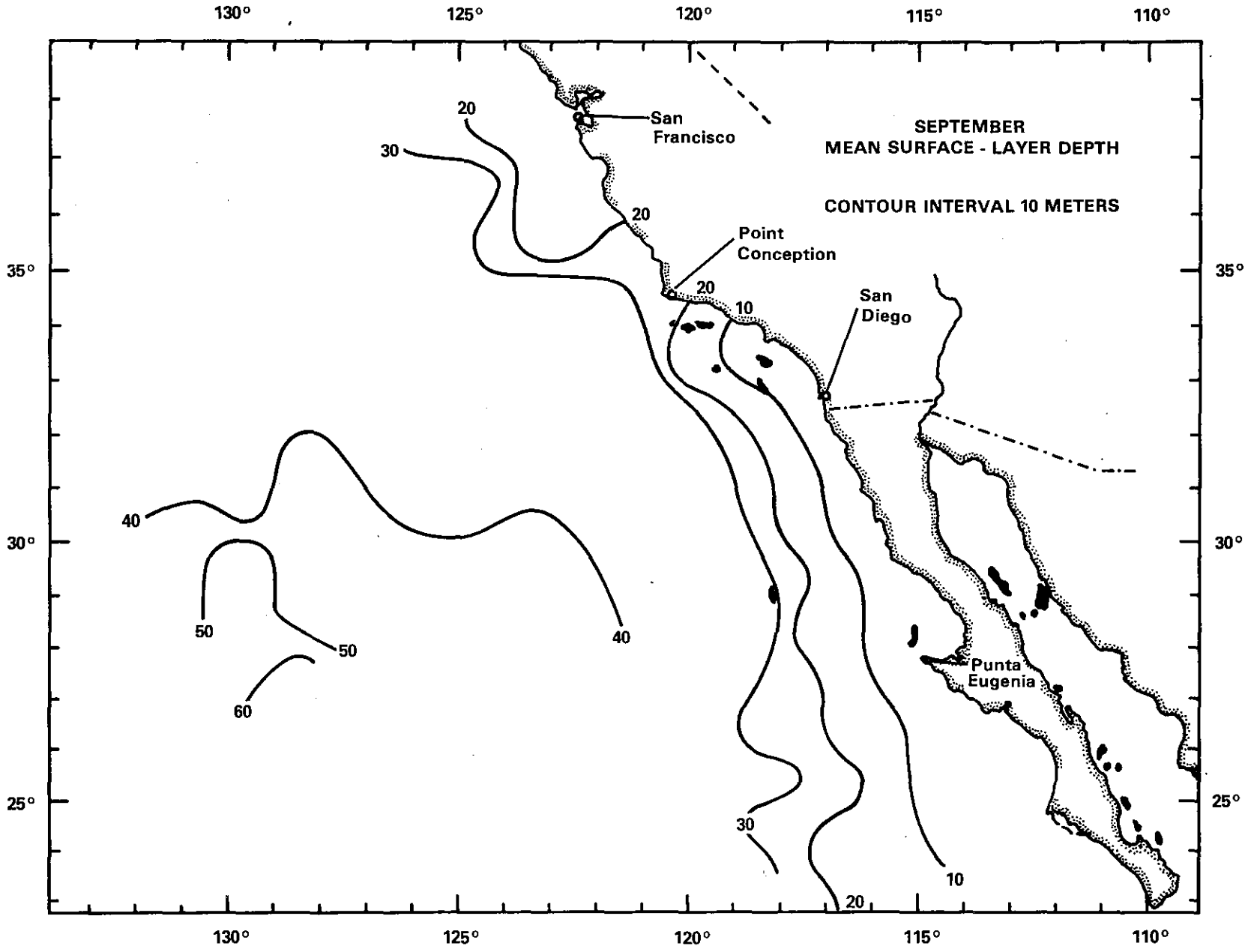

Figure 5.24(d). Mean Surface-Layer Depth, September (Wyllie and Lynn, 1971)

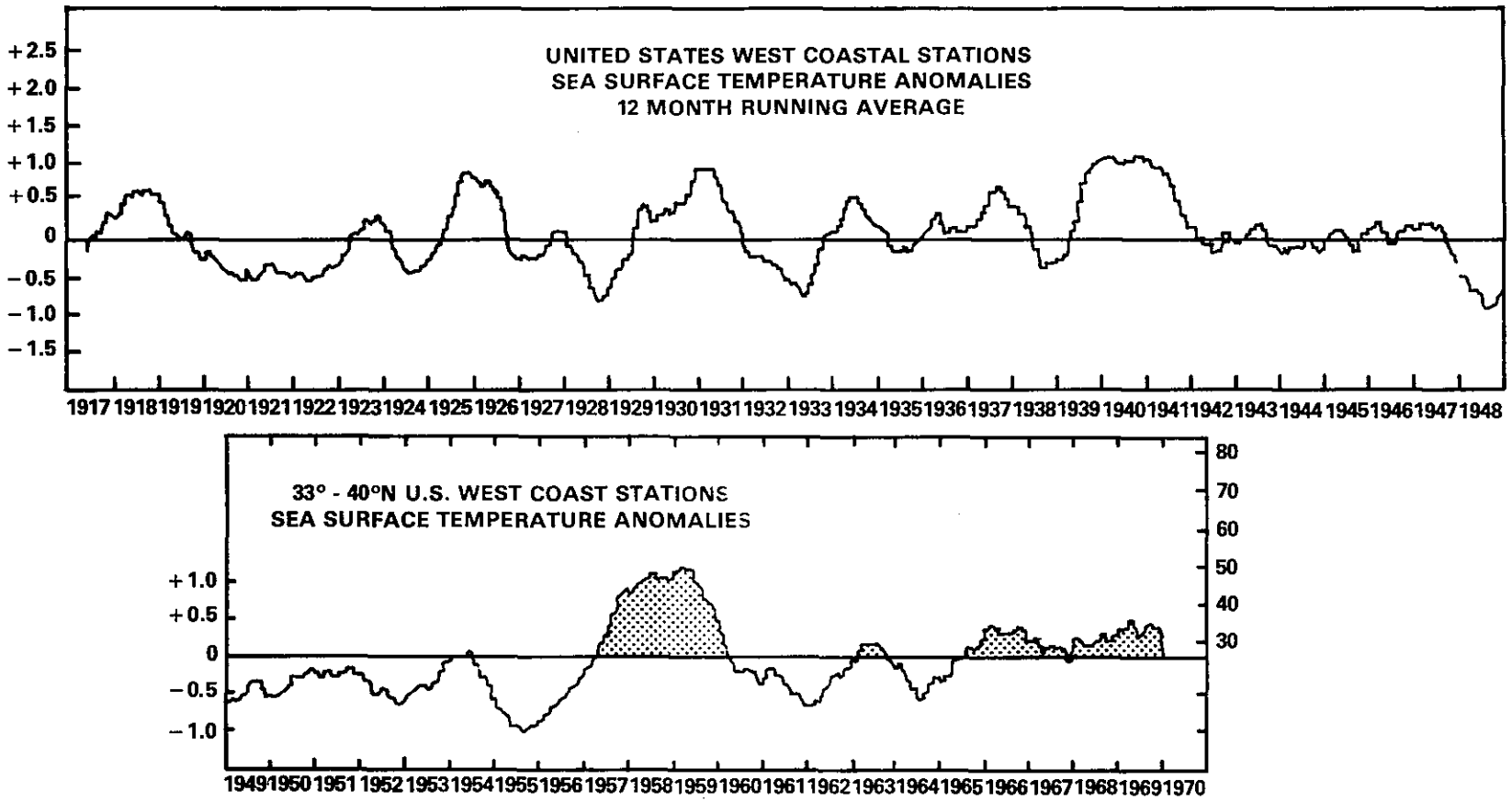

(a)

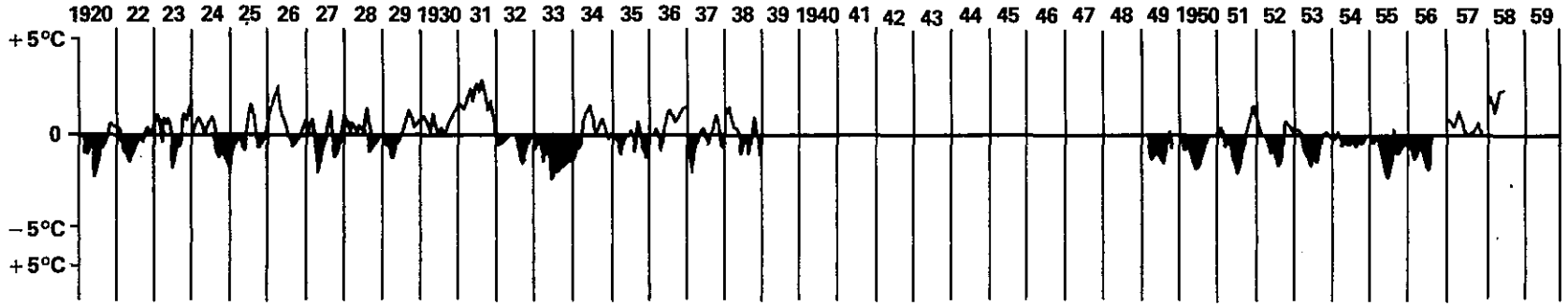

(b)

Figure 5.25 Water Temperature Anomalies (Reference 23)

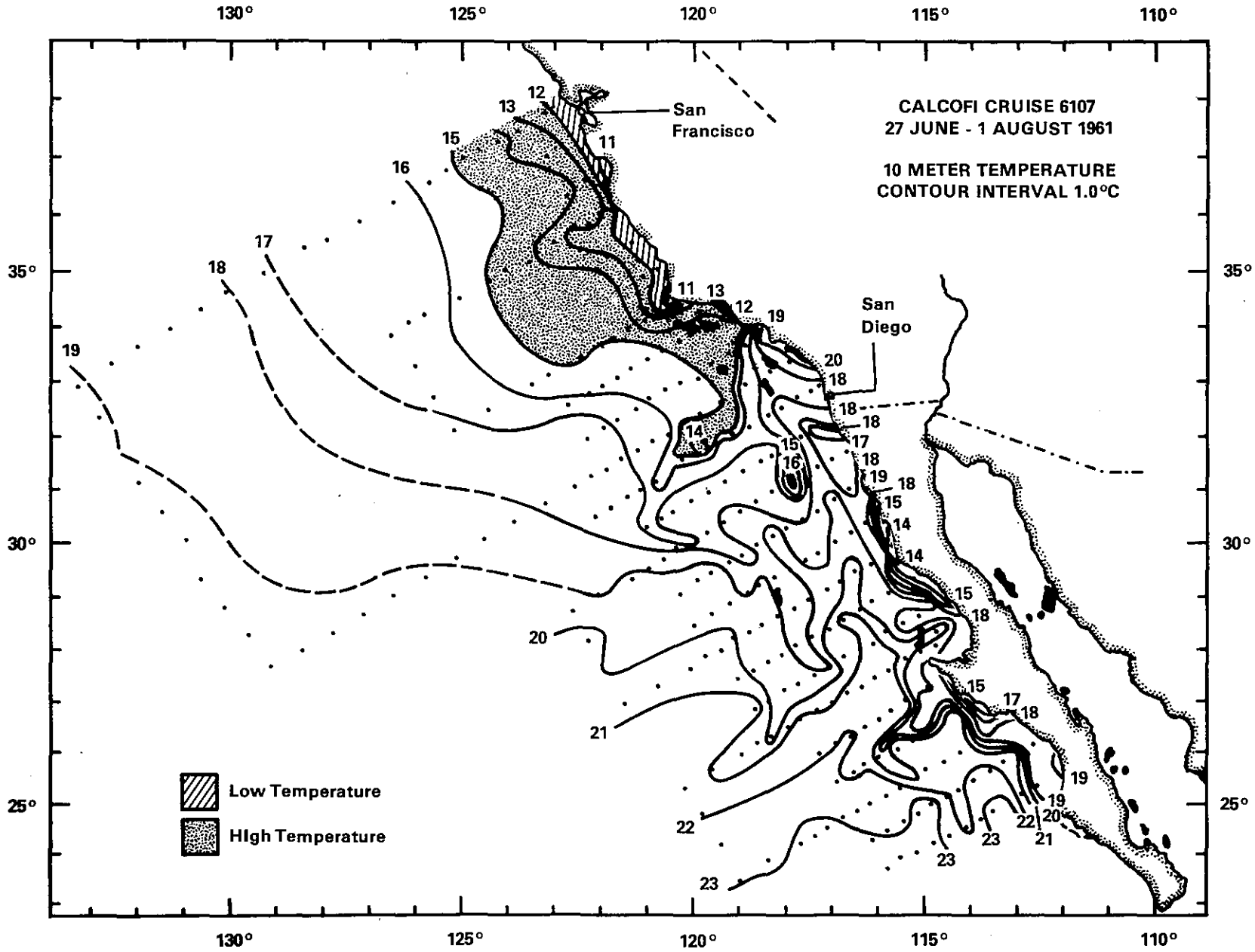

Figure 5.26 CALCOFI Cruise 6107 Contour Interval 1.0°C (Wyllie and Lynn, 1971)

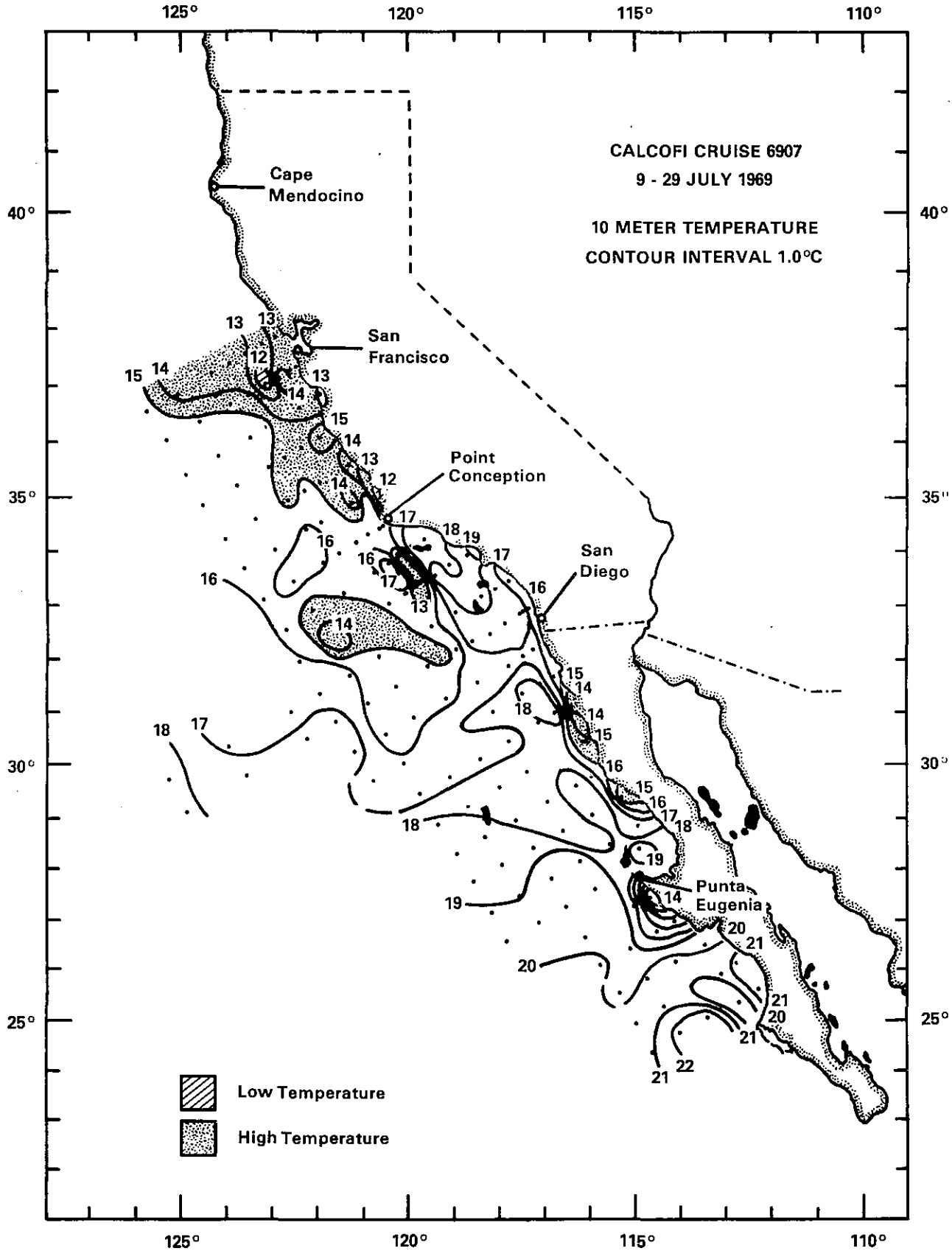

Figure 5.27 CALCOFI Cruise 6907 Contour Interval 1.0°C (Wyllie and Lynn, 1971)

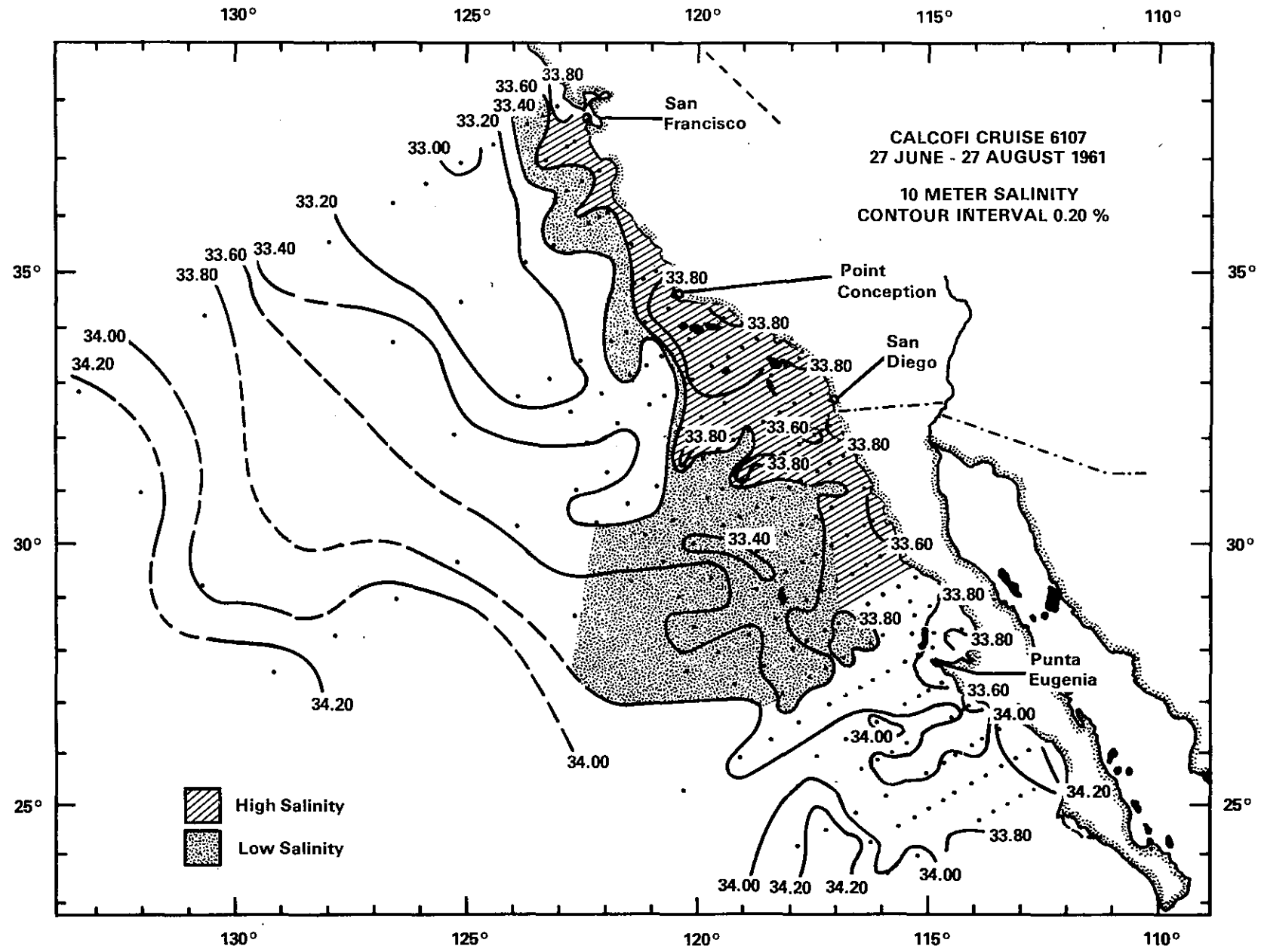

Figure 5.28 CALCOFI Cruise 6107 Contour Interval 0.20 percent (Wyllie and Lynn, 1971)

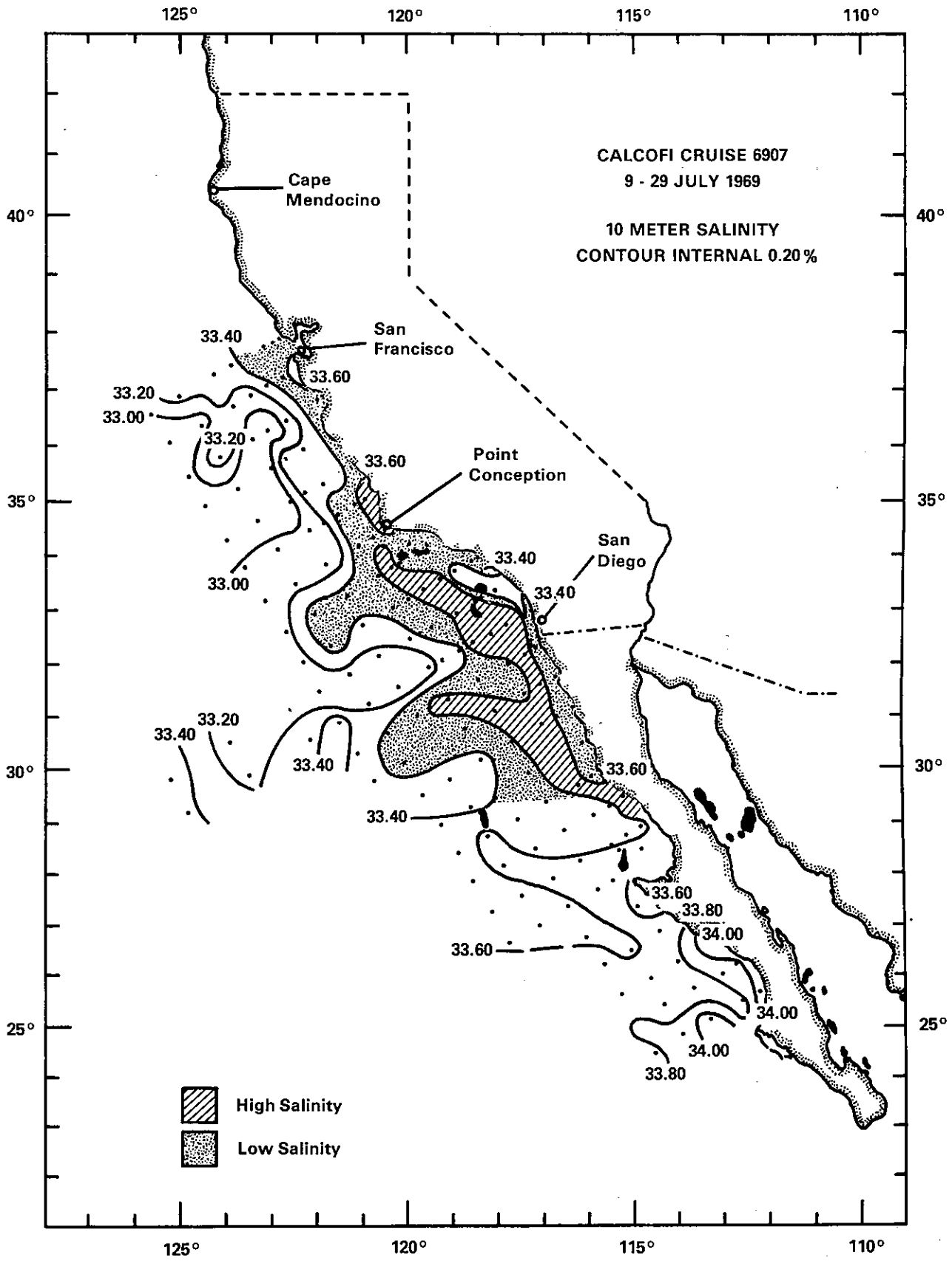

Figure 5.29 CALCOFI Cruise 6907 Contour Interval 0.20 percent (Wyllie and Lynn, 1971)

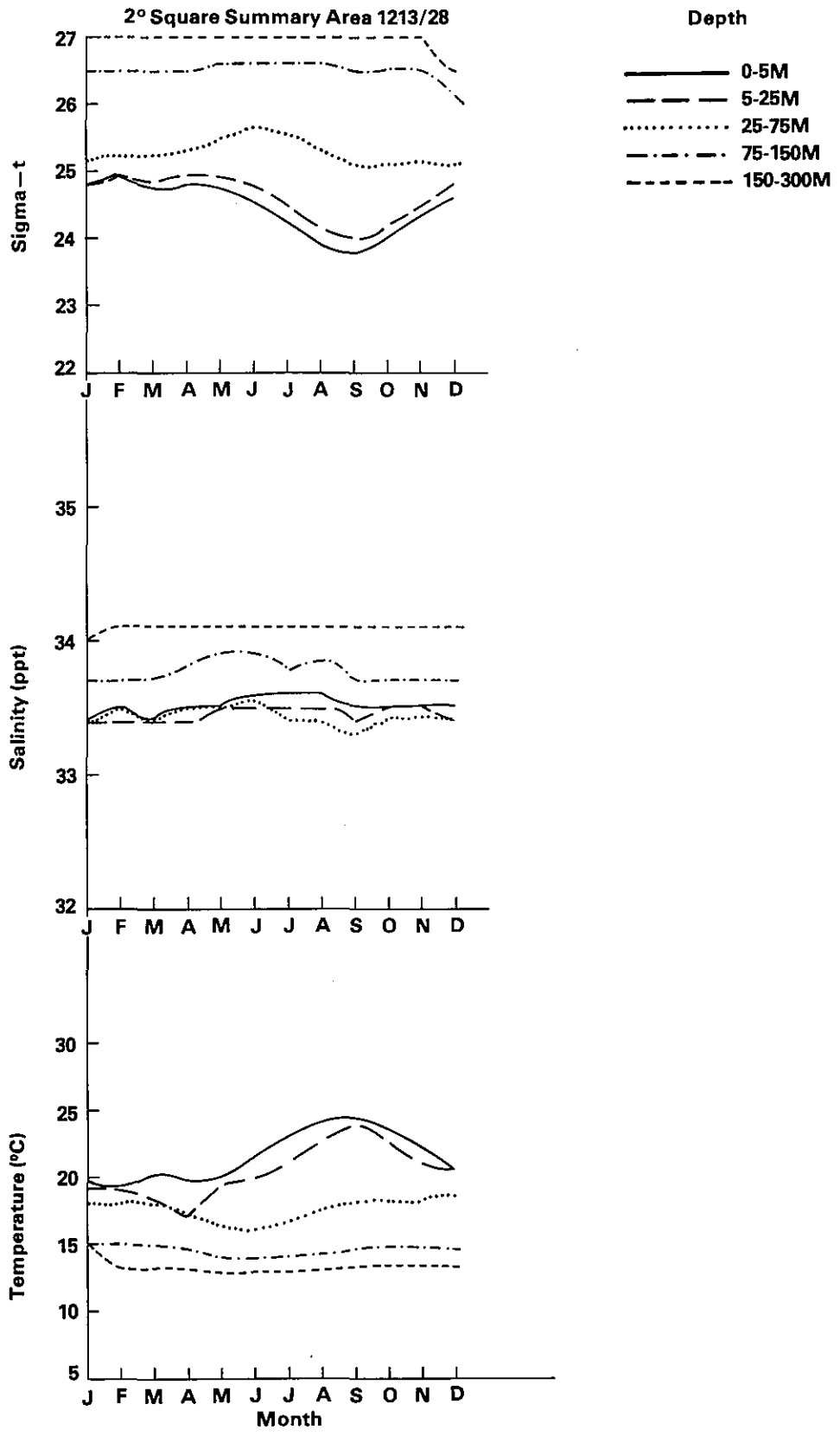

Figure 5.30(a) Monthly averages of temperature, salinity, and sigma-t for the layers indicated in the legend for the following summary areas: (a) 1213/28, (b) 1214/40, (c) 1214/46, (d) 1314/04. The locations of these areas are given in Figure 2.5.

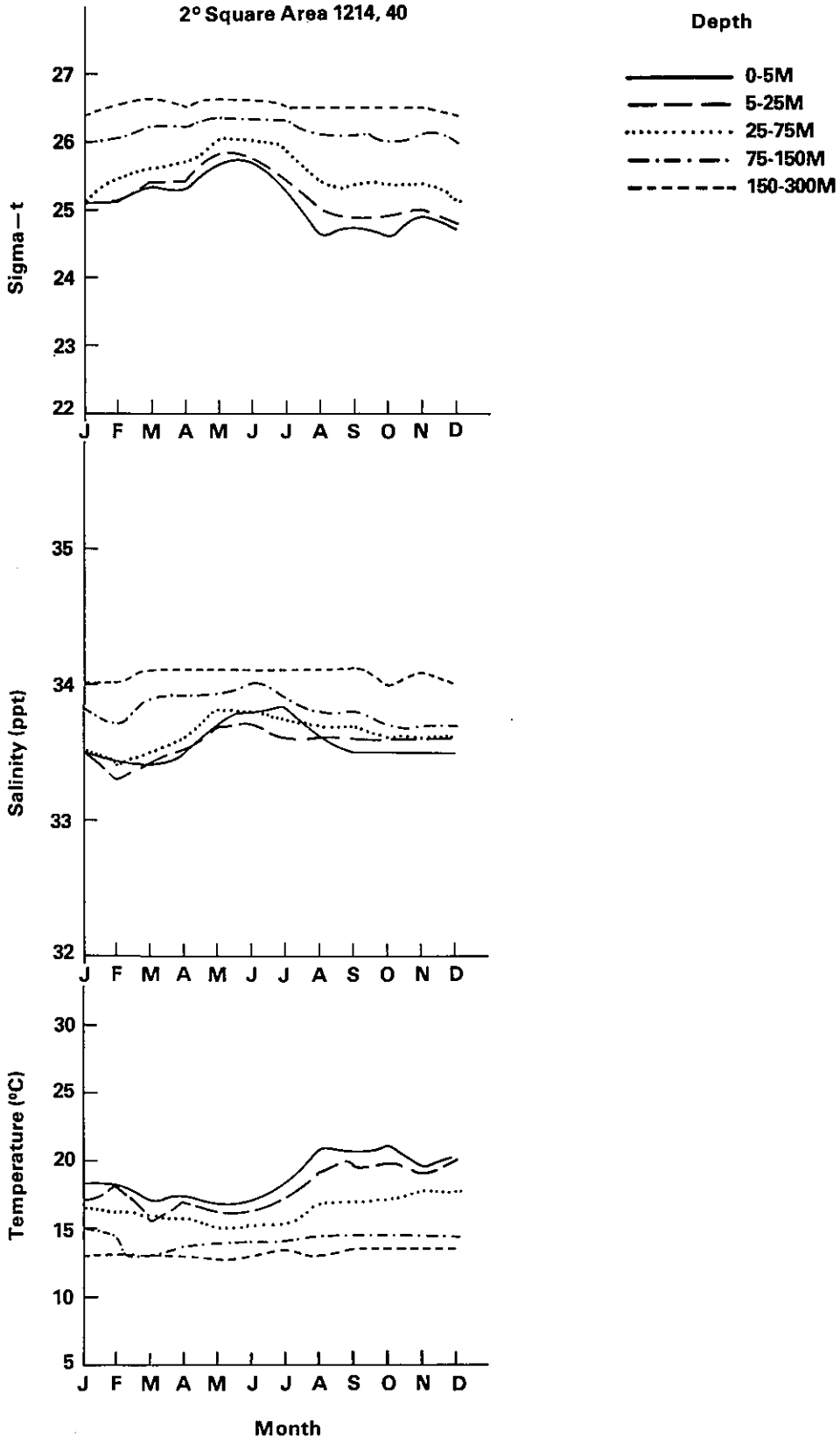

Figure 5.30(b). (Continued)

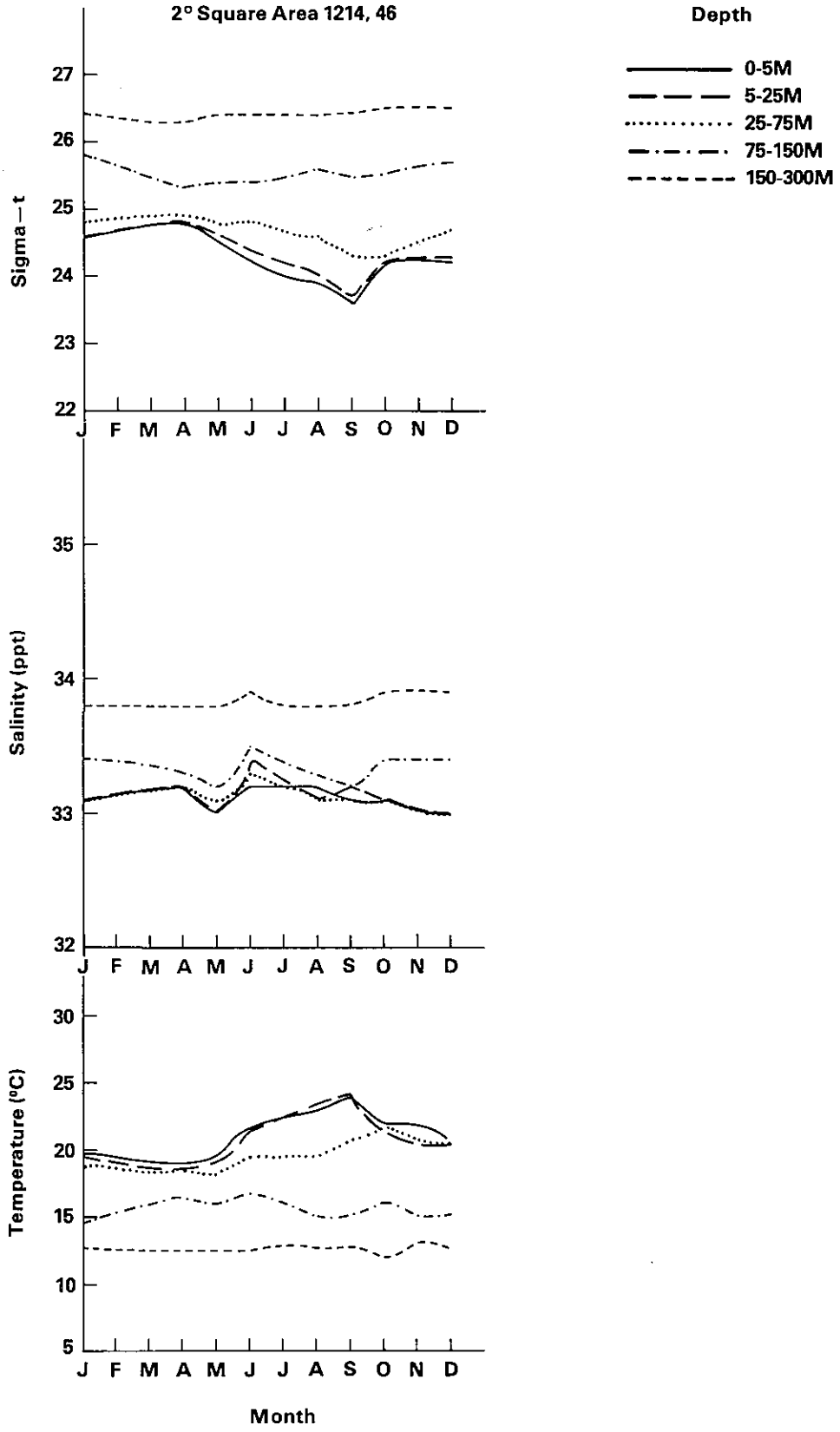

Figure 5.30(c). (Continued)

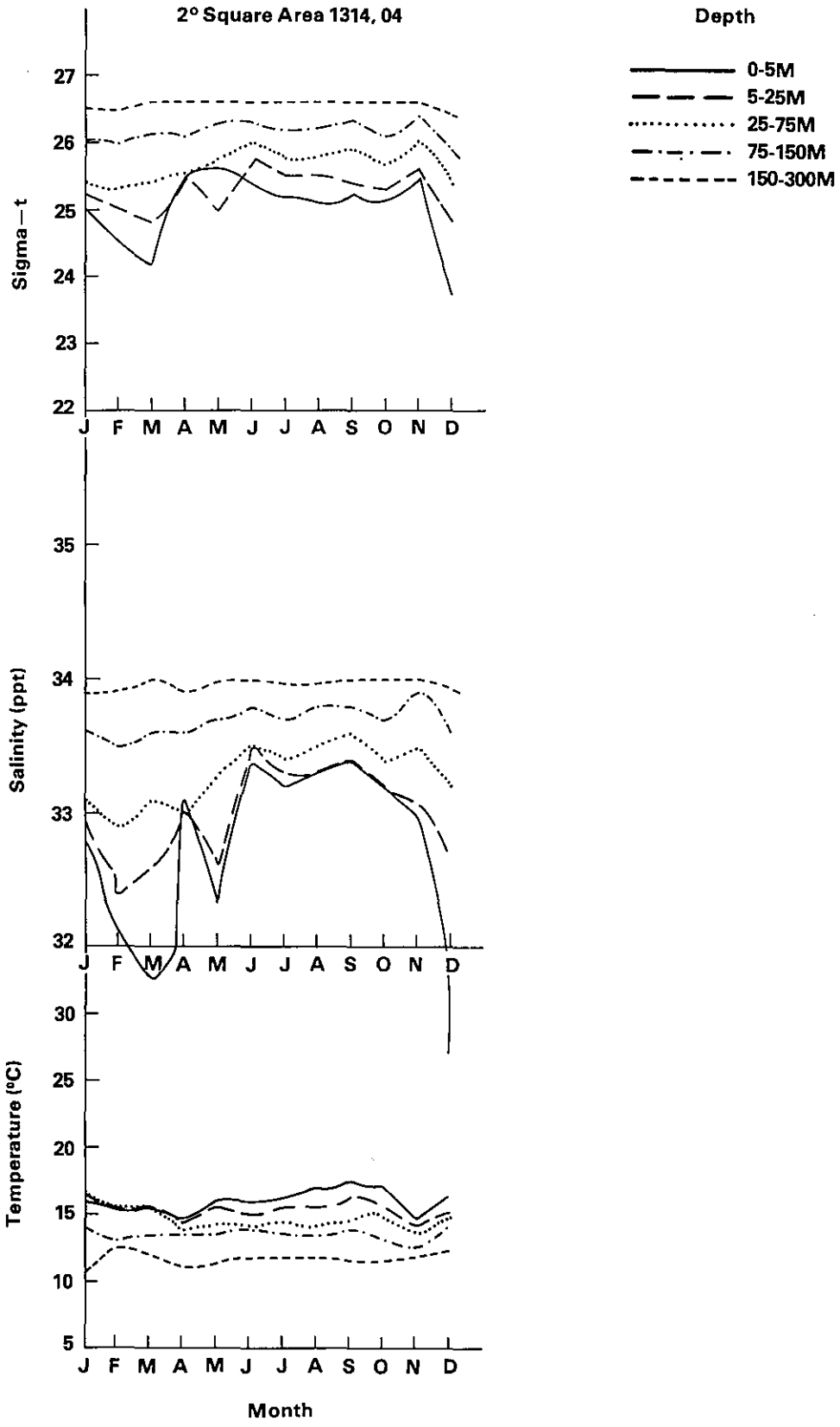

Figure 5.30(d). (Continued)

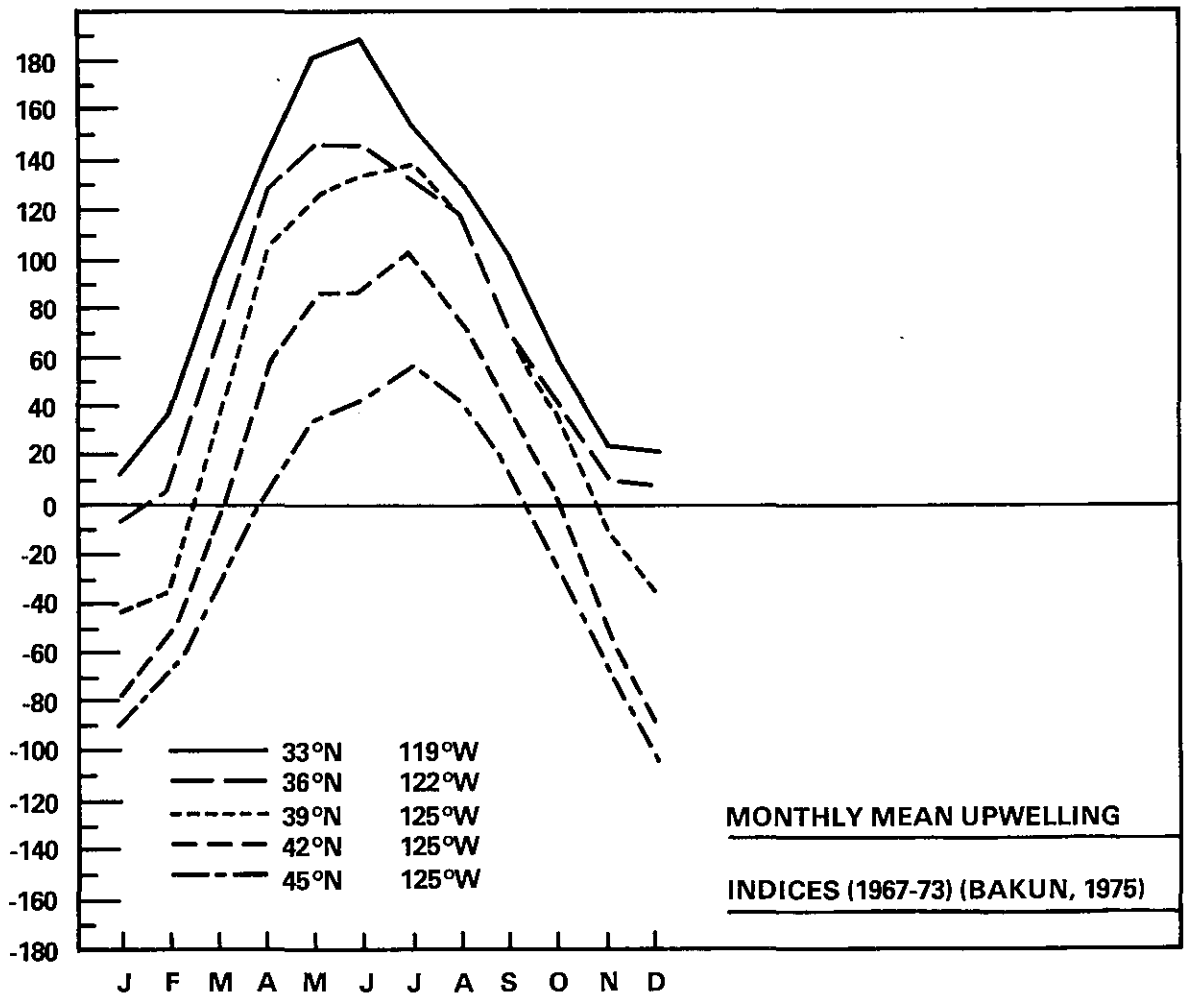

Figure 5.31. Seasonal variation of monthly mean upwelling indices, using results from Bakun (Reference 31). (The upwelling index is defined as the component of the computed Ekman Transport directed offshore.) Units are cubic meters-per second-per 100 m of shoreline.

6. NUTRIENT CHEMISTRY

S.W. Fehler

6.1 NITRATE

The data from the historical NODC archives are insufficient to draw any conclusions regarding the geographic distribution of nitrate. Only two one-degree squares (squares 61 and 62 of 10-degree square 1214) have a significant number of observations, and these have large standard deviations associated with the data (Figures 6.1 through 6.3). Square 1214-62 may show some influence of upwelling at the surface. The mean nitrate concentration during the Davidson season (December and January, Table 6.1) was 6.77 μg at/l (σ = 4.04); during the upwelling season (May-July, Table 6.2) the mean nitrate concentration was 8.95 μg at/l (σ = 5.52) but the differences are not statistically significant. The surface nitrate concentrations during the Oceanic season (September and October, Table 6.3) are significantly lower (μ = 2.42 μg at/l σ = 2.55 in square 1214-62) than during the other seasons (Figures 6.3 and 6.4).

The mean nitrate concentration increases with increasing depth. During the Oceanic season, the water structure is somewhat layered with lower nutrient concentrations in the surface region (0-25 m) overlaying the usual more concentrated regions. The increase of nitrate concentration with depth probably results from settling of detritus from dead organisms in combination with the microbial oxidation of ammonium to nitrate. This process is coupled to utilization of oxygen which results in a very strong statistical relationship between the apparent oxygen utilization and the nitrate concentration in a water mass (Reference 8). Thus, the dissolved oxygen concentration decreases with depth, whereas, the nitrate concentration increases with depth.

6.2 NITRITE

The limited number of nitrite observations in the NODC archives for the California region severely limits any discussion of the nitrite geographic distribution. During the Davidson season (December and January, Figure 6.5), there appears to be a region with elevated surface nitrite concentrations extending out from the San Francisco Bay, suggesting that the bay is the source of these high concentrations. A similar near-coastal elevation of surface nitrite concentration is found during the upwelling season (May through July, Figure 6.6). During the Oceanic period, there are not enough observations to draw any conclusions about the nitrite geographic distribution (Figure 6.7). The standard deviation of the nitrite observation is very large relative to the mean of the observations (Figure 6.8).

During the Davidson period of one-degree square 1214-62 (December and January, Table 6.4), nitrite concentrations are highest in the surface and near-surface waters, with the concentrations in the deepest water being the lowest. This behavior is distinctly unlike the other nutrients (nitrate, phosphate, and silicate) which typically have their greatest concentration at the greatest depth. During the Upwelling period (May through July, Table 6.5), the highest concentrations are typically at moderate depths (5-75 m), lower at the surface (0-5 m), and in the greatest depths (below 75 m). This variation with depth is also markedly different from the other nutrients and strongly suggests that it may be associated with the presence of marine phytoplankton or some associated activity such as predation. A quite similar depth distribution of nitrite concentration (Table 6.6) occurs during the Oceanic period (September and October). Unlike the other nutrients, the surface nitrite concentrations during the Oceanic period are not significantly different from those in the Davidson and Upwelling periods.

Table 6.1
Nitrate

DEGREE SQUARE		MONTH
1214	62	DECEMBER

STATISTICAL SUMMARY:

DEPTH RANGE	NUMBER SAMPLES	HIGHEST	LOWEST	RANGE	MEAN	STANDARD DEVIATION
ALL DEPTHS	155	48.100	0.0	48.100	18.245	11.826
0–5 M	22	17.900	0.0	17.900	8.745	6.784
5–25 M	29	21.800	0.0	21.800	9.924	7.512
25–75 M	31	30.200	0.0	30.200	12.419	8.985
75–150 M	18	27.700	3.200	24.500	18.044	7.397
150–300 M	24	35.100	7.900	27.200	24.329	5.897
BELOW 300 M	31	48.100	19.600	28.500	34.003	6.345

DEGREE SQUARE		MONTH
1214	62	JANUARY

STATISTICAL SUMMARY:

DEPTH RANGE	NUMBER SAMPLES	HIGHEST	LOWEST	RANGE	MEAN	STANDARD DEVIATION
ALL DEPTHS	159	40.000	1.600	38.400	17.828	10.255
0–5 M	23	14.400	2.500	11.900	8.191	2.769
5–25 M	29	18.800	1.600	17.200	9.655	3.603
25–75 M	31	24.200	3.800	20.400	12.164	4.633
75–150 M	22	24.500	8.800	15.700	17.095	3.829
150–300 M	22	32.700	17.500	15.200	23.841	3.754
BELOW 300 M	32	40.000	25.900	14.100	34.019	4.299

Table 6.2
Nitrate

DEGREE SQUARE	MONTH
1214 62	MAY

STATISTICAL SUMMARY:

DEPTH RANGE	NUMBER SAMPLES	HIGHEST	LOWEST	RANGE	MEAN	STANDARD DEVIATION
ALL DEPTHS	209	42.700	0.500	42.200	23.474	9.813
0–5 M	37	22.700	0.500	22.200	10.903	6.340
5–25 M	35	25.400	3.900	21.500	16.194	5.061
25–75 M	41	30.900	10.900	20.000	22.790	4.642
75–150 M	23	31.900	16.300	15.600	24.848	4.004
150–300 M	31	34.300	24.800	9.500	29.310	2.658
BELOW 300 M	42	42.700	27.500	15.200	36.224	3.942

DEGREE SQUARE	MONTH
1214 62	JUNE

STATISTICAL SUMMARY:

DEPTH RANGE	NUMBER SAMPLES	HIGHEST	LOWEST	RANGE	MEAN	STANDARD DEVIATION
ALL DEPTHS	200	45.300	2.500	42.800	23.074	10.086
0–5 M	35	20.700	2.500	18.200	9.406	4.710
5–25 M	32	21.900	3.900	18.000	15.384	4.599
25–75 M	39	28.100	13.900	14.200	22.226	3.180
75–150 M	25	30.500	15.300	15.200	25.040	4.096
150–300 M	32	38.900	15.600	23.300	29.381	4.782
BELOW 300 M	37	45.300	28.800	16.500	36.765	3.996

DEGREE SQUARE	MONTH
1214 62	JULY

STATISTICAL SUMMARY:

DEPTH RANGE	NUMBER SAMPLES	HIGHEST	LOWEST	RANGE	MEAN	STANDARD DEVIATION
ALL DEPTHS	168	46.000	0.200	45.800	22.372	11.089
0–5 M	25	17.800	0.200	17.600	5.728	5.579
5–25 M	28	24.700	0.200	24.500	13.507	6.754
25–75 M	33	29.500	7.600	21.900	21.454	5.010
75–150 M	20	30.600	19.500	11.100	25.560	3.352
150–300 M	24	33.200	19.800	13.400	27.954	3.721
BELOW 300 M	38	46.000	26.900	19.100	35.447	4.102

Table 6.3
Nitrate

DEGREE SQUARE	MONTH
1214 62	SEPTEMBER

STATISTICAL SUMMARY:

DEPTH RANGE	NUMBER SAMPLES	HIGHEST	LOWEST	RANGE	MEAN	STANDARD DEVIATION
ALL DEPTHS	112	43.200	0.0	43.200	17.147	13.674
0–5 M	19	9.200	0.100	9.100	3.063	2.619
5–25 M	19	13.200	0.0	13.200	3.505	4.199
25–75 M	26	26.800	0.400	26.400	13.081	7.929
75–150 M	13	30.300	17.300	13.000	23.177	3.812
150–300 M	17	41.000	18.700	22.300	28.235	6.672
BELOW 300 M	18	43.200	33.600	9.600	37.461	2.776

DEGREE SQUARE	MONTH
1214 62	OCTOBER

STATISTICAL SUMMARY:

DEPTH RANGE	NUMBER SAMPLES	HIGHEST	LOWEST	RANGE	MEAN	STANDARD DEVIATION
ALL DEPTHS	228	44.300	0.100	44.200	17.635	13.281
0–5 M	31	11.400	0.100	11.300	2.406	2.994
5–25 M	36	11.500	0.100	11.400	3.411	2.967
25–75 M	48	23.400	1.300	22.100	11.712	5.872
75–150 M	27	25.400	8.700	16.700	19.255	3.576
150–300 M	33	32.600	11.800	20.800	25.967	5.293
BELOW 300 M	53	44.300	17.200	27.100	35.555	4.552

Table 6.4
Nitrite

DEGREE SQUARE		MONTH
1214	62	DECEMBER

STATISTICAL SUMMARY:

DEPTH RANGE	NUMBER SAMPLES	HIGHEST	LOWEST	RANGE	MEAN	STANDARD DEVIATION
ALL DEPTHS	158	0.620	0.0	0.620	0.121	0.150
0–5 M	23	0.500	0.0	0.600	0.223	0.179
5–25 M	29	0.580	0.0	0.580	0.192	0.157
25–75 M	31	0.620	0.010	0.610	0.179	0.181
75–150 M	18	0.300	0.0	0.300	0.062	0.074
150–300 M	24	0.070	0.0	0.070	0.027	0.018
BELOW 300 M	33	0.100	0.0	0.100	0.032	0.028

DEGREE SQUARE		MONTH
1214	62	JANUARY

STATISTICAL SUMMARY:

DEPTH RANGE	NUMBER SAMPLES	HIGHEST	LOWEST	RANGE	MEAN	STANDARD DEVIATION
ALL DEPTHS	188	1.210	0.0	1.210	0.185	0.217
0–5 M	26	1.020	0.030	0.990	0.273	0.189
5–25 M	33	1.090	0.040	1.050	0.325	0.236
25–75 M	42	1.210	0.010	1.200	0.270	0.246
75–150 M	32	0.830	0.0	0.830	0.108	0.181
150–300 M	24	0.080	0.0	0.080	0.030	0.025
BELOW 300 M	31	0.180	0.0	0.180	0.044	0.050

Table 6.5
Nitrite

DEGREE SQUARE	MONTH
1214 62	MAY

STATISTICAL SUMMARY:

DEPTH RANGE	NUMBER SAMPLES	HIGHEST	LOWEST	RANGE	MEAN	STANDARD DEVIATION
ALL DEPTHS	207	0.650	0.0	0.650	0.190	0.143
0–5 M	38	0.390	0.050	0.340	0.237	0.102
5–25 M	33	0.450	0.040	0.410	0.294	0.092
25–75 M	38	0.650	0.020	0.630	0.302	0.147
75–150 M	24	0.370	0.0	0.370	0.193	0.113
150–300 M	31	0.380	0.0	0.380	0.085	0.085
BELOW 300 M	43	0.160	0.0	0.160	0.041	0.031

DEGREE SQUARE	MONTH
1214 62	JUNE

STATISTICAL SUMMARY:

DEPTH RANGE	NUMBER SAMPLES	HIGHEST	LOWEST	RANGE	MEAN	STANDARD DEVIATION
ALL DEPTHS	226	0.850	0.0	0.850	0.220	0.195
0–5 M	38	0.560	0.010	0.550	0.260	0.168
5–25 M	36	0.650	0.030	0.620	0.329	0.155
25–75 M	49	9.850	0.020	0.830	0.337	0.229
75–150 M	32	0.480	0.0	0.480	0.168	0.152
150–300 M	33	0.670	0.010	0.660	0.118	0.138
BELOW 300 M	38	0.390	0.0	0.390	0.056	0.072

DEGREE SQUARE	MONTH
1214 62	JULY

STATISTICAL SUMMARY:

DEPTH RANGE	NUMBER SAMPLES	HIGHEST	LOWEST	RANGE	MEAN	STANDARD DEVIATION
ALL DEPTHS	222	0.520	0.0	0.520	0.109	0.130
0–5 M	31	0.320	0.0	0.320	0.098	0.093
5–25 M	37	0.520	0.0	0.520	0.201	0.158
25–75 M	45	0.470	0.0	0.470	0.205	0.138
75–150 M	32	0.280	0.0	0.280	0.060	0.085
150–300 M	32	0.350	0.0	0.350	0.045	0.078
BELOW 300 M	45	0.140	0.0	0.140	0.025	0.033

Table 6.6
Nitrite

DEGREE SQUARE		MONTH
1214	62	SEPTEMBER

STATISTICAL SUMMARY:

DEPTH RANGE	NUMBER SAMPLES	HIGHEST	LOWEST	RANGE	MEAN	STANDARD DEVIATION
ALL DEPTHS	113	1.150	0.0	1.150	0.182	0.215
0–5 M	19	0.520	0.0	0.520	0.229	0.160
5–25 M	19	0.930	0.0	0.930	0.223	0.231
25–75 M	26	1.150	0.030	1.120	0.336	0.288
75–150 M	13	0.400	0.020	0.380	0.135	0.130
150–300 M	17	0.150	0.0	0.150	0.055	0.039
BELOW 300 M	19	0.110	0.0	0.110	0.032	0.029

DEGREE SQUARE		MONTH
1214	62	OCTOBER

STATISTICAL SUMMARY:

DEPTH RANGE	NUMBER SAMPLES	HIGHEST	LOWEST	RANGE	MEAN	STANDARD DEVIATION
ALL DEPTHS	240	0.660	0.0	0.660	0.125	0.158
0–5 M	33	0.640	0.0	0.640	0.189	0.182
5–25 M	39	0.560	0.0	0.560	0.162	0.153
25–75 M	52	0.660	0.0	0.660	0.243	0.198
75–150 M	29	0.280	0.0	0.280	0.074	0.067
150–300 M	34	0.190	0.0	0.190	0.036	0.044
BELOW 300 M	53	0.140	0.0	0.140	0.027	0.027

6.3 PHOSPHATE

Orthophosphate (as $H_2 PO_4^-$ and HPO_4^{2-} ions with negligible amounts of PO_4^{3-} or free phosphoric acid) is the major inorganic form of phosphorus in seawater (Reference 11) utilized by phytoplankton. Organic phosphorus compounds found in estuarine and marine waters (Reference 12) may equal or exceed the concentration of inorganic orthophosphate. Many species of phytoplankters contain enzyme systems (i.e., alkaline phosphatases and acid phosphatases) which can hydrolyze the extracellular organic phosphates to inorganic orthosphosphate (References 13, 14, 15 and 16). The phytoplankton can then take up the inorganic phosphate and utilize it for growth.

The geographic distribution of archived surface layer phosphate observations in the NODC data is more extensive than for the other nutrients. No clear patterns or gradients exist in any season within the area of this report (Davidson, Upwelling, and Oceanic, Figures 6.9, 6.10 and 6.11 respectively). Some small-scale (i.e., one-degree square) patchiness is seen when the average phosphate concentrations are examined, but these differences in concentrations are statistically insignificant. The surface phosphate concentrations are not significantly different during the Davidson (December and January, Figure 6.9) and Upwelling seasons (May through July, Figure 6.10) but may be somewhat lower in the Oceanic season (September and October, Figure 6.11).

The large-scale variations in surface layer orthophosphate concentration in the Pacific are related to surface divergence; high in cyclones and regions of upwelling, and low in anticyclones (Reference 18). Zooplankton population is positively correlated with the phosphate concentration in the Pacific gyres (Reference 17).

Phosphate and orthophosphate (Reference 19) concentrations increase with depth during each season (Tables 6.7, 6.8, and 6.9). The increase with depth is usually related to the settling of the detrital remains of living organisms, although this process can be obscured by the presence of differing water mass having differing life histories and thus, differing phosphate concentrations.

Organic phosphorus compounds are hydrolyzed and oxidized by microbial action during the detrital settling process. Living phytoplankton and zooplankton can also excrete organic phosphorus (References 20 and 21). The oxidative process consumes oxygen, and in deep water there is usually a strong negative correlation between the orthophosphate concentration and the dissolved oxygen (see Reference 6).

6.4 SILICON

Geochemical and biological processes affect the concentration of silicon in seawater which is generally undersaturated with respect to dissolved silicon (References 22 and 23). Rapid growth by diatoms or other silicon-requiring organisms can deplete the silicon in a given water mass; however, the silicon may redissolve into seawater following the death of the organisms.

The solubility of silicon varies with the temperature and ionic state of the seawater. The presence of aluminum and magnesium ions may cause amorphous silica to precipitate, whereas increased temperature and pH increases its solubility. Most silica in seawater probably exists as orthosilicic acid ($Si(OH)_4$), which is in equilibrium with ionized silicate (mostly $SiO(OH)_3$). The usual analysis for silicate, involving the colorimetric analysis of the product of an acid molybdate reaction, probably responds to some extent to colloidal and solid silica as well as the ionic silicate. However, diatoms can utilize all of the silicon that responds to the usual assay (Reference 24). In one study, it has been suggested that the silicon available in the seawater passed through ten phytoplankton life cycles in one season (Reference 25).

Table 6.7
Phosphate

DEGREE SQUARE	MONTH
1214 62	DECEMBER

STATISTICAL SUMMARY:

DEPTH RANGE	NUMBER SAMPLES	HIGHEST	LOWEST	RANGE	MEAN	STANDARD DEVIATION
ALL DEPTHS	148	3.770	0.400	3.370	1.869	0.875
0–5 M	21	1.480	0.400	1.080	1.110	0.360
5–25 M	28	2.110	0.420	1.690	1.158	0.460
25–75 M	28	2.010	0.500	1.510	1.317	0.471
75–150 M	17	2.450	1.160	1.290	1.800	0.348
150–300 M	22	3.530	1.970	1.560	2.473	0.351
BELOW 300 M	32	3.770	2.550	1.220	3.092	0.303

DEGREE SQUARE	MONTH
1214 62	JANUARY

STATISTICAL SUMMARY:

DEPTH RANGE	NUMBER SAMPLES	HIGHEST	LOWEST	RANGE	MEAN	STANDARD DEVIATION
ALL DEPTHS	204	3.600	0.490	3.110	1.580	0.820
0–5 M	29	1.270	0.500	0.770	0.890	0.184
5–25 M	36	1.380	0.490	0.890	0.920	0.197
25–75 M	50	1.720	0.490	1.230	1.144	0.323
75–150 M	33	2.060	0.760	1.300	1.622	0.311
150–300 M	24	3.250	1.610	1.640	2.256	0.322
BELOW 300 M	32	3.600	2.620	0.980	3.076	0.262

Table 6.8
Phosphate

DEGREE SQUARE	MONTH
1214 62	MAY

STATISTICAL SUMMARY:

DEPTH RANGE	NUMBER SAMPLES	HIGHEST	LOWEST	RANGE	MEAN	STANDARD DEVIATION
ALL DEPTHS	231	3.700	0.320	3.380	2.129	0.778
0–5 M	41	2.020	0.320	1.700	1.156	0.517
5–25 M	38	2.070	0.760	1.310	1.482	0.394
25–75 M	42	2.520	1.480	1.040	1.991	0.230
75–150 M	24	2.770	1.890	0.880	2.259	0.208
150–300 M	34	3.090	2.220	0.870	2.564	0.196
BELOW 300 M	52	3.700	2.570	1.130	3.136	0.249

DEGREE SQUARE	MONTH
1214 62	JUNE

STATISTICAL SUMMARY:

DEPTH RANGE	NUMBER SAMPLES	HIGHEST	LOWEST	RANGE	MEAN	STANDARD DEVIATION
ALL DEPTHS	250	3.580	0.210	3.370	1.966	0.780
0–5 M	39	1.820	0.210	1.610	0.973	0.463
5–25 M	38	2.060	0.490	1.570	1.359	0.479
25–75 M	58	2.660	0.480	2.180	1.839	0.420
75–150 M	37	2.510	1.040	1.470	2.126	0.326
150–300 M	37	3.160	1.460	1.700	2.420	0.308
BELOW 300 M	41	3.580	2.490	1.090	3.098	0.277

DEGREE SQUARE	MONTH
1214 62	JULY

STATISTICAL SUMMARY:

DEPTH RANGE	NUMBER SAMPLES	HIGHEST	LOWEST	RANGE	MEAN	STANDARD DEVIATION
ALL DEPTHS	252	3.550	0.100	3.450	1.980	0.863
0–5 M	33	1.620	0.100	1.520	0.675	0.473
5–25 M	41	2.060	0.150	1.910	1.198	0.511
25–75 M	48	2.310	0.770	1.540	1.790	0.384
75–150 M	35	2.810	1.870	0.940	2.157	0.195
150–300 M	37	2.880	1.550	1.330	2.452	0.235
BELOW 300 M	58	3.550	2.180	1.370	3.023	0.259

Table 6.9
Phosphate

DEGREE SQUARE		MONTH
1214	62	SEPTEMBER

STATISTICAL SUMMARY:

DEPTH RANGE	NUMBER SAMPLES	HIGHEST	LOWEST	RANGE	MEAN	STANDARD DEVIATION
ALL DEPTHS	116	3.570	0.140	3.430	1.641	0.982
0–5 M	17	1.020	0.180	0.840	0.586	0.243
5–25 M	20	1.400	0.140	1.260	0.701	0.403
25–75 M	25	2.080	0.500	1.580	1.305	0.482
75–150 M	12	2.220	0.960	1.260	1.759	0.320
150–300 M	18	2.930	1.010	1.920	2.243	0.499
BELOW 300 M	24	3.570	1.330	2.240	3.011	0.456

DEGREE SQUARE		MONTH
1214	62	OCTOBER

STATISTICAL SUMMARY:

DEPTH RANGE	NUMBER SAMPLES	HIGHEST	LOWEST	RANGE	MEAN	STANDARD DEVIATION
ALL DEPTHS	252	3.660	0.360	3.300	1.751	0.947
0–5 M	34	1.060	0.380	0.680	0.702	0.170
5–25 M	41	1.230	0.360	0.870	0.738	0.223
25–75 M	55	1.840	0.640	1.200	1.315	0.327
75–150 M	31	2.260	1.300	0.960	1.835	0.226
150–300 M	35	2.900	1.830	1.070	2.389	0.268
BELOW 300 M	56	3.660	2.540	1.120	3.112	0.280

The data for silicate in the historical NODC archives is minimal and limits the ability to draw inferences regarding the geographic distribution. During the Davidson season (December and January, Figure 6.13), and during the Upwelling season (May-July, Figure 6.14), concentrations of silicate decrease in the offshore direction. During upwelling, several one-degree squares (1213-39, 1214-40, 51, 62, 73) show surface silicate concentrations which are higher than in the other seasons (Figure 6.14). Silicate data is almost nonexistent during the Oceanic period (September and October, Figure 6.15).

One-degree square 1214-62 is one of the few squares with a reasonable number of observations during the three major hydrographic seasons. During all periods (Oceanic, Davidson, and Upwelling) (Tables 6.10, 6.11, and 6.12), there is a significant and consistent gradient of increasing silicate concentration with depth (Figure 6.16). The surface concentrations (0-5 m) during the Davidson period are not statistically different from the Upwelling season (Tables 6.10 and 6.11) but are larger than concentrations associated with the Oceanic season (Table 6.12).

Table 6.10
Silicate

DEGREE SQUARE	MONTH
1214 62	DECEMBER

STATISTICAL SUMMARY:

DEPTH RANGE	NUMBER SAMPLES	HIGHEST	LOWEST	RANGE	MEAN	STANDARD DEVIATION
ALL DEPTHS	97	143.000	8.000	135.000	37.515	28.784
0–5 M	15	20.000	10.000	10.000	16.267	3.453
5–25 M	17	24.000	9.000	15.000	17.471	4.274
25–75 M	19	29.000	8.000	21.000	20.105	7.187
75–150 M	10	36.000	17.000	19.000	28.600	5.967
150–300 M	13	54.000	28.000	26.000	41.769	7.769
BELOW 300 M	23	143.000	46.000	97.000	82.043	22.471

DEGREE SQUARE	MONTH
1214 62	JANUARY

STATISTICAL SUMMARY:

DEPTH RANGE	NUMBER SAMPLES	HIGHEST	LOWEST	RANGE	MEAN	STANDARD DEVIATION
ALL DEPTHS	127	90.000	4.000	86.000	23.795	20.441
0–5 M	20	28.000	4.000	24.000	11.500	5.472
5–25 M	25	23.000	4.000	19.000	11.000	3.926
25–75 M	34	32.000	4.000	28.000	14.912	6.492
75–150 M	19	29.000	15.000	14.000	21.789	3.809
150–300 M	13	57.000	28.000	29.000	35.769	8.043
BELOW 300 M	16	90.000	47.000	43.000	70.688	12.536

Table 6.11
Silicate

DEGREE SQUARE		MONTH
1214	62	MAY

STATISTICAL SUMMARY:

DEPTH RANGE	NUMBER SAMPLES	HIGHEST	LOWEST	RANGE	MEAN	STANDARD DEVIATION
ALL DEPTHS	143	129.000	0.0	129.000	35.217	25.121
0–5 M	27	25.000	0.0	25.000	11.852	8.511
5–25 M	27	34.000	2.000	32.000	18.926	8.311
25–75 M	29	36.000	17.000	19.000	28.241	4.933
75–150 M	16	42.000	28.000	14.000	35.375	4.924
150–300 M	21	62.000	34.000	28.000	47.333	8.163
BELOW 300 M	23	129.000	45.000	84.000	79.391	23.616

DEGREE SQUARE		MONTH
1214	62	JUNE

STATISTICAL SUMMARY:

DEPTH RANGE	NUMBER SAMPLES	HIGHEST	LOWEST	RANGE	MEAN	STANDARD DEVIATION
ALL DEPTHS	161	119.000	1.000	118.000	30.839	23.532
0–5 M	25	31.000	1.000	30.000	12.600	10.239
5–25 M	27	46.000	2.000	44.000	17.185	10.503
25–75 M	38	44.000	3.000	41.000	21.395	11.171
75–150 M	26	52.000	9.000	43.000	28.038	10.505
150–300 M	20	65.000	16.000	49.000	40.650	12.407
BELOW 300 M	25	119.000	45.000	74.000	73.240	19.477

DEGREE SQUARE		MONTH
1214	62	JULY

STATISTICAL SUMMARY:

DEPTH RANGE	NUMBER SAMPLES	HIGHEST	LOWEST	RANGE	MEAN	STANDARD DEVIATION
ALL DEPTHS	131	93.000	2.000	91.000	28.519	20.486
0–5 M	19	15.000	2.000	13.000	6.053	3.951
5–25 M	24	27.000	2.000	25.000	12.167	7.251
25–75 M	27	32.000	5.000	27.000	21.741	7.719
75–150 M	20	39.000	24.000	15.000	30.150	4.017
150–300 M	18	47.000	21.000	26.000	37.778	5.917
BELOW 300 M	23	93.000	44.000	49.000	63.435	13.024

Table 6.12
Silicate

DEGREE SQUARE	MONTH
1214 62	SEPTEMBER

STATISTICAL SUMMARY:

DEPTH RANGE	NUMBER SAMPLES	HIGHEST	LOWEST	RANGE	MEAN	STANDARD DEVIATION
ALL DEPTHS	92	108.000	3.000	105.000	29.250	27.611
0–5 M	15	11.000	3.000	8.000	7.400	2.230
5–25 M	17	15.000	3.000	12.000	7.706	3.350
25–75 M	20	34.000	7.000	27.000	16.450	8.763
75–150 M	10	35.000	18.000	17.000	24.800	6.070
150–300 M	13	63.000	26.000	37.000	42.231	11.344
BELOW 300 M	17	108.000	51.000	57.000	77.824	17.618

DEGREE SQUARE	MONTH
1214 62	OCTOBER

STATISTICAL SUMMARY:

DEPTH RANGE	NUMBER SAMPLES	HIGHEST	LOWEST	RANGE	MEAN	STANDARD DEVIATION
ALL DEPTHS	127	101.000	1.000	100.000	28.039	26.230
0–5 M	20	15.000	2.000	13.000	7.400	4.627
5–25 M	23	16.000	1.000	15.000	7.217	4.134
25–75 M	27	29.000	4.000	25.000	15.815	6.343
75–150 M	15	34.000	14.000	20.000	22.067	5.885
150–300 M	18	60.000	22.000	38.000	39.500	11.020
BELOW 300 M	24	101.000	44.000	57.000	74.083	16.154

REFERENCES

1. Cline, J.D. and F.A. Richards, 1972. Oxygen Deficient Conditions and Nitrate Reduction in the Eastern Tropical North Pacific Ocean, Limnology and Oceanography, **17**, pp. 885–900.

2. Eppley, R.W., E.H. Renger, E.L. Venrick, and M.M. Mullin, 1973. A Study of Plankton Dynamics and Nutrient Cycling in the Central Gyre of the North Pacific Ocean, Limnology and Oceanography, **18**, pp. 534–551.

3. Goering, John J., Richard C. Dugdale and David W. Menzel, 1966. Estimates of in situ Rates of Nitrogen Uptake by Trichodesmium sp. in the Tropical Atlantic Ocean, Limnology and Oceanography, **18**, pp. 534–550.

4. Goering, J.J., 1968. Denitrification in the Oxygen Minimum Layer of the Eastern Tropical Pacific Ocean. Deep-Sea Research, **15**, pp. 157–164.

5. Goering, John J., D.D. Wallen and R.M. Nauman, 1970. Nitrogen Uptake by Phytoplankton in the Discontinuity Layer of the Eastern Subtropical Pacific Ocean, Limnology and Oceanography, **15**, pp. 789–796.

6. Malone, T.C., 1971. The Relative Importance of Nannoplankton and Netplankton as Primary Producers in the California Current System. Limnology and Oceanography, **69**, pp. 799–820.

7. McCarthy, J.J., 1972. The Uptake of Urea by Natural Populations of Marine Phytoplankton, Limnology and Oceanography, **17**, pp. 739–748.

8. North, B.B., 1975. Primary Amines in California Coastal Waters: Utilization by Phytoplankton. Limnology and Oceanography, **20**, pp. 20–27.

9. Thomas, W.H. and D.L.R. Seibert, 1974. Distribution of Nitrate, Phosphate, and Silicate in the California Current Region, 1969, California Cooperative Oceanic Fisheries Investigation, Atlas #20.

10. Aaronson, S. and N.H. Patni, 1976. The Role of Surface and Extracellular Phosphatases in the Phosphorus Requirement of Ochromonas, Limnology and Oceanography, **21**, pp. 838–845.

11. Armstrong, F.A.J., 1965. Phosphorus in Chemical Oceanography, Vol. 1, J.P. Riley & G. Skirrow (Eds.), Academic Press, N.Y.

12. Berns, D.S., P. Holohan, and E. Scott, 1966. Urease Activity in Blue-Green Algae, Science, **152**, pp. 1077–1078.

13. Cline, J.D. and F.A. Richards, 1972. Oxygen Deficient Conditions and Nitrate Reduction in the Eastern Tropical North Pacific Ocean, Limnology and Oceanography, **17**, pp. 885–900.

14. Eppley, R.W., J.L. Coatsworth, and L. Solórzano, 1969. Studies of Nitrate Reductase in Marine Phytoplankton. Limnology and Oceanography, **14**, pp. 194–205.

15. Eppley, R.W., E.H.Renger, E.L. Venrick, and M.M. Mullin, 1973. A Study of Plankton Dynamics and Nutrient Cycling in the Central Gyre of the North Pacific Ocean, Limnology and Oceanography, **18**, pp. 534–551.

16. Jeffries, C.D., 1964. Intracellular Microbial Urease, Nature, pp. 202, 930.

REFERENCES (continued)

17. Hargrave, B.T. and G.H. Green, 1968. Phosphorus Excretion by Zooplankton, Limnology and Oceanography, **13**, pp. 332–342.

18. Holm-Hensen, O., J.D.H. Strickland and T.M. Williams, 1966. A Detailed Analysis of Biologically Important Substances in a Profile off Southern California, Limnology and Oceanography, **11, (4)**, pp. 548–561.

19. Ketchum, B.H., N. Corwin and K.J. Keen, 1955. The Significance of Organic Phosphorus Determinations in Ocean Waters, Deep-Sea Res., **2**, pp. 172–181.

20. Kuenzler, E.J. and J.P. Perras, 1965. Phosphatases of Marine Algae, Biol. Bull., **128**, pp. 271–284.

21. Kuenzler, E.J., 1979. Dissolved Organic Phosphorus Excretion by Marine Phytoplankton, J. Phycol., **6**, pp. 7–13.

22. Leftley, J.W. and P.J. Syrett, 1973. Urease and ATP: Urea Amidolyase Activity in Unicellular Algae, J. Gen. Microbiol., **77**, pp. 109–115.

23. Perry, M.J., 1972. Alkaline Phosphatases Activity in Subtropical Central North Pacific Waters Using a Sensitive Fluorometric Method, Mar. Biol. **15**, pp. 113–119.

24. Reid, J.L., Jr., On Circulation, Phosphate-Phosphorus Cont., and Zooplankton Volumes in the Upper Part of the Pacific Ocean, Limnology and Oceanography, pp. 287–306.

25. Yentsch, C.M., C.S. Yentsch and J.P. Perras, 1970. Alkaline Phosphatase Activity in the Tropical Marine Blue-Green Algae, Oscillatoria Erythraea (Trichodesmium), Limnology and Oceanography, **17**, pp. 772–774.

26. Armstrong, F.A.J., 1965. Silicon in Chemical Oceanography, Vol. 1, J.P. Riley and G. Skirrow (Eds.), Academic Press, N.Y.

27. Cooper, L.H.N., 1933. Chemical Constituents of Biological Importance in the English Channel November 1930 – January 1932, Part I, Phosphate, Silicate, Nitrate, Nitrite, Ammonia, J. Mar. Biol., U.K., **18**, 677.

28. Cooper, L.H.N., 1933. Chemical Constituents of Biological Importance in the English Channel, June 1932 – December 1932, Part III, Phosphate, Silicate, Nitrate, Hydrogen Ion Concentration with a Comparison with Wind Records, J. Mar. Biol., U.K., **19**, 55.

29. Katatan, A. and J.P. Riley, 1979. Rate of Dissolution of Diatom Silica Walls in Seawater, Marine Bio., **55**, pp. 29–35.

30. Lewin, J.C., 1955. Silicon Metabolism in Diatoms, J. Gen. Physiol., Part 1, **39**, p. 11.

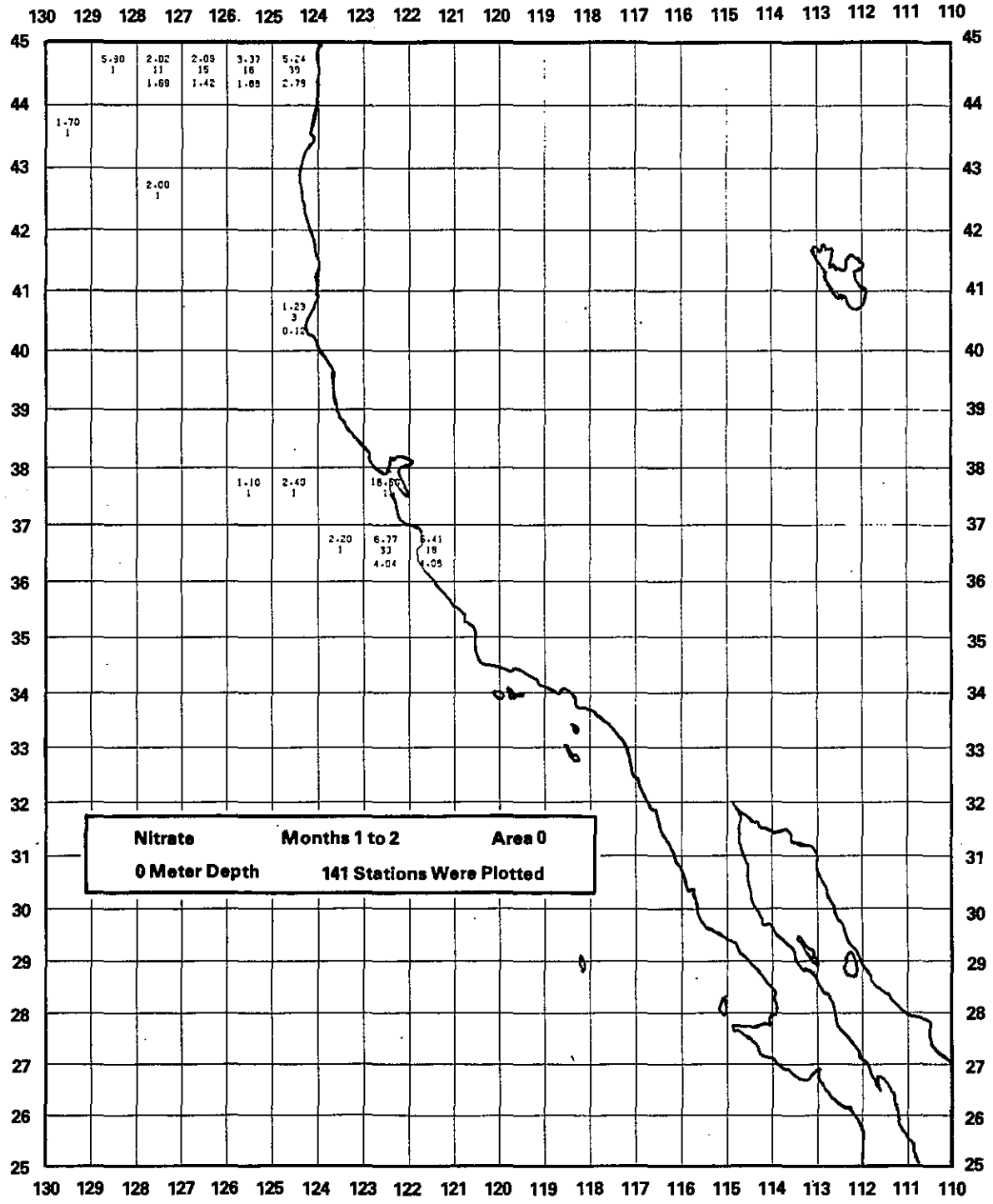

Figure 6.1. Geographic distribution of surface nitrate concentrations during December and January (mid-Davidson season). The numbers in each square, from top to bottom, are the mean, number of observations, and standard deviation.

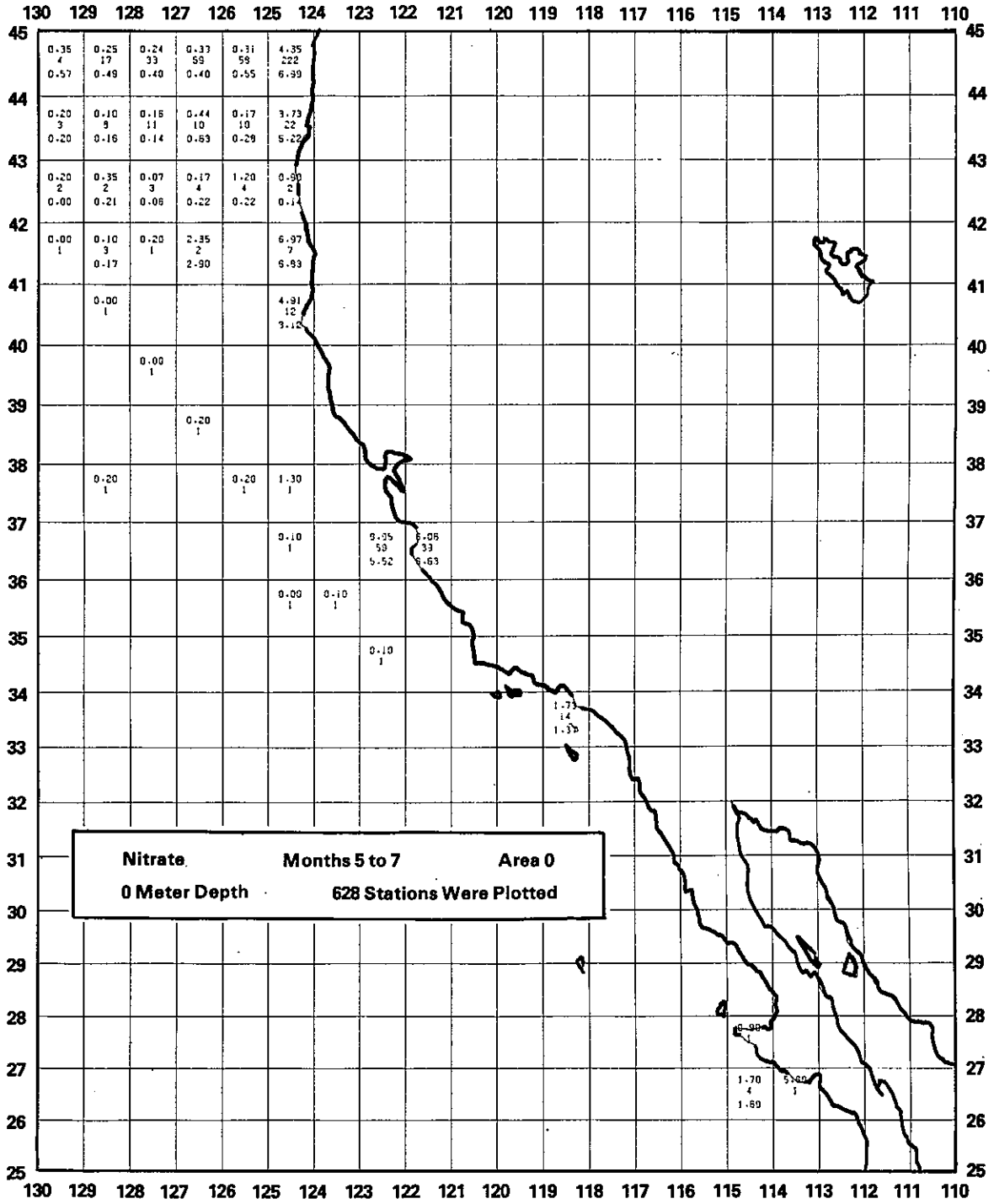

Figure 6.2. Geographic distribution of surface nitrate concentrations from May-July (the Upwelling season). The numbers in each square, from top to bottom, are the mean, number of observations, and standard deviation.

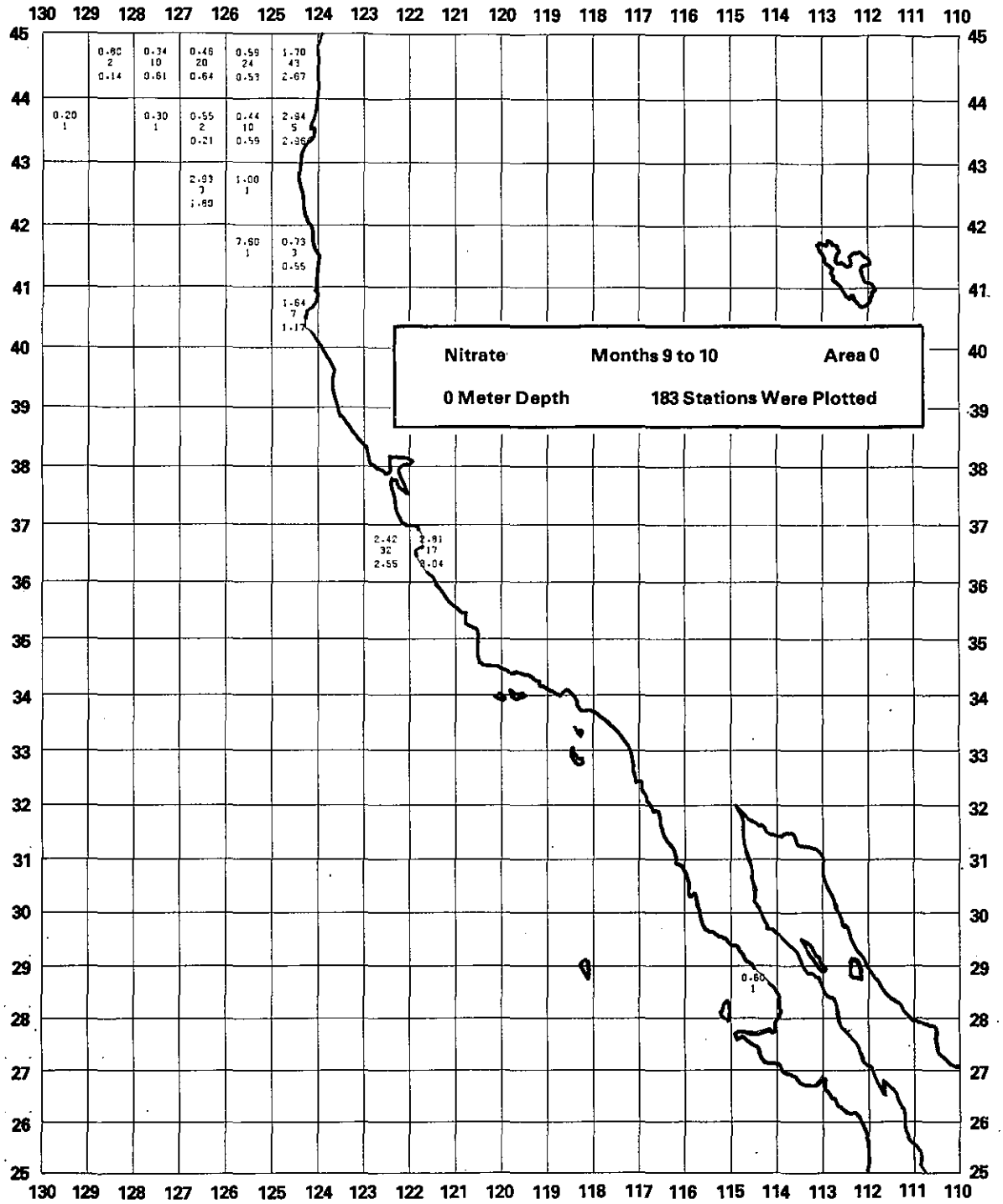

Figure 6.3. Geographic distribution of surface nitrate concentrations during September and October (the Oceanic season). The numbers in each square from top to bottom, are the mean, number of observations, and the standard deviation.

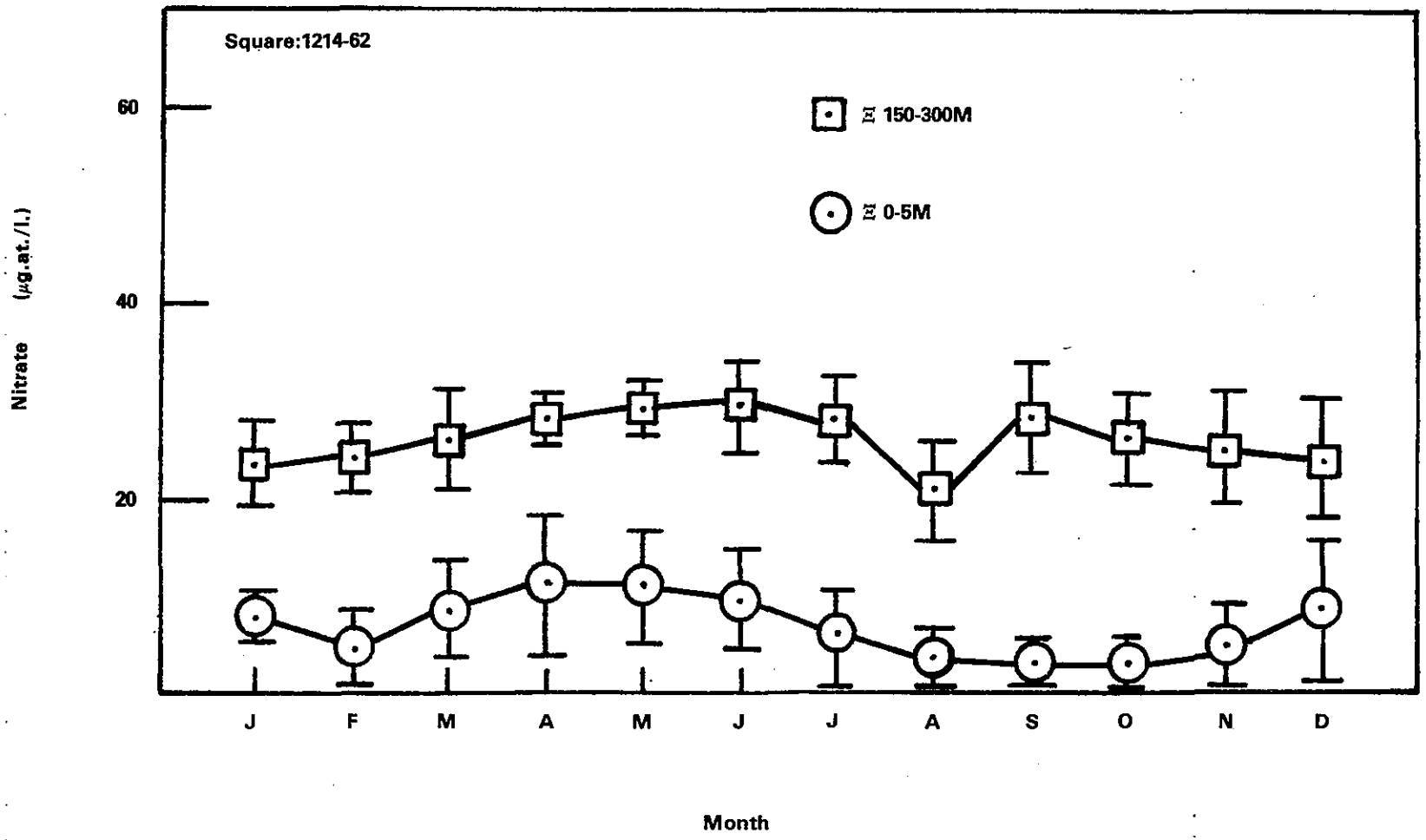

Figure 6.4. Plot of nitrate by month for 0-5 m (⊙) and 150-300 m (⊡). The error bars represent ± one standard deviation.

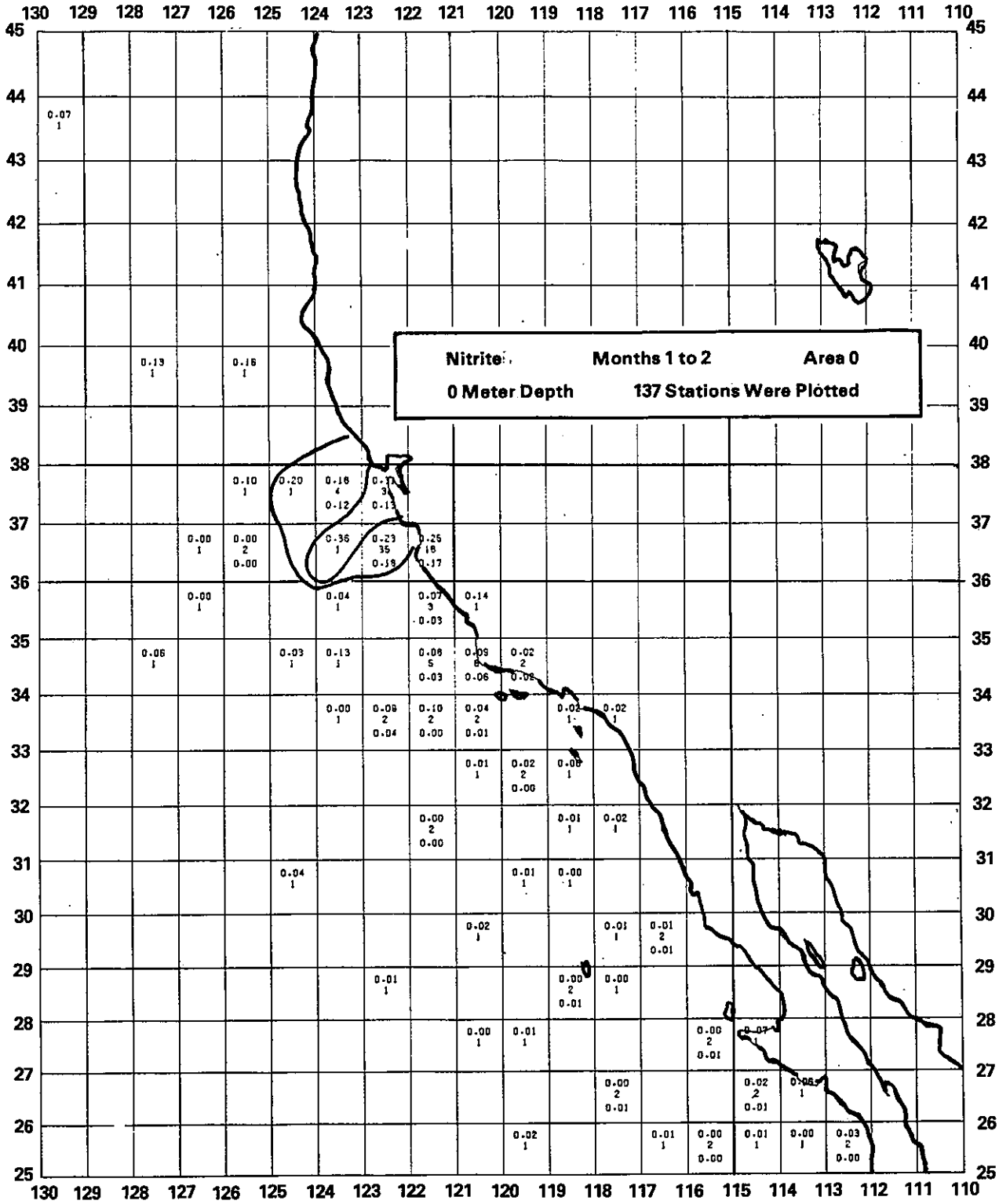

Figure 6.5. Geographic distribution of surface nitrite concentrations during December and January (mid-Davidson season). The numbers in each square, from top to bottom, are the mean, number of observations, and standard deviation.

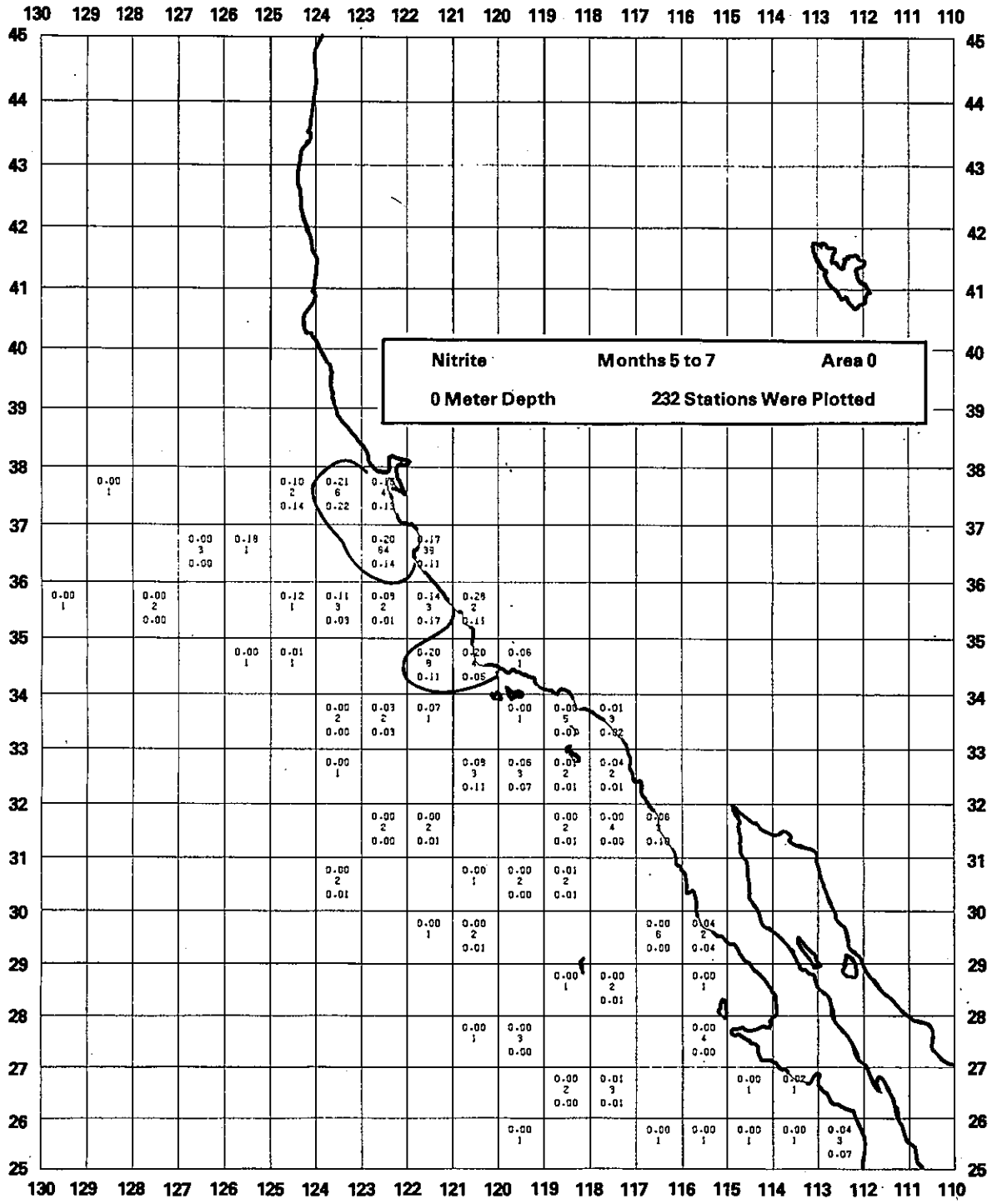

Figure 6.6. Geographic distribution of surface nitrite concentrations from May through July (mid-Upwelling season). The numbers in each square from top to bottom, are the mean, number of observations, and standard deviation.

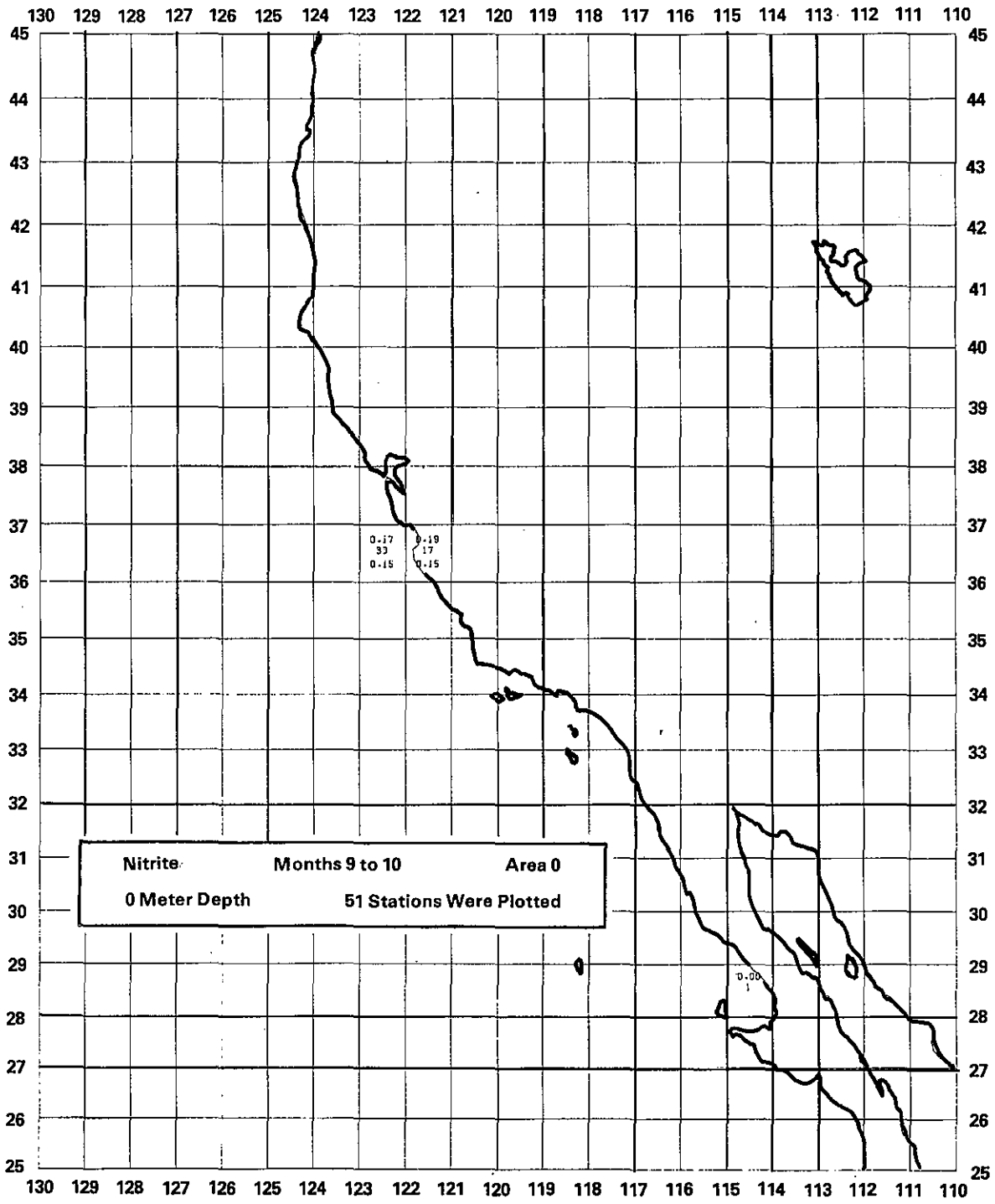

Figure 6.7. Geographic distribution of surface nitrite concentrations during September and October (Oceanic season). The numbers in each square, from top to bottom, are the mean, number of observations, and the standard deviation.

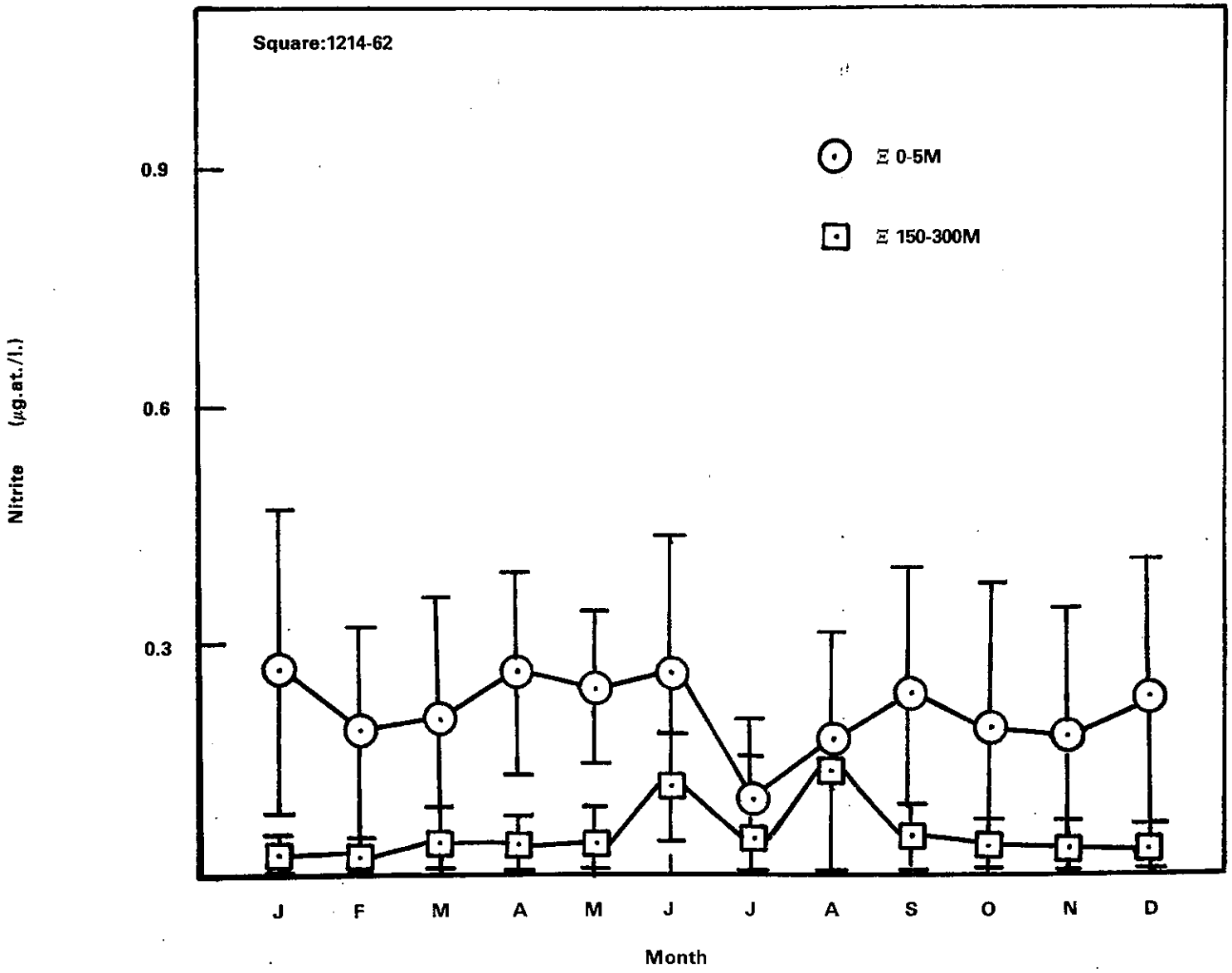

Figure 6.8. Plot of nitrite by month for 0-5 m (⊙) and 150-300 m (⊡). The error bars represent ± one standard deviation.

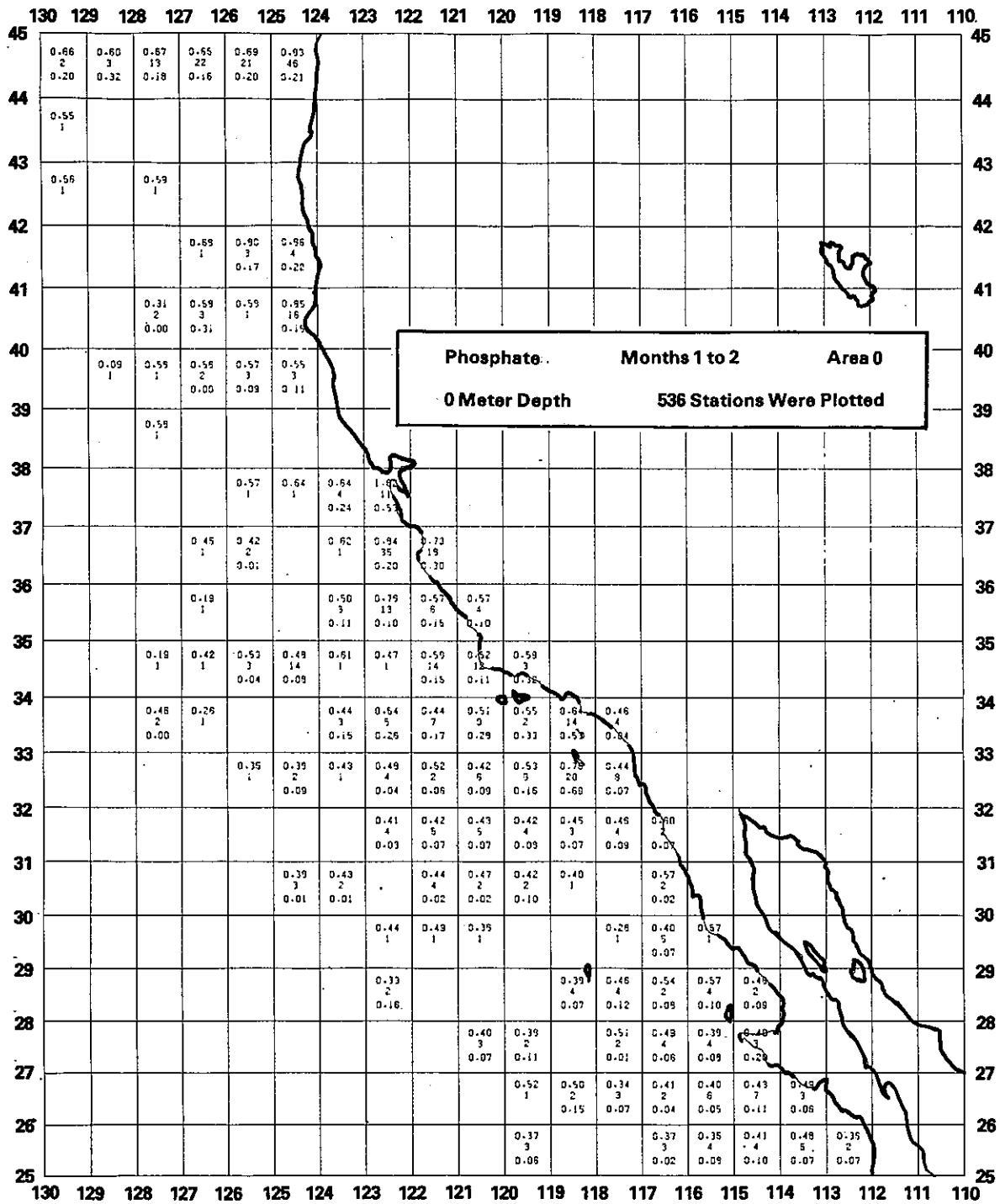

Figure 6.9. Geographic distribution of surface phosphate concentrations during December and January (mid-Davidson season). The numbers in each square, from top to bottom, are the mean, number of observations, and standard deviations.

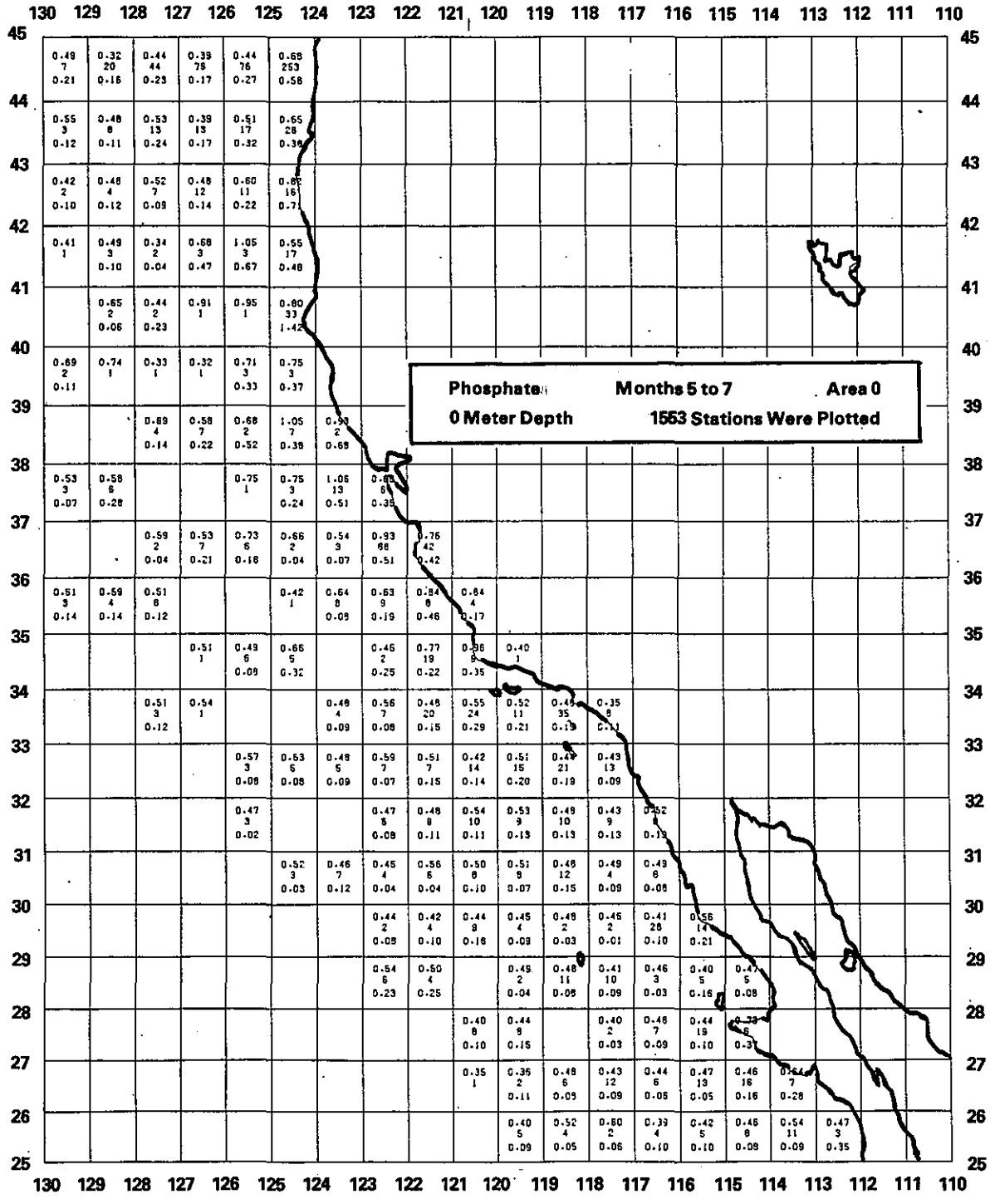

Figure 6.10. Geographic distribution of surface phosphate concentrations from May through July (mid-Upwelling season). The numbers in each square, from top to bottom, are the mean, number of observations, and the standard deviation.

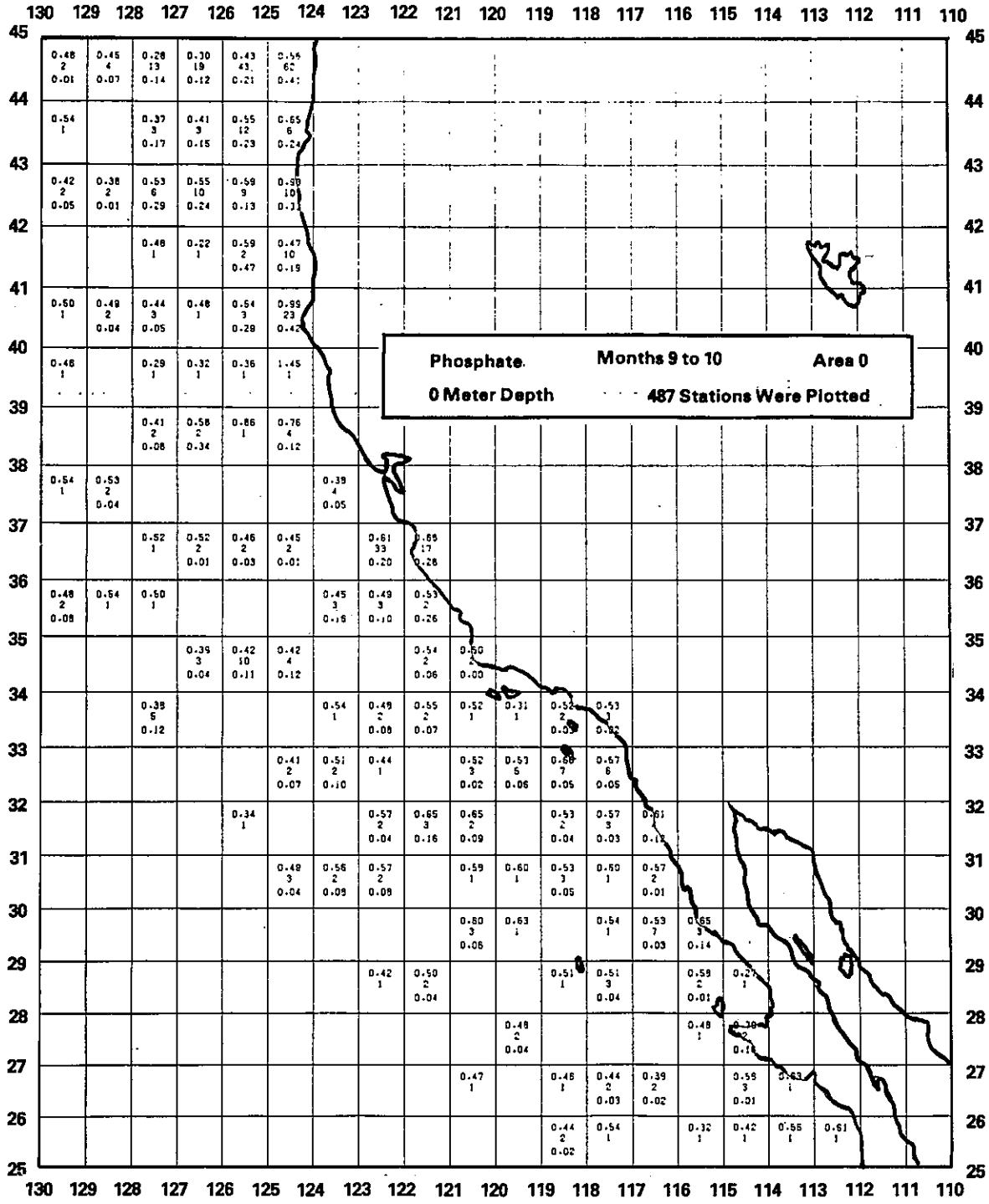

Figure 6.11. Geographic distribution of surface phosphate concentrations during September and October (Oceanic season). The numbers in each square, from top to bottom, are the mean, number of observations, and standard deviation.

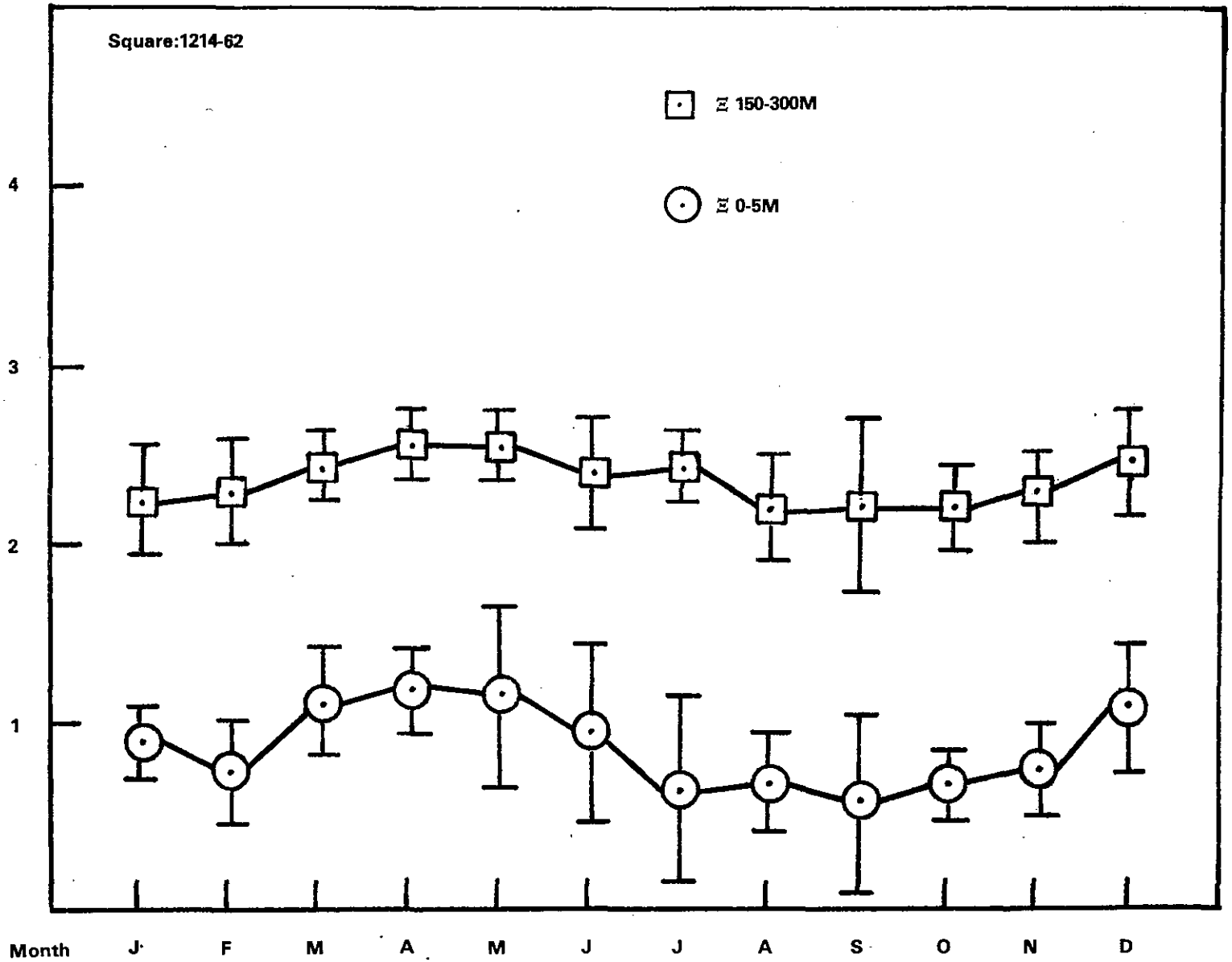

Figure 6.12. Plot of phosphate concentration by month at 0-5 m (⊙) and 150-300 m (⊡) depth. The error bars represent ± one standard deviation.

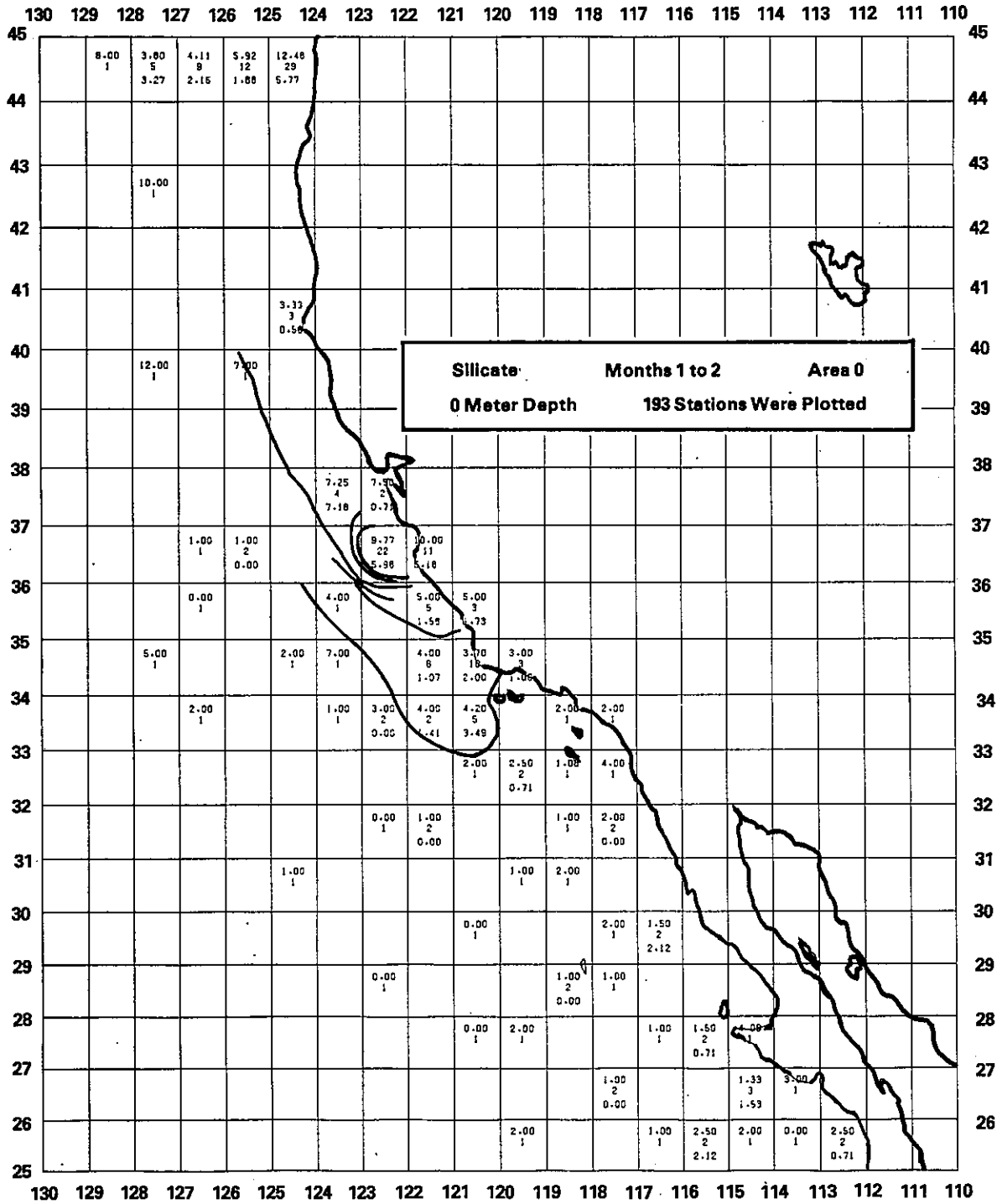

Figure 6.13. Geographic distribution of surface silicate concentrations during December and January (mid-Davidson season). The numbers in each square, from top to bottom, are the mean, number of observations, and the standard deviation.

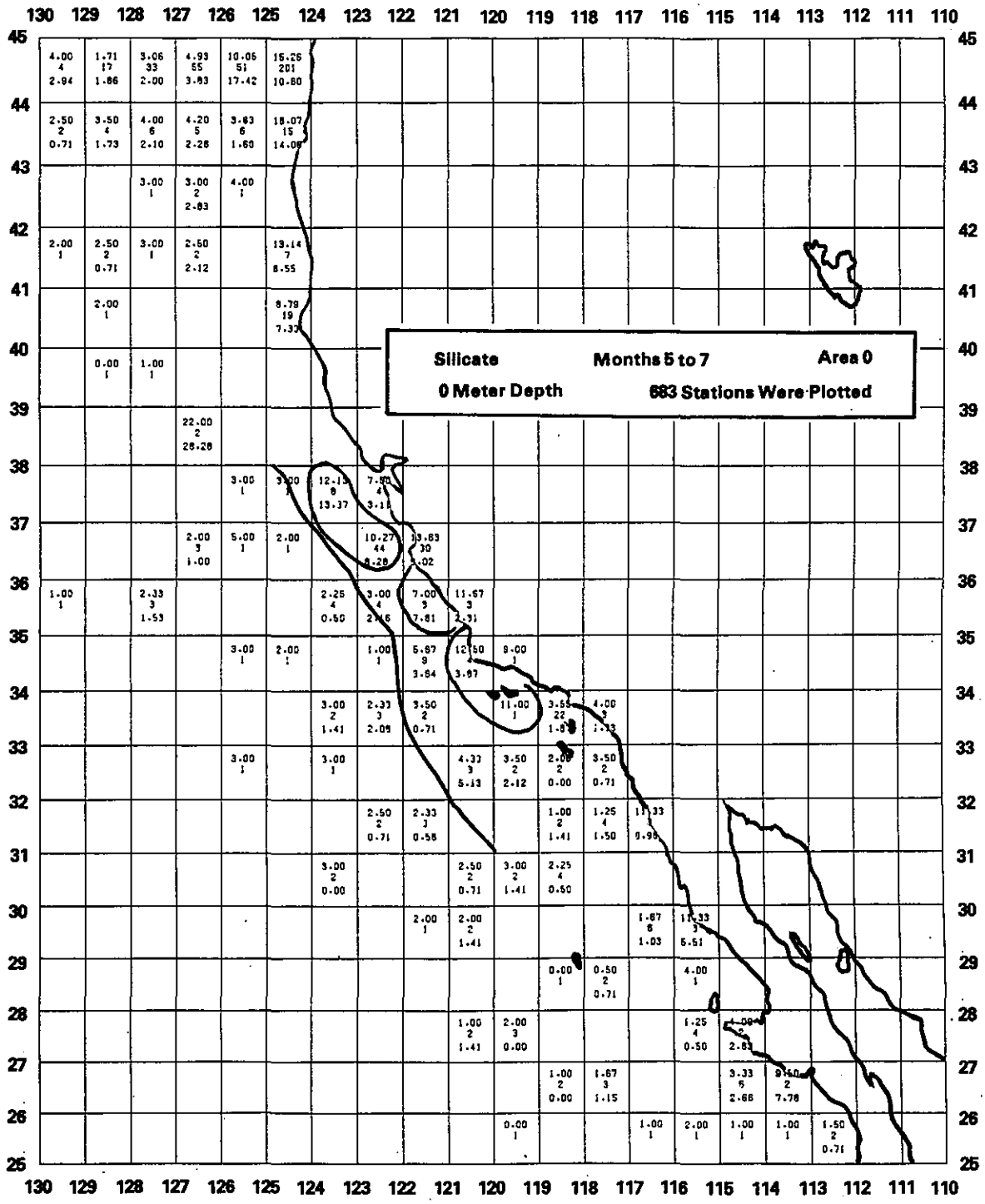

Figure 6.14. Geographic distribution of surface silicate concentrations from May through July (mid-Upwelling season). The numbers in each square, from top to bottom, are the mean, number of observations, and the standard deviation.

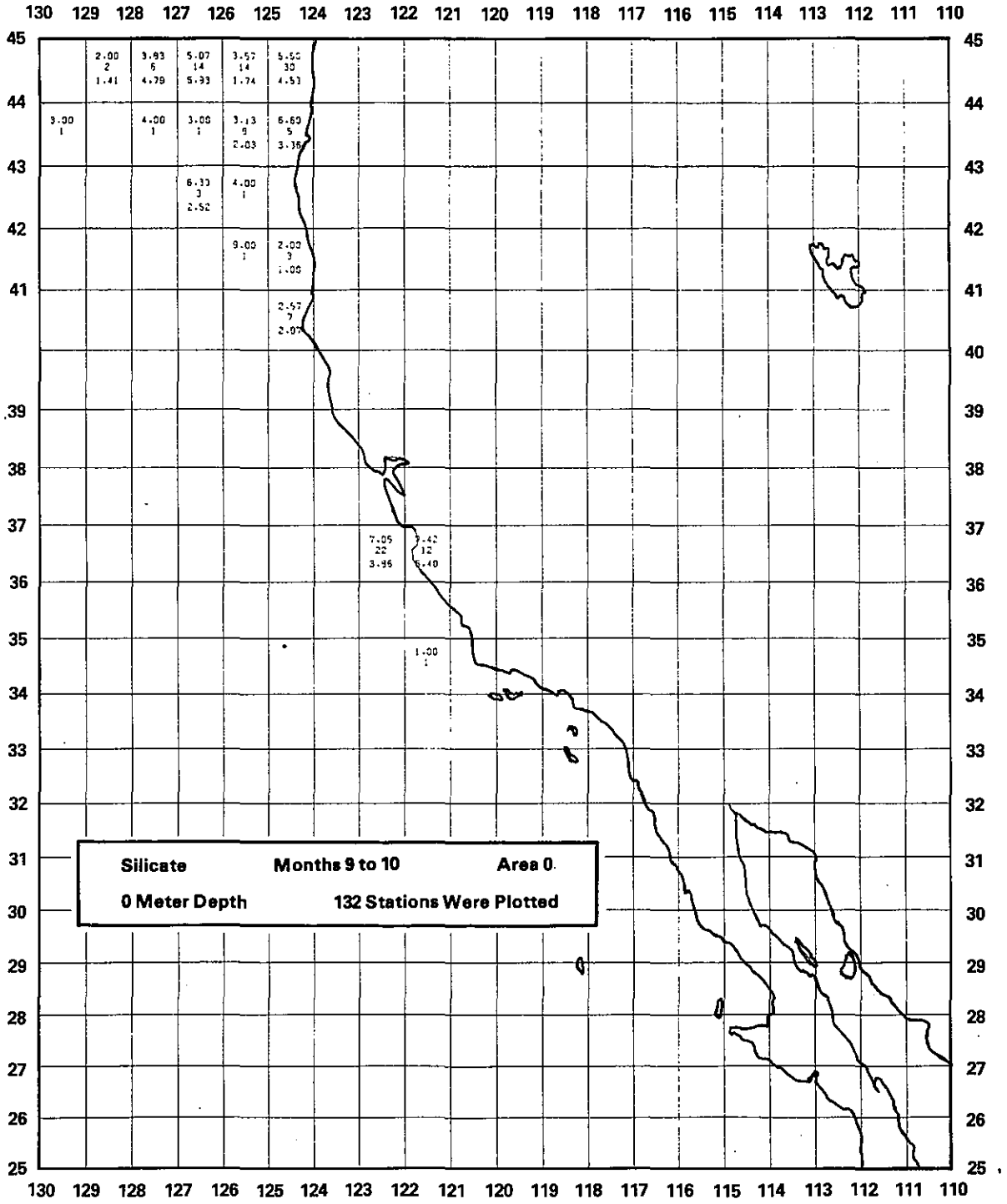

Figure 6.15. Geographic distribution of surface silicate concentrations during September and October (Oceanic season). The numbers in each square, from top to bottom, are the mean, number of observations, and the standard deviation.

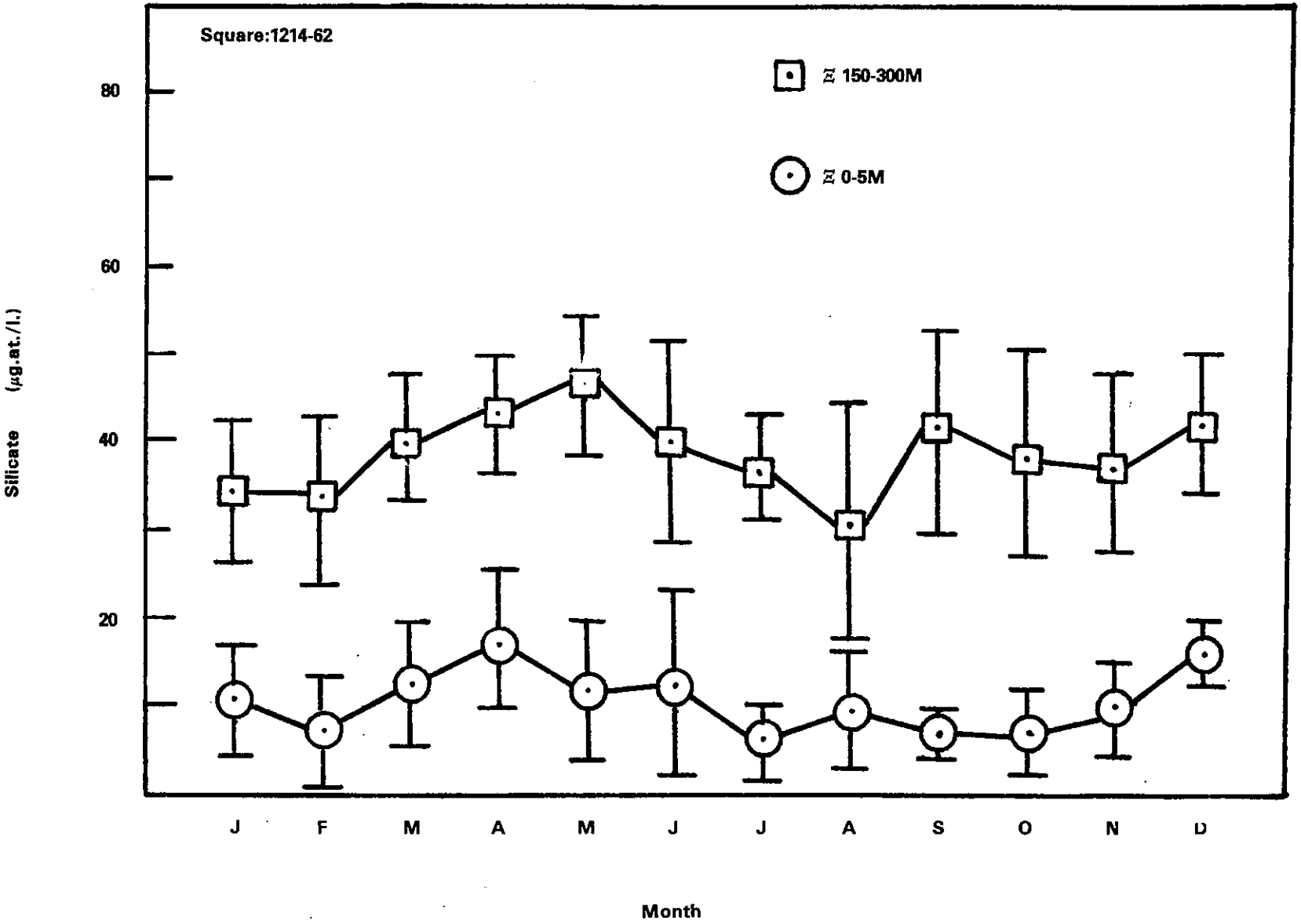

Figure 6.16. Plot of silicate by month for 0-5 m (⊙) and 150-300 m (⊡) depth. The error bars represent ± one standard deviation.

7. WATER ELEVATION COMPONENTS AND COMPARATIVE RISKS

M. D. Earle and K. Bush

7.1 INTRODUCTION

This chapter describes and compares the components that contribute to the total water elevation. These include storm surges, astronomical tides, seasonal and long-term sea level changes, tsunamis, waves, and wave setup. Water elevations measured by coastal tide gauges include contributions from storm surges, astronomical tides, seasonal sea level changes, and long-term sea level changes. These components can be separated by analysis of water elevation data but the total elevation is of primary importance for practical applications.

Seasonal sea level changes, particularly for northern California, are associated with extratropical storms and therefore, highest water elevations and storm surges occur in the winter. In addition, there has been a very slow long-term rise in sea level relative to land at most California tide stations. Extreme total water elevations as a function of recurrence interval generally increase from southern to northern California, e.g., the one hundred year recurrence interval for storm surge changes from approximately 0.6 m (2 ft) in southern to approximately 1 m (3 ft) in northern California.

For comparison, astronomical tides, which are predictable and are not normally a problem, have a typical range of about 2 m (6 ft) at most California tide stations. Limited numerical modeling substantiates the low elevations of extreme storm surges and provides estimates of storm surge elevation decrease over the continental shelf relative to the elevation at the coast. Because of the narrow continental shelf, astronomical tides over the shelf can be considered nearly equal to those measured at reasonably exposed coastal tide stations. The characteristics, particularly the relatively low elevations, of storm surges along the California coast make it probable that adequate information for specific engineering and environmental applications can be developed from more detailed analysis of measured water elevations at tide stations without the use of complex numerical models.

Tsunamis produce the highest water elevations along the California coast, however, very infrequently. Tsunamis generated near the Aleutian Trench and Peru-Chile Trench are a major threat to California but there is a low probability that destructive tsunamis will be locally generated near the California coast. The most destructive tsunami to affect California occurred in March, 1964, resulting from a severe Alaskan earthquake. Extensive damage due to this tsunami occurred in the vicinity of Crescent City where the maximum water elevation was approximately 6.3 m above mean lower low water.

Modeling procedures allow calculation of tsunami elevations over the continental shelf but offshore elevations are not usually critical for engineering applications. Because of very infrequent tsunami occurrences and significant modifications due to local effects, it is difficult to estimate extreme tsunami elevations as a function of recurrence interval from observations. Numerical modeling by the U.S. Army Corps of Engineers has been used to provide tsunami elevations, including a statistical superposition of astronomical tides, for recurrence intervals of one hundred and five hundred years along the California coast. A main feature of extreme tsunamis is their substantial location variability with values ranging from approximately 1.5 m (5 ft) to approximately 4.5 m (15 ft) for a one hundred year recurrence interval. High current velocities that may occur in shallow or constricted areas are another potential hazard of tsunamis.

Wave characteristics are related to prevailing weather patterns, storm climatology, unique geographical effects such as offshore islands off southern California, coastline configuration and orientation, and variations in offshore bottom topography. Spatial variation of deep water wave conditions depends mainly on occurrences of extratropical storms which primarily affect northern California during winter. However, swell from winter extratropical storms is sometimes a cause of major coastal damage along the southern California coast.

Typical wave and extreme wave probability distributions were developed from a 1951-1974 wave hindcast for six deep water locations. In general, wave conditions become more severe progressing northward and most severe conditions occur in the winter. Values of wave persistence, which refer to durations of wave heights above and below specified wave heights, are summarized in this chapter. For southern California, very infrequently occurring tropical storms do not affect typical wave conditions but do determine extreme wave heights over long time periods. One hundred year recurrence interval deep water significant wave heights are approximately 9 m (30 ft) off southern California and approximately 11 m (36 ft) off northern California. Wave setup is an increase in water elevation near the coast and is associated with breaking waves. Wave setup at the coast due to extreme waves, ranges from 0.9 m (3 ft) to 1.5 m (5 ft) and is generally larger than storm surge elevations. Nearshore wave conditions can vary greatly over relatively short distances due to complicated bottom topography, coastal configurations and orientations, and wave sheltering by offshore islands. Substantial, but feasible, computer modeling efforts would be required to accurately calculate nearshore wave conditions based on deep water wave conditions but the best present procedure is to use nearshore wave measurements which are becoming increasingly available.

7.2 STORM SURGES, ASTRONOMICAL TIDES, AND SEA LEVEL CHANGES

Severe winds off California are relatively weak and of shorter durations than for other U.S. coastal regions. Severe winds are due mainly to extratropical storms and very infrequent weak tropical storms off southern California. Relative importance of storm surges compared to other water elevation components is affected by offshore and onshore topography, and the narrow continental shelf causes smaller storm surges than would otherwise occur for the same wind conditions on other coasts.

Water elevation data from tide stations includes the combined effects of astronomical tides, storm surges, and sea level changes. These data, which are obtained from the NOS, provide predicted astronomical tides and tidal datums (reference levels) such as mean sea level. Useful analysis results are provided in References 1 and 2. Storm surges are measured as water elevations that exceed predicted astronomical tides. Table 7.1 lists values, to the nearest 0.1 ft, of the most important water elevation and tidal datum parameters at the tide stations shown in Figure 7.1.

Cumulative probability distributions of water elevation (Figure 7.2) can be used directly to estimate the probability that a given water elevation or predicted tide will or will not be exceeded. Cumulative probability distribution curves for predicted astronomical tides flatten out for probabilities greater than about 99.9 percent, indicating that extreme astronomical tide heights do not greatly exceed more frequently occurring astronomical tide heights.

At all stations along the California coast, the highest measured water elevation each year during the period 1933-1977 occurred during the winter months of December-January, due to extratropical storms. Secondary maxima occur during June and July in southern coastal areas due to late season severe extratropical storms and to prevailing winds.

Water elevation is also affected by variations in annual mean sea level (the average of hourly measured water elevations over one year), which are due to long term variations of meteorological and oceanographic conditions as well as such large-scale conditions as eustatic sea level changes and tectonic effects. Along most of the California coast, mean sea level has been rising relative to mean sea level for the 1941-1959 National Tidal Datum Epoch. A sea level elevation rise of approximately 0.005 ft/year has occurred at San Francisco.

Table 7.1
Water Elevations and Tidal Datum Parameters at Selected California Tide Stations.
All values are in feet and are relative to mean lower low water. Unless otherwise indicated,
all values were referenced during analysis to the presently used National Tidal Datum Epoch, 1941-1959.

Station	Mean Low Water	Mean Tide Level	Mean Sea Level	Mean High Water	Mean Higher High Water	Diurnal Range
Crescent City	1.2	3.7	3.7	6.3	6.9	6.9
San Francisco	1.1	3.1	3.0	5.1	5.7	5.7
Los Angeles	0.9	2.8	2.8	4.7	5.4	5.4
Santa Monica	0.9	2.8	2.7	4.6	5.4	5.4
Newport	0.9	2.8	2.7 (1956-61)	4.6	5.3	5.3
La Jolla	0.9	2.7	2.7	4.5	5.2	5.2
San Diego	0.9	3.0	2.9	5.0	5.7	5.7

Because of the narrow width of the California continental shelf, astronomical tides over the shelf can be considered nearly equal to those measured at reasonably exposed coastal tide stations. Storm surge elevations are more sensitive to varying widths of the shelf and the ratio of the offshore storm surge elevation to the coastal storm surge elevation may change substantially with location along the coast and distance offshore. At a depth of 100 ft, storm surge elevations range from 60-90 percent of coastal elevations; at a depth of 300 ft the range is 15-70 percent, and at a depth of 500 ft the range is 10-60 percent of the coastal elevations. With a very narrow shelf, smaller decreases in offshore storm surge elevations occur because the wind-induced surge near the coast is small compared to the atmospheric-induced surge both at the coast and in deeper water.

7.2.1 Extreme Water Elevations

Astronomical high tides (relative to mean lower low water) that are equaled or exceeded on the average once per year along the California coast tend to decrease southward along the coast, ranging from a high of 8.8 ft at Crescent City to a low of 7.0 ft at Newport and La Jolla, although the value at San Diego, 7.6 ft, is greater than any other except that at Crescent City. These values are barely less than the largest astronomical high tide values expected over very long time periods as determined from astronomical tide cumulative probability distributions.

Figure 7.3 shows extreme water elevations (relative to mean lower low water) at selected tide stations along the California coast for recurrence intervals of 5, 25, and 100 years. The results are based on a least squares fit of a log-normal probability distribution to measured extreme water elevations at each station. The record length varied from 22 years at Newport to 54 years at Los Angeles. These high water elevation values are the storm still water elevations which would be used for structural design purposes when tsunamis and wave setup are not important. They include both storm surges and astronomical tides.

Storm surge elevations alone as a function of return period were estimated by subtracting mean higher high water elevation values from the total water elevation values shown in Figure 7.3. The average mean higher high water values were computed from monthly information provided in Reference 1 for those months during which the greatest water elevations occurred at each station and are based on 19 years of predicted astronomical tides. The estimated storm surge elevations range from 1.9 to 2.5 ft for a recurrence interval of 5 years, 2.0 to 2.8 ft for a

recurrence interval of 25 years, and 2.1 to 3.1 ft for a recurrence interval of 100 years. Elevation values typically decrease from north to south along the coast from Crescent City to Newport, and then increase slightly from Newport to San Diego. Model-computed extreme storm surges which (Reference 3) range from 1 to 3 ft, verify the approximate range of storm surges computed from measured water elevations.

7.3 TSUNAMIS

A tsunami is a system of very long wave length gravity waves principally generated by intense submarine earthquakes. Typical tsunami periods range from several minutes to a few hours and typical wave lengths are on the order of 50 miles. Even in deep water, tsunamis are shallow water waves so that their propagation speed is $\sqrt{gd}$ [1] where g is the acceleration due to gravity and d is depth. Propagation speeds are typically several hundred miles per hour. Tsunami wave heights are a few feet or less in deep water. The low wave heights and long wave lengths in deep water usually prevent tsunami detection in the open ocean. As a tsunami approaches coastal regions, significantly increased wave heights may result from wave refraction, shoaling and local resonance, and are highly variable location to location.

Susceptibility of a coastline to tsunamis from different generation areas depends partly on orientation of the coastline relative to orientations of sea floor vertical displacements along fault lines that produce tsunamis. There are many seismically active fault zones capable of generating tsunamis in the Pacific Ocean but only tsunamis produced near the Aleutian Trench and Peru-Chile Trench are a major threat to California. Historical tsunami data for California verifies that these regions are of primary importance. There is a low probability that destructive tsunamis will be locally generated off the coast of California (Reference 4). Characteristic fault movements off California are expected to be mainly horizontal so that small local tsunamis rather than large tsunamis would be generated. The Mendocino Escarpment, which is approximately perpendicular to the coast near Eureka, is potentially capable of producing tsunamis but these tsunamis would travel approximately parallel to the coast and tsunami elevations at the coast would be relatively small.

7.3.1 Observed Tsunami Heights

In general, maximum tsunami elevations are obtained from tide gauge measurements, when the measurement limit of the tide gauge is not exceeded, and are essentially equal to the maximum elevations at the tide gauge locations, which are usually in harbors. For coastal engineering design applications, tsunami runup is often an important consideration. Runup is the increase in water level as a tsunami runs up onto the land and is very location dependent. As noted in Reference 5, values of runup are usually, but not always, similar to values of tsunami elevation at the shoreline. Procedures for calculation of runup and other tsunami parameters useful for engineering projects are provided in Reference 6.

The most destructive tsunami to affect California occurred in March 1964, the result of a severe Alaskan earthquake. Extensive damage occurred in the vicinity of Crescent City where the maximum water elevation was approximately 6.3 m above mean lower low water. This value is based on observation and post-tsunami surveys, since the tide gauge was destroyed. For comparison, the maximum non-tsunami water elevation at the Crescent City tide station between 1933 and 1978 was about 3.1 m above mean lower low water. Damaging tsunamis also affected northern California in 1946 and 1960. Reference 7 describes damage due to these tsunamis and references additional tsunami descriptions for the northern California coast.

Tsunami elevations decrease with increasing distance from the coast and become negligible for practical applications in the open ocean beyond the continental shelf. The rate of decrease depends on the topography of the continental shelf and slope, and changes with location. Although the best procedure for evaluating this offshore decrease

in elevation is to use a two-dimensional model such as that described in Reference 4, the one-dimensional analytical solution used in Reference 8 provides a reasonable estimate of this decrease. For the 1964 Crescent City tsunami, the offshore elevation computed by this method is 50 percent of the coastal elevation at a distance of approximately 2.5 nautical miles (4.6 km) from the coast, and the elevation decreases rapidly from this point seaward. In general, offshore tsunami elevations are not critical for engineering applications, both because of infrequent tsunami occurrences and because the offshore water elevation during a tsunami changes relatively slowly so that forces on structures are not excessive.

7.3.2 Tsunami Recurrence Intervals

Because of the variability of tsunami elevations with location along the coast and the fact that very few tsunamis affect a given location, it is difficult to accurately develop an observed tsunami elevation probability distribution function for extrapolation to infrequently occurring recurrence intervals. Numerical modeling is necessary to determine extreme tsunami elevations as a function of recurrence interval. For the California coast, the most extensive available modeling studies for planning and coastal engineering purposes have been conducted by the Waterways Experiment Station of the U.S. Army Corps of Engineers (References 8, 9, and 4).

Figure 7.4 provides tsunami runup, combined with astronomical tides, relative to mean sea level and as a function of position along the California coast based on the previous studies (References 8, 9, and 4) by the Corps of Engineers. Mean sea level relative to mean lower low water at selected California tides stations is given in Table 7.1. The purpose of Figure 7.4 is to indicate the range of 100- and 500-year recurrence interval tsunami runup values and the substantial coastal variability. Comparisons of 100-year recurrence intervals for tsunami runup in Figure 7.4 to similar values of 1 to 3 ft for storm surges show the dominant importance of tsunamis at the coast. Away from the immediate vicinity of the coast, tsunamis are of little importance and wind-generated waves are of primary importance.

Another hazard to structures is the relatively high current velocities associated with tsunamis. According to one study (Reference 7), the major effects of several recent California tsunamis were strong currents in harbors and bays, with velocities as high as 25 mph reported. These currents are most severe in shallow areas or where water is passing through a narrow channel or river mouth, and may not cause substantial damage to properly designed and constructed structures.

7.4 WAVES

Weather that causes wave conditions for the California coast and continental shelf is essentially the same as that which causes small storm surges for these areas. Most reported coastal damage in southern California is due to swell from winter extratropical storms further to the north but the largest waves affecting southern California are caused by infrequent tropical storms. Swell from extratropical storms in the Southern Hemisphere also affects southern California. During the winter, northern California is directly affected by extratropical storms so that wave heights are substantially higher in winter than in summer.

Wave height values that are given in this chapter are for significant wave height which is the average height of the one-third highest waves in a wave record. Given significant wave height, other wave heights such as root-mean-square wave heights, average height of the 1/10 highest waves, or probable maximum wave height for a given number of waves can be approximately calculated from a Rayleigh distribution (Reference 10). The ratio of significant wave height to root-mean-square wave height is 1.42. For engineering applications, the average wave height of the 1/10 highest waves and the probable maximum wave height for 1,000 waves are used frequently. Ratios of these values to the significant wave height are 1.27 and 1.86 respectively. Waves, particularly high waves, are not symmetrical about the mean water elevation and most of the wave, the wave crest elevation, is above the mean water elevation. The crest elevation that corresponds to a given wave height can be calculated by procedures found in Reference 11.

7.4.1 Typical Waves

Figure 7.5 provides significant wave height cumulative probability distributions at the six offshore locations shown in Figure 7.1. These results are based on a 1951-1974 hindcast with a significant wave height sea and swell model by the U.S. Navy Fleet Numerical Weather Central (FNWC). An intercomparison of significant wave heights cumulative probability distributions from Summary of Synoptic Meteorological Observations (SSMO), FNWC hindcasts, and ship observations in a one degree square area near FNWC location 3 is presented in Figure 7.6. An intercomparison of wave period data summaries is presented in Figure 7.7. Comparisons of the FNWC hindcast statistics to nearby ship wave observation statistics from the NCC and from Reference 14 show good agreement except at locations 5 and 6 where FNWC results provide greater probabilities for higher waves. A possible reason is that wave statistics for ship observations are based on the highest of the sea wave height or the swell wave height, while FNWC statistics are based on a combination of sea and swell wave heights. Use of statistical results from this hindcast instead of less accurate ship observations provides a slightly conservative estimate of wave heights. Because of winter extratropical storms, higher waves occur more often off northern California than off southern California. Monthly distributions and wave period statistics are given in Reference 12, which describes the 1951-1974 hindcast. Wave periods are most often between 6 s and 12 s with longer wave periods occurring off northern California during winter extratropical storms. Southern California experiences some long period swell from these winter storms and from winter extratropical storms that occur in the Southern Hemisphere during the Northern Hemisphere summer. Southern Hemisphere swell, which is not included in the FNWC hindcast, is occasionally refracted to cause damaging wave heights at the coast (Reference 13).

Wave persistence refers to durations of wave heights above and below given specified wave heights. Table 7.2 provides average durations for significant wave heights at FNWC hindcast locations 1, 3, and 6.

7.4.2 Extreme Waves

Extreme wave conditions can seldom be determined from measurements or observations over short time periods. Ship wave observations are poor data for determination of extreme wave conditions because ships attempt to avoid high seas, and visual estimates of very high waves are often not accurate. An accepted approach for calculation of extreme wave conditions is the use of past meteorological conditions, which are known with reasonable accuracy for long time periods, with wave hindcast models. The best currently available (1979) hindcast of deep water wave conditions off California covers the time period 1951-1974 and was made with the U.S. Navy Fleet Numerical Weather Central (FNWC) sea and swell model.

For determination of extreme wave heights, combined sea and swell significant wave heights greater than the larger of 5 m or the significant wave height that is exceeded on the average once per year were tabulated. Only the largest significant wave height during an individual storm was considered. Log-normal probability distributions were least-squares fit to cumulative probability distributions of tabulated wave heights at each station. Extrapolation of the log-normal distributions provided probabilities of extreme waves which were related to recurrence intervals. The recurrence interval, or return period, for a given wave height is the average time interval between occurrences of wave heights equal to or greater than the given wave height. Recurrence intervals for wave periods were similarly determined but individual hindcast wave periods were assigned probabilities of their corresponding wave heights. Extreme deep water significant wave heights as a function of recurrence interval and location are shown in Figure 7.8. Occurrences and severities of winter extratropical storms increase moving northward and account for the general increase in extreme wave heights toward the north. Extratropical storms also account for a northward increase in wave periods associated with extreme wave heights. 100-year recurrence interval periods corresponding to the extreme waves in Figure 7.5 increase from approximately 12 seconds at station 6 to approximately 15 seconds

Table 7.2
Annual Persistence of Favorable and Unfavorable
Significant Wave Heights

Average Duration (days) for Significant
Wave Heights Less Than

Location	1 meter	3 meters	6 meters
1	3.0	17.5	193.4
3	3.2	29.4	968.7
6	2.8	22.8	approaches infinity

Average Duration (days) for Significant
Wave Heights Greater Than

Location	1 meter	3 meters	6 meters
1	3.9	1.7	1.3
3	3.8	1.4	1.0
6	5.9	1.4	approaches zero

at station 1. Five-year recurrence interval wave periods increase from approximately 10 seconds at station 6 to approximately 13 seconds at station 1. North of San Francisco, deep water wave direction probability distributions for significant wave heights greater than 5 m have a primary peak for waves from approximately the south-southwest and a secondary peak for waves from the northwest. These directions are associated with directions of high wind speeds during winter extratropical storms. South of San Francisco, waves with significant wave heights greater than 5 m are mainly from the west-northwest to northwest directions, which correspond to primary directions of higher than normal wind speeds throughout the year.

Tropical storms seldom affect southern California and are never important off northern California. The FNWC hindcast does not include tropical storms. The most severe tropical storm to affect southern California occurred in September 1939, and wave hindcasts (Reference 13) indicate a maximum significant wave height of approximately 9 m with a corresponding period of about 14 s. Off southern California, these values should be used as extreme wave upper limits for recurrence intervals greater than approximately 25 years.

Extreme wave conditions from the FNWC 1951-1974 hindcast compare reasonably well with earlier and simpler hindcasts. A comparison with extreme wave heights determined by a statistical method (Reference 15) that uses maximum mean monthly wind speeds shows that the statistical method substantially overestimates wave heights as a function of recurrence interval.

7.4.3 Nearshore Waves and Wave Setup

Wave conditions near and at the California coast, particularly the southern California coast, are extremely variable due to effects of offshore bottom topography, coastal configuration, orientation of coastal segments, and offshore islands. Nearshore wave data (Figure 7.9), collected by the U.S. Army Coastal Engineering Research Center

(Reference 16), the California Coastal Engineering Data Network (operated by the Institute of Marine Resources, Scripps Institution of Oceanography), and the California Coastal Data Program (sponsored by the South Pacific Division, U.S. Army Corps of Engineers) are available and provide examples of wave height and period probability distributions at several coastal locations (Figure 7.10).

Wave setup is an increase in mean water elevation between the location of breaking waves and the shoreline and is related to the momentum flux of incoming waves. Near the location of breaking waves, there is a decrease in mean water elevation called wave setdown. Wave setup and wave setdown do not need to be considered in deeper water beyond the breaker zone. The occurrence of high waves and the associated setup, near times of higher than normal astronomical tides, can result in higher than normal water elevations along the coast. Considerable coastal damage can occur due to waves superimposed on these high water elevations and due to wave runup on structures and beaches. The procedures described in Reference 11 were used to calculate wave setup for 100-year recurrence interval wave heights and periods along the California coast and for the September 1939 tropical storm that affected southern California. For typical California offshore bottom slopes, extreme wave setup ranges from 0.9 m to 1.5 m.

REFERENCES

1. Harris, D. L., 1979. Tide and Tidal Datums for the United States, U.S. Army Coastal Engineering Research Center Report, in press.

2. Smith, R. A. and R. J. Leffler, 1978. Sea Level Variations and Highest Water Levels Along the California Coast, National Ocean Survey, National Oceanic and Atmospheric Administration.

3. Bodine, B. R., Storm Surge on the Open Coast, 1971. Fundamentals and Simplified Prediction, U.S. Army Corps of Engineers Coastal Engineering Research Center Technical Memorandum No. 35.

4. Houston, J. R. and A. W. Garcia, 1978. Type 16 Flood Insurance Study: Tsunami Predictions for West Coast of the Continental United States, U.S. Army Engineer Waterways Experiment Station Study for Federal Insurance Administration, U.S. Army Engineer Waterways Experiment Station Technical Report H-78-26.

5. Houston, J. R. and H. L. Butler, 1979. A Numerical Model for Tsunami Inundation, U.S. Army Engineer Waterways Experiment Station Technical Report HL-79-2.

6. Wiegel, R. L., 1970. "Tsunamis," Earthquake Engineering, pp. 253-306.

7. Magoon, O. T., 1965. Structural Damage by Tsunamis, in Coastal Engineering: Santa Barbara Specialty Conference, American Society of Civil Engineers, pp. 35-68.

8. Houston, J. R., and A. W. Garcia, 1974. Type 16 Flood Insurance Study: Tsunami Predictions for Pacific Coastal Communities, U.S. Army Engineer Waterways Experiment Station Study for Federal Insurance Administration, U.S. Army Engineer Waterways Experiment Station Technical Report H-74-3.

9. Garcia, A. W., and J. R. Houston, 1975. Type 16 Flood Insurance Study: Tsunami Predictions for Monterey and San Francisco Bays and Puget Sound, U.S. Army Engineer Waterways Experiment Station Study for Federal Insurance Administration, U.S. Army Engineer Waterways Experiment Station Technical Report H-75-17.

10. Longuet-Higgins, M. S., 1952. "On the Statistical Distribution of the Heights of Sea Waves," Journal of Marine Research, Vol. 2, No. 3, pp. 245–266.

11. U.S. Army Coastal Engineering Research Center, 1977. Shore Protection Manual, Vol. 1 and 2, U.S. Government Printing Office Stock Number 008-022-00113-1, third edition.

12. Meteorology International Incorporated, 1977. Deep Water Wave Statistics for the California Coast, prepared for the California Department of Navigation and Ocean Development, 6 volumes.

13. Horrer, P. L., 1950. Southern Hemisphere Swell and Waves from a Tropical Storm at Long Beach, California, Beach Erosion Board Bulletin, 4(3).

14. Naval Weather Service Detachment, National Climatic Center, 1976. Summary of Synoptic Meteorological Observations (SSMO), Vol. 5 (NTIS No. AD-A022 578).

15. Quayle, R. G., and D. C. Fulbright, 1975. Extreme Wind and Wave Return Periods for the U.S. Coast, Mariners Weather Log, Environmental Data and Information Service, National Oceanic and Atmospheric Administration, pp. 67-70.

16. Thompson, E., 1977. Wave Climate at Selected Locations Along U.S. Coasts, U.S. Army Coastal Engineering Research Center Technical Report Number 77-1.

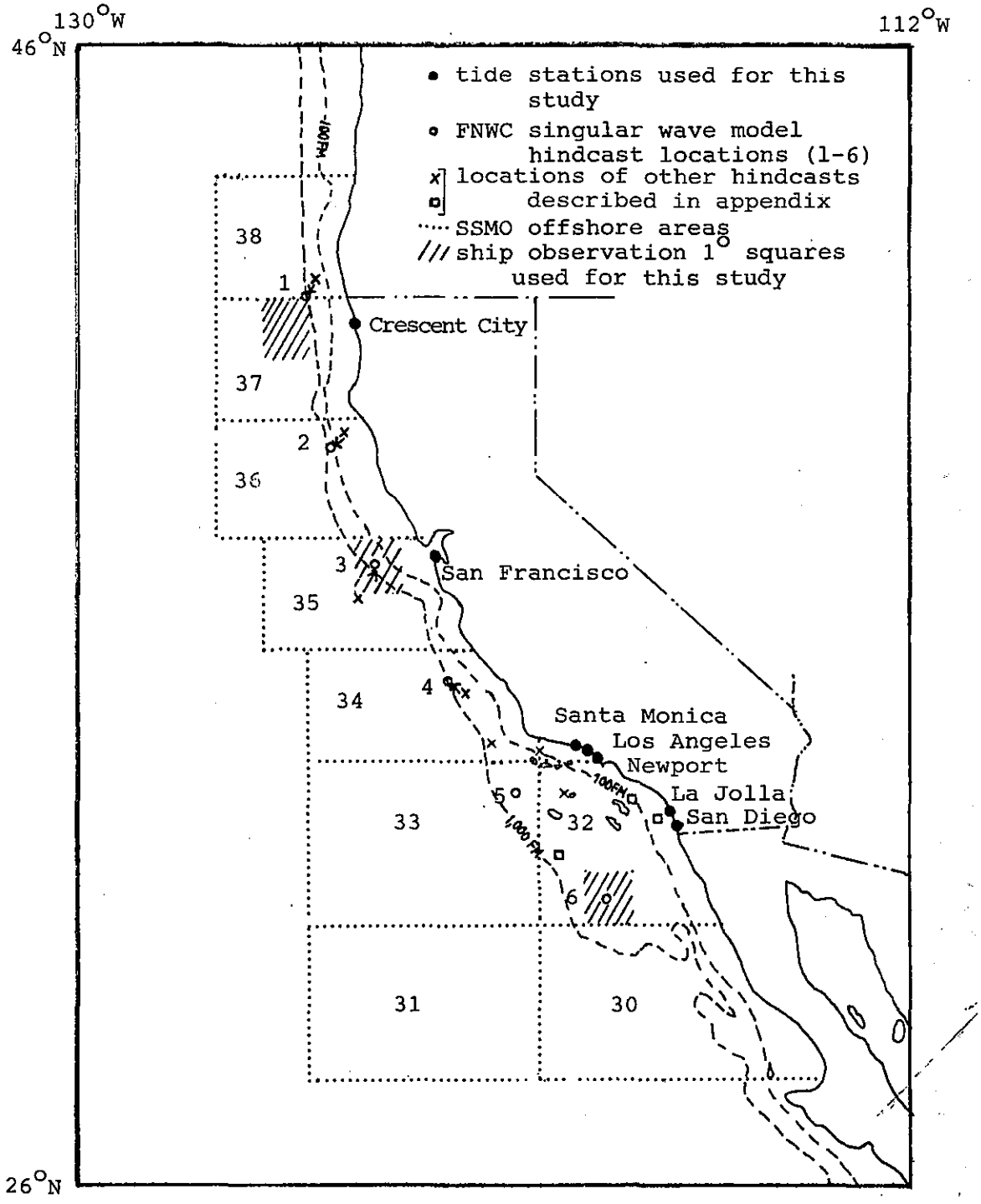

Figure 7.1. Locations of California Offshore Wave Information and of Long-term Tide Stations

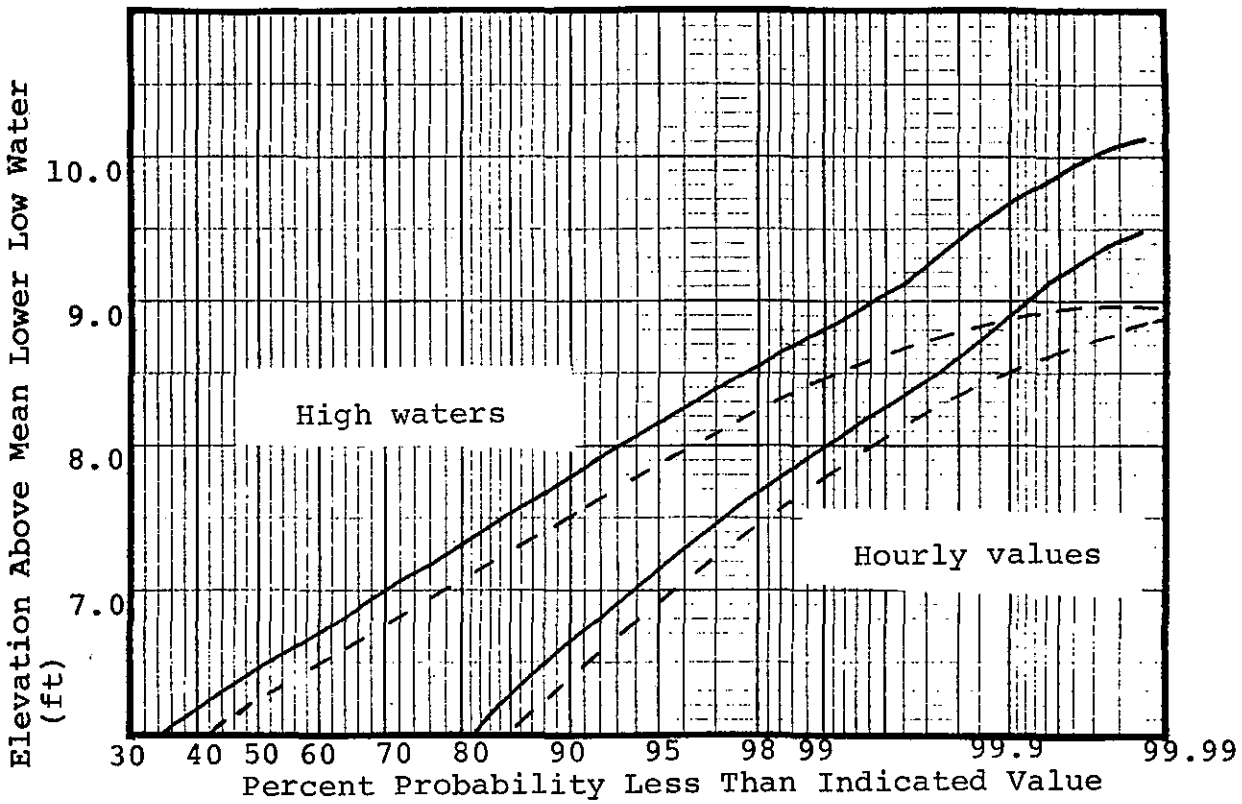

Figure 7.2. Water Elevation Cumulative Probability Distributions, Crescent City.
Measured elevations (—), Predicted astronomical tides (---).
Measured elevations are for 1941-1959.

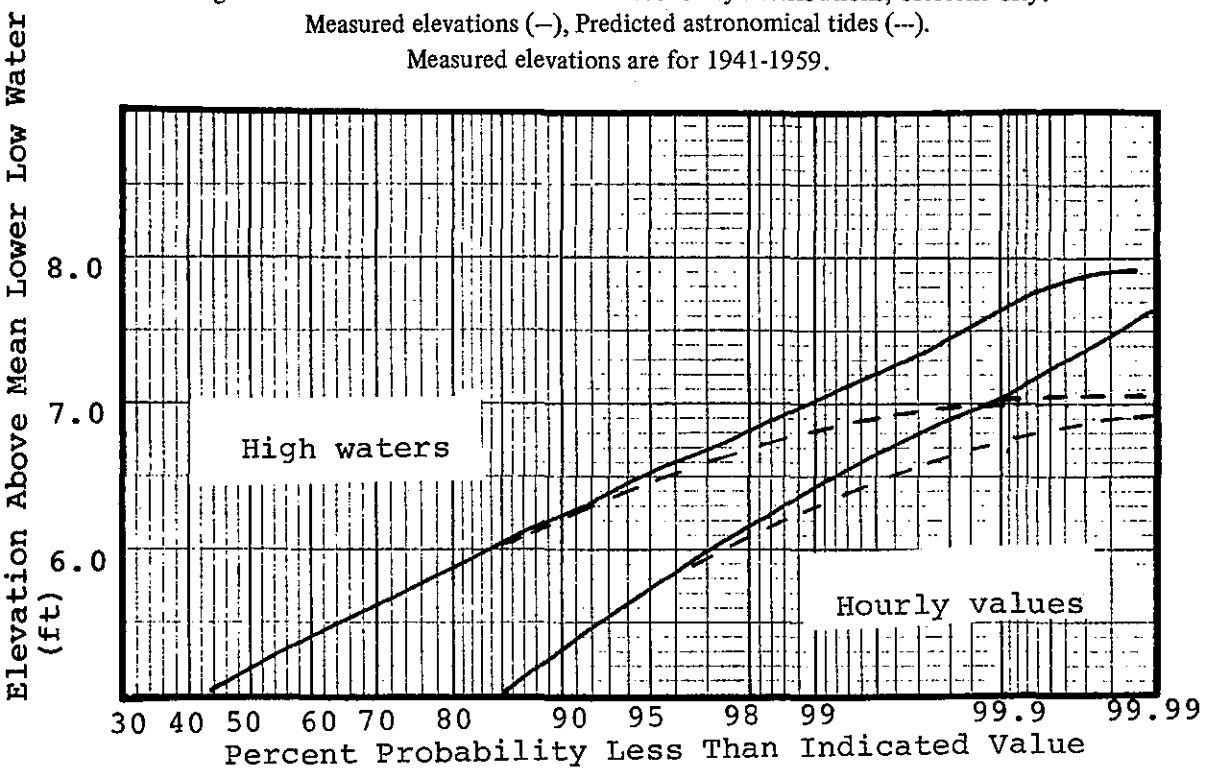

Figure 7.2 (cont). Water Elevation Cumulative Probability Distributions, San Francisco.
Measured elevations (—), Predicted astronomical tides (---).
Measured elevations are for 1941-1959.

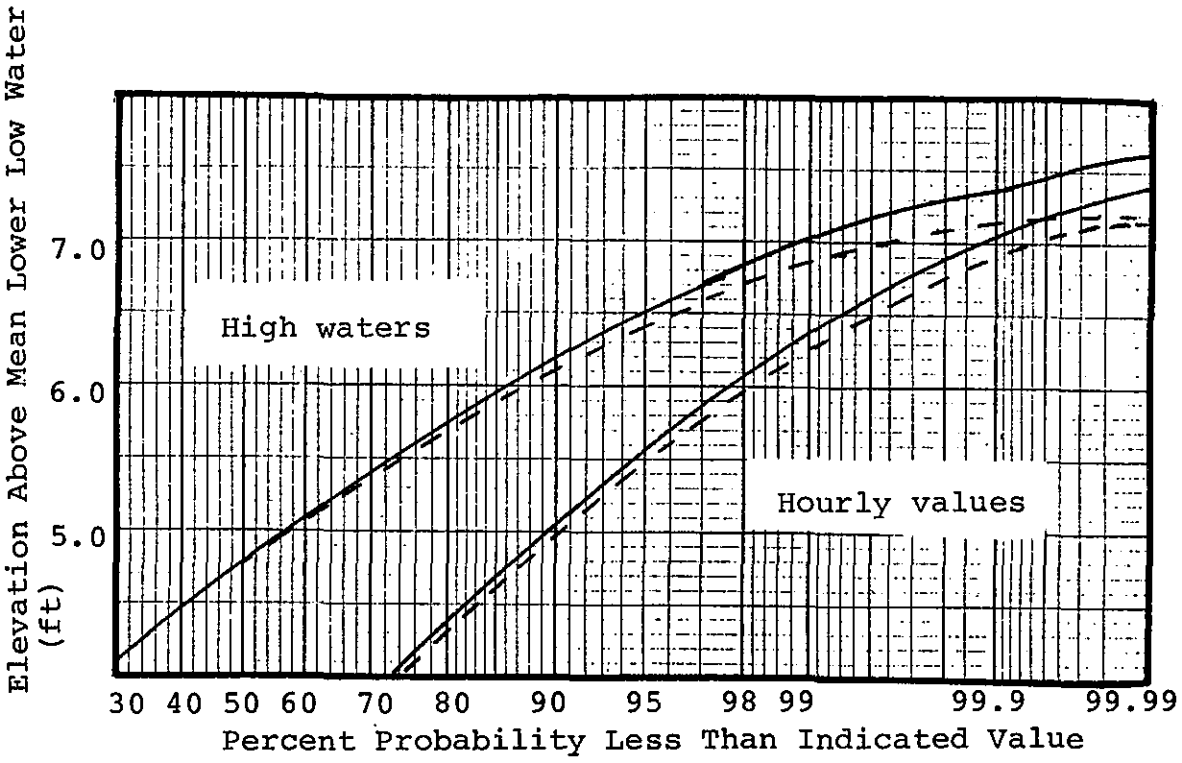

Figure 7.2 (cont). Water Elevation Cumulative Probability Distributions, Los Angeles.
Measured elevations (–), Predicted astronomical tides (---).
Measured elevations are for 1941-1959.

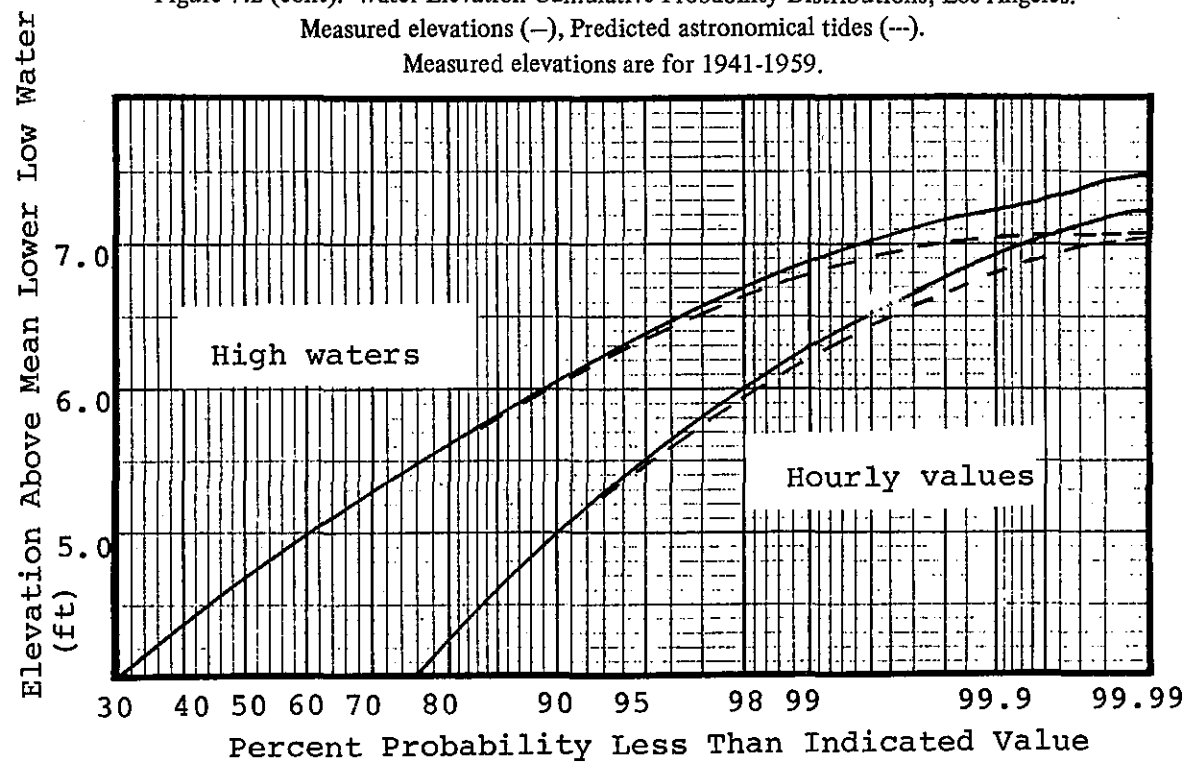

Figure 7.2 (cont). Water Elevation Cumulative Probability Distributions, Newport.
Measured elevations (–), Predicted astronomical tides (--).
Measured elevations are for 1955-1974.

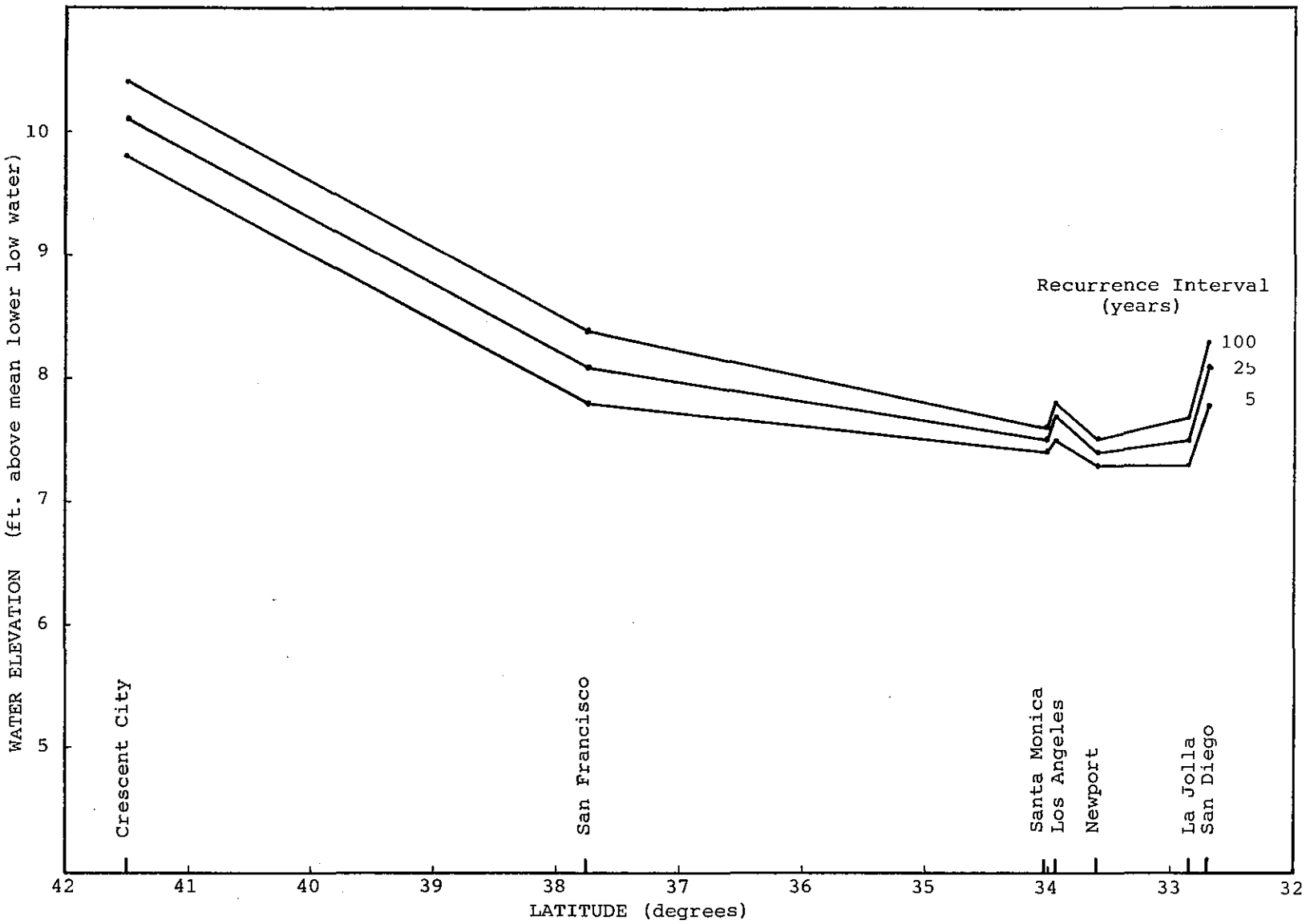

Figure 7.3. Extreme Storm Surge and Astronomical Tide Water Elevation as a Function of Recurrence Interval and Latitude Along the California Coast

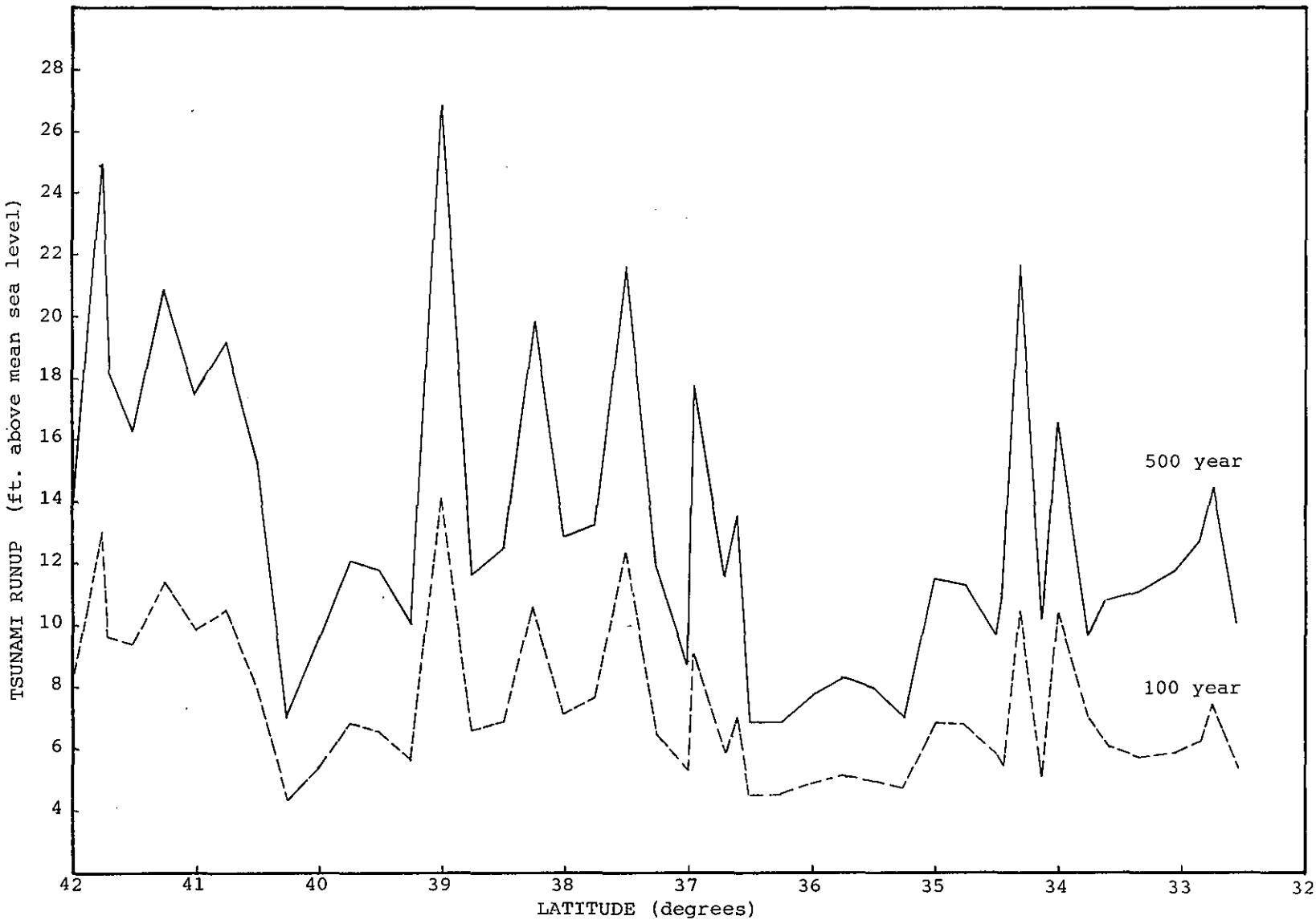

Figure 7.4. Tsunami Runup as a Function of Recurrence Interval and Latitude Along the California Coast

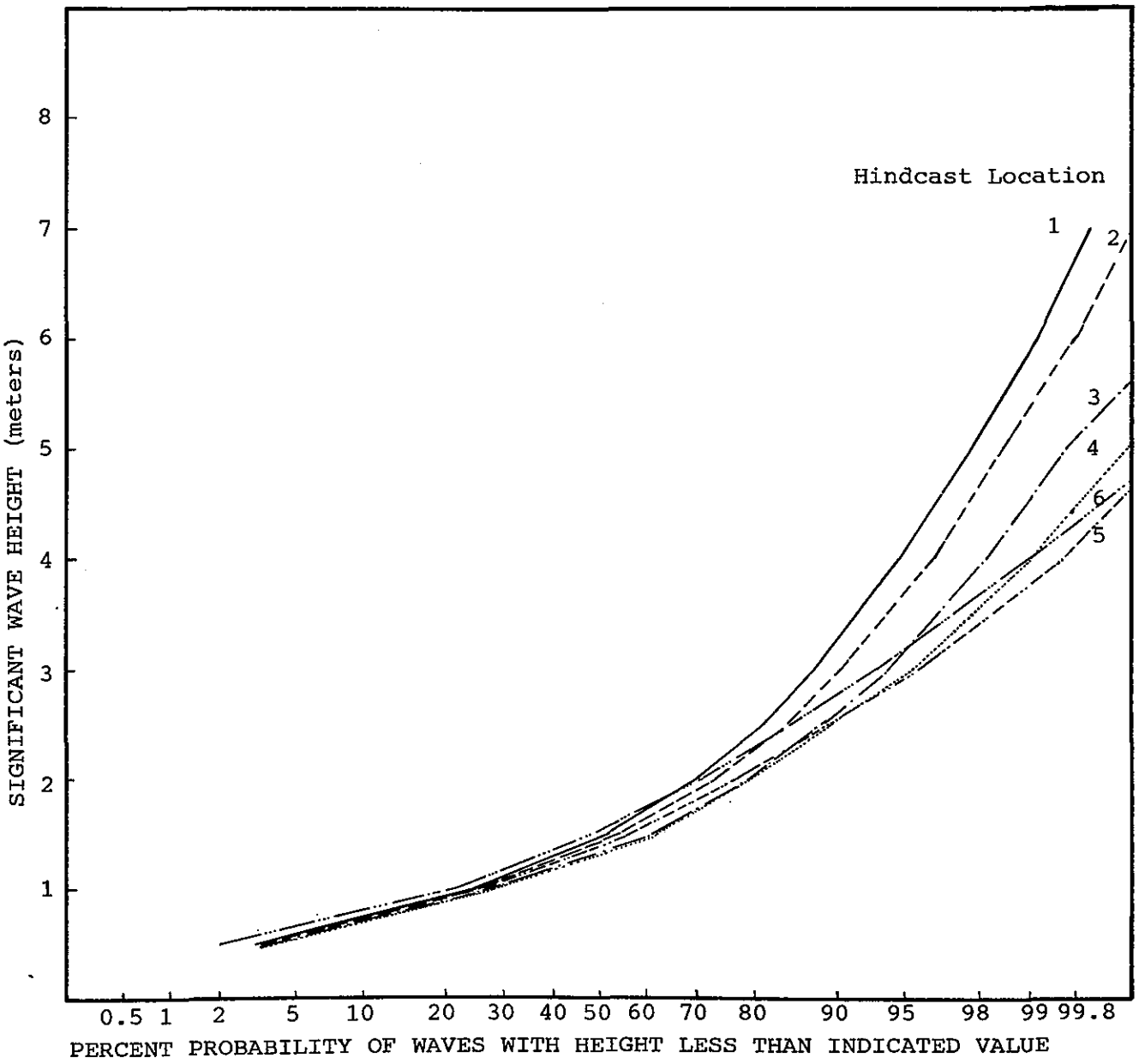

Figure 7.5 Annual Deep Water Significant Wave Height Cumulative Probability Distributions
Based on FNWC 1951-1974 Hindcast (Figure 7.1)

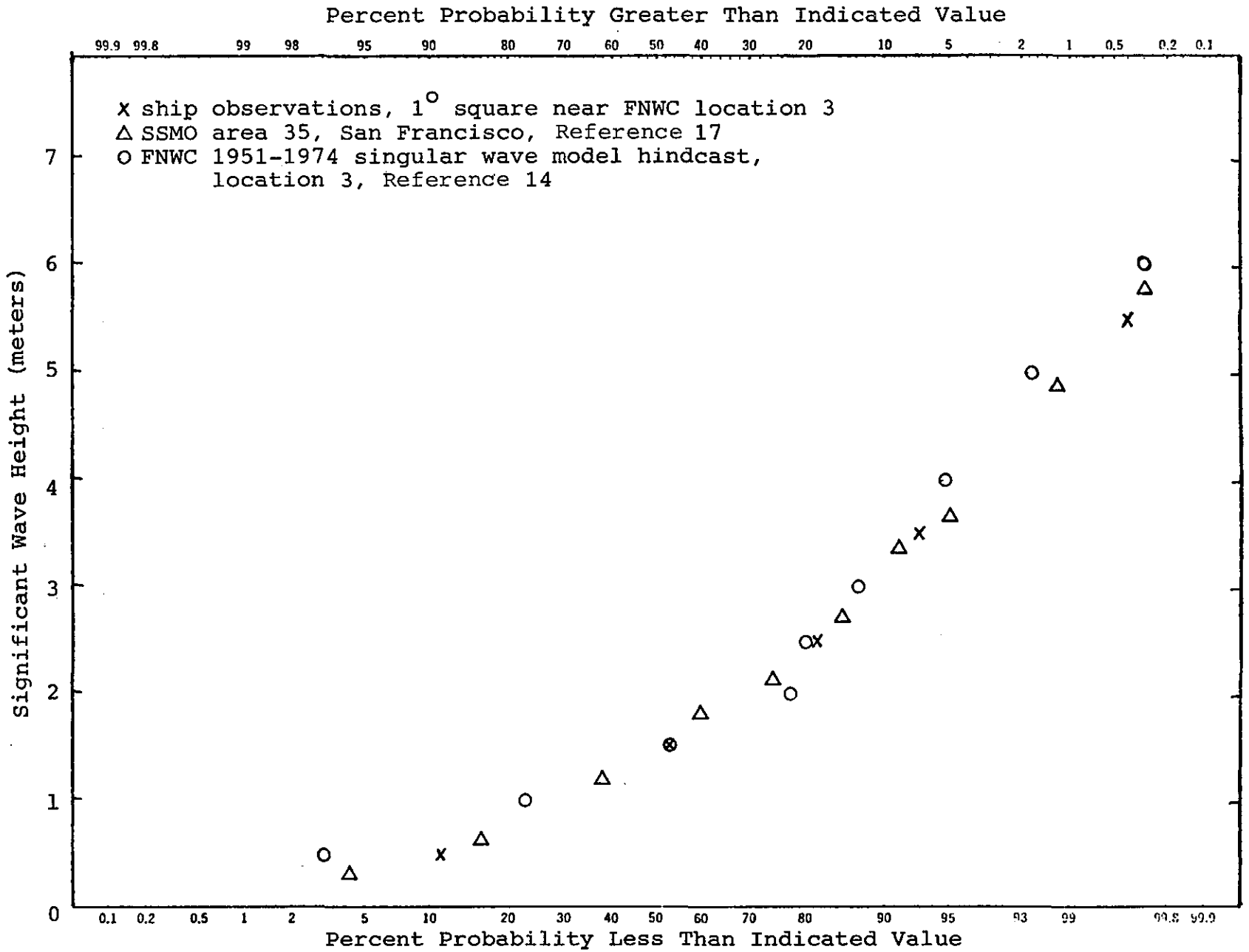

Figure 7.6 Comparisons of Wave Height Cumulative Probability Distributions Near FNWC 1951-1974 Hindcast Location 3 (Figure 7.1), January

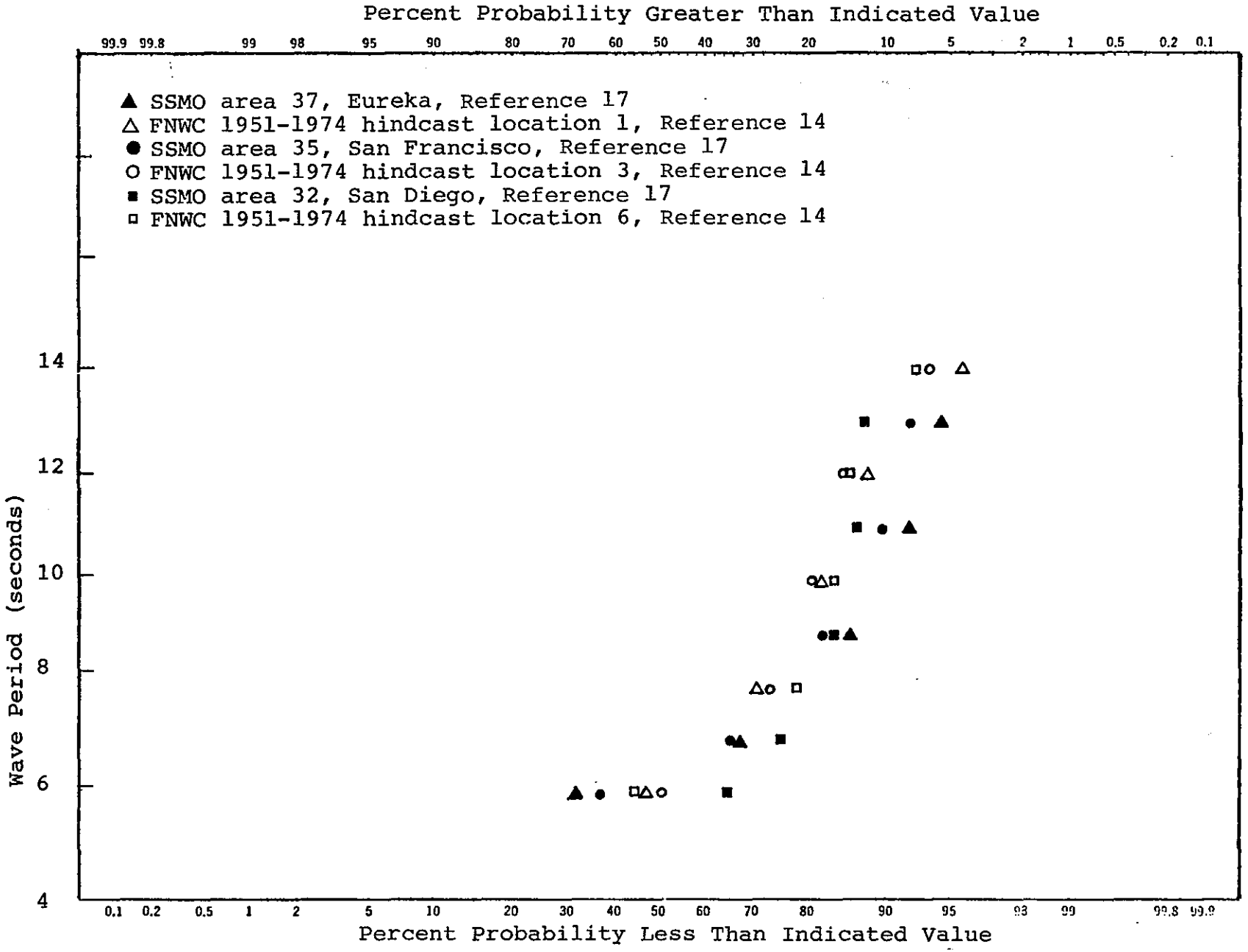

Figure 7.7 Comparison of Wave Period Cumulative Probability Distributions Near FNWC 1951-1974 Hindcast Locations 1, 3, and 6 (Figure 7.1), Annual (all years)

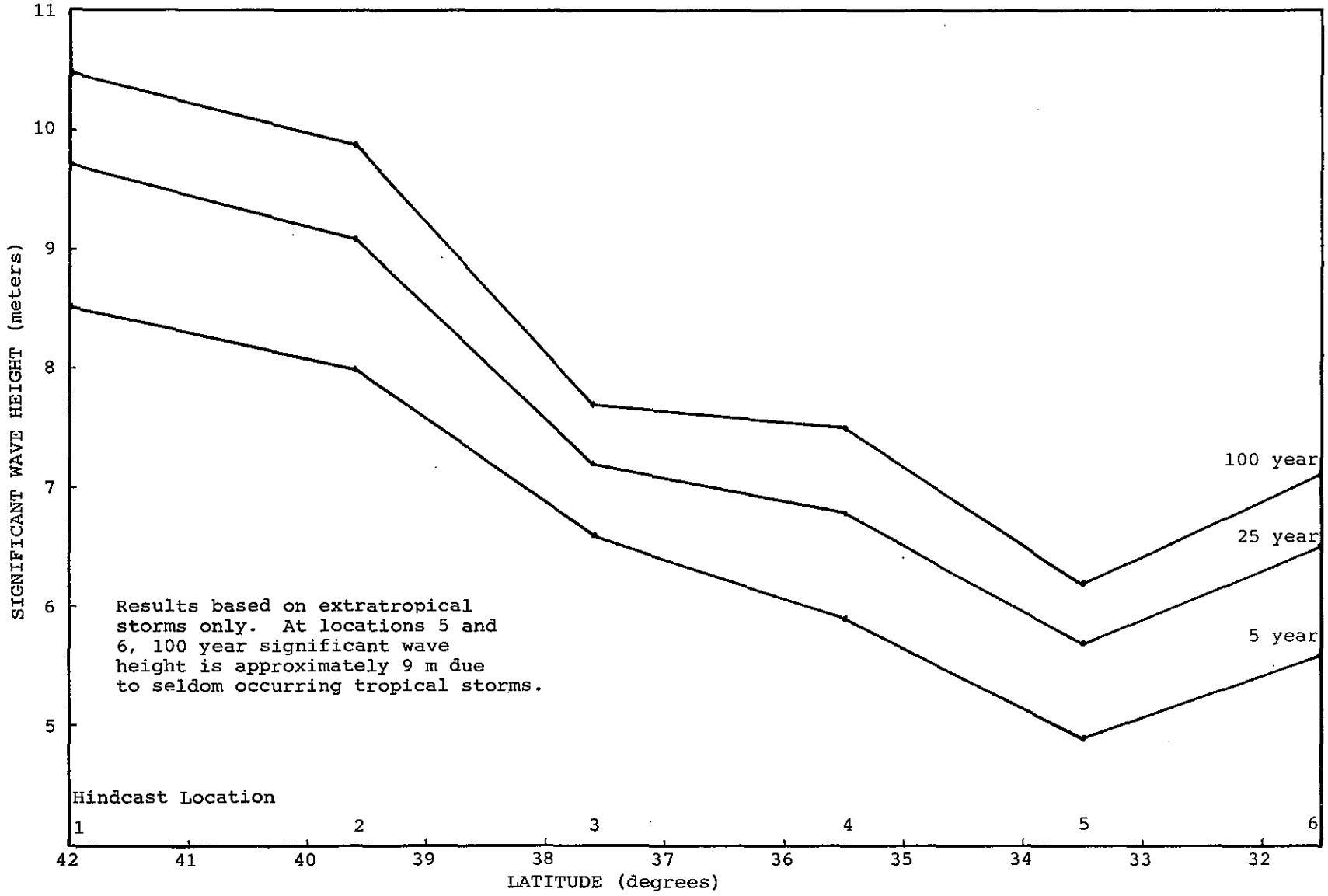

Figure 7.8. Extreme Deep Water Significant Wave Height as a Function of Recurrence Interval and Latitude Based on FNWC 1951-1974 Hindcast

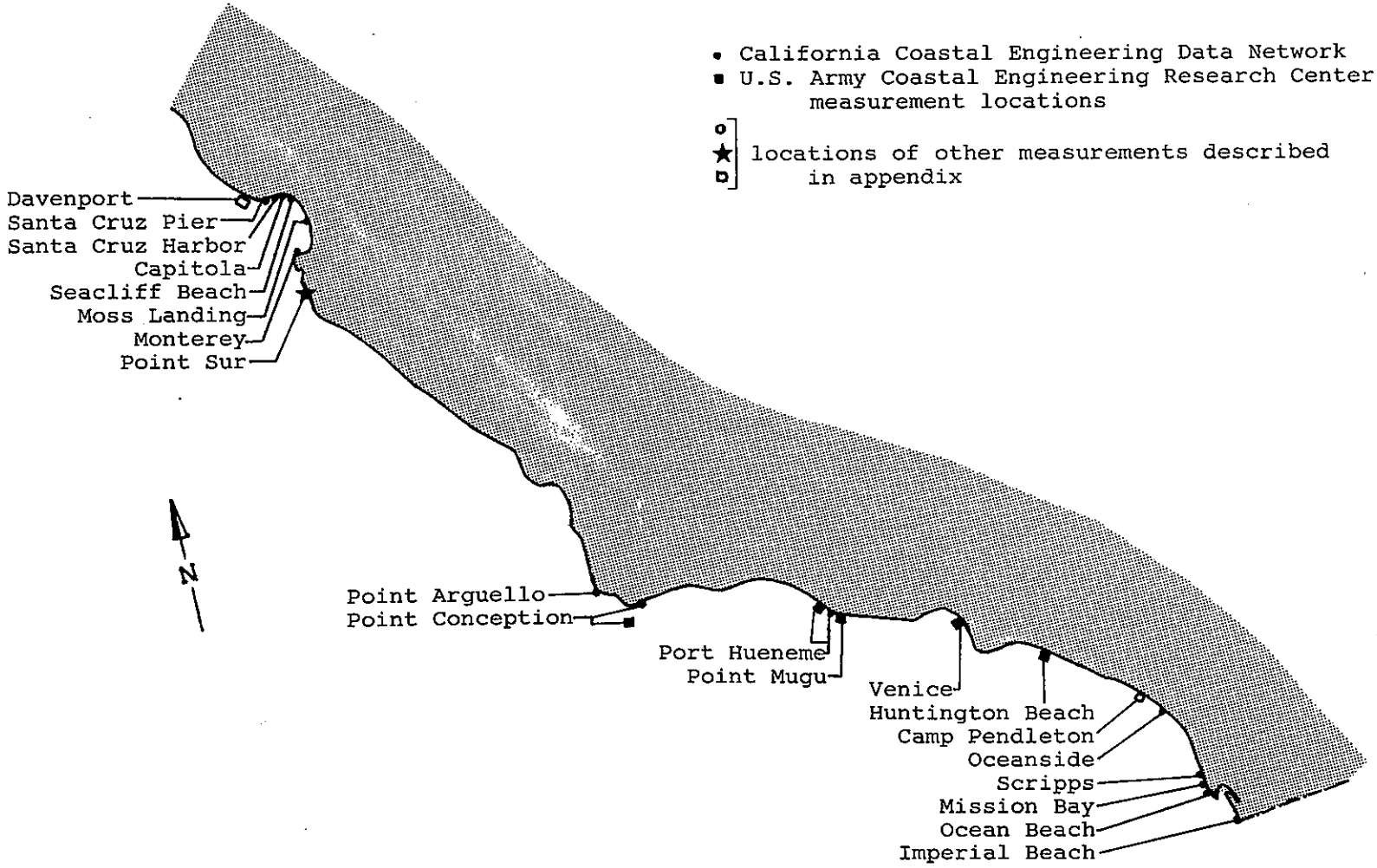

Figure 7.9. Locations of California Coastal Wave Measurements

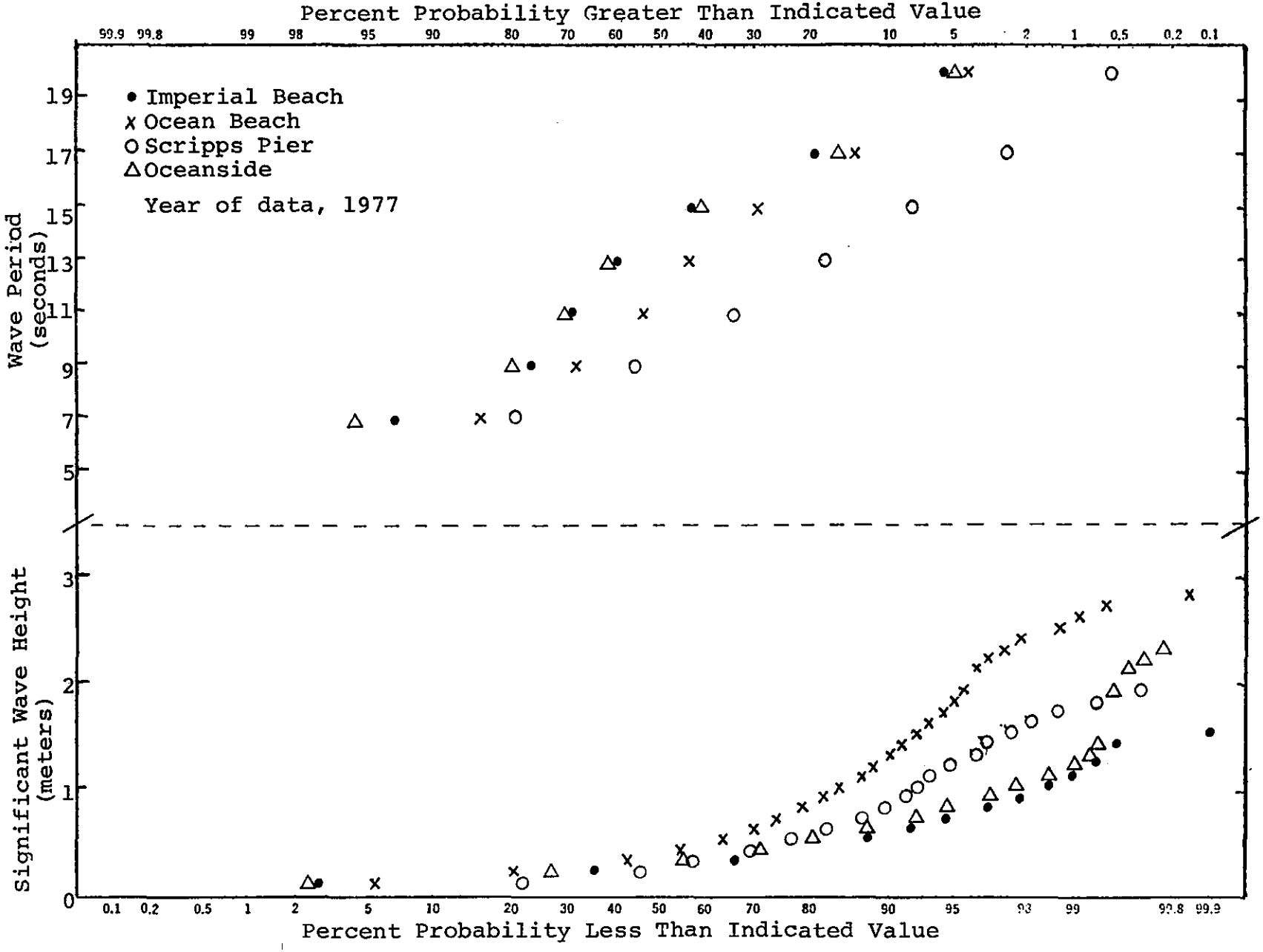

Figure 7.10 Cumulative Probability Distributions for Significant Wave Height and Period of Maximum Wave Energy at Four Southern California Coastal Locations for the California Coastal Engineering Data Network[11]

8. CONCLUSIONS AND RECOMMENDATIONS

8.1 INTRODUCTION

The physical variables studied in this report (i.e., wind velocity, ocean current velocity, temperature, salinity, density) significantly affect the movement and fate of spilled oil. These variables also have significant effect on the spreading of drill cuttings, muds, formation waters, and other waste products associated with marine mineral exploration and exploitation. Ocean wind waves, storm surge, and tsunamis have been analyzed primarily because these phenomena could pose hazards to marine structures and operations. In this, the concluding chapter of this report, the adequacy of the archived data in meeting the environmental information requirements for these variables is examined and recommendations are made for future work.

8.2 CONCLUSIONS

8.2.1 Meteorological Variables

The data base used in this study (coastal stations and summaries for 1° square areas) is adequate to identify the large-scale atmospheric circulation and its seasonal changes. However, this resolution is too crude to be able to depict the mean standing mesoscale eddies in the vicinity of Cape Mendocino and the Santa Barbara Islands. The data base does not allow us to study the sea breeze, but there have been some studies of extreme conditions of inland penetration of pollutants from urban sources. The existing data network allows only a crude estimate of the seaward extent of the land breeze.

The dispersion of atmospheric pollutants depends crucially on the static stability of the atmosphere, but measures of the stability over the water are not routinely available. Stabilities at the land stations are not representative of the open water and cannot be used. The best assumption one can make is that the boundary layer over the water is extremely stable and atmospheric pollutants will be transported with little dispersion over the ocean. During the day when the prevailing onshore flow is enhanced by the sea breeze, and the air over the land is more unstable than the air over the water, pollutants will be dispersed through a deeper layer. At night, when the land breeze is developed, nearshore pollutant sources will be carried seaward.

8.2.2 Water Masses and Physical Properties

Classification of water masses in the California POCS region by correlation based on STD/Nansen cast data yielded three characteristic structures:

- Southern water structure–equatorial in origin and transported northward along the coast by the California Countercurrent system.
- Subarctic structure (also termed California water)–transported southeastward in the California Current.
- Variant of the southern water–however, is slightly warmer and more saline than southern water and is found in the Southern California Bight.

The stratification is more highly developed in the southern water, reducing vertical mixing of particles at the sea surface, especially in late summer and early fall. There are far fewer observations in the Californian water than in the southern water, which implies that knowledge of the distribution of the Californian water is less complete than that of the southern water.

A rather diffuse frontal zone, typically running westward from the San Francisco Bay region, separates the southern water from the Californian water. It is apparent that most of the waters off Central California constitute a mixing zone for these water masses, as often noted in the literature (References 1 and 2). The archived data are, however, insufficient to delineate the details of this zone (e.g., whether the zone is characterized by distinct fronts or whether it is entirely a diffuse region). These limitations preclude quantitative characterization of mixing in the Central California region.

Another water mass which appears in the northeastern part of the study area is the outflow from the Columbia River, which spreads southward in spring and summer, as low salinity plume overlying denser oceanic water. Few observations off northern California are available for examination of this water. The existence of this water along the coast may be masked by the effects of upwelling, which transports high salinity water to the sea surface.

The distribution of water masses is determined largely by the currents. The California Current transports Californian water southward in the upper 200 m. The Countercurrent system, especially the Undercurrent, transports southern water northward along the coast. It appears that below the 500 m depth of the California Current, there is a diffuse northward flow of southern water beyond the continental slope.

Seasonal modification of the water masses is affected largely by the annual solar heating cycle and by the onset of upwelling, resulting from seasonal variations in wind stress. As early as 1936, Skogsberg (Reference 3) recognized that the seasonal march in water mass properties in the Central California region can be classified in three seasons: an Upwelling Season in spring in which northerly winds strengthen; the Davidson Current breaks up into eddies; and upwelling of cold, salty water from 200 m depth commences. In late summer, and early autumn, the mean upwelling relaxes somewhat corresponding to reduced wind stress. This period is called the Oceanic Season. In winter, monthly mean northerly winds are light, observed winds are often from the south and northward surface flow, and the Davidson Current is found adjacent to the coast.

The T-S correlation could potentially provide useful information in determining the origin of currents (e.g., southern or northern), the time of onset of currents (e.g., the Davidson Current onset is characterized by an increase in temperature and salinity), and advection time scales (e.g., the time of transit of the Columbia River plume). Unfortunately, insufficient data are available to make these inferences, particularly with the latter two situations.

The three season concept can be applied to the southern California and northern California areas, except that in southern California, the seasons begin earlier and progress northward along the coast so that the upwelling season may begin in January off Los Angeles, but may not begin until April off Crescent City. The time of onset of each season may vary by several weeks from year to year. During the Upwelling Season, isopleths of temperature, salinity, and density rise toward the coast, and large near-surface vertical gradients occur. In winter, the isopleths slope downward toward the coast, and gradients are less intense. Temperature is the variable which undergoes the largest seasonal variation. Far offshore, west of 120°W, the temperature of the upper layers follows the annual atmospheric heating cycle, lagged about one month. Further inshore, upwelling complicates the pattern and significantly reduces the temperature range between Point Conception and Cape Mendocino, because cold subsurface water is being upwelled during the heating season. Furthermore, during winter, the Davidson Current transports warm water northward, further reducing annual variability. Seasonal temperature variability increases slowly with distance to the north and south of Central California.

Evaporation and precipitation are less influential than upwelling in the seasonal salinity march. However, they do produce rather incoherent salinity fluctuations several hundred kilometers from shore. Nearshore, near the coast between 28° and 34°N, the effects of upwelling in spring and/or the Countercurrent in winter tend to cancel, keeping seasonal salinity variations small.

Also, near shore, especially in the regions of intense upwelling, near Point Conception and Cape Mendocino, the upwelling seems to be the major factor determining seasonal variations in near-surface density. For example, off Cape Mendocino, near-surface density typically reaches a maximum during the Upwelling Season and a minimum during the Davidson Current period when downwelling may occur. In the Southern California Bight area, near-surface density is still highest in the Upwelling Season and lowest in December and January. Dissolved oxygen concentration appears to follow the cycle of temperature. Below 150 m, seasonal variability of temperature, salinity, and density is small.

Mean vertical mixing potential was examined qualitatively by means of charts of mixed layer depth and vertical profiles of Brunt-Vaisala frequency. Only the area below San Francisco was considered because available data were insufficient in the northern part of the study area for this analysis. In general, it appears that the strongest vertical mixing occurs offshore in winter and early spring when thermal convection and extratropical storms deepen the mixed layer. The weakest vertical mixing occurs in late summer in the Southern California Bight region, when solar heating and weakened winds result in maximum intensification of the thermocline and hence maximum buoyancy force in the upper layers. Between Point Conception and Cape Mendocino, it seems likely that the mean upwelling would involve an upward transport and thus confine particulate matter to the surface, where seaward Ekman transport would tend to move the material offshore.

In general, the archive temperature, salinity, and dissolved oxygen concentration data are adequate to describe monthly variations at 100 km resolution in the Southern California Bight, particularly near large population centers. In other areas, particularly northwest of San Francisco, there is a dearth of observations and only seasonal descriptions can be made. The data are also insufficient to resolve the hydrographic features associated with the California Countercurrent system, whose component circulations would have a significant influence on the advection and dispersion of spilled pollutants and drilling muds.

In general, the archived data are insufficient to delineate the synoptic and mesoscale features, such as river plumes, fronts, upwelling zones. Most of the data available on these phenomena is qualitative and has been obtained by remote sensing. Convective and dynamic circulations associated with these features could result in either dispersion or concentration of spilled pollutants, depending on the patterns of convergences and divergences.

8.2.3 Circulation

The major deficiency in the circulation data archive is the lack of current meter observations. The national archive contains only 31 useable current meter records, with recording periods longer than one week. Most of these meters were deployed in the vicinity of the shelf break near a topographic feature known as Cordell Bank, near 38°N. Only two of the meters were deployed off Northern California and two in the Southern California Bight. Most of the currents from the meters located near Cordell Bank showed evidence of topographic steering, implying that current directions along the shelf break probably vary significantly with location. However, there are not enough measurements to estimate pertinent spatial scales. Mean current direction often differs significantly from mean direction determined by ship drift or by geostrophic calculation, although the magnitudes of all these measurements are generally on the order 5 cm/sec. This disparity in direction could result from three factors:

- Large shear between the surface and subsurface currents, evidenced by the current meter data (see Chapter 4)

- Large interannual variability, evidenced by the current meter data for different years and by the low values of persistence for the ship drift (see Chapter 4)

- Strong local topographic effects, evidenced by the current meter observations (see Chapter 4)

The factors suggest that caution should be used in accepting available mean current vectors as reliable estimates of long term means. Furthermore, the spatial scales of mean flow determined from the current meters appear to be small in this location; hence, the mean current observations should not be extrapolated far from the measurement site.

It is clear that, at the present time, the number of current meter observations is insufficient to provide useful input to oil spill advection models (Reference 4), which typically require current vectors on a ½° grid. For this purpose, the only alternative is to use either ship drift observations, or geostrophic calculations plus a wind drift factor. The desired ½° resolution cannot be obtained in the California POCS region with present ship drift or geostrophic current data, except in a few small regions off southern California near population centers. However, seasonal charts of 1° mean current vectors on a 1° grid were prepared from the mean geostrophic current-plus-mean wind stress current, as well as from ship drift. The two sets of charts generally agreed in both magnitude and direction. Unfortunately, the averaging interval required to obtain statistical stability would have obscured important presumed details of flow, such as the possible eddy between San Francisco and Monterey Bays (Reference 5). The quantity of data in each data set is insufficient to recommend the exclusive use of one chart over the other. In application, both charts must be consulted to fill data voids.

The inhomogeneity of the observations precluded calculation of a reliable estimate of error associated with these charts. The only available validation procedure compared the charts with the general body of scientific knowledge on California circulation as summarized in Reference 5. This comparison shows that there is agreement typically in the general seasonal circulation patterns. Details of flow (e.g., eddies other than the Southern California Eddy), upwelling zones, and the circulations on the shelf are not shown. Some of these features can be seen in the subjectively analyzed monthly dynamic topographic charts (Figures 4.2 through 4.13), but it is not clear whether these features are real or are artifacts of the analysis resulting from large interannual variability.

In terms of what can be said about the mean currents, generally, we have found good agreement between the analysis of archived data and Hickey's (Reference 5) extensive review and synthesis of the general circulation in the California POCS region.

The main branches of this general circulation are typical of eastern boundary currents (Reference 6) and include the equatorward flowing California Current, the poleward flowing California Undercurrent and Davidson Currents, and the counterclockwise Southern California Eddy. Mean speeds in all of these currents are typically slow, on the order of 10 cm/sec for surface currents and 5 cm/sec for subsurface currents. A few previous investigators have found mean speeds as high as 12.5-25 cm/sec in the California Current but in light of the archived data, these seem rather high. There are streaks of higher mean current speed, on the order of 20 cm/sec, but these are not typical of the flow field as a whole. The depth to which the California Current extends is not well known, but it probably extends below 200 m depth, since analysis of dynamic topography at 200 m depth shows poleward flow inshore of a line running roughly parallel to the coast, about 200-300 km offshore, depending on season and equatorward flow seaward of that line.

Storm surges are generated by local winds and increase in elevation along the California coast from south to north. Maximum elevation occurred in winter due to extratropical storms. Storm surge elevations range from 1 to 3 feet, which is less than the astronomical tide range of 5 to 7 feet. Therefore, the information provided here is considered adequate for planning, environmental assessments, and many engineering applications. Because of the small

elevations in extreme storm surges, information adequate for almost all applications could be developed by detailed analysis of existing water elevation data. Such an analysis would eliminate the need for developing advanced numerical models.

Extreme wind wave conditions are the determining factor for the design of fixed offshore and coastal structures. The main sources of damaging waves are winter extratropical storms. Occurrences and severities of these storms increase moving northward along the California coast and account for the general increase in wave heights toward the north. Extratropical storms also account for a northward increase in wave periods associated with extreme wave heights. North of San Francisco, the highest waves generally approach from the south-southwest. South of San Francisco, the highest waves are mainly from the west-northwest to northwest. In Southern California, wave damage primarily results from extratropical storms in the North Pacific and Gulf of Alaska.

Tropical storms seldom affect Southern California and are never important off Northern California. Considerable damage can result to coastal structures from wave setup. However, for typical California offshore bottom slopes, extreme wave setup ranges from 0.9 to 1.5 m, with 1.5 m a suitable upper limit for general planning and environmental assessments.

8.3 RECOMMENDATIONS

8.3.1 Circulation and Water Masses

The most urgent requirement for developing an archive data base adequate to the requirements of OCS development is to estimate the magnitudes of the atmospheric and oceanic forcing functions and the magnitudes and phase delays of the ocean response. The circulation on the shelf must be measured and the relationships between the shelf and slope water determined. The only practicable approach to meet this requirement is to carefully design a set of experiments to delineate the time and space scales of variability and exchanges with the deep ocean required to develop circulation models.

An important first step in developing this program would be the synthesis of results of the extensive experimental work done off the coasts of Oregon and Washington in, for example, the Coastal Upwelling Experiment (CUE) program. This could be done quickly by one or more of the CUE participants at the University of Washington or Oregon State University.

From this study, time and space scales of variability could be inferred (e.g., in terms of shelf width and atmospheric forcing) for the California coast, and detailed planning begun for field measurements. Results available to date (Reference 8) indicate an alongshelf scale of perhaps 200 km, and an across-shelf scale of perhaps 25 km. Therefore, a probable observation scheme would include linear arrays of current meter moorings perpendicular to the coastline and extending outward over the continental slope.

The area of greatest need for such measurements is in the Santa Barbara Channel – Point Conception region. This area is not only important in terms of location of lease blocks, but is of great importance oceanographically, since Point Conception is the border between the Southern California Eddy and the coastal circulation off Central California. Westward moving flow in the Eddy south of Point Conception may continue westward as part of the Eddy, or may branch northward as the Davidson Current or Undercurrent. Strong upwelling and mixing (both vertical and horizontal) preclude a simple dynamic description of this area based on available information. The exchange of shelf water between the Southern California Bight and the shelf area to the north is poorly understood.

The measurements required in this region would require deployment of lines of moored current meters, temperature and salinity sensors, ocean pressure gauges, and surface floats supporting meteorological instruments. The arrays would also be deployed in proximity to long-term sea level gauges, and extend seaward, approximately perpendicular to the coast. A few such arrays should be deployed and maintained in position for several years to acquire long-term data.

The value of these measurements in the Point Conception area could be greatly enhanced by coordinating the field program with a National Science Foundation-funded program, the Coastal Ocean Dynamics Experiment (CODE) (Reference 10) to be conducted off the California coast through March 1983 and briefly described below.

CODE measurements will be built around two four-month, small-scale experiments, CODE-1 (April-July, 1981) and CODE-2 (April-July, 1982). During these experiments, the CODE utilized current meters, temperature and salinity sensors, and bottom pressure gauges, and extensive ship and aircraft surveys. In addition, some larger scale, long-term measurements are being made during the period April 1981 through March 1983 from buoys moored along the 90 m and 130 m isobaths, with instruments deployed at the depths indicated in Figure 8.1.

One of these buoys deployed off the San Francisco coast (where coastal sea levels are available) monitors alongshelf current. A current meter mooring at the 400 m isobath (LT_3 in Figure 8.1) with meters at 11, 75, 150, 250, and 350 m, and a bottom pressure gauge (LP_0 in Figure 8.1) on the 130 m isobath, was deployed within the CODE measurement area for the 16-month period April 1981 through July 1982. Another current meter mooring is on the 90 m isobath (LT_2 in Figure 8.1). Several other bottom pressure gauges will be maintained within the CODE measurement area for either the 16-month or two-year period, all on either the 130 or 60 m isobaths. A coastal tide gauge station will be maintained inshore of the bottom pressure gauges. This will permit second-order fluctuations in across-shelf sea level gradient to be observed. The deployment schedule for these instruments is shown in Figure 8.2. (Note that bottom pressure gauges will be deployed on the 130 m isobath off three other coastal sea level stations—Crescent City, Shelter Cove, and Point San Luis, Figure 8.1--but only during the small-scale experiments.)

The BLM could maximize the information gained from deploying current meter arrays in the Point Conception area by means of a plan similar to that shown in Figure 8.1. Current meters, bottom pressure gauges, and T-S sensors should be deployed off Santa Barbara, Point Arguello, and Point San Luis in the same manner as in the CODE program for the corresponding time intervals. If additional funds are available, moorings should be deployed off Monterey and San Francisco to link the observation networks with the CODE buoys and thus greatly extend the space scales that the observational array is capable of sensing. Hydrographic and aircraft ART measurements should be made periodically through the moored arrays (monthly, if possible). The extension of the observed spatial scales of current variability is important, because long wave length oscillations (e.g., shelf waves) are believed to be an important component of the circulation off California (Reference 5) and could result in significant transport of pollutants.

In addition to extending the Point Conception array, a third priority measurement program would be a small-scale observational net between Point Arguello and Santa Barbara, with instrumentation deployed again in the CODE configuration. Hydrographic and aircraft ART measurements should be made to coincide with CODE intense small-scale measurements (Figure 8.1) to provide information on mixing. During the measurements, satellite images should be analyzed for passage of eddies, fronts, and meanders. Sea level data should be obtained from the NOS gauges at Point San Luis, Point Arguello, Santa Barbara, Long Beach, and San Diego. Meteorological data would be obtained from the NDBO buoys deployed by BLM, as well as from the Point Arguello Coast Guard Station, and NWS weather stations to the north and south.

The above experiment has been presented only as a concept. The detailed planning and analysis would require many dedicated principal investigators with extensive knowledge of the local hydrography and circulation. Before embarking on a major field program, coordination should be effected with other programs, such as SCCWRP, CALCOFI, and other principal investigators who may be deploying oceanographic instrumentation. The measurements described above will not suffice alone, however, in providing BLM with the information required to assess possible impacts resulting from oil and gas developments. These measurements must be incorporated in one or more dynamical or statistical circulation models and subsequently, oil spill trajectory models. These models would assist in the planning of further observational programs in that forcing variables and geographic subregions of critical importance to the prediction of the ocean circulation could be identified from model results.

Consideration should also be given to exploiting new technology, such as CODAR, satellite-tracked drogues, and undersea acoustic ranges for monitoring nearshore currents. Current transport between the channel islands could be monitored with GEK sensors similar to those deployed in the Straits of Florida. These transport measurements would be combined with densely sampled STD sections across the channels between (e.g., Santa Catalina and the mainland) to provide budgets of dissolved substances and hence, the inference of pollutant residence times.

8.3.2 Air Pollution

In order to depict more adequately the mesoscale and diurnal circulations and their impact on airborne pollution, it is necessary to deploy a dense network of buoys in the coastal region. They should possess the capabilities to measure wind direction and speed, and surface currents.

8.3.3 Water Elevations

Nearshore wave conditions can vary over relatively short distances due to complex bathymetry, coastal configuration, and sheltering by offshore islands, particularly for Southern California. A substantial modeling effort, which might couple a nearshore model to the U.S. Navy Fleet Numerical Weather Central (spectral) hindcast procedure, would probably yield good results, but is probably unnecessary for most of BLM's applications for site-specific wave information. The best procedure is to use nearshore wave measurements which are becoming increasingly available. The greatest need for practical application is for additional long-term nearshore wave measurement.

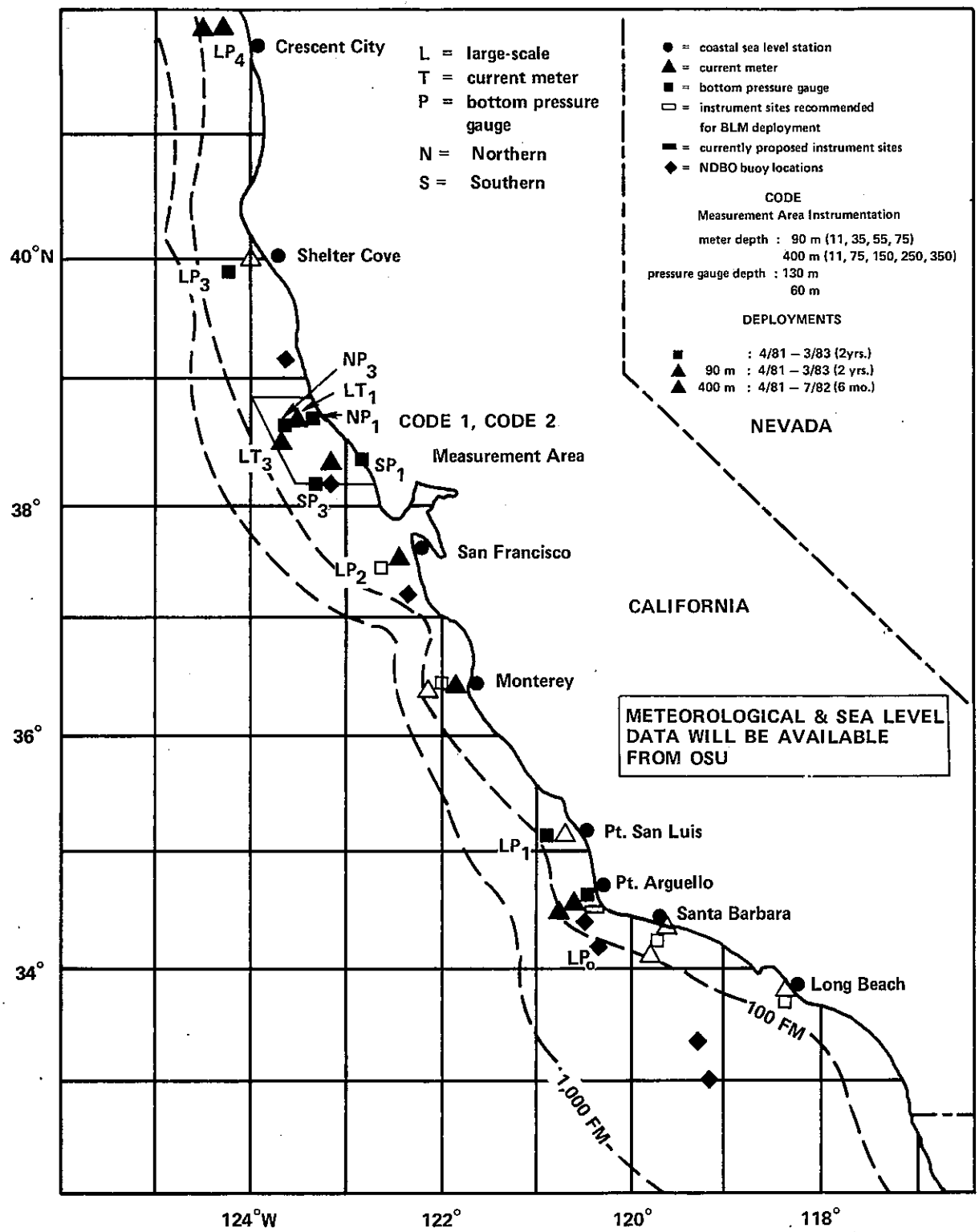

Figure 8.1. Map of the California POCS Region Showing Locations of CODE Observations and Proposed Complementary Observations (indicated by open figures) by BLM.

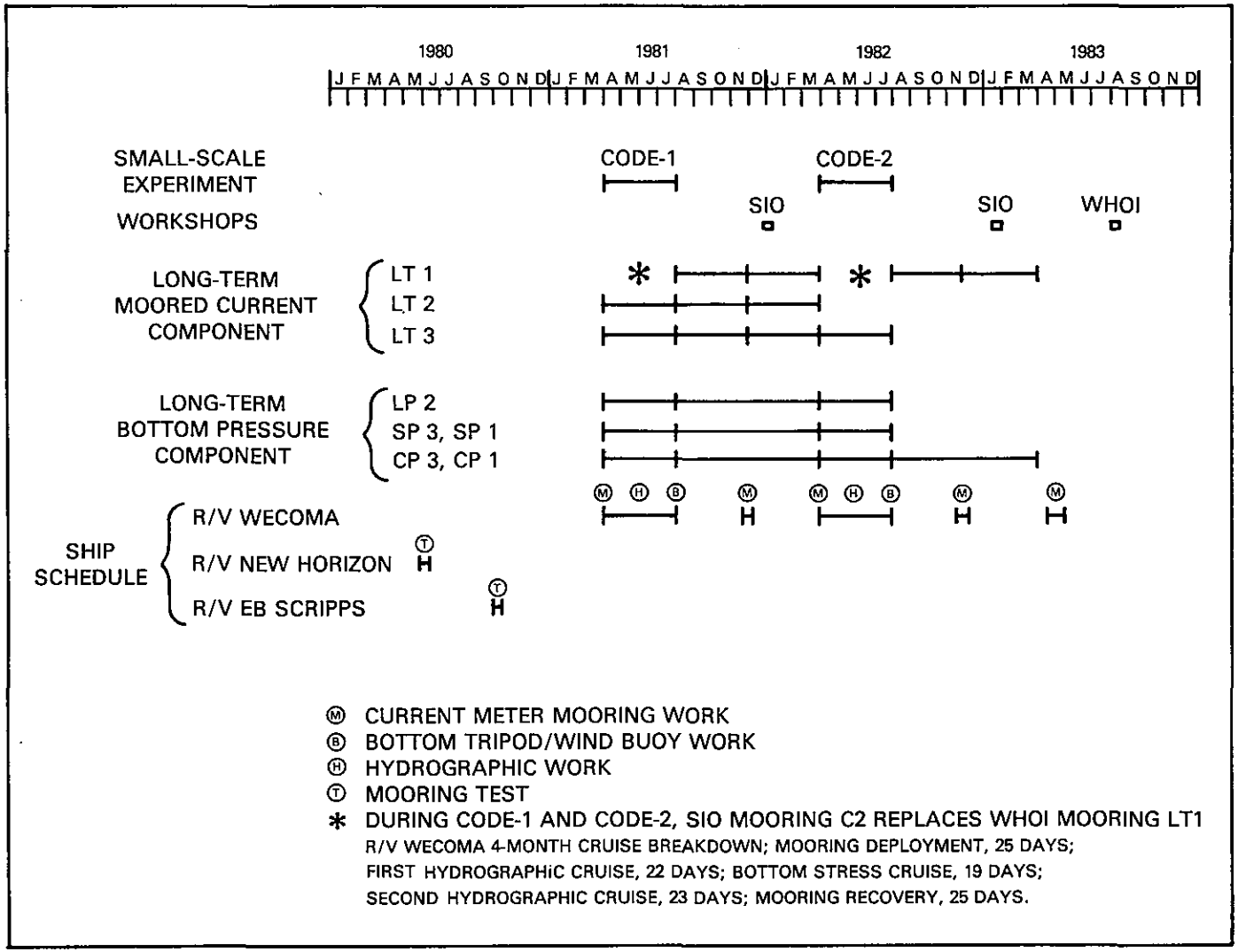

Figure 8.2. The proposed schedule of activities during CODE, including the time periods of the small-scale experiments CODE-1 and CODE-2 and the long-term arrays LT1-LT3. The timing of the projected ship schedule is also shown. Schedule as of February 22, 1980 (Reference 10).

☆U.S. GOVERNMENT PRINTING OFFICE: 1982-360-997/2119